DISTRIBUTION STATEMENT A
Approved for Public Release
Distribution Unlimited

Annual Research Briefs – 2003

Center for Turbulence Research

December 2003

20040210 105

Annual Research Briefs – 2003

Center for Turbulence Research

December 2003

DISTRIBUTION STATEMENT A
Approved for Public Release
Distribution Unlimited





CONTENTS

Preface 1

Macroscopic models of radiative transfer as applied to computation of the radiation field in the solar atmosphere. J.-F. RIPOLL & A.A. WRAY 3

Subgrid scale modeling in solar convection simulations using the ASH code. Y-.N. YOUNG, M. MIESCH, AND N.N. MANSOUR 15

Dynamic turbulence modelling in large-eddy simulations of the cloud-topped atmospheric boundary layer. M.P. KIRKPATRICK, N.N. MANSOUR, A.S. ACKERMAN AND D.E. STEVENS 23

Particle size distributions in atmospheric clouds. R. PAOLI & K. SHARIFF 39

Simulation of inviscid compressible multi-phase flow with condensation. P. KELLENERS 49

Large-eddy simulation of stratocumulus-topped atmospheric boundary layers with dynamic subgrid-scale models. I. SENOCAK 69

Numerical simulation of protoplanetary vortices H. LIN, J.A. BARRANCO AND P.S. MARCUS 81

The effect of surface topography on the nonlinear dynamics of Rossby waves. S.I. ABARZHI, O. DESJARDINS, H. PITSCH 91

Nonlinear gulf stream interaction with the deep western boundary current system: observations and a numerical simulation. D. DIETRICH, A. MEHRA, R. HANEY, M. J. BOWMAN, AND Y.H. TSENG 101

Numerical simulation of regional circulation in the Monterey Bay region. Y.H. TSENG, D.E. DIETRICH & J.H. FERZIGER 115

Testing of RANS turbulence models for stratified flows based on DNS data. S.K. VENAYAGAMOORTHY, J.R. KOSEFF, J.H. FERZIGER, AND L.H. SHIH 127

Unstructured LES of reacting Multiphase flows in realistic gas turbine combustors. F. HAM, S. APTE, G. IACCARINO, X. WU, M. HERRMANN, G. CONSTANTINESCU, K. MAHESH, AND P. MOIN 139

A Eulerian-Lagrangian model to simulate two-phase particulate flows. S.V. APTE, K. MAHESH, AND T. LUNDGREN 161

New type of the interface evolution in the Richtmyer-Meshkov instability. S.I. ABARZHI AND M. HERRMANN 173

Modeling primary breakup: A three-dimensional Eulerian level set /vortex sheet method for two-phase interface dynamics. M. HERRMANN 185

Fragmentation under the scaling symmetry and turbulent cascade with intermittency. M. GOROKHOVSKI 197

"Hypothetical" heavy particles dynamics in LES of turbulent dispersed two-phase channel flow. M. GOROKHOVSKI AND A. CHTAB 205

A Domain decomposition parallelization of the Fast Marching Method. M. HERRMANN 213

A Cartesian adaptive level set method for two-phase flows. F. HAM, AND Y.-N. YOUNG 227

Turbulent mixing of multiphase flow. Y.-N. YOUNG, J. FERZIGER, F.E. HAM AND M. HERRMANN 239

The effect of the density ratio on the nonlinear dynamics of the unstable fluid surface. S.I. ABARZHI 251

Quadrature moments method for the simulation of turbulent reactive flows. V. RAMAN, H.PITSCH AND R. O. FOX. 261

A self contained mapping closure approximation for scalar mixing. G. HE & Z. ZHANG 277

Stochastic mixing model with power law decay of variance. S. FEDOTOV, M. IHME AND H. PITSCH 285

Large-eddy simulation of conductive flows at low magnetic Reynolds number. B. KNAEPEN AND P. MOIN 297

DNS and LES of a shear-free mixing layer. B. KNAEPEN, O. DEBLIQUY AND D. CARATI 307

On the Computation of space-time correlations by large eddy simulations. G. HE, M. WANG, AND S. LELE 319

Grid-independent large-eddy simulation in turbulent channel flow using three-dimensional explicit filtering. J.GULLBRAND 331

Advanced signal processing for integrated LES-RANS simulations: Anti-aliasing filters. J.U. SCHLUTER 343

Integrated RANS-LES computations of turbomachinery components: Generic compressor/diffuser. J. SCHLUTER, X. WU, S. KIM, J.J. ALONSO, AND H. PITSCH 357

Toward immersed boundary simulation of high Reynolds number flows. G. KALITZIN AND G. IACCARINO 369

Numerical and experimental investigation of the turbulent flow in a ribbed serpentine passage. G. IACCARINO, G. KALITZIN, AND C. ELKINS 379

RANS simulation of the separated flow over a bump with active control. G. IACCARINO, C. MARONGIN, P. CATALANO, M. AMATO 389

Constrained aeroacoustic shape optimization using the surrogate management framework. A.L. MARSDEN, M. WANG & J. DENNIS 399

Rough-wall channel analysis using suboptimal control theory. O. FLORES, J. JIMENEZ, AND J. TEMPLETON 413

Unfolding of proteins: Thermal and mechanical unfolding. J. HUR & E. DARVE 425

Numerical simulation of high drag reduction in a turbulent channel flow with polymer additives. Y. DUBIEF 439

MHD turbulence at moderate magnetic Reynolds number. B. KNAEPEN, S. KASSINOS, AND D. CARATI 449

Linearly forced isotropic turbulence. T.S. LUNDGREN 461

Transition in hypersonic flows including high-temperature gas effects. C. STEMMER 475

Appendix: Center for Turbulence Research 2003 Roster 481

Preface

This volume contains the 2003 Annual Progress Reports of the postdoctoral fellows and visiting scholars of the Center for Turbulence Research. In 2003 CTR sponsored 19 resident Postdoctoral Fellows, 5 Senior visiting scholars, 4 doctoral students and hosted 9 Research Associates. The volume contains progress reports on a wide range of subjects reflecting the impact of the dynamic subgrid scale model on new application areas, and the close association of CTR with efforts funded at Stanford University by the Department of Energy, the Air Force Office of Scientific Research and the U.S Office of Naval Research. The development of core technology for gas turbine application remains the largest component of CTR's effort. This reflects the support received by CTR from NASA's Ultra Efficient Engine Technology Program in turbulent combustion research. Close coordination with the efforts supported by DOE's ASCI program at Stanford enables rapid transfer of progress in fundamental understanding and modeling to realistic aircraft engine simulations. Several reports show progress in simulation of multiphase flows in general, and sprays in particular. Level set methods have been developed to model the primary breakup of sprays, and adaptive level set methods have been applied to study three-dimensional breakup of drops. A new Eulerian-Lagrangian formation shows great potential for the extension of particle methods to the dense regime in sprays. Advances in multiphase flow simulation enabled new studies in other problems such as the Richtmyer-Meshkov instability. Major progress has been made in transferring the multiphase technology to the unstructured LES code being developed to simulate realistic gas turbine combustors. Simulation of the flow in turbine blade cooling passages shows the power of the immersed boundary technique in enabling realistic simulations in complex geometry, and is a good example of the continuing and indispensable research at CTR on numerical methods. The increased number of reports on geophysical and astrophysical applications reflects an active effort at CTR to contribute to all of NASA's enterprises. Close collaborations with scientists from NASA's Solar Dynamics Observatory (SDO) project have been established. New macroscopic models of radiative transfer are being developed for application to the soot problem in combustion and to atmospheric and solar simulations. The application of improved sub-grid scale models in cloud simulations show great potential in improving the predictive capability of atmospheric codes. Early indications point to a similar success in improving simulations of the sun interior. New transport equations for sparse particle systems such as clouds, have been derived and will be applied to cloud seeding by aircraft contrails. Ocean modeling is becoming of increased importance to NASA in support of its mission to understand and protect our home planet. Efforts in this area have focused on simulating regional ocean patterns. Other efforts show continued support by CTR of fundamental studies in turbulence and other multiscale phenomena. These theoretical efforts have been the seed of new ideas and will continue to be of interest to CTR.

We thank Millie Chethik for day-to-day management of the Center and editing these briefs. Special thanks are due to Dr. Massimiliano Fatica for his help with the final preparation of this report.

Parviz Moin
Nagi N. Mansour

This volume is available as a .pdf file on the Web at http://ctr.stanford.edu

Macroscopic models of radiative transfer as applied to computation of the radiation field in the solar atmosphere

By J.-F. Ripoll, A. A. Wray

1. Motivation and objectives

The *two stream method*, also called the *two-flux approximation*, distinguishes between incoming and outgoing radiation for improved accuracy relative to one-stream methods while retaining reduced numerical cost relative to full RTE solutions (Mihalas & Mihalas 1984; Siegel & Howell 2001). It assumes different radiation from each source, each uniform over its half-space, which constitutes the weak point of the method.

This concept has recently been used by Dubroca & Klar (2002), where they derive a unidimensional macroscopic moment radiation model for each stream; they call this a half moment model. The pressure closure is obtained by using maximization of entropy (Minerbo 1978), which allows them to avoid any isotropic assumption about the radiative intensities.

In this paper a new three dimensional half-moment model for radiative transfer is presented for a gray medium. It describes the evolution of the zeroth and first directional half moments of the radiative intensity. The closure is provided, similarly to Dubroca & Klar (2002), by the maximum entropy concept. This work generalizes that model to three dimensions.

The splitting of the direction of propagation Ω into two pieces, Ω^+ and Ω^-, in Dubroca & Klar (2002) was done by cutting the Ω-space in a static sense, meaning that the same definition of $+$ and $-$ was used at all points in the domain. This direction splitting is clearly the best, at least the most intuitive one, for unidimensional problems, but this is not necessarily true for multi-dimensional problems. As a matter of fact, and in contrast, the splitting is here done dynamically according to the direction of the total radiative flux at each point. At any point of the domain, our model considers that the radiative flux defines the main direction of propagation, the positive direction Ω^+, and a negative one, in the opposite direction, Ω^-. This dynamic way of splitting the domain of directions appears to be a natural one for multidimensional problems.

This particular choice for the splitting also allows the pressure model to be analytically computed, which is not the case for a static definition of the half moments. However, it does have a very unfortunate consequence: since the half spaces Ω^+ and Ω^- are dependent on the radiative flux, they become variable in time and space. The integration of the radiative transfer equation (RTE) over these subspaces is then complicated. Nevertheless, if the radiation is assumed isotropic in the plane perpendicular to the direction of propagation, which we believe is a reasonable assumption for a two-direction model, the integration of the RTE over these spaces can be done. Unfortunately, the integration introduces unclosed border terms involving the intensity in this plane. A closure will then be provided below by a model for this intensity.

In order to derive the radiative pressure tensor and then to be able to close the system,

a further assumption is necessary: the positive component of the flux is assumed to be nearly parallel to the total flux, the negative one becoming then necessarily anti-parallel. This is obviously true in one dimension, but not in general, and constitutes our main assumption in the pressure derivation. It holds nevertheless exactly in two important limits: at radiative equilibrium and for strongly anisotropic radiation.

The model presented here (the derivation being done in Ripoll & Wray (2003)), called the $M_1^{1/2}$ model, is a hyperbolic system consisting of a total of eight equations in three dimensions, four equations for each direction. Each half model has the classical form of a macroscopic moment model in which the pressure tensor is constructed from the well-known Eddington tensor with a particular Eddington factor. Moreover, different source and border terms occur. The latter introduce couplings between the macroscopic and microscopic quantities and between the + and − streams, through the intensity in the plane perpendicular to the flux.

One of the major advantages of this model is that independent incoming and outgoing boundary conditions are allowed, which is not possible with full moment models. Moreover, the flux stays limited by the speed of light and the underlying intensity, which can always be deduced from the macroscopic quantities. The flux is described by a Planck function at radiative equilibrium or by one (or two) Dirac function(s) in one (or two) direction(s) of propagation in the anisotropic limit(s). Furthermore, the maximum entropy closure, which has been often applied to radiative transfer (see for instance (Ripoll 2004)) will be shown as a very useful and powerful concept allowing the derivation of new accurate, well-defined, and robust models.

The main theoretical application of the half moment model, treated in this paper, is its reduction to a full moment model, called M_1^+, for the particular but important case of a hot, opaque source radiating in a cold transparent (or semi-transparent) medium for very specific applications, such as stellar interiors or atmospheres, or combustion problems. This model consists of four equations and is derived from the half moment model with fairly simple arguments. The model is tested on a simple test case for different values of the opacity and will be shown to give very good results, better than those obtained from either the P_1 or M_1 closures. For all problems presented in this paper, the solutions obtained by the new models are compared with those obtained by using a ray-tracing solver of the RTE. It will be shown numerically, partially here and mostly in Ripoll & Wray (2003), that the M_1^+ model constitutes an improvement of the existing closures and may be particularly useful for treating radiation in stellar interiors or atmospheres.

The problem of a modeled solar atmosphere, in which the opacity is roughly approximated by that at a wavelength of $500\,nm$ (Vernazza *et al.* 1981), will be solved and discussed. The radiation field is obtained from the M_1^+ model at reasonable accuracy.

The structure of the paper is as follows. In section 2, the model $M_1^{1/2}$ is presented. In section 3, for the particular case of a hot, opaque source radiating into a cold medium, the half moment model is reduced to the M_1^+ model. In section 4, we first solve a simple and academic problem to validate the models, followed by a simplified solar atmosphere.

2. The Half-Moment Model

2.1. *The radiative transfer equation*

The radiative transfer equation in an non-scattering, emitting, and absorbing gray medium is given by

$$\frac{1}{c}\partial_t I + \mathbf{\Omega}\cdot\nabla I = \sigma\mathcal{B}(\nu,T) - \sigma I, \tag{2.1}$$

where the intensity $I = I(t,\mathbf{r},\mathbf{\Omega},\nu)$ is a function of the time t, the position $\mathbf{r}$, the direction of propagation $\mathbf{\Omega}$ and the frequency ν. The Planck radiative intensity $\mathcal{B}$ describes the isotropic emission of the medium at frequency ν and temperature T. Here c is the velocity of light and σ, the spectral absorption coefficient or opacity, is assumed to be independent of ν. By integrating the RTE over frequency and introducing the quantity $J(t,\mathbf{r},\mathbf{\Omega}) = \int_0^\infty I(t,\mathbf{r},\mathbf{\Omega},\nu)\,d\nu \equiv \langle I\rangle_\nu$ †, we obtain

$$\frac{1}{c}\partial_t J + \mathbf{\Omega}\cdot\nabla J = \frac{\sigma a}{4\pi}T^4 \ - \sigma J, \tag{2.2}$$

where the constant a is given by $a = (8\pi^5 k^4)/(15h^3c^3)$.

2.2. *Derivation of the Half-Moment Model*

Two half spaces, defined by the direction of propagation of the radiation, are introduced, splitting the domain $\mathbf{\Omega}$ into 2 disjoint pieces, $\mathbf{\Omega}^+$ and $\mathbf{\Omega}^-$, such that $\mathbf{\Omega} = \mathbf{\Omega}^+ \cup \mathbf{\Omega}^-$, $\mathbf{\Omega}^+ \cap \mathbf{\Omega}^- = \emptyset$, and

$$\mathbf{\Omega}^+ = \{\mathbf{\Omega} \ / \ \mathbf{F}_R/F_R\cdot\mathbf{\Omega} \geq 0\}, \tag{2.3}$$

$$\mathbf{\Omega}^- = \{\mathbf{\Omega} \ / \ \mathbf{F}_R/F_R\cdot\mathbf{\Omega} < 0\}, \tag{2.4}$$

where $\mathbf{F}_R$ designates the radiative flux and F_R its norm‡. $\mathbf{\Omega}^\pm$ are then two unit half spheres, obtained by cutting the sphere $\mathbf{\Omega}$ by the plane perpendicular to the flux vector $\mathbf{F}_R$, $P_\perp = \{\Omega \ / \ \mathbf{F}_R\cdot\mathbf{\Omega} = 0\}$.

The three first moments, E_R, $\mathbf{F}_R$, and $\mathbf{P}_R$, respectively the radiative energy, flux vector and pressure tensor, of the radiative intensity I according to the frequency and the direction are defined by

$$E_R = \frac{1}{c}\langle J\rangle_\Omega \quad \mathbf{F}_R = \langle \mathbf{\Omega} J\rangle_\Omega, \quad \mathbf{P}_R = \frac{1}{c}\langle \mathbf{\Omega}\otimes\mathbf{\Omega} J\rangle_\Omega, \tag{2.5}$$

In a similar way, the half moments ${E_R}^\pm$, $\mathbf{F}_R^\pm$, and $\mathbf{P}_R^\pm$ are defined by

$${E_R}^\pm = \frac{1}{c}\langle J\rangle_{\mathbf{\Omega}^\pm}, \quad \mathbf{F}_R^\pm = \langle \mathbf{\Omega} J\rangle_{\mathbf{\Omega}^\pm}, \quad \mathbf{P}_R^\pm = \frac{1}{c}\langle \mathbf{\Omega}\otimes\mathbf{\Omega} J\rangle_{\mathbf{\Omega}^\pm}, \tag{2.6}$$

By construction, the following properties hold

$$E_R = {E_R}^+ + {E_R}^-, \quad \mathbf{F}_R = \mathbf{F}_R^+ + \mathbf{F}_R^-, \quad \mathbf{P}_R = \mathbf{P}_R^+ + \mathbf{P}_R^-. \tag{2.7}$$

Three unit vectors of propagation $\mathbf{n}$, $\mathbf{n}^+$, $\mathbf{n}^-$ are defined according to the direction of the radiative flux and half fluxes:

$$\mathbf{n} = \mathbf{F}_R/F_R, \quad \mathbf{n}^+ = \mathbf{F}_R^+/F_R^+, \quad \mathbf{n}^- = \mathbf{F}_R^-/F_R^-, \tag{2.8}$$

It is assumed herein that the positive component of the flux can be taken to be approximately parallel to the flux itself, $\mathbf{n}^\pm \simeq \pm\mathbf{n}$ (hypothesis **H1**). This assumption is true

† We will denote the integration of a function f over the variables X, Y, Z as $\langle f\rangle_{X,Y,Z}$

‡ for the sake of brevity, the norm of a vector $\mathbf{v}$ will be always denoted as v.

when the radiation is isotropic or strongly anisotropic but is less accurate in intermediate cases. As a consequence of the previous definitions, the negative component of the flux then becomes anti-parallel to the flux $\mathbf{F}_R$. The previous relationship among the radiative fluxes can then be rewritten as

$$\mathbf{F}_R = F_R^+ \mathbf{n}^+ + F_R^- \mathbf{n}^- \simeq F_R^+ \mathbf{n} - F_R^- \mathbf{n}. \tag{2.9}$$

Integrating the radiative transfer equation (2.2) over each half direction $\mathbf{\Omega}^\pm$, leads to

$$\int_{\mathbf{\Omega}^\pm} \partial_t J \, d\mathbf{\Omega} + \int_{\mathbf{\Omega}^\pm} \mathbf{\Omega} \cdot \nabla J \, d\mathbf{\Omega} = \frac{1}{2} c\sigma a T^4 - c\sigma E_R^\pm. \tag{2.10}$$

Multiplying the radiative transfer equation (2.2) by $\mathbf{\Omega}$ and integrating over the half directions $\mathbf{\Omega}^\pm$ leads to

$$\frac{1}{c} \int_{\mathbf{\Omega}^\pm} \partial_t \mathbf{\Omega} J \, d\mathbf{\Omega} + c \int_{\mathbf{\Omega}^\pm} \mathbf{\Omega} \otimes \mathbf{\Omega} \cdot \nabla J \, d\mathbf{\Omega} = \frac{1}{4} c\sigma a T^4 \mathbf{n}^\pm - \sigma \mathbf{F}_R^\pm. \tag{2.11}$$

The two subspaces $\mathbf{\Omega}^\pm$ have been chosen in order to partition the domain in a physically natural way and to allow the radiative pressure to be closed (see section 2.3). But the partitioning causes the bounds of integration over $\mathbf{\Omega}^\pm$ to depend on the flux and hence on x, y, z, t, and so disallows commuting derivatives and integrals over $\mathbf{\Omega}^\pm$. Nevertheless, it has been possible to perform these integrals. The following relationships hold provided that the radiation is assumed to be isotropic in the plane perpendicular to the direction of the flux (hypothesis **H2**), for example if described or modeled by a radiative intensity $I_\perp$ such as that in the next section.

$$\int_{\mathbf{\Omega}^\pm} \partial_t J \, d\mathbf{\Omega} \simeq \partial_t E_R^\pm, \tag{2.12}$$

$$\int_{\mathbf{\Omega}^\pm} \mathbf{\Omega} \cdot \nabla J \, d\mathbf{\Omega} \simeq \nabla \cdot \mathbf{F}_R^\pm - \pi J_\perp \nabla \cdot \mathbf{n}^\pm, \tag{2.13}$$

$$\int_{\mathbf{\Omega}^\pm} \partial_t \mathbf{\Omega} J \, d\mathbf{\Omega} \simeq \partial_t \mathbf{F}_R^\pm - \frac{\pi}{c} J_\perp \partial_t \mathbf{n}^\pm, \tag{2.14}$$

$$\int_{\mathbf{\Omega}^\pm} \mathbf{\Omega} \otimes \mathbf{\Omega} \cdot \nabla J \, d\mathbf{\Omega} \simeq \nabla \cdot \mathbf{P}_R^\pm, \tag{2.15}$$

where $J_\perp = \langle I_\perp \rangle_\nu$. These relationships are derived in Ripoll & Wray (2003) using assumption (**H2**) which leads to canceling of two of the border terms in (2.12) and in (2.15) and to a simple form of (2.13) and (2.14). Thus, the $M_1^{1/2}$ model is given in three dimension by

$$\partial_t E_R^\pm + \nabla \cdot \mathbf{F}_R^\pm - \pi J_\perp \nabla \cdot \mathbf{n}^\pm = \frac{1}{2} c\sigma a T^4 - c\sigma E_R^\pm, \tag{2.16}$$

$$\frac{1}{c} \partial_t \mathbf{F}_R^\pm - \frac{\pi}{c} J_\perp \partial_t \mathbf{n}^\pm + c \nabla \cdot \mathbf{P}_R^\pm = \frac{1}{4} c\sigma a T^4 \mathbf{n}^\pm - \sigma \mathbf{F}_R^\pm. \tag{2.17}$$

The closure of the model will be provided by models for the radiative pressure and $J_\perp$ in the next section.

2.3. *Closure of the Half-Moment Model*

2.3.1. *A model for the pressure*

A special radiative intensity I^* with the following form is chosen

$$I^*(t,\mathbf{r},\mathbf{\Omega},\nu) = I(T^*(t,\mathbf{r},\mathbf{\Omega}),\nu) = \frac{2h\nu^3}{c^2}\left[\exp\left(\frac{h\nu}{kT^*}\right)-1\right]^{-1}, \tag{2.18}$$

in which

$$T^*(t,\mathbf{r},\mathbf{\Omega}) = \frac{T}{B(1-\mathbf{A}\cdot\mathbf{\Omega})}, \tag{2.19}$$

and where $\mathbf{A}$ and B are defined on $\mathbf{\Omega}^+$ and $\mathbf{\Omega}^-$ as follows

$$\mathbf{A} = \begin{cases} A^+\mathbf{n}^+ & \text{on} \quad \mathbf{n}\cdot\mathbf{\Omega}\geq 0 \\ A^-\mathbf{n}^- & \text{on} \quad \mathbf{n}\cdot\mathbf{\Omega}<0 \end{cases} \quad \text{and} \quad B = \begin{cases} B^+ & \text{on} \quad \mathbf{n}\cdot\mathbf{\Omega}\geq 0 \\ B^- & \text{on} \quad \mathbf{n}\cdot\mathbf{\Omega}<0 \end{cases}. \tag{2.20}$$

This intensity, determined by the so-called maximum entropy closure, provides a way to close the radiative pressure $\mathbf{P}_R$ by approximating it with $\mathbf{P}_R^*$, computed from I^*. This constitutes the third and last assumption (**H3**) used here to derive the $M_1^{1/2}$ model.

If the scalar B and the vector $\mathbf{A}$ are defined from the two constraints $E_R = \langle I^*\rangle_{\nu,\mathbf{\Omega}}$ and $\mathbf{F}_R = \langle \mathbf{\Omega}\, I^*\rangle_{\nu,\mathbf{\Omega}}$, then the intensity I^*, defined in (2.18), maximizes the radiative entropy under these constraints (Minerbo 1978). The subdivision into $\mathbf{\Omega}^+$ and $\mathbf{\Omega}^-$ does not change this property, and as a direct consequence of (2.7) we have that the restricted intensities $I^*_{|\mathbf{\Omega}^\pm}$ maximize the radiative entropy under the constraints $E_R{}^\pm = \langle I^*\rangle_{\nu,\mathbf{\Omega}^\pm}$ and $\mathbf{F}_R^\pm = \langle \mathbf{\Omega} I^*\rangle_{\nu,\mathbf{\Omega}^\pm}$. Unfortunately, it is not possible to obtain a closed form for the pressure using these constraints directly; instead we use **H1** to approximate the constraints as follows

$$\left\langle I^*(\mathbf{n}^\pm)\right\rangle_{\nu,\mathbf{\Omega}^\pm} \simeq \langle I^*(\pm\mathbf{n})\rangle_{\nu,\mathbf{\Omega}^\pm} \quad \text{and} \quad \left\langle I^*(\mathbf{n}^\pm)\right\rangle_{\nu,\mathbf{\Omega}^\pm} \simeq \langle \mathbf{\Omega} I^*(\pm\mathbf{n})\rangle_{\nu,\mathbf{\Omega}^\pm}, \tag{2.21}$$

The abbreviated notation $I^*(\mathbf{n}^\pm)$ is used to denote I^* as defined using $\mathbf{A}$ in (2.20), and $I^*(\pm\mathbf{n})$ denotes I^* using instead

$$\mathbf{A} = A^+\mathbf{n}^+ \simeq A^+\mathbf{n} \quad \text{on} \quad \mathbf{n}\cdot\mathbf{\Omega}\geq 0 \quad ; \quad \mathbf{A} = A^-\mathbf{n}^- \simeq -A^-\mathbf{n} \quad \text{on} \quad \mathbf{n}\cdot\mathbf{\Omega}<0, \tag{2.22}$$

which corresponds to the use of **H1** in the definition (2.20). The computation of $\mathbf{A}$, from now approximated by (2.22), and B is shown in done in Ripoll & Wray (2003). Actually, the assumption **H1** was not needed before this point of the derivation.

The radiative pressure tensor $\mathbf{P}_R^\pm$ is approximated by $\mathbf{P}_R^{\pm *}$, computed in Ripoll & Wray (2003), and is written

$$\begin{aligned}\mathbf{P}_R^\pm &= \int_{\mathbf{\Omega}^\pm} \mathbf{\Omega}\otimes\mathbf{\Omega} J\, d\mathbf{\Omega} \simeq \int_{\mathbf{\Omega}^\pm} \mathbf{\Omega}\otimes\mathbf{\Omega} J^*(\mathbf{n}^\pm)\, d\mathbf{\Omega} = \mathbf{P}_R^{\pm *} \simeq \int_{\mathbf{\Omega}^\pm} \mathbf{\Omega}\otimes\mathbf{\Omega} J^*(\pm\mathbf{n})\, d\mathbf{\Omega} \\ &\simeq \mathbf{P}_R^*(\mathbf{f}^\pm, E_R{}^\pm) = \mathbf{D}_R^\pm E_R{}^\pm = \mathbf{D}_R(\mathbf{f}^\pm) E_R{}^\pm\end{aligned}$$

where $\mathbf{D}_R^\pm$ has the form of the well-known Eddington tensor evaluated for an anisotropy $\mathbf{f}^\pm = \mathbf{F}_R^\pm/(cE_R{}^\pm)$, given by

$$\mathbf{D}_R^\pm = \mathbf{D}_R(\mathbf{f}^\pm) = \frac{1-\chi(f^\pm)}{2}\,\mathbf{Id} + \frac{3\chi(f^\pm)-1}{2}\,\frac{\mathbf{f}^\pm\otimes\mathbf{f}^\pm}{f^{\pm 2}}, \tag{2.23}$$

in which the Eddington factor χ is

$$\chi(f^{\pm}) = \frac{8f^{\pm 2}}{1+6\,f^{\pm}+\sqrt{1+12\,f^{\pm}-12\,f^{\pm 2}}} \text{ if } f^{\pm} > 0.5 \text{ and } \chi(f^{\pm}) = 1/3 \text{ elsewhere.} \tag{2.24}$$

There is then no coupling between outgoing and incoming radiation in the pressure model. The isotropic and anisotropic limits ($f \to 0$ and $f \to 1$) of the model, which define its range of validity are discussed in Ripoll & Wray (2003). The corresponding range of $f^{\pm}$ is $[1/2, 1]$; this range will hold numerically as well if the limitation on the Eddington factor χ is enforced as in (2.24), but not otherwise. The Eddington factor is hence in total agreement with the domain of definition of $f^{\pm}$. Without this limitation on χ, $f^{\pm}$ lower than $1/2$ implies a radiative intensity defined, problematically, in terms of an $\mathbf{A}$ with a negative norm.

2.3.2. *A model for $I_{\perp}$ and $J_{\perp}$*

The radiative intensity I^*, which has been used to derive mean absorption coefficient (Ripoll *et al.* 2001), can be used as well to model the border terms coming from the integration, since I^* is isotropic in the plane perpendicular to the flux and we have

$$I_{\perp}^{*\,\pm} = \frac{2h\nu^3}{c^2}\left[\exp(\frac{h\nu T}{kB^{\pm}}) - 1\right]^{-1}, \tag{2.25}$$

since $\mathbf{A}^{\pm} \cdot \mathbf{\Omega} = 0$ for $\mathbf{\Omega} \in P_{\perp}$ and $B^{\pm}$ is given in Ripoll & Wray (2003). $I_{\perp}^{*\,\pm}$ is a Planck function evaluated in $T_R^{\pm}$ when radiation are isotropic and vanishes when radiation are anisotropic in the direction of the flux. The main problem of this model is that the intensity is reconstructed from the plus and minus macroscopic quantities. There is then two intensities $I_{\perp}^{*\,\pm}$, which should have the same value in $P_{\perp}$, but nothing can guaranteed it. The definition of $I_{\perp}^{*}$ in $P_{\perp}$ in then not obvious and we propose simply an average of the two values $I_{\perp}^{*\,\pm}$.

$$I_{\perp} \simeq I_{\perp}^{*} \simeq \frac{I_{\perp}^{*\,+} + I_{\perp}^{*\,-}}{2} \quad ; \quad J_{\perp} \simeq J_{\perp}^{*} \simeq \frac{J_{\perp}^{*\,+} + J_{\perp}^{*\,-}}{2}, \tag{2.26}$$

where $J_{\perp}^{*\,\pm}$ is given by

$$J_{\perp}^{*\,\pm} = \frac{aT^4}{4\pi B^{\pm 4}} = \frac{aT_R^{\pm 4}}{4\pi}\frac{6(1-A^{\pm})^3}{3-3A^{\pm}+A^{\pm 2}} \tag{2.27}$$

$$= \frac{3}{16\pi}aT_R^{\pm 4}\frac{\left(1-2f^{\pm}+\sqrt{-12f^{\pm 2}+12f^{\pm}+1)}\right)^3}{f^{\pm}(6f^{\pm}+1+\sqrt{-12f^{\pm 2}+12f^{\pm}+1})}, \tag{2.28}$$

$J_{\perp}^{*\,\pm}$ is a function of $T_R^{\pm}$ and $f^{\pm}$ which decrease from their isotropic values $J_{\perp}^{*\,\pm^{iso}} = aT_R^{\pm 4}/2\pi$ (note that $J_{\perp}^{*\,\pm^{eq}} = aT^4/4\pi$ at equilibrium) to their anisotropic values $J_{\perp}^{*\,\pm^{aniso}} = 0$. Moreover, it can be seen that $J_{\perp}^{*\,iso} = E_R/4\pi$ could constitute a rough model for $J_{\perp}$.

One could think the average (2.26) is arbitrary and any average of the form $J_{\perp}^{*} \simeq (aJ_{\perp}^{*\,+} + bJ_{\perp}^{*\,-})/(a+b)$ could have been chosen. Actually, $a = 1$ and $b = 1$ is the only combination allowing the model (2.26) to get the exact isotropic value $J_{\perp} = E_R/(4\pi) = (E_R^{+} + E_R^{-})/(4\pi)$. (The demonstration is obvious using (2.28) with $f^{\pm} \to 1/2$ in (2.26)).

Finally, the 8 equations in three dimension of the $M_1^{1/2}$ model are

$$\partial_t E_R^{\pm} + \nabla \cdot \mathbf{F}_R^{\pm} - \pi J_{\perp}^* \nabla \cdot \mathbf{n}^{\pm} = \frac{1}{2} c\sigma a T^4 - c\sigma E_R^{\pm}, \tag{2.29}$$

$$\frac{1}{c}\partial_t \mathbf{F}_R^{\pm} - \frac{\pi}{c} J_{\perp}^* \partial_t \mathbf{n}^{\pm} + c\nabla \cdot \left(\mathbf{D}_R(\mathbf{f}^{\pm})\, {E_R}^{\pm}\right) = \frac{1}{4} c\sigma a T^4 \mathbf{n}^{\pm} - \sigma \mathbf{F}_R^{\pm}, \tag{2.30}$$

and have been derived using the three assumptions **H1**, **H2**, and **H3**. The positive and negative quantities are then only coupled by the model for $J_{\perp}^*$ given in (2.26)-(2.28), which constitutes the last approximation, and when the full moment are reconstructed.

3. A new 3D moment model for a hot opaque medium emitting in a cold medium

From the half moment model, a new moment model is derived for a particular, but nevertheless important, case: a hot opaque source emitting in a cold medium. It can be seen in (2.29)-(2.30) that the non-linearity of the radiative pressure does not allow reducing a closed full moment model from the sum of the two half-moment models in the general case. As a matter of fact, this sum leads to

$$\partial_t E_R + \nabla \cdot \mathbf{F}_R = c\sigma a T^4 - c\sigma E_R, \tag{3.1}$$

$$\frac{1}{c}\partial_t \mathbf{F}_R + c\nabla \cdot (\mathbf{D}_R(\mathbf{f}^+) {E_R}^+ + \mathbf{D}_R(\mathbf{f}^-) {E_R}^-) = -\sigma \mathbf{F}_R, \tag{3.2}$$

where the border terms have canceled when added, as did the half emission terms of the flux equations, and where a pressure remains which is expressed in terms of unclosed quantities.

From this system, it is however possible to reconstruct a full closed moment model in the particular case of a hot, opaque opaque source emitting in a cold, transparent (or semi-transparent) medium. We will discuss at the end of this section how the source and the exterior medium must be characterized with regard to their temperature and opacity.

We now discuss the two domains in this particular problem.

1) First, inside the hot, opaque source where radiation can be considered as nearly isotropic ($f^{\pm} \simeq 0.5$), the linear P_1 limit holds for both half-moment models since in this limit

$$\mathbf{P}_R \simeq \lim_{f^{\pm} \to 1/2} (\mathbf{D}_R^+ E_R^+ + \mathbf{D}_R^- E_R^-) = \frac{1}{3}(E_R^+ + E_R^-) = \frac{1}{3} E_R \tag{3.3}$$

The condition $f^{\pm} \simeq 0.5$ implies $f \simeq 0$. We will assume for this model that radiation can be considered isotropic for $f < 0.5$. It should be noticed that radiation is usually considered nearly isotropic for $f < 0.3$ (the P_1 validity domain); we assume that it is possible to extend this range to $f < 0.5$ without too much impact on the solution because, for many applications, the anisotropic factor f is predominantly either close to 0 or 1. The latter case will be handled next.

2) Within the cold, transparent medium, a cold equilibrium is assumed for the negative half moments while the positive ones are strongly anisotropic due to the radiating source, implying $f^+ >> 0.5$.

The exterior medium is assumed to be cold enough such that $E_R^- << E_R^+$ and $\|{F_R}_i^-\| << \|{F_R}_i^+\|$ (or indifferently ${F_R}_i^- << {F_R}_i^+ \; \forall i = 1..3$). Then $E_R \simeq E_R^+$ and $F_R \simeq F_R^+$ lead to $f \simeq f^+$ and hence $f >> 0.5$. Finally, using these approximations

$$\mathbf{P}_R = \mathbf{D}_R{}^+ E_R^+ + \mathbf{D}_R{}^- E_R^- \simeq \mathbf{D}_R(f^+) E_R^+ \simeq \mathbf{D}_R^+(f) E_R. \tag{3.4}$$

It must be noticed now that the Eddington factor $\mathbf{D}_R^+(f)$, given in (2.23)-(2.24) is limited by construction to $D_R^+ = 1/3$ when $f^+ < 0.5$, and since $f^+ \simeq f$, this leads to the P_1 closure when radiation is isotropic. This tensor then naturally makes the transition from $D_R^+ = 1/3$ to $D_R^+(f)$. Thus the same full moment model is found to be valid inside the hot, opaque medium and the cold one and is able to establish the transition. The radiation field is hence fully described by this model, called here M_1^+, which is written

$$\partial_t E_R + \nabla \cdot \mathbf{F}_R = c\sigma a T^4 - c\sigma E_R, \tag{3.5}$$

$$\frac{1}{c}\partial_t \mathbf{F}_R + c\nabla \cdot \left(\mathbf{D}_R^+(f)\, E_R\right) = -\sigma \mathbf{F}_R, \tag{3.6}$$

with

$$\mathbf{D}_R^+(f) = \frac{1-\chi^+(f)}{2}\,\mathbf{Id} + \frac{3\chi^+(f)-1}{2}\,\frac{\mathbf{f}\otimes\mathbf{f}}{f^2} \tag{3.7}$$

and

$$\chi^+(f) = \frac{8f^2}{1+6f+\sqrt{1+12f-12f^2}} \text{ if } f > 0.5 \text{ and } \chi(f) = 1/3 \text{ elsewhere.} \tag{3.8}$$

This four equation model gives equations for the full moments and for a range of the anisotropy $f \in [0,1]$. It should be noticed here that this reduction to a full-moment system is only possible because the positive flux always radiates in the full flux direction, whatever this direction is. With a classical splitting of the flux, where the positive component of the flux is statically defined, such a reduction is not possible since incoming and outgoing radiation cannot be distinguished.

This model describes radiation emitted by a source which is isotropic inside (P_1 must be valid inside) and radiating into a exterior domain in a strongly anisotropic way. This signifies that this exterior medium is not radiating much compared to the source, but might for example absorb part of emitting radiation of the source provided that it does not re-radiate towards the source. Moreover, if the exterior medium is too opaque or too hot, the anisotropy factor will stay lower than 0.5 and the model will simply reduce to P_1.

The domain of validity of M_1^+ is then quite large. It will be valid in many applications where the main interest is to compute the heat loss of a source by radiation in a non-remitting medium, in particular for luminous flames and fires burning in ambient air and for stars radiating into their thin atmospheres.

We will see in the next section that this model gives results very close to those obtained by a RTE ray-tracing solver.

4. Numerical Results

4.1. *A black hot sphere radiating into an infinite semi-transparent cold gas*

The first case is a hot black sphere of radius $r = 1$ which emits at an intensity $I_s = 1$ into an infinite absorbing cold gas ($T = 0$) of two different and small opacities $\sigma = 0.1, 0.01$. In terms of macroscopic quantities, we have inside the sphere: $E_{R_s}^{\pm} = 2\pi$, $\mathbf{F}_{R_s}^{\pm} = \pm\pi$, $E_{R_s} = 4\pi$ and $\mathbf{F}_{R_s} = 0$.

For this case the positive flux will remain positive and the negative quantities, which vanish, do not need to be computed. Moreover, the exact value of $J_\perp$, which here is simply $J_\perp = 0$, is used. The outgoing boundary conditions are $\partial_r {E_R}^+ = 0$, $\partial_r \mathbf{F}_R^+ = 0$ at

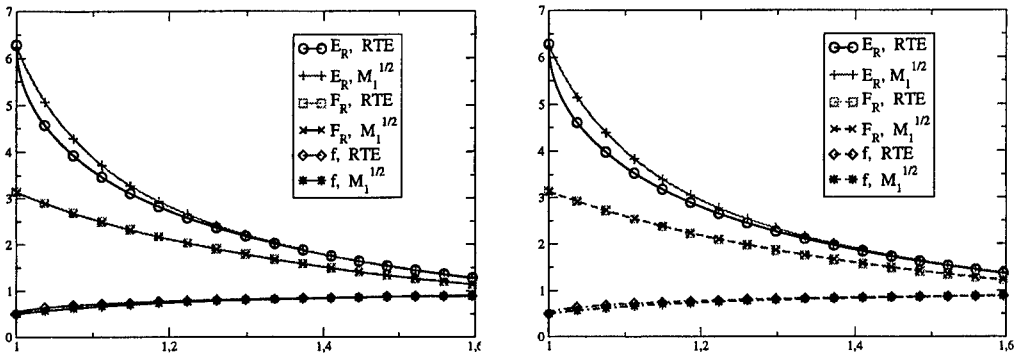


FIGURE 1. Radiative quantities: energy, flux and anisotropy. Left: $\sigma = 0.1$. Right: $\sigma = 0.01$

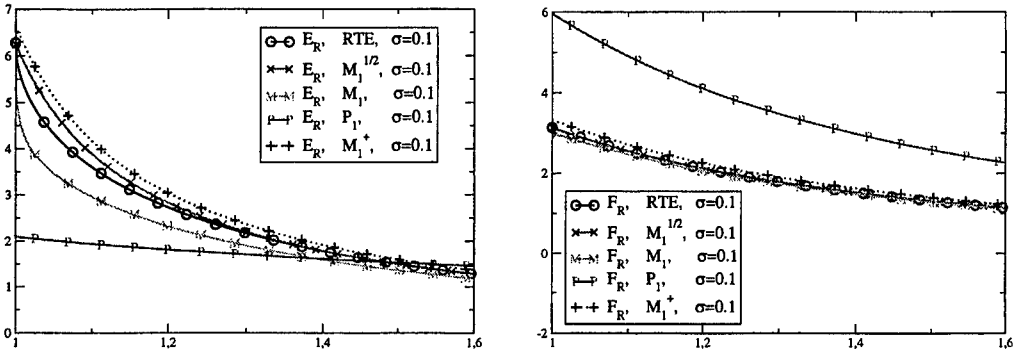


FIGURE 2. Comparison between 5 models for $\sigma = 0.1$. Left: Radiative Energy. Right: Radiative Flux.

$r = 1.6$, similarly $\partial_r E_R = 0$, $\partial_r \mathbf{F}_R = 0$ for the full moment models, in order to simulate an infinite domain.

We compare in Fig. 1, the steady states of the radiative energy, flux, and anisotropic factor given by $M_1^{1/2}$ to those obtained by the RTE solver for $\sigma = 0.1, 0.01$. Results are in very good agreement for each of these quantities.

We compare in Fig. 3-2, both radiative energy and flux obtained by five models for these opacities: RTE, $M_1^{1/2}$, M_1, P_1 and the new M_1^+. Results obtained by the RTE and the $M_1^{1/2}$ solvers were presented in the two previous figures. The full moment methods M_1, P_1 and M_1^+ are solved from inside the hot sphere since no boundary conditions can be prescribed at $r = 1$, contrary to the RTE and the $M_1^{1/2}$ solvers. M_1^+ is in its range of applicability and gives results almost as good as those of $M_1^{1/2}$. It might be presumed that the small difference between them comes from the difference of the boundary conditions. In all cases, P_1 gives mostly wrong results (for $\sigma = 0.01$, the anisotropic factor $f = \mathbf{F}_R/E_R$ found by P_1 at $r = 1.0$ is around 5, meaning a speed of light five times overestimated). Surprisingly, M_1 gives a good computation of the flux for all cases, but a rough computation of the energy.

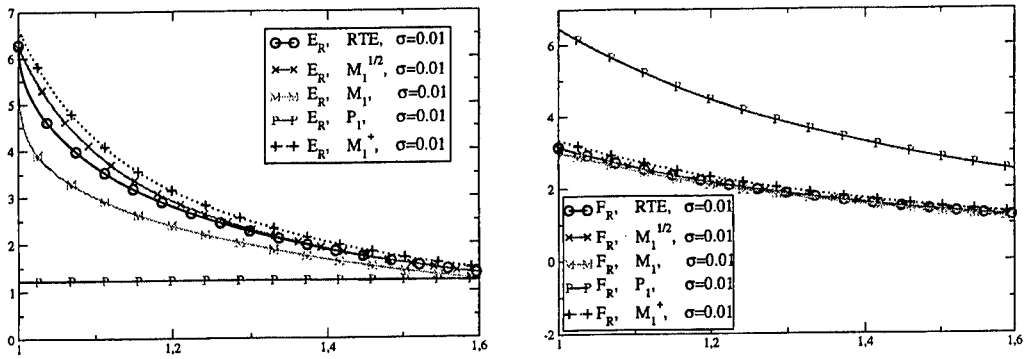


FIGURE 3. Comparison between 5 models for $\sigma = 0.01$. Left: Radiative Energy. Right: Radiative Flux.

These results valid the models and let presume that they will provide an accurate description of radiative fields of the solar atmosphere, which presents the same main characteristics of this simple geometry.

4.2. *Computation of the radiation field of the solar atmosphere*

The temperature and opacity profiles of the sun are taken from Stix (1989). These values are obtained from model C of Vernazza *et al.* (1981) and are representative of a quiet sun. The temperature and opacity profiles are truncated before the transition layer to the corona, which is here considered as a zero density zone. Confronted with the difficulty of determining mean absorption coefficients for the solar atmosphere, which are needed to model the opacity, we obtained the opacity from the optical depth τ at $500\,nm$ ($\sigma = \partial\tau_{500}/\partial r$).

The interior of the sun is assumed to be opaque enough to be represented by a black body emitting at $6910K$, which is the temperature at $25\,km$ below the surface. Outgoing boundary conditions are identical to the previous case. In Fig 4, the M_1^+ in spherical coordinates with spherical symmetry is solved and compared to the RTE ray tracing solution for the solar atmosphere.

The radiative temperature computed by M_1^+ is coincident with the one computed by the RTE solver close to the sun. Far away, the M_1^+ model finds a different plateau value (between $4960K$ and $4938K$) from the RTE solver (between $4700K$ and $4650K$). At $r = 6.97 \times 10^8\,m$, the error in the radiative temperature from the M_1^+ model, which finds $4950K$ instead of $4682K$, is 5.72%. At $r = 6.98 \times 10^8\,m$, the error is 6%. The radiative flux computed by both models presents, close to the sun, a small spike followed by a smooth bump close to the surface which is due to the opacity profile. The error of the flux computed by $M1^+$ is maximal at the top of the spike where it reaches 17%, while at the top of the bump the error is around 10%. Outside this highly variable zone, the profile of the radiative flux is computed with a precision of 5% by the M_1^+ model. Moreover, it should be noticed that, in this particular example, radiation is near isotropic ($f \simeq 0.5$), a condition in which the error introduced by M_1^+ is maximal, but it remains as we can see very admissible.

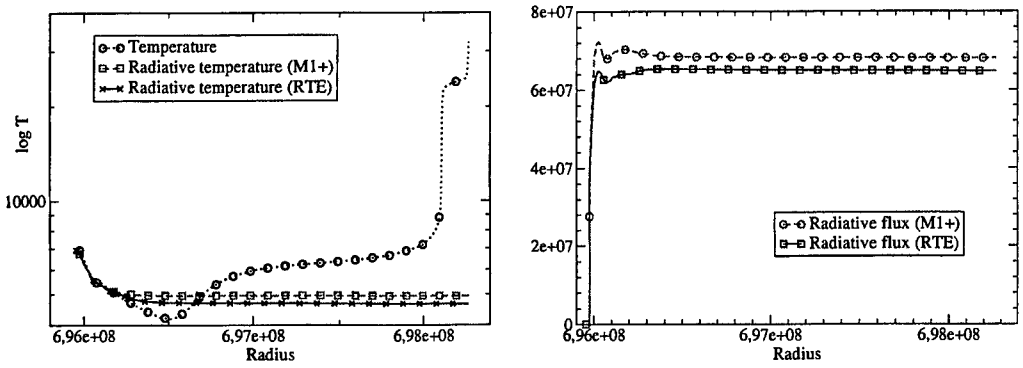


FIGURE 4. Radiation field of the sun atmosphere. Left: Radiative and matter Temperatures. Right: Radiative Flux.

5. Conclusion

A new three dimensional half moment model, called $M_1^{1/2}$, has been derived using a dynamic definition of the half quantities and the maximum entropy closure. The direction space is cut into two pieces according to the direction of propagation of the total flux, at each time and position. This splitting allows the radiative pressure to be closed, using the standard maximum entropy closure, with approximate constraints, but introduces non-trivial border terms.

By assuming that radiation is isotropic in the plane perpendicular to the flux, $P_\perp$, which seems admissible for a two-flux model, the radiative transfer equation has been integrated on these moving half-directional spaces. The integration is difficult but leads to small and simple expressions; the border terms account for the rotation needed to set the directional space in the direction of the flux. The value of the intensity in $P_\perp$ must be known, and a model for this quantity has been proposed.

An immediate application of this work has been presented: for the particular case of a three dimensional hot, opaque source emitting into a non re-emitting medium, the half moment model has been reduced to a new full moment model, called here M_1^+.

The model is here tested for the case of a hot one-dimensional Gaussian source radiating into media of various opacities. Very good agreement has been shown between the RTE and the $M_1^{1/2}$ model independently of the opacity. The relevance and the correctness of the closure has been shown, in one dimension, for a case theoretically similar to the solar atmosphere.

The radiation field of a solar atmosphere with an approximate opacity has been computed with the M_1^+ model. The results of M_1^+ are not as good as those presented in the previous theoretical problem: the error is always around 5% for all unknowns, except in a small transitional zone where the flux error reaches its maximal value of 17%. The solar problem close to the surface, being near isotropic, is a case for which the accuracy of M_1^+ should be lowest, but is nevertheless found to be admissible.

REFERENCES

DUBROCA, B. & KLAR A. 2002 Half moment closure for radiative transfer equations. *J. Comp. Phys* **180**, 584–596.

MIHALAS D. & MIHALAS B. W. 1984 *Foundation of radiation hydrodynamics.* Oxford University Press, New York.

MINERBO, G. N. 1978 Maximum entropy eddington factors. *J. Quant. Spectrosc. Radiat. Transfer* **20**, 541–545.

RIPOLL, J.-F. 2004 An averaged formulation of the M_1 radiation model with presumed with mean absorption coefficients and probability density functions for turbulent flows. *JQSRT* **83**, 493–517.

RIPOLL, J.-F., DUBROCA, B. & DUFFA, G. 2001 Modelling radiative mean absorption coefficients. *Comb. Th. and Mod.* **5** (3), 261–275.

RIPOLL, J.-F. & WRAY, A. A. 2003 A Half-Moment Model for Radiative Transfer in a 3D Gray Medium and its Reduction to a Moment Model for Hot, Opaque Sources. *Submitted.*

SIEGEL, R. C. & HOWELL, J. R. 2001 *Thermal radiation heat transfer.* 4^{th} Ed., Taylor and Francis.

STIX, M. 1989 *The sun. An introduction.* Springer-Verlag.

VERNAZZA, J. E., AVRETT, E. H. & LOESER, R. 1981.*Astrophys. J. Suppl.* **45**, 635.

Subgrid scale modeling in solar convection simulations using the ASH code

By Y.-N. Young, M. Miesch† and N. N. Mansour

1. Motivation and objectives

The turbulent solar convection zone has remained one of the most challenging and important subjects in physics. Understanding the complex dynamics in the solar convection zone is crucial for gaining insight into the solar dynamo problem. Many solar observatories have generated revealing data with great details of large scale motions in the solar convection zone. For example, a strong differential rotation is observed: the angular rotation is observed to be faster at the equator than near the poles not only near the solar surface, but also deep in the convection zone. On the other hand, due to the wide range of dynamical scales of turbulence in the solar convection zone, both theory and simulation have limited success. Thus, cutting edge solar models and numerical simulations of the solar convection zone have focused more narrowly on a few key features of the solar convection zone, such as the time-averaged differential rotation. For example, Brun & Toomre (2002) report computational finding of differential rotation in an anelastic model for solar convection. A critical shortcoming in this model is that the viscous dissipation is based on application of mixing length theory to stellar dynamics with some *ad hoc* parameter tuning.

The goal of our work is to implement the subgrid scale model developed at CTR into the solar simulation code and examine how the differential rotation will be affected as a result. Specifically, we implement a Smagorinsky-Lilly subgrid scale model into the ASH (anelastic spherical harmonic) code developed over the years by various authors. Readers are referred to (Clune *et al.* 1999) and (Miesch 1998) for a detailed description of the ASH code. This paper is organized as follows. In §2 we briefly formulate the anelastic system that describes the solar convection. In §3 we formulate the Smagorinsky-Lilly subgrid scale model for unstably stratified convection. We then present some preliminary results in §4, where we also provide some conclusions and future directions.

2. The anelastic equations of motions

In the solar convection zone, the depth extends over many density scale heights and thus the effects of stratification need to be captured despite the fact that acoustic timescales are much shorter than the large-scale convection timescales. An appropriate approach is to filter out sound waves while maintaining the density stratification, namely the anelastic approximation first proposed by Gough (1969) and later adapted to the solar convection zone by Gilman & Glatzmaier (1981). In stellar models, a fluid layer is unstable if the layer is superadiabatic. The degree of superadibaticity is quantified as

† High Altitude Observatory, National Center for Atmospheric Research, Boulder, Colorado, 80301

(Gilman & Glatzmaier 1981)

$$\epsilon \equiv -\frac{d}{C_P}\left(\frac{\partial s}{\partial r}\right)_0, \tag{2.1}$$

where d is the depth of the convection zone, C_P the specific heat capacity at constant pressure, s the entropy, and r the radial coordinate. The entropy gradient is calculated at some fiducial level in the convection zone. In the sun, the departure from adiabaticity in the convection zone is extremely small (Christensen-Dalsgaard *et al.* 1993),

$$\epsilon \leq 10^{-4}. \tag{2.2}$$

If we assume that the velocity in the horizontal (transverse to gravity) directions is mostly driven by pressure gradients, the coupling between vertical and horizontal velocities leads to the following relationship between the convection velocity v and sound speed c_s

$$\mathcal{M} \equiv \frac{v}{c_s} \sim \sqrt{\epsilon} \ll 1, \tag{2.3}$$

where $\mathcal{M}$ is the Mach number of the flow.

The basic idea in the anelastic approximation is to expand the variables in terms of the small parameter ϵ, and collect terms of the zeroth and first orders. As is usually found in perturbation theory, the zeroth order equations describe the basic state, which remain stationary over timescales at which the first order variables vary. The fundamental equations are the compressible, stratified Navier-Stokes equations in a rotating reference frame

$$\rho\left(\frac{\partial \mathbf{v}}{\partial t} + (\mathbf{v}\cdot\nabla)\mathbf{v}\right) = -\nabla P + \rho\mathbf{g} + 2\mathbf{v}\times\Omega_0 + \nabla\cdot\mathcal{D}, \tag{2.4}$$

$$\rho\Theta\frac{\partial s}{\partial t} + \rho\Theta\mathbf{v}\cdot\nabla s = -\nabla\cdot q + 2\nu\rho\left(e_{ij}e_{ij} - \frac{1}{3}(\nabla\cdot\mathbf{v})^2\right) - \rho\mathcal{E}, \tag{2.5}$$

$$\frac{\partial \rho}{\partial t} + \nabla\cdot(\rho\mathbf{v}) = 0, \tag{2.6}$$

where s is the entropy, Θ is the temperature, and $\mathcal{E}$ is the nuclear energy generation rate. The viscous stress $\mathcal{D}$ is defined as

$$\mathcal{D} \equiv 2\rho\nu\left(e_{ij} - \frac{1}{3}(\nabla\cdot\mathbf{v})\delta_{ij}\right), \tag{2.7}$$

and q is the composite non-convective heat flux, defined as

$$q \equiv -\kappa\rho\Theta\nabla s - \kappa_r\rho C_p\nabla\Theta. \tag{2.8}$$

and the various transport coefficient such as the viscosity ν, thermal diffusion κ, and radiative thermal diffusion κ_r are assumed to be functions of the radial coordinate only.

Upon substituting the variables expanded in terms of the small parameter ϵ, at zeroth order we obtain the hydrostatic equation. Denoting the zeroth order terms with a subscript 0, the equations at the leading order are

$$\frac{\partial P_0}{\partial r} + \Lambda = -\rho_0 g, \tag{2.9}$$

$$P_0 = \mathcal{R}\rho_0\Theta_0, \tag{2.10}$$

where Λ is the radial gradient of a mean turbulent pressure

$$\Lambda \equiv \langle [\rho_0(\mathbf{v}\cdot\nabla)\mathbf{v} - \nabla\cdot\mathcal{D} - 2\rho_0(\mathbf{v}\times\Omega_0)]_r\rangle_t\,. \tag{2.11}$$

The angular brackets in Equation (2.11) denote horizontal averages, and the square brackets denote the radial component of the enclosed vector. We evaluate Λ only as we update the reference state (denoted with a subscript 0).

At the next order, we obtain the anelastic equations for compressible, stratified fluids

$$\frac{\partial \rho_0\mathbf{v}}{\partial t} + \rho_0(\mathbf{v}\cdot\nabla)\mathbf{v} = -\nabla P + \nabla\cdot\mathcal{D} + \rho\mathbf{g} + 2\rho_0(\mathbf{v}\times\Omega_0) + \Lambda\hat{r}, \tag{2.12}$$

$$\begin{aligned}\rho_0\Theta_0\frac{\partial s}{\partial t} + \rho_0\Theta_0\mathbf{v}\cdot\nabla(s_0+s) = \nabla\cdot(\kappa\rho_0\Theta_0\nabla(s_0+s) + \kappa_r\rho_0 C_p\nabla(\Theta_0+\Theta)) \\ +2\nu\rho_0\left(e_{ij}e_{ij} - \frac{1}{3}(\nabla\cdot\mathbf{v})^2\right) - \rho_0\mathcal{E},\end{aligned} \tag{2.13}$$

$$\nabla\cdot(\rho_0\mathbf{v}) = 0, \tag{2.14}$$

and

$$\frac{\rho}{\rho_0} = \frac{P}{P_0} - \frac{\Theta}{\Theta_0} = \frac{P}{\gamma P_0} - \frac{s}{C_p}. \tag{2.15}$$

We note that both the reference state and perturbation terms have been retained in Equation (2.13) because the gradient of the reference state entropy (s_0) varies in amplitude from $\mathcal{O}(\epsilon)$ in the convection zone to $\mathcal{O}(1)$ in the convectively stable region. This scaling is also true for the term involving thermal diffusion of the reference temperature ($\kappa_r\partial\Theta_0/\partial r$). We retain the term $\kappa_r\partial\Theta/\partial r$ because we wish to allow for small deviations of the radiative heat flux from spherical symmetry.

The viscosity coefficient ν is assumed to be a function of the reference density ρ_0. The functional dependence is obtained from mixing length theory, and the specific value is chosen in an *ad hoc* fashion for a given numerical resolution and combination of parameters. Our main goal in this work is to replace these "mixing length" viscosity and thermal diffusivity with those based on Smagorinsky subgrid scale model. More details will be presented in §3.

The reference state is crucial in the simulation of the anelastic system. In the ASH code, the reference state is updated only every few hundred steps of advancing the anelastic equations. During the update process, the following equations are solved simultaneously for the reference pressure P_0 and density ρ_0:

$$\frac{1}{C_P}\frac{ds_0}{dr} = \frac{1}{\gamma}\frac{d\ln P_0}{dr} - \frac{d\ln\rho_0}{dr}, \tag{2.16}$$

$$\frac{dP_0}{dr} = -\rho_0 g. \tag{2.17}$$

Using the reference entropy gradient (ds_0/dr) and gravity ($g(r)$) profiles from the previous time step, Equations (2.16) and (2.17) are solved for the reference pressure and density. Figure 1 is an example from one of the ASH simulations. With similar reference states and viscosity profiles to those illustrated in figure 1, simulations of the ASH code have successfully generated differential rotation profiles that are similar to the solar observations. An example from ASH simulations is illustrated in figure 2. The numerical resolution for figure 2 is $65\times128\times256$ in the radial, latitudinal, and azimuthal

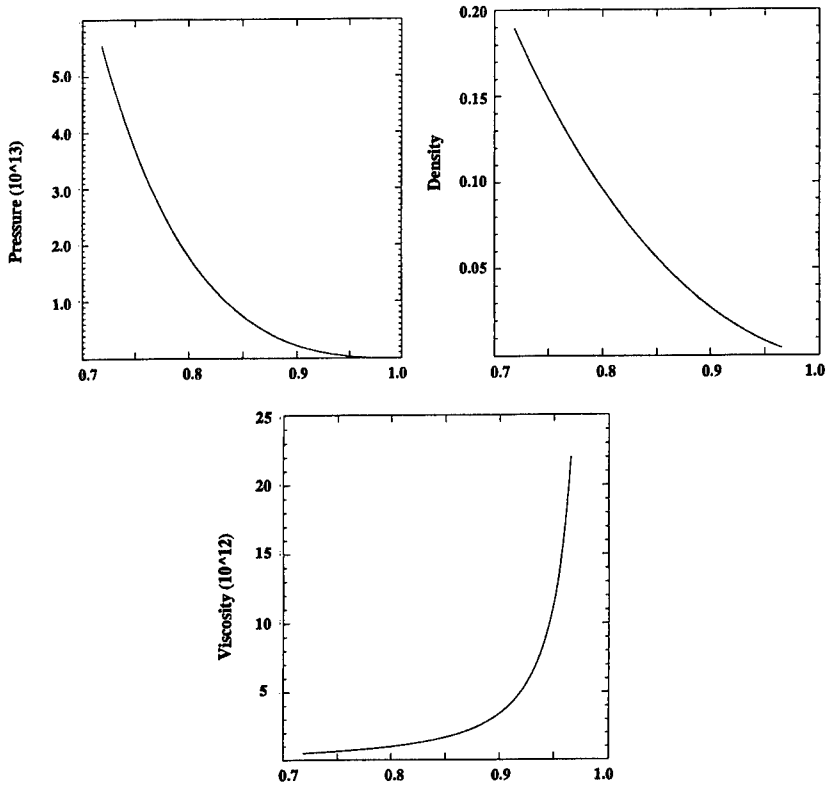


FIGURE 1. Reference state from ASH simulations, the horizontal axis is radial coordinate in units of solar radius. Panel (a): Reference pressure (dyne/cm^2) within the convection zone. Panel (b): Reference density (g/cm^3). Panel (c): the "mixing length" viscosity (cm^2/sec) as a function of r.

directions. The left panel is a filled contour plot of the averaged angular velocity as a function of latitude and radius, while the right panel shows the angular velocity at five latitudes as a function of radius from the bottom to the top of the convection zone. For this particular case, the viscosity is a prescribed function of radius as shown in figure 1(c), and the Prandtl number is fixed at 1/4. This corresponds to the AB case in Brun & Toomre (2002), in which the differential rotation inside the convection zone is most prominent among all the simulation data presented in Brun & Toomre (2002). Figure 2 is from simulations conducted on the NASA/Ames SGI cluster with different initial conditions. A typical differential rotation from solar helioseismic observations is shown in figure 2(c) (same as figure 1(b) in Brun & Toomre (2002)). The close similarity between observational solar differential rotation and the simulation data shows great promise that better results may be obtainable if the conveciton model is refined by building in more physics. For example, the viscosity and thermal diffusivity may be replaced by better dynamical models. Addition of a mechanism to couple the convection zone with the tachocline below may result in better agreement between simulation and observational data. As a preliminary initiative we have undertaken is to first improve the model for viscosity using Smagorinsky-Lilly's model.

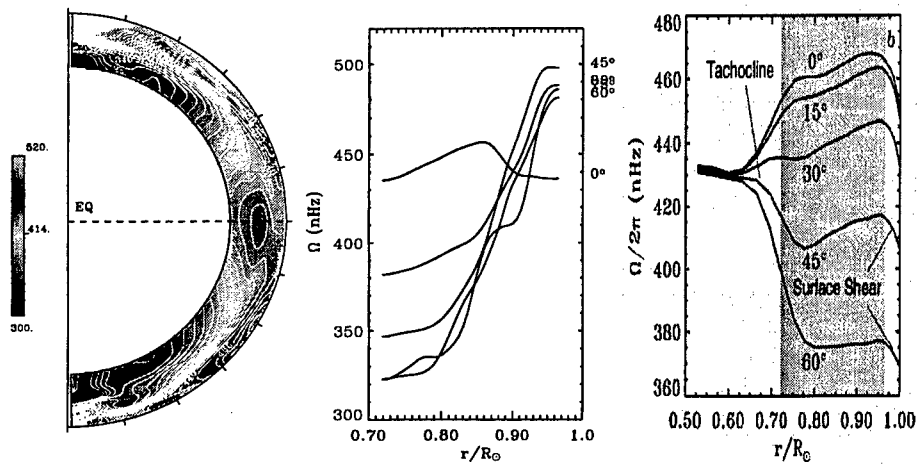


FIGURE 2. Panels (a) and (b): Differential rotation for the AB case in Brun & Toomre (2002) with different initial conditions. Panel (c) is the time-averaged rotation rates from five years of GONG data.

3. Smagorinsky-Lilly subgrid scale model

The principle underlying the Smagorinsky subgrid scale model is the balance of production of subgrid-scale turbulent kinetic energy and dissipation of isotropic turbulence energy at the characteristic eddy size. Let the subgrid turbulent production rate be denoted by $\mathcal{P}$, then for a given turbulent viscosity ν_T, the subgrid turbulent production rate is

$$\mathcal{P} = 2\nu_T e_{ij} e_{ij}. \tag{3.1}$$

The dissipation at scale l is $\sim q^3/l$, where q is a characteristic turbulent velocity. Finally, to find an expression for ν_T in terms of the resolved quantities, we utilize the Prandtl's assumption: $\nu_T = C_1 q l$, and upon substituting q into the dissipation rate and equating dissipation and production rates, we obtain the Smagorinsky subgrid scale model

$$\nu_T = (C_s l)^2 \sqrt{2 e_{ij} e_{ij}}, \tag{3.2}$$

where C_s is a constant in the range of $0.1 \leq C_s \leq 0.3$. Lilly (1962) later extended the Smagorinsky model to turbulence in unstably stratified convection. Due to the stratification an additional parameter, the Richardson number, appears in the expression for the eddy viscosity. The idea that led to Lilly's eddy viscosity is very similar to the above argument underlying the Smagorinsky model: buoyancy production or consumption must also be accounted for in the subgrid energy balance. Thus in the stratified case, the dissipation consists of contribution from both eddy dissipation and thermal diffusion. The Smagorinsky-Lilly eddy viscosity is simply the modified Smagorinsky model with the inclusion of stratification effect

$$\nu_T = (C_s l)^2 \sqrt{2 e_{ij} e_{ij}} \left[1 - \frac{\kappa_T}{\nu_T} Ri_f \right]^{0.5}. \tag{3.3}$$

Here κ_T is the eddy thermal diffusivity, and the flux Richardson number is defined as

$$Ri_f \equiv \frac{g}{2 e_{ij} e_{ij}} \frac{\partial \ln \theta}{\partial r}. \tag{3.4}$$

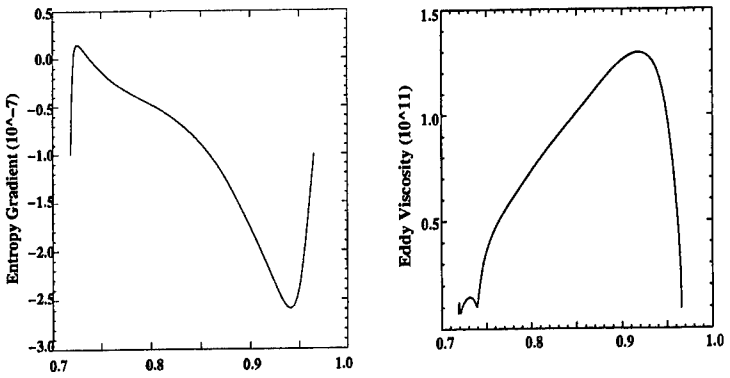


FIGURE 3. The left pannel is the reference entropy gradient (erg/g K m) and the right pannel is the averaged Smagorinsky-Lilly viscosity (cm^2/sec) as functions of r in units of solar radius.

Alternatively, the flux Richardson number can also be defined through entropy as

$$Ri_f \equiv \frac{g}{2e_{ij}e_{ij}} \frac{\partial s_0/\partial r}{C_p}, \tag{3.5}$$

where $\partial s_0/\partial r$ is the reference entropy gradient. In spherical geometry, we choose the length scale l as

$$l \equiv \left(\frac{\Delta(r) r^2}{L_{max}(L_{max}+1)} \right)^{1/3}, \tag{3.6}$$

where $\Delta(r)$ is the radial grid spacing at location r, L_{max} is the maximum (latitudinal) angular mode index.

Figure 3 shows the reference entropy gradient and the averaged Smagorinsky-Lilly viscosity as a function of radius. Near the bottom of the convection zone, the reference entropy gradient is positive, implying a stably stratified region. This corresponds to the small bump seen in the Smagorinsky-Lilly viscosity profile.

In the simulations we start from a stationary configuration with a negative reference entropy gradient throughout the convection zone. The boundary conditions for the velocity are stress free, which are not necessarily realistic but numerically convenient. As we are mostly interested in the differential rotation profile in the convection zone, the parameters and initial reference state are chosen to be the same as the AB case in Brun & Toomre (2002). We first obtain a turbulent convection zone using the mixing length viscosity and thermal diffusivity. As the simulation progresses, the differential rotation profile reaches a statistically stationary state. We then replace the mixing length viscosity and thermal diffusivity with the Smagorinsky-Lilly model with some prescribed constant coefficient C_s. At present we average Smagorinsky-Lilly's eddy viscosity over latitudinal and azimuthal angles. Strictly speaking this is inconsistent with the energy balance principle that gives rise to the eddy viscosity. We are now implementing a local, three-dimensional version of the Smagorinsky-Lilly model, which requires a considerably tedious alteration of the ASH code. For the following results, we present ASH simulations using the averaged Smagorinsky-Lilly eddy viscosity as a test study to see how the differential rotation may differ from that obtained with the "mixing length" viscosity and thermal diffusivity.

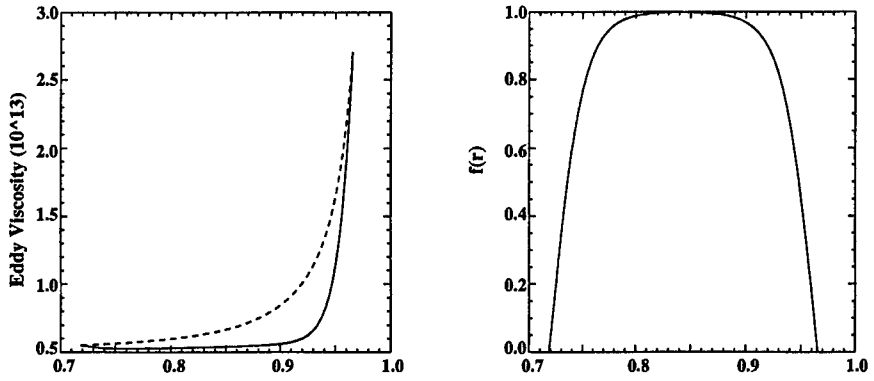


FIGURE 4. Eddy viscosity (cm^2/sec) using the length scale defined in Equation (4.1) (solid line) and the mixing length viscosity (dashed line). On the right is the functional form of $f(r)$ used in constructing the eddy viscosity.

4. Preliminary results and future directions

Our experiences so far show that the averaged Smagorinsky-Lilly eddy viscosity (as shown in figure 3) is too small, and simulations (with resolutions $65 \times 128 \times 256$) blow up soon after the Smagorinsky-Lilly viscosity is activated. A significant difference between the mixing length viscosity and the averaged Smagorinsky-Lilly viscosity is that the eddy viscosity is much smaller at the boundaries. Similar issues arise in large eddy simulations of the atmospheric flows, and it is usually necessary to incorporate a smooth transition from the eddy viscosity to a wall-model viscosity near the boundary. In the solar case, we can combine the mixing length viscosity with the eddy viscosity using a choice of length scale l as follows

$$l^2 = f(r) l_{SL}^2 + (1 - f(r)) l_M^2, \tag{4.1}$$

where l_{SL} is the length scale in Equation (3.6) and l_M is defined as

$$l_M \equiv \frac{1}{C_s} \left(\frac{\nu_M}{\sqrt{2 e_{ij} e_{ij}} \sqrt{1 - Rif}} \right)^{0.5} \tag{4.2}$$

Here $f(r)$ consists of two error functions so that $f(r) = 1$ in the bulk of the convection zone, and $f(r) = 0$ at the boundaries of the convection zone. Figure 4 shows the resultant eddy viscosity (left panel) for a given choice for $f(r)$ (right panel). Figure 5 shows the differential rotation at a instant in time from simulations using the length scale in Equation (4.2).

It is clear from comparing figure 5 and figure 2 that the differential rotation rates are very different near the top of convection zone. In fact the solar observation suggests that the rotation rates decrease near the top of convection zone, which is the opposite of the trend in figure 5. However, near the bottom and in the bulk of the convection zone, the rotation rates from the ASH simulations using the combined eddy viscosity are very similar to those in figure 2. This implies that we may expect to find similar differential rotation profile once we implement a better model than Equation (4.2) for the eddy viscosity near the top of convection zone. Better results may be obtained as well once we implement the fully local Smagorinsky-Lilly's eddy viscosity.

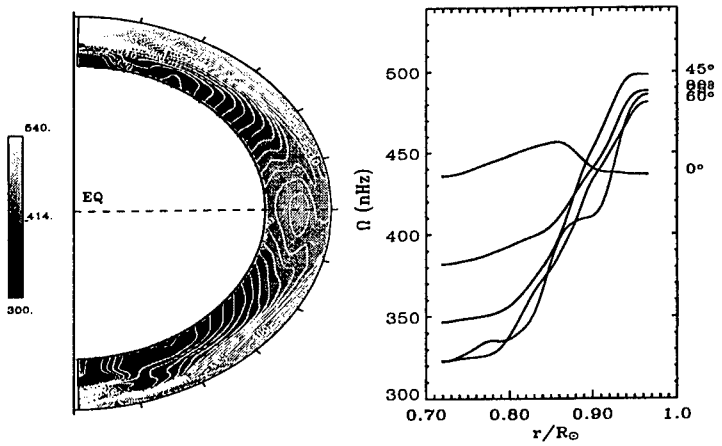


FIGURE 5. Panels (a) and (b): Differential rotation using the eddy viscosity with a transition to the mixing length viscosity near the boundaries of convection zone.

REFERENCES

BRUN, A. S. & TOOMRE, J. 2002 Turbulent convection under the influence of rotation: sustaining a strong differential rotation. *Astrophysical Journal* **570**, 865.

CHRISTENSEN-DALSGAARD, J., PROFFITT, C. R. & THOMPSON, M. J. 1993 Effects of diffusion on solar models and their oscillation frequencies. *Astrophysical Journal* **403**, L75.

CLUNE, T. C., ELLIOTT, J. R., MIESCH, M. S. & TOOMRE, J. 1999 Computational aspects of a code to study rotating turbulent convection in spherical shells. *Parallel Computing* **25**, 361.

GILMAN, P. A. & GLATZMAIER, G. A. 1981 Compressible convection in a rotating spherical shell. I. Anelastic equations. *Astrophysical Journal Suppl.* **45**, 335.

GOUGH, D. O. 1969 The anelastic approximation for thermal convection. *J. Atmo. Sci.* **26**, 448.

LILLY, D. K. 1962 On the numerical simulation of buoyant convection. *Tellus* **24**, 148.

MIESCH, M. S. 1998 Turbulence and convection in stellar and interstellar environments. PhD thesis. University of Coloardo, Boulder.

Dynamic turbulence modelling in large-eddy simulations of the cloud-topped atmospheric boundary layer

By M. P. Kirkpatrick, N. N. Mansour, A. S. Ackerman †, and D. E. Stevens ‡

1. Motivation and Objectives

The use of large eddy simulation, or LES, to study the atmospheric boundary layer dates back to the early 1970s when Deardorff (1972) used a three-dimensional simulation to determine velocity and temperature scales in the convective boundary layer. In 1974 he applied LES to the problem of mixing layer entrainment (Deardorff 1974) and in 1980 to the cloud-topped boundary layer (Deardorff 1980*b*). Since that time the LES approach has been applied to atmospheric boundary layer problems by numerous authors.

While LES has been shown to be relatively robust for simple cases such as a clear, convective boundary layer (Mason 1989), simulation of the cloud-topped boundary layer has proved more of a challenge. The combination of small length scales and anisotropic turbulence coupled with cloud microphysics and radiation effects places a heavy burden on the turbulence model, especially in the cloud-top region. Consequently, over the past few decades considerable effort has been devoted to developing turbulence models that are better able to parameterise these processes. Much of this work has involved taking parameterisations developed for neutral boundary layers and deriving corrections to account for buoyancy effects associated with the background stratification and local buoyancy sources due to radiative and latent heat transfer within the cloud (see Lilly 1962; Deardorff 1980*a*; Mason 1989; MacVean & Mason 1990, for example). In this paper we hope to contribute to this effort by presenting a number of turbulence models in which the model coefficients are calculated dynamically during the simulation rather than being prescribed *a priori*.

The dynamic procedure, first proposed by Germano *et al.* (1991), computes model coefficients using information contained in the resolved velocity and scalar fields. In this sense dynamic models can be considered self-calibrating, a feature that makes them an appealing choice for dealing with the complex interactions between the hydrodynamics, radiation and cloud microphysics occurring within clouds. Nevertheless, while dynamic turbulence models have been used with considerable success for complex engineering flows (see Boivin *et al.* 2000; Branley & Jones 2001, for example), their application to atmospheric flows has been very limited.

The objective of this paper is to present a set of dynamic turbulence models written in a form appropriate for large eddy simulations of the atmospheric boundary layer in which the flow is described using equations of motion in anelastic form . The models are tested using simulations of a nocturnal marine stratocumulus cloud observed during during the second Dynamics and Chemistry of Marine Stratocumulus (DYCOMS-II) field experiment. This test case includes a number of features that typically cause problems

† NASA Ames, Earth Science Division
‡ Lawrence Livermore National Laboratory

in simulations of the atmospheric boundary layer, including the presence of a strong temperature inversion at the level of the cloud top, and positive feedback loops involving turbulent entrainment across the inversion, radiation and cloud microphysics. As such, these simulations provide a good test for the utility of our models. Simulations are performed using the atmospheric boundary layer LES code, DHARMA, (Stevens & Bretherton 1999; Stevens *et al.* 2000), with dynamic turbulence models computed using the new LLAMA code presented here.

2. Dynamic turbulence models for the anelastic equations

The dynamics of the cloud-topped atmospheric boundary layer can be described using equations for conservation of mass, momentum, liquid water potential temperature and total water mixing ratio. These equations are written in the anelastic form of Ogura & Phillips (1962) in which the thermodynamic variables such as pressure p are decomposed into an isentropic base state p_0 (corresponding to a uniform potential temperature θ_0) and a dynamic component. Following Clark (1979), the dynamic component is further decomposed into an initial environmental deviation in hydrostatic balance p_1 and a time-evolving dynamic perturbation p_2 to give

$$p(x,y,z,t) = p_0(z) + p_1(z) + p_2(x,y,z,t). \tag{2.1}$$

After subtracting hydrostatic balances, the resulting continuous equations are written,

$$\frac{\partial \varrho_0 u_i}{\partial t} + \frac{\partial(\varrho_0 u_i u_j)}{\partial x_j} = -\frac{\partial p_2}{\partial x_i} + \delta_{i3} g \frac{\varrho_0 \theta_{v2}}{\theta_0} - \epsilon_{ijk} \varrho_0 f_j u_k + H_{u_i}, \tag{2.2}$$

$$\frac{\partial \varrho_0 \theta_l^*}{\partial t} + \frac{\partial(\varrho_0 \theta_l^* u_j)}{\partial x_j} = H_{\theta_l^*}, \tag{2.3}$$

$$\frac{\partial \varrho_0 q_t}{\partial t} + \frac{\partial(\varrho_0 q_t u_j)}{\partial x_j} = H_{q_t}, \tag{2.4}$$

$$\frac{\partial(\varrho_0 u_j)}{\partial x_j} = 0. \tag{2.5}$$

Here u_i are the Cartesian components of the velocity vector, ϱ the density, δ_{ij} the Kronecker delta, ϵ_{ijk} the permutation tensor, f_j the Coriolis parameter, g the acceleration due to gravity, q_t the total water mixing ratio and $\theta_l^* = (\theta_l - \theta_0)/\theta_0$ a scaled liquid water potential temperature. Total water mixing ratio is the sum of the liquid and vapour mixing ratios,

$$q_t = q_c + q_v = \frac{\varrho_c + \varrho_v}{\varrho_d}, \tag{2.6}$$

where ϱ_c, ϱ_v and ϱ_d are the density of the condensed water, water vapour and dry air respectively. Liquid water potential temperature is defined as

$$\theta_l = \theta - \frac{L q_c}{C_{pd} \pi_0}. \tag{2.7}$$

Here L is the latent heat of vaporisation, C_{pd} the specific heat at constant pressure for dry air and $\pi_0 = \left(\frac{p_0}{p_{ref}}\right)^{\frac{R_d}{C_p}}$ with p_{ref} a reference pressure and R_d the gas constant of dry air. The virtual potential temperature θ_v appearing in the buoyancy term of the

momentum equations is given by

$$\theta_v = \theta + \theta_0 \left[\left(\frac{R_d}{R_v} - 1 \right) q_v - q_c \right], \tag{2.8}$$

where R_v is the gas constant for water vapour. The terms H_{u_i}, $H_{\theta_l^*}$ and H_{q_t} are source terms that include parameterisations for physical processes such as radiation, precipitation and the effects of the global atmospheric circulation.

In a large eddy simulation, the equations are filtered to remove from the solution those fluctuations that cannot be resolved by the numerical method. For the anelastic equations it is convenient to use a density-weighted or Favre filter, where a Favre filtered variable is defined as $\widetilde{\phi} = \overline{\varrho\phi}/\overline{\varrho}$. Application of this filter to the equations gives

$$\frac{\partial \overline{\varrho}_0 \widetilde{u}_i}{\partial t} + \frac{\partial (\overline{\varrho}_0 \widetilde{u}_i \widetilde{u}_j)}{\partial x_j} = -\frac{\partial \overline{p}_2}{\partial x_i} + \delta_{i3} g \frac{\overline{\varrho}_0 \widetilde{\theta}_{v2}}{\theta_0} - \epsilon_{ijk} \overline{\varrho}_0 \widetilde{u}_k f_j + H_{u_i} - \frac{\partial \tau_{ij}}{\partial x_j}, \tag{2.9}$$

$$\frac{\partial \overline{\varrho}_0 \widetilde{\theta}_l^*}{\partial t} + \frac{\partial (\overline{\varrho}_0 \widetilde{\theta}_l^* \widetilde{u}_j)}{\partial x_j} = H_{\theta_l^*} - \frac{\partial \gamma_{\theta_l^*}}{\partial x_j}, \tag{2.10}$$

$$\frac{\partial \overline{\varrho}_0 \widetilde{q}_t}{\partial t} + \frac{\partial (\overline{\varrho}_0 \widetilde{q}_t \widetilde{u}_j)}{\partial x_j} = H_{q_t} - \frac{\partial \gamma_{q_t}}{\partial x_j}, \tag{2.11}$$

$$\frac{\partial (\overline{\varrho}_0 \widetilde{u}_j)}{\partial x_j} = 0, \tag{2.12}$$

with subgrid scale stresses and fluxes given by

$$\tau_{ij} = \overline{\varrho}_0 \left(\widetilde{u_i u_j} - \widetilde{u}_i \widetilde{u}_j \right), \tag{2.13}$$

$$\gamma_{\theta_l^*} = \overline{\varrho}_0 \left(\widetilde{\theta_l^* u_j} - \widetilde{\theta}_l^* \widetilde{u}_j \right), \tag{2.14}$$

$$\gamma_{q_t} = \overline{\varrho}_0 \left(\widetilde{q_t u_j} - \widetilde{q}_t \widetilde{u}_j \right). \tag{2.15}$$

We have assumed here that f_j is constant so that the Coriolis term is linear - an assumption that is valid when the domain is small compared to the Rossby radius of deformation. The source terms H are shown without an overbar since they are parameterisations rather than exact terms.

The Smagorinsky model (Smagorinsky 1963) for the subgrid scale stress is

$$\tau_{ij}^a = \tau_{ij} - \frac{1}{3} \delta_{ij} \tau_{kk} = -2 \overline{\varrho}_0 K_m \widetilde{D}_{ij} C_B, \tag{2.16}$$

where $\widetilde{D}_{ij}$ is the strain rate tensor,

$$\widetilde{D}_{ij} = \frac{1}{2} \left(\frac{\partial \widetilde{u}_i}{\partial x_j} + \frac{\partial \widetilde{u}_j}{\partial x_i} \right) - \frac{1}{3} \delta_{ij} \frac{\partial \widetilde{u}_k}{\partial x_k}. \tag{2.17}$$

Here and elsewhere in this paper the superscript ^{a} is used to denote the anisotropic part of a tensor. The eddy viscosity K_m is given by

$$K_m = C \Delta^2 \left| \widetilde{D} \right|, \tag{2.18}$$

with $\left| \widetilde{D} \right| = \sqrt{2 \widetilde{D}_{ij} \widetilde{D}_{ij}}$ and C a dimensionless coefficient. Stratification effects are ac-

counted for using the correction of Lilly (1962),

$$C_B = (1 - Ri_{sgs})^{1/2} \qquad Ri_{sgs} < 1 \tag{2.19}$$

$$C_B = 0 \qquad Ri_{sgs} \geq 1, \tag{2.20}$$

where the subgrid scale flux Richardson number is estimated using

$$Ri_{sgs} = \frac{g/\theta_0 \, \partial\widetilde{\theta}_v/\partial z}{Pr_{sgs}|\widetilde{D}|^2}. \tag{2.21}$$

Pr_{sgs} is the subgrid scale turbulent Prandtl number, which we set to a constant value of $Pr_{sgs} = 0.4$.

The mixed model of Bardina *et al.* (1983), combines the Smagorinsky model with the scale similarity model of Bardina *et al.* (1980). The model is derived by rewriting the subgrid scale stress tensor in terms of resolved and unresolved parts of the velocity field $u_i = \widetilde{u}_i + u_i'$ using the decomposition of Germano (1986). For the anelastic equations this decomposition takes the form

$$\tau_{ij} = L_{ij}^* + C_{ij}^* + R_{ij}^*, \tag{2.22}$$

where the modified Leonard, cross and SGS Reynolds terms are

$$L_{ij}^* = \overline{\varrho}_0(\widetilde{\widetilde{u}_i\widetilde{u}_j} - \widetilde{\widetilde{u}}_i\widetilde{\widetilde{u}}_j) \tag{2.23}$$

$$C_{ij}^* = \overline{\varrho}_0(\widetilde{\widetilde{u}_i u'_j} + \widetilde{u'_i\widetilde{u}_j} - \widetilde{\widetilde{u}}_i\widetilde{u'}_j - \widetilde{u'}_i\widetilde{\widetilde{u}}_j) \tag{2.24}$$

$$R_{ij}^* = \overline{\varrho}_0(\widetilde{u'_i u'_j} - \widetilde{u'}_i\widetilde{u'}_j). \tag{2.25}$$

The modified Leonard term, which contains only resolved scale quantities, can be calculated explicitly leaving the modified cross and SGS Reynolds terms to be parameterised using the Smagorinsky model,

$$\tau_{ij} = L_{ij}^* - 2\overline{\varrho}_0 C\Delta^2 \left|\widetilde{D}\right| \widetilde{D}_{ij} C_B. \tag{2.26}$$

Martin *et al.* (2000) note that, with the mixed model, the isotropic part of the subgrid scale stress τ_{ij} can be represented at least partially by the isotropic part of the modified Leonard term. In fact they obtained the closest agreement with experiment for their compressible flow test cases when they assumed that the isotropic part of L_{ij}^* models the whole of $\frac{1}{3}\delta_{ij}\tau_{kk}$. We have adopted the same approach in Eq.(2.26).

In dynamic versions of these models, the model coefficient C is calculated dynamically. To achieve this, a test filter is applied to the velocity and scalar fields to extract information from the smallest resolved scales. Application of a spatial test filter (denoted here by a caret) to the filtered momentum equations gives

$$\frac{\partial\widehat{\overline{\varrho}_0\widetilde{u}_i}}{\partial t} + \frac{\partial(\widehat{\overline{\varrho}_0\widetilde{u}_i\widetilde{u}_j})}{\partial x_j} = -\frac{\partial\widehat{\overline{p}_2^*}}{\partial x_i} + \delta_{i3}g\frac{\widehat{\overline{\varrho}_0\widetilde{\theta}_{v2}}}{\theta_0} - \epsilon_{ijk}\widehat{\overline{\varrho}_0\widetilde{u}_k}f_j + H_{u_i} - \frac{\partial\widehat{\tau}_{ij}}{\partial x_j}. \tag{2.27}$$

In order to rewrite this equation in a form similar to Eq.(2.9) we adopt a Favre test filter $\breve{\phi} = \widehat{\varrho\phi}/\widehat{\varrho}$ giving

$$\frac{\partial\widehat{\overline{\varrho}}_0\breve{\widetilde{u}}_i}{\partial t} + \frac{\partial(\widehat{\overline{\varrho}}_0\widetilde{u}_i\breve{\widetilde{u}}_j)}{\partial x_j} = -\frac{\partial\widehat{\overline{p}_2^*}}{\partial x_i} + \delta_{i3}g\frac{\widehat{\overline{\varrho}}_0\breve{\widetilde{\theta}}_{v2}}{\theta_0} - \epsilon_{ijk}\widehat{\overline{\varrho}}_0\breve{\widetilde{u}}_k f_j + H_{u_i} - \frac{\partial\widehat{\tau}_{ij}}{\partial x_j}. \tag{2.28}$$

Since density varies only in the z direction, this equation can be simplified considerably

by using two-dimensional horizontal test filter rather than a three-dimensional one. The Favre test filter is then equivalent to a spatial test filter,

$$\breve{\widehat{\phi}} \equiv \widehat{\widehat{\phi}}, \tag{2.29}$$

and the density field is unchanged by the test filtering operation, that is,

$$\widehat{\overline{\varrho}}_0 = \overline{\varrho}_0. \tag{2.30}$$

From Eqs.(2.29) and (2.30), with horizontal test filtering Eq.(2.28) becomes

$$\frac{\partial \overline{\varrho}_0 \widehat{\widetilde{u}}_i}{\partial t} + \frac{\partial (\overline{\varrho}_0 \widehat{\widetilde{u}_i \widetilde{u}_j})}{\partial x_j} = -\frac{\partial \widehat{\overline{p}_2^*}}{\partial x_i} + \delta_{i3} \widehat{\overline{\varrho}}_2 g - \epsilon_{ijk} \overline{\varrho}_0 \widehat{\widetilde{u}}_k f_j + H_{u_i} - \frac{\partial \widehat{\tau}_{ij}}{\partial x_j}. \tag{2.31}$$

Extracting the resolved stress $\mathcal{L}_{ij} = \overline{\varrho}_0(\widehat{\widetilde{u}_i \widetilde{u}_j} - \widehat{\widetilde{u}}_i \widehat{\widetilde{u}}_j)$ then gives

$$\frac{\partial \overline{\varrho}_0 \widehat{\widetilde{u}}_i}{\partial t} + \frac{\partial (\overline{\varrho}_0 \widehat{\widetilde{u}}_i \widehat{\widetilde{u}}_j)}{\partial x_j} = -\frac{\partial \widehat{\overline{p}_2^*}}{\partial x_i} + \delta_{i3} \widehat{\overline{\varrho}}_2 g - \epsilon_{ijk} \overline{\varrho}_0 \widehat{\widetilde{u}}_k f_j + H_{u_i} - \frac{\partial \widehat{\tau}_{ij}}{\partial x_j} - \frac{\partial \mathcal{L}_{ij}}{\partial x_j}. \tag{2.32}$$

Alternatively, application of the grid and test filters together to the continuous equations gives

$$\frac{\partial \overline{\varrho}_0 \widehat{\widetilde{u}}_i}{\partial t} + \frac{\partial (\overline{\varrho}_0 \widehat{\widetilde{u}}_i \widehat{\widetilde{u}}_j)}{\partial x_j} = -\frac{\partial \widehat{\overline{p}_2^*}}{\partial x_i} + \delta_{i3} \widehat{\overline{\varrho}}_2 g - \epsilon_{ijk} \overline{\varrho}_0 \widehat{\widetilde{u}}_k f_j + H_{u_i} - \frac{\partial T_{ij}}{\partial x_j}, \tag{2.33}$$

where

$$T_{ij} = \overline{\varrho}_0 \left(\widehat{\widetilde{u}_i \widetilde{u}_j} - \widehat{\widetilde{u}}_i \widehat{\widetilde{u}}_j \right). \tag{2.34}$$

Comparison of Eqs.(2.32) and (2.33) gives the Germano identity,

$$\mathcal{L}_{ij} = T_{ij} - \widehat{\tau}_{ij}. \tag{2.35}$$

The dynamic procedure assumes that the same parameterisation that is used to parameterise the SGS stress at the grid filter level τ_{ij} can be used to model the test level stress T_{ij}. The test level stress for the Smagorinsky and mixed models are written as

$$T_{ij}^a = -2\overline{\varrho}_0 C \widehat{\Delta}^2 \left| \widehat{\widetilde{D}} \right| \widehat{\widetilde{D}}_{ij} \widehat{C}_B, \tag{2.36}$$

and

$$T_{ij} = L_{ij}^{*T} - 2\overline{\varrho}_0 C \widehat{\Delta}^2 \left| \widehat{\widetilde{D}} \right| \widehat{\widetilde{D}}_{ij} \widehat{C}_B, \tag{2.37}$$

respectively. Here $\widehat{C}_B$ is given by

$$\widehat{C}_B = \left(1 - \widehat{Ri}_{sgs}\right)^{1/2} \qquad \widehat{Ri}_{sgs} < 1 \tag{2.38}$$

$$\widehat{C}_B = 0 \qquad \widehat{Ri}_{sgs} \geq 1, \tag{2.39}$$

with the test level Richardson number given by

$$\widehat{Ri}_{sgs} = \frac{g/\theta_0 \, \partial \widehat{\widetilde{\theta}}_v / \partial z}{Pr_{sgs} |\widehat{\widetilde{D}}|^2}. \tag{2.40}$$

The test level modified Leonard term in the mixed model L_{ij}^{*T} is found by decomposing T_{ij}

in a manner similar to the decomposition of τ_{ij} (see Eq.(2.22)). Substituting $u_i = \widehat{\widetilde{u}}_i + u_i''$ into Eq.(2.34) gives

$$T_{ij} = L_{ij}^{*T} + C_{ij}^{*T} + R_{ij}^{*T}, \tag{2.41}$$

where the modified Leonard, cross and Reynolds terms at the test level are

$$L_{ij}^{*T} = \overline{\varrho}_0(\widehat{\widehat{\widetilde{u}}_i\widetilde{u}_j} - \widehat{\widehat{\widetilde{u}}}_i\widehat{\widetilde{u}}_j) \tag{2.42}$$

$$C_{ij}^{*T} = \overline{\varrho}_0(\widehat{\widehat{\widetilde{u}}_i u_j''} + \widehat{\widetilde{u}_i''\widetilde{u}_j} - \widehat{\widehat{\widetilde{u}}}_i\widehat{\widetilde{u}_j''} - \widehat{\widetilde{u}_i''}\widehat{\widetilde{u}}_j) \tag{2.43}$$

$$R_{ij}^{*T} = \overline{\varrho}_0(\widehat{\widetilde{u}_i''u_j''} - \widehat{\widetilde{u}_i''}\widehat{\widetilde{u}_j''}). \tag{2.44}$$

In Eqs.(2.36-2.44) we have again used the fact that we assume a horizontal test filter so that Eqs.(2.29-2.30) can be used to simplify the equations.

The decomposition shown in Eqs.(2.42-2.44) is different from that derived by Zang *et al.* (1993), who used a decomposition based on $u_i = \widetilde{u}_i + u_i'$ at both the grid and test level, rather than the form $u_i = \widehat{\widetilde{u}}_i + u_i''$ used here for the test level. As noted by Vreman *et al.* (1994), the latter is more consistent with the dynamic procedure since the test level stress should be written in terms of test filtered velocity components in order to make the test level parameterisations analogous to those used at the grid level.

Substituting the parameterisations for the subgrid scale stress τ_{ij} (Eq.(2.26)) and test level stress T_{ij} (Eq.(2.37)) into the Germano identity (Eq.(2.35)) gives

$$\begin{aligned}\overline{\varrho}_0(\widehat{\widetilde{u}_i\widetilde{u}_j} - \widehat{\widetilde{u}}_i\widehat{\widetilde{u}}_j) = \; & \overline{\varrho}_0(\widehat{\widehat{\widetilde{u}}_i\widetilde{u}_j} - \widehat{\widehat{\widetilde{u}}}_i\widehat{\widetilde{u}}_j) - 2\overline{\varrho}_0 C\widehat{\Delta}^2 \left|\widehat{\widetilde{D}}\right| \widehat{\widetilde{D}}_{ij}\widehat{C}_B \\ & -\overline{\varrho}_0(\widehat{\widetilde{u}_i\widetilde{u}_j} - \widehat{\widetilde{u}}_i\widetilde{u}_j) + 2\overline{\varrho}_0 C\Delta^2 \widehat{\left|\widetilde{D}\right| \widetilde{D}_{ij}} C_B.\end{aligned} \tag{2.45}$$

Removing the constant factor $\overline{\varrho}_0$, and contracting tensors using the least squares approach of Lilly (1992) gives an equation for the model coefficient in the dynamic mixed model,

$$C\Delta^2 = -\frac{< M_{ij}(\mathcal{L}_{ij}^* - H_{ij}) >}{< 2M_{kl}M_{kl} >}, \tag{2.46}$$

where

$$\mathcal{L}_{ij}^* = \widehat{\widetilde{u}_i\widetilde{u}_j} - \widehat{\widetilde{u}}_i\widehat{\widetilde{u}}_j, \tag{2.47}$$

$$M_{ij} = \alpha^2 \left|\widehat{\widetilde{D}}\right| \widehat{\widetilde{D}}_{ij}\widehat{C}_B - \widehat{\left|\widetilde{D}\right| \widetilde{D}_{ij}} C_B, \tag{2.48}$$

$$H_{ij} = (\widehat{\widehat{\widetilde{u}}_i\widetilde{u}_j} - \widehat{\widehat{\widetilde{u}}}_i\widehat{\widetilde{u}}_j) - (\widehat{\widetilde{u}_i\widetilde{u}_j} - \widehat{\widetilde{u}}_i\widetilde{u}_j), \tag{2.49}$$

α is the ratio of the test and grid filters

$$\alpha = \widehat{\Delta}/\Delta, \tag{2.50}$$

and $< >$ indicates averaging on horizontal planes. Equivalently, for the dynamic Smagorinsky model,

$$C\Delta^2 = -\frac{< M_{ij}\mathcal{L}_{ij}^{*a} >}{< 2M_{kl}M_{kl} >}. \tag{2.51}$$

The models outlined above use the original dynamic procedure of Germano *et al.* (1991) and require averaging in homogeneous directions to remain stable. Ghosal *et al.*

(1995) recast the dynamic procedure as a constrained variational problem and used this approach to develop a "dynamic localization model" that does not require averaging. This model, however, requires the solution of an integral equation and is computationally expensive. A less expensive alternative proposed by Piomelli & Liu (1995) involves finding an approximate solution to the integral equation by using the value of C at the previous time step to give a first approximation C^*. Applying their procedure gives localised versions of the models. The coefficient for the localised dynamic Smagorinsky model is given by

$$C = -\frac{(\mathcal{L}_{ij}^{*a} - 2\widehat{C^* B_{ij}})A_{ij}}{2A_{kl}A_{kl}}. \tag{2.52}$$

where,

$$A_{ij} = \alpha^2 \Delta^2 \left|\widehat{\widetilde{D}}\right| \widehat{\widetilde{D}}_{ij} \widehat{C}_B, \tag{2.53}$$

$$B_{ij} = \Delta^2 \left|\widetilde{D}\right| \widetilde{D}_{ij} C_B. \tag{2.54}$$

The coefficient for the localised dynamic mixed model is

$$C = -\frac{(\mathcal{L}_{ij}^{*} - H_{ij} - 2\widehat{C^* B_{ij}})A_{ij}}{2A_{ij}A_{ij}}, \tag{2.55}$$

with A_{ij} and B_{ij} given by Eqs.(2.53) and (2.54) respectively and H_{ij} given by Eq.(2.49).

We note here that by using a horizontal test filter we have reduced the complexity of our models considerably. With three-dimensional test filtering the models would be of similar complexity to the equivalent dynamic models for compressible flow whereas, when a horizontal filter is used, the models for the anelastic equations become similar to those for incompressible flow. In fact, if the discretisation operator is taken as being equivalent to the first level of grid scale Favre filtering (that is, we assume implicit filtering at the grid scale), then the only difference in the implementation occurs in the mixed model, where the second grid scale filter in the formula for H_{ij} (Eq.(2.49)) is a Favre filter that must be applied explicitly.

An interesting feature of the localised dynamic model is that, if unconstrained, it can calculate negative values for the model coefficient, and thus predict regions of negative eddy viscosity. While such regions may be interpreted as regions of backscatter, or energy transfer from small to large scales, Ghosal *et al.* (1995) and Carati *et al.* (1995) note that the dynamic Smagorinsky model has no information about how much energy is actually available in the subgrid scales. Consequently, there is no mechanism by which such a "counter-gradient diffusion" model for backscatter can be turned off once all the subgrid scale energy has been removed. For this reason we chose to clip the eddy viscosity at zero. For the localised model backscatter is therefore included. For the plane averaged dynamic Smagorinsky model, however, the effect of backscatter is included in an average sense through a reduction of the plane averaged model coefficient. As noted above, in the mixed model the Leonard term allows backscatter, so there is no need to resort to using a negative eddy viscosity.

The Smagorinsky and mixed models for the subgrid scale fluxes of the scalar variables

are written

$$\gamma_\phi = -\overline{\varrho}_0 C_\phi \Delta^2 \left|\widetilde{D}\right| \frac{\partial \widetilde{\phi}}{\partial x_j} C_B, \tag{2.56}$$

$$\gamma_\phi = \overline{\varrho}_0 (\widetilde{\widetilde{\phi}\widetilde{u}_j} - \widetilde{\widetilde{\phi}}\widetilde{\widetilde{u}}_j) - \overline{\varrho}_0 C_\phi \Delta^2 \left|\widetilde{D}\right| \frac{\partial \widetilde{\phi}}{\partial x_j} C_B. \tag{2.57}$$

Here ϕ is a generic scalar representing θ_l^* or q_t. The mixed model includes a term representing the scalar equivalent of the modified Leonard term,

$$L_{\phi j}^* = \overline{\varrho}_0 (\widetilde{\widetilde{\phi}\widetilde{u}_j} - \widetilde{\widetilde{\phi}}\widetilde{\widetilde{u}}_j). \tag{2.58}$$

Equations for the model coefficients are then written in a form analogous to that used for the subgrid scale stress. For the plane averaged dynamic Smagorinsky model,

$$C_\phi \Delta^2 = -\frac{< F_j E_j >}{< F_k F_k >}, \tag{2.59}$$

where the resolved flux E_j is given by

$$E_j = \widehat{\widetilde{\phi}\widetilde{u}_j} - \widehat{\widetilde{\phi}}\widehat{\widetilde{u}}_j, \tag{2.60}$$

and

$$F_j = \alpha^2 \left|\widehat{\widetilde{D}}\right| \frac{\partial \widehat{\widetilde{\phi}}}{\partial x_j} \widehat{C}_B - \left|\widetilde{D}\right| \widehat{\frac{\partial \widetilde{\phi}}{\partial x_j}} C_B. \tag{2.61}$$

For the dynamic mixed model,

$$C_\phi \Delta^2 = -\frac{< F_j (E_j - G_j) >}{< F_k F_k >}, \tag{2.62}$$

where

$$G_j = (\widehat{\widehat{\widetilde{\phi}\widetilde{u}_j}} - \widehat{\widehat{\widetilde{\phi}}}\widehat{\widehat{\widetilde{u}}_j}) - (\widehat{\widetilde{\phi}\widetilde{u}_j} - \widehat{\widetilde{\phi}}\widehat{\widetilde{u}}_j). \tag{2.63}$$

The coefficient for the localised dynamic Smagorinsky model is given by

$$C_\phi = -\frac{(E_j - \widehat{C_\phi^* Q_j}) P_j}{P_k P_k}, \tag{2.64}$$

where

$$P_j = \alpha^2 \Delta^2 \left|\widehat{\widetilde{D}}\right| \frac{\partial \widehat{\widetilde{\phi}}}{\partial x_j} \widehat{C}_B, \tag{2.65}$$

$$Q_j = \Delta^2 \left|\widetilde{D}\right| \frac{\partial \widetilde{\phi}}{\partial x_j} C_B. \tag{2.66}$$

The coefficient for the localised dynamic mixed model is

$$C_\phi = -\frac{(E_j - G_j - \widehat{C_\phi^* Q_j}) P_j}{P_k P_k}, \tag{2.67}$$

with P_j and Q_j given by Eqs.(2.65) and (2.66) respectively, and G_j given by Eq.(2.63).

Close to the rough surface at the bottom of the domain the size of the turbulent eddies decreases and the turbulence models described above do not give the correct dissipation.

The standard Smagorinsky model is over-dissipative while the dynamic models are under-dissipative. With the standard Smagorinsky model we use a damping function suggested by Mason (1994),

$$\frac{1}{\Delta^{*2}} = \frac{1}{\Delta^2} + \frac{1}{(k(z+z_0))^2}, \tag{2.68}$$

where k is the Von Kàrmàn constant and z_0 the roughness length. With all models we also add a surface layer stress term suggested by Brown *et al.* (2001). This stress takes the form

$$\tau_{sfc} = -\int C_{sfc} a(z) \rho_0 |\boldsymbol{u}| \phi dz, \tag{2.69}$$

where C_{sfc} is a scaling factor, a(z) a smoothing function, $|\boldsymbol{u}|$ the horizontal wind speed and ϕ the dependent variable. At present we follow Chow & Street (2002) and choose C_{sfc} to give τ_{sfc} equal to half the surface flux at the first grid point above the wall.

3. Simulation results

The test case chosen for the simulations is the first research flight (RF01) of the second Dynamics and Chemistry of Marine Stratocumulus (DYCOMS-II) field experiment. The computational domain extends 3.2km in the two horizontal directions and 1.5km in the vertical direction, with $96 \times 96 \times 128$ cells in the x, y and z directions respectively. Cell-spacing is uniform in the horizontal directions and stretched in the vertical direction to give cells of height 5m close to the bottom surface and in the vicinity of the inversion. This grid is typical of that currently used in large eddy simulations of the atmospheric boundary layer. The spatial discretisation uses a second-order centered scheme with no flux limiting, while time integration uses a second order Runge-Kutta scheme. The simulation is integrated over a period of four hours. Further details of the simulation set-up are described in Kirkpatrick *et al.* (2003) and will not be repeated here.

In the following we compare results obtained with four of the SGS turbulence models described above: the standard Smagorinsky (SM), dynamic Smagorinsky (DSM), dynamic mixed (DMM) and localised dynamic Smagorinsky model (LDSM). The standard Smagorinsky model uses a constant coefficient of $C_S = C^{1/2} = 0.18$ and a Prandtl number of $Pr_{sgs} = 0.4$. For reference, we also show results obtained with no SGS model.

Figure 1 shows vertical profiles of condensed water, liquid water potential temperature, eddy viscosity and diffusivities and SGS Prandtl number predicted by the various models. These profiles are calculated by averaging over horizontal planes as well as over a time period of 30 minutes. All profiles are calculated for the last half hour of the simulation, that is for $t = 3.5 - 4$h. The dynamic Smagorinsky models give quantitatively similar profiles to the standard Smagorinsky model. LDSM gives somewhat higher average eddy viscosity and diffusivities than DSM. This is because negative values of eddy viscosity predicted by LDSM are clipped, whereas with DSM conditions that would produce local negative values have the effect of reducing the plane average. The unclipped model coefficient profiles for DSM and LDSM (not shown) were found to be almost identical. The dynamic mixed model gives lower values of eddy viscosity and diffusivity because the Leonard term component of the SGS stress is included separately. All models predict a SGS turbulent Prandtl number close to the standard value of 0.4 through most the boundary layer, although DSM predicts an increase to a value of approximately 2 in the region just below the inversion. The reason for this behaviour, which is not seen with the other models, is not clear at present.

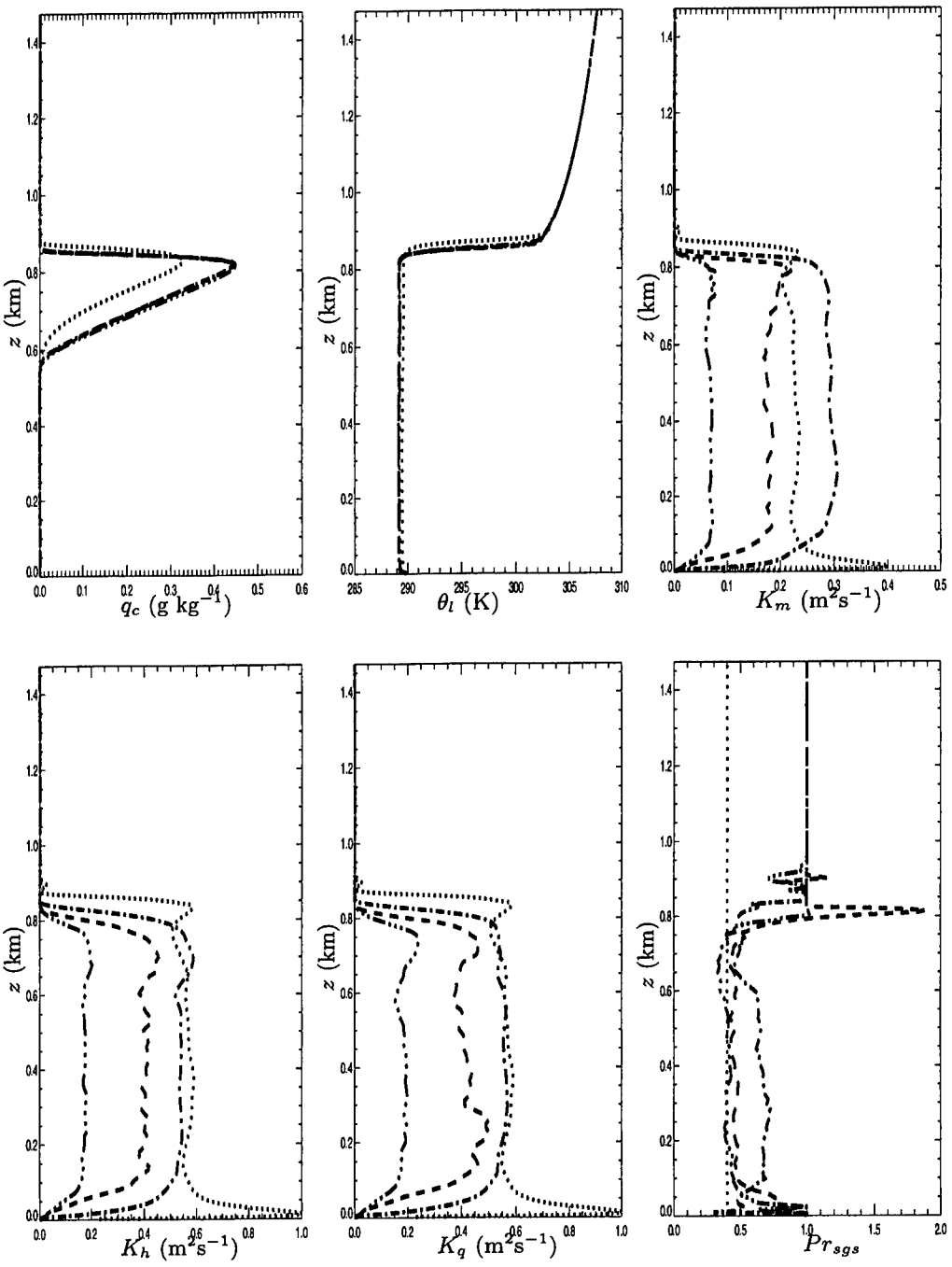


FIGURE 1. Vertical profiles of condensed water, liquid water potential temperature, eddy viscosity and diffusivities, and SGS Prandtl number: ··· SM, – – – DSM, – · – LDSM, – ··· – DMM.

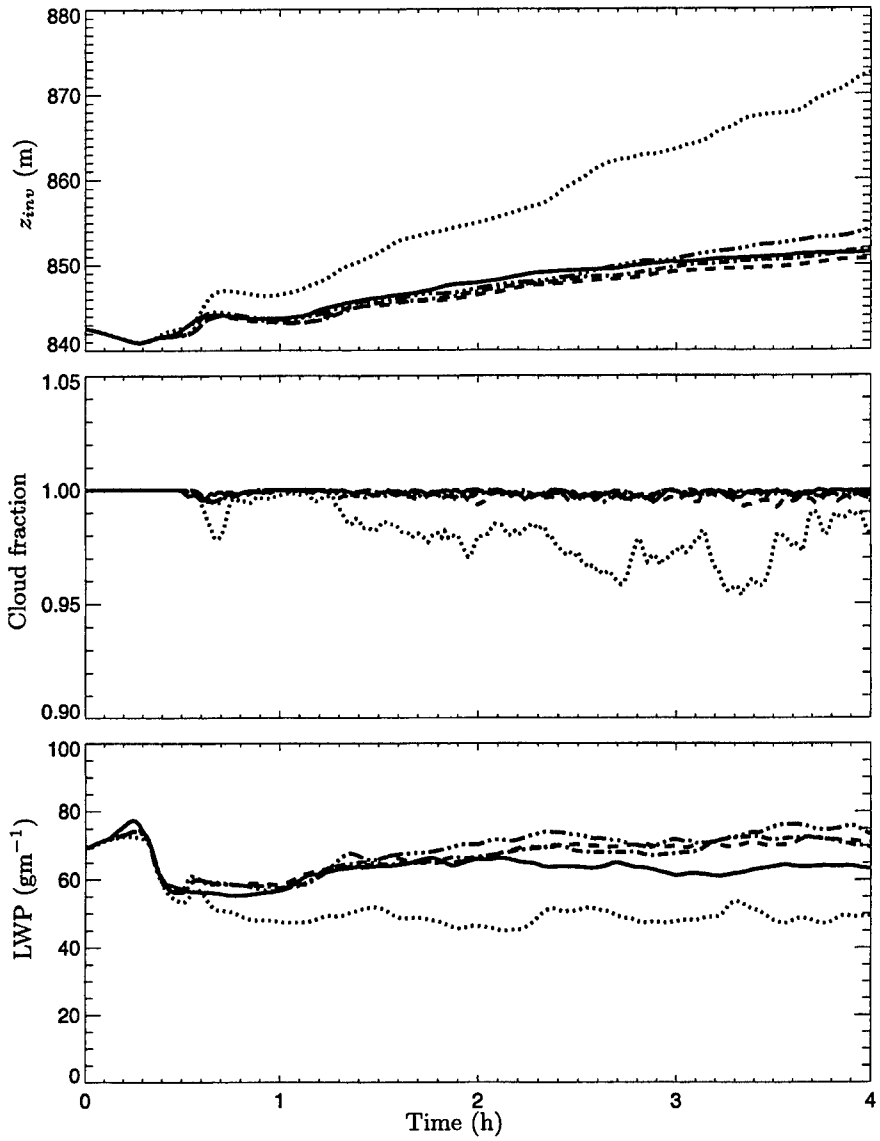


FIGURE 2. Time series of inversion height, cloud fraction and liquid water path: —— no SGS model, ··· SM, – – – DSM, – · – LDSM, – ··· – DMM.

Figure 2 shows time series of inversion height z_{inv}, liquid water path LWP and cloud fraction. The entrainment rate E can be estimated from the rate of change of z_{inv} using the formula,

$$E = \frac{dz_{inv}}{dt} - w_{sub}. \tag{3.1}$$

Here w_{sub} is the subsidence velocity, which for the present case is estimated to be -0.3cms^{-1}. dz_{inv}/dt is calculated as the average rate of change over the period $t = 2-4$h. The dynamic Smagorinsky models give an entrainment rate of approximately 0.36-

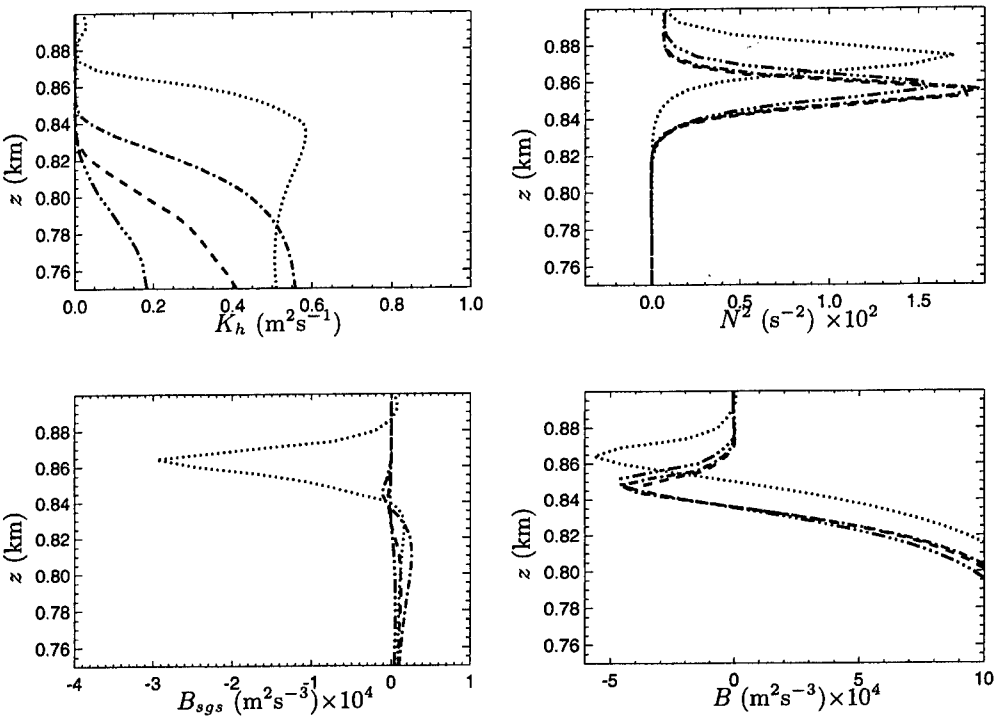


FIGURE 3. Eddy diffusivity, buoyancy frequency, and SGS and resolved buoyancy production at cloud-top: ··· SM, – – – DSM, – · – LDSM, – ···· – DMM.

0.37cms^{-1}, while the dynamic mixed model gives 0.40cms^{-1}. These results are in excellent agreement with the entrainment rate $E = 0.38 \pm 0.04$cms^{-1} estimated from observational measurements. The standard Smagorinsky model, however, overpredicts entrainment significantly giving $E \approx 0.55$cms^{-1}. The entrainment rate with no SGS model is 0.34cms^{-1}, which is slightly lower than that obtained with the dynamic models, but still within the error bounds of the observational measurements. The observed liquid water path and cloud fraction remained approximately constant during the experiment. This is also well predicted with dynamic models and no SGS model, while with the standard Smagorinsky model the results for these parameters again deviate significantly.

To help explain these differences, Figure 3 shows a comparison of the eddy diffusivity K_h, squared buoyancy frequency N^2, resolved buoyancy production B and subgrid scale buoyancy production B_{sgs}. Subgrid scale buoyancy production is approximated as

$$B_{sgs} \approx -K_h N^2. \tag{3.2}$$

The buoyancy frequency is calculated using a method described by Stevens *et al.* (2002). This approach is an extension of the work of MacVean & Mason (1990) and takes into account changes in stability that occur when subgrid scale mixing causes condensation or evaporation. Figure 3 shows the eddy diffusivity predicted by the standard Smagorinsky model decreasing through the inversion as a result of the stable stratification which drives the buoyancy correction coefficient C_B in the model to zero (see Eq.(2.16)). There is, however, a significant overlap region in which both the eddy diffusivity and buoyancy frequency are large. From Figure 3 and Eq.(2.16) it is clear that this overlap region

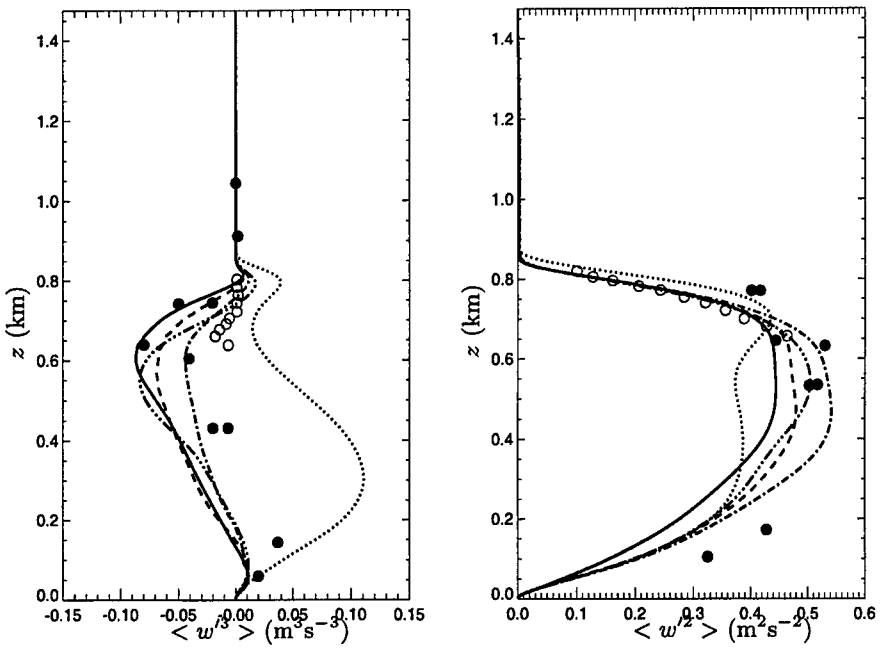


FIGURE 4. Second and third moments of vertical velocity. Simulation results (resolved component only): ——— no SGS model, ··· SM, – – – DSM, – · – LDSM, – ···· – DMM. Measurements: radar data (open circles), *in situ* measurements (filled circles).

also constitutes a zone of negative subgrid scale buoyancy production. Meanwhile the resolved buoyancy production with SM is similar to that seen with the other models. Negative buoyancy production is associated with conversion of mechanical energy into potential energy. In the present case this is interpreted as turbulence doing work to mix the warmer air above the inversion with cooler boundary-layer air below. Thus, the extra $-B_{sgs}$ provided by the standard Smagorinsky model is the cause of the enhanced entrainment rate seen with this model. Excessive entrainment of warm, dry air across the inversion then leads to the observed reduction of cloud fraction and liquid water path.

The same effect is not seen with the dynamic models which damp the model coefficient so that it becomes zero just *below* the inversion. Consequently there is no overlap region and no region of significant negative SGS buoyancy production. By coincidence, the same effect is also achieved when no SGS model is used, which explains the similarity between the results obtained with the dynamic models and no SGS model for large scale parameters such as entrainment rate, liquid water path and cloud fraction.

Figure 4 shows vertical profiles for the second and third moments of the resolved vertical velocity component compared with the observational measurements. The second moment is well predicted in the dynamic model simulations, with numerical results in excellent agreement with observations. The shape of the profiles obtained with the dynamic models is also typical of a well-mixed boundary layer as is expected for nocturnal stratocumulus. In contrast, the simulation using the standard Smagorinsky model does not agree as well with the observations and gives a two-peaked profile. Such a profile indicates a decoupling of the cloud layer and sub-cloud layer which is not apparent in the observational results.

The differences in profiles of the third moment are even more striking. The standard Smagorinsky model gives reasonable results in the surface layer, but does not give the negative values observed in the cloud layer. The dynamic models, on the other hand, give good agreement with the observations throughout the boundary layer, although, close to the surface they appear to under-predict the magnitude of this statistic somewhat. More work is required on the surface layer model to improve this.

4. Future work

The results presented in this paper clearly demonstrate the utility of dynamic turbulence models for atmospheric simulations. There is, however, much work still to be done. At present we are using a second-order accurate scheme for the spatial-discretisation. Consequently the numerical errors are of a similar magnitude to the terms associated with the subgrid scale models. The authors are currently working on a fourth-order scheme to resolve this issue. More work is also required in refining the surface layer model, especially where it is applied in combination with the dynamic models. As discussed above, dynamic models tend to underpredict the dissipation in the surface layer. This is because as the surface is approached the energetic eddies are no longer resolved and the assumptions underlying the dynamic procedure break down. While the current surface layer model helps to overcome these issues, the surface layer velocity and scalar profiles still deviate significantly from profiles predicted by similarity theory.

REFERENCES

BARDINA, J., FERZIGER, J. H. & REYNOLDS, W. C. 1980 Improved subgrid scale models for large eddy simulation. AIAA paper 80-1357.

BARDINA, J., FERZIGER, J. H. & REYNOLDS, W. C. 1983 Improved turbulence models based on large eddy simulation of homogeneous, incompressible, turbulent flows. *Tech. Rep.* TF-19. Stanford University, Thermosciences Division, Dept. of Mech. Engr.

BOIVIN, M., SIMONIN, O. & SQUIRES, K. D. 2000 On the prediction of gas-solid flows with two-way coupling using large eddy simulation. *Phys. Fluids* **12**, 2080–2090.

BRANLEY, N. & JONES, W. P. 2001 Large eddy simulation of a turbulent non-premixed flame. *Combust. and Flame* **127**, 1914–1934.

BROWN, A. R., HOBSON, J. M. & WOOD, N. 2001 Large-eddy simulation of neutral turbulent flow over rough sinusoidal ridges. *Bound.-Layer. Meteorol.* **98**, 411–441.

CARATI, D., GHOSAL, S. & MOIN, P. 1995 On the representation of backscatter in dynamic localization models. *Phys. Fluids* **7** (3), 606–616.

CHOW, F. K. & STREET, R. L. 2002 Modeling unresolved motions in LES of field-scale flows. In *15th Symposium on Boundary Layers and Turbulence, 15-19 July.*

CLARK, T. L. 1979 Numerical simulations with a three-dimensional cloud model: Lateral boundary condition experiments and multicellular severe storm simulations. *J. Atmos. Sci.* **36**, 2191–2215.

DEARDORFF, J. W. 1972 Convective velocity and temperature scales for the unstable planetary boundary layer and Rayleigh convection. *J. Atmos. Sci.* **27**, 1211–1213.

DEARDORFF, J. W. 1974 Three-dimensional numerical study of turbulence in an entraining mixed layer. *Bound.-Layer. Meteorol.* **7**, 199–226.

DEARDORFF, J. W. 1980*a* Stratocumulus-capped mixed layers derived from a 3-dimensional model. *Bound.-Layer. Meteorol.* **18** (4), 495 – 527.

DEARDORFF, J. W. 1980*b* Stratocumulus-capped mixed layers derived from a three-dimensional model. *Bound.-Layer. Meteorol.* **18**, 495–527.

GERMANO, M. 1986 A proposal for a redefinition of the turbulent stresses in the filtered Navier-Stokes equations. *Phys. Fluids* **29** (7), 2323–2324.

GERMANO, M., PIOMELLI, U., MOIN, P. & CABOT, W. H. 1991 A dynamic subgrid-scale eddy viscosity model. *Phys. Fluids* **A 3** (7), 1760–1765.

GHOSAL, S., LUND, T. S., MOIN, P. & AKSELVOLL, K. 1995 A dynamic localization model for large-eddy simulation of turbulent flows. *J. Fluid Mech.* **286**, 229–255.

KIRKPATRICK, M. P., ACKERMAN, A. S., MANSOUR, N. N. & STEVENS, D. E. 2003 Dynamic turbulence models for large-eddy simulations of the cloud-topped atmospheric boundary layer. In prep. for submission to J. Atmos. Sci.

LILLY, D. K. 1962 On the numerical simulation of buoyant convection. *Tellus* **14** (2), 148 – 172.

LILLY, D. K. 1992 A proposed modification of the Germano subgrid scale closure method. *Phys. Fluids* **A 4**, 633–635.

MACVEAN, M. K. & MASON, P. J. 1990 Cloud top entrainment instability through small-scale mixing and its parameterization in numerical models. *J. Atmos. Sci.* **47** (8), 1012–1030.

MARTIN, M. P., PIOMELLI, U. & CANDLER, G. V. 2000 Subgrid-scale models for compressible large-eddy simulations. *Theor. Comp. Fluid Dyn.* **13**, 361–376.

MASON, P. 1989 Large-eddy simulation of the convective atmospheric boundary-layer. *J. Atmos. Sci.* **46** (11), 1492–1516.

MASON, P. J. 1994 Large-eddy simulation: A critical review of the technique. *Quart. J. Royal Meteor. Soc.* **120** (515/pt.A), 1–26.

OGURA, Y. & PHILLIPS, N. 1962 Scale analysis of deep and shallow convection in the atmosphere. *J. Atmos. Sci.* **19**, 173–179.

PIOMELLI, U. & LIU, J. 1995 Large eddy simulation of rotating channel flows using a localized dynamic model. *Phys. Fluids* **7**, 839–848.

SMAGORINSKY, J. 1963 General circulation experiments with the primitive equations, I. The basic experiment. *Mon. Weath. Rev.* **91**, 99–164.

STEVENS, D. E., ACKERMAN, A. S. & BRETHERTON, C. S. 2002 Effects of domain size and numerical resolution on the simulation of shallow cumulus convection. *submitted to J. Atmos. Sci.* .

STEVENS, D. E., BELL, J. B., ALMGREN, A. S., BECKNER, V. E. & RENDLEMAN, C. A. 2000 Small-scale processes and entrainment in a stratocumulus marine boundary layer. *J. Atmos. Sci.* **57** (4), 567–581.

STEVENS, D. E. & BRETHERTON, C. S. 1999 Effects of resolution on the simulation of stratocumulus entrainment. *Quart. J. Royal Meteor. Soc.* **125** (554/pt.B), 425–439.

VREMAN, B., GEURTS, B. & KUERTEN, H. 1994 On the formulation of the dynamic mixed subgrid-scale model. *Phys. Fluids* **6** (12), 4057–4059.

ZANG, Y., STREET, R. & KOSEFF, J. R. 1993 A dynamic mixed subgrid-scale model and its application to recirculating flows. *Phys. Fluids* **A 5** (12), 3186–3196.

Particle size distributions in atmospheric clouds

By **Roberto Paoli & Karim Shariff †**

In this note, we derive a transport equation for a spatially integrated distribution function of particles size that is suitable for sparse particle systems, such as in atmospheric clouds. This is done by integrating a Boltzmann equation for a (local) distribution function over an arbitrary but finite volume. A methodology for evolving the moments of the integrated distribution is presented. These moments can be either tracked for a finite number of discrete populations ("clusters") or treated as continuum variables.

1. Introduction

Particles are present in atmospheric clouds in several forms such as liquid droplets, non-volatile aerosols or ice crystals. Their microphysical properties control many processes such as the production of rain in stratocumulus clouds and radiation through cirrus clouds. These properties depend on the way particles interact with the surrounding air, through fluid-dynamic and thermodynamic processes. As these processes usually take place at small spatial scales, the interaction of particles with atmospheric turbulence is an important, though complex, problem in cloud physics (Shaw 2003). From a computational point of view, two major factors contribute to this complexity. First is the very high turbulence Reynolds number and the large range of spatial scales (Vaillancourt & Yau 2000; Shaw 2003): for convective clouds, the ratio of energy-containing to dissipative length scales is $\mathcal{O}(10^5)$, while the Reynolds number of the largest eddies is $\mathcal{O}(10^6$ to $10^7)$. The second factor is that the mean distance λ between particles is of the order of the Kolmogorov scale η. Thus, if one contemplated direct numerical simulation (DNS) where all spatial scales are resolved, then one would have to track individual particles. Since DNS resolution is not affordable for these flows, Eulerian formulations for the liquid/solid phase are widely used in the simulation of clouds. These formulations fall into two main classes. The first is a "two fluid model" where particles are modeled as a continuum having a local mass density per unit volume. This approach carries no information about the distribution of the particle size. In the second approach, some physical properties (e.g. the mean radius) of some "ensemble" of particles are explicitly computed at each physical location $\mathbf{x}$. The concept of particle size distribution at a point at this stage of our discussion is ambiguous but will be clarified later. A standard procedure used in two-phase flow models (e.g. Williams 1965; Cotton & Anthes 1989; Crowe *et al.* 1998) to describe an ensemble of particles is to define a distribution function f, in a manner analogous to the kinetic theory of gases. In kinetic theory, a distribution function $f(\mathbf{x},\mathbf{v};t)$ is defined where $f(\mathbf{x},\mathbf{v};t)\,\delta\mathbf{x}\,\delta\mathbf{v}$ represents the number of molecules that at time t are between $\mathbf{x}$ and $\mathbf{x}+\delta\mathbf{x}$ and whose velocity is between $\mathbf{v}$ and $\mathbf{v}+\delta\mathbf{v}$. It is assumed that, as $(\delta\mathbf{x},\delta\mathbf{v})\rightarrow 0$, the phase volume still contains a sufficently large population of molecules that statistics can be used. This is usually true in gasdynamics because the mean free path of molecules is much smaller than the continuum scale one

† NASA Ames Research Center, Moffett Field, CA 94035

cares about. The extension of this appraoch to particles other than molecules is formally straightforward (see for example the book by Williams 1965), as long as the continuum description remains valid. In the case of atmospheric clouds however, $\lambda \simeq \eta$ so that only a few particles rather than a population are present in a volume $V = \mathcal{O}(\eta^3)$. The object of this note is first to derive a transport equation for an integrated distribution function $\mathcal{F}_0$, describing an ensemble of particles inside an arbitrary but finite volume V_0. Then, this approach is specialized to atmopsheric clouds. Finally, a methodology is proposed to solve for the moments of the distribution function $\mathcal{F}_0$.

2. Distribution function in atmospheric clouds

Let us consider a population of particles in a cloud from an ensemble of realizations. At any time t, each particle p occupies the position $\mathbf{x}_p(t)$ in physical space, moves with velocity $\mathbf{u}_p(t)$ and changes its radius $r_p(t)$. This population can be represented in a phase space, defined by the generalized coordinates $\mathbf{q}(t)$ and evolving via the generalized velocities $\mathbf{U}(\mathbf{q}(t))$:

$$\mathbf{q}(t) = \begin{bmatrix} r(t) \\ \mathbf{x}(t) \\ \mathbf{u}(t) \end{bmatrix}, \quad \mathbf{U}(\mathbf{q}(t)) = \frac{d\mathbf{q}}{dt} = \begin{bmatrix} \dot{r}(\mathbf{q}(t)) \\ \mathbf{u}(\mathbf{q}(t)) \\ \mathbf{F}(\mathbf{q}(t)) \end{bmatrix} \tag{2.1}$$

where $\mathbf{x}$ and $\mathbf{u}$ are the spatial coordinates and velocities, $\mathbf{F}$ is the functional law of the force per unit mass acting on the particle and $\dot{r}$ is the functional law of the growth rate of its radius. At any time t, each particle of the population occupies a point $\mathbf{q}(t)$ in this space. Instead of tracking each particle we wish to follow the evolution of a distribution function $f(\mathbf{q}(t); t)$ of the population. This is defined in such a way that

$$f(\mathbf{q}(t); t)\ \delta Q(t) \tag{2.2}$$

is the number of particles that at time t are inside a cube of volume $\delta Q(t)$ in phase space, located between the coordinates $\mathbf{q}(t)$ and $\mathbf{q}(t) + \delta\mathbf{q}(t)$. After a time dt, this volume has a value $\delta Q(t+dt)$ and the diagonally opposite corners of the cube are mapped to $\mathbf{q}(t+dt)$, and $\mathbf{q}(t+dt) + \delta\mathbf{q}(t+dt)$, respectively. At the same time, each particle can change its $\mathbf{q}$ and the particle number can vary because of evaporation or coagulation. To derive a transport equation for f we need to relate these quantities. For the sake of clarity, we will drop the explicit dependence on t in all variables, and define $t' \equiv t + dt$, and $\mathbf{q}' \equiv \mathbf{q}(t+dt)$. Then we have

$$\mathbf{q}' = \mathbf{q} + \mathbf{U}(\mathbf{q})\, dt \tag{2.3}$$

$$\mathbf{q}' + \delta\mathbf{q}' = \mathbf{q} + \delta\mathbf{q} + \mathbf{U}(\mathbf{q} + \delta\mathbf{q})\, dt \tag{2.4}$$

The last term in (2.4) can be expanded as $\mathbf{U}(\mathbf{q}+\delta\mathbf{q}) = \mathbf{U}(\mathbf{q}) + (\nabla_{\mathbf{q}}\mathbf{U})\delta\mathbf{q}$ where $\nabla_{\mathbf{q}}\mathbf{U}$ is the gradient of $\mathbf{U}$ in phase space. Substituting (2.3) into (2.4) one gets

$$\delta\mathbf{q}' = (\mathbf{I} + dt\, \nabla_{\mathbf{q}}\mathbf{U})\, \delta\mathbf{q} \tag{2.5}$$

The change of phase space volume $\delta Q' - \delta Q$ is related to the divergence of the generalized velocity $\mathbf{U}$ by

$$\frac{\delta Q' - \delta Q}{\delta Q} = (\nabla_{\mathbf{q}} \cdot \mathbf{U})\, dt + \mathcal{O}(dt^2) \tag{2.6}$$

Let $K(\mathbf{q};t)$ describe the general rate of gain or loss of particle number due to coagulation or evaporation,

$$f(\mathbf{q}';t')\,\delta Q' = f(\mathbf{q};t)\,\delta Q + K(\mathbf{q};t)dt\,\delta Q \tag{2.7}$$

Substituting (2.3), (2.4) and (2.6) into (2.7) and expanding gives:

$$\left[f+\left(\frac{\partial f}{\partial t}+\nabla_{\mathbf{q}}f\cdot\mathbf{U}\right)dt+\mathcal{O}(dt^2)\right]\left[1+\nabla_{\mathbf{q}}\cdot\mathbf{U}\,dt+\mathcal{O}(dt^2)\right]\,\delta Q = f\,\delta Q+K dt\,\delta Q \tag{2.8}$$

where all quantitites are evaluated at t. Taking the limit $dt \to 0$ and neglecting higher order infinitesimals gives a Boltzmann equation

$$\frac{\partial f}{\partial t}+\nabla_{\mathbf{q}}\cdot(f\,\mathbf{U}) = K \tag{2.9}$$

Finally, inserting the different components of $\mathbf{q}$ and $\mathbf{U}$ by means of (2.1) gives the more usual form employed in two-phase flow literature (e.g. Williams 1965):

$$\frac{\partial f}{\partial t}+\nabla_{\mathbf{x}}\cdot(f\,\mathbf{u})+\nabla_{\mathbf{u}}\cdot(f\,\mathbf{F})+\frac{\partial(f\,\dot{r})}{\partial r} = K \tag{2.10}$$

The term $\mathbf{F}$ in (2.10) is the aerodynamic drag induced by the flow on particles, $\mathbf{F} \approx (\mathbf{u}_p - \mathbf{u}_f)/\tau_p$ (see Crowe *et al.* 1998) where $\mathbf{u}_f$ is the fluid velocity and $\tau_p = 4\rho_p r_p^2/18\mu$ is a relaxation time. If the size of the particle r_p is small, τ_p is also small and the particle velocity immediately adjusts to the flow velocity. In the following, we restrict our analysis to this case, so there is no dependence on $\mathbf{F}$ in (2.10):

$$\frac{\partial f}{\partial t}+\nabla_{\mathbf{x}}\cdot(f\,\mathbf{u})+\frac{\partial(f\,\dot{r})}{\partial r} = K \tag{2.11}$$

3. Integrated distribution

We now derive an integrated version of (2.11). Consider a point $\mathbf{x}_0$ in physical space and an arbitrary (but finite) volume $V_0(\mathbf{x}_0(t)$ around it. Then, a space integrated distribution function $\mathcal{F}_0(r,\mathbf{x}_0;t)$ can be defined as

$$\mathcal{F}_0(r,\mathbf{x}_0;t) = \int_{V_0} f(r,\mathbf{x};t)\,dV_0(\mathbf{x}) \tag{3.1}$$

so that $\mathcal{F}_0(r,\mathbf{x}_0;t)\,\delta r$ represents the number of particles that at time t are inside a finite volume V_0 around $\mathbf{x}_0$ and whose radius is in between r and $r+\delta r$ (the dimensions of this function are $[\mathcal{F}_0] = L^{-1}$ whereas $[f] = L^{-1}\times L^{-3}$). The mean ψ_0 within the volume V_0 of any quantity $\psi(r,\mathbf{x};t)$ associated with each particle is

$$\psi_0(r,\mathbf{x}_0;t) = \frac{1}{\mathcal{F}_0(r,\mathbf{x}_0;t)}\int_{V_0} f(r,\mathbf{x};t)\,\psi(r,\mathbf{x};t)\,dV_0(\mathbf{x}) \tag{3.2}$$

Let us introduce a local coordinate $\mathbf{y}$ around $\mathbf{x}_0$, $\mathbf{x} = \mathbf{x}(\mathbf{x}_0,\mathbf{y}) = \mathbf{x}_0 + \mathbf{y}$, so that

$$\nabla_{\mathbf{x}}\cdot(\bullet) = \nabla_{\mathbf{x}_0}\cdot(\bullet)+\nabla_{\mathbf{y}}\cdot(\bullet). \tag{3.3}$$

Using (3.2) for $\mathbf{u}$ and $\dot{r}$, their integral values over V_0 become

$$\mathbf{u}_0(r,\mathbf{x}_0;t) = \frac{1}{\mathcal{F}_0(r,\mathbf{x}_0;t)}\int_{V_0} f(r,\mathbf{x}_0+\mathbf{y};t)\,\mathbf{u}(r,\mathbf{x}_0+\mathbf{y};t)\,dV_0(\mathbf{y}) \tag{3.4}$$

$$\dot{r}_0(r,\mathbf{x}_0;t) = \frac{1}{\mathcal{F}_0(r,\mathbf{x}_0;t)}\int_{V_0} f(r,\mathbf{x}_0+\mathbf{y};t)\,\dot{r}(r,\mathbf{x}_0+\mathbf{y};t)\,dV_0(\mathbf{y}) \tag{3.5}$$

Using (3.3) to express the divergence term $\nabla_{\mathbf{x}} \cdot (f\,\mathbf{u}) = \nabla_{\mathbf{x}_0} \cdot (f\,\mathbf{u}) + \nabla_{\mathbf{y}} \cdot (f\,\mathbf{u})$, a transport equation for $\mathcal{F}_0$ can be derived by integrating (2.11) inside volume V_0:

$$\int_{V_0} \frac{\partial f}{\partial t}\, dV_0 + \nabla_{\mathbf{x}_0} \cdot \left(\int_{V_0} f\,\mathbf{u}\, dV_0 \right) + \int_{V_0} \nabla_{\mathbf{y}} \cdot (f\,\mathbf{u})\, dV_0 + \frac{\partial}{\partial r} \left(\int_{V_0} f\,\dot{r}\, dV_0 \right) = \int_{V_0} K\, dV_0 \tag{3.6}$$

As in general $\mathbf{x}_0$ and V_0 vary in time, we need to switch volume integration and time derivative in the first term of the above equation. Using Leibnitz rule and (3.1), one has:

$$\frac{\partial \mathcal{F}_0}{\partial t} \equiv \frac{\partial}{\partial t} \int_{V_0} f\, dV_0 = \int_{V_0} \frac{\partial f}{\partial t}\, dV_0 + \oint_{S_0} f\,\dot{\mathbf{S}}_f \cdot \mathbf{n}_0\, dS_0 \tag{3.7}$$

where S_0 is the surface around V_0 and $\dot{\mathbf{S}}_f$ is the velocity of S_0 with respect to the fixed reference frame. Using (3.7), Gauss theorem and the definitions (3.4) and (3.5) in (3.6), and introducing the relative velocity with respect to S_0, $\mathbf{w} = \mathbf{u} - \dot{\mathbf{S}}_f$, finally gives

$$\frac{\partial \mathcal{F}_0}{\partial t} + \nabla_{\mathbf{x}_0} \cdot (\mathcal{F}_0\,\mathbf{u}_0) + \frac{\partial (\mathcal{F}_0\,\dot{r}_0)}{\partial r} + \oint_{S_0} f\,\mathbf{w} \cdot \mathbf{n}_0\, dS_0 = K_0 \tag{3.8}$$

which is a Boltzmann equation for the integral distribution function $\mathcal{F}_0$. Equation (3.8) formally differs from (2.11) because of the surface integral in the left-hand side. This contains the (unknown) local distribution function f, which must be modeled in some way. Note, however, that if V_0 is a material volume, then $\mathbf{u} = \dot{\mathbf{S}}_f$ on S_0, and the surface flux goes to zero.

Ergodic hypothesis

In the previous derivation we had to introduce an ensemble of realizations in order to derive a local Boltzmann equation which we then integrated over a finite volume. We now make the hypothesis that V_0 is large enough to contain a population of particles that we can by-pass the ensemble. In other words, we hypothesize that the integrated Boltzmann equation (3.8) is valid for a single realization if V_0 is large enough. Typically, the grid size in cloud codes is $\Delta \geq 1\,m$ while $\lambda \simeq \eta \approx 10^{-3}\,m$, so each grid cell contains at least 10^9 particles.

3.1. *Ensemble averages*

The total number of particles N_0 in spatial volume V_0 can be obtained by integrating $\mathcal{F}_0$ over all possible radii,

$$N_0(\mathbf{x}_0; t) = \int_0^\infty \mathcal{F}_0(r, \mathbf{x}_0; t)\, dr. \tag{3.9}$$

Using (3.9), the ensemble average $\langle \psi_0 \rangle$ of any variable ψ is obtained by integrating (3.2) over r:

$$\langle \psi_0 \rangle\, (\mathbf{x}_0; t) = \frac{1}{N_0(\mathbf{x}_0; t)} \int_0^\infty \psi_0(r, \mathbf{x}_0; t)\, \mathcal{F}_0(r, \mathbf{x}_0; t)\, dr \tag{3.10}$$

In particular, the ensemble velocity and radius growth rate are

$$\langle \mathbf{u}_0 \rangle\, (\mathbf{x}_0; t) = \frac{1}{N_0(\mathbf{x}_0; t)} \int_0^\infty \mathbf{u}_0(r, \mathbf{x}_0; t)\, \mathcal{F}_0(r, \mathbf{x}_0; t)\, dr,$$

$$\langle \dot{r}_0 \rangle\, (\mathbf{x}_0; t) = \frac{1}{N_0(\mathbf{x}_0; t)} \int_0^\infty \dot{r}_0(r, \mathbf{x}_0; t)\, \mathcal{F}_0(r, \mathbf{x}_0; t)\, dr \tag{3.11}$$

For further analysis, it will be useful to introduce the mean radius, $\langle r_0 \rangle$, and the variance, $\langle \Delta r_0^2 \rangle$, of the population. Using (3.2), these are given by

$$\langle r_0 \rangle (\mathbf{x}_0; t) = \frac{1}{N_0(\mathbf{x}_0; t)} \int_0^\infty r \, \mathcal{F}_0(r, \mathbf{x}_0; t) \, dr \tag{3.12}$$

$$\langle \Delta r_0^2 \rangle (\mathbf{x}_0; t) = \frac{1}{N_0(\mathbf{x}_0; t)} \int_0^\infty [r - \langle r_0 \rangle (\mathbf{u}_0; t)]^2 \, \mathcal{F}_0(r, \mathbf{x}_0; t) \, dr \tag{3.13}$$

Note that $\mathbf{u}(r, \mathbf{y}; t)$ and $\langle \mathbf{u}_0 \rangle (\mathbf{x}_0; t)$ (same for $\dot{r}$ and $\langle \dot{r}_0 \rangle$) have a different physical meaning: $\mathbf{u}(\mathbf{y})$ represents the velocity of a particle in a neighboorood of $\mathbf{y}$. On the other hand, $\mathbf{u}_0(\mathbf{x}_0)$ represents a statistical average within a population of particles and is a continuum velocity field, associated to any point, $\mathbf{x}_0$, of the physical domain. Indeed, one could, in principle, obtain $\langle \mathbf{u}_0 \rangle$ and $\langle \dot{r}_0 \rangle$ as

$$\langle \mathbf{u}_0 \rangle = \frac{1}{N_0} \sum_{p=1}^{N_0} \mathbf{u}_p \, , \quad \langle \dot{r}_0 \rangle = \frac{1}{N_0} \sum_{p=1}^{N_0} \dot{r}_p \tag{3.14}$$

where $\mathbf{u}_p$ and $\dot{r}_p$ are the velocity and the radius growth rate of particle p inside V_0. In the limit of $N_0 \to \infty$, (3.11) and (3.14) are equivalent but we only have access to $\mathcal{F}_0$ because the details concerning $\mathbf{u}_p$ and $\dot{r}_p$ of each physical particle are unknown.

The next step is to relate the continuum fields $\langle \mathbf{u}_0 \rangle$ and $\langle \dot{r}_0 \rangle$ to the corresponding flow variables. As we do not consider here any force acting on particles (Sec. 2), they are simply convected by the fluid. Therefore, there is no reason why two particles of the same population and different radius should have different velocities, i.e. $\mathbf{u}_0$ is statistically uncorrelated with r,

$$\mathbf{u}_0(r, \mathbf{x}_0; t) \equiv \langle \mathbf{u}_0 \rangle (\mathbf{x}_0; t) = \mathbf{u}_f(\mathbf{x}_0; t) \tag{3.15}$$

where $\mathbf{u}_f(\mathbf{x}_0; t)$ is the fluid velocity at $\mathbf{x}_0$. The same arguments, cannot be applied to $\dot{r}_0$, i.e. $\dot{r}_0 \neq \langle \dot{r} \rangle_0$, because each particle of the population may have a different growth rate due to different "reactions" to turbulent fluctuations in the flow-field, as discussed next.

4. Particle growth by condensation

The growth of the radius of a single particle in a medium at rest can be simply derived by considering a diffusion equation for water vapor on a particle surface (Pruppacher & Klett (1997) p. 502) and is given by

$$\frac{dr}{dt} = \frac{D \, (\rho_v - \rho_v^s(T))}{\Gamma \rho_w \, r} = \frac{D \, S}{\Gamma \rho_w \, r} \tag{4.1}$$

where D is the diffusion coefficient of water vapor in air and Γ is the psychrometric correction associated with the latent heat of condensation; and ρ_w is the density of either water or ice. The vapor densities ρ_v and $\rho_v^s(T)$ are evaluated, respectively, at some "ambient" condition far from the particle and at the surface of the particle (which coincides with the saturation value because vapor there is in thermodynamic equilibrium with water/ice). Thus, in such a single-particle picture, the radius growth rate is only controlled by the supersaturation $S = \rho_v - \rho_v^s$. As first pointed out by Srivastava (1989) (see also Khvorostyanov & Curry 1999), this description cannot be extended straightforwardly to a population of particles. In fact, even in the absence of turbulence and uniform S initially, the available vapor in a cloud is not equally distributed among all particles

because of their random spatial distribution, so that the effective supersaturation available at a droplet surface ("microsaturation"), can differ significantly from the overall ensemble averaged supersaturation ("macrosaturation") (Srivastava 1989). In addition, in a turbulent cloud, each particle "reacts" in a different way to turbulent fluctuations in the flow-field: for example, if a supersaturation fluctuation arises, it will be absorbed by each particle through a complex diffusional process of vapor involving all elements of the population (Srivastava 1989). Several approaches have been developed in the atmospheric science literature (Pruppacher & Klett 1997) to try to solve this complex problem. One of these, the so-called "stochastic condensation" approach performs Reynolds averaging on the equation for condensational growth, resulting in covariances that can be though as "Reynolds stresses" (Shaw 2003). In particular, we follow Khvorostyanov & Curry (1999) (see also Pruppacher & Klett (1997) p.505) who use kinetic theory to relate the micro- and macro-saturation in a cloud. Their arguments are as follows. For the moment consider the situation where the particle radius is so small to be comparable with the mean free path of vapor molecules. In this case, one should account for the Brownian motion of molecules, that is the diffusion associated to the (random) molecular impact on particles surface. As shown by Pruppacher & Klett (1997), this can be done in (4.1) by introducing a modified diffusion coefficient $D^*(r)$ which depends linearly on the radius r (Pruppacher & Klett (1997) p.506). It can be argued (Crowe *et al.* 1998; Khvorostyanov & Curry 1999) that the effects of turbulent fluctuations of vapor density or in supersaturation is similar to Brownian motion, whereas the molecular impact on particles is substituted by their interaction with turbulent eddies (note that this picture can also be extended to account for equivalent Brownian dispersion of particles, induced by fluctuating fluid forces rather than density fluctuations) (Crowe *et al.* 1998). The "micro" supersaturation S_p available to particle p of an ensemble is

$$S_p = \frac{\langle S_0 \rangle}{\langle r_0 \rangle} r_p \tag{4.2}$$

where $\langle S_0 \rangle (\mathbf{x}_0; t)$ is the ensemble supersaturation available to the population within volume V_0. It represents the supersaturation that would be at $\mathbf{x}_0$ if there were no particles, then it can be thught as the fluid supersaturation at $\mathbf{x}_0$, $\langle S_0 \rangle (\mathbf{x}_0; t) = S_f(\mathbf{x}_0; t)$. Using (4.2) and the previous formalism ($r_p \to r$; $S_p \to S(r, \mathbf{y})$; $\dot{r}_p \to \dot{r}(r, \mathbf{y})$), one gets to

$$\frac{S(r, \mathbf{y})}{r} = \frac{\langle S_0 \rangle}{\langle r_0 \rangle} = \frac{S_f}{\langle r_0 \rangle} \tag{4.3}$$

$$\dot{r}(r, \mathbf{y}) = \frac{DS(r, \mathbf{y})}{\Gamma \rho_w r} = \frac{DS_f}{\Gamma \rho_w \langle r_0 \rangle} \tag{4.4}$$

Substituting (4.3) and (4.4) into (3.11) finally gives

$$\langle \dot{r}_0 \rangle = \frac{1}{N_0(\mathbf{x}_0; t)} \int_0^\infty \mathcal{F}_0 \dot{r}_0 \, dr = \int_0^\infty \int_{V_0} f \frac{DS(r, \mathbf{y})}{\Gamma \rho_w r} \, dV_0 \, dr \equiv \frac{D S_f}{\Gamma \rho_w \langle r_0 \rangle} \tag{4.5}$$

5. Method of moments

Even neglecting the surface term, (3.8) is a p.d.e. in four-dimensional space $(r, \mathbf{x}_0; t)$ that can only be solved numerically. Some atmospheric cloud codes solve a transport equation for a distribution function by discretizing the particle size r in a finite number of bins, at each grid location (although it is not explicitly mentioned, they are conceptually discretizing (3.8) with neglected surface terms).

In this section, we present a simulation strategy based on the method of moments proposed in Paoli *et al.* (2002). The moments m_k of the distribution $\mathcal{F}_0$ are defined by

$$m_k(\mathbf{x}_0;t) = \int_0^\infty r^k \mathcal{F}_0(r,\mathbf{x}_0;t)\,dr \tag{5.1}$$

Multiplying (3.8) by r^k gives

$$\frac{\partial}{\partial t}\left(\int_0^\infty r^k \mathcal{F}_0\,dr\right) + \nabla_{\mathbf{x}_0}\cdot\left(\int_0^\infty r^k \mathcal{F}_0\,\mathbf{u}_0\,dr\right) = -\mathcal{F}_0\dot{r}_0 r^k|_0^\infty + k\int_0^\infty r^{k-1}\mathcal{F}_0\dot{r}_0\,dr \tag{5.2}$$

Using (3.15), (4.5) and (5.1) and assuming that $\mathcal{F}_0 \to 0$ sufficiently fast as $r \to \infty$, (5.2) becomes

$$\frac{\partial m_k}{\partial t} + \nabla_{\mathbf{x}_0}\cdot(\mathbf{u}_f\, m_k) = \frac{D\,S_f}{\Gamma\,\rho_w\,\langle r_0\rangle}\,k\,m_{k-1} \tag{5.3}$$

Under all assumptions made, (5.3) describes the evolution of the moments of the integral distribution function $\mathcal{F}_0$. An attractive property, deriving from the microsaturation model (4.2), is that the evolution of the k^{th} moment only depends on the previous order moment which allows one to close the system (5.3) without any further assumptions and without presuming the shape of $\mathcal{F}_0$. Using (3.9)–(3.13) and (5.1), the zero and the first two moments are easily found and are related to the ensemble average radius and variance,

$$m_0 = N_0\,, \quad m_1 = N_0\,\langle r_0\rangle\,, \quad m_2 = N_0\left[\langle \Delta r_0^2\rangle + \langle r_0\rangle^2\right]. \tag{5.4}$$

The corresponding evolution equations are (we put $\alpha \equiv D/\Gamma\rho_w$)

$$\frac{\partial N_0}{\partial t} + \nabla_{\mathbf{x}_0}\cdot(\mathbf{u}_f\, N_0) = 0 \tag{5.5}$$

$$\frac{\partial m_1}{\partial t} + \nabla_{\mathbf{x}_0}\cdot(\mathbf{u}_f\, m_1) = \alpha S_f \frac{N_0^2}{m_1} \tag{5.6}$$

$$\frac{\partial m_2}{\partial t} + \nabla_{\mathbf{x}_0}\cdot(\mathbf{u}_f\, m_2) = 2\,\alpha S_f N_0 \tag{5.7}$$

These equation are coupled to the continuum fluid phase through $\mathbf{u}_f$ and S_f. In particular, an increase in particle radius by condensation implies vapor depletion $\dot{\rho}_v$, with

$$\dot{\rho}_v = -\int_0^\infty 4\pi\rho_w r^2 \dot{r}_0 \mathcal{F}_0\,dr = -\frac{4\pi\rho_w D}{\Gamma\rho_w}\frac{S_f}{\langle r_0\rangle}\int_0^\infty r^2\mathcal{F}_0\,dr = -4\pi\rho_w\alpha S_f\frac{N_0 m_2}{m_1} \tag{5.8}$$

The usual convection-diffusion-reaction equation for a scalar Y_v in conservative form ($\rho_v \equiv Y_v\,\rho_f$ where ρ_f is the total gas phase density) then becomes:

$$\frac{\partial \rho_v}{\partial t} + \nabla_{\mathbf{x}_0}\cdot(\mathbf{u}_f\,\rho_v) + \nabla_{\mathbf{x}_0}\cdot(\rho_f D\,\nabla_{\mathbf{x}_0} Y_v) = \dot{\rho}_v = -4\pi\rho_w\alpha S_f\frac{N_0 m_2}{m_1} \tag{5.9}$$

Under all approximations made, (5.5)-(5.7) and (5.9) (together with Navier-Stokes equations) describe the evolution of the first moments of the size distribution of a population of particles. These moments can be solved by using either an Eulerian or a Lagrangian description as discussed next.

Eulerian description

In this case, one has to solve for m_k using (5.5)–(5.7) with the further condition that the volume V_0 is constant in time (in discretized form it can be the volume of a grid cell). It is worth mentioning that $\mathcal{F}_0$ and m_k are continuous functions of space (not grid averages!),

so their gradients contain all spatial fluctuations in a turbulent flow. In particular, if they are filtered in a LES approach, the correlations $\overline{m_k\,\mathbf{u}_f}$ and $\overline{m_k\,S_f}$ exist at subgrid scale level and must be modeled.

An approximate Lagrangian method

Let us devide the total number of particles in the cloud into N_c "clusters", each containing a fixed number, N_j, of particles (where $j = 1,..,N_c$). The position of each cluster is assumed to evolve according to

$$\frac{d\mathbf{x}_0^j}{dt} = \mathbf{u}_f(\mathbf{x}_0^j) \tag{5.10}$$

where $\mathbf{x}_0^j$ is the center of the volume V_0^j containing cluster j and $\mathbf{u}_f(\mathbf{x}_0^j)$ is the fluid velocity at $\mathbf{x}_0^j$. Note that we are assuming that the cluster advects rigidly without deforming. Introducing the total derivative $d()/dt = \partial()/\partial t + \nabla_{\mathbf{x}_0}()\mathbf{u}_f$ in (5.5)–(5.7), one can "track" the moments of each cluster j as (note that the zeroth moment equation, $N_j = const$ is now trivial)

$$\frac{dm_1^j}{dt} = \alpha S_f \frac{N_j^2}{m_1^j} \tag{5.11}$$

$$\frac{dm_2^j}{dt} = 2\,\alpha S_f N_j \tag{5.12}$$

where $S_f \equiv S_f(\mathbf{x}_0^j)$ is the fluid supersaturation at $\mathbf{x}_0^j$. The advantage of the Lagrangian approach is that the surface term in (3.8), which was neglected to get to (5.5)–(5.7), is now zero because V_0^j is a material volume, $\mathbf{u} = \dot{\mathbf{S}}_f^j$ on S_0^j for all j.

6. Conclusions

In this note we derived a transport equation for the radius distribution function of a population of particles in an atmospheric cloud. We used a simple stochastic condensation model for the radius growth (taken from the atmospheric science literature) to relate the microsaturation around each particle to the macrosaturation of the entire population. Finally, we described a procedure to solve for the moments of the distribution, and showed that this can be either used in Eulerian continuum formulations or Lagrangian tracking of "clusters" of particles. Future plans include testing of this method by comparison with DNS of homogeneus and isotropic turbulence and individual particle tracking; and application of the method to natural and contrail-generated cirrus.

REFERENCES

COTTON, W. R. & ANTHES, R. A. 1989 *Storm and Cloud Dynamics.* Academic Press.

CROWE, C., SOMMERFELD, M. & TSUJI, Y. 1998 *Multiphase Flows with Droplets and Particles.* CRC Press.

KHVOROSTYANOV, V. I. & CURRY, J. A. 1999 Toward the Theory of Stochastic Condensation in Clouds. Part I: A general kinetic equation *J. Atmos. Sci.*, **56**, 3985-3996.

PAOLI, R., HÉLIE, J., POINSOT, T. & GHOSAL, S. 2002 Contrail formation in aircraft wakes using large eddy simulation *Proc. 2002 Summer Program* Center for Turbulence Research, Stanford University, Stanford, CA .

PRUPPACHER, H. R. & KLETT, J. D. 1997 *Microphysics of Clouds and Precipitation.* Kluwer Academic Publishers, Dordrecht, The Netherlands.

ROGERS, R. R. & YAU, M. K. 1989 *A short course in Cloud Physics.* Butterworth-Heinemann.

SHAW, R. A. 2003 Particle-Turbulence Interactions in Atmospheric Clouds. *Annu. Rev. Fluid Mech.* **35**, 183-227.

SRIVASTAVA, R. C. 1989 Growth of cloud Drops by Condensation: A criticism of currently accepted theory and a new approach *J. Atmos. Sci.*, **46**, 869-887.

VAILLANCOURT, P. A. & YAU, M. K. 2000 Review of Particle-Turbulence Interactions and Consequences for Cloud Physics *Bull. Am. Meteorol. Soc.*, **81**, 285-298.

WILLIAMS, F. A. 1965 *Combustion Theory* Addison-Wesley Publishing Company.

Simulation of inviscid compressible multi–phase flow with condensation

Philip Kelleners †

Condensation of vapours in rapid expansions of compressible gases is investigated. In the case of high temperature gradients the condensation will start at conditions well away from thermodynamic equilibrium of the fluid. In those cases homogeneous condensation is dominant over heterogeneous condensation. The present work is concerned with development of a simulation tool for computation of high speed compressible flows with homogeneous condensation. The resulting flow solver should preferably be accurate and robust to be used for simulation of industrial flows in general geometries.

1. Introduction

A substance below its critical temperature can be present in either gaseous or liquid phase, depending on the pressure, and is referred to as a vapour. Vapours present in a mixture of gases and vapours, when subjected to expansion can condensate and form liquid droplets. This phenomenon is observed in e.g. aircraft tip vortices and in industrial flows like steam turbines. Condensation in flows of gas mixtures at high speed has been investigated by, among others; Wegener (1969), Hill (1966), Campbell (1989), Schnerr et al. Schnerr (1996), Dohrmann (1989), Mundinger (1994), Adam (1996) and van Dongen et al. Luijten (1999), Luijten (1998), Prast (1997) and Lamanna (2000). Expansion in nozzles of gases to supersonic speeds has often been used to investigate the physics of condensation. Condensation in the flow around airfoil sections and in steam turbines has been investigated to a large extent. At the University of Twente a numerical tool has been developed to simulate transonic flows with condensation in confined geometries. The solver operates on the basis of a finite volume method using unstructured meshes. It has been observed that results obtained with the solver are very sensitive to accurate shock prediction, and fine shock resolution in the flow field, especially in cases of strong interaction between the gasdynamic shock and the condensation process. The focus of the present work is to improve the accuracy and robustness of the flow solver by improving solid wall boundary treatment and spatial reconstruction for simulations with second order spatial accuracy.

2. Physics of Condensation during Rapid Expansion

Below its critical temperature, a fluid can be in gaseous or liquid phase. The thermodynamical region of coexistence of vapour and liquid in equilibrium in bulk substances is given by the Clausius-Clapeyron relation. For rapid expansions of vapour this coexistence region is passed without the fluid attaining equilibrium. The vapour is saturated expressed by the saturation ratio;

† Address: Engineering Fluid Dynamics, Mechanical Engineering - University of Twente, P. O. Box 217, 7500 AE Enschede, The Netherlands

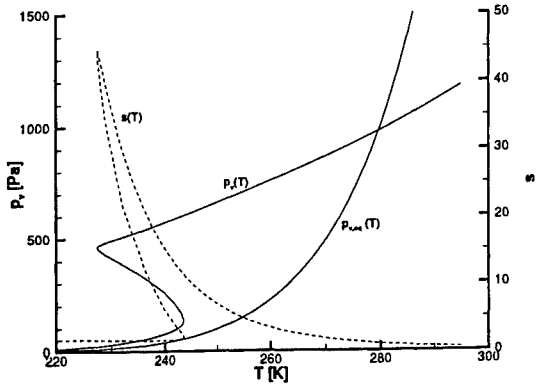


FIGURE 1. Expansion of air–water mixture in nozzle–S2, partial vapour pressures and saturation ratio s (dashed)

$$s = \frac{n_v}{n_{v,eq}} \tag{2.1}$$

where n_v and $n_{v,eq}$ are the number of moles of the vapour in the actual mixture and the mixture in equilibrium, respectively. For pressures as high as atmospheric pressure equation 2.1 can be replaced by the more conventional expression:

$$s = \frac{p_v}{p_{v,eq}} \tag{2.2}$$

where p_v is the actual partial vapour pressure in the mixture and $p_{v,eq}$ is the equilibrium partial vapour pressure at the same thermodynamic conditions. s, p_v and $p_{v,eq}$ are plotted in figure 1 for the expansion of an air–water mixture, as functions of temperature.

The curve for the coexistence of liquid and vapour ($p_{v,eq}$) divides the plane given by pressure and temperature into two regions. For pressures higher than the coexistence pressure the substance under consideration (water) is present in liquid form while in equilibrium state. For lower pressures the substance will be present as water–vapour while in equilibrium. The expansion in the nozzle, as given by the partial vapour pressure p_v, is so quick that the water–vapour will not immediately condense under equilibrium conditions. This is the case as the characteristic time of the gasdynamic flow is much smaller than the time needed to form the first onsets of the new liquid phase. For the nozzle flow at hand this is due to the high–cooling rate in the nozzle. So the water–vapour expands further, driving the air–water–vapour mixture well away from equilibrium, as indicated by the saturation ratio which attains values as high as 40. In case $s > 1$ the fluid is said to be super–saturated. Formation of small liquid clusters, nuclei, at high super–saturation is the first stage of the condensation process that starts in order to reestablish equilibrium. On these newly formed nuclei, the super–saturated vapour condenses as a second step until equilibrium is reached, the process of droplet growth. This can be seen in figure 1 by the decrease in partial vapour pressure and the increase in temperature. With so much liquid already present, the remainder of the condensation process due to droplet growth takes place very close to thermodynamic equilibrium of the water, indicated by the saturation close to one, for the remainder of the expansion.

The process described above is the process of homogeneous condensation. In contrast, the process of heterogeneous condensation is droplet growth on foreign, already present particles. However, for high cooling speeds and consequentially high super–saturation the number of new nuclei formed exceeds any realistic number of foreign particles by several orders of magnitude. For the present applications only homogeneous condensation processes are of importance.

An effect resulting from condensation is the release of latent heat during the condensation process, indicated by the increase in temperature during condensation in the previous example of nozzle flow. The latent heat L is defined as

$$L = h_v - h_l \tag{2.3}$$

with h_v and h_l the enthalpy of the gaseous and liquid phase, respectively. The latent heat is the enthalpy needed to evaporate a unit mass of liquid. It is a material property.

3. Nucleation and Droplet Growth models

From the previous treatment of condensation during rapid expansion, it is observed that the condensation process consists of two consecutive stages. The first one is the formation of liquid nuclei, nucleation, the second one is the condensation of vapour molecules on the already present nuclei, making these grow in the process of droplet growth. In the following, a brief treatment is given of the physical background of both nucleation and droplet growth together with the presentation of the models used to simulate these processes.

3.1. *Nucleation*

Under super–saturation vapour molecules can condense on liquid already present or on foreign objects. In the absence of both, the vapour molecules can form small clusters. As a result of the clustering, an additional phase needs to be formed, the interface between the liquid inside the cluster and the gas outside of the cluster. The interface can be regarded as infinitely thin. At the interface there is surface tension. Thus the creation of an interface requires energy. For very small clusters, the surface effects are dominant over volume related effects. As a result the formation of the interface represents an energy barrier in the formation process of the nucleus. If the energy involved in the clustering of the vapour molecules is less than required in the formation of the interface surface, the cluster will disintegrate immediately following its formation. Therefore at near equilibrium conditions, super–saturations close to one, it is highly unlikely, that a realistic number of stable nuclei in a volume at macro scale will be formed although clusters are constantly formed and falling apart. The previous notion results in formulation of formation enthalpy of critically sized stable nuclei, and the number densities in which these stable nuclei are likely to come into existence. The creation enthalpy of one liquid droplet under equilibrium conditions is given by Dohrmann (1989):

$$\Delta G = 4\pi r^2 \sigma - nkT \ln(s) \tag{3.1}$$

where, ΔG is the change in Gibbs enthalpy, r is the radius of the droplet, σ is the droplet surface tension in a plane with no curvature, n is the number of molecules in the droplet, k is the Boltzmann constant, and T is the temperature. In accordance with classical nucleation theory, we note that a stable nucleus will be created when the function for ΔG attains a local maximum. ΔG at this maximum is:

$$\Delta G = \frac{4}{3}\pi r^{*2}\sigma \tag{3.2}$$

with r^*, the radius of this critical sized droplet being given by:

$$r^* = \frac{2\sigma}{\rho_l R_v T \ln(s)} \tag{3.3}$$

where ρ_l is the density of the liquid in the droplet, and R_v is the gas constant of the vapour. The number of droplets created is given by the nucleation rate. For the nucleation rate several models are available, Classical Nucleation Theory CNT–model (Wegener 1969) and the Internally Consistent Classical Theory, ICCT–model (Luijten 1998). In the present work, the CNT–model is applied:

$$J = \frac{\rho_v^2}{\rho_l}\sqrt{\frac{2\sigma}{\pi m^3}}\exp\left(-\frac{16\pi}{3}\frac{\sigma^3}{m\rho_l^2 R_v^3 T^3 \ln^2(s)}\right) \tag{3.4}$$

where ρ_v is the density of the vapour and m is the mass of one vapour molecule.

3.2. *Droplet Growth*

The droplet growth model to be applied depends on the regime in which droplet growth takes place. For pressures of the order of atmospheric pressure droplet growth is based on a balance between condensation of vapour molecules onto droplets, and evaporation of vapour molecules from the droplet. For pressures 1 to 2 orders of magnitude higher, droplet growth is diffusion–controlled. In the present work, high pressure effects are not taken into account. Therefore the Hertz–Knudsen droplet growth model (Hill 1966) can be applied. The droplet growth rate is:

$$\frac{dr}{dt} = \frac{\alpha}{\rho_l}\left(\frac{p_v}{\sqrt{2\pi R_v T}} - \frac{p_{s,r}}{\sqrt{2\pi R_v T_d}}\right) \tag{3.5}$$

where α is an accommodation coefficient usually taken equal to one, T_d is the droplet temperature in the present work equal to the surrounding gas temperature and $p_{s,r}$ is the partial super–saturated vapour pressure over a curved radius of curvature r given by:

$$p_{s,r} = p_{v,eq}\exp\left(\frac{2\sigma}{\rho_l R_v T r_{hl}}\right) \tag{3.6}$$

where r_{hl} is the Hill droplet radius. This radius is computed as an averaged radius over the complete population of droplets at hand. This radius, of course, depends on the distribution function of the droplets.

4. Description of the Liquid Phase

Until now only, the creation and growth rate of a single droplet, and the creation rate, nucleation rate, of new droplets has been treated. Next to that, the size and form of individual droplets and the size and distribution of the droplet population need to be computed. As the number of droplets in the flow cases at hand typically range between 10^{12} and 10^{22} number of droplets per unit mass, it is impossible to describe individual droplets. One alternative approach is to define classes of droplets of similar radius, the class–model. This approach naturally extends to a description of the distribution of the

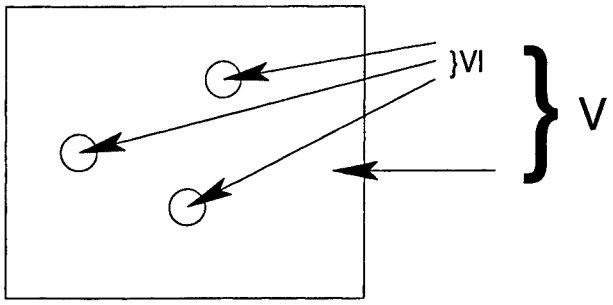


FIGURE 2. Liquid droplets in control volume

droplets. For the nozzle flow problems at hand, the typical range of radii of the droplets will be between 2.10^{-10} and 1.10^{-7}. This would require an impractical high number of droplet-classes, making the class-model computationally very expensive. Hill's method of moments is computationally less intensive at the cost of some of the resolution of the droplet distribution. As for the problems at hand, the total amount of liquid generated and the strong interaction between the gasdynamic flow and the condensation process is of primary interest, the loss of resolution of the droplet distribution is no severe penalty.

4.1. *Hill's Method of Moments*

Consider a control volume as depicted in figure 2. In the control volume a mixture of an ambient gas, and a vapour in its gaseous and its liquid state is present. A first assumption is that all liquid is present in the form of spherical droplets. Conservation of the mass in the control volume gives:

$$M = M_a + M_v + M_l \tag{4.1}$$

where M is the total mass in the control volume, M_a is the mass of the ambient gas, M_v is the mass of the condensible substance in gaseous form and M_l is the mass of the same substance in liquid form. The ambient air is assumed to be permanently above its critical temperature. The dimensionless liquid mass fraction g is defined as:

$$g = \frac{M_l}{M} = \frac{\rho_l V_l}{\rho V} = \rho_l \frac{V_l}{\rho V} \tag{4.2}$$

With the final notation emphasis is placed on the next assumption; the liquid mass present in the control volume is regarded to be incompressible. Therefore ρ_l is taken constant. The liquid mass fraction is a function of time. The density of the complete mixture; gas, vapour and liquid ρ, is dependent of time, as are the volume occupied by the liquid V_l and the total control volume V. This gives:

$$g(t) = \rho_l \frac{V_l(t)}{\rho(t)V(t)}.$$

The volume occupied by the liquid V_l is given by the following integral:

$$V_l(t) = \int_0^t \frac{4}{3}\pi r^3(t,\tau)J(\tau)V(\tau)d\tau \tag{4.3}$$

where $J(\tau)$ is the nucleation rate per unit volume and $V(\tau)$ is the size of the control

volume, at the moment of nucleation. The volume occupied by the droplets is given by $\frac{4}{3}\pi r^3(t,\tau)$. The function $r(t,\tau)$ describes the radius of the droplet, from its time of creation, $r(\tau_0,\tau_0)$ where this radius is equal to the critical radius as given in equation 3.3, $r(\tau_0,\tau_0) = r^*$, up to the present radius of the droplet at time t. Under the integral the product $J(\tau_0)V(\tau_0)$ acts as a weight function for the contribution of the liquid volume of the droplets created at time τ_0 to the total amount of liquid formed at time t. The liquid mass fraction now becomes:

$$g(t) = \rho_l \frac{\int_0^t \frac{4}{3}\pi r^3(t,\tau) J(\tau) V(\tau) d\tau}{\rho(t) V(t)}$$

If the considered lump of mass, liquid and gas–vapour mixture, is at rest, or flows along a stream–line, the fraction $\frac{M_v+M_l}{M_a}$ is fixed. This is identical to the assumption that the droplets do not move relative to the surrounding gas mixture. This is known as the no–slip condition in Hill's Method of Moments. This can be expressed as:

$$dM = 0 \Rightarrow M = \rho(\tau)V(\tau) = \rho(t)V(t)$$

The liquid mass fraction can be rewritten (Hagmeijer 2001):

$$g(t) = \rho_l \int_0^t \frac{4}{3}\pi r^3(t,\tau) \frac{J(\tau)}{\rho(\tau)} d\tau.$$

However, the function $r(t,\tau)$ is not readily available in closed form. The droplet growth rate $\frac{dr}{dt}$ is known in closed form. Therefore $g(t)$ is differentiated with respect to time:

$$\begin{aligned}
\frac{dg}{dt} &= \rho_l \frac{d}{dt} \int_0^t \frac{4}{3}\pi r^3(t,\tau) \frac{J(\tau)}{\rho(\tau)} d\tau \\
&= \rho_l \int_0^t \frac{4}{3}\pi 3 r^2(t,\tau) \frac{dr(t,\tau)}{dt} \frac{J(\tau)}{\rho(\tau)} d\tau + \rho_l \frac{4}{3}\pi r^3(t,t) \frac{J(t)}{\rho(t)} \\
&= \rho_l \frac{4}{3}\pi r^{*3} \frac{J(t)}{\rho(t)} + 3\rho_l \int_0^t \frac{4}{3}\pi r^2(t,\tau) \frac{dr(t,\tau)}{dt} \frac{J(\tau)}{\rho(\tau)} d\tau.
\end{aligned}$$

In this analysis, it is assumed, that at the initial time $t = 0$ there is no liquid present in the control volume. A third assumption is that the present droplet growth rate is independent of the present radius of the droplet. This assumption is certainly not true for very small droplets because of the dependency of the surface tension on the droplet radius, however the assumption is valid for droplets with larger radii.

$$\frac{dr}{dt} \neq \frac{dr}{dt}(r(t,\tau)) \tag{4.4}$$

This implies that, the present value of $\frac{dr}{dt}$, the droplet growth rate, is *independent* of its history. So it can be written:

$$\frac{dr}{dt} = \frac{dr}{dt}(t). \tag{4.5}$$

In this case, it is allowed to take the variation of the radius with time out of the integral:

$$\frac{dg}{dt} = \rho_l 4/3\pi r^{*3} \frac{J(t)}{\rho(t)} + 3\frac{dr}{dt}(t)\rho_l \int_0^t 4/3\pi r^2(t,\tau)\frac{J(\tau)}{\rho(\tau)}d\tau.$$

Careful inspection of the right–hand side of the relation above shows, that the original integral has reappeared; but with the power of the radius reduced by one, and multiplied by the power of the function r and the droplet growth rate. Following this observation, it is helpful to employ the following definition of a liquid moment:

$$Q_n(t) \equiv \int_0^t r^n(t,\tau)\frac{J(\tau)}{\rho(\tau)}d\tau.$$

Q_3 is closely related to the liquid mass fraction:

$$g(t) = \rho_l \frac{4}{3}\pi Q_3(t) \Rightarrow \frac{dg(t)}{dt} = \rho_l \frac{4}{3}\pi \frac{dQ_3(t)}{dt}.$$

The variation of this liquid moment $Q_n(t)$ with time is very much similar to expression of $\frac{dg}{dt}$:

$$\begin{aligned}\frac{dQ_n}{dt} &= r^{*n}(t)\frac{J(t)}{\rho(t)} + n\frac{dr}{dt}(t)\int_0^t r^{n-1}(t,\tau)\frac{J(\tau)}{\rho(\tau)}d\tau \\ &= r^{*n}(t)\frac{J(t)}{\rho(t)} + n\frac{dr}{dt}(t)Q_{n-1}\end{aligned}$$

which is a recurrent relation for the differentiation of Q_n. First consider the formulation of the relevant liquid moments:

$$\begin{aligned}Q_3 &= \int_0^t r^3(t,\tau)\frac{J(\tau)}{\rho(\tau)}d\tau \\ Q_2 &= \int_0^t r^2(t,\tau)\frac{J(\tau)}{\rho(\tau)}d\tau \\ Q_1 &= \int_0^t r(t,\tau)\frac{J(\tau)}{\rho(\tau)}d\tau \\ Q_0 &= \int_0^t \frac{J(\tau)}{\rho(\tau)}d\tau.\end{aligned}$$

Inspection of the last moment, Q_0, shows that there is no longer a functional dependence of t in the integral. So the differentiation of this last liquid moment can be expected to be different from the higher liquid moments:

$$\frac{dQ_0}{dt} = \frac{d}{dt}\left(\int_0^t \frac{J(\tau)}{\rho(\tau)}d\tau\right) = \frac{J(t)}{\rho(t)}.$$

This last result is fortunate, as it shows, that the logical expansion defined by the recurrence relation for the liquid moments, is not continued for $n < 0$. So there is no closure problem for the solution of the set of moments. The system of ordinary differential equations, to determine the liquid moment Q_3 now becomes:

$$\begin{aligned}
\frac{dQ_3}{dt} &= r^{*3}\frac{J(t)}{\rho(t)} + 3\frac{dr}{dt}(t)Q_2 \\
\frac{dQ_2}{dt} &= r^{*2}\frac{J(t)}{\rho(t)} + 2\frac{dr}{dt}(t)Q_1 \\
\frac{dQ_1}{dt} &= r^{*}\frac{J(t)}{\rho(t)} + \frac{dr}{dt}(t)Q_0 \\
\frac{dQ_0}{dt} &= \frac{J(t)}{\rho(t)}
\end{aligned}$$

In this system the variables represent the following quantities:

- Q_3 is proportional to the sum of all droplet volumes,
- Q_2 is proportional to the sum of all droplet surface areas,
- Q_1 is proportional to the sum of all droplet radii,
- Q_0 is the present number of droplets.

Now it is assumed that the droplet growth rate $\frac{dr}{dt}(t)$ is given only by the present local thermodynamic and chemical state, and not by the spatial gradients of r in the flow domain. In this case, $\frac{\partial r(t)}{\partial x_i} = 0$. By addition of the product of vector Q and the continuity equation for mass, the system of ordinary differential equations above can be rewritten in strong–conservation form:

$$\begin{aligned}
\frac{\partial \rho Q_3}{\partial t} + \frac{\partial \rho Q_3 u_i}{\partial x_i} &= r^{*3}J(t) + 3\frac{dr}{dt}(t)\rho Q_2 \\
\frac{\partial \rho Q_2}{\partial t} + \frac{\partial \rho Q_2 u_i}{\partial x_i} &= r^{*2}J(t) + 2\frac{dr}{dt}(t)\rho Q_1 \\
\frac{\partial \rho Q_1}{\partial t} + \frac{\partial \rho Q_1 u_i}{\partial x_i} &= r^{*}J(t) + \frac{dr}{dt}(t)\rho Q_0 \\
\frac{\partial \rho Q_0}{\partial t} + \frac{\partial \rho Q_0 u_i}{\partial x_i} &= J(t)
\end{aligned}$$

$$g(t) = \rho_l \frac{4}{3}\pi \frac{(\rho Q_3(t))}{\rho}$$

Where x_i and u_i are the spatial coordinates, and the velocity components in spatial direction respectively, r^*, J and $\frac{dr}{dt}(t)$ are given by the laws formulated for the creation and growth of a single droplet. The above set of equations gives the integral properties of the droplet distribution. So details of individual droplets are not available. To be able to compute a radius needed for droplet growth laws, Hill defined (Hill 1966) an averaged radius as:

$$r_{hl} = \sqrt{\frac{Q_2}{Q_0}} \tag{4.6}$$

Reason for application of Q_2 in calculation of r_{hl}, is the dominance of surface effects in droplet growth, hence the application of the integral surface quantity Q_2.

5. Thermodynamic State of Gas–Liquid Mixtures

The change of phase from vapour to liquid releases latent heat to the surrounding mixture. Due to the condensation, the fractions of the gases in the mixtures change. Both processes result in a change of the thermodynamic state of the mixture. To model these changes regard the enthalpy of the mixture:

$$Mh = M_a h_a + M_v h_v + M_l h_l$$

where $h = H/M$ is the specific enthalpy. By application of the previously defined dimensionless mass fraction $g = \frac{M_l}{M}$:

$$h = (1 - g_{max})h_a + (g_{max} - g)h_v + gh_l.$$

Application of the definition of the latent heat $L = h_v - h_l$ and the definition $c_p = \left(\frac{\partial h}{\partial T}\right)_{p,g}$ results in:

$$c_p = (1 - g_{max})c_{p_a} + (g_{max} - g)c_{p_v} + g(c_{p_v} - \frac{\partial L}{\partial T}_p). \tag{5.1}$$

Under the assumption $\frac{p_v}{\rho_v} - \frac{p}{\rho_l} \approx \frac{p_v}{\rho_v}$, a similar expression can be derived for the isochoric specific heat coefficient $c_v = \left(\frac{\partial e}{\partial T}\right)_{V,g}$:

$$c_v = (1 - g_{max})c_{v_a} + (g_{max} - g)c_{v_v} + g(c_{p_v} - \frac{\partial L}{\partial T}_v). \tag{5.2}$$

With these relations for the specific heat coefficients, the gas constant R_{mix} and the dimensionless ratio γ_{mix} can be computed similar to the case of an ideal gas, $R_{mix}(g, L) = c_p - c_v$ and $\gamma_{mix}(g, L) = \frac{c_p}{c_v}$. Both R and γ are now functions depending on the mass fraction g and the relation for the latent heat L. Derived quantities like pressure p and speed of sound c can be shown (Mundinger 1994) to be:

$$p = \rho R(g, l)T \qquad c^2 = \gamma(g, L)\frac{p}{\rho}.$$

6. Model of Inviscid Flow with Condensation

Based on Reynolds numbers for typical flow problem of interest the flow is assumed to be inviscid. The Euler equations are used to describe the flow. Together with Hill's Method of Moments, the models for nucleation and droplet growth and an equation of state they form a closed set of equations:

$$\frac{\partial}{\partial t}\int_V \underline{\phi}' dv + \int_{S=\partial V} \underline{\underline{F}}(\underline{\phi}') \cdot \underline{ds} = \int_V \underline{W}(\underline{\phi}')dv \tag{6.1}$$

where $\underline{\phi}'$ is the vector with the conserved quantities, $\underline{\underline{F}}(\underline{\phi}')$ the flux vector, and $\underline{W}(\underline{\phi}')$ is the source term:

$$\underline{\phi}' = \begin{bmatrix} \rho \\ \rho\underline{u} \\ \rho E \\ \rho Q_3 \\ \rho Q_2 \\ \rho Q_1 \\ \rho Q_0 \end{bmatrix} \quad \underline{\underline{F}}(\underline{\phi}') = \begin{bmatrix} \rho\underline{u} \\ \rho\underline{u}\underline{u} + \underline{\underline{I}}p \\ \rho\underline{u}H \\ \rho\underline{u}Q_3 \\ \rho\underline{u}Q_2 \\ \rho\underline{u}Q_1 \\ \rho\underline{u}Q_0 \end{bmatrix} \quad \underline{W}(\underline{\phi}') = \begin{bmatrix} 0 \\ \underline{0} \\ 0 \\ r^{*3}J(t) + 3\frac{dr}{dt}(t)\rho Q_2 \\ r^{*2}J(t) + 2\frac{dr}{dt}(t)\rho Q_1 \\ r^{*}J(t) + \frac{dr}{dt}(t)\rho Q_0 \\ J(t) \end{bmatrix} \tag{6.2}$$

where $\rho, \underline{u}, p$ are the density, the velocity and the pressure of the mixture. $E = e + \frac{1}{2}\|\underline{u}\|^2$ and $H = E + \frac{p}{\rho}$ are the total energy and the total enthalpy of the mixture. Q_i is the i–th moment in Hill's Method of Moments. The thermal equation of state reads:

$$p = \rho R(g, L)T \tag{6.3}$$

and the caloric equation of state:

$$e = c_v(g, L)T. \tag{6.4}$$

7. Finite Volume Discretization

With the definition of the control volume averaged ϕ_i:

$$\underline{\phi}_i = \frac{1}{V_i}\int_{V_i} \underline{\phi}' dv$$

equation 6.1is semi–discretized as:

$$\frac{\partial \phi_i}{\partial t} V_i + \sum_{j=1}^{n} \underline{f}(\phi_{i,j}) \cdot \underline{s}_{i,j} = w(\underline{\phi}) V_i$$

The summation of discrete fluxes $\sum_{j=1}^{n} \underline{f}(\phi_{i,j}) \cdot \underline{s}_{i,j}$ is computed using an edge–based data structure as described in Jameson (1986), Barth (1989) and Barth (1994). For every edge the indices of the 2 control volumes connected by the edge are stored, as well as the three spatial components of the surface normal vector of the surface between the two control volumes. The length of the surface normal vector is equal to the magnitude of the surface area. This edge–based approach allows for a cell–centered or a vertex–centered use of the original mesh, without significant changes to the flux computation algorithm. The fluxes are computed, by solving a local one–dimensional Riemann problem for every surface using an approximate Riemann solver. This is implemented in the flow solver for edges oriented in every possible direction in three–dimensional space. Two–dimensional problems with meshes in two independent directions can be regarded as a subclass of the full three–dimensional problem. The same holds for quasi one–dimensional or truly one–dimensional flow problems. With proper definition of additional boundary surfaces in the case of quasi one–dimensional flows, all flows can be computed using the same flow–solver regardless of the mesh being fully three-dimensional, two–dimensional or quasi or truly one–dimensional. The preprocessor, to the flow solver, generating the edge–based data structure from the meshes needs only to insert zeros for the edge–related surface normals

in the directions not relevant for the particular mesh. To date, pre–processors have been written for meshes consisting of line elements for one–dimensional meshes, triangular elements for unstructured two–dimensional meshes, quadrilaterals for structured monoblock two–dimensional meshes, and tetrahedral elements for three–dimensional meshes. However, the edge–based data structure allows simple extension to multiblock meshes, meshes constructed by hexahedra and hybrid meshes. This requires only the pre–processor for the particular element(s) to be developed, and minor additions to the domain boundary treatment in the flow solver. The flow solver has successfully completed simulations for one–, two– and three–dimensional flows. The great advantage of this approach is that almost all testing during development can be done for flow problems in one and two–dimensions decreasing development time, as formulation of one and two–dimensional flow problems and generation of one– and two–dimensional meshes is much less time consuming than in the full three–dimensional case. There is a penalty in the case of computation of one– and two–dimensional flows. For the one–dimensional case the momentum fluxes in the two spatial directions perpendicular to the main spatial direction are computed but not used. In the case of the Euler–equations this would result in 66% increased computational expense. In the two–dimensional case this increased computational expense is 25%. In the case of the computation of the Euler–equations and Hill's momentum equations, this computational overhead drops to 28% in the one–dimensional case, and 12% in the two dimensional case. However, the number of grid points for flow problems in two–dimensions and one–dimensions is one and two orders lower respectively. So the computational overhead is completely negligible next to the enormous advantage of simple and faster testing in lower dimensions.

Eigenvalue–analysis Kelleners (2001) of the complete system of Euler–equations with the Hill Momentum equations has shown that the additional eigenvalues due to the Hill equations are all real and have value $\underline{u}$. So the liquid moments $Q_0..Q_3$ are convected downstream along streamlines, and no new acoustic waves are introduced. The computation of the flux is identical to the case of flow without condensation, with only additional transport equations for the liquid moments.

The presence of the source terms in the Hill momentum equations results in the complete system of partial differential equations being a stiff system. Wishing to use an explicit time–stepping method as a relaxation method to compute a steady state, the fact that the system is stiff would lead to an unacceptable small time–step requirement due to the source terms. To circumvent this time–step restriction a fractional time–stepping method is used as proposed by Oran and Boris, Oran (1987) the differential equation of the form:

$$\frac{d\phi}{dt} + f(\phi) = w(\phi)$$

the solution procedure is split into:

$$\frac{d\phi^*}{dt_1} = -f(\phi^n) \tag{7.1}$$

$$\frac{d\phi^{n+1}}{dt_2} = w(\phi^*) \tag{7.2}$$

where the time–step operator for the first step can be any conventional explicit operator, e.g. Euler–forward or Runge–Kutta. The time step–operator for the second time step

needs to be able to cope with the possible large magnitude of the source $w(\phi^*)$, (see Oran 1987; Mundinger 1994)

The two following subsections highlight two topics which require detailed attention in the case of development of a spatial second–order accurate finite–volume method. For other topics like, flux splitting or flux limiting, see Jameson (1995) and Liou (1996).

7.1. *Higher Order Spatial Reconstruction*

To achieve good accuracy on meshes with moderate vertex densities the computational method must be at least second order. Whereas computation of first–order spatial accuracy allows for the storage location of the cell–averaged value to be located anywhere inside the control volume, this point should preferably be located at the geometric center of gravity for higher–order spatial accuracy. Use of the center of gravity circumvents severe penalties to the applicable CFL–number of individual control volumes. Higher–order reconstructions of cell–averaged data should conserve the cell–averaged value. In case of second–order reconstruction it can be proven that use of the center of gravity satisfies this requirement:

$$\underline{u}(\underline{x}) = \underline{u}_{cg} + \frac{\partial \underline{u}}{\partial \underline{x}}_{cg} (\underline{x} - \underline{x}_{cg}) \tag{7.3}$$

where $\underline{u}_{cg}$ is the cell–averaged value positioned at the center of gravity. $\underline{u}(\underline{x})$ integrated over the control volume gives:

$$\frac{1}{V}\int_V \underline{u}(\underline{x})dv = \frac{1}{V}\int_V \underline{u}_{cg}dv + \frac{1}{V}\int_V \frac{\partial \underline{u}}{\partial \underline{x}}_{cg} (\underline{x} - \underline{x}_{cg})dv \tag{7.4}$$

The first term on the right–hand side gives the cell–averaged value. The second term on the right hand side is zero. The gradient $\frac{\partial \underline{u}}{\partial \underline{x}}_{cg}$ can be moved in front of the integral. The remaining integral is the static moment about the center of gravity, and necessarily zero. For vertex–centered control volumes, the movement of the cell storage location, from cell-vertex to center of gravity of the control volume, is largest for control volumes at the physical boundaries of the domain.

7.2. *Linear Reconstruction at Domain Boundaries*

The assumption of linear reconstruction in the control volume in the case of second–order spatial accuracy, requires special attention at the domain boundaries. At solid wall boundaries the pressure part of the flux needs to be calculated. Question is, how the pressure must be integrated along the solid wall boundary surface for the resulting flux integral along the complete boundary of the control volume to be of second–order spatial accuracy. It is assumed that fluxes vary linearly over the control volume. Reconstruction of the flux at the solid wall boundary is therefore similar to linear reconstruction from the cell averaged state of the conservative variables throughout the control volume. The latter requires the computation of gradient the $\frac{\partial \phi}{\partial \underline{x}}$ at the center of the control volume. Green–Gauss reconstruction is often used for computation of this gradient Barth (1994); Aftosmis (1995). Green–Gauss reconstruction is easily implemented using the edge–based data structure. Starting point is Gauss' divergence theorem:

$$\int_V \nabla(\phi)dv = \int_s \phi d\underline{s} \tag{7.5}$$

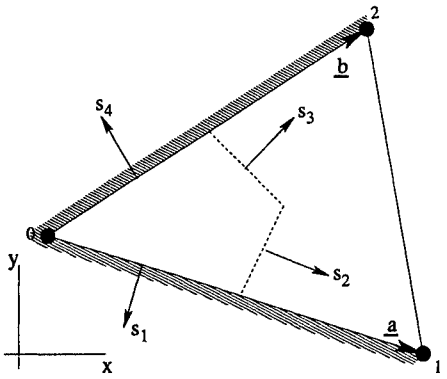


FIGURE 3. Median dual mesh control volume sharing sides with a physical boundary

which is rewritten in discrete form:

$$\nabla(\phi) = \frac{1}{V}\sum_i \phi_i \underline{s}_i \tag{7.6}$$

As an example the linear distribution of ϕ along a domain boundary for a control volume being the median dual to a two–dimensional triangular element is given, see figure 3. The volume V is the surface area associated with vertex 0 in the case of the median dual mesh is:

$$V = \frac{1}{6}\|\underline{a} \times \underline{b}\|$$

To evaluate equation 7.6, the outward pointing surface vectors $\underline{s}_1 ... \underline{s}_4$, and the mean values of the quantity $\phi_1 ... \phi_4$ need to be determined.

$$\begin{aligned}
\underline{s}_1 &= \frac{1}{2}\underline{a} \times \underline{e}_z \\
\underline{s}_2 &= (\frac{1}{3}\underline{b} - \frac{1}{6}\underline{a}) \times \underline{e}_z \\
\underline{s}_3 &= (\frac{1}{6}\underline{b} - \frac{1}{3}\underline{a}) \times \underline{e}_z \\
\underline{s}_4 &= -\frac{1}{2}\underline{b} \times \underline{e}_z
\end{aligned}$$

where $\underline{e}_z = \underline{e}_x \times \underline{e}_y$. ϕ_i is computed similar as would be the case for a median dual mesh volume embedded entirely in the physical domain. The value for ϕ_i at surfaces $\underline{s}_2$ and $\underline{s}_3$ is interpolated:

$$\begin{aligned}
\phi_{\underline{s}_2} &= \frac{1}{2}(\phi_0 + \phi_1) \\
\phi_{\underline{s}_3} &= \frac{1}{2}(\phi_0 + \phi_2)
\end{aligned}$$

At the surfaces $\underline{s}_1$ and $\underline{s}_4$ it is assumed that there exists a linear distribution of ϕ along the surface of the following form:

$$\phi = \omega\phi_0 + (1-\omega)\phi_i$$

The allowable value of ω is between zero and one. Substitution of $\underline{s}_i$ and ϕ_i in equation 7.6 ultimately gives:

$$\nabla(\phi) = \frac{1}{V}\sum_i \phi_i \underline{s}_i =$$

$$\begin{array}{lll} ((3\omega - \frac{3}{2})\phi_0 & +(\frac{5}{2} - 3\omega)\phi_1 & -\phi_2) \\ ((-3\omega + \frac{3}{2})\phi_0 & +\phi_1 & +(-\frac{5}{2} + 3\omega)\phi_2) \end{array} \quad \begin{array}{l} \frac{1}{a_x b_y - a_y b_x} \\ \frac{1}{a_x b_y - a_y b_x} \end{array} \begin{pmatrix} a_y \\ -a_x \end{pmatrix} + \begin{pmatrix} b_y \\ -b_x \end{pmatrix}$$

To compute the value of ω, the gradient $\nabla(\phi)$ is also computed assuming a linear distribution of ϕ in the triangle given by the vectors $\underline{a}$ and $\underline{b}$.

$$\phi(x) - \phi_0 = \alpha(x - x_0) + \beta(y - y_0)$$

The gradient for this linear distribution is:

$$\nabla(\phi) = \begin{pmatrix} \frac{\partial \phi}{\partial x} \\ \frac{\partial \phi}{\partial y} \end{pmatrix} = \begin{pmatrix} \alpha \\ \beta \end{pmatrix}$$

Using the data in vertices 1 and 2, ϕ_1, ϕ_2 a system can be derived, which can be solved for $\begin{pmatrix} \alpha \\ \beta \end{pmatrix}$. The solution of this system is:

$$\begin{pmatrix} \alpha \\ \beta \end{pmatrix} = \begin{pmatrix} a_x & a_y \\ b_x & b_y \end{pmatrix}^{-1} \begin{pmatrix} \phi_1 - \phi_0 \\ \phi_2 - \phi_0 \end{pmatrix}$$

Both expressions for $\nabla(\phi)$ are equal to one–another. Formulating this identity, and noting that it must be true for any value of ϕ_0, ϕ_1, ϕ_2, it can be shown that:

$$\omega = \frac{5}{6}$$

Returning to the assumption that the wall pressure flux is linearly distributed along the domain boundary surfaces, in a manner similar as any reconstructed scalar ϕ, the weights $\frac{5}{6}$ and $\frac{1}{6}$ can be applied to compute the integral of the pressure over the domain boundary surfaces. E.g. for surface $\underline{s}_4$ this becomes:

$$p_{\underline{s}_4}\underline{s}_4 = (\frac{5}{6}p_0 + \frac{1}{6}p_2)\underline{s}_4.$$

It should be stressed that the value of ω depends on the type of element at the domain boundary, (e.g. triangle, tetrahedron or brick) and the manner in which the control volume is defined (e.g. cell–centered or vertex–centered median dual mesh).

8. Results

The simulation tool described above has been used to compute solutions to flow problems of internal and external flows, adiabatic flows and flows with condensation. The cases presented below have been computed using the following layout of the solution algorithm. Node–centered finite–volume scheme, using median dual mesh cells. Explicit time stepping of the homogeneous equations as described in equation 7.2 using the second order Heun–method. For second order spatial resolution, application of a least–squares

algorithm for computation of spatial gradients in the flow field. Reconstruction of limited second–order states at the control volume interfaces using minimum–maximum restrictions formulated by Barth (1989), and a limiter function by Venkatakrishnan as presented in Aftosmis (1995). Fluxes computed using flux splitting according to Eberle. Computation of the time–updates due to the source terms as mentioned in equation 7.2 using a fractional time stepping method as presented in Mundinger (1994). Inflow boundaries conserving entropy and total enthalpy at infinity upstream for a general equation of state, outflow boundaries maintaining downstream static pressure in case of subsonic outflow, or simple first–order extrapolation of flow quantities in case of supersonic flow. At solid walls application of linear pressure distribution along the outward facing surfaces, as presented in section 7.2. Heat effects due to condensation, are taken into account by inclusion of both the gaseous and liquid phase into the energy conservation equation. This results in strong two–way coupling of the condensation process and the gasdynamics. All computations related to the equation of state, or material properties have been programmed into separate library routines. These libraries are called upon by the routines solving the conservation equations. This produces additional computational overhead, but should allow for quick implementation of different equations of state. In the present form of the flow solver only an equation of state for an ideal gas is implemented.

8.1. *Condensation in Nozzle Ba–120*

Flows with condensation in nozzle Ba–120, designed by Bartlmä, were investigated both experimentally and numerically by Schnerr and co–workers (see Mundinger 1994). Flows for two different humidities are presented in figure 4. The stagnation conditions for both flows in figure 4 are:

$s_0[\%]$	$T_0[K]$	p_0 [pa]
42.1	298.8	100900
49.3	297.1	100900

The expansion of the air–water–vapour mixture gives rise to condensation in the flow field downstream of the nozzle throat. This is seen by the steep rise in the nucleation rate. Following the creation of the nuclei is the process of droplet growth indicated by the rise of the liquid mass fraction $\frac{g}{g_{max}}$. The release of latent heat to the flow, induces a shock in both cases. However the shock-strength in the case of the higher humidity is much larger, and as a result the nucleation pulse is terminated abruptly. In both cases, the continuing expansion due to nozzle divergence results in condensation of almost all of the water–vapour at nozzle station $x = .15[m]$. In the Mach–isoline plot of the flow with higher humidity, the reflection of the curved shock–wave from the nozzle wall is nicely visible.

8.2. *Condensation in Vortex Flow*

To study the process of condensation in vortical flow, a very slender delta wing has been placed inside a tube, see figure 5. At the inlet of the tube a mixture of air–water–vapour flows in at Mach 1.55. The humidity of the mixture at stagnation condition is as low as 1.1%. The wing induces a vortex in the flow field. In the vortex core there is considerable loss of total pressure, clearly visible in figure 6. The vortex spirals downstream in the tube in a helical form. In the low pressure region in the vortex on the upper side of the wing, super–saturation occurs, resulting in large nucleation rate, see figure 7. Note that the region with the highest nucleation rates remains restricted to the front half of the wing close to the apex. This is a consequence of the droplet growth lowering the levels of super–saturation considerably once the first liquid droplets are created in great numbers.

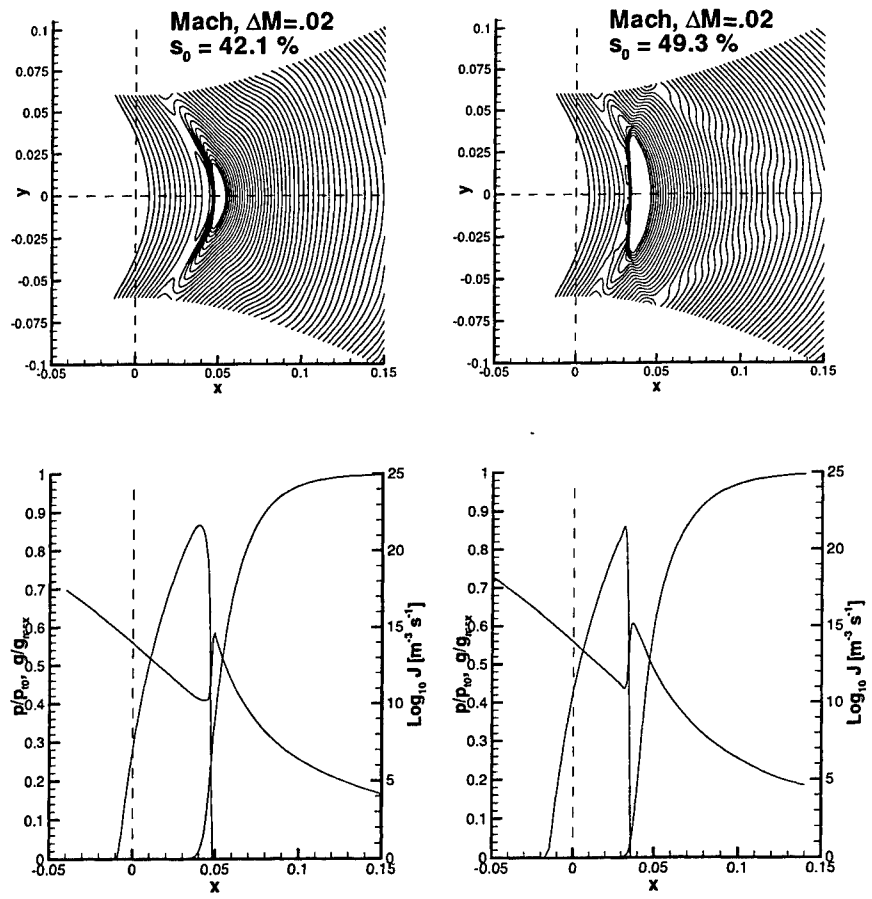


FIGURE 4. Flow with condensation in nozzle Ba120, flow from left to right. Humidity at stagnation condition for left figure: $s_0 = 42.1\%$, right figure $s_0 = 49.3\%$. Mach iso–lines in upper figures, only iso–lines for $M > 1$ are drawn. Nucleation rate J, dimensionless pressure $\frac{p}{p_{t0}}$, and liquid mass fraction $\frac{g}{g_{max}}$ in lower figures. Dashed lines indicate center line, and position of nozzle throat

The dimensionless liquid mass fraction $\frac{g}{g_{max}}$ is plotted in figure 8. On the second half of the upper side of the wing, almost all of the water is present in liquid form. Beyond the trailing edge of the wing, some evaporation of the liquid water occurs, but the main part of the water is convected downstream in liquid form. As the vortex is diffusing over the cross–sections of the tube, so is the cloud of water droplets, as can be noted from the similar shapes of the iso–lines of both the total pressure in figure 6 and the liquid mass fraction in figure 8

9. Conclusions

A brief treatment has been given on condensation in high speed flows. Because of large temperature gradients, the condensation can start well away from thermodynamic equi-

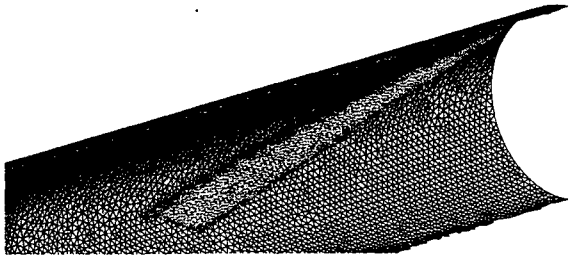


FIGURE 5. Layout of the delta wing, which produces the vortex. For clarity only one half of the tube wall is shown. Flow from upper right corner to lower left corner.



FIGURE 6. Total pressure, p_t

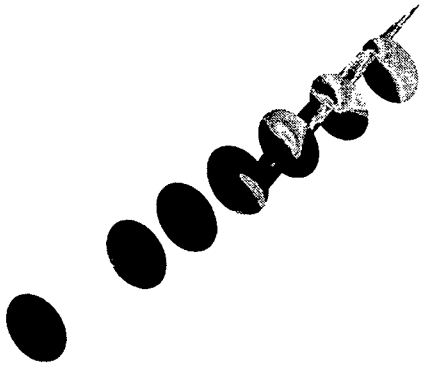


FIGURE 7. Nucleation rate, J plotted on a log–scale.



FIGURE 8. Liquid mass fraction, g.

librium, leading to fog–like clouds consisting of many small droplets. Basic nucleation and droplet–growth models have been presented. A thorough derivation of the integral description of the liquid phase, Hill's Method of Moments has been given. The complete model describing inviscid compressible multi–phase flow with condensation and its finite–volume discretization have been given. Two aspects of the implementation of the finite–volume method for achieving second–order spatial accuracy have been highlighted. Results presented for a two–dimensional flow problem, and a fully three–dimensional flow problem have been computed using one and the same flow solver. The benefit of developing only one single flow solver is clearly felt. From the case of higher humidity in nozzle Ba–120, a strong interaction between gasdynamics and condensation can already be seen. Higher humidities will lead to unsteady flow. Both experimental and numerical data is already available from Schnerr and co–workers. A future extension of the flow solver to take into account unsteady flow should be made. For flows with condensation in vortices simulations should be performed using the full Navier–Stokes equations, to validate the assumption of inviscid flow, made in this work. Improvements must be made with respect to accuracy and robustness of the solution algorithm, to make results of the simulation tool less dependent on grid quality, but the last problem is universal to CFD–methods.

10. Acknowledgments

Thanks are extended to Dr. T. J. Barth of CTR, (Center for Turbulence Research - NASA Ames) for fruitful discussions on consistent reconstruction of higher order spatial states, Dr. N. N. Mansour for creating a productive and enjoyable working environment at CTR, and to Prof. Dr. Ir. H. W. M. Hoeijmakers of Engineering Fluid Mechanics - University of Twente for proofreading of the present work, and continuing support. Funding for this work was provided by RIACS - Research Institute for Advanced Computer Science at NASA Ames Research Center, the JM Burgerscentrum - Research School for Fluid Mechanics in the Netherlands, and TIM - Twente Institute of Mechanics the Netherlands (IMPACT Institute of Mechanics, Processes, And Control - Twente).

REFERENCES

ADAM, S. 1996 Numerische und experimentelle Untersuchung instationärer Düsenströmungen mit Energiezufuhr durch homogene Kondensation, *PhD Thesis*, Universität Karlsruhe (TH), Germany.

AFTOSMIS, M., GAITONDE, D., SEAN TAVARES, T. 1995 Behaviour of Linear Reconstruction Techniques on Unstructured Meshes, *AIAA Journal*, Vol. 33, No. 11, 2038–2049.

BARTH, T.J., JESPERSEN, D.C. 1989 The Design and Application of Upwind Schemes on Unstructured Meshes, *AIAA Paper* 89-0366, AIAA 27th Aerospace Sciences Meeting, Reno, January 1989.

BARTH, T.J. 1995 Aspects of Unstructured Grids and Finite–Volume Solvers for the Euler and Navier–Stokes Equations *VKI Lecture Series* 1994-05, Revised February 1995.

CAMPBELL, J.F., CHAMBERS, J.R., RUMSEY, C.L. 1989 Observation of Airplane Flowfields by Natural Condensation Effects, *AIAA Journal*, Vol. 26, No. 7, 593–604.

DOHRMANN, U. 1989 Ein numerisches Verfahren zur Berechnung stationärer transsonischer Strömungen mit Energiezufuhr durch homogene Kondensation, *PhD Thesis*, Universität Karlsruhe (TH), Germany.

HAGMEIJER, R. 2001 *Private communication*, University of Twente.

HILL, P.G. 1966 Condensation of Water Vapour during Supersonic Expansion in Nozzles, *Journal of Fluid Mechanics*, Vol. 25, part 3, pp. 593–620.

JAMESON, A., BAKER, T.J., WEATHERILL, N.P. 1986 Calculation of Inviscid Transonic Flow Over a Complete Aircraft, *AIAA Paper* 86-0103, AIAA 24th Aerospace Sciences Meeting, Reno, January 1986.

JAMESON, A. 1995 Analysis and Design of Numerical Schemes for Gas Dynamics 1 Artificial Diffusion, Upwind Biasing, Limiters and Their Effect on Accuracy and Multigrid Convergence, *RIACS Technical Report* 94.15, International Journal of Computational Fluid Dynamics, Vol. 4, pp. 171-218.

LAMANNA, G. 2000 On Nucleation and Droplet Growth in Condensing Nozzle Flows, *PhD Thesis*, Eindhoven University of Technology, The Netherlands, ISBN 90-386-1649-X.

LIOU, M.S. 1996 A Sequel to AUSM: AUSM+, *Journal of Computational Physics*, Vol 129, 364–382, Academic Press Inc.

LUIJTEN, C.C.M. 1998 Nucleation and Droplet Growth at High Pressure, *PhD Thesis*, Eindhoven University of Technology, the Netherlands, ISBN 90-386-0747-4.

LUIJTEN, C.C.M., VAN DONGEN, M.E.H. 1999 Nucleation at high pressure. 1. Theoretical considerations, *Journal of Chemical Physics*, Vol. 111, Number 18.

MUNDINGER, G. 1994 Numerische Simulation instationärer Lavaldüsenströmungen mit Energiezufuhr durch homogene Kondensation, *PhD Thesis*, Universität Karlsruhe (TH), Germany.

ORAN, E.S., BORIS, J.P. 1987 Numerical Simulation of Reactive Flow, Elsevier Science Publishing Co., Inc. New York, ISBN 0-444-01251-6.

PRAST, B. 1997 Condensation in Supersonic Expansion Flows; Theory and Numerical Evaluation, Eindhoven: Stan Ackermans Institute, Ontwerpers opleiding Computational Mechanics.

KELLENERS, P.H., PUT, F., HAGMEIJER, R., HOEIJMAKERS, H.W.M. 2001 Development if a Numerical Method for the Simulation of Condensing Real Gas Flows, *ICMF-2001* paper 152, International Conference on Multiphase Flow, New Orleans, May 2001.

SCHNERR, G.H., MEIER, G.E.A. 1996 Control of Flow Instabilities and Unsteady Flows, *International Center for Mechanical Sciences, Courses and Lectures*, - No. 369, Springer Verlag, New York.

WEGENER, P.P. 1969 Nonequilibrium Flows, Part 1, Marcel Dekker, New York and London.

Large-eddy simulation of stratocumulus-topped atmospheric boundary layers with dynamic subgrid-scale models

By Inanc Senocak

1. Motivation and objectives

Earth's climate and its geographical variation is strongly influenced by cloud coverage. It is estimated that about 50% of the earth is covered by clouds at any given time, providing a shield from solar radiation. Radiative energy transfer and its interaction with clouds play an important role in the thermal structure and stratification of the atmosphere. For instance, clouds have high reflectivity in the visible wavelengths, thus providing relative cooling of the atmosphere. They also absorb strongly in the infrared wavelengths, resulting in heating of the atmosphere (Salby 1996).

Condensation is the major physical process that is responsible for cloud formation. Clouds can be classified into four broad categories, namely: cumulus, cirrus, nimbus and stratus (Rogers & Yau 1989). Many other classifications can be derived from combinations of these four broad categories. A comprehensive description can be found in Scorer & Wexler (1967). Among various types of clouds, marine stratocumulus clouds have received increased attention because of the important role they play in the global radiation budget. Marine stratocumulus clouds cover about 25% of the Earth's ocean at any instant. These are low-level clouds that exist below 1.5 km with several hundred meters in thickness and they rarely produce precipitation. Their horizontal coverage is extensive and more homogeneous than other type of clouds. Their appearance is grey and a wavy undersurface is typical (Kantha & Clayson 2000; Heymsfield 1993; Mason 1975).

The structure of the marine stratocumulus cloud-topped atmospheric boundary layer is driven by both cloud-top radiative cooling and positive buoyancy flux from the surface that maintains the atmospheric boundary layer in a well-mixed turbulent state. Above the cloud layer, negative buoyancy flux has a stabilizing effect, suppressing the turbulence there (Kantha & Clayson 2000). The entrainment of dry air from above the cloud layer induces evaporative cooling and entrained air parcel can sink further down enhancing the turbulent mixing within the clouds, known as cloud top entrainment instability (Deardorff 1980*a*). Clearly, the structure of cloud-topped atmospheric boundary is more complicated than a cloud-free atmospheric boundary layer due to strong interactions among cloud microphysics, turbulent motions and the radiative energy transfer.

In large-eddy simulation (LES), three-dimensional, large unsteady flow structures are resolved and the effects of the unresolved scales are modeled. A filtering operation is applied to the governing equations to distinguish between the resolved scales that are computed and smaller scales that are modeled. LES has been widely applied to simulate atmospheric boundary layers, partly because of the difficulties involved in observational studies and field experiments (Stevens & Lenschow 2001). An extensively studied topic is LES of cloud-free convective atmospheric boundary layers. The salient features of these boundary layers have been compared to observations and well documented (Kantha

& Clayson 2000). The presence of clouds complicates the problem due to additional physics and reliable numerical simulations of cloud-topped boundary layer is still an active research area. In the following, several representative studies are briefly mentioned to help describe the current state of the knowledge.

An early study on three-dimensional modeling of cloud-topped atmospheric boundary layer is by Deardorff (1980*b*). He studied the structure of turbulence and entrainment within stratocumulus layers with and without cloud-top radiative cooling and suggested that simulations need high resolution at the inversion. It was also found that a functional dependence on Richardson number helps correlate the entrainment rate. Deardorff (1980*a*) has defined a criterion for the cloud top entrainment instability. It was found that entrainment rate increases decisively when the equivalent potential temperature gradient across the cloud top drops below a critical value. It was also shown that a strong instability can lead to stratocumulus breakup leading to a scattered cumulus layer. Tag & Payne (1987) indicated that in addition to Deardorff's criterion, the vertical motions should exceed a threshold for the cloud breakup to occur.

Moeng (1986) studied the structure of a stratus-topped boundary layer using LES. It was found that the vertical component of the turbulent kinetic energy is generated by buoyancy and a portion of this energy is redistributed in the horizontal directions due to pressure effects. It was also shown that turbulence is generated more effectively by surface heating than cloud-top cooling.

Bohnert (1993) tested the dynamic procedure for LES of cloud-topped boundary layer. Simple parametrization for cloud microphysics and radiation were adopted. The dynamic model results were compared to the results of SGS model that were optimized in an ad-hoc fashion. The results were found to be comparable. The importance of SGS modeling in predicting cloud breakup was also highlighted.

Stevens *et al.* (2000) investigated the dependence of an LES model on mesh resolution, numerical schemes and SGS model. They provided simulations of varying resolutions for the simulation of stratocumulus topped marine boundary layer. Different SGS models and advection schemes were tested. It was found that thickness of the inversion layer, depth of entraining eddies and shape of the vertical velocity spectra is influenced by mesh resolution. Motions at the inversion were found to be underresolved even for the finest resolution. The entrainment rate was found to depend on both numerical and SGS dissipation.

Duynkerke, Zhang & Jonker (1995) performed an observational study to describe the microphysical and turbulent structure of stratocumulus observed during the Atlantic Stratocumulus Transition Experiment (ASTEX). The turbulence kinetic energy budget, velocity and temperature variance, and vertical fluxes were calculated. The entrainment was found to be very efficient, which resulted in reduction of turbulent kinetic energy production due to buoyancy. It was also shown that water vapor flux, liquid water flux, and drizzle rate have the same magnitude.

Stevens *et al.* (1998) presented an LES study of the ASTEX case. They adopted a drop-size resolving cloud microphysics model that enabled them to perform simulations with and without drizzle. It was found that inclusion of drizzle in modeling leads to sharp decrease in entrainment and turbulent kinetic energy generation by buoyancy. The authors have hypothesized that shallow, well-mixed radiatively driven stratocumulus cannot persist in the presence of heavy drizzle.

Duynkerke *et al.* (1999) did a comparison of actual ASTEX observations with computations obtained from LES and one-dimensional single column models. The buoyancy

flux obtained from LES agrees well with the observations. The authors concluded that drizzle has small influence on the buoyancy flux, although significant uncertainty exists in its parametrization.

The objective of the present study is to evaluate the dynamic procedure in LES of stratocumulus topped atmospheric boundary layer and assess the relative importance of subgrid-scale modeling, cloud microphysics and radiation modeling on the predictions. The simulations will also be used to gain insight into the processes leading to cloud top entrainment instability and cloud breakup. In this report we document the governing equations, numerical schemes and physical models that are employed in the Goddard Cumulus Ensemble model (GCEM3D). We also present the subgrid-scale dynamic procedures that have been implemented in the GCEM3D code for the purpose of the present study.

2. Numerical formulation

The numerical model used in this study to simulate cloud-topped atmospheric boundary layers is the Goddard Cumulus Ensemble model(GCEM3D). Its main features are described in Tao & Simpson (1993), Simpson & Tao (1993) and Tao *et al.* (2003).

2.1. *Governing equations*

Acoustic waves are part of the solution of the compressible Navier-Stokes equations and very small time steps are needed to resolve them. On the other hand, acoustic waves do not impact the dynamics of thermal convection for low Mach number flows. Therefore, the governing equations of motion are simplified by filtering out the sound waves from them. The resulting set of equations is known as the anelastic equations (Ogura & Phillips 1962). In deriving these equations the basic assumption is to decompose the thermodynamic state variables into a horizontally averaged base quantity, which only depends on altitude, and a perturbation quantity, which depends on both time and space, as follows

$$\begin{aligned} p(x,y,z,t) &= p_o(z) + p'(x,y,z,t), \\ \rho(x,y,z,t) &= \rho_o(z) + \rho'(x,y,z,t), \\ T(x,y,z,t) &= T_o(z) + T'(x,y,z,t), \end{aligned} \tag{2.1}$$

where p is the pressure, ρ is the density of moist air and T is the temperature. The following moist equation of state is used in deriving the momentum equations

$$p = \rho RT(1 + 0.61q_v), \tag{2.2}$$

where R is the gas constant for dry air and q_v is the mixing ratio of water vapor. The pressure is nondimensionalized according to a reference pressure (p_o) value

$$\pi = (\frac{p}{p_o})^{R/C_p}, \tag{2.3}$$

where C_p is the specific heat of dry air at constant pressure. The potential temperature is defined as

$$\theta = \frac{T}{\pi}. \tag{2.4}$$

The anelastic form of the filtered continuity equation reads as follows

$$\frac{\partial(\rho_o \bar{u}_i)}{\partial x_i} = 0. \tag{2.5}$$

The filtered momentum equations, using the f-plane approximation, are written as

$$\frac{\partial \bar{u}_i}{\partial t} + \frac{1}{\rho_o}\frac{\partial(\rho_o \bar{u}_i \bar{u}_j)}{\partial x_j} = -C_p \theta_o \frac{\partial \pi'}{\partial x_i} + \frac{\partial \tau_{ij}}{\partial x_j} + g_i\left(\frac{\theta'}{\theta_o} + 0.61 q_v' - q_l\right) + F_{coriolis}, \tag{2.6}$$

where g_i is the gravitational acceleration. The Coriolis term that appears in the momentum equations is written as

$$F_{coriolis} = [2\omega sin\phi u_2, -2\omega sin\phi u_1, 0], \tag{2.7}$$

where ω is the angular velocity of the Earth and ϕ gives the latitude. τ_{ij} represents the subgrid scale stress tensor and its particular form is described in section 2.3. The primed variables represent deviation from horizontally averaged quantities.

The equations for potential temperature θ and the water vapor mixing ratio q_v are written as follows

$$\frac{\partial \bar{\theta}}{\partial t} + \frac{1}{\rho_o}\frac{\partial(\rho_o \bar{\theta} \bar{u}_i)}{\partial x_i} = -\frac{\partial \gamma_i^{\theta}}{\partial x_i} + \frac{L_v}{C_p}(c - e_c - e_r) + \frac{L_f}{C_p}(f_s + f_g - m_s - m_g) + \frac{L_s}{C_p}(d_{ice} - s_{ice}) + Q_{rad}, \tag{2.8}$$

$$\frac{\partial \bar{q}_v}{\partial t} + \frac{1}{\rho_o}\frac{\partial(\rho_0 \bar{q}_v \bar{u}_i)}{\partial x_i} = -\frac{\partial \gamma_i^{q_v}}{\partial x_i} + (c - e_c - e_r) + (d_{ice} - s_{ice}), \tag{2.9}$$

where L_v, L_f and L_s are the latent heats of condensation, fusion and sublimation, respectively. The quantities $c, e_c, e_r, f, m, d_{ice}, s_{ice}$ represent the rates of condensation, evaporation of cloud droplets, evaporation of rain drops, freezing of rain drops, melting of snow and graupel/hail, deposition of ice particles and sublimation of ice particles, respectively. The particular forms for these phase change rates are not explicitly formulated. Instead, a saturation adjustment scheme is adopted that calculates the amount of phase change rate in order to remove any supersaturated vapor and/or subsaturation of cloud water. The saturation adjustment scheme is described in Soong & Ogura (1973) and Tao, Simpson & McCumber (1989). γ_i^{ϕ} is the subgrid scale flux of the scalar, which is explained in section 2.3. Q_{rad} is the source due to radiative heat transfer. It is described in section 2.4.

2.2. *Cloud microphysics model*

The formulation of the cloud microphysical processes is based on solving scalar transport equations for each hydrometeor species. The transport equations for cloud water (q_c), cloud ice (q_{ice}), rain (q_r), snow (q_s), graupel/hail (q_g) are written as

$$\frac{\partial \bar{q}_c}{\partial t} + \frac{1}{\rho_o}\frac{\partial(\rho_o \bar{q}_c \bar{u}_i)}{\partial x_i} = -\frac{\partial \gamma_i^{q_c}}{\partial x_i} + (c - e_c) + T_{q_c}, \tag{2.10}$$

$$\frac{\partial \bar{q}_{ice}}{\partial t} + \frac{1}{\rho_o}\frac{\partial(\rho_o \bar{q}_{ice} \bar{u}_i)}{\partial x_i} = -\frac{\partial \gamma_i^{q_{ice}}}{\partial x_i} + (d_{ice} - s_{ice}) + T_{q_{ice}}, \tag{2.11}$$

$$\frac{\partial \bar{q}_r}{\partial t} + \frac{1}{\rho_o}\frac{\partial(\rho_o \bar{q}_r \bar{u}_i)}{\partial x_i} - \frac{1}{\rho_o}\frac{\partial(\rho_o \bar{q}_r U_r)}{\partial x_3} = -\frac{\partial \gamma_i^{q_r}}{\partial x_i} + (m_s + m_g - f_s - f_g - e_r) + T_{q_r}, \tag{2.12}$$

$$\frac{\partial \bar{q}_s}{\partial t} + \frac{1}{\rho_o}\frac{\partial(\rho_o \bar{q}_s \bar{u}_i)}{\partial x_i} - \frac{1}{\rho_o}\frac{\partial(\rho_o \bar{q}_s U_s)}{\partial x_3} = -\frac{\partial \gamma_i^{q_s}}{\partial x_i} + (d_s - s_s - m_s + f_s) + T_{q_s}, \tag{2.13}$$

$$\frac{\partial \bar{q}_g}{\partial t} + \frac{1}{\rho_o}\frac{\partial(\rho_o \bar{q}_g \bar{u}_i)}{\partial x_i} - \frac{1}{\rho_o}\frac{\partial(\rho_o \bar{q}_g U_g)}{\partial x_3} = -\frac{\partial \gamma_i^{q_g}}{\partial x_i} + (d_g - s_g - m_g + f_g) + T_{q_g}, \quad (2.14)$$

where V_r, V_s and V_g are the fall speeds of rain, snow and graupel, respectively. Their values are obtained from parameterizations. γ_i^{ϕ} is the subgrid-scale flux of the scalar. T_ϕ represents the microphysical transfer rates between the hydrometeor species. A total of 27 different processes are considered and the reader is referred to Lin, Farley & Orville (1983) for details of their formulation. To illustrate the parameterizations of these processes, only the microphysical transfer rate of rain T_{q_r} is described in this report. For instance, if the temperature is above $0°C$, then the production term for rain is given by the following equation

$$T_{q_r} = P_{RACW} + P_{RAUT} + P_{SACW} + P_{GACW} - P_{GMLT} - P_{SMLT} + P_{REVP}(1-\delta_1). \quad (2.15)$$

The terms on the right hand side of the above equation are the accretion of cloud water by rain, autoconversion of cloud water to form rain, accretion of cloud water by snow, accretion of cloud water by graupel, melting of graupel to form rain, melting of snow to form rain, evaporation of rain, respectively. The accretion of rain by cloud water P_{RACW} is written as

$$P_{RACW} = \frac{\pi E_{rw} n_{0r} a q_c \Gamma(3+b)}{4\lambda_r^{3+b}}, \quad (2.16)$$

where E_{rw} is the collection efficiency, which is assumed to be 1, n_{0r} is the intercept parameter of the rain drop size distribution, Γ is the gamma function, λ_r is the slope parameter in rain size distribution and a, b are empirical constants. Exponential size distributions are assumed for rain, snow and graupel/hail. The explicit forms of other transformation rates are documented in Lin *et al.* (1983).

2.3. *Subgrid-scale turbulence models*

Three turbulence closure models will be considered for comparison. These are the subgrid-scale kinetic energy model of Klemp & Wilhelmson (1978),which is the base turbulence model in the GCEM3D code, the dynamic Smagorinsky model of Germano *et al.* (1991) and the localized dynamic Smagorinsky model of Piomelli & Liu (1995). The implementation of dynamic turbulence models by Kirkpatrick (2002) has been coupled to the GCEM3D code. In the following sections these models are briefly explained.

2.3.1. *Subgrid-scale kinetic energy model*

A transport equation for subgrid-scale turbulent kinetic energy is solved, which is then used to specify the eddy viscosity. The influence of buoyancy on the turbulent motions is also modeled. The equation for subgrid-scale turbulent kinetic energy is written as

$$\frac{\partial E}{\partial t} + \frac{1}{\rho_o}\frac{\partial(\rho_o E \bar{u}_i)}{\partial x_j} = \overline{gw'(\frac{\theta'}{\theta_o} + 0.61q_v' - q_l')} - \tau_{ij}\frac{\partial \bar{u}_i}{\partial x_j} + \frac{\partial}{\partial x_j}(K_m \frac{\partial E}{\partial x_j}) - \frac{C_e}{\Delta}E^{3/2}, \quad (2.17)$$

$$\Delta = (\Delta x \Delta y \Delta z)^{1/3},$$
$$K_m = C_m \Delta E^{1/2},$$
$$\tau_{ij} = \frac{2}{3}E\delta_{ij} - K_m(\frac{\partial \bar{u}_i}{\partial x_j} + \frac{\partial \bar{u}_j}{\partial x_i}), \quad (2.18)$$

where K_m is the turbulent eddy viscosity, Δ is the filter width. The empirical constants C_e and C_m have the values of 0.7 and 0.2,respectively. The subgrid-scale scalar fluxes

are modeled as

$$\gamma_i^{\phi} = K_h \frac{\partial \phi}{\partial x_i}, \tag{2.19}$$

where $K_h/K_m = 3$ is used. The buoyancy flux in a saturated area is computed as

$$\overline{w'(\frac{\theta'}{\theta_o} + 0.61 q_v' - q_l')} = -AK_h \frac{\partial \theta_e}{\partial z} + K_h \frac{\partial q_t}{\partial z}, \tag{2.20}$$

where

$$A = \frac{1}{\theta_o} \frac{1 + \frac{1.61 \varepsilon L q_v}{R_d T}}{1 + \frac{\varepsilon L^2 q_v}{C_p R_d T^2}}, \tag{2.21}$$

and $\varepsilon = 0.622$.

In an unsaturated area, the buoyancy flux is computed as follows:

$$\overline{w'(\frac{\theta'}{\overline{\theta}} + 0.61 q_v' - q_l')} = -K_h (\frac{1}{\overline{\theta}} \frac{\partial \theta}{\partial z} + 0.61 \frac{\partial q_v}{\partial z}). \tag{2.22}$$

2.3.2. *Dynamic Smagorinsky model*

Smagorinsky model (Smagorinsky 1963) is commonly used in LES to model the subgrid scale stresses. It is based on eddy viscosity assumption and can be written as

$$\tau_{ij} - \frac{1}{3} \delta ij \tau_{kk} = -2C\Delta^2 |\bar{S}| \bar{S}_{ij}, \tag{2.23}$$

where C is a dimensionless parameter and $|\bar{S}| = \sqrt{2\bar{S}_{ij}\bar{S}_{ij}}$. The filtered strain rate is defined as

$$\bar{S}_{ij} = \frac{1}{2} (\frac{\partial \bar{u}_i}{\partial x_j} + \frac{\partial \bar{u}_j}{\partial x_i}). \tag{2.24}$$

Germano *et al.* (1991) have introduced the dynamic procedure that offers advantages over the original Smagorinsky model. In this model the parameter C is computed at each time step from the information already available in the resolved velocity field. The basic formalism behind the dynamic Smagorinsky model is explained in the following.

The dynamic model involves filters of different sizes. In addition to the grid filter, a test filter is introduced. The subgrid scale stress tensor based on the grid filter and the test filter are written respectively as

$$\begin{aligned} \tau_{ij} &= \overline{u_i u_j} - \bar{u}_i \bar{u}_j, \\ T_{ij} &= \widehat{\overline{u_i u_j}} - \hat{\bar{u}}_i \hat{\bar{u}}_j, \end{aligned} \tag{2.25}$$

where the symbols overbar and the hat represent the grid and test filtering operations, respectively. Applying the test filter to τ_{ij} and subtracting it from T_{ij} yields the following identity (Germano, 1992)

$$L_{ij} = T_{ij} - \hat{\tau}_{ij} = \widehat{\bar{u}_i \bar{u}_j} - \hat{\bar{u}}_i \hat{\bar{u}}_j. \tag{2.26}$$

The significance of this identity is that it can be computed from the large eddy field. Germano *et al.* (1991) have utilized this identity to dynamically compute the coefficient of the Smagorinsky model as follows.

$$L_{ij} - \frac{1}{3} \delta_{ij} L_{kk} = \alpha_{ij} C - \widehat{\beta_{ij} C}, \tag{2.27}$$

where

$$\alpha_{ij} = -2\widehat{\Delta}^2\widehat{\bar{S}}\widehat{\bar{S}}_{ij},$$
$$\beta_{ij} = -2\Delta^2\bar{S}\bar{S}_{ij}. \tag{2.28}$$

For atmospheric boundary layers, where the horizontal directions are assumed to homogenous, the filtering operation is applied only in the horizontal direction and C is assumed to be independent of the homogeneous directions and taken out of the filtering operator. Equation (2.27) is rearranged to the following form

$$L_{ij} - \frac{1}{3}\delta_{ij}L_{kk} = CM_{ij}, \tag{2.29}$$

where

$$M_{ij} = \alpha_{ij} - \widehat{\beta}_{ij}. \tag{2.30}$$

Following the method described in Lilly (1992), the coefficient C is computed so as to minimize the sum of the squares of the residuals of equation (2.29).The numerator and the denominator are averaged over the horizontal (x,y)-plane.

$$C(z,t) = \frac{\langle M_{ij}L_{ij}\rangle_{xy}}{\langle M_{kl}M_{kl}\rangle_{xy}}. \tag{2.31}$$

Once C is calculated, the subgrid scale stress tensor, given in equation (2.23) is computed. In a similar approach, the subgrid-scale flux of a scalar ϕ can be computed dynamically Moin *et al.* (1991). If we consider the following eddy diffusivity subgrid-scale model

$$\gamma_i = -\frac{\nu_t}{Pr_t}\frac{\partial\bar{\phi}}{\partial x_i}, \tag{2.32}$$

where the kinematic eddy viscosity is computed with the dynamic Smagorinsky model as $\nu_t = C\Delta^2|\bar{S}|$. The dynamic procedure can also be applied to compute the turbulent Prandtl number Pr_t. The subgrid-scale scalar flux based on the test filter scale is written as

$$G_i = -\frac{C\hat{\Delta}^2}{Pr_t}|\hat{\bar{S}}|\frac{\partial\hat{\bar{\phi}}}{\partial x_i} \tag{2.33}$$

The test and grid scale fluxes are related to each other by the following identity

$$P_i = G_i - \hat{\gamma}_i = \widehat{\bar{\phi}\bar{u}_i} - \hat{\bar{\phi}}\hat{\bar{u}}_i = -C\frac{\hat{\Delta}^2|\hat{\bar{S}}|}{Pr_t}\frac{\partial\hat{\bar{\phi}}}{\partial x_i} + C\frac{\widehat{\Delta^2|\bar{S}|}}{Pr_t}\frac{\partial\bar{\phi}}{\partial x_i}. \tag{2.34}$$

The above equation can be recast into the following form

$$P_i = -\frac{C}{Pr_t}R_i. \tag{2.35}$$

Following the suggestion of Lilly (1992), a least squares procedure is applied to compute the value of Pr_t. Note that the value of C is determined earlier.

$$\frac{1}{Pr_t} = -\frac{1}{C}\frac{\langle P_iR_i\rangle_{xy}}{\langle R_mR_m\rangle_{xy}} \tag{2.36}$$

After calculating the Pr_t, equation (2.31) is used to compute the subgrid scale flux of a scalar.

2.3.3. *Approximate localized dynamic Smagorinsky model*

The dynamic Smagorinsky model is not general for flows with no homogeneous direction, because of the need for averaging in the homogeneous directions. Ghosal *et al.* (1995) have addressed the mathematical inconsistencies and proposed a new formulation for the dynamic procedure that makes it applicable to arbitrary inhomogeneous flows. They have also provided formal justifications for the ad-hoc procedures that have been adopted in the early versions of the dynamic model.

The mathematical inconsistency in previous versions comes from the fact that space and time dependent coefficient C is simply taken out of the filtering operation. In the variational formulation of Ghosal *et al.* (1995), C is kept inside and an integral equation needs to be solved at each time step to determine C. This method is referred to as the dynamic localization model.

The solution of an integral equation is costly. Piomelli & Liu (1995) have followed a simpler approach and proposed the approximate localized dynamic model. In the following this method is briefly described.

Equation (2.27) is recast in the following form.

$$-C\alpha_{ij} = L^a_{ij} + \widehat{C^*\beta_{ij}}, \tag{2.37}$$

where

$$L^a_{ij} = L_{ij} - \frac{1}{3}\delta_{ij}L_{kk}. \tag{2.38}$$

An estimated value C^* is assumed, which is the value of C from the previous time step. Along with this approximation, a least squares procedure is applied to compute C as given below

$$C = -\frac{(L^a_{ij} + \widehat{C^*\beta_{ij}})\alpha_{ij}}{\alpha_{mn}\alpha_{mn}}. \tag{2.39}$$

The same iterative idea applies to equation (2.31) to compute the Pr_t of the subgrid-scale flux of a scalar quantity.

2.4. *Radiation model*

In an effort to describe the physical models in GCEM3D code in a single document, we briefly summarize the basic formalism of the radiation modeling.

The plane parallel assumption is typically adopted to model the radiative energy transfer. The convenience of the assumption comes from the fact that the properties of the atmosphere vary sharply with height due to its stratification, hence, the medium is regarded as horizontally homogeneous (Salby 1996).

The intensity of a radiation pencil, traversing a distance ds along the direction of its propagation, changes due to absorbtion, scattering and emission, which can be described by the following equation (Liou 2002).

$$dI_\lambda = -K_\lambda \rho I_\lambda ds + j_\lambda \rho ds, \tag{2.40}$$

where k_λ is the mass extinction cross section due to absorbtion and scattering and j_λ is the source function due to emission and scattering. In plane-parallel assumption, it is convenient to define an optical thickness as

$$\tau = \int_{z'}^{\infty} k_\lambda dz, \qquad dz = \mu ds, \qquad \mu = \cos\theta, \tag{2.41}$$

where z is the vertical direction and θ is the angle between the path of radiation and the

vertical, which is specifically called the zenith angle. The basic equation, describing the radiative energy transfer in plane-parallel atmospheres is written as

$$\mu \frac{dI(\tau;\mu,\phi)}{d\tau} = I(\tau;\mu,\phi) - J(\tau;\mu,\phi). \tag{2.42}$$

The source function J is defined as

$$J(\tau;\mu,\phi) = \frac{\tilde{\omega}}{4\pi}\int_0^{2\pi}\int_{-1}^{1} I(\tau;\mu',\phi')P(\mu,\phi;\mu',\phi')d\mu' d\phi' + \frac{\tilde{\omega}}{4\pi}F_o P(\mu,\phi;-\mu_0,\phi_0)e^{-\tau/\mu_0} - (1-\tilde{\omega})B[T(\tau)], \tag{2.43}$$

where $P(\mu,\phi;\mu',\phi')$ is the phase function, which gives the angular distribution of scattered energy as a function of direction, ϕ is the azimuthal angle, $\tilde{\omega}$ is the single scattering albedo, $B[T(\tau)]$ is the Planck's function representing the blackbody emission of the medium, and F_o is the solar irradiance at the top of atmosphere. Upon solution of equation (2.43), the flux density F_λ and the total flux density F are computed based on the following definitions

$$F_\lambda^{\uparrow\downarrow}(\tau) = 2\pi\int_0^1 I_\lambda^{\uparrow\downarrow}(\tau,\pm\mu)\mu d\mu \qquad , F = \int_0^\infty F_\lambda d\lambda. \tag{2.44}$$

The heating rate due to radiation that appears in the potential temperature equation, Q_{rad}, is then computed as

$$Q_{rad} = -\frac{1}{\rho_0 C_p}\frac{dF(z)}{dz}. \tag{2.45}$$

Equation (2.43) is an integrodifferential equation and its numerical solution is quite involved due to sharp variation of the atmospheric properties with height. The computation of radiation fluxes involves spectral, vertical and directional integrations. Because the absorbtion coefficient varies sharply with wave number, the spectral integration is the most CPU intensive part. However, the major difficulty comes from the dependence of the absorbtion coefficient on pressure and temperature. Hence, effective parametrization is an important part in the numerical solution of equation (2.42). Different approaches are adopted depending on the nature of the radiation problem. A detailed account of atmospheric radiation modeling can be found in Liou (2002).

The radiative transfer model that is incorporated into the GCEM code is documented in Chou & Suarez (1996*a*,*b*).The radiation scheme can model the absorbtion due to water vapor, CO_2, O_3, and O_2, and scattering by clouds, aerosols and molecules. Fluxes are integrated almost over the full spectrum, ranging from 0.175 μm to 10μm. The radiation field is divided into three distinct regions. In the ultraviolet and photosynthetically active regions, the spectrum is divided into 8 bands, in which single O_3 absorption coefficient and Rayleigh scattering coefficient is used for each band. The infrared region is divided into three bands and the k-distribution method is applied with ten absorption coefficients in each band. The δ-Eddington approximation is used to compute the reflection and transmission of a cloud and aerosol-laden layer. Two-stream adding method is then used to compute the fluxes.

2.5. *Numerical schemes*

In GCEM3D code, the governing equations are discretized on a staggered grid. The momentum equations are solved using the second order central difference scheme for the

spatial derivatives and the second order accurate leap-frog scheme for temporal derivatives. A time smoother is adopted to avoid the time splitting problem associated with the leap-frog scheme. Forward time differencing and the multi-dimensional positive definite advection transport algorithm (MPDATA) of Smolarkiewicz & Grabowski (1990) are used to solve the scalar transport equations. A direct solver (FFT) is utilized for the solution of the pressure Poisson equation. The GCEM3D code has been parallelized to run on the SGI Origin clusters using OpenMP (Jin *et al.* 2003).

Lateral boundary conditions are periodic and free slip boundary conditions are imposed on the top and bottom boundaries for all the variables except the vertical velocity that vanishes at the top and bottom boundary.

3. Future work

The sugrid-scale turbulence models described in the previous section will be tested with progressively refined mesh resolutions, adopting the ASTEX field experiment as the test case. The relative influence of subgrid-scale modeling, cloud microphysics and radiation modeling on the predictions will be investigated. The simulations will also be used to gain insight into the processes leading to the cloud top entrainment instability and cloud breakup. Additionally, the dynamic modeling subroutine will be parallelized to speed up the overall computation.

Preliminary computations produced comparable results of wind speeds, soundings of cloud water and potential temperature among the subgrid-scale models considered. However, the computations also indicated problems with the top boundary resulting in spurious cloud formation and unstable stratification. A possible cure to the problem might be to use a Rayleigh absorbing layer, which is commonly used in atmospheric simulations, in the proximity of the top boundary to damp the vertically propagating gravity waves.

In this report we have briefly documented the governing equations and physical models that are employed in the GCEM3D code. We have also described the subgrid-scale dynamic procedures that have been introduced to the GCEM3D code in this study. We are in the process of double checking the implementation and the results. The findings of the present study will be published in the open literature.

REFERENCES

BOHNERT, M. 1993 A numerical investigation of cloud-topped planetary boundary layers. PhD thesis, Stanford University.

CHOU, M. D. & SUAREZ, M. J. 1996*a* An efficient thermal infrared radiation parameterization for use in general circulation models. NASA Technical Memorandum vol:3 no:104606.

CHOU, M. D. & SUAREZ, M. J. 1996*b* A solar radiation parameterization (CLIRAD-SW) for atmospheric studies. NASA Technical Memorandum vol:15 no:104606.

DEARDORFF, J. W. 1980*a* Cloud top entrainment instability. *J. Atmos. Sci* **37**, 131–147.

DEARDORFF, J. W. 1980*b* Stratocumulus-capped mixed layers derived from a three-dimensional model. *Boundary-Layer Meteorol.* **18**, 495–527.

DUYNKERKE, P. G., JONKER, P. J., CHLOND, A., ZANTEN, M. C. V., CUXART, J., CLARK, P., SANCHEZ, E., MARTIN, G., LENDERINK, G. & TEIXEIRA, J. 1999 Intercomparison of three- and one-dimensional model simulations and aircraft observations stratocumulus. *Boundary-Layer Meteorol.* **92**, 453–487.

DUYNKERKE, P. G., ZHANG, H. & JONKER, P. J. 1995 Microphysical and turbulent structure of nocturnal stratocumulus as observed during ASTEX. *J. Atmos. Sci.* **52**, 2763–2777.

GERMANO, M., PIOMELLI, U., MOIN, P. & CABOT, W. H. 1991 A dynamic subgrid-scale eddy viscosity model. *Phys. Fluids* **3**, 1760–1765.

GHOSAL, S., LUND, T. S., MOIN, P. & AKSELVOLL, K. 1995 A dynamic localization model for large-eddy simulation of turbulent flows. *J. Fluid Mech.* **286**, 229–255.

HEYMSFIELD, A. J. 1993 Microphysical structures of stratiform and cirrus clouds. In *Aerosol-Cloud-Climate Interactions* (ed. P. V. Hobbs), *International Geophysics Series*, vol. 54, pp. 97–121. Academic Press.

JIN, H., JOST, G., JOHNSON, D. & TAO, W. K. 2003 Experience on the parallelization of a cloud modeling code using computer-aided tools. *Tech. Rep.* NAS-03-006. NAS Division, NASA Ames Research Center.

KANTHA, L. H. & CLAYSON, C. A. 2000 *Small Scale Processes in Geophysical Fluid Flows*. Academic Press.

KIRKPATRICK, M. P. 2002 Turbulence modelling in large-eddy simulations of the cloud-topped atmospheric boundary layer. Annual Research Briefs, Center for Turbulence Research, NASA-Ames/Stanford Univ.

KLEMP, J. B. & WILHELMSON, R. B. 1978 The simulation of three-dimensional convective storm dynamics. *J. Atmos. Sci.* **35**, 1070–1096.

LILLY, D. K. 1992 A proposed modification of the Germano subgrid-scale closure method. *Phys. Fluids* **4**, 633–635.

LIN, Y.-L., FARLEY, R. D. & ORVILLE, H. D. 1983 Bulk parameterization of the snow field in a cloud model. *J. Clim. Appl. Meteor.* **22**, 1065–1092.

LIOU, K. N. 2002 *An Introduction to Atmospheric Radiation*, 2nd edn. Academic Press.

MASON, P. J. 1975 *Clouds, Rain and Rainmaking*. Cambridge University Press.

MOENG, C. H. 1986 Large-eddy simulation of a stratus-topped boundary layer. Part-1: Structure and budgets. *J. Atmos. Sci* **43**, 2886–2900.

MOIN, P., SQUIRES, K., CABOT, W. H. & LEE, S. 1991 A dynamic subgrid-scale model for compressible turbulence and scalar transport. *Phys. Fluids* **3**, 2746–2757.

OGURA, Y. & PHILLIPS, N. 1962 Scale analysis of deep and shallow convection in the atmosphere. *J. Atmos. Sci* **19**, 173–179.

PIOMELLI, U. & LIU, J. 1995 Large-eddy simulation of rotating channel flows using a localized model. *Phys. Fluids* **7**, 839–848.

ROGERS, R. R. & YAU, M. K. 1989 *A Short Course in Cloud Physics*, 3rd edn. Butterworth-Heinemann.

SALBY, M. L. 1996 *Fundamentals of Atmospheric Physics*. Academic Press.

SCORER, R. & WEXLER, H. 1967 *Cloud Studies in Colour*. Pergamon Press.

SIMPSON, J. & TAO, W. K. 1993 Goddard Cumulus Ensemble model. Part 2: Applications for studying cloud precipitating processes and for NASA TRMM. *Terr. Atmos. Ocean Sci.* **4**, 73–116.

SMAGORINSKY, J. 1963 General circulation experiments with the primitive equations. I. The basic experiment. *Mon. Weather Rev.* **91**, 99–164.

SMOLARKIEWICZ, P. K. & GRABOWSKI, W. W. 1990 The multidimensional positive definite advection transport algorithm: Nonoscillatory option. *J. Comput. Phys,* **86**, 355–375.

SOONG, S. T. & OGURA, Y. 1973 A comparison between axisymmetric and slab-symmetric cumulus cloud models. *J. Atmos. Sci* **30**, 879–893.

STEVENS, B., COTTON, W. R., FEINGOLD, G. & MOENG, C.-H. 1998 Large-eddy simulations of strongly precipitating, shallow, stratocumulus-topped boundary layers. *J. Atmos. Sci.* **55**, 3616–3638.

STEVENS, B. & LENSCHOW, D. H. 2001 Observations, experiments, and large eddy simulation. *Bull. Amer. Meteor. Soc.* **82**, 283–294.

STEVENS, D. E., BELL, J. B., ALMGREN, A. S., BECKNER, V. E. & RENDLEMAN, C. A. 2000 Small-scale processes and entrainment in a stratocumulus marine boundary layer. *J. Atmos. Sci.* **57**, 567–581.

TAG, P. M. & PAYNE, S. W. 1987 An examination of the breakup of marine stratus: A three-dimensional numerical investigation. *J. Atmos. Sci* **44**, 208–223.

TAO, W. K. & SIMPSON, J. 1993 Goddard Cumulus Ensemble model. Part 1: Model description. *Terr. Atmos. Ocean Sci.* **4**, 35–72.

TAO, W. K., SIMPSON, J., BAKER, D., BRAUN, S., M. D. CHOU, B. F., JOHNSON, D., KHAIN, A., LANG, S., LYNN, B., SHIE, C. L., STARR, D., SUI, C. H., WANG, Y. & WETZEL, P. 2003 Microphysics, radiation and surface processes in the Goddard Cumulus Ensemble (GCE) model. *Meteorol. Atmos. Phys.* **82**, 97–137.

TAO, W. K., SIMPSON, J. & MCCUMBER, M. 1989 An ice-water saturation adjustment. *Mon. Weather. Rev.* **117**, 231–235.

Numerical simulation of protoplanetary vortices

By H. Lin, J.A. Barranco † AND P.S. Marcus ‡

1. Introduction

The fluid dynamics within a protoplanetary disk has been attracting the attention of many researchers for a few decades. Previous works include, to list only a few among many others, the well-known α-prescription of Shakura & Sunyaev (1973), the convective and instability study of Stone & Balbus (1996) and Hawley *et al.* (1999), the Rossby wave approach of Lovelace *et al.* (1999), as well as a recent work by Klahr & Bodenheimer (2003), which attempted to identify turbulent flow within the disk. The disk is commonly understood to be a thin gas disk rotating around a central star with differential rotation (the Keplerian velocity), and the central quest remains as how the flow behavior deviates (albeit by a small amount) from a strong balance established between gravitational and centrifugal forces, transfers mass and momentum inward, and eventually forms planetesimals and planets.

In earlier works (Barranco & Marcus 2000; Barranco *et al.* 2000; Lin *et al.* 2000) we have briefly described the possible physical processes involved in the disk; we have proposed the existence of long-lasting, coherent vortices as an efficient agent for mass and momentum transport. In particular, Barranco *et al.* (2000) provided a general mathematical framework that is suitable for the asymptotic regime of the disk; Barranco & Marcus (2000) addressed a proposed vortex-dust interaction mechanism which might lead to planetesimal formation; and Lin *et al.* (2002), as inspired by general geophysical vortex dynamics, proposed basic mechanisms by which vortices can transport mass and angular momentum. The current work follows up on our previous effort. We shall focus on the detailed numerical implementation of our problem. We have developed a parallel, pseudo-spectral code to simulate the full three-dimensional vortex dynamics in a stably-stratified, differentially rotating frame, which represents the environment of the disk. Our simulation is validated with full diagnostics and comparisons, and we present our results on a family of three-dimensional, coherent equilibrium vortices.

2. Governing equations

Scaling issues have been discussed in both Barranco *et al.* (2000) and Lin *et al.* (2002), and shall not be repeated. Here we simply list the governing equations that we propose to solve numerically, namely

$$\frac{\partial \bar{\rho}\mathbf{v}}{\partial t} + \bar{\rho}(\mathbf{v}\cdot\nabla\mathbf{v}) = -2\bar{\rho}\Omega_o\mathbf{z}\times(\mathbf{v}-\bar{\mathbf{v}}) - \nabla\tilde{p} - \tilde{\rho}\Omega_o^2 z\mathbf{z}, \tag{2.1}$$

$$\nabla\cdot(\bar{\rho}\mathbf{v}) = 0, \tag{2.2}$$

$$\frac{\partial T}{\partial t} + \mathbf{v}\cdot\nabla T = -(\gamma-1)T_o\left(1+\frac{\tilde{p}}{\bar{p}}\right)\frac{v_z z}{H_o^2} - \frac{T}{\tau_{rad}(z)}, \tag{2.3}$$

† Department of Astronomy, University of California, Berkeley
‡ Department of Mechanical Engineering, University of California, Berkeley

$$\frac{\tilde{p}}{\bar{p}} = \frac{\tilde{\rho}}{\bar{\rho}} + \frac{\tilde{T}}{T_o}. \tag{2.4}$$

Here the equations are written in a rotating frame with an angular velocity Ω_o, x is the streamwise (ϕ) direction, y is the radial (r) direction, z is the direction about which the frame is rotating, and $\mathbf{z}$ is its corresponding unit vector. In our notation system $\bar{\rho}$, $\bar{p}$, T_o and $\bar{\mathbf{v}}$ denote the base state density, pressure, temperature and velocity, respectively, and their forms will be given shortly. The tilde quantities $\tilde{\rho}$ and $\tilde{p}$ denote the deviations of density and pressure from the base states, respectively, and γ is the ratio of specific heats. Finally H_o is the scale hight of the disk and τ_{rad} is a radiation time scale. Compared with the governing equations (4.1-4.4) of Lin *et al.* (2002), we have further expanded the energy equation making use of the anelastic continuity equation (2.2); we have also linearized the equation of state to obtain equation (2.4) which is consistent with our current low-Mach number asymptotic regime.

We nondimensionalize equations (2.1-2.4) with the following scales:

$$[L] = H_o, \quad [\mathbf{v}] = c_s, \quad [t] = \frac{[L]}{[\mathbf{v}]} = \frac{1}{\Omega_o},$$

$$[\rho] = \rho_o, \quad [p] = \rho_o c_s^2 = p_o, \quad [T] = T_o,$$

where c_s is the speed of sound, ρ_o is a characteristic density, and T_o is the characteristic (base) temperature. The resulted *dimensionless* equations are

$$\frac{\partial \bar{\rho}\mathbf{v}}{\partial t} = -\bar{\rho}(\mathbf{v}\cdot\nabla)\mathbf{v} - 2\bar{\rho}\mathbf{z}\times(\mathbf{v}-\bar{\mathbf{v}}) - \nabla\tilde{p} - \tilde{\rho}z\mathbf{z}, \tag{2.5}$$

$$\nabla\cdot(\bar{\rho}\mathbf{v}) = 0, \tag{2.6}$$

$$\frac{\partial T}{\partial t} = -\mathbf{v}\cdot\nabla T - (\gamma-1)\left(1+\frac{\tilde{p}}{\bar{p}}\right)v_z z - \frac{T}{\tau_{rad}(z)}, \tag{2.7}$$

$$\tilde{p} = \tilde{\rho} + \bar{\rho}\tilde{T}. \tag{2.8}$$

The base states, as discussed in Lin *et al.* (2002), are given (in *dimensionless* form) as:

$$\bar{p} = \bar{\rho} = \bar{\rho}_o(y)\exp\left(-\frac{z^2}{2}\right), \tag{2.9}$$

$$\bar{\mathbf{v}} = \frac{3}{2}y\mathbf{x}, \tag{2.10}$$

where $\bar{\rho}_o(y)$ represents the radial variation of the base density, and $\mathbf{x}$ is the unit vector in the x direction. The dimensionless base temperature, which is assumed to be constant, simply becomes $T_o = 1$. For the radiation time τ_{rad}, we currently assume the following dimensionless form,

$$\tau_{rad}(z) = \tau_o\exp\left(-z^2\right).$$

We set τ_o to be approximately 10^6 times that of the orbital period (denoted τ_{orb}). When such a value is assumed there is almost no radiative dissipation at the midplane, and the radiation time scale is comparable to the orbital period close to the upper and lower boundaries of the disk. The radiation scheme captures only the long term dissipative behavior of the disk, and has a negligible effect on dynamics that have time scales comparable with orbital periods.

Equations (2.5-2.8), together with appropriate boundary conditions, are the set of equations we solve numerically.

3. Numerical scheme

Before presenting in detail the numerical algorithm, it is appropriate to address a few of the special challenges involved in the system we are trying to solve. First, we have a base shear flow in a rotating frame as indicated by equation (2.10). For this kind of problem it is natural to think about a sliding-box formulation, as it has been implemented by Rogallo (1981) and Hawley *et al.* (1999). Two of the current authors (J.A.B. and P.S.M.) have also developed a similar algorithm to solve the system of equations (2.5-2.8) using the sliding-box methodology. In this sliding-box formulation, flow in the radial direction is artificially periodic after subtraction of the convection ensued from the base shear flow, and the vertical direction is represented in Chebyshev series to capture the non-periodic buoyancy (gravity) force. Nonetheless, because in the current code we aim to represent a non-periodic radial thermodynamic (potential-vorticity) background (see discussions in Lin *et al.* (2002)), we can no longer assume the artificial periodicity in y, and functions in this direction should be instead represented in Chebyshev series. This complication forces us to assume an artificial periodicity in the vertical direction under the current framework of a Fourier-Fourier-Chebyshev representation, and we shall have more discussions regarding this point later. Secondly, we account for density variation (albeit with a simplified form) *via* the anelastic continuity equation (2.6), and capture the stably-stratified physics through a vertically decaying density $\bar{\rho}$, a temperature (energy) evolution equation (2.7), and a buoyancy (gravity) force term in the momentum equation (2.5). Thirdly, because the base density has the fast-decaying form of equation (2.9) (*e.g.* at $z = \pm 3H_o$, the base density decays to only 1% of its value at the midplane), it should be carefully treated to avoid numerical instability. Finally, the coherent vortices we are trying to identify assumes full three-dimensional structures for reasons discussed in Barranco *et al.* (2000).

We solve equations (2.5-2.8) with a pseudo-spectral scheme. We represent functions in the x and z direction with Fourier series, and functions in the y direction by Chebyshev series. Because of the artificial periodicity in the z direction, we have to replace the variable z in the buoyancy force term $\tilde{\rho}z$ with a new periodic function z^* that equals z for most of the domain, but comes back to zero to enforce periodicity toward the upper and lower boundaries (see Figure 1). Because the base density $\bar{\rho}$ (and hence momentum, energy, *etc.*) becomes very small where z^* has the largest deviation from z, and because our vortices have a compact structure around $z = 0$, the influence of this replacement of z with z^* is assumed to be minimal.

For time integration we adopt a Leap-Frog scheme for calculation of the nonlinear terms. Our algorithm can be compactly written as

$$\hat{\mathbf{u}}^{M+1} = \mathbf{u}^{M-1} + 2\Delta t(\mathbf{n}^M - \tilde{\rho}^M z^* \mathbf{z}), \tag{3.1}$$

$$\nabla^2 \tilde{p}^M = \nabla \cdot \hat{\mathbf{u}}^{M+1}, \qquad \left[\frac{\partial \tilde{p}^M}{\partial y} = \frac{1}{2\Delta t}\hat{u}_y^{M+1}\right]_{y=\pm 1}, \tag{3.2}$$

$$\mathbf{u}^{M+1} = \hat{\mathbf{u}}^{M+1} - 2\Delta t \nabla \tilde{p}^M, \tag{3.3}$$

$$T^{M+1} = (T^{M-1} + 2\Delta t n_T) e^{-2\Delta t/\tau_{rad}}, \tag{3.4}$$

where

$$\mathbf{u} \equiv \bar{\rho}\mathbf{v} \tag{3.5}$$

is momentum and our working variable, the superscript M denotes quantities at the M^{th} time step, $\mathbf{n}$ is the sum of the nonlinear terms on the RHS of equation (2.5) excluding the

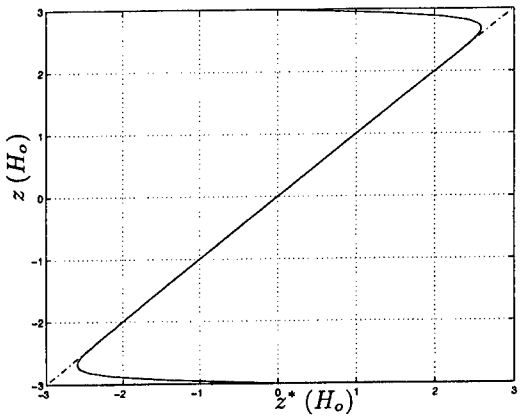


FIGURE 1. The artificially enforced periodic function z^* (solid), compared with the original linear function z (dash-dotted). In this plot the vertical domain extends from $-3H_o$ to $3H_o$; the value of the base density $\bar{\rho}$ at the upper and lower boundaries ($z \approx \pm 3H_o$) is about 1% of its value at the midplane ($z = 0$). Our vortex structure, as we shall present later, is compact in z and primarily assumes the domain from $-H_o$ to H_o.

buoyancy force, and n_T is the sum of the nonlinear terms on the RHS of equation (2.7) excluding the radiation term. The Helmholtz equation (3.2) is inverted to solve for pressure which consequently enforces the divergence free condition (2.6) at the $(M+1)^{th}$ step. In our code we have also implemented a τ-method that ensures equation (2.6) is satisfied for all Chebyshev modes. We found that the latter method improves numerical stability. For boundary conditions, we are currently implementing no-flow condition at $y = \pm 1$ (which is enforced by the pressure boundary condition when solving for $\tilde{p}^M$ in (3.2)). The advantage of doing this is to contain our flow and enforce conservation laws within the computational domain. Finally we apply a 6^{th} order hyperviscosity/hyperdiffusion on both the momentum and energy equations to ensure numerical stability.

Note that we have not adopted the more commonly practiced Adams-Bashforth (for nonlinear terms) and Crank-Nicolson (for pressure) time-integration scheme. This is because the current Leap-Frog scheme has better performance in terms of avoiding the instability caused by the large density variation of $\bar{\rho}$ in the vertical direction. Note also that when inverting the Helmholtz problem (3.2) for $\tilde{p}^M$, the $\hat{\mathbf{u}}^{M+1}$ term on the RHS contains a buoyancy term $\tilde{\rho}^M z^*$, in which the density $\tilde{\rho}^M$ is related to the pressure $\tilde{p}^M$ *via* the equation of state (2.8). This coupling problem is resolved by an iterative method. We use $\tilde{\rho}^{M-1}$ as the initial value $\tilde{\rho}_0^M$ to enter the iteration on the RHS of equation (3.2). Once the pressure $\tilde{p}_0^M$ is obtained by inverting the Helmholtz problem, it is used to obtain a new density function using

$$\tilde{\rho}_{i+1}^M = \tilde{p}_i^M - \bar{\rho}\tilde{I}^M, \tag{3.6}$$

which subsequently enters the Helmholtz solver as the new density. we found that ~ 5 times of this procedure give excellent convergence at an acceptable computational cost.

To improve the speed of the code we have also implemented a "faster" variation of our algorithm. This implementation is based on the following consideration. We can rewrite the momentum and energy equations as

$$\frac{\partial \mathbf{u}}{\partial t} = -\sigma y \frac{\partial \mathbf{u}}{\partial x} + \mathbf{n} - \nabla\tilde{p} - \tilde{\rho} z^* \mathbf{z}, \tag{3.7}$$

$$\frac{\partial T}{\partial t} = -\sigma y \frac{\partial T}{\partial x} + n_T - \frac{T}{\tau_{rad}}, \tag{3.8}$$

where $\sigma = \frac{3}{2}$ is the shear rate of the base flow, and $\mathbf{n}$ and n_T are the same as previously defined. In this case, however, we further exclude the base-shear convection terms. The base shear flow poses a major constraint on the size of the time-step if calculated explicitly, whereas the flow structure we are interested in is only a small deviation from this base flow (Barranco *et al.* 2000). We therefore separate the base convective terms $-\sigma y \frac{\partial \mathbf{u}}{\partial x}$ and $-\sigma y \frac{\partial T}{\partial x}$ and treat them analytically. Our new algorithm, in which the base convection is represented in terms of waves, is written

$$\hat{\mathbf{u}}^{M+1} = e^{-2ic\Delta t}\mathbf{u}^{M-1} + e^{-ic\Delta t}2\Delta t(\mathbf{n}^M - \nabla\tilde{p}^{M-1} - \tilde{\rho}^{M-1}z^*\mathbf{z}), \tag{3.9}$$

$$\mathbf{u}^{M+1} = \hat{\mathbf{u}}^{M+1} - 2\Delta t[\nabla(\tilde{p}^M - \tilde{p}^{M-1}) + (\tilde{\rho}^M - \tilde{\rho}^{M-1})z^*\mathbf{z}], \tag{3.10}$$

$$T^{M+1} = (e^{-2ic\Delta t}T^{M-1} + e^{-ic\Delta t}2\Delta t n_T^M)e^{-2\Delta t/\tau_{rad}}. \tag{3.11}$$

Here $c \equiv k_x\sigma y$, that is, these exponents are applied for each wave number k_x in the x direction and at each point y in the transverse domain. This formula assumes the form of a semi-implicit, predictor-corrector algorithm of second-order accuracy. Again a Helmholtz problem is solved to obtain pressure and enforce continuity equation, and an iterative method is used to simultaneous obtain $\tilde{p}^M$ and $\tilde{\rho}^M$. In this new algorithm our effective flow number is calculated from

$$|\tilde{\mathbf{v}}| = |\mathbf{v} - \bar{\mathbf{v}}| \ll |\bar{\mathbf{v}}|.$$

Because the maximum value of $\tilde{\mathbf{v}}$ is typically only 1/5 that of $\bar{\mathbf{v}}$, we can use significantly larger time steps.

Our algorithms are implemented for parallel computation using MPI, with a communication algorithm for FFT provided by Dr. Alan Wray. We test and run our code on the *SGI Origin 2000* clusters at NASA Ames. We have performed diagnostics such as conservation of mass, momentum and energy. Aside from the results that we shall present below, we have also tested finer resolutions for convergence. We have followed the standard diagnostic procedures and the details shall not be presented here.

4. Results

We now present our computational results for three dimensional vortices. We shall be seeking the *existence* of three-dimensional, coherent vortices which can survive in an environment such as that of the protoplanetary disk. We will call these vortices henceforth *"equilibrium"* vortices.

Because we seek vortices that are in dynamic equilibrium with their environment, a natural approach would be to generalize the idea of the well-known Moore-Saffman vortices (see, *e.g.* Saffman (1992)) to three dimensions. In Lin *et al.* (2002) we have discussed columnar Moore-Saffman vortices, which are quasi-two-dimensional objects. In the following we present results for three-dimensional vortices, which resemble Moore-Saffman vortices in the horizontal planes, but have compact support in the vertical direction. Before we start it is useful to list the vorticity-aspect-ratio relation given by Moore-Saffman theory:

$$\frac{\tilde{\omega}_z}{\sigma} = \lambda\frac{\lambda+1}{\lambda-1}, \tag{4.1}$$

where $\tilde{\omega}_z$ is the strength of the constant vorticity patch superimposed on the shear, and $\lambda < 1$ is the ratio of the semi-axes of the elliptic patch.

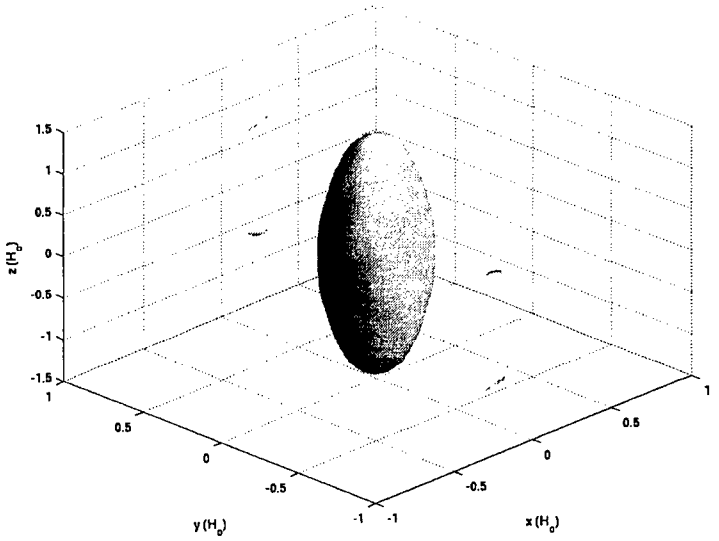


FIGURE 2. Three-dimensional vortex structure in the absence of shear. Here we show the isosurface at the value $\tilde{\omega}_z = -1$, and at the time $t = 20\ \tau_{orb}$. Our computational resolution is $128 \times 64 \times 96$ on a computational domain of $8 \times 2 \times 6$ (not entirely shown in this graph).

4.1. *Vortices without shear*

We first present a relatively simple case in which we set the shear to be zero, that is, $\sigma = 0$. This case will facilitate a comparison with our later results where we see the effects of a strong shear on the vortex. As the initial condition, we specify a vorticity function as

$$\tilde{\omega}_z = \begin{cases} \omega_o \exp\left(-\frac{z^2}{2}\right), & \sqrt{x^2+y^2} \le r_o \\ 0, & \sqrt{x^2+y^2} > r_o \end{cases}, \tag{4.2}$$

where $\omega_o = -2.25$, $r_o = 0.25$ is the radius of the circular patches (note that from (4.1) $\lambda \to 1$ when $\sigma \to 0$), and the Gaussian distribution renders the vortex compact in z. We have set $\tilde{\rho}$ to give an initial hydrostatic balance in the vertical direction.

The vortex goes through a brief (on the scale of turn-around time) and slight adjustment and then evolves into an equilibrium shape that is coherent for many (we have tested up to 120) turn-around times. See Figure 2.

4.2. *Vortices in a Keplerian shear*

Similar to the case without shear, we start with an initial guess that is close enough to the equilibrium state. We specify our initial vorticity function as

$$\tilde{\omega}_z = \begin{cases} \omega_o \exp\left(-\frac{z^2}{2}\right), & x^2/a^2 + y^2/b^2 \le 1 \\ 0, & \sqrt{x^2/a^2 + y^2/b^2} > 1 \end{cases}, \tag{4.3}$$

where $\omega_o = -0.625$, and the semi-axes are specified as $a = 0.25$ and $b = 1.0$. At the midplane $z = 0$, the elliptical vortex patch satisfied exactly the Moore-Saffman relation (4.1), and again the vorticity strength decreases with a Gaussian distribution away from the midplane. Similarly we have specified the initial $\tilde{\rho}$ such that the flow is in hydrostatic balance. Note that we have specified a lower value for ω_o. This is because J.A.B. and P.S.M. found that lower vorticity strength (albeit still of a moderate Rossby number)

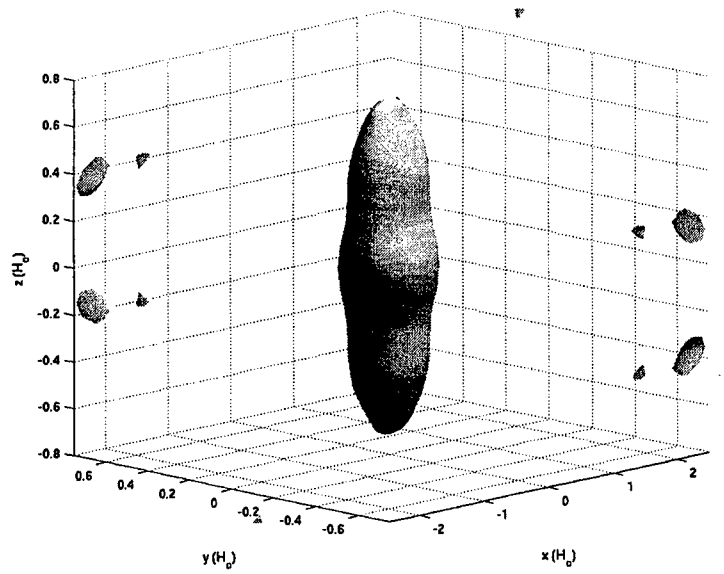


FIGURE 3. Elongated three-dimensional vortex structure in a Keplerian shear ($\sigma = 1.5$). Here we show the isosurface at the value of $\tilde{\omega}_z = -0.55$, and at the time $t = 20\,\tau_{orb}$. Our computational resolution is $128 \times 64 \times 96$ on a computational domain of $8 \times 2 \times 6$ (not entirely shown in this graph).

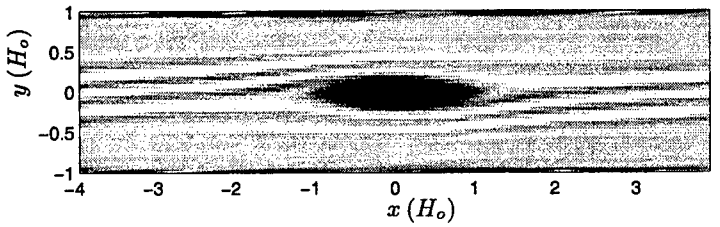


FIGURE 4. Contour plot of same vortex structure as shown in Figure 3 at the midplane $z = 0$. In this plot darker color designate the more negative values of $\tilde{\omega}_z$, and the black spot at the center is our equilibrium vortex patch. At the midplane the vortex is almost exactly Moore-Saffman.

induces fewer thermodynamic oscillations in the vertical direction and therefore aids coherence.

The resulting equilibrium vortex (after a few turn-around times from the initialization) is shown in both Figures 3 and 4. In Figure 3 we show an isosurface plot of the vertical vorticity $\tilde{\omega}_z$. When compared with Figure 2, the vortex is stretched by the shear and has a elongated shape in the horizontal directions (Figure 4).

Figure 5 illustrates the evolution of the vertical vorticity profile $\tilde{\omega}_z$ in time. The vorticity quickly adjusts, on turn-around-time scales, to an equilibrium distribution that is maintained for a much longer period. (We have tested up to 60 turn-around times in this case.) Note that, close to the midplane, the vorticity goes through small-amplitude oscillations. This is because at $z = 0$ there is no gravitation and the flow is at its least stably stratified.

Finally we compare our results (henceforth denoted as *"current"*) with those from a sliding-box implementation (denoted *"sliding-box"*) that has been developed by J.A.B.

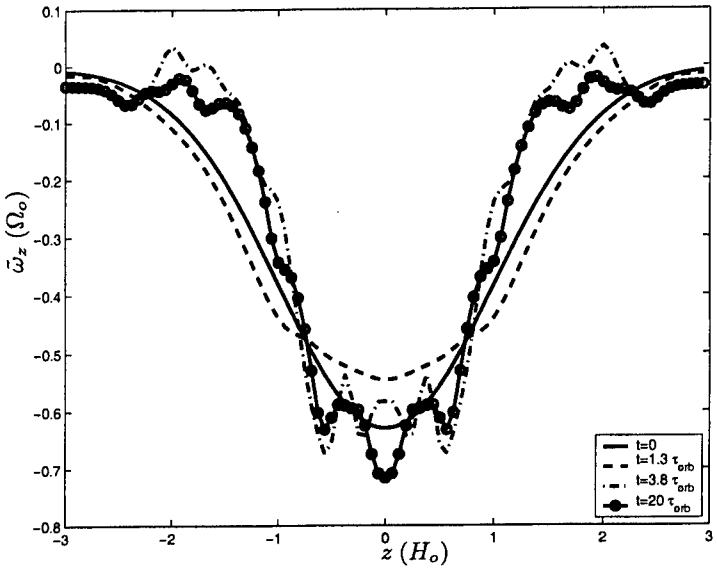


FIGURE 5. Time evolution of vertical vorticity profile $\tilde{\omega}_z(z)$ for vortices shown in Figure 3 and 4. The vorticity starts with a Gaussian distribution (solid), goes through quick adjustment (dash) and evolves into an equilibrium shape (dot-dash and line-circle).

and P.S.M. The most significant difference between these two codes lies in the boundary conditions. For the streamwise x direction, a natural periodicity is assumed for both methods. For the other two (transverse and vertical) directions, our current implementation has an artificial periodicity in z and enforces a no-flow condition in y, whereas the sliding box formulation assumes a shear-convected periodicity in y and a no-flow condition in z. The agreement between these two implementations is an important validation of the results from both.

In Figure 6 we show the comparison of the equilibrium vorticity $\tilde{\omega}_z$ along the three major axes. We initialize with the same vorticity distribution that is given by equation (4.3). The velocity, pressure and density functions are obtained satisfying both the hydrostatic balance and the boundary conditions in each of the implementations. The flows then evolve and we compare our results after 20 orbital periods. The results indicate excellent agreement between the methods.

The most significant difference lies in the vorticity distribution along the z axis. This difference can be better illustrated by a contour plot of $\tilde{\omega}_z$ along the $x = 0$ slice (Figure 7). The difference in $\tilde{\omega}_z(0, 0, z)$ is primarily manifested as a smaller vortex size in the current method. Nonetheless, the equilibrium shapes of these vortices agree well with each other, and, most strikingly, the black-and-white stripe patterns emanating away from the vortices are almost exactly reproduced in both of the methods, even though the boundary conditions are very different. These patterns are speculated to be gravity waves. Both the gravity waves and the difference in vortex size require more detailed study in the future.

5. Future Work

In the present paper we have shown the numerical implementation, as well as our results on three-dimensional, equilibrium vortices. We have compared and validated our

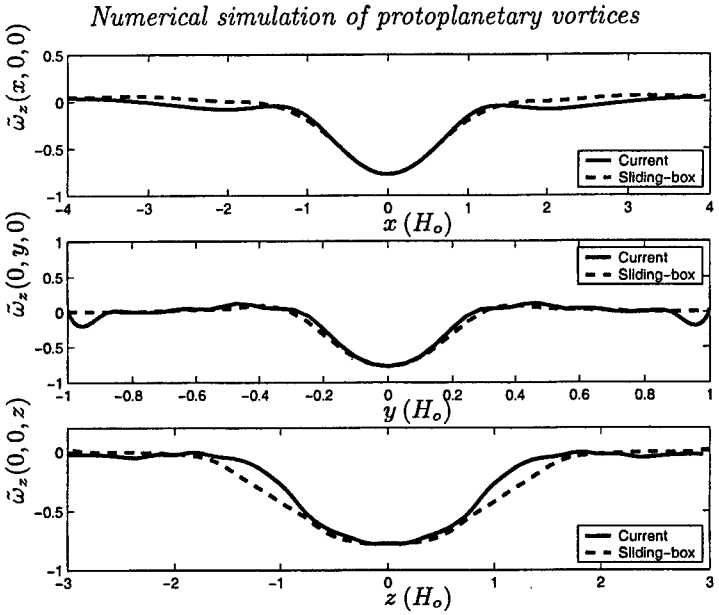


FIGURE 6. Comparison of equilibrium vorticity distribution against a sliding-box calculation along the three major axes of the vortex structure.

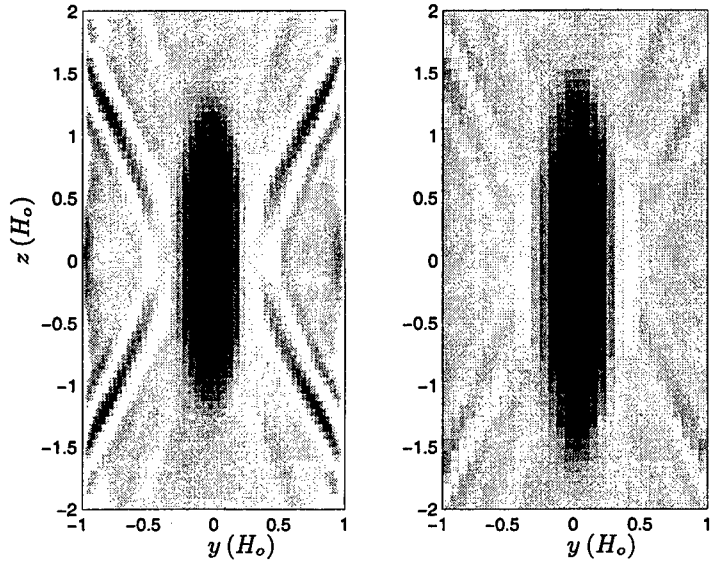


FIGURE 7. Comparison of equilibrium vorticity distribution against a sliding-box calculation. Here we plot the function $\tilde{\omega}_z(0,y,z)$, and the darker color correspond to the more negative values. The very black patches in the middle are our equilibrium vortex structures. Result from the current method is shown in the left graph, and that from the sliding-box method is shown to the right.

results with an alternative, sliding-box method. A few of the issues that we shall be immediately looking into next are as follows. First, even though we have identified a family of equilibrium vortices from one particular form of initialization, we should also seek other possible forms of equilibrium vortices. For example, we have tried the combi-

nation of different decaying exponents in (4.3) and different vorticity strength ω_o, and found equilibrium vortices under certain conditions. (This work is still in progress and is not presented here.) Second, we have preferred a no-flow condition in the y direction, primarily because of its advantage in diagnosing the conservation laws. This more rigid boundary condition should be relaxed or modified in the future to better reflect the physics of the disk. Finally, the purpose of the current numerical implementation has been to overcome the limitation of the sliding-box formulation, and eventually simulate a radial (y) thermodynamic (potential-vorticity) background. Our ultimate goal would be to generate coherent vortices from such a (baroclinic) background, as well to as to study the dynamical migration and deformation of such vortices; with these achieved we will be ready to address their relevance to the greater problem of angular momentum and mass transport within protoplanetary disks.

Acknowledgments

H.L. thanks Dr. Karim Shariff and Dr. Alan Wray of NASA Ames for very constructive insights and discussions.

REFERENCES

BARRANCO, J.A. & MARCUS, P.S. 2000 Vortices in protoplanetary disks and formation of planetesimals. In *Proceedings of the 2000 Summer Program*, 97-108. Center for Turbulence Research, Stanford University.

BARRANCO, J.A., MARCUS, P.S. & UMURHAN, O.M. 2000 Scalings and asymptotics of coherent vortices in protoplanetary disks. In *Proceedings of the 2000 Summer Program*, 85-95. Center for Turbulence Research, Stanford University.

HAWLEY, J.F., BALBUS, S.A. & WINTERS, W.F. 1999 Local hydrodynamic stability of accretion disks. *ApJ* **518**, 394-404.

KLAHR, H.H. & BODENHEIMER, P. 2003 Turbulence in accretion disks: vorticity generation and angular momentum transport via the global baroclinic instability. *ApJ* **582**, 869-892.

LIN, H., BARRANCO, J.A. & MARCUS, P.S. 2002 Vortex dynamics and angular momentum transport in accretion disks. In *Center for Turbulence Research Annual Research Briefs 2002*, 289-299. Stanford University.

LOVELACE, R.V.E., LI, H., COLGATE, S.A. & NELSON, A.F. 1999 Rossby wave instability of Keplerian accretion disks. *ApJ* **513**, 805-810.

ROGALLO, R.S. 1981 Numerical experiments in homogeneous turbulence. *NASA Tech. Mem.* **81315**, 1-91.

SAFFMAN, P.G. 1992 *Vortex Dynamics.* Cambridge University Press.

SHAKURA, N.I. & SUNYAEV R.A. 1973 Black holes in binary systems. Observational appearance. *Astron. Astrophys.* **24**, 337-355.

STONE, J.M. & BALBUS, S.A. 1996 Angular momentum transport in accretion disks via convection. *ApJ* **464**, 264-372.

The effect of surface topography on the nonlinear dynamics of Rossby waves

By S.I. Abarzhi, O. Desjardins, H. Pitsch

1. Motivation and objectives

Boussinesq convection in rotating systems attracts a sustained attention of the fluid dynamics community, because it has intricate non-linear dynamics (Cross & Hohenberg 1993) and plays an important role in geophysical and astrophysical applications, such as the motion of the liquid outer core of Earth, the Red Spot in Jupiter, the giant cells in the Sun etc. (Alridge *et al.* 1990). A fundamental distinction between the real geo- and astrophysical problems and the idealized laboratory studies is that natural systems are inhomogeneous (Alridge *et al.* 1990). Heterogeneities modulate the flow and influence significantly the dynamics of convective patterns (Alridge *et al.* 1990; Hide 1971). The effect of modulations on pattern formation and transition to turbulence in Boussinesq convection is far from being completely understood (Cross & Hohenberg 1993; Aranson & Kramer 2002).

It is generally accepted that in the liquid outer core of the Earth the transport of the angular momentum and internal heat occurs via thermal Rossby waves (Zhang *et al.* 2001; Kuang & Bloxham 1999). These waves been visualized in laboratory experiments in rotating liquid-filled spheres and concentric spherical shells (Zhang *et al.* 2001; Kuang & Bloxham 1999). The basic dynamical features of Rossby waves have been reproduced in a cylindrical annulus, a system much simpler than the spherical ones (Busse & Or 1986; Or & Busse 1987). For convection in a cylindrical annulus, the fluid motion is two-dimensional, and gravity is replaced by a centrifugal force, (Busse & Or 1986; Or & Busse 1987). Hide (1971) has suggested that the momentum and heat transport in the core might be influenced significantly by so-called bumps, which are heterogeneities on the mantle-core boundary. To model the effect of surface topography on the transport of momentum and energy in the liquid outer core of the Earth, Bell & Soward (1996), Herrmann & Busse (1998) and Westerburg & Busse (2001) have studied the nonlinear dynamics of thermal Rossby waves in a cylindrical annulus with azimuthally modulated height.

The models of Bell & Soward (1996), Herrmann & Busse (1998), and Westerburg & Busse (2001) considered different regimes of the flow, and reported analytical and numerical solutions for the system of conservation laws. Bell & Soward (1996) assumed periodic boundary conditions in the radial direction and neglected the viscous friction in the fluid interior. They found two types of convective patterns depending on the modulation amplitude: Rossby waves for small modulation amplitude and traveling waves with long azimuthal length scale for large modulation amplitude. Herrmann & Busse (1998) and Westerburg & Busse (2001) have accounted for the viscous friction in the fluid interior, neglected the friction produced by the Eckman layer, assumed no-slip boundary conditions in the radial direction, and found Rossby waves with quasi-periodic dependecies in space and in time. Both rigorous studies, the work by Bell & Soward (1996), and by Herrmann & Busse (1998) and Westerburg & Busse (2001) compliment each other and

identify several important features of the modulated convection. A need still remains for a model, which quantitatively and qualitatively describes the effect of modulations on Rossby waves in a wide range of the forcing parameters and convection intensity, and which can compare this inhomogeneous system to other pattern-forming systems (Cross & Hohenberg 1993; Aranson & Kramer 2002). Here we suggest a model to study the effect of surface topography on the nonlinear dynamics of thermal Rossby waves.

2. Pattern-forming system with modulated forcing

For rotating cylindrical annulus with homogeneous boundary conditions, the nonlinear dynamics of thermal Rossby waves are described by a complex Ginzburg-Landau equation in terms of amplitude A, whose magnitude determines the convection intensity, and whose phase describes changes in the position and direction of the convective rolls. We refer the reader to Busse & Or (1986) and Or & Busse (1987) for details. For heterogeneous systems, a rigorous derivation of the amplitude equation from the conservation laws has not been accomplished yet (Cross & Hohenberg 1993; Aranson & Kramer 2002). To model the nonlinear dynamics of slightly inhomogeneous systems, one usually applies the Ginzburg-Landau equation with forcing. As an example, one may consider pattern formation in the presence of a mode associated with a conserved physical quantity, such as the Rayleigh-Benard convection driven by surface tension, which has been considered by Siggia & Zippelius (1981), Tribelsky & Velarde (1996), Matthews & Cox (2000). Other examples are convection in liquid crystals driven by a stochastic electric field (Meyer *et al.* 1987; Wu & Andereck 1990; Roder *et al.* 1997), and the study of the effect of time-periodic forcing on an oscillatory system (Elphick *et al.* 1987; Coullet *et al.* 1990; Hemming & Kapral 2000).

Convection in a rotating cylindrical annulus with inhomogeneous boundaries differs from the foregoing pattern-forming systems. The surface modulation is not a slowly relaxing Goldstone mode as in the models with a conserved physical quantity (Siggia & Zippelius 1981; Tribelsky & Velarde 1996; Matthews & Cox 2000). The modulation does not result in an Ising-Bloch bifurcation as in the model with time-periodic forcing (Elphick *et al.* 1987; Coullet *et al.* 1990; Hemming & Kapral 2000), and its amplitude does not change with time, in contrast to the system with stochastic forcing (Meyer *et al.* 1987; Wu & Andereck 1990; Roder *et al.* 1997). To study the effect of surface topography on the dynamics of thermal Rossby waves, the Ginzburg-Landau equation with spatially periodic and time-independent forcing is a proper model. The equation has the form:

$$\frac{\partial A}{\partial T} = \beta \frac{\partial^2 A}{\partial Y^2} + \Delta_0 A + D|A|^2 A + \left(\delta e^{ikY} + \delta^* e^{-ikY}\right) A\,. \tag{2.1}$$

Here T and Y are the slow time and coordinate, A is the complex amplitude, the values of β and D are complex numbers with $\beta = \beta_r + i\beta_i$, $D = D_r + iD_i$, the subscripts r and i mark the real and imaginary parts, $\Delta_0 \sim (R - R_{cr})$ is real with R_{cr} being the critical Raleigh number (Cross & Hohenberg 1993; Busse & Or 1986; Or & Busse 1987; Aranson & Kramer 2002). The forcing amplitude and the absolute value of the wave-vector are δ and k respectively, where the asterisk marks the complex conjugate. The system (2.1) is slightly inhomogeneous and $|\delta|k \ll 1$.

Without forcing, $\delta = 0$, the values of β, D, Δ_0 in the equation (2.1) can be derived from the incompressible Navier-Stokes and energy equations for $R \sim R_{cr}$ (Busse & Or

1986; Or & Busse 1987). In agreement with the stability criterion the real parts of β and D obey the relations $\beta_r > 0$ and $D_r < 0$ (Cross & Hohenberg 1993; Aranson & Kramer 2002). The dynamics of the convective rolls are descirbed by the traveling waves with $A = \bar{A} = A_0 e^{iqy+i\gamma T}$, where

$$A_0^2 = -\frac{(\Delta_0 - \beta_r q^2)}{D_r}, \qquad \gamma = -\beta_i q^2 + D_i A_s \,. \tag{2.2}$$

This solution appears for $\Delta_0 > \beta_r q^2$, and depicts the pattern formation of thermal Rossby waves without forcing.

If the value of Δ_0 is finite and the modulation amplitude is small, $|\delta| \ll |\Delta_0|$, the explicit dependence on the Y coordinate in equation (2.1) can be eliminated. We present the amplitude A in (2.1) in the form $A = \bar{A} + \tilde{A}$, where $\bar{A} = A_0 e^{iqy+i\gamma T}$ from (2.2), and the term $\tilde{A} = A_1 + A_2 + ...$ appears due to the forcing with $A_n = \left(a_n e^{-inkY} + b_n e^{inkY}\right) e^{iqY+i\gamma T}$, $n = 1, 2, \ldots$. In this way we obtain

$$A = e^{iqY+i\gamma T}\left[A_0 + a_1 e^{-ikY} + b_1 e^{ikY} + a_2 e^{-2ikY} + b_2 e^{2ikY} + ...\right] . \tag{2.3}$$

Substituting the expression (2.3) in (2.1) and expanding the equation (2.1) in terms of small $|\delta/\Delta_0|$, we can derive a system of the coupled equations of the Ginzburg-Landau type:

$$\frac{\partial A_0}{\partial T} = \left[f_0 + DA_0^2 + 2D\left(a_1 a_1^\star + b_1 b_1^\star + a_1 b_1\right)\right] A_0 + a_1 \delta^\star + b_1 \delta \,, \tag{2.4}$$

$$\frac{\partial a_1}{\partial T} = f_1^- a_1 + db_1^\star + \left[D\left(a_1 a_1^\star + 2b_1 b_1^\star\right) a_1 + 2DA_0\left(a_1^\star a_2 + a_2 b_1 + b_1 b_2^\star\right)\right] + A_0\delta + a_2\delta^\star \tag{2.5}$$

$$\frac{\partial b_1}{\partial T} = da_1^\star + f_1^+ b_1 + \left[D\left(2a_1 a_1^\star + b_1 b_1^\star\right) b_1 + 2DA_0\left(a_1 a_2^\star + a_1 b_2 + b_1^\star b_2\right)\right] + A_0\delta^\star + b_2\delta, \tag{2.6}$$

$$\frac{\partial a_2}{\partial T} = f_2^- a_2 + db_2^\star + \left[DA_0\left(2a_1 b_1^\star + a_1^2\right)\right] + a_1\delta + a_3\delta^\star \,, \tag{2.7}$$

$$\frac{\partial b_2}{\partial T} = da_2^\star + f_2^+ b_2 + \left[DA_0\left(2a_1^\star b_1 + b_1^2\right)\right] + b_1\delta^\star + b_3\delta \ldots \tag{2.8}$$

where $f_0 = \Delta_0 - \beta q^2 - i\gamma$, $f_n^\pm = \Delta_0 - \beta\left(q \pm nk\right)^2 - i\gamma + 2DA_0^2$, $d = DA_0^2$, and the Y-dependence of the values A_0, a_n, b_n has been neglected for the sake of simplicity.

The nonlinear dynamics in the system (2.4-2.8) depend on the forcing parameters and the convection intensity, with the modulation wave-vector k being the key factor for pattern formation. Below we briefly describe several limiting cases.

In the linear approximation in $|\delta/\Delta_0| \ll 1$, the solution (2.2) satisfies equation (2.4), while the equations (2.5,2.6) are reduced to:

$$\frac{\partial a_1}{\partial T} = f_1^- a_1 + db_1^\star + A_0\delta, \qquad \frac{\partial b_1}{\partial T} = da_1^\star + f_1^+ b_1 + A_0\delta \,. \tag{2.9}$$

The linear system (2.9) has steady solutions with

$$a_1 = A_1 = -\frac{A_0\delta\left(\left(f_1^+\right)^* - d\right)}{\left(f_1^-\left(f_1^+\right)^* - dd^*\right)}, \qquad b_1^* = B_0^* = -\frac{A_0\delta\left(f_1^- - d^*\right)}{\left(f_1^-\left(f_1^+\right)^* - dd^*\right)}. \tag{2.10}$$

The solutions (2.2,2.3,2.10) are stable for $Re[\sigma] < 0$, where the Liapunov exponents σ obey the equation

$$(\sigma + 2f_0)\left[\left(\sigma - f_1^-\right)\left(\sigma - \left(f_1^+\right)^*\right) - dd^*\right] = 0\,. \tag{2.11}$$

For the large-scale modulations with $k/q \ll 1$, pattern formation is quite complicated. In the interval $\beta_r q^2 < \Delta_0 < F_r$, the pure solution with A_0 from (2.2) and $a_1 = b_1 = 0$ occurs, where $F_r = F_r(D,\beta)$ and $F_r > \beta_r$. For $\Delta_0 > F_r q^2$, this solution becomes unstable, and the modulated pattern (2.3,2.10) appears. In the limit of $(k/q) \to 0$, the values of $|a_1|, |b_1|$ increase as $|\delta/\Delta_0|(q/k)^2$, and result in a growth of the higher-order terms in the system (2.5-2.8). A nonlinear coupling among the amplitudes a_n and b_n yields then a solution with $|a_n/A_0|$, $|b_n/A_0| \gg |\delta/\Delta_0|$, yet keeping $|a_n/A_0| \ll 1$. In this case the system (2.5-2.8) is reduced to

$$\frac{\partial a_1}{\partial T} = f_1^- a_1 + db_1^* + \left[D\left(a_1 a_1^* + 2b_1 b_1^*\right)a_1 + 2DA_0\left(a_1^* a_2 + a_2 b_1 + b_1 b_2^*\right)\right], \tag{2.12}$$

$$\frac{\partial b_1}{\partial T} = da_1^* + f_1^+ b_1 + \left[D\left(2a_1 a_1^* + b_1 b_1^*\right)b_1 + 2DA_0\left(a_1 a_2^* + a_1 b_2 + b_1^* b_2\right)\right], \tag{2.13}$$

$$\frac{\partial a_2}{\partial T} = f_2^- a_2 + db_2^* + \left[DA_0\left(2a_1 b_1^* + a_1^2\right)\right], \tag{2.14}$$

$$\frac{\partial b_2}{\partial T} = da_2^* + f_2^+ b_2 + \left[DA_0\left(2a_1^* b_1 + b_1^2\right)\right]. \tag{2.15}$$

From (2.12-2.15) we obtain

$$a_n = A_n e^{inGT}, \qquad b_n = B_n e^{inGT}, \qquad n = 1,2,3\,, \tag{2.16}$$

with A_2, B_2 dependent on $A_1 = A_1(\Delta_0, k, q)$ and $B_1 = B_1(\Delta_0, k, q)$. Using the solvability conditions for real A_1, B_1, in (2.12-2.15), we derive the dispersion relation $G = G(\Delta_0, k, q)$. It is remarkable that $G \sim \gamma$ for small q and for $(k/q) \ll 1$. The solutions and their stability analysis are quite cumbersome and not presented here.

For the small-scale forcing with $k/q \gg 1$, the modulated state (2.3,2.10) is stable for all $\Delta_0 > 0$. The nonlinear dynamics in this case are governed by terms proportional to δ in (2.5-2.8), and the nonlinear solutions are steady. With $a_2 = b_2 = 0$, equations (2.4,2.5) are reduced to

$$\frac{\partial a_1}{\partial T} = A_0\delta + D\left(a_1 a_1^* + 2b_1 b_1^*\right)a_1\,, \tag{2.17}$$

$$\frac{\partial b_1}{\partial T} = A_0\delta^* + D\left(2a_1a_1^* + b_1b_1^*\right)b_1\,, \tag{2.18}$$

and for small but finite $|\delta/\Delta_0|$ in the system (2.17,2.18)

$$a_1, b_1 \sim A_0|\delta/\Delta_0|^{2/3}\,. \tag{2.19}$$

We conclude that the large-scale forcing eventually results in the occurrence of Rossby waves with quasi-periodic time-dependence. The convective pattern (2.3,2.16) consists of three traveling waves with different group velocities. The dynamics of this pattern depends on the convection intensity and the forcing wave-vector, yet it is independent of the forcing amplitude. In contrast, the small-scale forcing produces spatially modulated convective patterns with dynamics governed by the forcing amplitude.

3. Numerical results

To obtain numerical solutions of the complex amplitude A in (2.1), we non-dimensionalize this equation first using the length of the domain L, the reference time scale Δ_0^{-1}, and the initial magnitude of A_0. This leads to the following equation:

$$\frac{\partial A'}{\partial T'} = \beta'\frac{\partial^2 A'}{\partial Y'^2} + A' + D'|A'|^2A' + \tilde{\delta}'A' \tag{3.1}$$

The initial solution of the problem has the form $A = A_0e^{iqY}$, and the forcing is defined as $\tilde{\delta} = \delta e^{ikY} + \delta^* e^{-ikY}$. The non-dimensional quantities are given by $A' = A/A_0$, $Y' = Y/L$, $T' = T\Delta_0$, $\beta' = \beta/\Delta_0L^2$, $D' = DA_0^2/\Delta_0$ and $\tilde{\delta}' = \tilde{\delta}/\Delta_0$, and with the wavenumbers k and q being $k' = kL$ and $q' = qL$.

We solve equation (3.1) on a domain of length $L = 10$ with periodic boundary conditions. We replace the complex equation by a set of two equations for the real and imaginary parts of A. This set of equations is discretized using a second order central difference scheme in space. A fully implicit solver is used in time.

For these computations we choose $\Delta_0 = 100$ and $A_0 = 1$. The values of β and D are taken to match experiments of Herrmann & Busse (1998); Westerburg & Busse (2001). The three remaining parameters are the forcing amplitude δ and the ratio between the two wavenumbers k and q. Several cases have been computed with $\delta/\Delta_0 = 0.1, 0.2, 0.4, 0.6, 0.8, 1$, and $(k/q) = 1/10, 1/3, 1, 3, 10$. The space is discretized with a 300 points mesh, and the time step is chosen to be $\Delta T = 0.05$.

Figure 1 presents the real part of A' in (3.1) for the case with no forcing. The pattern has the form of the traveling wave, and its dynamics agrees qualitatively and quantitatively with the solution (2.2).

Figures 2, 3, and 4 show the real part of the amplitude, and the spatial and temporal Fourier transforms in the case of large-scale forcing with $k/q = 1/3$ and $\delta/\Delta_0 = 0.2$. Three traveling waves with different group velocities, described in (2.19), are clearly visible on the Figure 2. The spatio-temporal characteristics of the pattern are in good agreement with the results in (2.16). Figure 3 shows that the asymptotic dynamics of

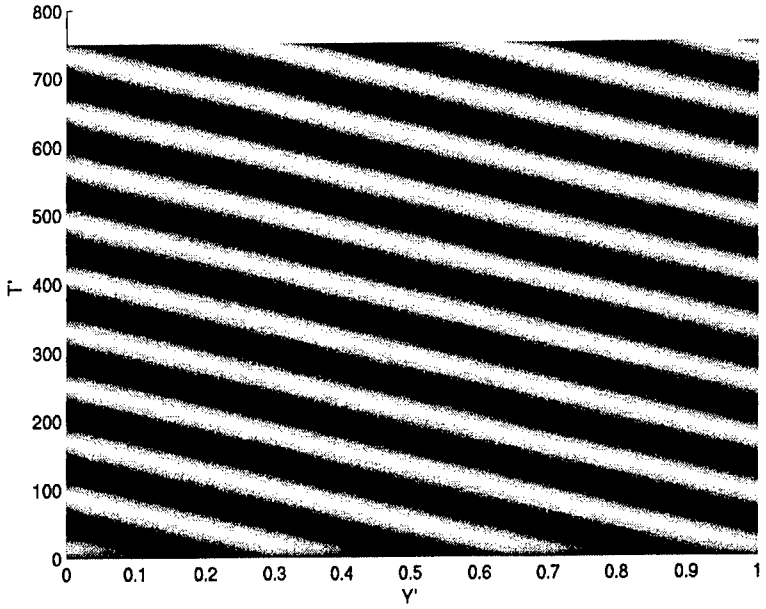


FIGURE 1. Rossby waves with no forcing

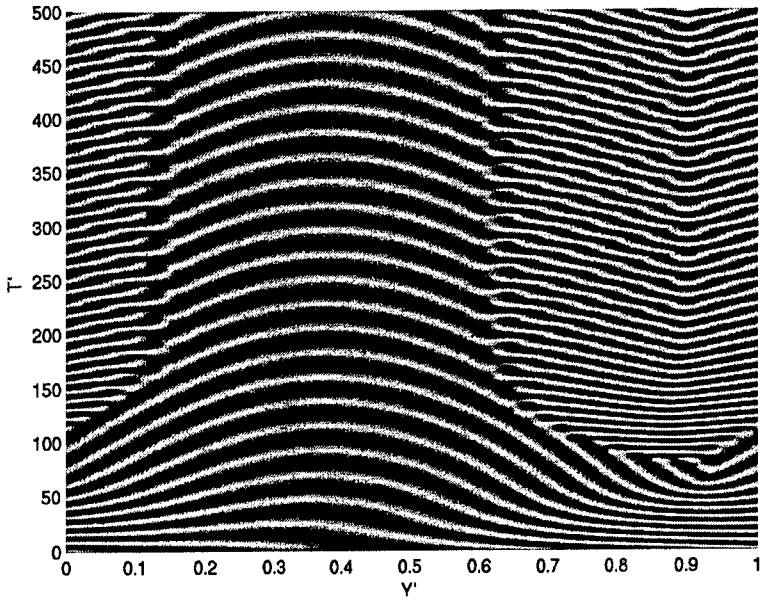


FIGURE 2. Real part of the amplitude in the case of large-scale modulation

the pattern are highly nonlinear, and there exist three major spatial modes associated with the wavevectors q, $q-k$ and $q+k$. Temporal Fourier transforms of the pattern on presented Figure 4 clearly show the existence of a low frequency, associated with small $(\gamma - G) \ll \gamma$ in (2.16). The other modes on Figure 4 correspond to γ in the equation (2.2) and $(\gamma + G) \sim 2\gamma$ in the solution (2.16). We conclude that the large-scale forcing

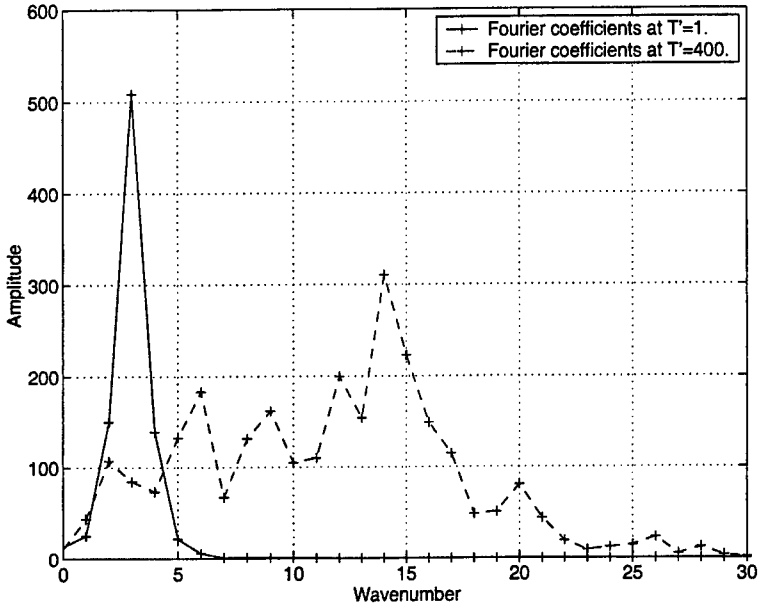


FIGURE 3. Spatial Fourier transform of the amplitude in the case of large-scale modulation

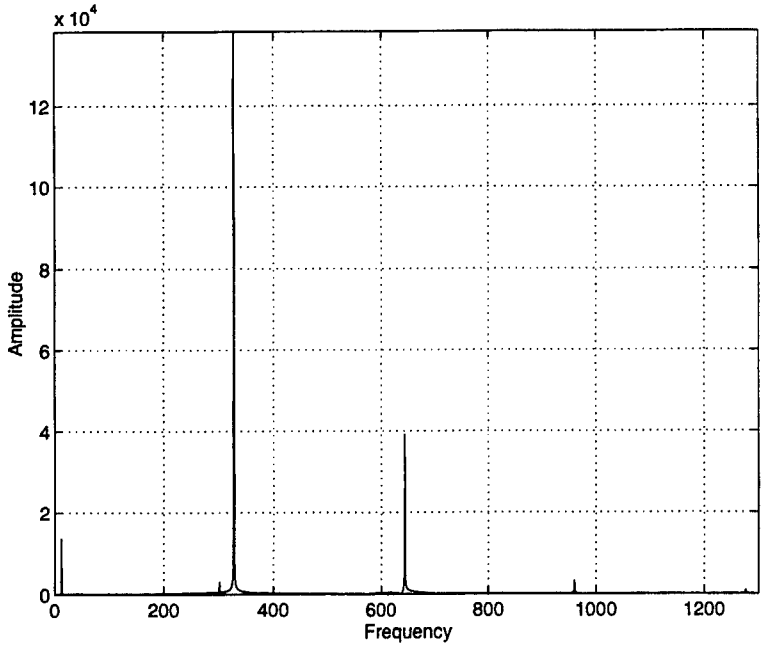


FIGURE 4. Temporal Fourier transform of the amplitude in the case of large-scale modulation

influences the Rossby waves significantly, and forms a pattern modulated in space and quasi-periodically in time.

Figures 5, 6, and 7 present the real part of the amplitude, and the spatial and temporal Fourier transforms in the case of small-scale forcing with $k/q = 10$ and $\delta/\Delta_0 = 0.1$. The pattern formation in this case differs significantly from that of the large-scale modula-

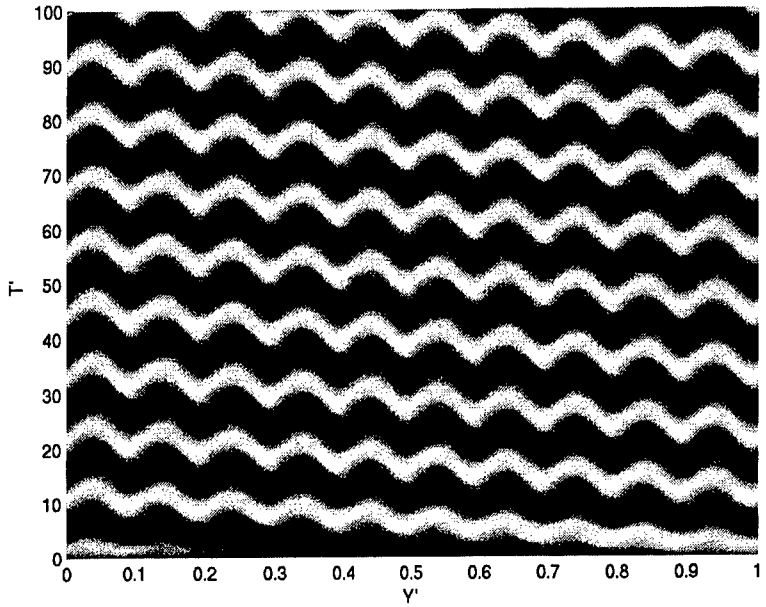


FIGURE 5. Real part of the amplitude in the case of small-scale modulation

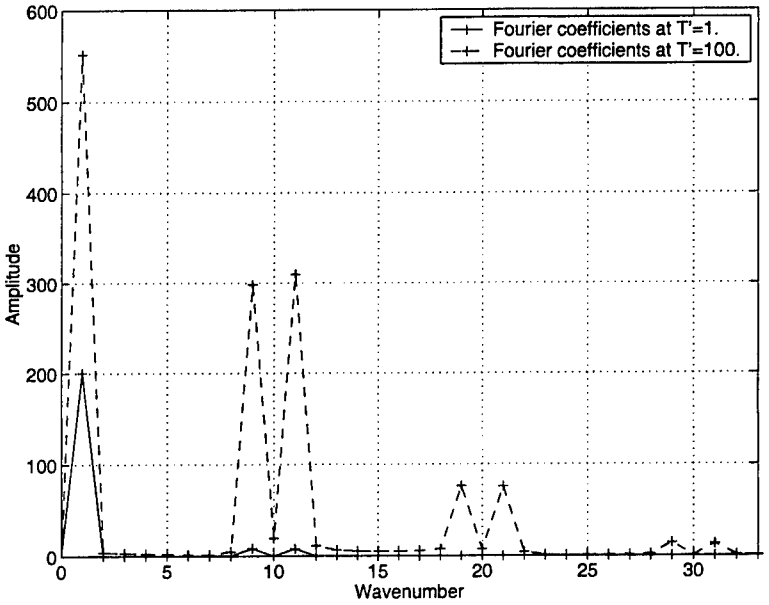


FIGURE 6. Spatial Fourier transform of the amplitude in the case of small-scale modulation

tions. Figures 5, 6, and 7 clearly show the formation of spatially modulated Rossby waves, in agreement with the solution (2.19). Figure 6 demonstrates that the spatial dynamics of the pattern are described by the modes associated with the wavevectors q, $q-k$ and $q+k$. Temporal Fourier transforms of the pattern shown on Figure 7 indicate that there

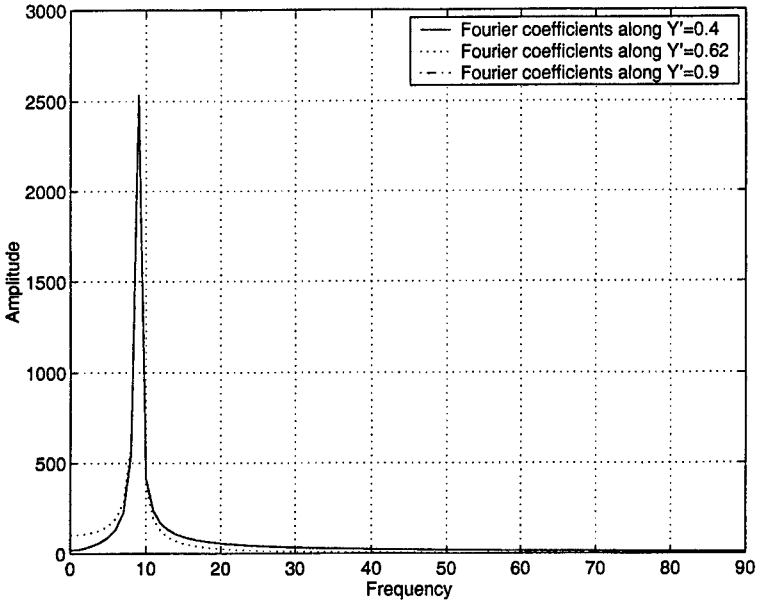


FIGURE 7. Temporal Fourier transform of the amplitude in the case of small-scale modulation

is only one frequency in the system, which is associated with γ in (2.2). We conclude that the small-scale forcing modulates Rossby waves in space, (2.19).

4. Discussion

In the present work, we studied the effect of surface topography on the nonlinear dynamics of thermal Rossby waves. The foregoing results show that the interaction of Rossby waves with spatially modulated forcing gives rise to a quasi-periodic behavior in space as well in time. The large-scale forcing results in the appearance of interacting traveling waves, whose dynamics depend strongly on the forcing wavevector and weakly on the convection intensity, and are insensitive to the forcing amplitude. In contrast, the small-scale forcing generates spatially modulated patterns, but does not influence their temporal dependence. In this case, the pattern dynamics are governed by the forcing amplitude and the convection intensity.

Our model captures the main properties of the linear and weakly nonlinear solutions obtained in Bell & Soward (1996) and Westerburg & Busse (2001). On the other hand, the model describes the influence of modulations on the dynamics of Rossby waves in a wide range of the forcing parameters and convection intensity, and predicts the new properties of the nonlinear dynamics. Our results are in a good qualitative agreement with the observations by Westerburg & Busse (2001).

REFERENCES

ALRIDGE, K., BLOXHAM, J., DEHANT, V. *et al.* 1990 Core-Mantle interactions. *Surv. Geophys.* **11**, 329–353.

ARANSON, I. & KRAMER, L. 2002 The world of the complex Ginzburg-Landau equation. *Rev. Mod. Phys.* **74**, 99–143.

BELL, P. & SOWARD, A. 1996 The influence of surface topography on rotating convection. *J. Fluid Mech.* **313**, 147–180.

BUSSE, F. & OR, A. 1986 Convection in a rotating cylindrical annulus - thermal Rossby waves. *J. Fluid Mech.* **166**, 173–187.

COULLET, P., LEGA, J., HOUCHMANZADEH, B. *et al.* 1990 Breaking chirality in nonequilibrium systems. *Phys. Rev. Lett.* **65**, 1352–1355.

CROSS, M. & HOHENBERG, P. 1993 Pattern formation outside of equilibrium. *Rev. Mod. Phys.* **65**, 851–1112.

ELPHICK, C., IOOSS, G. & TIRAPEGUI, E. 1987 Normal-form reduction of time-periodically driven differential equations. *Phys. Lett.* **A 120**, 459–463.

HEMMING, C. & KAPRAL, R. 2000 Resonantly forced inhomogeneous reaction-diffusion systems. *Chaos* **10**, 720–730.

HERRMANN, J. & BUSSE, F. 1998 Stationary and time dependent convection in the rotating cylindrical annulus with modulated height Phys. *Phys. Fluids* **10**, 1611–1620.

HIDE, R. 1971 Geostrophic motion of a non-homogeneous fluid. *J. Fluid Mech.* **49**, 745.

KUANG, W. & BLOXHAM, J. 1999 Numerical modeling of magnetohydrodynamic convection in a rapidly rotating spherical shell: Weak and strong field dynamo action. *J. Comp. Phys.* **153**, 51–81.

MATTHEWS, P. & COX, S. 2000 Pattern formation with a conservation law. *Nonlinearity* **13**, 1293–1320.

MEYER, C., AHLERS, G. & CANNELL, D. 1987 Initial stages of pattern formation in Rayleigh-Bnard convection. *Phys. Rev. Lett.* **59**, 1577–1580.

OR, A. & BUSSE, F. 1987 Convection in a rotating cylindrical annulus. 2. Transitions to asymmetric and vacillating flow. *J. Fluid Mech.* **174**, 313–326.

RODER, J., RODER, H. & KRAMER, L. 1997 Linear stability analysis of bifurcations with a spatially periodic, fluctuating control parameter. *Phys. Rev.* **E 55**, 7068–7078.

SIGGIA, E. & ZIPPELIUS, A. 1981 Pattern selection in Rayleigh-Benard convection near threshold. *Phys. Rev. Lett.* **47**, 835–838.

TRIBELSKY, M.I. & VELARDE, M.G. 1996 Short-wavelength instability in systems with slow long-wavelength dynamics. *Phys. Rev.* **E 54**, 4973–4981.

WESTERBURG, M. & BUSSE, F. 2001 Finite-amplitude convection in the presence of finitely conducting boundaries. *J. Fluid Mech.* **432**, 351–367.

WU, M. & ANDERECK, C. 1990 Effect of extrenal noise on the Fredericksz transition in a nematic liquid crystal. *Phys. Rev. Lett.* **65**, 591–594.

ZHANG, K., EARNSHAW, P., LIAO, X. *et al.* 2001 On inertial waves in a rotating fluid sphere. *J. Fluid Mech.* **437**, 103–119.

Nonlinear Gulf Stream interaction with the deep western boundary current system: observations and a numerical simulation

By David E. Dietrich, Avichal Mehra †, Robert L. Haney ‡, Malcolm J. Bowman ¶ AND Yu-Heng Tseng

1. Motivation and objectives

Gulf Stream (GS) separation near its observed Cape Hatteras (CH) separation location, and its ensuing path and dynamics, is a challenging ocean modeling problem. If a model GS separates much farther north than CH, then northward GS meanders, which pinch off warm core eddies (rings), are not possible or are strongly constrained by the Grand Banks shelfbreak. Cold core rings pinch off the southward GS meanders. The rings are often re-absorbed by the GS. The important warm core rings enhance heat exchange and, especially, affect the northern GS branch after GS bifurcation near the New England Seamount Chain. This northern branch gains heat by contact with the southern branch water upstream of bifurcation, and warms the Arctic Ocean and northern seas, thus playing a major role in ice dynamics, thermohaline circulation and possible global climate warming. These rings transport heat northward between the separated GS and shelf slope/Deep Western Boundary Current system (DWBC). This region has nearly level time mean isopycnals. The eddy heat transport convergence/divergence enhances the shelfbreak and GS front intensities and thus also increases watermass transformation. The fronts are maintained by warm advection by the Florida Current and cool advection by the DWBC. Thus, the GS interaction with the DWBC through the intermediate eddy field is climatologically important.

Besides GS separation and mean path, realistic simulation of GS natural variability is important. GS separation occurs (by definition) when the shelfbreak current from the Florida Straits angles toward deeper water. If it does not separate at CH, the observed separation location, but separates much later as is common in North Atlantic Ocean models, it then remains too close to the shelfbreak to allow northward (shoreward) meanders to develop freely and pinch off warm core eddies (rings). The distance from the mean GS current to shelfbreak must be at least comparable to the Rossby radius of deformation for this to happen. The highly energetic, nonlinear turbulent GS system provides a significant amount of geophysical "noise" to the climate system. Such "noise" may affect climate through fundamentally nonlinear stochastic resonance (Velez-Belchi et al. 2001); such resonance may be associated with nonlinear effects of changes relating to freshwater sources and sinks (Rossby and Nilsson 2003), changes of North Atlantic Deep Water formation (Rahmstorf and Alley 2002) and nonlinear GS interaction with the DWBC seen in results of the present study. Such variability may be natural in the ocean by itself. For example, even with annual cycle forcing, constructed using observed annual cycle

† Mississippi State University
‡ Naval Postgraduate School
¶ State University of New York at Stony Brook

surface wind, heat flux and freshwater source/sink conditions, there may be significant interannual variability, as seen in Mediterranean Sea modeling studies (Fernandez et al. 2003). Another example of particularly strong natural interannual variability is the Gulf of Mexico (Dietrich et al. 1997), which is dominated by the Loop Current and its irregular major eddy shedding, independent of annual cycle forcing, having a mean time-scale of about 270 days.

Two recent major North Atlantic Basin model comparison studies are: DYNAMO (1997) and DAMEE-NAB (2000). None of the DYNAMO models at 1/3° horizontal resolution was able to simulate the observed GS separation at CH. This failure using only moderate horizontal resolution was not unexpected, because of the importance of fine-scale vorticity dynamics and bathymetry near CH (Dengg et al. 1996). Coastal abutments such as CH often lead to boundary current separation; examples are ubiquitous in nature, a prime example being the Black Sea whose coastal circulation is dominated by recirculation eddies in the wakes of coastal abutments (Staneva et al. 2001). Besides isobath curvature near the CH abutment, the upstream convergence of isobaths also plays an important role in GS separation (Stern 1998).

In the DAMEE model intercomparison experiment using HR (Hellerman and Rosenstein 1983) climatological wind forcing, all but one of the models failed to simulate GS separation at CH. The exception was ROMS (Haidvogel et al. 2000), which got GS separation at the proper location without resolving the major CH coastal abutment. Hurlburt and Hogan (2000) report that when sufficient resolution is used to address nonlinear GS separation dynamics at CH using the NLOM model (Hurlburt and Thompson 1980), realistic GS separation and other inherently nonlinear features are well simulated using HR winds, *even though* the linear version of the same model shows unrealistic wind-stress-curl-induced GS separation for 11 different wind stress climatologies including HR winds (Townsend et al. 2000). The linear effects of wind stress curl do not explain the observed GS separation and path, but instead give two paths, both very different from the observed one. Thus, the ROMS low resolution GS separation at CH is surprising.

Herein, we adapt the DieCAST ocean model to the North Atlantic/Caribbean Sea/Gulf of Mexico system in order to explore GS separation and ensuing dynamics. Base case results are discussed, focusing on GS interaction with the DWBC during a 75-year simulation. In follow up to this base case, closely related sensitivity studies (Dietrich et al. 2003b) show significant effects of horizontal viscosity and diffusivity, especially relating to the thin, narrow DWBC and its effects on GS separation.

The DieCAST ocean model adaptation for the present North Atlantic study is described in Section 2. In Section 3, the modeled North Atlantic general circulation is compared with observations, focusing on the GS and DWBC. Results before and after the establishment of the DWBC show dramatic effects of the DWBC on the GS separation and path. Further discussion of the significance of the DWBC is given in Section 4. Conclusion and future work are given in Section 5.

2. Model and Experiment Design

We use the z-level DieCAST ocean model adapted to the North Atlantic Ocean/ Caribbean Sea/ Gulf of Mexico system. The duo grid model runs at about 200 model days per day of computer time on a PC using a single 2.0 gigahertz P4.

The model uses:

a) fourth-order accurate numerical approximations for all terms, except a conventional

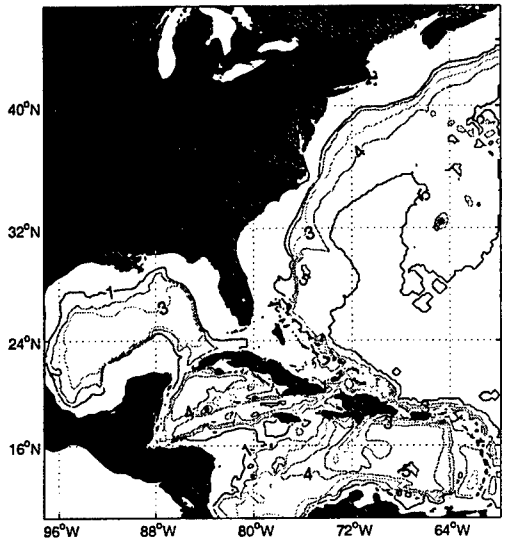


FIGURE 1. Western (1/6° resolution £ne grid) domain bathymetry (depth is in km).

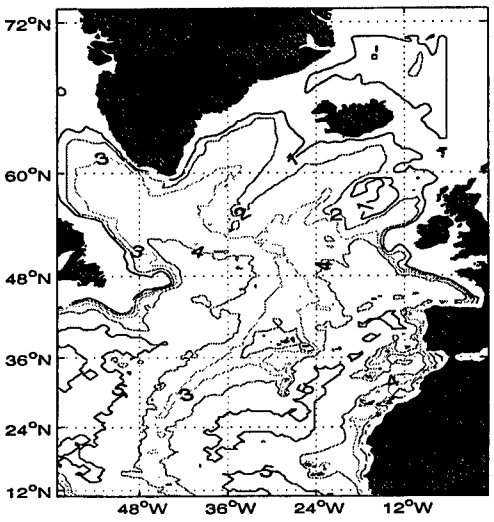


FIGURE 2. Eastern (1/2° deg resolution coarse grid) domain bathymetry (depth is in km) showing shelf-break bathymetry in the shortcircuited Arctic Ocean.

second-order accurate hydrostatic vertical pressure gradient, in a semi-collocated control volume framework (Sanderson and Brassington 1998);

b) an incompressibility algorithm having low numerical dispersion associated with its required interpolations (Dietrich 1997)

The semi-collocated grid avoids the large numerical dispersion resulting from evaluating the large Coriolis term on the conventional staggered Arakawa "C" grid. Fourth-order accurate advection further reduces numerical dispersion. Thus, the model is formally accurate in all significant respects. It is also robust using very low total (explicit plus numerical) dissipation.

The model domain covers the North Atlantic basin from 10° N to 73° N and from 97.5° W to 0° W. To reduce the computation required, a duo grid approach is used; the grids are coupled using upwind-based boundary flux approximations as used by Dietrich and Mehra (1998) for the Santa Barbara Channel nested in the California Current system. The western North Atlantic, Gulf of Mexico and Caribbean Sea require high resolution to resolve the GS separation region and critical narrow straits. West of 60° W, 1/6° resolution is used; east of 60° W, 1/2° resolution is used. The grids are fully two-way coupled each time step, with one coarse grid cell overlap (3 × 3 fine grid cells). The results are virtually seamless at the duo grid interface (Dietrich 2002). There are 30 model layers, geometrically expanding from 41.6 m thick at the top to 738 m thick at the bottom (maximum depth 5000 m). Open southern boundary conditions are derived from a one degree global implementation of the DieCAST ocean model.

Figure 1 shows the western domain bathymetry. Figure 2 shows the eastern domain and has lower resolution than Figure 1. To avoid potentially disastrous unphysical vortex stretching in the northeast corner of the eastern domain, the real bathymetry is replaced by a shelfbreak patterned after the shortcircuited Arctic Ocean, rather than using a conventional vertical wall approach.

To resolve the critical Caribbean Sea passages and reduce computation, the duo grid

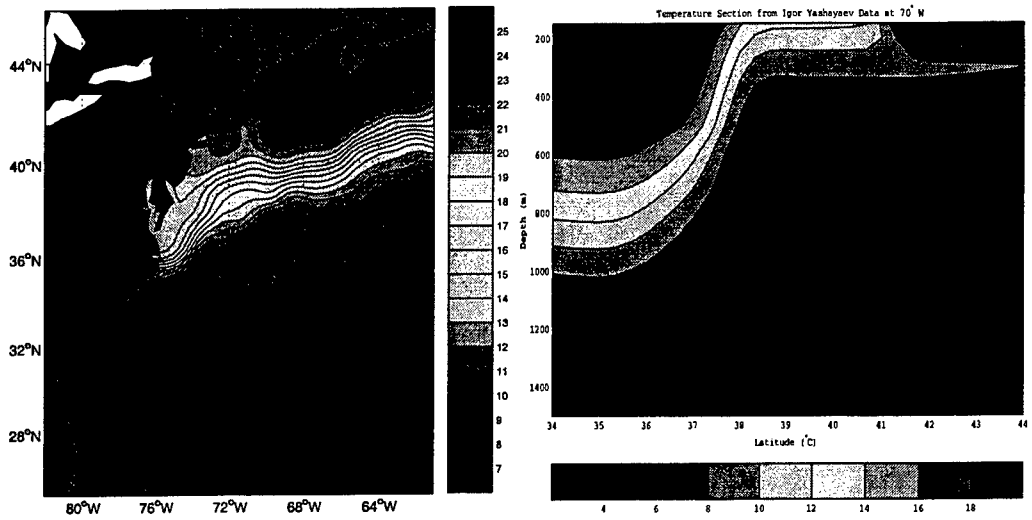


FIGURE 3. Surface layer annual mean Yashayaev temperature ($°C$) climatology in the western domain GS region (west of 60 deg W) of the duo grid DieCAST north Atlantic model (left panel); Vertical/latitudinal cross-section of annual mean Yashayaev potential temperature ($°C$) climatology at 70 deg W, showing highly nonlinear, non-diffusive flattening of isopycnals between Gulf Stream and Grand Banks (right panel).

interface is placed just east of the important Caribbean Sea passages, and the western fringe of the Labrador Sea (west of 60° W) is excluded and an idealized shelfbreak is used along 60° W in the eastern domain (Figure 2), again to minimize unrealistic vortex stretching. Surface boundary conditions are derived from monthly climatology. The wind forcing is by monthly average HR climatological winds. Levitus climatology is used for initial conditions and for surface thermohaline forcing until model year 13, when it is replaced by an improved (less smoothed) surface climatology (Yashayaev 2002). The annual mean surface temperature in the GS region from Yashayaev climatology (Figure 3) is consistent with the observed GS separation near CH.

Below-surface-layer model temperature is restored toward climatology in a buffer zone 20 gridpoints wide along open northern lateral boundaries. Salinity is not restored, because that does not conserve salt material and has no physical basis. Instead, a 0.2 Sv (1 Sverdrup equals one million cubic meters per second) inflow of freshwater is spread uniformly along the open northern boundary to parameterize Arctic Ocean net river inflow (Bacon et al. 2002) and a 0.018 Sv Gulf of St. Lawrence freshwater volume source is also specified (Chapman and Beardsley 1989). Heat and freshwater fluxes at the sea surface are computed such that the model multi-year mean annual cycle of surface temperature and salinity follow the observed climatological annual cycle (Dietrich et al. 2003a). This new surface buoyancy flux condition avoids problems (reduced annual cycle amplitudes and phase lags, and excessive damping of surface fronts) attributed to conventional restoring (Killworth et al. 2000).

All *externally* specified inflows are in the eastern, coarse grid domain; these are added to the western boundary inflow from the fine grid western domain and to the integrated evaporation-precipitation (e-p) to get a net eastern domain inflow (derived as described by Dietrich et al. 2003a); then, the total inflow is subtracted uniformly at the southern boundary (about 0.02 Sv as it turns out) to be consistent with incompressibility. An alternate approach, not used here, is to apply this volume correction at the surface (e.g.,

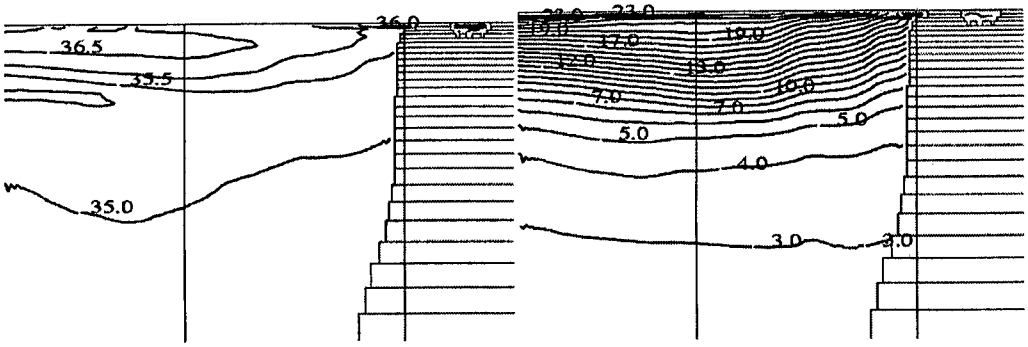


FIGURE 4. Vertical/latitudinal cross-sections at 70 deg W of time-averaged salinity (left) and temperature (right) during years 0-5.

in a global model having closed lateral boundaries), using the mean diffusivity between the top two layers to maintain observed climatological annual cycle surface layer salinity. This approach is consistent with the long-term climatological state (near zero mean sea level change) and with the rigid-lid approximation used in this model, in which there can be no mean surface height change. Thus, the rigid lid is slightly porous; the divergence of the barotropic mode (vertically integrated horizontal velocity) is very small but not exactly zero.

In the western (1/6° resolution) domain, we use constant horizontal viscosity and diffusivity of 10 m^2/sec. Based on the scale of the CH abutment curvature ($\sim$ 100 km) and GS velocity ($\sim$ 1 m/sec), this gives Reynolds number $O(10,000)$ for the primary GS separation scale. The Rossby number for these scales is $O(0.1)$. Both domains use near-molecular background vertical viscosity and diffusivity, with modified Pacanowski and Philander Richardson number based mixing as described by Staneva et al. (2001). Thus, the inertia terms are strong in the CH region, as necessary (but not sufficient, as a robust DWBC is also required, as will be shown here) for nonlinear inertial separation.

3. Results

3.1. *Before and After DWBC Interaction with GS Separation*

The transient GS behavior during the first five model years is strikingly different from the long-term behavior (Figures 4 - 6). During the first model year (not shown), bathymetry-induced strong inertial dynamics lead to early partial GS separation near CH. However, the separated portion of the model GS moves northward to the Grand Banks shelfbreak during the next few model years. It then moves back southward to its observed CH separation point and mean downstream path after about 10 model years, and remains close to the mean observed path throughout years 10−75 (end of the present simulation).

It follows that model intercomparisons of the GS region before 10 years of simulation, such as done under DAMEE, are of limited value, especially when overly diffused, highly unstable (baroclinically) Levitus climatology is a basis for model comparison, even for time averaged model results, as will be seen below.

Figures 4 and 5 shows vertical/latitudinal cross-sections at 70° W of temperature averaged during years 1 − 5 and years 66 − 75 respectively. There is clearly a strong flattening of isopycnal surfaces (well approximated by isotherms) between the DWBC and

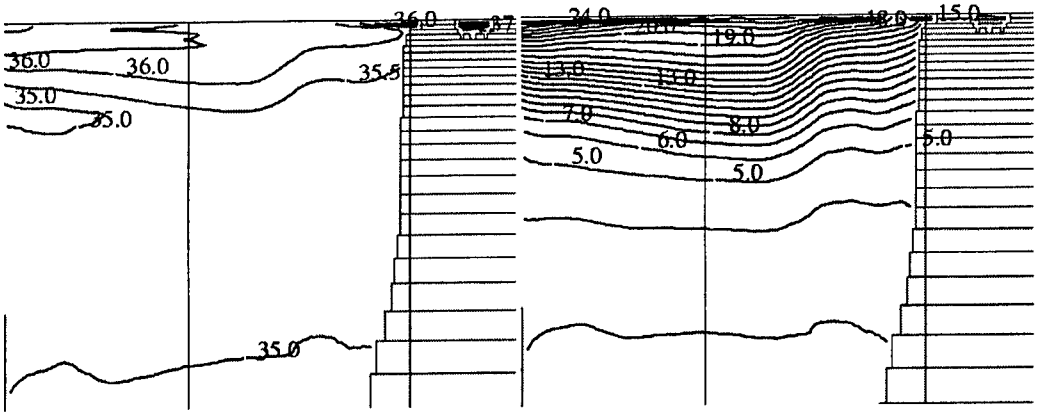


FIGURE 5. Vertical/latitudinal cross-sections at 70 deg W of time-averaged salinity (left) and temperature (right) during years 66-75.

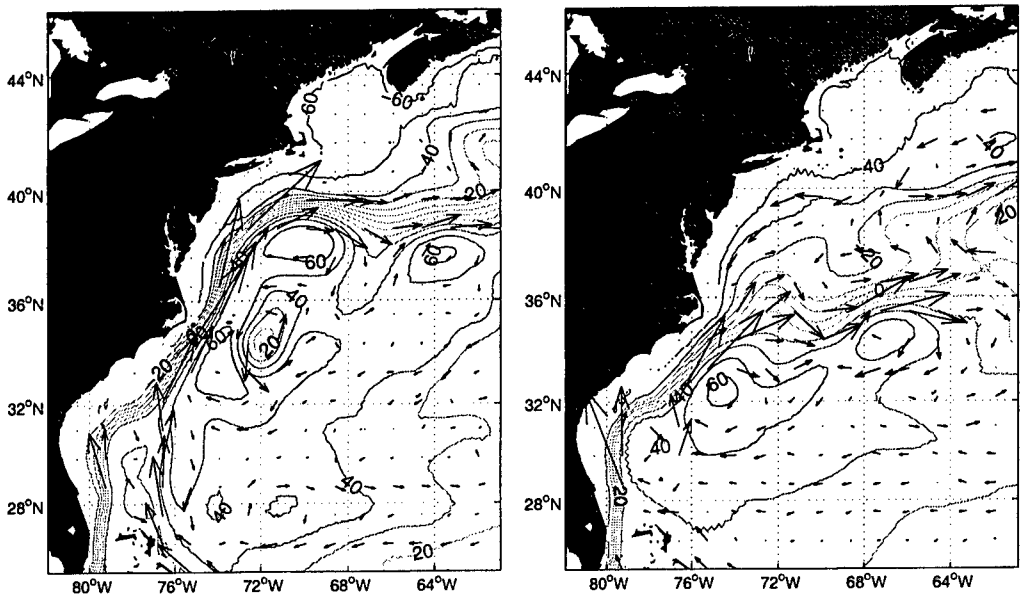


FIGURE 6. Time mean seasurface height (cm) and 700 m depth velocity vectors in the 1/6° resolution western domain during years 0 – 5 (left) and during years 66 – 75 (right).

GS core during the latter years (Figure 5), as in observations (Figure 3). Also during the latter years, there is a strong deepwater GS jet and front outcropping, as in observations.

Figure 6 shows the time mean surface pressure with superposed 700 m depth time-averaged velocity vectors during years 1 – 5 and years 66 – 75. The color shaded contour field is the time mean surface height. The arrows are time mean velocity vectors at 700m depth. The mean Gulf Stream front is the boundary between the green and light blue. The slight northward bend into the mid Atlantic Bight (a.k.a. "New York Bight") reflects warm core eddies that separate from northern tips of Gulf Stream meanders (mostly far downstream from Cape Hatteras), some of which slowly propagate all the way back to the Cape Hatteras region where they rejoin the Gulf Stream. Nearly all of the "blue water" in the mid Atlantic Bight (a.k.a. "New York Bight") is cold water that has upwelled

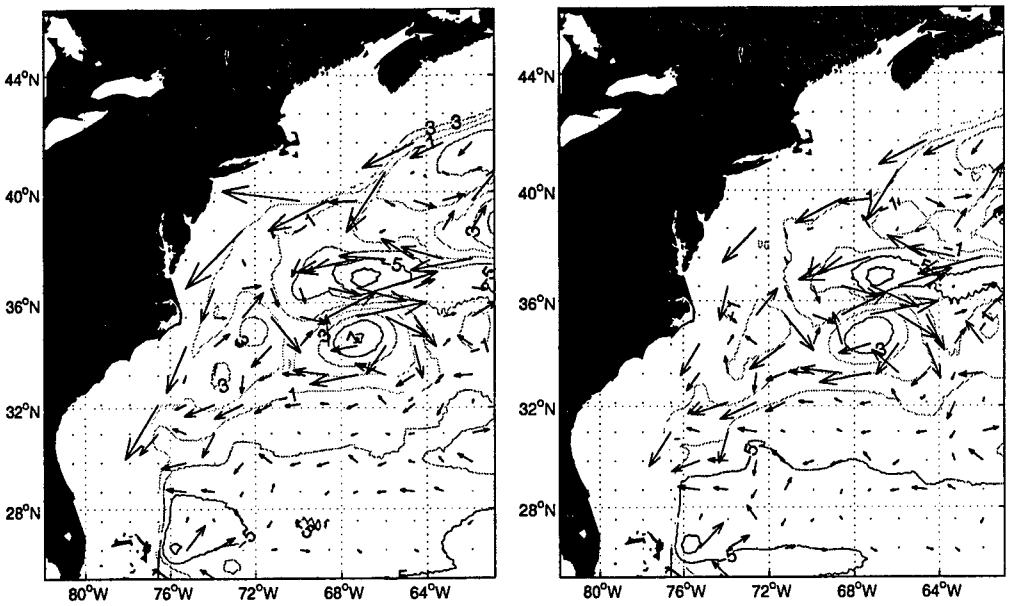


FIGURE 7. Time mean pressure and velocity vectors in the 1/6° resolution western domain during years 66 – 75 at levels 1474 m (left) and 2020 m (right).

along the shelfbreak between south Florida and the mid Atlantic Bight region; this water recirculates back to the northern seas and Arctic Ocean after heat exchange with the warmer green water that recirculates southward along with the other "warmer colors" that indicate higher surface elevations. Apparently, the DWBC, indicated by the deep velocity vectors during years 66 – 75, but missing during years 1 – 5, plays a big role in the observed mean GS path.

The DWBC extends to more than 2000 m depth in the model results (Figure 7). After turning sharply counterclockwise near CH most of the DWBC current travels eastward to well off-shore, before turning southward, crossing under the GS and turning back towards the coast. Transient eddies are significant throughout the depth, and dominate in the deeper levels where the mean flow is smaller.

These figures show the dramatic effect of the DWBC on the GS and the major flattening of isopycnal surfaces that occurs after the DWBC dense water reaches the Grand Banks shelfbreak region. Dietrich et al. (2003b) find that a realistically narrower western Labrador Sea shelfbreak significantly intensifies the DWBC, resulting in even more strongly flattened isopycnals than seen in Figure 5, more like Yashayaev climatology (Figure 3). Higher model resolution may further intensify the DWBC, but is not addressed.

The negative contours in Figure 6 intersect the U.S. mainland coast *nearly* tangentially; this reflects upwelled DWBC water on the west side of the Florida Strait, as consistent with the cool coastal climatological temperature (Figure 3) and model temperature that is close to the climatology. This upwelling reflects a secondary circulation effect associated with bottom friction and mixing of offshore GS jet momentum into the slower moving coastal water. The strong GS jet effects dominate over local wind forcing, unlike the California Current system (Haney et al. 2001).

Thus, even the nearshore part of the coastal current, which is shoreward of the upwelled coastal water indicated by the negative contours in Figure 6, separates almost completely

at CH and forms the north wall of the separated GS. As noted above, this does not occur as a linear response to the HR winds used in this study.

The explanation of the interesting strong GS/DWBC interaction indicated by Figures 4-6 is as follows. The Levitus climatology used to initialize the model is unrealistically baroclinic between the observed GS mean location and the Grand Banks shelfbreak, reflecting diffusive smoothing of climatological data. The resulting baroclinic eddies transport potential density southward (mainly by northward heat transport) and flatten potential density contours in the deep offshore water, leading to strong isopycnal slopes in the shelfbreak region and much weaker slopes along the observed mean GS axis. Thus, there is a northward displacement of the GS front to the Grand Banks shelfbreak during the first few model years and a corresponding wrong GS path. Only after full establishment of the DWBC along the Grand Banks shelfbreak, which takes about 10 model years to occur, does the front move southward to its observed location. This is the time scale required for densest DWBC water formed in the GIN Sea to reach the Grand Banks.

Thus, overly diffusive models, carefully tuned to the diffuse Levitus climatology, can closely match this climatology. However, *it is impossible to tune models requiring such large diffusion to the observed flattened time averaged non-diffused climatological isopycnals* (Figure 3). This can only be done by a model such as the present DieCAST model configured with low diffusion (Figure 5).

Thus, the DWBC water plays a major material role in model GS separation. In a limited-area model having specified DWBC inflow, Thompson and Schmitz (1989) came to a similar conclusion. The role is analogous to the inner wall of rotating annulus experiments, except the cold water source is by advection of the dense DWBC water rather than by conduction at the wall. The GS, in turn, plays a role analogous to the outer wall of the rotating annulus experiments. Amplitude vacillation in those experiments is accompanied by flattening of interior isotherms due to baroclinic instability (Pfeffer et al. 1974), which by its very nature results in such flattening. This also characterizes the atmospheric index cycle.

3.2. *Other Significant Results*

A large northern recirculation gyre occurs between the GS and the Grand Banks shelfbreak at depth > 700 m. This gyre entrains and recirculates some of the DWBC water. Figure 8a shows its far north source, the East Greenland Current, flowing over the Denmark Strait, which preconditions even deeper water formation in the Labrador Sea. On the east side of the Denmark Strait, a fragment of the North Atlantic Gyre flows into the GIN Sea as observed. Notably, such two-way flow separated by a strong front occurs in spite of the coarse $1/2°$ resolution used in the eastern domain of the present model. The sill overflow quickly becomes a quasi-balanced bottom density current, as the Coriolis terms quickly arrest any initial downslope flow (away from shore) to give a quasi-balanced along-isobath flow with deep water and lower pressure to the left (looking downstream); a slow, frictionally induced cross-isobath (away from shore) flow toward deeper water occurs in the bottom boundary layer.

Figure 9 shows the time mean rms velocity deviation from the time mean velocity at 700m depth in the Denmark Strait region, where dense sill level water spills "over the dam (sill)" into a bottom density current. This shows that the deep eddy activity is concentrated in the DWBC region (along the shelfbreak), where significant vortex stretching is driven by energy-releasing sinking dense DWBC water along the shelfbreak and by locally strong interaction with GS water near the northeast coast of the Flemish Cap (45 deg W, 47 deg N). The vortex stretching, as the potential energy is released,

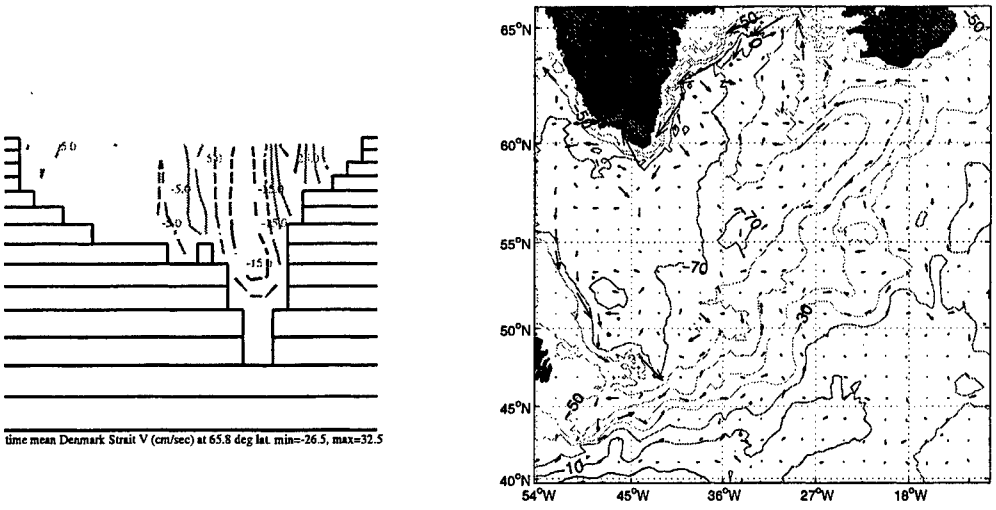


FIGURE 8. (a) Vertical/longitudinal cross-section of time mean latitudinal velocity across Denmark Strait in the coarse 1/2° resolution model eastern domain (left panel); (b) Time mean surface height and velocity vectors at 700 m depth in the Denmark Strait region (right panel).

results in turbulent mixing of the East Greenland Current (Arctic Ocean source) water with the North Atlantic Gyre water. The saddle point structure of the time average surface height (Figure 8b) reflects the sill bathymetry, and also shows the mean watermass paths leading to turbulent interaction. Thus, Figures 8-9 indicate inertial, turbulent interaction between the East Greenland Current and North Atlantic Gyre south of the Denmark Strait, even with the relatively coarse 1/2° resolution in this region. The sill overflow is an important part of the thermohaline circulation, and the associated locally strong mixing is important to watermass dynamics.

While some of the DWBC upwells on the north side of the GS separation point, some of it continues southward. Some of the southward branch upwells on along the shelfbreak between CH and the Bahamas. The cool coastal temperatures in both the Yashayaev climatology and the model results in this region reflect this upwelling. Horizontal advection by the Florida Current from the south that warms the coastal region is balanced by vertical advection and mixing. Such vertical circulation is forced by a combination of bottom drag and entrainment of coastal water into the strong GS current. This indirect circulation intensifies the GS front, thereby affecting development of eddies through baroclinic instability, especially after GS separation. Thus, in this narrow coastal region, the upwelled undercurrent water is entrained into the Florida Current from the south; this is a region of significant watermass mixing. Unlike the wind forced coastal jet of the California Current system (Haney et al. 2001), local wind effects may be secondary in such an energetic current system.

These mean results, calculated on a modern PC, are more realistic than the recent state-of-the-art results by Chao et al. 1996 despite requiring less overall resolution. Using realistic HR winds which, unlike the winds they used, do not *force* separation at CH (Townsend et al. 2000), the mean path of the model GS is very close to the observed mean path, starting with a realistic trajectory from the observed separation point. Further downstream, the separated upwelled coastal water bifurcates from the GS core, similar to the two-branch separated Gulf Stream in the linear response to HR winds noted by

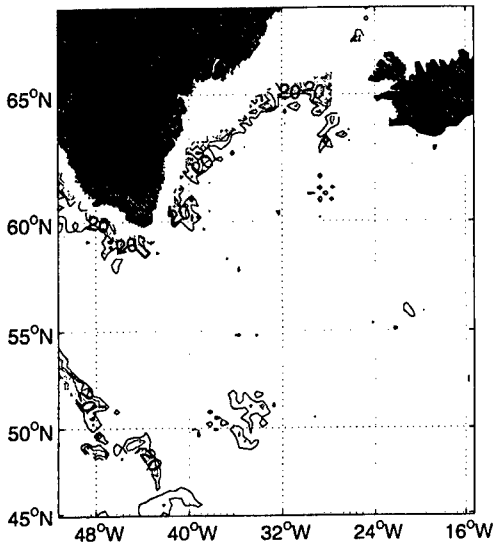


FIGURE 9. Time mean rms velocity deviation from the time mean velocity at 700 m depth in the Denmark Strait region.

Townsend et al. (2000), but is also influenced by interaction with the New England Seamount Chain, as indicated by the animation from Figure 10 (shown in `ftp://ssc.erc.msstate.edu/pub/mehra/nab_duo/OMO/year69-70.AVI.gz`).

Figure 10 shows a sequence of the surface currents during model year 70. A major cold core eddy (often called a ring) pinches off the southern tip of a southward GS meander around day 85. Around day 100, a warm core pinches off a northward meander. Later, another warm core develops as a result of GS interaction with the New England Seamount Chain. There is a deep northward secondary flow generated by blocking of the deep GS flow, which also steers the northern GS surface current fringe northward into a developing warm core ring, as discussed by Hurlburt and Thompson (1984). This GS bifurcation is a prevailing feature in model results, as indicated by Figure 6. The GS straightens out to its observed mean path after these two major eddy pinchoffs. These results are consistent with observations of transient small-scale features in and around the GS. The results of Chao et al. (1996) do not show such fine-scale features.

Several times per year, buoyant warm-core eddies pinch off northward meanders of the GS and drift westward and southwestward back through the Middle Atlantic Bight, as also seen in Figure 10. They become imbedded in the Middle Atlantic Bight shelfslope current and ultimately entrained back into the GS near CH (e.g. Bowman and Duedall 1975). However, the volume of slope water entrained, including its eddies, is only a fraction of the total $O(100$ Sv) GS transport. Full separation of the warm GS water occurs at CH, including a small volume of much cooler DWBC water upwelled along the shelfbreak between the Florida Strait and the Middle Atlantic Bight.

Also in the Figure 10 sequence, the Gulf of Mexico Loop Current penetrates northward and pinches off a major warm core eddy. The Dry Tortuga cyclone plays a significant role, as do other cyclonic frontal eddies that originate along the Yucatan shelfbreak, some of which merge into the Dry Tortuga eddy when the Loop Current is well extended into the Gulf of Mexico. Some frontal cyclones also pass through the Florida Strait. Before the major warm core eddy pinchoff, the Loop Current takes the shape of a square

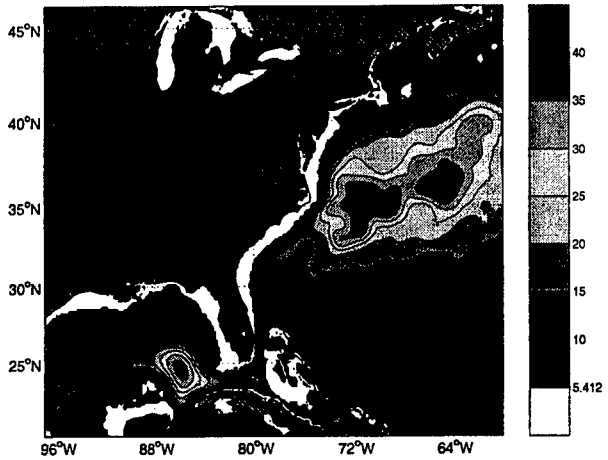


FIGURE 11. Root mean square deviation of surface height from years 66 – 75 time mean in western 1/6° resolution domain.

with rounded corners due to frontal eddy effects. The Loop Current takes a right angle turn into the Florida Strait after eddy shedding. Westward propagating anticyclones prevail in the Caribbean Sea, and there is a semi-permanent cyclonic recirculation in the southwestern Caribbean Sea corner. These details are consistent with observations and earlier modeling results (e.g. Dietrich et al. 1997).

Figure 11 shows rms seasurface height anomaly derived from the model results. In general, the rms value is 30 – 45 cm along the separated GS axis all the way to the New England Seamount region near the eastern boundary of the 1/6° resolution grid. Thus, vigorous transient eddies populate the modeled GS region with root-mean-square surface height anomaly amplitudes comparable to those in nature (DYNAMO 1997, Figure 8.6). The rms anomaly in the Gulf of Mexico region is also close to the observed, as in earlier Gulf of Mexico studies with DieCAST (Dietrich 1997; Dietrich et al. 1997). The rms value in the coarse resolution domain east of 60° W (not shown) is smaller, but there is a local maximum of about 20 cm along the shelfbreak at the south edge of the Flemish Cap. Coupling to low resolution coarse grid domain may cause reduced rms values near the eastern boundary in the fine grid domain.

4. DWBC Interaction with Methane Hydrates: Potential for Global Warming

Accurate DWBC simulation is important, because it not only affects the GS path as shown in Section 3, but the DWBC path also affects potential catastrophic release of vast amounts of methane gas from methane hydrates stored on the shelf slope below depths where methane freezes (about 4° C, depending also on pressure-depth). It is thought that this methane, after escaping to the atmosphere, may oxidize and add huge amounts of CO_2 (Katz et al. 1999), a greenhouse gas that, unlike the water vapor by-product, does not precipitate out, thus leading to global warming.

As suggested by Lai (2003), strongly exothermic biogeochemical processes occuring within the methane bubbles generated in the ocean depths (Kennett et al. 2000) may significantly warm the DWBC, lead to positive feedback, including by DWBC recirculation in the northern seas and Arctic ocean, and affect thermohaline circulation including Arctic and northern seas stratification through annual cycle ice melting/freezing. These

processes are coupled to the GS. The nonlinear GS/DWBC system dynamics may lead to accelerating methane release and sudden global warming. As further noted by Lai (2003), this possibility demands careful study, due to observed recent global warming (IPCC 2001) and oxygen depletion (Joos et al. 2003) in the ocean depths near the methane hydrate levels. A major concern is that anthropogenic perturbation of the system may lead to even stronger catastrophic warming than the about 10° C Arctic temperature rise that occurred in $10 - 20$ years at the end of the last glacial maximum (Rossby and Nilsson 2003).

The GS path affects the location and intensity of North Atlantic deep water formation, which occurs mainly in the northern seas and Arctic Ocean and feeds the DWBC after spilling over the GIN Sea sills. Its changes would alter the location and temperature of the DWBC, possibly augmenting the potential catastrophic greenhouse gas induced warming noted above. Modeling the DWBC water is a big challenge relating to GS separation. Dense fluid in a thin, narrow, bottom density current must travel from its high latitude source region to the Grand Banks shelfbreak without excessive numerical dissipation and dispersion, in order to have sufficient intensity to realistically affect the energetic GS separation and ensuing dynamics; this travel takes $O(10)$ years.

The dense narrow thin DWBC is not resolved by the climatological data used to initialize the model. Thus, it must develop spontaneously in the model. This dense shelfslope water forms in the northern seas, and takes more than a year to reach the Grand Banks from the Labrador Sea, and $O(10)$ years to reach there from the GIN Sea. In order for it to arrive at CH with sufficient intensity to properly affect GS separation and path, it must not be overly diluted by numerical dispersion and dissipation.

5. Conclusion and future work

Results presented herein show that one may simulate GS dynamics and separation from the coast realistically in a marginally eddy-resolving simulation by using a model having a) low total (physical plus numerical) dissipation; b) fourth-order accurate advection with its associated low numerical dispersion; c) further numerical dispersion reduction in the interpolations between grids; and d) fourth-order accurate horizontal pressure gradient. Nonlinear dynamics are involved in GS separation and it thus seems necessary to resolve the major CH abutment. However, although bathymetry-induced strongly inertial dynamics may favor separation near CH, our results indicate that is not sufficient; a robust DWBC is also required. A robust DWBC requires that the DWBC water not be dispersed by numerical errors during the $O(10)$ years to travel from its source region to the Grand Banks shelfbreak region. The importance of the DWBC is enhanced by its interaction with methane hydrates, which may lead to global warming.

It would be interesting to nest a finer grid in the GS separation region to shed more light on the detailed dynamics of the GS separation, focusing on the vertical circulation in the region of GS separation and how this circulation connects the GS to the DWBC. The significance of simulating a realistic GS/DWBC system lies partly in its potential impact on climate through fundamentally nonlinear stochastic resonance effects that are known to occur in many nonlinear systems (Rahmstorf and Alley 2002).

REFERENCES

BACON, S., REVERDIN, G., RIGOR, I. G., & SMITH, H. M. 2002 A freshwater jet on the East Greenland shelf. 2002 Ocean Sciences Meeting.

BOWMAN, M. J. & DUEDALL, I. W. 1975 Gulf Stream meander in the vicinity of the New York Bight. *Gulfstream*, **1** (2), 6–7, 1975. NOAA, Washington, D.C.

CHAO, Y., GANGOPADHYAY, A., BRYAN, F. O. & HOLLAND, W. R. 1996 Modeling the Gulf Stream system: How far from reality?. *Geophys. Res. Lett.*, **23**, 3155–3158.

CHAPMAN, D. C. & BEARDSLEY, P. C. 1989 On the origin of shelf water in the Middle Atlantic Bight. *J. Phys. Oceanogr.*, **19**, 384–391.

DAMEE-NAB 2000 Data assimilation and model evaluation experiment - North Atlantic Basin. *Dyn. Atmos. Oceans.*, **32**, special DAMEE-NAB issue.

DENGG, J., BECKMANN, A. & GERDES R. 1996 The Gulf Stream separation problem. In: Krauss, W. (Ed.), The warmwatersphere of the North Atlantic Ocean. Gebr. Borntraeger, Berlin, 253–290.

DIETRICH, D. E. 1997 Application of a modified "A" grid ocean model having reduced numerical dispersion to the Gulf of Mexico circulation. *Dynamics of Atmospheres and Oceans*, **27**, 201–217.

DIETRICH, D. E. 2002 Duo-resolution North Atlantic Ocean/Gulf of Mexico model. 2002 Ocean Sciences Meeting.

DIETRICH, D. E., HANEY R. L., FERNANDEZ V., JOSEY S. & TINTORE, J. 2003a Air-sea fluxes based on observed annual cycle surface climatology and ocean model internal dynamics: a precise, non-damping, zero-phase-lag approach applied to the Mediterranean Sea. under revision.

DIETRICH, D. E., LIN, C. A., MESTAS-NUNEZ, A. & KO, D.-S. 1997 A high resolution numerical study of Gulf of Mexico fronts and eddies. *Meteorol. Atmos. Phys.*, **64**, 187–201.

DIETRICH, D. E. & MEHRA, A. 1998 Sensitivity studies in the Santa Barbara Channel using the DieCAST ocean model. Proceedings of the Santa Barbara Channel Quality Review Board Meeting, San Diego, February, 1998.

DIETRICH, D. E., MEHRA, A., RICHMAN, J., BOWMAN, M. J., LAI, C. A. & TSENG, Y. H. 2003b Nonlinear Gulf Stream interaction with the Deep Western Boundary Current System: bathymetry and dissipation sensitivity (to be submitted).

DYNAMO 1997 Dynamics of North Atlantic models. Simulation and assimilation with high resolution models. Institure fur Meereskunde an der Univsrsitat Kiel, 334.

FERNANDEZ, V., DIETRICH, D. E., HANEY, R. L. & TINTORE, J. 2003. Mesoscale, seasonal and interannual variability in the Mediterranean Sea using the DieCAST ocean model. Submitted to *J. Marine Systems* (in revision).

HAIDVOGEL, D. B., ARANGO, H. G., HEDSTROM, K., BECKMANN, A., MALONOTTE-RIZZOLI, P. & SHCHEPETKIN, A. F. 2000 Model evaluation experiments in the North Atlantic Basin: simulations in nonlinear terrain-following coordinates. *Dyn. Atmos. Oceans.*, **32**, 239–281.

HANEY, R. L., HALE, R. A. & DIETRICH, D. E. 2001 Offshore propagation of eddy kinetic energy in the California Current. *JGR-Oceans*, **106**, 709–717.

HELLERMAN, S. & ROSENSTEIN, M. 1983 Normal monthly wind stress over the world ocean with error estimates. *J. Phys. Oceanogr.*, **13**, 1093–1104.

HURLBURT, H. E. & HOGAN, P. J. 2000 Impact of 1/8 deg to 1/64 deg resolution on Gulf Stream model-data comparisons in basin-scale subtropical Atlantic Ocean models. *Dyn. Atmos. Oceans.*, **32**, 283–329.

HURLBURT, H. E. & THOMPSON, J. D. 1980 A numerical study of Loop Current intrusions and eddy shedding. *J. Phys. Oceanogr.*, **10**, 1611–1651.

HURLBURT, H. E. & THOMPSON, J. D. 1984 Preliminary results from a numerical study of the New England Seamount chain influence on the Gulf Stream. Proc. of the Workshop on Predictability of Fluid Motions, Amer. Inst. Phys., G. Hollaway, Ed.

IPCC 2001 Climate change 2001: The scientific basis. Cambridge University Press, Cambridge, U.K. 881.

JOOS, F., PLATINER, G.-K., STOCKER, T. F., KORTZINGER, A. & WALLACE, D. W. R., 2003 Trends in marine dissolved oxygen: Implications for ocean circulation changes and the carbon budget. EOS, *Transactions Ameri. Geophy. Union*, **84**, 197–201.

KATZ, M. E., PAK, D. K., DICKENS, G. R. & MILLER, K. G. 1999 The source and fate of massive carbon input during the latest paleocene thermal maximum. *Science*, **286**, 1531–1533.

KENNETT, J. P., CANNARIATO, K. G., HENDY, I. L. & BEHL, R. J. 2000 Carbon isotopic evidence for methane hydrate instability during Quaternary Interstadials. *Science*, **288**, 128–133.

KILLWORTH, P. D., SMEED, D. A. & NURSER, A. J. G. 2000 The effects on ocean models of relaxation toward observations at the surface. *J. Phys. Oceanogr.*, **30**, 160–174.

LAI, C.-C. A. 2003 personal communications.

PFEFFER, R. L., BUZYNA, G. & FOWLIS, W. W. 1974 Synoptic features and energetics of wave-amplitude vacillation in a rotating, differentially heated fluid. *J. Atmos. Sci.*, **31**, 622–645.

RAHMSTORF, S. & ALLEY, R. B. 2002 Stochastic resonance in glacial climate. *EOS*, 19 March 2002 (lead article).

ROSSBY, T. & NILSSON, J. 2003 Current switching as the cause of rapid warming at the end of the last Glacial Maximum and Younger Dryas. *Geophys. Res. Lett.*, **30**. In press.

SANDERSON, B.G. & BRASSINGTON, G. 1998 Accuracy in the context of a control-volume model. *Atmosphere-Ocean*, **36**, 355–384.

STANEVA, J. V., DIETRICH, D. E., STANEV, E. V. & BOWMAN, M. J. 2001 Rim current and coastal eddy mechanisms in an eddy-resolving Black Sea general circulation model. *J. Marine Systems*, special issue on the Black Sea, **31**, 137–157.

STERN, M. E. 1998 Separation of a density current from the bottom of a continental slope. *J. Phys. Oceanogr.*, **28**, 2040–2049.

THOMPSON, J. D. & SCHMITZ, W. J. 1989 A limited-area model of the Gulf Stream: design, initial experiments and model-data intercomparison. *J. Phys. Oceanogr.*, **19**, 791–814.

TOWNSEND, T. L., HURLBURT, H. E. & HOGAN, P. J. 2000 Modeled Sverdrup flow in the North Atlantic from 11 different wind stress climatologies. *Dyn. Atmos. Oceans.*, **32**, 373–417.

VELEZ-BELCHI, P., ALVAREZ, A., COLET, P., TINTORE, J. & HANEY, R. L. 2001 Stochastic resonance in the thermohaline circulation. *Geophys. Res. Lett.*, **28**, 2053–2056.

YASHAYAEV, I. 2002 Personal communication.
http://www.mar.dfo-mpo.gc.ca/ science/ocean/woce/climatology/naclimatology.htm

Numerical simulation of regional circulation in the Monterey Bay region

By Y. H. Tseng, D. E. Dietrich †, AND J. H. Ferziger

1. Motivation and objectives

Monterey Bay is located 100 km south of San Francisco and is one of several large bays on the West Coast of the United States. This area is important due to the abundance of marine life. The regional circulation in the Monterey Bay area is tightly coupled to the California Current System (CCS) and highly correlated to the coastal upwelling. In the offshore region, flow is dominated by a broad, weak, equatorward flowing current, the California Current (CC). The CC extends offshore to a distance of $900 - 1000$ km and flows year-round. Within about 100 km of the coast, two narrow poleward flowing boundary currents have been found, the Inshore Countercurrent (IC) and the California Undercurrent (CU). The IC is a weak current that varies seasonally, appearing in fall and winter, and transports shallow, upper layer water. The CU is a narrow ($10 - 50$ km) relatively weak subsurface flow and transports warm, saline equatorial water. The CU is strongest at around $100 - 300$ m depth and has a mean speed of approximately 15 cm/s (Pierce *et al.* 2000) at all latitudes on the West Coast throughout the year.

While many experimental studies have examined the flow in the vicinity of Monterey Bay, there are only a few numerical studies focusing on the regional circulation. These previous modeling studies have mostly used simplified dynamics, domains, and forcing, with coarse spatial resolution or/and short integration times. However, there are some significant interannual variations, including large scale effects relating to El Nino/Southern Oscillation dynamics and smaller scale noise due to fronts and eddies. The regional circulation in this region is very complex and difficult to model correctly.

The objective of this study is to produce a high-resolution numerical model of Monterey Bay area in which the dynamics are determined by the complex geometry of the coastline, steep bathymetry, and the influence of the water masses that constitute the CCS. Our goal is to simulate the regional-scale ocean response with realistic dynamics (annual cycle), forcing, and domain. In particular, we focus on non-hydrostatic effects (by comparing the results of hydrostatic and non-hydrostatic models) and the role of complex geometry, i.e. the bay and submarine canyon, on the nearshore circulation. To the best of our knowledge, the current study is the first to simulate the regional circulation in the vicinity of Monterey Bay using a non-hydrostatic model. Section 2 introduces the high resolution Monterey Bay area regional model (MBARM). Section 3 provides the results and verification with mooring and satellite data. Section 4 compares the results of hydrostatic and non-hydrostatic models. Finally, conclusions and future work are drawn in section 5.

† AcuSea Inc., Albuquerque, New Mexico

2. Monterey Bay area regional model (MBARM)

2.1. *Numerical methods*

In order to study the regional circulation in the vicinity of Monterey Bay while avoiding numerical errors introduced by the σ-coordinate and non-hydrostatic effects, we used the non-hydrostatic, z-level, mixed Arakawa A and C grid, fourth-order accurate Dietrich/Center for Air-Sea Technology (DieCAST) ocean model, which provides high computational accuracy and low numerical dissipation and dispersion. The numerical procedures are detailed in Dietrich & Lin (2002) and Tseng (2003).

The Coriolis terms are evaluated on the 'a' grid and thus have no spatial interpolation error, which is a significant advantage for a dominant term (Dietrich 1997). Fourth-order central differencing is used in the control volume approximation to compute all advection and horizontal pressure gradient terms, except adjacent to boundaries where second-order accuracy is used. All control volumes are collocated (e.g. momentum, energy, salinity and the incompressibility approximation to mass conservation) and are all enforced on the same set of control volumes. The model uses a rigid-lid approximation. At the regional ocean scale, the 'slow modes' (low frequency, long time scale motions) dominate the ocean circulation. Use of a rigid lid excludes the 'fast mode' associated with barotropic free surface waves. The rigid-lid approximation does not affect internal gravity wave speeds. Thus, it does not affect geostrophic adjustment of the baroclinic mode that dominates the general circulation. The rigid-lid approximation also simplifies the treatment of open boundaries because it greatly reduces the range of frequencies that must be addressed.

2.2. *Model descriptions*

The Monterey Bay area regional model (MBARM) is one-way coupled to a larger scale California current system DieCAST model and uses the immersed boundary method to represent the coastal geometry and bathymetry (Tseng & Ferziger 2003) in the local model. The domain of MBARM extends from 36.1° to 37.4°N and from the California coast out to 122.9°W (Figure 1); the horizontal grid size is uniformly 1/72° ($\approx 1.5\ km$) for the medium grid, and 1/108° ($\approx 1\ km$) for the fine grid. The vertical grid has 28 levels. The surface buoyancy flux is computed by nudging both the temperature and the salinity toward Levitus' monthly climatology (Levitus 1982). This is equivalent to adding heat and/or freshwater to the top layer. This salinity condition, although widely used, has little physical basis and does not conserve salt material exactly (Dietrich *et al.* 2003), but it has little effect in the region modeled because the salinity field is strongly constrained by the open boundary inflows; freshwater sources from rivers and precipitation, and sinks from evaporation have only minor effect in this region. The wind stress is from Hellerman and Rosenstein's monthly climatology (Hellerman & Rosenstein 1983). The southeastward winds intensify during spring and summer and weaken during fall and winter.

Bathymetry is unfiltered USGS 250 m resolution topography. The bottom topography and the coastal geometry are adequately represented by the immersed boundary module (Tseng & Ferziger 2003). The sea floor is insulated and partial-slip as parameterized by a nonlinear bottom drag coefficient of 0.002. Significant momentum exchange with the California Current System occurs through the open boundary.

The model is one-way coupled from a larger scale CCS model (Haney *et al.* 2001) which has resolution 1/12°. The MBARM is initialized by interpolation of the coarse CCS model results after two years of simulation. All open boundary conditions are based on boundary fluxes. A pure upwind advective scheme is used at the three lateral open

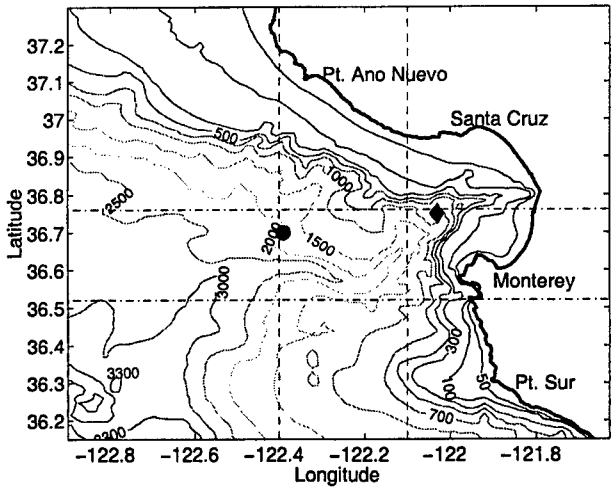


FIGURE 1. The model domain of Monterey Bay area and bathymetry. Locations of moorings M1, M2 are marked by a circle and a diamond, respectively. '–.': lines at latitude $36.52°N$ and $36.76°N$, '––': lines at longitude $122.4W$ and $121.1°W$. The horizontal uniform grid is shown by the dotted lines (Every sixth grid is shown).

boundaries (north, south, and west) for all variables:

$$\frac{\partial \phi}{\partial t} + U_n \frac{\partial \phi}{\partial n} = 0 \tag{2.1}$$

where

$$\frac{\partial \phi}{\partial n} = \begin{cases} (\phi - \phi_o)/\Delta x_n & U_n \geq 0 \\ (\phi_i - \phi)/\Delta x_n & U_n < 0 \end{cases} \tag{2.2}$$

and U_n is the normal velocity on the open boundary. ϕ represents any of the three velocity components, temperature or salinity at the boundary. ϕ_o is the variable on the open boundary obtained from the CCS model and ϕ_i is the variable at one grid point inside the open boundary, Δx_n is the grid spacing in the direction normal to the boundary. Thus, large scale data are advected inward at an inflow boundary and the interior data is advected outward at an outflow boundary.

It has been argued that the primitive equations are ill-posed when an inappropriate open boundary condition is used. If the proper number of boundary conditions is not specified, the solution of the primitive equations will lead to the exponential growth of energy and numerical instability (Oliger & Sundstrom 1978). According to Oliger & Sundstrom (1978) and Mahadevan *et al.* (1996), the numerical problem is well-posed if the velocity vector, salinity, and temperature are specified at the inflow boundary condition and the normal velocity is specified at the outflow boundary. The above open boundary treatment satisfies these requirements and is well-posed. Palma & Matano (2000) investigated the performance of combinations of OBCs using POM. They found that the best overall performance of OBCs was a flow relaxation scheme for barotropic modes, a radiation condition for baroclinic modes, and combined advection and relaxation for the scalar field. In fact, the current scheme corresponds to a simplified version of the scheme suggested by Palma & Matano (2000).

3. Results

3.1. *General description*

Using Levitus' surface climatological forcing (temperature and salinity), the simulation reproduces many important features of the observed annual cycle of the CCS including the strengthening of the equatorward jet in spring and the weakening of the jet in autumn and winter. Coastal eddies occur primarily near some major headlands, especially Point Ano Nuevo, Pacific Grove and Point Sur. To examine the general circulation in the vicinity of Monterey Bay, we focus on the annual mean flow and seasonal variability.

3.1.1. *Annual mean flow*

The mean velocity fields for a simulation year at various depths (10.1, 50, 100, 300, 400, 700 m) are shown in Figure 2. As mentioned before, the major features in the Monterey Bay area are the shallow, equatorward, broad California Current and two narrow poleward boundary currents (California Undercurrent and Inshore Current) along the coast. These flows are seen in Figure 2. The surface flow is affected by surface wind forcing. Vertical shear layers appear at moderate depth ($50 - 200$ m). The mean velocity pattern clearly delineates the extent of poleward flow associated with the inshore currents.

Collins *et al.* (2000) estimated the upper 1000 m depth-averaged mean velocity based on 19 cruises conducted from April 1988 to April 1991. They reported a west-northwestward ($290°T - 310°T$) flow with a mean speed of $3.7 - 5.3$ cm/s at four inshore stations C1-C4 (at latitude $36.3°N$, $33 - 65$ km away from the shore). We estimate the one-year depth-averaged annual mean flow along the line connecting the four inshore stations C1-C4 (Collins *et al.* 2000). The mean magnitude is 4.7 cm/s with direction $301°T$. The annual mean flow in the current study is in good agreement with observation. The result shows that the current one-way coupling at lateral boundary and the surface forcing are appropriate. More detailed comparison with observation is provided in the following section.

3.1.2. *Seasonal variability*

Summer and winter mean velocity fields at several depths (10.1, 100, 300, 700 m) are shown in Figures 3 and 4 for a simulation year. The along-shore component of the wind stress has been shown to be a key ingredient for generating realistic vertical and horizontal structures and the surface equatorward and subsurface poleward currents. These currents are baroclinically and barotropically unstable, resulting in the generation of meanders, filaments and eddies.

In summer, defined as May to July (Figure 3), the equatorward flow strengthens and dominates the flow from a depth of 100 m to the surface. This equatorward flow is forced by upwelling-favorable winds. A weak cyclonic eddy is observed within Monterey Bay, and is associated with the equatorward flow past a coastal bay. There is also a large-scale, anti-cyclonic eddy around 50 km from the coast that extends down to depth 100 m where the eddy is stretched significantly by the coastal bathymetry. The subsurface northward flow exists below depth 300 m during spring which is consistent with the year round northward flow associated with the CU. The transition from CC to CU occurs around depth $200 - 500$ m and the strongest CU occurs at depth 300 m, which is consistent with previous observations. These flows are tightly coupled with the large scale California current system model through open boundary.

The southward flow in the upper ocean strengthens and tends to move offshore, forming the filaments observed in the satellite images. Point Sur is the location where the

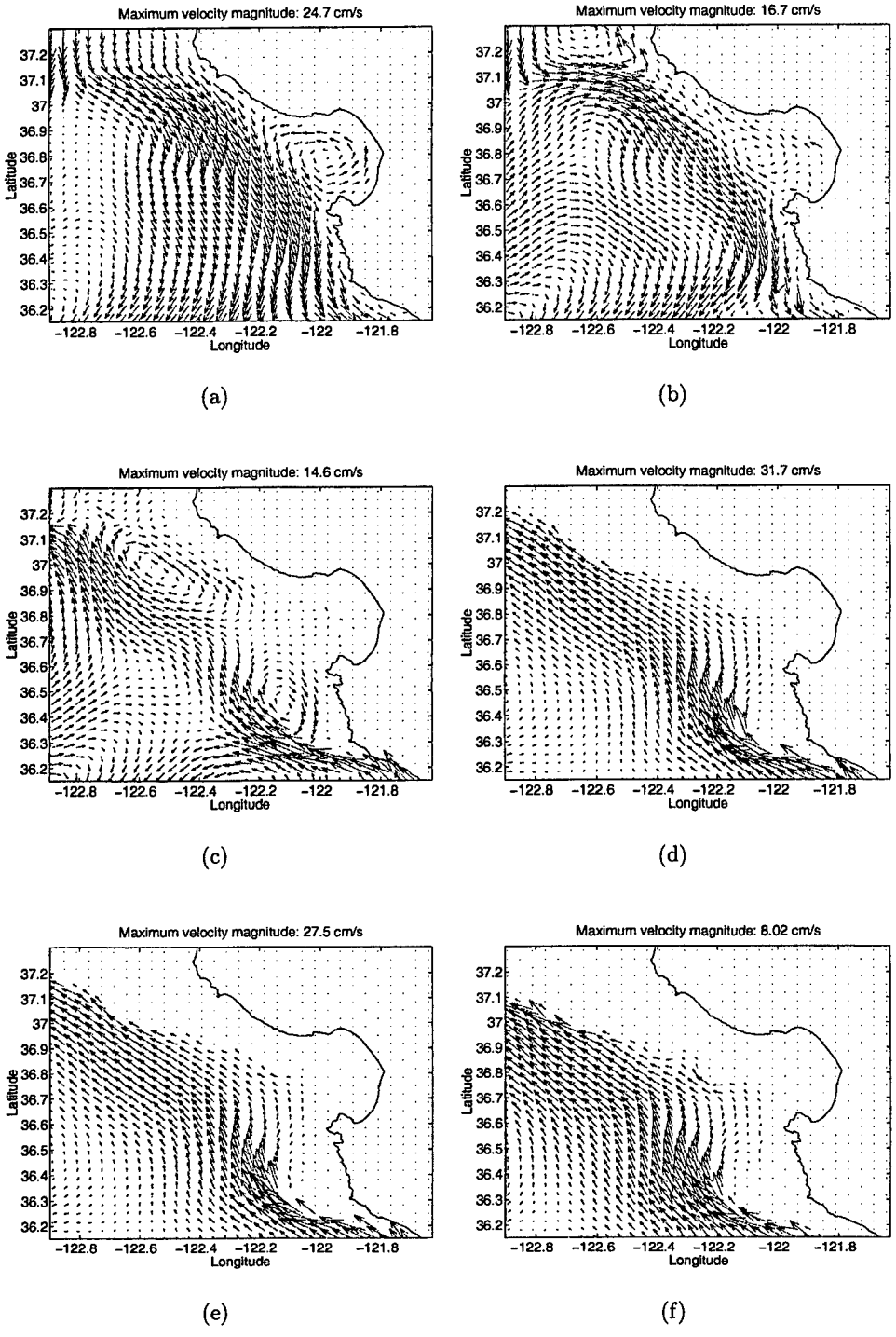


FIGURE 2. The annual mean velocity field at various depths for a year. At depth (a) 10.1 m, (b) 50 m, (c) 100 m, (d) 300 m, (e) 400 m,(f) 700 m.

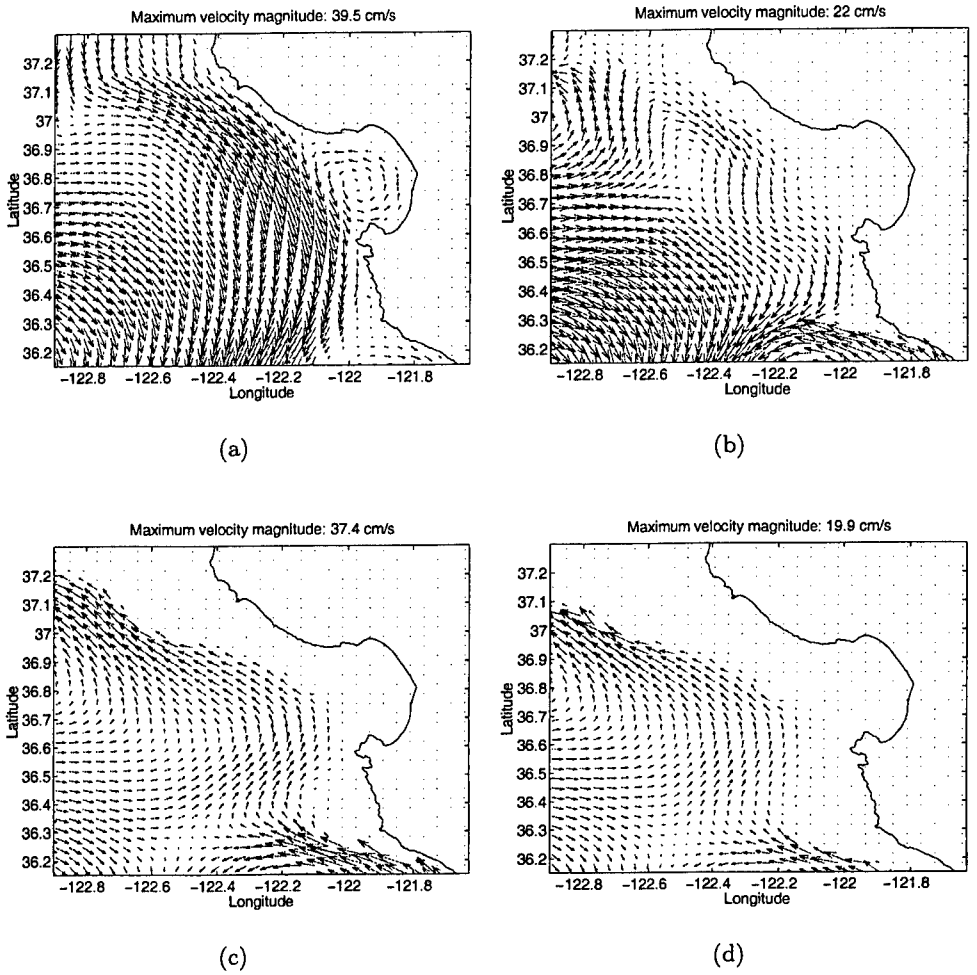


FIGURE 3. The mean velocity field at various depths during summer. At depth (a) 10.1 m, (b) 100 m, (c) 300 m, (d) 700 m.

offshore flow is most significant and satellite images also show that filaments occur there frequently. The current simulation shows this to be an effect of local topography on the enhancement of flow toward steep bathymetry and the steering effect of the Pacific Grove headland. The same conclusion was suggested by observations (Ramp *et al.* 1997). We still see the CU at depth, and the undercurrent follows the contours of coastal bathymetry closely.

Autumn is the season in which the dominant flow changes from equatorward to poleward in the upper ocean. By October upwelling favorable circulation occurs much less frequently, and near-surface flow along the central coast is under the influence of the northward flowing Davidson Current, which generally reaches its maximum speed at the surface in December. Figure 4 shows the mean flow in wintertime (November to January) at several depths. The velocity fields at all levels show very similar spatial structure. The CCS is dominated by the poleward flow. A narrow equatorward flow can still be observed

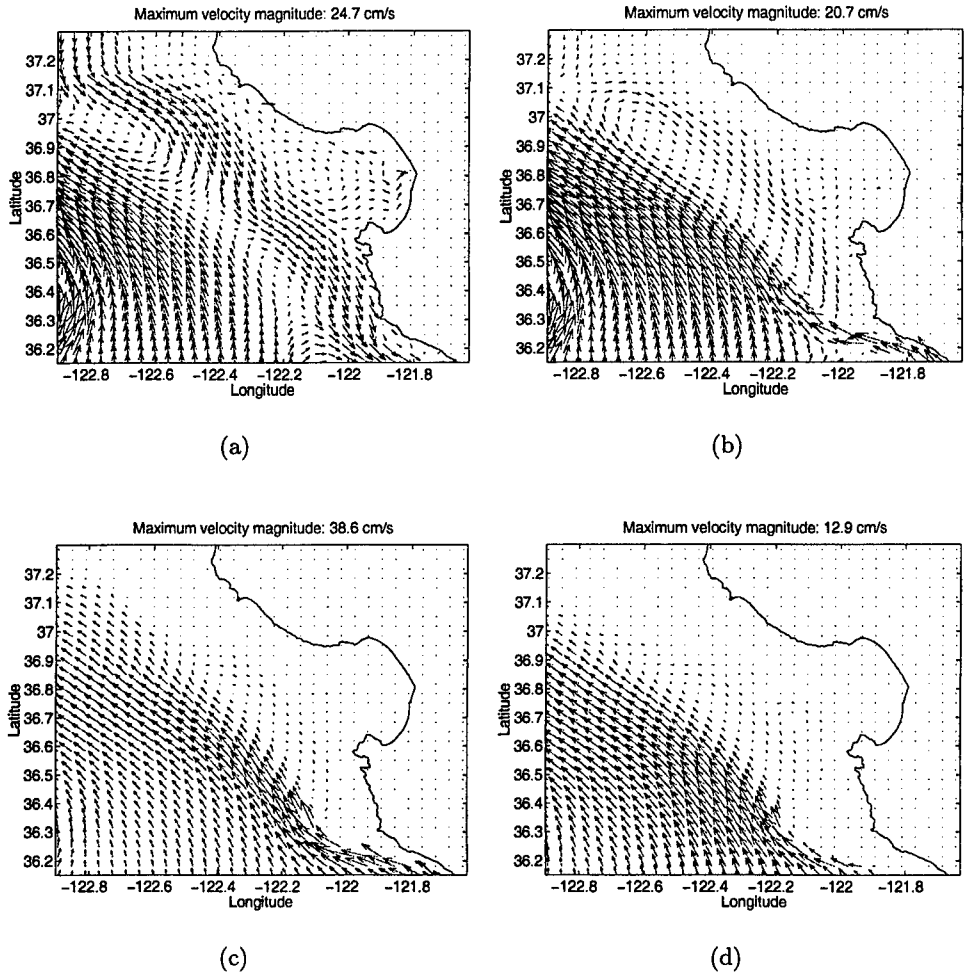


FIGURE 4. The mean velocity field at various depths during winter. At depth (a) 10.1 m, (b) 100 m, (c) 300 m, (d) 700 m.

in the shallow region. The poleward currents off Point Sur usually flow toward the northwest (along-shore), while the summer equatorward currents flow toward the southwest rather than southeastward along the large-scale bathymetry. This feature of the flow is reproduced by the simulation and can likely be attributed to the local topography, which tends to steer currents from the north offshore (Ramp *et al.* 1997).

3.2. *Comparison with mooring data*

We compare the model temperatures with those measured by Sea-Bird MicroCAT CTDs mounted on MBARI's M1 (122.03°W, 36.75°N) and M2 (122.39°W, 36.70°N) surface moorings (for location, see Figure 1). Since the model is forced by the average climatology at the sea surface, we do not expect the model to match the observations exactly.

The observed time series of temperatures at the M1 and M2 mooring stations display an annual cycle with cold temperatures during upwelling seasons and warmer temperatures during the rest of the year. The seasonal variation is more significant near the surface than

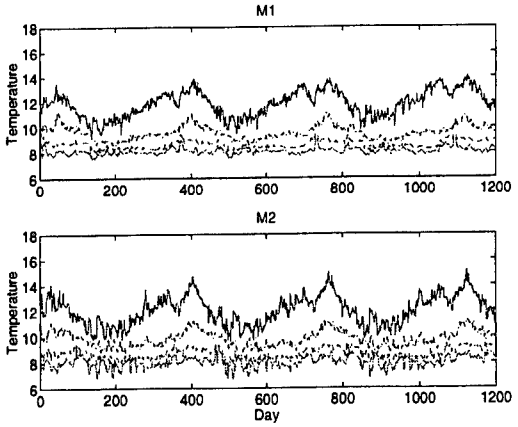


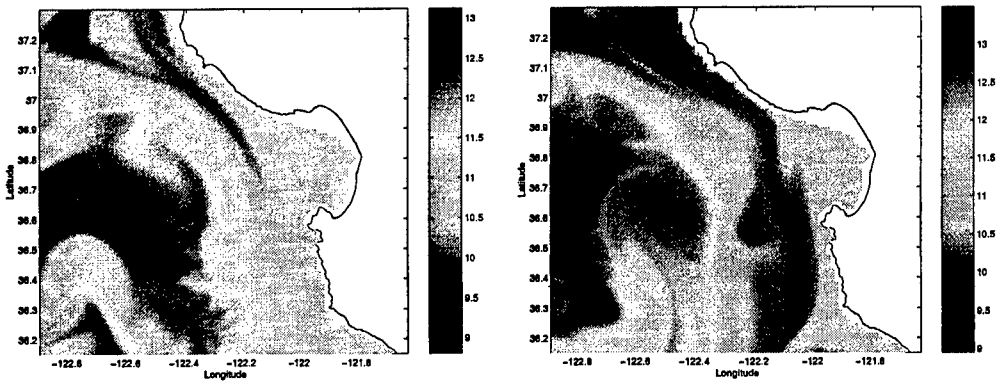
FIGURE 5. Model time series of temperature at stations M1 (top) and M2 (bottom) for three simulation years. The model repeats smoothly after 40 days, thus showing that the annual cycle is accurately responded. The depths from top to bottom are 10 m, 100 m, 200 m and 300 m.

at depth. The model results are shown in Figure 5 for the M1 and M2 mooring locations, respectively. The results repeat annually, showing that the model has been run long enough that the results are independent of the initial state. The model results reproduce many of the observed trends. These include the annual variation in temperature, cooling of surface and subsurface temperatures during spring upwelling, warming water masses during summer and early autumn, and slight cooling during late autumn. The near surface temperature (10 m) at M2 varies between $10 - 15°$ which is in the same range as the observations. The temperature at M1 is $1 - 2°$ lower than that at M2, which is again consistent with the measurements. At depth 300 m, the temperature varies from $7 - 9°$ at both the M1 and M2 stations, consistent with the observational data. The most important result of the simulation is the fact that, as in the observation, the annual cycle is evident and well reproduced in the simulation.

3.3. *Comparison with other observation results*

During periods of upwelling-favorable winds (spring and summer), there is a band of cold water which flows equatorward across the mouth of Monterey Bay with typical near-surface speeds of $20 - 30 cm/s$. Figures 6(a)-(b) show the surface temperature for day 109 and day 113 and contain a typical spring upwelling event. The upwelling centers are found north and south of Monterey Bay near Points Ano Nuevo and Sur (Figure 6(b)). Point Ano Nuevo has been identified to be the source of cold, salty near-surface water frequently seen in the bay (Rosenfeld *et al.* 1994). The upwelled (cold) water is advected southward across the bay and then breaks into two streams: one water mass moves offshore and the other equatorward. A warm anticyclonic feature is often found off the mouth of Monterey Bay, or just south of it (Ramp *et al.* 1997). This feature was also seen in advanced very high resolution radiometer (AVHRR) imagery. The simulation produces patterns very similar to those observed in the satellite images. A warm anticyclone is also apparent in the simulation. Meanders of the California current with anticyclonic circulation have often been reported (Breaker & Broenkow 1994; Ramp *et al.* 1997).

Within the bay, a cyclonic circulation is often observed (Breaker & Broenkow 1994). This circulation is caused mainly by the coastal geometry. The cyclonic circulation within Monterey Bay is consistent with the observed circulation.



(a) Day 109 (b) Day 113

FIGURE 6. The surface temperature field for day 109 and day 113.

4. Hydrostatic versus Non-Hydrostatic modeling

The growth of meanders and filaments of upwelled water has been demonstrated in many previous studies using hydrostatic models. However, it is still not clear how the non-hydrostatic mode affects the circulation in a coastal region with complex bathymetry and upwelling. Casulli & Stelling (1998) assessed the effects of the hydrostatic approximation in various applications and found that the hydrostatic model is not accurate in some cases. The hydrostatic approximation breaks down when the vertical acceleration is significant compared to the buoyancy force.

The vertical momentum and the non-hydrostatic pressure component cannot be neglected when the bottom topography changes abruptly on scales small compared to the local Rossby radius of deformation (e.g. near continental shelf edges and in deep canyons). Chao & Shaw (2002) studied coastal upwelling meanders and filaments using a non-hydrostatic model. Their idealized model does not include complex bathymetry, coastal irregularity or unsteady wind forcing. Their results show that the growth rates of meanders and filaments are enhanced by non-hydrostatic effects. Here we explore the impact of the hydrostatic approximation by comparing results from hydrostatic and non-hydrostatic versions of the DieCAST model applied to Monterey Bay.

It is noteworthy that hydrostatically modeled systems actually have more total energy than the corresponding non-hydrostatic systems. Specifically, the potential energy decrease due to sinking dense fluid and rising warm fluid goes entirely into horizontal kinetic energy according to the hydrostatic equations. Vertical acceleration senses no inertia, generally leading to larger vertical acceleration than would occur when inertia terms are included in the vertical momentum equation. The hydrostatic approximation is well posed and robust in spite of its lack of energy conservation; the horizontal kinetic energy is limited by the potential energy release and the vertical kinetic energy is limited, in turn, by its relation to horizontal velocity through the incompressibility equation.

The vertical velocity differences between the hydrostatic and non-hydrostatic models at various depths are shown in Figure 7. They are large along the canyon wall at all depths. These results show that rapid changes in slope cause vertical accelerations which violate the hydrostatic approximation. Vertical acceleration associated with the bores produced

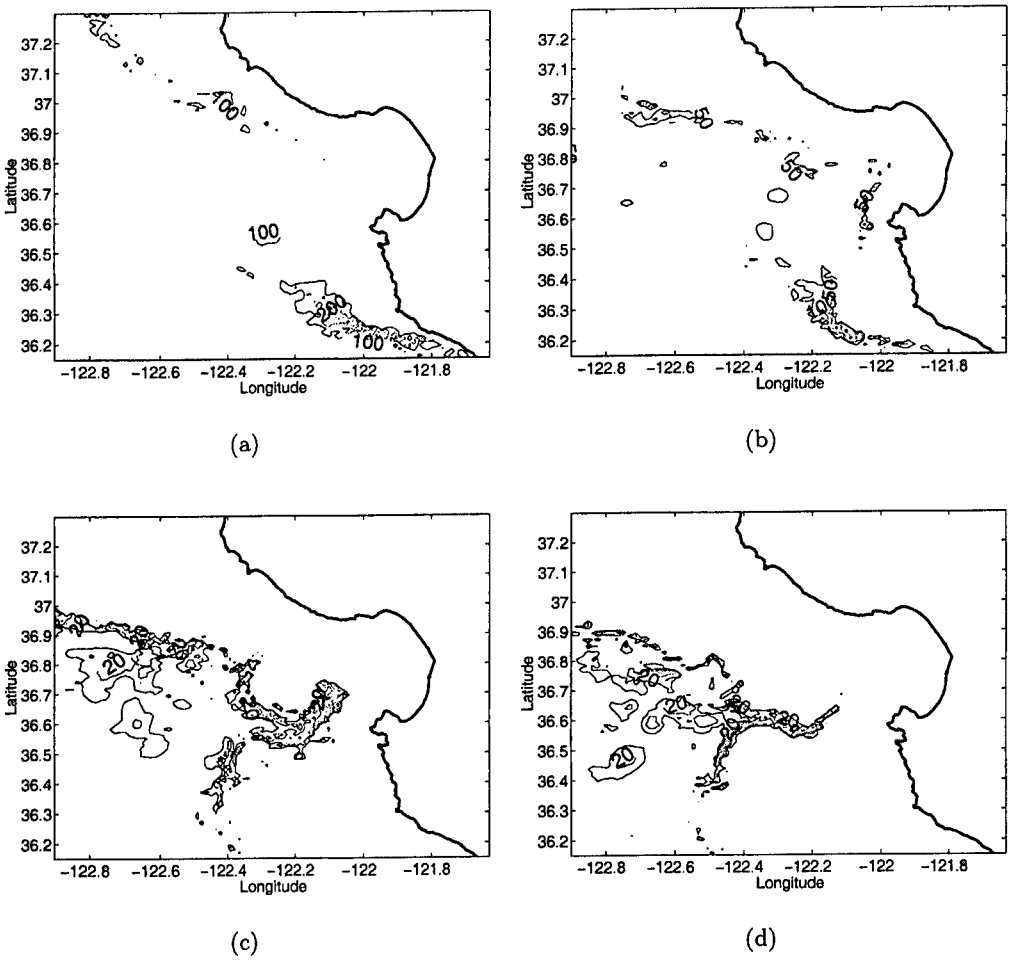


FIGURE 7. The contour of vertical velocity difference ($m/week$) between the hydrostatic and non-hydrostatic models at various depths. (a) 100 m, (b) 700 m, (c) 1500 m, (d) 2000 m, The difference is based on monthly averaged vertical velocity during June (day 150-180).

by internal wave reflection at topography is also poorly represented by the hydrostatic model (Legg & Adcroft 2003). In realistic topography, alongslope tides produce internal hydraulic jumps and solitary wave packets as they flow over corrugations. This is not well represented by hydrostatic models.

5. Conclusion and future work

The high resolution, non-hydrostatic MBARM was used to investigate the regional ocean circulation in the Monterey Bay area. The model reproduces several known features of the general circulation in the vicinity of Monterey Bay. The Monterey Bay area circulation is highly correlated to the CCS so the surface flow pattern in spring/summer is different from that in autumn/winter. Within the bay a cyclonic circulation is often

observed. This feature is a result of coastal geometry. A warm anticyclone is often seen near the mouth of Monterey Bay. In particularly, non-hydrostatic effects play an important role in determining the non-linear dynamics of the nearshore circulation. The non-linear non-hydrostatic dynamics are enhanced by the complex coastal geometry and cannot generally be ignored in regions of steep bathymetry or where the Rossby radius of deformation is small; sometimes it is even negative, leading to strongly nonhydrostatic convection.

The current MBARM uses one-way coupling to allow information from the CCS to enter the coastal region. In order to examine their dynamical interactions, full two-way coupling is needed in the future. Two-way nesting will generate much smoother results and remove artificial fronts when the boundary flow switches between outflow and inflow. To better understand the dynamics of the coastal region, which is strongly affected by coastal perturbations and bathymetry, non-hydrostatic effects should be further investigated using non-hydrostatic coastal model with simplified coastal geometry, e.g. an idealized bay and an idealized submarine canyon. The current simulation results identify some important non-hydrostatic effects. However, realistic topography and forcing complicate the analysis and understanding of the physical process. Detailed analysis is required to quantify non-hydrostatic effects on the overall circulation.

REFERENCES

BREAKER, L. C. & BROENKOW, W. W. 1994 The circulation of Monterey Bay and related processes. *Oceanogr. and Marine Bio.* **32**, 1-64.

CASULLI, V. & STELLING, G. S. 1998 Numerical simulation of 3D quasi-hydrostatic, free-surface flow. *J. Hydrau. Eng.* **124**, 678-686.

CHAO, S. Y. & SHAW P. T. 2002 Nonhydrostatic aspects of coastal upwelling meanders and filaments off eastern ocean boundaries. *Tellus* **54(A)**, 63-75.

COLLINS, C. A., GARFIELD, N., RAGO, T. A., RISCHMILLER, F. W. & CARTER, E. 2000 Mean structure of the inshore countercurrent and California undercurrent off Point Sur, California. *Deep-Sea Res. II* **47**, 765-782.

DIETRICH, D. E. 1997 Application of a modified "a" grid ocean model having reduced numerical dispersion to the gulf of Mexico circulation. *Dyn. Atmos. Oceans* **27**, 201-217.

DIETRICH, D. E. & LIN, C. A. 2002 Effects of hydrostatic approximation and resolution on the simulation of convective adjustment. *Tellus* **54(A)**, 34-43.

DIETRICH, D. E., HANEY, R. L., FERNANDEZ, V., POSEY, S. & TINTORE, J. 2003 Model-determined surface heating and freshwater sources using a precise, non-damping nudging approach. *J. Mar. Systems (accepted).*

HANEY, R. L., HALE, R. A. & DIETRICH, D. E. 2001 Offshore propagation of eddy kinetic energy in the California Current. *J. Geophys. Res.* **106**, 11709-11717.

HELLERMAN, S. & ROSENSTEIN, M. 1983 Normal monthly wind stress over the world ocean with error estimates. *J. Phys. Oceanogr.* **13**, 1093-1104.

LEGG, S. & ADCROFT, A. 2003 Internal wave breaking at concave and convex continental slopes. *J. Phys. Oceanogr.* **33**, 2224-2246.

LEVITUS, S. 1982 Climatological atlas of the world oceans. *NOAA Prof. Pap.* U.S. Govt. Print Off., 173.

MAHADEVAN, A. AND OLIGER, J. & STREET, R. L. 1996 A nonhydrostatic mesoscale ocean model. Part I: Well-posedness and scaling. *J. Phys. Oceanogr.* **26**, 1868-1880.

OLIGER, J. & SUNDSTROM, A. 1978 Theoretical and practical aspects of some initial boundary value problems in fluid dynamics. *SIAM J. Appl. Math.* **35**, 419-446.

PALMA, E. D. AND MATANO, R. P. 2000 On the implementation of open boundary condition for a general circulation model: The three-dimensional case *J. Geophys. Res.* **105**, 8605-8627.

PIERCE, S.D. , SMITH, R. L., KOSRO, P. M., BARTH, J. A. & WILSON, C. D. 2000 Continuity of the poleward undercurrent along the eastern boundary of the mid-latitude Pacific. *Deep-Sea Res. II* **47**, 811-829.

RAMP, S. R., ROSENFELD, L. K., TISCH, T. D. & HICKS, M. R. 1997 Moored observations of the current and temperature structure over the continental slop off central California, 1, A basic description of the variability. *J. Geophys. Res.* **102**, 22877-22902.

ROSENFELD, L. K., SCHWING, F. B., GARFIELD, N. & TRACY, D. E. 1994 Bifurcated flow from an upwelling center: A cold water source for Monterey Bay. *Cont. Shelf Res.* **14**, 931-964.

TSENG, Y. H. & FERZIGER, J. H. 2003 A ghost-cell immersed boundary method for flow in complex geometry. *J. Compu. Phys. (in press).*

TSENG, Y. H. 2003 *On the development of a ghost-cell immersed boundary method and its application to large eddy simulation and geophysical fluid dynamics.* Ph. D. Dissertation, Stanford University.

Testing of RANS turbulence models for stratified flows based on DNS data

By S. K. Venayagamoorthy †, J. R. Koseff†, J. H. Ferziger† AND L. H. Shih†.

1. Motivation and objectives

Stably stratified flows such as those in the atmosphere or in large water bodies such as the ocean, lakes, estuaries and reservoirs are prevalent in the natural environment. The presence of the buoyancy force due to the stratification may have a substantial effect on the flow development and mixing processes, and hence influence the distribution of scalar substances such as pollutants, suspended sediments, in the environment.

Today, there exist numerous turbulence models for calculating turbulent mixing in the environment. These models range from the simple eddy viscosity models to the more detailed large eddy simulations (LES) and direct numerical simulations (DNS) (Axell & Liungman 2001). However, both DNS and LES can be too computationally expensive (and often too idealized) for most geophysical and engineering applications. This limitation has restricted modelers to RANS approaches commonly based on turbulent kinetic energy (TKE) closure schemes. The most widely used RANS models today are two equation models which solve two transport equations for the properties of the turbulence from which the eddy viscosity can be computed. The best known of these models is the k-ϵ model which requires the solutions of the turbulent kinetic energy equation (a component of essentially all current multi-equation models) and dissipation of turbulent kinetic energy equation (Ferziger *et al.* 2003).

In most geophysical flows, turbulence occurs at the smallest scales and one of the two most important additional physical phenomena to account for is stratification (the other being rotation). In this paper, the main objective is to investigate proposed changes to RANS turbulence models which include the effects of stratification more explicitly. These proposed changes were developed using a DNS database on stratified and sheared homogenous turbulence developed by Shih *et al.* (2000) and are described more fully in Ferziger *et al.* (2003). The data generated by Shih *et al.* (2000) (hereinafter referred to as SKFR) are used to study the parameters in the k-ϵ model as a function of the turbulent Froude number, Fr_k. A modified version of the standard k-ϵ model based on the local turbulent Froude number is proposed. The proposed model is applied to a stratified open channel flow, a test case that differs significantly from the flows from which the modified parameters were derived. The turbulence modeling and results are discussed in the next two sections followed by suggestions for future work.

† Environmental Fluid Mechanics Laboratory, Stanford University, CA 94305-4020

2. Turbulence modeling based on DNS data

2.1. *The Data*

The DNS data of SKFR are used to develop parameterizations of modeling coefficients typically found in RANS models (e.g. C_μ) as functions of quantities that define the local state of the turbulence (Fr_k etc.).

SKFR performed DNS of stratified homogeneous turbulent shear flows. The data have been extensively discussed by SKFR and hence the discussion will not be repeated here. However, it is important to realize that the data provide all of the properties of the turbulence up to second order statistics. The subset of the data used in this study consists of the highest initial Taylor microscale Reynolds number runs ($Re_{\lambda 0} = 89$). The value of $Re_{\lambda 0} = 89$ is relatively high for direct numerical simulations but not high enough to produce results that are independent of Reynolds number effects. It is nevertheless, high enough that the effects of the other parameters should be accurately represented. All the data used for this study were taken from the latter parts of the SKFR runs in order to ensure that the turbulence was fully developed. The physical time was non-dimensionalized as St where S is the shear rate defined as:

$$S = \frac{\partial U}{\partial z} \tag{2.1}$$

As discussed by Ferziger *et al.* (2003), the turbulence does not become fully developed until sometime later than $St > 2$. Most of the runs were continued until St = 12-14. In our present study, only the data for times between $St = 8$ and the end of the run were used. To render the plots less confusing, the data is averaged over this time period. In total, 37 runs were used to derive the results given below. Each run is characterized by the initial Reynolds number (which is the same for all the runs) and the gradient Richardson Ri_g (defined in equation 2.2) which has a fixed value for each run.

$$Ri_g = \frac{N^2}{S^2} \tag{2.2}$$

where N is the buoyancy frequency defined as:

$$N = \left(\frac{-g}{\rho} \frac{\partial \rho}{\partial z} \right)^{1/2} \tag{2.3}$$

2.2. *k-ϵ model*

k-ϵ is a commonly used two equation model, of which many variations have been suggested. Here, we base our proposed modifications on the standard version of the k-ϵ model. In the presence of stratification, the turbulent kinetic energy equation can be written as:

$$\frac{Dk}{Dt} = P - \epsilon - B + D_k \tag{2.4}$$

where P is the rate of production of TKE, which is given, for simple shear flows like the SKFR flows, by:

$$P = -\overline{u'w'}S \tag{2.5}$$

B is the buoyancy flux given by:

$$B = -\frac{g}{\rho_0}\overline{\rho' w'}. \tag{2.6}$$

C_μ	$C_{\epsilon 1}$	$C_{\epsilon 2}$	σ_k	σ_ϵ
0.09	1.44	1.92	1.0	1.3

TABLE 1. Values of constants in the k-ϵ model (Rodi, 1980)

D_k is the transport term (equal to zero for the SKFR flows) modeled using the gradient-diffusion hypothesis as:

$$D_k = \frac{\partial}{\partial z}\left(\frac{\nu_t}{\sigma_k}\frac{\partial k}{\partial z}\right) \tag{2.7}$$

and ϵ, the rate of dissipation of the turbulent kinetic energy, is modeled in an analogous way to equation (2.4):

$$\frac{D\epsilon}{Dt} = C_{\epsilon 1}\frac{P\epsilon}{k} - C_{\epsilon 2}\frac{\epsilon^2}{k} - C_{\epsilon 3}\frac{B\epsilon}{k} + D_\epsilon \tag{2.8}$$

where D_ϵ is the transport term (equal to zero for the SKFR flows) modeled again using the gradient-diffusion hypothesis as:

$$D_\epsilon = \frac{\partial}{\partial z}\left(\frac{\nu_t}{\sigma_\epsilon}\frac{\partial \epsilon}{\partial z}\right) \tag{2.9}$$

The eddy viscosity is then given by:

$$\nu_t = C_\mu \frac{k^2}{\epsilon} \tag{2.10}$$

and the eddy diffusivity is:

$$\kappa_t = \frac{\nu_t}{Pr_t} \tag{2.11}$$

where Pr_t is the turbulent Prandtl number. The constants that are commonly used are given in Table 1.

The value for the buoyancy parameter $C_{\epsilon 3}$ is a matter of much discussion. Various values have been suggested, e.g. Rodi (1987) suggests a value of $0 < C_{\epsilon 3} < 0.29$, Baum & Caponi (1992) suggest $C_{\epsilon 3} = 1.14$ and Burchard & Baumert (1995) have argued that $C_{\epsilon 3}$ should have negative values. It turns out from our studies that this is a very sensitive parameter for stratified flows.

2.3. *Proposed parametrizations*

Several parameters have been suggested to characterize the effects of the stratification, the most obvious of which is the gradient Richardson number defined in equation (2.2). However, Ferziger *et al.* (2003) argue that this is not the best choice as it represents the forcing rather than the properties of the turbulence. As pointed out by SKFR, the turbulent Froude number gives better correlations. It can be defined based on the quantities computed from the k-ϵ model as:

$$Fr_k = \frac{\epsilon}{Nk} \tag{2.12}$$

Further, it is also noted that there is a gradient Richardson number at which turbulence

energy neither grows nor decays called the stationary Richardson number Ri_{gs}. Holt *et al.* (1992) showed that Ri_{gs} is a function of the Reynolds number at least at smaller values of Re. If, in equations (2.4) and (2.8), we set $Dk/Dt = D\epsilon/Dt = 0$, and eliminate ϵ, then for homogeneous flows, the following relation is obtained:

$$Ri_{fs} = \frac{B}{P} = \frac{C_{\epsilon 2} - C_{\epsilon 1}}{C_{\epsilon 2} - C_{\epsilon 3}} \tag{2.13}$$

where Ri_{fs} is the flux Richardson number. Applying the gradient diffusion modeling concept to both B and P in equation (2.13) yields:

$$Ri_{fs} = \frac{Ri_{gs}}{Pr_t} \tag{2.14}$$

where it is found that $Pr_t \approx 1$ in the stationary flow cases. Hence we assume that Ri_{fs} and Ri_{gs} are equivalent in the discussion that follows.

We choose to insist that $C_{\epsilon 3}$ be zero at the stationary state in order to satisfy the constraint that the model predicts the existence of a stationary state under the conditions determined by SKFR. Rearranging equation (2.13) and using the generally accepted value of 0.25 for the stationary Richardson number at high turbulence Reynolds number, we get:

$$C_{\epsilon 2} = \frac{C_{\epsilon 1}}{1 - Ri_{fs}} \tag{2.15}$$

The functional dependence of the stationary Richardson number Ri_{gs} on the turbulence Reynolds number Re_k defined in equation (2.16) was given by SKFR as shown in equation (2.17).

$$Re_k = \frac{k^2}{\epsilon \nu} \tag{2.16}$$

$$Ri_{fs} \approx Ri_{gs} = \frac{0.25}{1 + 103/Re_k} \tag{2.17}$$

Any of the parameters in the model ϵ equation can be allowed to vary as a function of the turbulent Froude number but only one parameter (or combination of parameters) can be derived from the model dissipation equation and the DNS data, enforcing a limitation on the choices that can be made. In this study, the parameters that are chosen to depend on the stratification are $C_{\epsilon 3}$ and C_μ, while $C_{\epsilon 1}$ and $C_{\epsilon 2}$ are independent of the stratification. We do however include the effect of the Reynolds number on $C_{\epsilon 2}$ as discussed earlier through equations (2.15) and (2.17).

The buoyancy parameter $C_{\epsilon 3}$ can be calculated from DNS data using the model ϵ equation as a function of Fr_k. To accomplish this, we compute $(1/\epsilon)d\epsilon/dt$ from the SKFR data by fitting a least square straight line to log ϵ as a function of time over the time range used in all of the data fitting. We then solve equation (2.8) for $C_{\epsilon 3}$ using equation (2.15) for $C_{\epsilon 2}$ (as discussed by Ferziger *et al,* 2003). The resulting values are plotted in Figure 1. Unfortunately, there is no clear trend in the data to suggest any definitive fit. However, the data indicates that $C_{\epsilon 3}$ is of order unity in the strongly stratified region and possibly shows a slight increase with increasing Fr_k. The fit we used for this study is also shown in Figure 1 and is given by equation (2.18). This correlation is based on the observation that the mixing efficency peaks at about Fr_k of 0.4 - 0.5 for the SKFR data and $C_{\epsilon 3}$ should be zero there. It should be noted that the data does not extend into the very strongly stratified regime (i.e. very low Fr_k values). It is a regime that has a

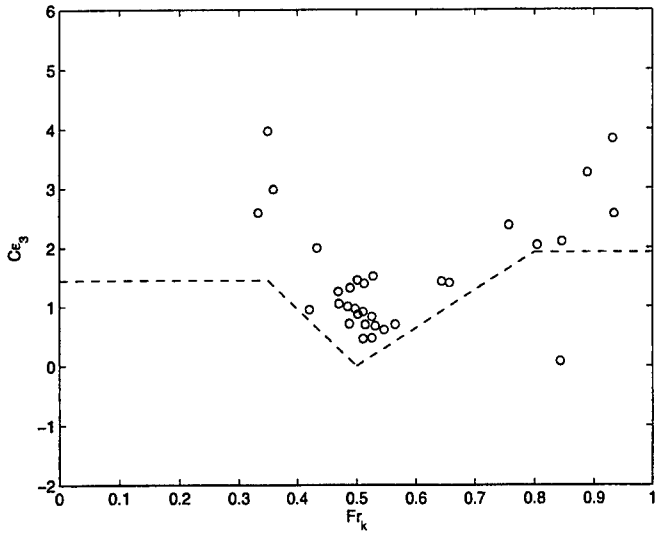


FIGURE 1. Buoyancy parameter $C_{\epsilon 3}$ as a function of the turbulent Froude number. o: values calculated from the SKFR data, – – – : fit given by (2.18).

mixture of internal waves and turbulence and care has to be exercised in applying any turbulence model in this regime.

$$C_{\epsilon 3} = \begin{cases} 1.44 & \text{for } Fr_k < 0.35 \\ 1.44 - 9.6(Fr_k - 0.35) & \text{for } 0.35 < Fr_k < 0.50 \\ 6.4(Fr_k - 0.5) & \text{for } 0.5 < Fr_k < 0.80 \\ 1.92 & \text{for } Fr_k > 0.80 \end{cases} \tag{2.18}$$

We note that Figure 1 indicates that a better fit to the data could be given but we felt it important to repeat the condition that $C_{\epsilon 3}$ be zero at $Fr_k = 0.5$.

The eddy viscosity parameter C_μ obtained from the data is plotted as function of Fr_k in Figure 2. The value of C_μ obtained from the SKFR data at large Fr_k (weak stratification) is lower than the typical value of 0.09. However, we fit the data such that C_μ reaches the asymptotic value of 0.09 at high Fr_k values. Thus:

$$C_\mu = \begin{cases} 0.125Fr_k^2 + 0.014Fr_k & \text{for } Fr_k < 0.35 \\ 0.006(Fr_k - 0.35)/(0.02 + 0.1(Fr_k - 0.35)) + 0.02 & \text{for } 0.35 < Fr_k < 0.60 \\ 0.08\tanh(Fr_k) + 0.01 & \text{for } Fr_k > 0.60 \end{cases} \tag{2.19}$$

The scalar transport can be modeled using the turbulent Prandtl number defined in equation (2.11). We plotted the turbulent Prandtl number as a function of the turbulent Froude number as shown in Figure 3. The curve fit shown in the figure is:

$$Pr_t = \begin{cases} 1.4 & \text{for } Fr_k < 0.35 \\ 1.4 - 0.55(1 - \exp(-7(Fr_k - 0.35)) & \text{for } Fr_k > 0.35 \end{cases} \tag{2.20}$$

where we have chosen to keep the Prandtl number constant in the highly stratified regions.

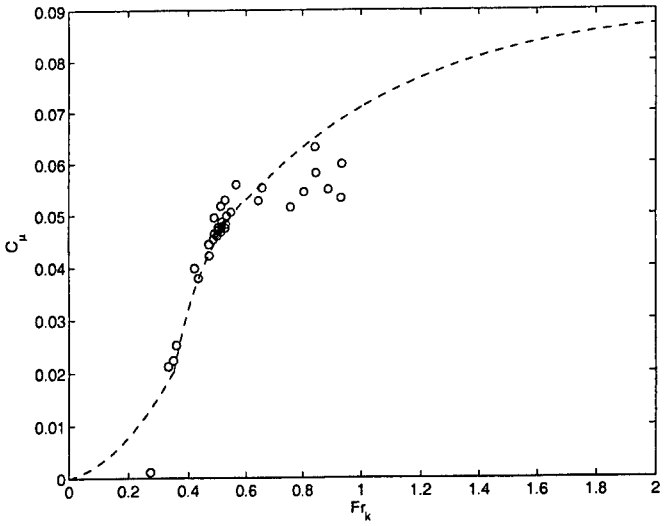


FIGURE 2. The eddy viscosity coefficient C_μ as a function of the turbulent Froude number. o: values derived from the SKFR data, – – – : correlation (2.19)

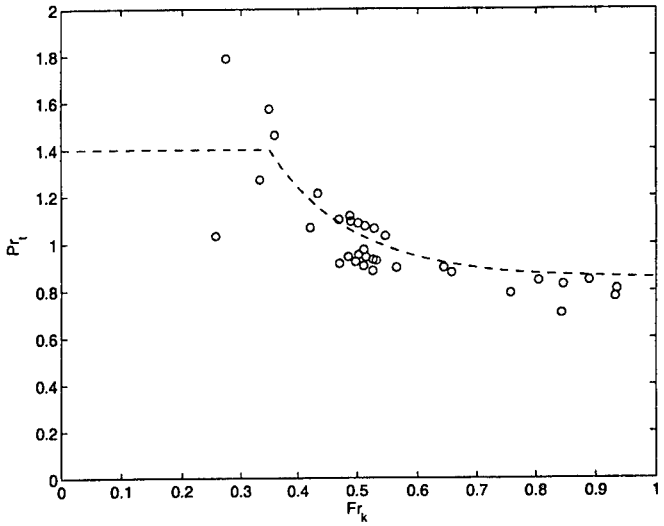


FIGURE 3. The turbulent Prandtl number as a function of the turbulent Froude number. o: values derived from the SKFR data, – – – : correlation (2.20)

3. Results and discussion

In order to test the proposed parameterization and compare it with other models, it is essential that we apply it to a flow that is significantly different from the homogenous flows from which the parameters were derived. We chose the stratified open channel flow as our test case. This is a flow for which direct numerical simulations and large eddy simulations have been performed by Garg *et al.* (2000) and Shih (2003).

The tests of the model were performed using a 1-D water column model called GOTM

(General Ocean Turbulence Model) developed by Burchard *et al.* (1999). The various turbulence closure schemes in GOTM are based on a modular format that enables easy incorporation in 3-D ocean circulation models and also allows for refinements or extensions to the turbulence models. The source code is available to the public on the Internet website www.gotm.net. We incorporated our proposed model into the GOTM code. Since none of the built in stability functions in GOTM modify their parameters based on depth, we had to adapt the code to modify the parameters in k-ϵ model discussed above to be depth dependent based on the local turbulent Froude number.

The test case we use is somewhat artificial. It is a pressure-gradient driven open channel flow in which the density is held fixed at both the lower solid boundary and the upper free surface and in some ways similar to the experiments done by Komori *et al.* (1983). The Reynolds number Re_τ and the Richardson number Ri_τ based on the shear velocity for all the test runs were 682 and 31 respectively. Previous studies by Garg *et al.* (2000) have shown that LES produces results that are in good agreement with DNS results for open channel flows. Hence we use an LES run with identical conditions to those in our test case to assess the predictions of our proposed model and that of the standard k-ϵ model with constant stability functions.

The flow was first allowed to develop to a converged solution (without stratification effects) using the standard k-ϵ model after which the stratification was imposed. The velocity and density profiles at the initial state (i.e. after spin up) are shown in Figure 4. Also shown in Figure 4, are the turbulent kinetic energy and dissipation profiles together with the turbulent Froude number and the turbulent Reynolds number profiles. Superimposed on these figures are the instantaneous LES profiles.

A total of four runs were done using different combinations of the modifications (outlined above) to the k-ϵ model so as to determine the most suitable combination of parameters that can match as closely as possible the LES results. The test runs discussed in this paper are outlined in Table 2. Run 1 is based the standard k-ϵ model with $C_{\epsilon 3} = 1.44$, while run 2 uses the proposed parametrizations. In run 3, we vary only the eddy viscosity parameter C_μ and turbulent Prandtl number Pr_t and keep both $C_{\epsilon 2}$ and $C_{\epsilon 3}$ constant as in run 1. Run 4 is an arbitrary case that was chosen to investigate the effects of just varying the turbulent Prandtl number using the correlation given by equation (3.1).

The velocity, density, turbulent kinetic energy, dissipation of the turbulent kinetic energy, turbulent Froude number and turbulent Reynolds number profiles at non-dimensional times $tu_*/h = 4.1$ and $tu_*/h = 14.6$ for the standard k-ϵ model (run 1) and the full modified version (run 2) together with the LES profiles are shown in Figures 5 and 6 respectively.

The full modified version of the proposed model (denoted by run 2) underperforms the k-ϵ model in terms of predicting the velocity profile in the channel especially at later times, as seen in Figure 6, even though it appears to capture the free surface velocity better. However, it does significantly better in predicting the evolution of the density profile, especially during the transient stages of the flow.

In run 3, both $C_{\epsilon 2}$ and $C_{\epsilon 3}$ are held at constant values equal to the ones used for the k-ϵ test run 1. It can be seen from the density profile in Figure 7 that the mixing is now predicted better for the highly stratified regions (i.e. low Froude numbers) in this run. However, this case underperforms the standard k-ϵ case for most of the lower half of the channel depth. The discrepancy between the LES and the RANS results given by runs 1 and 3 for the lower half of the channel depth indicates that in general the k-ϵ model allows too much mixing to occur from the bottom boundary. There is a strong

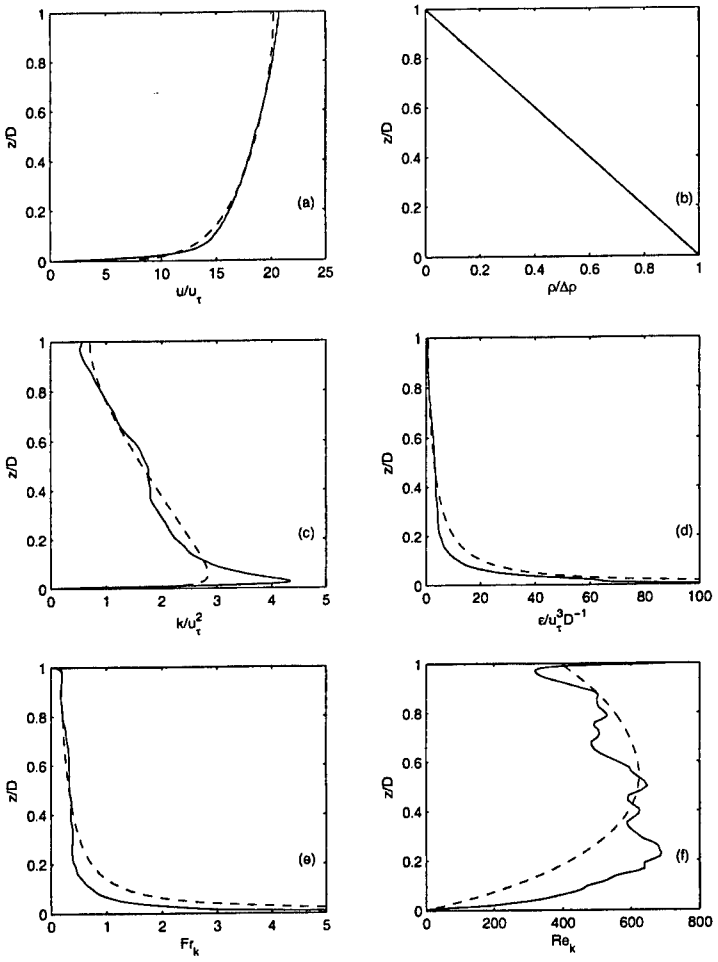


FIGURE 4. Initial profiles (a) velocity; (b) density; (c) tke; (d) dissipation; (e) turbulent Froude number Fr_k; (f) turbulent Reynolds number Re_k. — : LES results, – – – : k-ϵ results.

Run	C_μ	$C_{\epsilon 2}$	$C_{\epsilon 3}$	Pr_t	Remarks
1	0.09	1.92	1.44	0.85	Standard k-ϵ model
2	eq.(2.19)	eq. (2.15)	eq. (2.18)	eq. (2.20)	Full modified version
3	eq.(2.19)	1.92	1.44	eq. (2.20)	Varying C_μ and Pr_t only
4	0.09	1.92	1.44	eq. (3.1)	Varying Pr_t only

TABLE 2. Test runs used for evaluating the predictions by the modified k-ϵ model

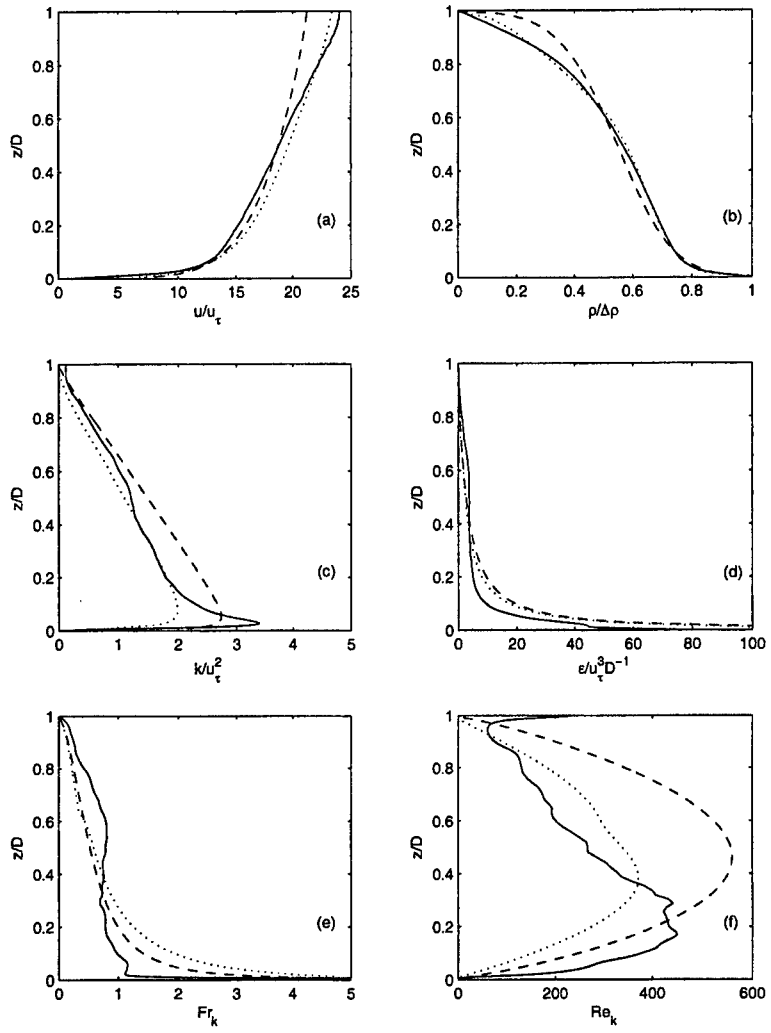


FIGURE 5. Profiles at $tu_*/h = 4.1$: (a) velocity; (b) density; (c) tke; (d) dissipation; (e) Fr_k; (f) Re_k. — : LES results; – – – : run 1; ··· : run 2.

possibility that the prescribed asymptotic value of 0.85 that the SKFR data suggests for the turbulent Prandtl number is low even though there are good engineering data that suggest this value is reasonable. However, other observations such as those due to Högstrom (1996) suggest a value of $Pr_t = 1$. In run 4, we use a different correlation for Pr_t such that it asymptotes to 1.0 at high Fr_k (see equation 3.1). The results as shown in Figure 7 indicate closer agreement with the LES results compared to runs 1 and 3 respectively. .

$$Pr_t = 0.4\exp(-2.5Fr_k) + 1.0 \qquad \text{for all } Fr_k \tag{3.1}$$

4. Conclusions and future work

Modifications of the k-ϵ model to account for stratification based on the SKFR data have been suggested and tested in this study. The test runs done on the stratified open

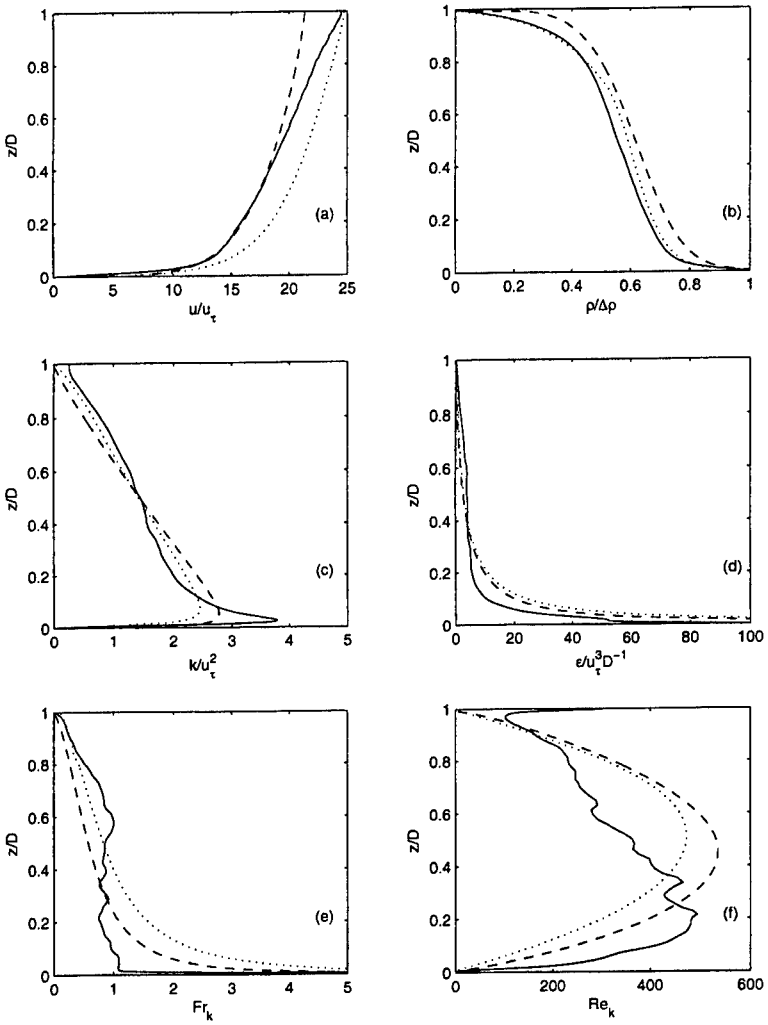


FIGURE 6. Profiles at $tu_*/h = 14.6$: (a) velocity; (b) density; (c) tke; (d) dissipation; (e) Fr_k; (f) Re_k. — : LES results; – – – : run 1; ··· : run 2.

channel flow highlight the importance of correctly modeling the turbulent Prandtl number Pr_t as well as the buoyancy parameter $C_{\epsilon 3}$. The results suggest that the turbulent Prandtl number should be close to unity for the neutrally stable flows. Further, it appears that the buoyancy parameter $C_{\epsilon 3}$ has to be prescribed as a value of the order of $C_{\epsilon 1}$ in order to correctly model the effects of the buoyancy force in the dissipation equation. The lack of a clear trend in $C_{\epsilon 3}$ as a function of Fr_k from the DNS data suggests that the strategy of setting $C_{\epsilon 3}$ equal to a constant is probably the most reasonable approach. The results of this paper are useful only in the regimes of weak to moderate stratification. Clearly further test cases should be performed where the effects of the stratification are more pronounced and where Fr_k is small over larger fraction of the flow depth. This will allow us to evaluate the effects of varying C_μ as function of Fr_k more precisely. Further work is also required to capture the boundary layer dynamics properly so that momentum balance can be achieved properly. We are also unable to comment on the transport models

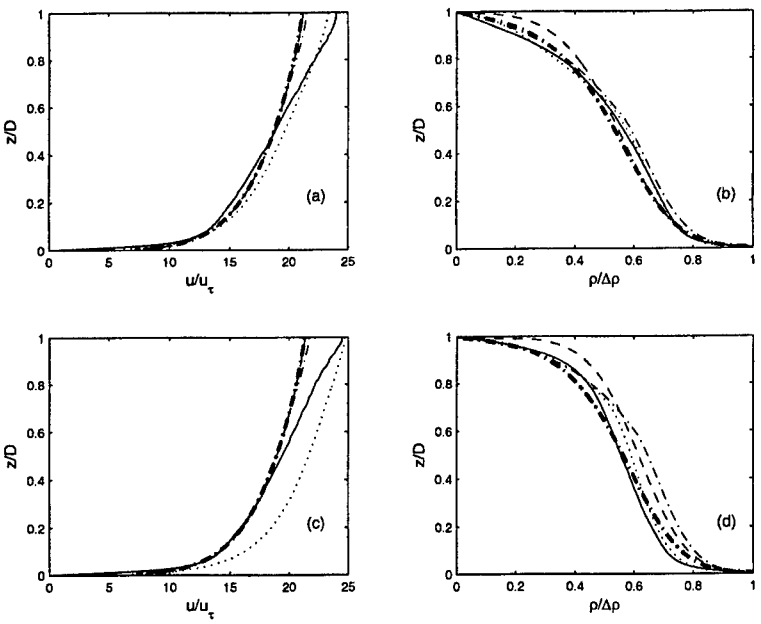


FIGURE 7. Velocity profiles (left) and density profiles (right). — : LES results; – – – : run1; ··· : run 2; – · – : run 3; – · – in bold : run 4 at $tu_*/h = 4.1$ (top) and $tu_*/h = 14.6$ (bottom).

(which may also depend on stratification) as the SKFR database is for homogeneous flows. It is important to obtain data for strongly stratified and inhomogeneous flows and apply them to the development of better models for stably stratified flows.

Acknowlegdements

SKV is grateful to Professor Parviz Moin for financial support through the Center for Turbulence Research. The authors would like to thank Professor Paul Durbin for his helpful comments. We would like to also thank Dr. Hans Burchard for providing extensive and invaluable assistance in the use of the GOTM model.

REFERENCES

AXELL, L. B. & LIUNGMAN, O. 2001 A one-equation turbulence model for geophysical applications: comparison with data and the k-ϵ model. *Env. Fluid Mech.* **1**, 71-106.

BAUM, E. & CAPONI, E. A. 1992 Modeling the effects of buoyancy on the evolution of geophysical boundary layers, *J. Geophys. Res.*, **97**, 15513-15527.

BURCHARD, H. & BAUMERT, H. 1995 On the performance of a mixed-layer model based on the k-ϵ turbulence closure, *J. Geophys. Res.* **100**, 8523-8540.

BURCHARD, H., BOLDING, K. & VILLARREAL, M. R. 1999 *GOTM, a General Ocean Turbulence Model, Theory, Implementation and Test cases,* European Commission, Report EUR 18745, 103pp.

FERZIGER, J. H., KOSEFF, J. R., SHIH, L. H. & VENAYAGAMOORTHY, S. K. 2003 RANS models for stratified turbulence based on DNS data, *Phys. Fluids*, in preparation.

GARG, R. K., FERZIGER, J. H., MONISMITH, S. G. & KOSEFF, J. R. 2000 Stably stratified turbulent channel flows: I. Stratifcation regimes and turbulent suppression mechanism, *Phys. Fluids*, **12**, 2569-2594.

HÖGSTROM, U. 1996 Review of some basic characteristics of the atmospheric surface layer, *Boundary-Layer Meteorol.*, **78**, 215-246.

HOLT. S. E., KOSEFF, J. R. & FERZIGER, J. H. 1992 A numerical study of the evolution and structure of homogeneous stably stratified sheared turbulence, *J. Fluid Mech.* **237**, 499-539.

KOMORI. S., UEDA, H., OGINO, F. & MIZUSHINA, T. 1983 Turbulence structure in stably stratified open-channel flow, *J. Fluid Mech.* **130**, 13.

RODI, W. 1987 Turbulence models and their application in Hydraulics - A state of the art review, *Int. Assoc. Hydr. Res.*, Rotterdam, The Netherlands.

RODI, W. 1980 Examples of calculation methods for flow and mixing in stratified flows, *J.Geophys. Res.*, **92**, 5305-5328.

SHIH. L. H. 2003 Numerical simulations of stably stratified turbulent flow *Phd dissertation,* Dept. of Civil and Env. Engr., Stanford Univ.

SHIH. L. H., KOSEFF, J. R., FERZIGER, J. H. & REHMANN, C. R. 2000 Scaling and parameterization of stratified homogeneous turbulent shear flow, *J. Fluid Mech.* **412**, 1-20.

Unstructured LES of reacting multiphase flows in realistic gas turbine combustors

By Frank Ham, Sourabh Apte, Gianluca Iaccarino, Xiaohua Wu, Marcus Herrmann, George Constantinescu†, Krishnan Mahesh‡ AND Parviz Moin

1. Motivation and objectives

As part of the Accelerated Strategic Computing Initiative (ASCI) program, an accurate and robust simulation tool is being developed to perform high-fidelity LES studies of multiphase, multiscale turbulent reacting flows in aircraft gas turbine combustor configurations using hybrid unstructured grids. In the combustor, pressurized gas from the upstream compressor is reacted with atomized liquid fuel to produce the combustion products that drive the downstream turbine. The Large Eddy Simulation (LES) approach is used to simulate the combustor because of its demonstrated superiority over RANS in predicting turbulent mixing, which is central to combustion.

CDP is the flagship LES code being developed by the combustor group to perform LES of reacting multiphase flow in complex geometry. CDP is named after the late Charles David Pierce (1969-2002) who made several lasting contributions to the LES of reacting flows and to this ASCI program. CDP is a parallel unstructured finite-volume code developed specifically for LES of variable density low Mach-number flows. It is written in Fortran 90, uses MPI, and has integrated combustion and spray modules. In the first five years of ASCI (1997-2002), the principle focus of the combustor group was the development and validation of an entirely new numerical method with the characteristics necessary for simultaneously accurate and robust LES on unstructured grids. These competing ends were both achieved by developing a method around the principle of discrete kinetic energy conservation (Mahesh *et al.* 2003). This numerical algorithm has now been extended to variable density, low-Mach number multiphase reacting flows.

In March of 2003, with the underlying numerics established and validated in a variety of flows, a major redesign and rewrite of the code was initiated. Called CDP-α, this new version of the code will have all the capabilities of the current code along with considerable improvements, all of which are considered critical to achieving the stated ASCI goal of a "major advance in engine simulation technology."

This paper summarizes the accomplishments of the combustor group over the past year, concentrating mainly on the two major milestones achieved this year:

- Large scale simulation: A major rewrite and redesign of the flagship unstructured LES code has allowed the group to perform large eddy simulations of the complete combustor geometry (all 18 injectors) with over 100 million control volumes.
- Multi-physics simulation in complex geometry: The first multi-physics simulations including fuel spray breakup, coalescence, evaporation, and combustion are now being performed in a single periodic sector ($1/18^{th}$) of an actual Pratt & Whitney combustor geometry.

† University of Iowa
‡ University of Minnesota

2. New CDP Code Development: CDP-α

In March of 2003, development of a new version of CDP, CDP-α, was initiated with the goal of performing large-scale simulation of the full Pratt & Whitney combustor. When completed, CDP=α will have all the capabilities of the existing CDP code, with the following improvements:

- Parallel preprocessing to allow unstructured simulations of 100 million control volumes or more,
- Faster, more scalable solvers based on geometric and/or algebraic multigrid methods,
- Particle/mesh load balancing capabilities,
- Integrated postprocessing capabilities, including the parallel computation and writing of plane and isosurface cuts of instantaneous or statistical data, and the seeding and tracking of massless Lagrangian particles,
- Generally improved code modularity and design, allowing users several levels of interaction with the code, and rapid implementation and testing of new models and capabilities,
- Regression testing and version control.

At the time of writing, the parallel preprocessor has been completed, and a cold flow (incompressible) version of CDP-α has been completed and verified against the old code in a variety of incompressible flow calculations. A Fortran 90 interface to the algebraic multigrid solver of LLNL's CASC group (Falgout *et al.* 2002) has been added as an option for solving the Poisson system, resulting in a significant overall speedup, although at a substantial memory overhead. Particle/mesh load balancing capabilities have been added and tested using model particle distributions. Details of these capabilities are described in the following subsections.

2.1. *Parallel Preprocessing*

CDP requires as input N_p separate grid partition files, where N_p is the number of processors that will be used for the LES. These partition files describe the grid (nodes, faces, control volumes) associated with a particular partition, and also contain the connectivity graph. The preparation of these N_p partition files is called preprocessing, and consists of four distinct steps:

- geometry definition
- grid generation
- grid partitioning
- reordering/redistribution

Up to now, the combustor group simulations have used a single-processor preprocessing strategy to generate and preprocess hybrid unstructured grids up to a maximum size of about 14 M control volumes (cv's). This is approximately the maximum size that can fit within the 8 GByte physical memory of the high-end workstation used for grid generation. At this size, the grid is extremely cumbersome to inspect for quality, and a more reasonable limit is about 5 M cv's.

To preprocess grids of order 100 M cv's, it was necessary to develop a new parallel preprocessor. Some recent aircraft simulations in the literature have used unstructured tetrahedral grids close to this size (25 to 60 M vertices) (Mavriplis & Pirzadeh 1999). These grids were generated using a two step approach. First an unstructured grid of several million vertices was generated and partitioned on a work-station. These partitions were subsequently refined using homothetic refinement on a supercomputer. This

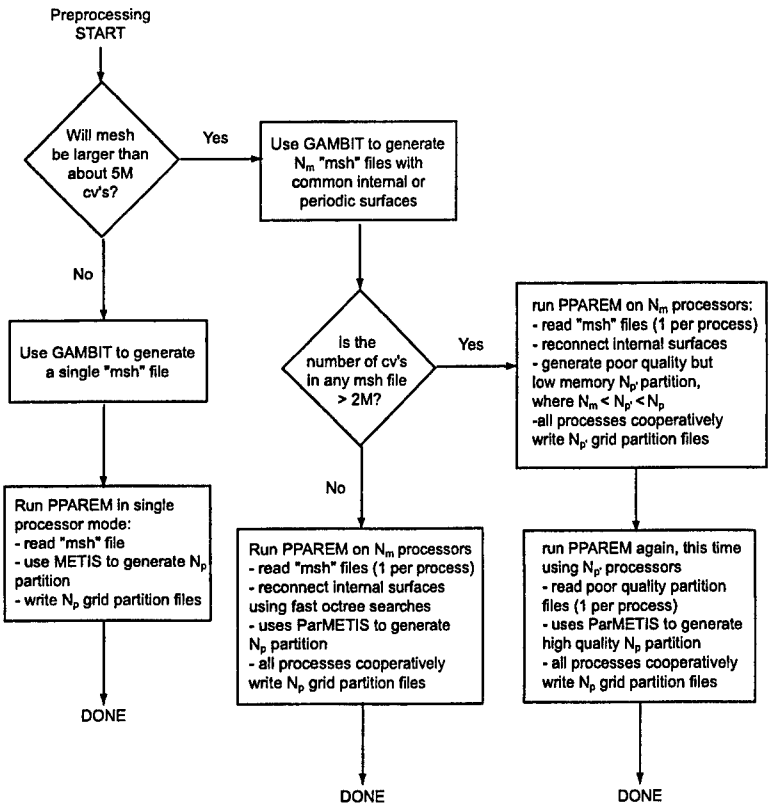


FIGURE 1. Flowchart for the Parallel Preprocessor based on Fluent's GAMBIT software for mesh generation, and our own preprocessing program called PPAREM (Parallel PArtition and REorder Mesh).

approach significantly reduces the cost of the initial grid generation, but gives up individual element control. This approach also requires a close coupling to the problem geometry during the refinement of elements along the boundary to ensure the grid remains boundary-conforming.

The present combustor simulations contain substantially more geometric complexity than the aircraft wing-body geometries typically used for simulation. Consequently, ensuring boundary conformity during refinement presents a significant challenge. Additionally, there are many regions of the geometry where control of the final grid distribution is desired, such as the geometric details of the injectors or dilution holes. Homothetic refinement without subsequent grid smoothing can introduce step-changes in the grid spacing that may adversely affect LES accuracy. For these reasons, the present parallel preprocessor was developed based on the idea of decomposing the combustor geometry into several geometrically-separated regions, and then separately generating the desired grid in each of these regions, ensuring only that shared surfaces have identical meshes. These meshes are then reassembled on the parallel computer using fast octree searches on the common face geometry.

Figure 1 illustrates the process of mesh generation using the CDP parallel preprocessor. Grid generation is still performed on a single high-end workstation using Fluent's commercial mesh generation software, GAMBIT. For mesh sizes less than about 5 mil-

TABLE 1. Parallel preprocessing of 35 M cv grid

exact cv count	35,140,896
number of msh files, N_m	18
number of final partitions, N_p	352
I/O:	
input msh files	3.72 GB
output partition files	3.01 GB
Wall clock time:	
PPAREM on N_m processors:	
read/parse msh files	504 s
octree reconnect geometry	28 s
N_p partition (ParMETIS)	45 s
write N_p partition files	1436 s
Total wall clock time	2013 s (34 min)

lion control volumes, the preprocessing is done in an entirely serial way, much as before. For larger meshes, however, the geometric decomposition approach described earlier is used, and GAMBIT is used to generate a number of separate mesh files. Our parallel preprocessing program PPAREM (Parallel PArtition and REorder Mesh) then reads and reconnects the global mesh, produces a high-quality partition that is independent of the present geometric decomposition using ParMETIS, and reorders and cooperatively writes the partition files using the MPI-I/O routines. Cooperative writing of the partition files represented a challenging programming task, but is the only theoretically scalable way to write the final partition.

The parallel preprocessor was used to prepare two large grids on LLNL's Frost for the cold flow full combustor simulations described in the next subsection. Grid sizes were approximately 35 M and 100 M cv's respectively. Due to the memory requirement of ParMETIS (approx. 0.4 GB per million cv's out of the total requirement of 0.5 GB per million CV's for PPAREM), it was necessary in the case of the 100 M cv grid to produce an intermediate partition using a low-memory but poor quality partitioning algorithm (simply binning the cv's based on global index). PPAREM was then run a second time on a larger number of processors using this poor quality partition as input. With more memory available, a high-quality partition was then calculated using ParMETIS. An alternative and presumably faster approach would be to increase the memory per processor by using more nodes. This was tried unsuccessfully up to 6 nodes for the 100 M case (i.e. 3 processors per node), at which point the "successive partitioning" strategy described previously was adopted.

Tables 1 and 2 summarize some key indices measured during preprocessing. The most expensive and apparently least scalable component of preprocessing is the cooperative reordering and writing of the partition files using MPI-I/O. In the worst case, however, preprocessing of the 100 M cv grid with 1024 partitions required 4.5 hours.

2.2. *Large-Scale Simulation*

In the process of verification and validation of CDP-α, a variety of incompressible cold flow simulations have been performed. The largest of these have been 35 M cv and 100 M cv simulations of the full P&W combustor (all 18 injectors). Figure 2 presents a snapshot

TABLE 2. Parallel preprocessing of 100 M cv grid – 2 cases

exact cv count	100,241,208	100,241,208
number of msh files, N_m	18	18
poor quality partitions, $N_{p'}$	96	96
final partitions, N_p	512	1024
I/O:		
input msh files	14.28 GB	14.28 GB
poor quality partition files	9.65 GB	9.65 GB
final partition files	8.86 GB	8.78 GB
Wall clock time:		
1. PPAREM on N_m processors:		
read/parse msh files	1550 s	1550 s
octree reconnect geometry	75 s	75 s
poor quality partition	2 s	2 s
write poor partition files	1538 s	1538 s
2. PPAREM on $N_{p'}$ processors:		
read poor quality partition	122 s	183 s
partition (ParMETIS)	387 s	501 s
write N_p partition files	6445 s	12385 s
Total wall clock time	10121 s (2.8 h)	16236 s (4.5 h)

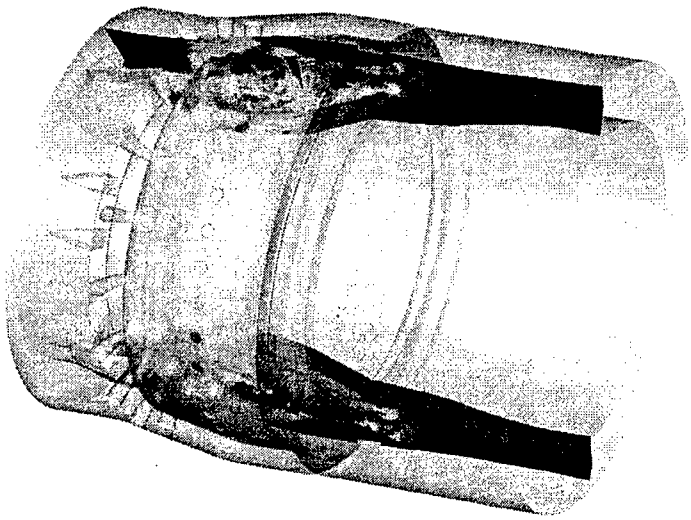


FIGURE 2. Geometry and contours of the instantaneous velocity magnitude on a plane cut through the full P&W 6000 combustor simulation, 35 M cv's.

of this simulation illustrating its substantial geometric complexity and fidelity. The maximum ratio of length scales (ratio of overall domain size to the smallest control volume sizes) is about 10^4. When the new code is completed and contains all the combustion and spray capability of the existing CDP, the ability to run such large simulations will allow the investigation of important physical phenomena, including azimuthal combustion instabilities. Their purpose at this point, however, is mainly for computer science.

2.2.1. *Multigrid*

Multigrid solvers will play an important role in achieving speed and scalability for the very large scale simulations made possible with the new code. As part of the CDP-α development, an interface was written to the hypre solvers of LLNL's CASC group (Falgout *et al.* 2002), and specifically the algebraic multigrid solver (AMG). Tests on large scale cold-flow simulations (35 M cv's on between 160 and 512 processors of Frost) where the existing preconditioned conjugate gradient solver (PCG) for pressure was replaced by AMG yielded a consistent overall speedup of over 4 times. At the largest problem size investigated of 100 M cv's, however, it was not possible to use AMG due to memory allocation errors, even when all 64 nodes of Frost were dedicated to this problem . Based on these results, the following modifications were made to the solver-related research in the combustor group:

- Although the existing CDP code will be phased out in the next few months as the combustion and spray capabilities are implemented and verified in CDP-α, the CDP-to-hypre interface was integrated into the old CDP code, where it has resulted in an overall speedup of over 2 $\times$ for the multiphysics reacting flow simulations. The effect of AMG on both the old and new codes is shown in figure 3.
- The combustor group's research into geometric multigrid has been given lower priority. While the performance of geometric multigrid should theoretically be superior to the algebraic method, both methods have the property of linear scalability, and the promising results from hypre's AMG have meant that combustor group computer science resources can be concentrated on other non-scalable bottlenecks associated with CDP, including parallel preprocessing and particle/mesh load balancing.
- LLNL's CASC group has been involved to help solve the memory problems associated with the very large scale simulations, and also to provide expertise in optimizing the variety of AMG settings for our simulations.

2.2.2. *Scalability*

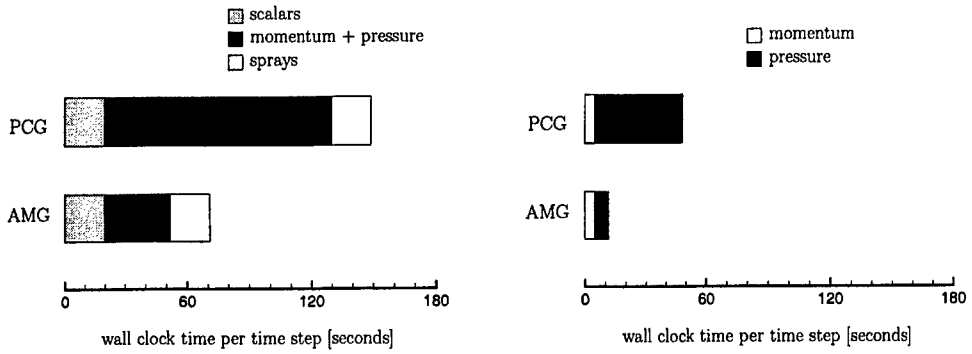
A scalability study of CDP-α has been performed on Frost. Figure 4 summarizes these results for the 35 M cv full combustor cold flow LES, showing acceptable scalability on up to 480 processors.

Although the full combustor simulation was also run with 100 M cv's on up to 64 nodes of Frost, this was only possible with the significantly slower PCG solver for pressure. Investigations of the code scalability at these larger problem sizes and over a greater range of processors will be made once the memory problems associated with the AMG solver have been solved.

2.2.3. *Code Performance*

Table 3 gives some of the key computer science indices for the new CDP-α code. The total memory requirement and total file size scale linearly with problem size, so these indices are reported per M cv's. We note that the AMG memory estimate is based on a number of smaller simulations made on 32 processors or fewer. Clearly such an aggregate memory requirement does not give the complete picture for large-scale simulations. Assuming linear scaling, the 100 M cv simulation should require 100 M $\times$ 3.5 GB = 350 GB, less than the physical memory available on 32 and certainly 64 nodes of Frost†. As discussed earlier, however, attempts to run the 100 M cv simulation with AMG on both 32 and 64 nodes of Frost resulted in memory allocation errors.

† Frost has 64 nodes with 16 GB/node and 16 processors/node



(a) old CDP, multiphysics LES (b) new CDP-α, cold flow LES

FIGURE 3. Speedup of the old and new CDP codes by changing the pressure solver from preconditioned conjugate gradient (PCG) to hypre's algebraic multigrid (AMG): a) Old CDP code, P&W reacting flow single sector simulation with 2 M cv's on 80 processors of Frost ($\approx 25,000$ cv's/processor). b) New CDP-α, cold flow LES of full combustor, 35 M cv's on 480 processors of Frost ($\approx 73,000$ cv's/processor).

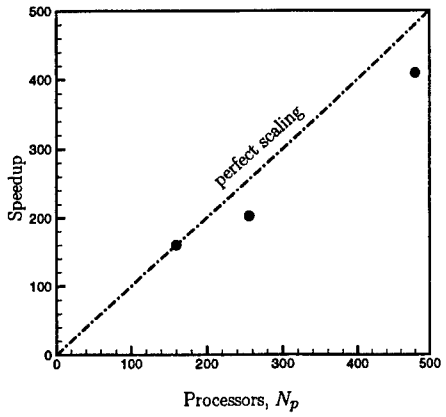


FIGURE 4. Scalability of the new CDP-α code on Frost (with hypre AMG solver for pressure). Problem is the cold flow LES of the full combustor geometry with 35 M cv's. Scaling is reported relative to the 160 processor case, which was the smallest number of Frost processors that could run this problem.

2.3. *Particle/Mesh Load Balancing*

The geometric locality of particles combined with the sequential nature of particle/mesh time advancement can create load imbalance. By integrating components of the parallel preprocessor with CDP-α, it was straight-forward to add particle/mesh load balancing capabilities to the new code. Because the code has very long run times relative to the startup time (i.e. reading the partition and restart files), we developed the load balancing strategy to work like a restart. When a threshold value of load imbalance is reached, a

TABLE 3. Some computer science indices for CDP-α

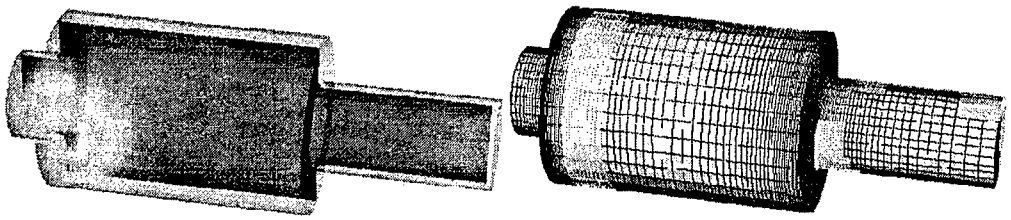
Total memory requirement	
- with PCG solver for pressure	1.5 GB per M cv's
- with AMG solver for pressure	3.5 GB per M cv's
I/O (MPI-2):	
- input partition files	0.10 GB per M cv's
- input restart or output result files	0.20 GB per M cv's
Floating point performance (Frost):	
- sustained Megaflops per processor	78.9 Mflops
- percentage of peak	5.3 %
- flops to memory references	0.294
Sample wall clock time (35 M cv on 480 processors of Frost, cold flow):	
- startup (read partition & restart files)	13 min
- 20,000 time steps at 11 s/step	61 h
- writing result/restart files	5 min
- cooperative writing 2D plane data file	1 min

new partition is calculated using the multi-constraint option available in ParMETIS. This new partition will have (approximately) the same number of cv's and particles on each processor. This new partition is then cooperatively written to files using the routines developed for the parallel preprocessor. The simulation is then stopped, and can be restarted using the new partition.

At the time of this writing, these capabilities have been tested on small problems using model particle cost distributions only. Figure 5 illustrates a model particle cost function and an initial 32-partitioning produced by the parallel preprocessor using ParMETIS in single-constraint mode. ParMETIS was then used to repartition the problem with the dual constraints of equal numbers of cv's *and* particles on each partition. The theoretical simulation timings for the initial partition and multi-constraint partition are shown in figure 6 a) and b) respectively. Times are normalized relative to the perfectly balanced case. For this particular particle distribution, the initial partition has a normalized computation time of over 4. Using a multi-constraint repartitioning, the normalized computation time is reduced to 1.04. This implies a speedup of about 4 $\times$, assuming no change in parallel efficiency. The multi-constrained partitioning does, however, increase the edge cut – in this case by about 40%. The extent to which this reduces the theoretical speedup will be determined when this load balancing capability is tested on real problems.

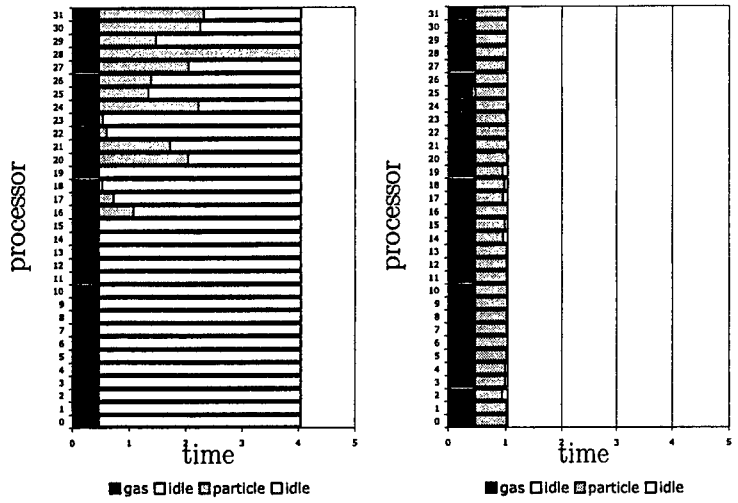
3. Spray Models in CDP

The objective of the spray simulation effort is to develop a numerical framework based on Lagrangian particle models to perform high-fidelity LES of reacting multiphase flows encountered in realistic gas-turbine combustion chambers. Three regimes of flow development are commonly observed inside these combustors (as shown in Fig. 7): 1) 'primary breakup regime' and 'dense regime', where the liquid film exhibits large scale coherent structures that interact with the gas-phase and disintegrate into filaments by forming Kelvin-Helmholtz type instability, 2) 'intermediate regime' where the liquid blobs formed



(a) model particle cost (b) initial 32-partitioning

FIGURE 5. Sample problem used to demonstrate particle/mesh load balancing capabilities in CDP-α.



(a) single-constraint 32-partition, edge cut = 18038, normalized time = 4.05

(b) multiple-constraint 32-partition, edge cut = 23043, normalized time = 1.04

FIGURE 6. Computation time on each processor for sample particle/mesh load balancing problem shown in figure 5.

undergo secondary breakup, and 3) 'dilute regime' where the droplets evaporate, the fuel vapor mixes with the surrounding hot gas giving turbulent spray flames. Droplet deformation and collision are also important features in the intermediate regime. Figure 7 summarizes the characterization of the spray formation into the three regimes, based on the ratio of the characteristic length scale of the liquid to the available grid resolution $\ell/\Delta x$ and the liquid phase volume fraction Θ_p.

The main task was to integrate models capturing these complex phenomena into the unstructured LES code (CDP), perform comprehensive validation simulations of each model, and initiate large-scale turbulent, multiphase, reacting flow simulation in realistic

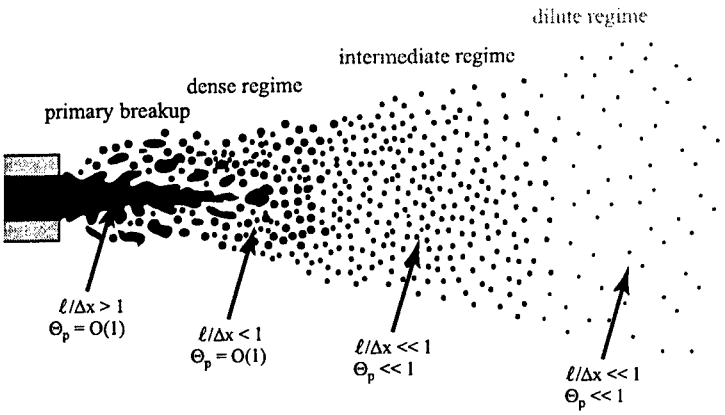


FIGURE 7. Regimes of spray formation defined by the ratio of the characteristic length scale of the liquid, ℓ, to the local grid spacing, Δx and the liquid phase volume fraction, Θ_p.

combustor geometry. A summary of Eulerian/Lagrangian equations with two-way coupling for interphase mass, momentum, and energy transport is given below. The subgrid models for sprays including secondary breakup, droplet deformation and drag, droplet evaporation, a hybrid particle-parcel approach for sprays, and accounting for finite-size effect of droplets in the dense spray regime are described in brief. Also, two novel approaches to more accurately simulate the initial 'primary breakup regime' and the 'dense regime' are briefly outlined.

3.1. *Gas-Phase Equations*

We solve the variable density, low-Mach number equations with two-way coupling between the gas-phase and liquid particles. The formulation is based on the flamelet/progress variable approach developed by Pierce & Moin (2001) for LES of non-premixed, turbulent combustion. The gas-phase continuity, scalar, and momentum equations are,

$$\frac{\partial \overline{\rho_g}\tilde{u_j}}{\partial x_j} = -\frac{\partial \overline{\rho_g}}{\partial t} + \overline{\dot{S}_m} \tag{3.1}$$

$$\frac{\partial \overline{\rho_g}\tilde{Z}}{\partial t} + \frac{\partial \overline{\rho_g}\tilde{Z}\tilde{u_j}}{\partial x_j} = \frac{\partial}{\partial x_j}(\overline{\rho_g}\tilde{\alpha_Z}\frac{\partial \tilde{Z}}{\partial x_j}) - \frac{\partial q_{Zj}}{\partial x_j} + \overline{\dot{S}_Z} \tag{3.2}$$

$$\frac{\partial \overline{\rho_g}\tilde{C}}{\partial t} + \frac{\partial \overline{\rho_g}\tilde{C}\tilde{u_j}}{\partial x_j} = \frac{\partial}{\partial x_j}(\overline{\rho_g}\tilde{\alpha_C}\frac{\partial \tilde{C}}{\partial x_j}) - \frac{\partial q_{Cj}}{\partial x_j} + \overline{\dot{\omega}_C} \tag{3.3}$$

$$\frac{\partial \overline{\rho_g}\tilde{u_i}}{\partial t} + \frac{\partial \overline{\rho_g}\tilde{u_i}\tilde{u_j}}{\partial x_j} = -\frac{\partial \overline{p}}{\partial x_i} + \frac{\partial(2\overline{\mu}\tilde{S_{ij}})}{\partial x_j} - \frac{\partial q_{ij}}{\partial x_j} + \overline{\dot{S}_i} \tag{3.4}$$

$$\tilde{\rho_g} = \tilde{\rho_g}(\tilde{Z}, \tilde{C}, \tilde{Z''}) \tag{3.5}$$

$$\tilde{S_{ij}} = \frac{1}{2}(\frac{\partial \tilde{u_i}}{\partial u_j} + \frac{\partial \tilde{u_j}}{\partial u_i}) - \frac{1}{3}\delta_{ij}\frac{\partial \tilde{u_k}}{\partial x_k} \tag{3.6}$$

where the unclosed transport terms in the momentum and scalar equations are grouped into the residual stress q_{ij}, and residual scalar flux $q_{Zj} and q_{Cj}$. The dynamic Smagorinsky

model by Moin *et al.* (1991) is used to close these subgrid terms as demonstrated by Pierce & Moin (2001). For a two-fluid (air + fuel) mixture, one conserved scalar (the mixture fraction, Z) and a non-conserved scalar (the progress variable, C) are solved. The gas-phase properties such specific heat, molecular weight, density, viscosity, heat-release, and source terms in the progress-variable equation, $\overline{\dot{\omega}_C}$, are obtained from lookup tables generated using flamelet theory for non-premixed combustion and are dependent on the local values of Z, C, and the subgrid mixture fraction fluctuations, $Z"$.

With the presence of the liquid phase and inter-phase mass, momentum, and energy transport, additional source terms are added into the continuity, scalar transport and momentum equations. As the droplets evaporate the heat of vaporization is taken from the gas-phase and there is evaporative cooling of the surrounding gas. This gives rise to a sink term in the energy equation. By assuming adiabatic walls and unity Lewis number, the energy and scalar equations have the same boundary conditions and are linearly dependent. Only one scalar equation (for mixture fraction, Z) is solved and other scalars including temperature are deduced using flamelet tables. The evaporative cooling effect (heat of vaporization) is accounted for in the equation of state during the generation of the flamelet tables. The heat content of the liquid fuel is taken into account by computing an effective gaseous fuel enthalpy and is used in solving the flamelet equations.

3.2. *Modeling Primary Breakup/Dense Regime*

The initial breakup of the turbulent liquid film into large coherent structures is called primary breakup. It is dominated by the interaction of the turbulent liquid film with the surrounding turbulent gas-phase giving rise to liquid surface instability waves. These interfacial instabilities are important in the overall spray evolution and droplet formation process. However, the dynamics of the phase interface is highly complex and as of today not well understood. It in fact remains one of the outstanding unresolved problems in the area of spray simulation how to model this initial breakup in turbulent environments correctly. The majority of the atomization modeling effort is based on Lagrangian particle tracking and secondary breakup mechanisms as described later. Implicit in these models are the assumptions that a) the characteristic length scale of the liquid, ℓ, is small compared to the grid size, Δx, and b) the liquid volume fraction Θ_p is small. Although these models are successful in predicting secondary breakup in the 'intermediate' and 'dilute' regimes, they are not applicable in the 'primary breakup' and 'dense' regime, because their basic assumptions are invalid.

Two different but in essence complementary approaches are being pursued within the group to correctly predict the 'primary breakup' and 'dense' regime. On the one hand, a novel Eulerian based Large Surface Structure model is being developed that explicitly tracks the larger scale dynamics of the phase interface, $\ell/\Delta x > 1$. On the other hand, Lagrangian spray models are being extended to the 'dense regime' by accounting for drop/particle sizes that are comparable to but still smaller than the grid size, $\ell/\Delta x < 1$.

3.2.1. *Large Surface Structure Model*

The objective of the Large Surface Structure (LSS) Model is to correctly capture the dynamics of the phase interface in the primary breakup regime. To this end, we propose to follow in principle the LES approach for turbulent flows. All interface dynamics occurring on scales larger than the grid size are explicitly resolved and captured by a Eulerian level set approach, whereas interface dynamics occurring on the subgrid scales are described by an appropriate subgrid model. Details of this model and some preliminary test cases and results are given in a separate paper in this annual research brief (Herrmann 2003).

3.2.2. *Modeling Finite-Size Droplets*

In a parallel effort, the Lagrangian framework is extended to account for drop/particle sizes that are comparable to but still smaller than the grid size, $\ell/\Delta x < 1$. The equations are based on the original spray formulation developed by Dukowicz (1980) which consists of Eulerian fluid and Lagrangian particle calculations, and accounts for the displacement of the fluid by the particles as well as the momentum interchange between them. The gas-phase equations given above are modified to take into account the volume fraction ($\Theta = 1 - \Theta_p$), where Θ_p represents the volume occupied by the liquid-phase in a given control volume. The gas-phase density, ρ_g and pressure p are then replaced by $(\rho_g\Theta)$ and $(p\Theta)$ in the gas-phase governing equations.

In brief, the Lagrangian particles are advanced using Lagrangian particle tracking. The particle volume fraction Θ_p is then computed on each grid point and then the gas-phase equations are advanced. Use of volume fraction, however, adds to numerical complexity and accurate numerical schemes conserving liquid mass are being developed. Apte *et al.* (2003c) summarize the theoretical formulation and present some preliminary test cases in particulate flows.

3.3. *Modeling Intermediate Regime*

The particle motion is simulated using the Basset-Boussinesq-Oseen (BBO) equations (Crowe *et al.* 1998). It is assumed that the density of the particle is much larger than that of the fluid ($\rho_p/\rho_g \sim 10^3$), particle-size is small compared to the turbulence integral length scale, and that the effect of shear on particle motion is negligible. The high value of density ratio implies that the Basset force and the added mass term are small and are therefore neglected. Under these assumptions, the Lagrangian equations governing the droplet motions become

$$\frac{d\mathbf{x}_p}{dt} = \mathbf{u}_p, \tag{3.7}$$

$$\frac{d\mathbf{u}_p}{dt} = D_p\left(\mathbf{u} - \mathbf{u}_p\right) + \left(1 - \frac{\rho_g}{\rho_p}\right)\mathbf{g} \tag{3.8}$$

where m_p is the mass of the droplet, $\mathbf{u}_p$ the particle velocity components, $\mathbf{u}$ gas-phase velocities interpolated to the particle location, ρ_p and ρ_g the particle and gas-phase densities, and $\mathbf{g}$ the gravitational acceleration. The drag force on a solid particle is modeled using a drag-coefficient, C_d,

$$D_{p_{solid}} = \frac{3}{4} C_d \frac{\rho_g}{\rho_p} \frac{|\mathbf{u}_g - \mathbf{u}_p|}{d_p} \tag{3.9}$$

where C_d is obtained from the nonlinear correlation (Crowe *et al.* 1998)

$$C_d = \frac{24}{Re}\left(1 + aRe_p^b\right). \tag{3.10}$$

Here $Re_p = d_p|\mathbf{u}_g - \mathbf{u}_p|/\mu_g$ is the particle Reynolds number. The above correlation is applicable for $Re_p \leq 800$. The constants $a = 0.15, b = 0.687$ yield the drag within 5% from the standard drag curve. Modifications to the solid particle drag are applied to compute drag on a liquid drop and are given below.

3.4. *Deformation and Drag Models*

In order to quantify the effect of droplet deformation on drag, Helenbrook & Edwards (2002) performed detailed resolved simulations of axisymmetric liquid drops in uniform gaseous stream. The simulations were performed using an *hp*-finite element method (Helenbrook 2002). An unstructured mesh of triangles which deforms with the interface along with a dynamic mesh adaptation algorithm was used allowing higher-order accuracy to be obtained even though there is a discontinuity at the interface. This gives results for the drag which are accurate to within 1%. Based on their computations for a range of density and viscosity ratios, range of Weber (We), Ohnesorge (Oh), and Reynolds numbers (Re), a correlation was developed that provides the amount of deformation in the form of ellipticity, E, which is defined as the ratio of the height to width of the drop. This is given as,

$$E = 1 - 0.11We^{0.82} + 0.013\sqrt{\frac{\rho_l}{\rho_g}\frac{\mu_g}{\mu_l}}Oh^{-0.55}We^{1.1} \tag{3.11}$$

where μ_l, μ_g are the viscosities of the liquid and gas and ρ_l, ρ_g are the densities, respectively. The non-dimensional Weber and Ohnesorge numbers are defined as, $We = \rho_g U^2 d_p/\sigma$ and $Oh = \mu_l/\sqrt{\rho_l \sigma d_p}$, where U is the relative velocity between the gas and liquid, d_p the diameter of the droplet, and σ the surface tension. Accordingly, $E < 1$ indicates that the drops have more width than height with deformation in the direction perpendicular to the relative velocity. These shapes are called oblate shapes. Similarly, $E > 1$ gives elongation in the direction of the relative velocity giving rise to prolate shapes. $E = 1$ implies spherical shapes.

The effect of droplet deformation is to change the drag force. This effect is modeled by using an effective equatorial droplet diameter, $d_p^* = d_p E^{-1/3}$. The particle Reynolds number is also modified, $Re_p^* = Re_p E^{-1/3}$ (Helenbrook & Edwards 2002). This is used in equations (3.9, 3.10) to obtain the modified drag. In addition the effect of internal circulation is modeled by changing the drag on a solid sphere as

$$\frac{D_{drop}}{D_{solid}} = \left(\frac{2 + 3\mu_l/\mu_g}{3 + 3\mu_l/\mu_g}\right)\left(1 - 0.03(\mu_g/\mu_l)Re_p^{0.65}\right) \tag{3.12}$$

3.5. *Stochastic Model for Secondary Breakup*

Performing simulations of primary atomization where one tracks the liquid-gas interface in realistic combustor geometries is computationally intensive. Development of numerical techniques based on hybrid Eulerian/Lagrangian Level-set/Particle tracking schemes to capture the primary atomization process is ongoing and will be implemented into CDP. However, the current status is to compute the atomization process using advanced stochastic secondary breakup models developed (Apte *et al.* 2003). Emphasis is placed on obtaining the correct spray evolution characteristics such as liquid mass flux, spray angle, and droplet size distribution. The liquid film is approximated by large drops with size equal to the nozzle diameter and undergoes deformation and breakup. The effect of high mass-loading on the gas-phase momentum transport is captured through two-way coupling between the two phases.

In this model, the characteristic radius of droplets is assumed to be a time-dependent stochastic variable with a given initial size-distribution. The breakup of parent blobs into secondary droplets is viewed as the temporal and spatial evolution of this distribution function around the parent-droplet size according to the Fokker-Planck (FP) differen-

tial equation. This distribution function follows a certain long-time behavior, which is characterized by the dominant mechanism of breakup:

$$\frac{\partial T(x,t)}{\partial t} + \nu(\xi)\frac{\partial T(x,t)}{\partial x} = \frac{1}{2}\nu(\xi^2)\frac{\partial^2 T(x,t)}{\partial x^2}. \tag{3.13}$$

where the breakup frequency (ν) and time (t) are introduced. Here, $T(x,t)$ is the distribution function for $x = \log(r_j)$, and r_j is the droplet radius. Breakup occurs when $t > t_{breakup} = 1/\nu$. The value of the breakup frequency and the critical radius of breakup are obtained by the balance between the aerodynamic and surface tension forces. The secondary droplets are sampled from the analytical solution of equation (3.13) corresponding to the breakup time-scale. The parameters encountered in the FP equation ($\langle\xi\rangle$ and $\langle\xi^2\rangle$) are computed by relating them to the local Weber number for the parent blob, thereby accounting for the capillary forces and turbulent properties. As new droplets are formed, parent droplets are destroyed and Lagrangian tracking in the physical space is continued till further breakup events.

3.6. *Modeling Dilute Regime*

Typical spray simulations do not resolve the temperature and species gradients around each droplet to compute the rate of evaporation. Instead, evaporation rates are estimated based on quasi-steady analysis of a single isolated drop in a quiescent environment (Faeth 1977, Faeth 1983). Multiplicative factors are then applied to consider the convective and internal circulation effects. We model the droplet evaporation based on a 'uniform-state' model. The Lagrangian equations governing particle mass and heat transfer processes are well summarized by Oefelein (1997) and are described in brief.

$$\frac{d}{dt}(m_p) = -\dot{m}_p \tag{3.14}$$

$$m_p C_{pl}\frac{d}{dt}(T_p) = h_p \pi d_p^2 (T_g - T_p) - \dot{m}_p \Delta h_v \tag{3.15}$$

where Δh_v is the latent heat of vaporization, m_p mass of the droplet, T_p temperature of the droplet, and C_{pl} the specific heat of liquid. The diameter of the droplet is obtained from its mass, $d_p = (6m_p/\pi\rho_p)^{1/3}$. h_p is the effective heat-transfer coefficient and is defined as

$$h_p = k_s \left(\frac{dT}{dr}\right)_{sg} / (T_g - T_s) \tag{3.16}$$

where k_s is the effective conductivity of the surrounding gas at the droplet surface. The subscript 's' stands for the surface of the droplet. The solutions to the mass and temperature equations for quiescent medium are obtained by defining Spalding mass and heat transfer numbers and making use of the Clausius-Clapeyron's equilibrium vapor-pressure relationship (Faeth 1977). In addition, several convective correction factors are applied to obtain spray evaporation rates at high Reynolds numbers (Faeth 1977, Faeth 1983).

3.7. *Hybrid Particle-Parcel Technique for Spray Simulations*

Performing spray breakup computations using Lagrangian tracking of each individual droplet gives rise to a large number of droplets ($\approx$ 10-30 million) very close to the injec-

tor. For LES, simulating all droplet trajectories would be ideal, however, this gives rise to severe load-balancing problems on parallel processors. We have developed a hybrid particle-parcel scheme to effectively reduce the number of particles tracked. A parcel or computational particle represents a group of droplets, N_{par}, with similar characteristics (diameter, velocity, temperature). During injection, new particles added to the computational domain are pure drops ($N_{par} = 1$). These drops move downstream and undergo breakup according to the secondary breakup model and produce new droplets.

The basic idea behind the hybrid-approach, is to collect all droplets in a particular control volume and group them into bins corresponding to their size and other properties such as velocity, temperature etc. The droplets in bins are then used to form a parcel by conserving mass, momentum and energy. The properties of the parcel are obtained by mass-weighted averaging from individual droplets in the bin. For this procedure, only those control volumes are considered for which the number of droplets increases above a certain threshold value. The number of parcels created would depend on the number of bins and the threshold value used to sample them. The parcel thus created then undergoes breakup according to the above stochastic sub-grid model, however, does not create new parcels. On the other hand, N_{par} is increased and the diameter is decreased by mass-conservation. This strategy reduces the total number of computational particles in the domain. In a real simulation with breakup and evaporation models, all the particles are clustered in a very small region close to the injector. This may still give rise to load-imbalance as only a few processors would solve the Lagrangian particle equations. Domain decomposition methods taking into account this load imbalance are being developed and will be tested in the present large-scale multi-physics simulation.

4. Validation Studies using CDP

A systematic and extensive validation effort of CDP code and the Lagrangian spray modules was initiated earlier and several simulations were performed to compare the LES predictions of gas and liquid/solid phases with the available experimental data. Apte *et al.* (2003a) first performed an LES of particle-laden swirling, co-annular jet and compared the results with the experiments of Sommerfeld & Qiu (1991). This validated the Lagrangian particle tracking scheme as well as the accuracy of the numerical method in swirling flows. In addition, development & validation of the secondary breakup model in simplified combustor geometries was also completed (Apte *et al.* 2003). This spray model validation effort was continued and applied to study model predictions for spray evaporation and breakup in complex geometries.

4.1. *Validation of Spray Breakup Model in PW Frontend Geometry*

The stochastic model along with the hybrid particle-parcel approach were used to simulate spray evolution from the Pratt and Whitney injector nozzle. Figure 8 shows the instantaneous snapshot of the spray field along with the injector geometry. The experimental data set was obtained by mounting the injector in a cylindrical plenum through which gas with prescribed mass-flow rate was injected. The gas goes through the main and guide swirler to create a swirling jet into the atmosphere. Liquid film is injected through the filmer surface which forms an annular ring. The liquid mass-flow rate corresponds to certain operating conditions of the gas-turbine engine. For this case, 3.2M grid points were used with high resolution near the injector. The domain decomposition is based on the optimal performance of the Eulerian gas-phase solver on 96 processors. Due to breakup, a large number of droplets are created in the vicinity of the injector. With

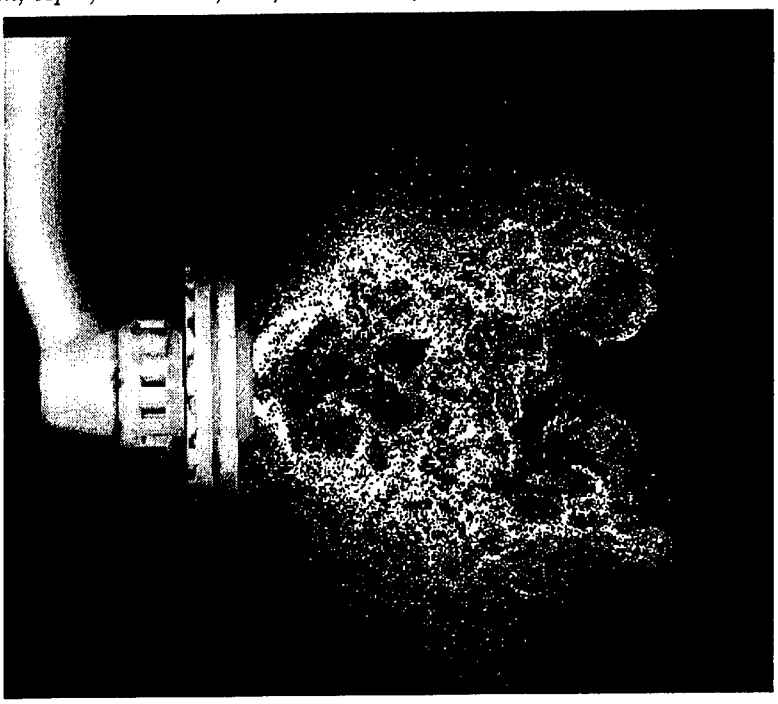


FIGURE 8. Spray evolution from a realistic gas-turbine injector: scatter plot shows the instantaneous droplet locations in $z = 0$ plane. Large size droplets are injected from the nozzle wall in an annular ring to form a hollow cone spray.

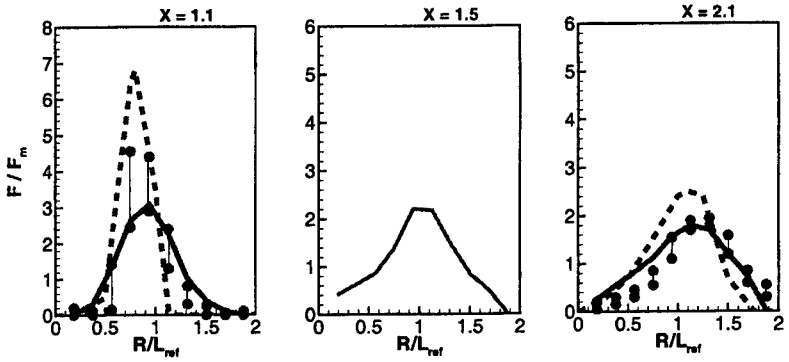


FIGURE 9. Comparison of radial variation of liquid axial mass flux at various axial locations, ---- P&W RANS with TAB model , ——— present LES with stochastic model, o — o experimental error bar.

the hybrid approach, the total number of computational particles tracked at stationary state is around 3.5M, which represents approximately 13M droplets. This includes around 150,000 parcels. The load-imbalance due to atomization was found to be significant as only $1/3^{rd}$ of the processors had more than 10,000 computational particles. We are looking into advanced load-balancing techniques to reduce this computational overhead due to sprays. CDP-(α) has the capability of dynamic load-balancing based on particle imbalance as shown earlier. This will be used to perform these simulations to

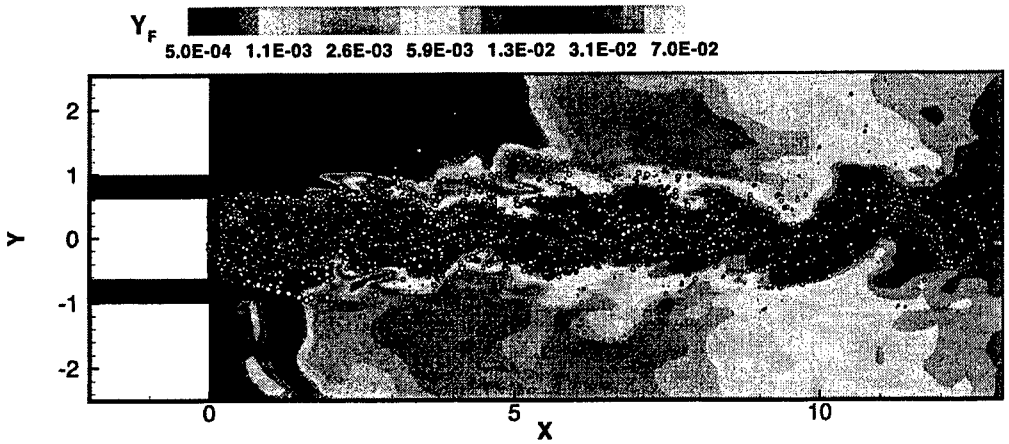


FIGURE 10. Instantaneous contours of ISO-propyl mass-fraction superimposed by droplet locations in $z = 0$ plane.

significantly improve the efficiency and speedup. It will also facilitate us to investigate advanced collision/coalescence models.

Figure (9) shows comparisons with the experimental data of radial variation of liquid mass-flowrates using LES with stochastic model for secondary breakup. Also shown are the predictions made by Pratt & Whitney's RANS-based simulation with a Taylor-Analogy Breakup (TAB) model. The LES results are generally in good agreement with the experiments. The liquid mass-flowrates basically relate to the spray angle and droplet size distributions obtained after breakup. The Sauter Mean Diameter (SMD) are well captured by the present LES simulation (within 7% of the experimental data). The diameter distributions when compared with the experimental data indicates a broad size-distribution as opposed to the one predicted by RANS with the TAB model. The size distribution also indicates presence of large number of small size droplets which could be attributed to the lack of models addressing droplet collision and coalescence. In addition, the initial droplet size at the injector nozzle is assumed to be constant in these simulations, whereas it may vary depending on the local conditions governing primary atomization. A further investigation with inclusion of collision models as well as using a size distribution at the inlet should be performed in order to accurately predict the spray characteristics.

4.2. *Validation of Spray Evaporation Model*

In order to validate the evaporation model and the variable density formulation in CDP, simulation of a coaxial non-swirling jet was performed following the configuration used in the experiments by Sommerfeld & Qiu (1998). This flow configuration was chosen because of its direct relevance in gas-turbine combustion chambers. In addition, in these experiments the boundary conditions for the liquid phase specifying the inlet droplet size distribution and their correlation with droplet velocity is well-defined. The gas-phase temperatures are not high enough to produce spray flames. This isolates the droplet evaporation problem from spray breakup and combustion and is very useful in validating the evaporation models used in CDP. Accordingly, only one scalar equation (mixture fraction) is solved and the gas-phase temperature is obtained from the ideal gas law.

The selection of droplet size and velocity at the injection surface is based on the given

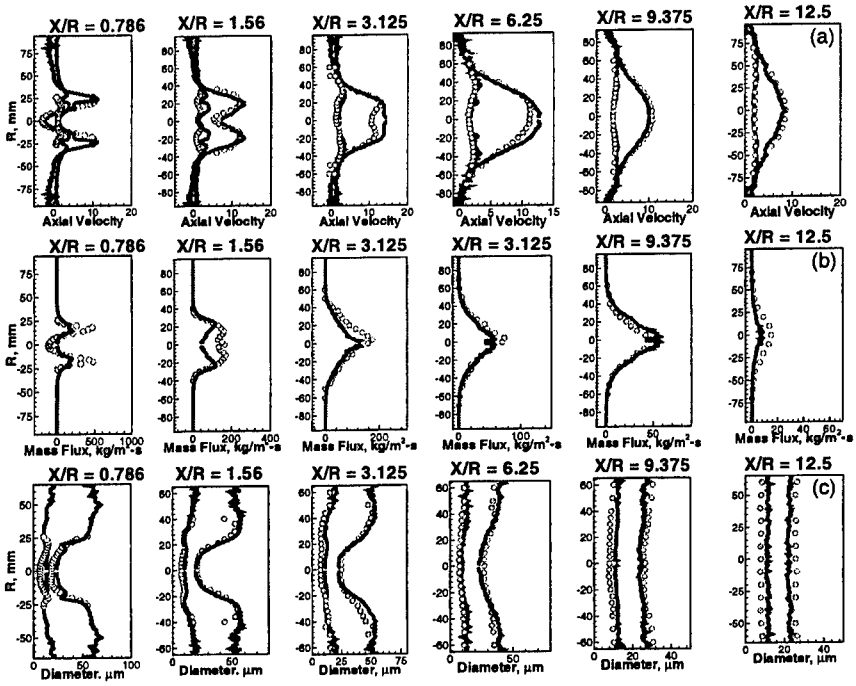


FIGURE 11. Comparison of radial variation of evaporation statistics at various axial locations with the experimental data of Sommerfeld & Qiu (1998), ——— LES, o experimental data: a) mean and *rms* of axial particle velocity, b) mean axial liquid mass flux, c) mean and *rms* of particle droplet diameter.

experimental PDF of size-velocity correlations. The grid used consists of 1.5M hexahedral cells and around 0.5M particles were present in the computational domain at stationary state. Figure (10) shows a snapshot of mixture fraction contours superimposed by scatter plot of ISO-propyl alcohol particles in a coaxial combustor. The droplets are injected near the inlet circular wall of cross-sectional diameter 40 mm. The droplet velocity-size correlation depicts a conical spray with a spray angle of around 60^0. Figure (11) shows the droplet statistics. The radial variations of mean and *rms* droplet velocity, mean axial mass flux, and mean and *rms* droplet diameter compared with experimental data of Sommerfeld & Qiu (1998) are shown. The profiles are in good agreement with the experimental data. The droplet mean diameter profile is typical of the hollow cone atomizer, where smaller droplets are found in the core region and larger droplets near the edge of the spray. Away from the inlet section, the droplet mean diameter distribution becomes more uniform over the cross-section and slowly decreases in the downstream direction because of evaporation. The axial mass-flux also decreases towards the exit due to evaporation and is well captured by the present simulation. At $x = 0$ and $x = 0.786$ the profiles of droplet mass flux show two-peaks associated to hollow-cone spray. Due to the recirculation region downstream of the center-body, the droplet mass-flux becomes negative. Further downstream spreading of the spray is hindered by the annular air-jets and maximum of the mass flux moves towards the centerline. These features are well captured by the present LES computation.

5. Large Scale Multi-physics Simulation using CDP

A multi-scale, multi-physics simulation of turbulent reacting flow in a realistic Pratt & Whitney combustor was initiated. This simulation includes all the complex models for spray breakup, evaporation, and turbulent combustion described in section(3). This simulation will serve as the first validation study of the reacting multiphase flow solver (CDP) in complex combustor geometry. Figure (12) shows the combustor geometry in the symmetry plane $z = 0$. The simulation is performed for a single injector which represents one sector of the full combustor containing 18 injectors. Liquid fuel (Jet-A) enters the combustion chamber through an annular ring at the injector exit. This liquid film is approximated by large drops of the size of the annulus radius. These drops are convected by the surrounding hot air, they break, evaporate, and the fuel vapor thus formed mixes with the surrounding air giving a non-premixed spray flame. The computational grid consists of 1.9M hybrid elements (hexes, pyramids, and tets) with fine resolution close to the injector.

The flamelet library for Jet-A fuel at gas-turbine engine operating conditions, was generated by using a surrogate fuel of 80% n-Decane and 20% 1-2-4 tri-methyl-benzene which closely follows the chemical kinetics and reaction rates of the Jet-A fuel. Around 1000 elementary reactions among 100 chemical species were used to generate these tables. The chemical kinetics of surrogate fuel was compared with original fuel in terms of prediction of pollutants in laminar flames and showed good agreement. In this multiphase simulation, the flamelet tables are generated by considering the heat of vaporization of the liquid fuel. This is obtained by using heat-content for an equivalent gaseous fuel which gives large densities in the pure fuel-vapor region ($Z = 1$).

Figure (12) shows instantaneous snapshots of progress variable (C), mixture fraction (Z), normalized temperature (T/T_0), and velocity magnitude (u_{mag}) in the $z = 0$ symmetry plane. Scatter plot of droplets forming a conical spray is also shown. A highly complex unsteady flame is observed in this simulation. High temperatures in the combustion chamber are reduced by large mass-influx through the dilution holes. This reduces the exit temperature considerably. Strong recirculation zone with conical spray flame is observed near the nozzle. The droplets evaporate completely close to injector and do not appear beyond ($x = 2$). The experimental data available for validation includes pressure drops across different components, mass-splits through the inner and outer dilution holes, and swirlers. The comparison of these quantities with the experimental data was shown to be within 10% for the cold flow simulation. Similar results are obtained for the reacting flow case. In addition, the exit plane temperature was measured at 5 locations. The temperature field is within 10-15% of the experimental data near the center. The predicted temperature near the walls is much lower and is still evolving with time indicating that the flow has not reached the statistically stationary state.

This computation was performed on 80 processors on Frost and involved around 0.5M computational particles. The algebraic multigrid solver (AMG) developed at Lawrence Livermore is used to solve the Poisson equation. The convergence rate of the AMG solver was compared with the conjugate gradient solver (PCG). For each time-step, the conjugate gradient solver typically requires 2000 iterations, whereas the AMG solver requires 10-12 cycles corresponding to 500-600 conjugate gradient iterations. The AMG-solver gave an overall speed-up of 2-3 times over the PCG solver and reduced the computational time substantially.

6. Summary

CDP is the flagship LES code developed by the combustor group to perform LES of reacting multiphase flow in complex geometry. CDP is named after the late Charles David Pierce (1969-2002) who made several lasting contributions to the LES of reacting flows and to the DOE's ASCI program. CDP is a parallel unstructured finite-volume code developed specifically for LES of variable density low Mach-number flows. It is written in Fortran 90, uses MPI, and has integrated combustion and spray modules. A wide range of simulations of multiphase, reacting turbulent flows have been performed using CDP. It has been shown that the predictive capability of CDP for complex flows in realistic gas-turbine configurations is good. A major redesign and rewrite of CDP has been initiated to improve and add to the current capabilities. In the past year, major accomplishments included the following milestones:

- Multi-physics simulation in complex geometry: The first multi-physics simulation including fuel spray breakup, coalescence, evaporation, and combustion is being performed in a single periodic sector ($1/18^{th}$) of an actual Pratt & Whitney combustor geometry.
- Large scale simulation: Performed large eddy simulations of the complete combustor geometry (all 18 injectors) with over 100 million control volumes using CDP-α.

Further development of CDP-α will include the implementation of advanced combustion and primary atomization models, and modification of the numerical algorithm to capture acoustic waves and combustion instabilities based on the compressible formulation of Wall *et al.* (2002). Several large-scale, multiphysics simulations in the PW combustor using one or more sectors will be performed to assess the accuracy of the overall formulation.

7. Acknowledegement

Support for this work was provided by the United States Department of Energy under the Accelerated Strategic Computing Initiative (ASCI) program.

REFERENCES

APTE, S. V., MAHESH, K., MOIN, P. & OEFELEIN, J.C. 2003a Large-eddy simulation of swirling particle-laden flows in a coaxial-jet combustor. *Int. J. Mult. Flow* **29**, 1311-1331.

APTE, S. V., GOROKHOVSKI, M. & MOIN, P. 2003b LES of atomizing spray with stochastic modeling of secondary breakup. *Int. J. Mult. Flow* **29**, 1503-1522.

APTE, S. V., MAHESH, K. & LUNDGREN, T. 2003c An Eulerian-Lagrangian model to simulate two-phase/particulate flows. *Annual Research Briefs*, 2003, Center for Turbulence Research.

CROWE, C., SOMMERFELD, M. & TSUJI, Y. 1998 Multiphase Flows with Droplets and Particles, CRC Press, Boca Raton, FL.

DELLENBACK, P.A., METZGER D.E. & NEITZEL, G.P. 1988 Measurements in Turbulent Swirling Flow Through an Abrupt Axisymmetric Expansion, *AIAA Journal*, **26**.

DUKOWICZ, J. K. 1980 A particle-fluid numerical model for liquid sprays. *J. Comput. Phys.* **35**, 229-253.

FAETH, G. 1977 Current status of droplet and liquid combustion. *Prog. Energy Combust. Sci.*, **3**: 191-224.

FAETH, G. 1983 Evaporation and combustion of sprays. *Prog. Energy Combust. Sci.*, **9**: 1-76.

HELENBROOK, B. T. 2002 A two-fluid spectral element method. *Comp. Meth. Appl. Mech. Eng.*, **191**, 273-294.

FALGOUT, R. D. AND YANG, U. M., "hypre: a Library of High Performance Preconditioners," in Computational Science - ICCS 2002 Part III, P.M.A. Sloot, C.J.K. Tan. J.J. Dongarra, and A.G. Hoekstra, Eds., Lecture Notes in Computer Science, **2331**, 632-641, 2002, Springer-Verlag. Also available as Lawrence Livermore National Laboratory technical report UCRL-JC-146175.

HELENBROOK, B. T. & EDWARDS, C. F. 2002 Quasi-steady Deformation and Drag of Uncontaminated Liquid Drops. *Int. J. Multi. Flows..*

HERRMANN, M. 2003 Modeling primary breakup: A three-dimensional Eulerian level set/vortex sheet method for two-phase interface dynamics. *Annual Research Briefs*, Center for Turbulence Research, 2003.

MAHESH, K., CONSTANTINESCU, G. & MOIN, P. 2003 A new time-accurate finite-volume fractional-step algorithm for prediction of turbulent flows on unstructured hybrid meshes. *J. Comput. Phys.*, to appear.

MAVRIPLIS, D. J. & PIRZADEH, S. 1999 NASA/CR-1999-208999ICASE Report No. 99-9Large-scale Parallel Unstructured Mesh Computations for 3D High-lift Analysis.

MOIN, P., SQUIRES, K., CABOT, W. & LEE, S. 1991 A dynamic subgrid model for compressible turbulence and scalar transport. *Physics of Fluids. A.*, **3**, pp. 2746-2757.

OEFELEIN, J. C. 1997 Simulation and analysis of turbulent multiphase combustion processes at high pressures, Ph.D. Thesis, The Pennsylvania State University, University Park, Pa.

PARMETIS http://www-users.cs.umn.edu/ karypis/metis/parmetis/

PIERCE, C.D. & MOIN, P. 2001 Progress variable approach for large eddy simulation of turbulent combustion. *Report TF - 80*, Flow Physics and Computation Division, Mechanical Engineering Dept., Stanford University, Stanford, California.

SCHLUTER, J. & PITSCH, H. 2002 Consistent boundary conditions for integrated LES/RANS simulations: LES inflow conditions, *Annual Research Briefs*, Center for Turbulence Research.

SOMMERFELD, M. & QIU, H.H. 1991 Detailed measurements in a swirling particulate two -phase flow by a phase - Doppler anemometer. *Int. J. of Heat and Fluid Flow* **12**(1), 20-28.

SOMMERFELD, M. & QIU, H.H. 1998 Experimental studies of spray evaporation in turbulent flow. *Int. J. Heat & Fluid Flow* **19**, 10-22.

WALL, C., PIERCE, C. D. & MOIN, P. 2002 A semi-implicit method for resolution of acoustic waves in low mach number flows. *J. Comp. Phys.*, **181** (2), 545–563.

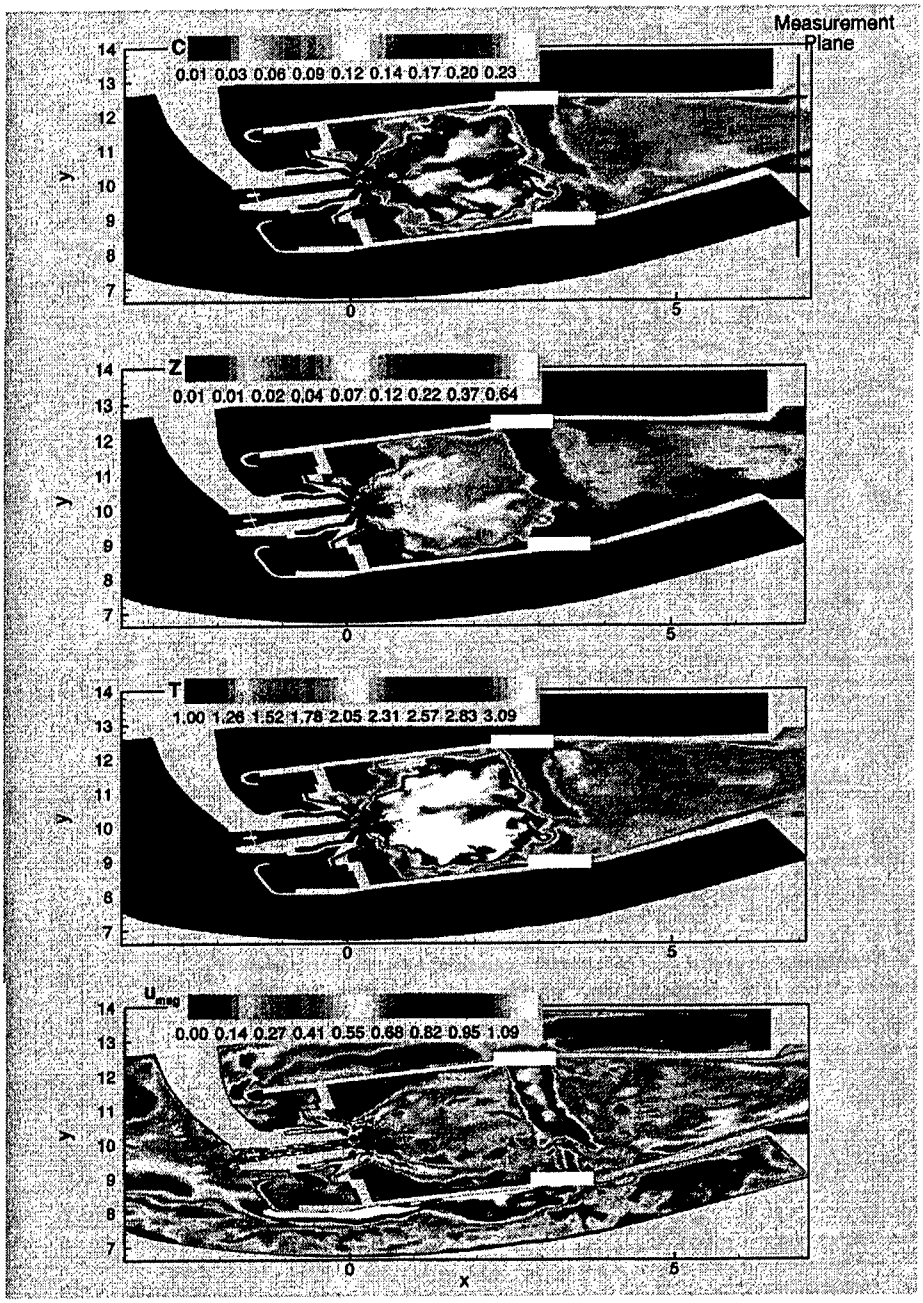


FIGURE 12. Instantaneous snapshots (from top to bottom) of progress variable, C, mixture fraction, Z, temperature normalized by inlet air temperature, T/T_0, and velocity magnitude, $\sqrt{u^2+v^2+w^2}$ superimposed with droplet scatter plot in Pratt & Whitney combustor, $z = 0$ plane. The geometry has been distorted.

A Eulerian-Lagrangian model to simulate two-phase/particulate flows

By S. V. Apte, K. Mahesh†, & T. Lundgren‡

1. Motivation and Objectives

Figure 1 shows a snapshot of liquid fuel spray coming out of an injector nozzle in a realistic gas-turbine combustor. Here the spray atomization was simulated using a stochastic secondary breakup model (Apte *et al.* 2003a) with point-particle approximation for the droplets. Very close to the injector, it is observed that the spray density is large and the droplets cannot be treated as point-particles. The volume displaced by the liquid in this region is significant and can alter the gas-phase flow and spray evolution. In order to address this issue, one can compute the dense spray regime by an Eulerian-Eulerian technique using advanced interface tracking/level-set methods (Sussman *et al.* 1994; Tryggvason *et al.* 2001; Herrmann 2003). This, however, is computationally intensive and may not be viable in realistic complex configurations. We therefore plan to develop a methodology based on Eulerian-Lagrangian technique which will allow us to capture the essential features of primary atomization using models to capture interactions between the fluid and droplets and which can be directly applied to the standard atomization models used in practice. The numerical scheme for unstructured grids developed by Mahesh *et al.* (2003) for incompressible flows is modified to take into account the droplet volume fraction. The numerical framework is directly applicable to realistic combustor geometries.

Our main objectives in this work are:

- Develop a numerical formulation based on Eulerian-Lagrangian techniques with models for interaction terms between the fluid and particles to capture the Kelvin-Helmholtz type instabilities observed during primary atomization.
- Validate this technique for various two-phase and particulate flows.
- Assess its applicability to capture primary atomization of liquid jets in conjuction with secondary atomization models.

2. Mathematical Formulation

Recent direct numerical simulations of large number of solid particles interacting through a fluid medium by Joseph and collaborators (Choi & Joseph 2001) show that a layer of heavy particles with fluid streaming above it can develop Kelvin-Helmholtz (K-H) instability waves whereas a layer of particles above a lighter fluid develops Rayleigh-Taylor instability. This suggests that the primary breakup of a liquid jet into a spray can be simulated by replacing the jet by a closely packed collection of droplets with some assumed size distribution. The K-H instability at the boundary between droplets and

† University of Minnesota
‡ University of Minnesota, Visiting Fellow Center for Turbulence Research

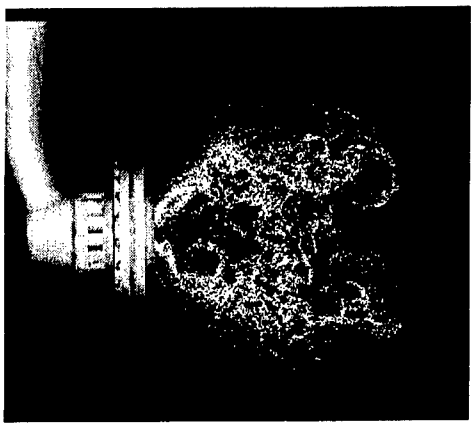


FIGURE 1. Snapshot spray from a gas-turbine fuel-injector.

fluid would initiate dispersal of droplets into a spray. Further breakup of these dispersed drops can be obtained by advanced secondary breakup models.

The formulation described below is a modification of the equations for spray computation developed by Dukowicz (1980) which consists of Eulerian fluid and Lagrangian particle calculations, and accounts for the displacement of the fluid by the particles as well as the momentum interchange between them. The modifications presented here are mainly in the details of modeling the interaction terms.

2.1. *Gas-Phase Equations*

The fluid mass for unit volume satisfies a continuity equation,

$$\frac{\partial}{\partial t}\left(\rho_f \Theta_f\right) + \nabla \cdot \left(\rho_f \Theta_f \mathbf{u}_f\right) = 0 \tag{2.1}$$

where ρ_f, Θ_f, and $\mathbf{u}_f$ are fluid density, volume fraction, and velocity, respectively. This indicates that the average velocity field of the fluid phase does not satisfy the divergence-free condition even if we consider an incompressible suspending fluid. The fluid momentum equation is given as

$$\frac{\partial}{\partial t}\left(\rho_f \Theta_f \mathbf{u}_f\right) + \nabla \cdot \left(\rho_f \Theta_f \mathbf{u}_f \mathbf{u}_f\right) = -\nabla\left(\Theta_f p\right) + \nabla \cdot \left(\mu_f \mathbf{D}_c\right) + \mathbf{F} \tag{2.2}$$

where p is the average dynamic pressure in the fluid phase, μ_f is the viscosity of the fluid phase, and $\mathbf{D}_c = \nabla \mathbf{u}_c + \nabla \mathbf{u}_c^T$ is the average deformation-rate of the fluid-particle composite, $\mathbf{u}_c$ is the composite velocity of the mixture, and F is the force per unit volume the particles exert on gas. These equations are derived in detail for constant density flows by Joseph & Lundgren (1990). For particulate flows and dilute suspensions at low Reynolds numbers, the fluid viscosity should be replaced by an effective viscosity μ^* by using Thomas (1965) correlation,

$$\mu^* = \mu_f \left(1 + 2.5\Theta_f + 10.05\Theta_f^2 + 0.00273 e^{16.6\Theta_f}\right) \tag{2.3}$$

2.2. *Particle-Phase Equations*

The evolution of particle-phase is governed by a Liouville equation for the particle distribution function $\Phi(\mathbf{x}_p, \mathbf{u}_p, \rho_p, V_p, t)$

$$\frac{\partial \Phi}{\partial t} + \nabla_{\mathbf{x}} \cdot (\Phi \mathbf{u}_p) + \nabla_{\mathbf{u}_p} \cdot (\Phi \mathbf{A}_p) = 0, \tag{2.4}$$

where $\mathbf{x}_p$ is the particle position, $\mathbf{u}_p$ particle velocity, ρ_p particle density, and V_p particle volume. $\mathbf{A}_p$ is the particle acceleration and $\mathbf{F}_p = m_p \mathbf{A}_p$ the total force acting on the particle of mass m_p and are given below. Here, $\nabla_{\mathbf{x}} \cdot$ and $\nabla_{\mathbf{u}_p} \cdot$ are the divergence operators with respect to space and velocity, respectively. The individual particle positions and velocities can be obtained by solving the Liouville equation in Lagrangian framework for each particle p:

$$\frac{d}{dt}(\mathbf{x}_p) = \mathbf{u}_p \tag{2.5}$$

$$m_p \frac{d}{dt}(\mathbf{u}_p) = F_p \tag{2.6}$$

2.2.1. *Particle Forces*

The main issue is to model the force on a particle. This may consist of the standard hydrodynamic drag force, dynamic pressure gradient, gradient of viscous stress in the fluid phase, a generalized buoyancy force, and inter-particle collision. The total acceleration of the particle A_p is given as,

$$A_p = D_p (\mathbf{u}_f - \mathbf{u}_p) - \frac{1}{\rho_p} \nabla p_p + \left(1 - \frac{\rho_f}{\rho_p}\right) \mathbf{g} + \mathbf{B}_p + \mathbf{A}_{cp} \tag{2.7}$$

Here $\mathbf{B}_p$ is the generalized buoyancy force and $\mathbf{A}_{cp}$ is the acceleration due to inter-particle forces. If $\rho_p >> \rho_g$ the pressure gradient, viscous, and buoyancy terms are usually negligible. In the present study, the generalized buoyancy force is also neglected for simplicity. It is shown later that, even without the presence of this buoyancy force, one can obtain lift of particles in a shear flow. The drag force is caused by the motion of a particle through the gas. The standard expression for D_p is used

$$D_p = \frac{3}{8} C_d \frac{\rho_f}{\rho_p} \frac{|\mathbf{u}_f - \mathbf{u}_p|}{R_p} \tag{2.8}$$

where C_d is the drag coefficient and is given by (Gidaspow 1994; Andrews & O'Rourke 1996)

$$C_d = \frac{24}{Re} \left(1 + a Re_p^b\right) \Theta_f^{-1.8}, \quad for \;\; Re_p < 1000 \tag{2.9}$$

$$= 0.44 \Theta_f^{-1.8}, \quad for \;\; Re_p \geq 1000 \tag{2.10}$$

where C_d is the drag coefficient for spherical particles, $R_p = (3V_p/4\pi)^{1/3}$ is the particle radius. The particle Reynolds number (Re_p) is given as

$$Re_p = \frac{2\rho_f \Theta_f |\mathbf{u}_f - \mathbf{u}_p| R_p}{\mu_f}. \tag{2.11}$$

There is an indirect collective effect in this drag term: when there is a dense collection of particles passing through the fluid interphase momentum exchange term in equation

(2.2) will cause $\mathbf{u}_g$ to approach the particle velocity, $\mathbf{u}_p$ thus decreasing the drag on a particle, a drafting effect.

The probability function Φ integrated over velocity and mass gives the probable number of particles per unit volume at $\mathbf{x}$ and t in the interval $(\mathbf{u}_p, \mathbf{u}_p + d\mathbf{u}_p), (\rho_p, \rho_p + d\rho_p), (V_p, V_p + dV_p)$. The particle volume fraction (Θ_p) is defined from the particle distribution function as,

$$\Theta_p = \int\int\int \Phi V_p dV_p d\rho_p d\mathbf{u}_p. \tag{2.12}$$

From continuity, the gas-phase volume fraction is obtained as $\Theta_f = 1 - \Theta_p$. The interphase momentum transfer function per unit volume in equation (2.2) is given as

$$\mathbf{F} = \int\int\int \Phi V_p \rho_p \left[D_p \left(\mathbf{u}_f - \mathbf{u}_p \right) - \frac{1}{\rho_p} \bigtriangledown p_p \right] dV_p d\rho_p d\mathbf{u}_p. \tag{2.13}$$

2.2.2. *Collision Force*

The acceleration of particles due to inter-particle interactions (A_{cp}) is an important term in dense particulate and two-phase flows. For dilute and lightly loaded configurations, the particle volume fraction (Θ_p) is small ($< 10\%$), the inter-particle collisions are negligible and probability of particles overlapping each other is low. For dense particulate flows, however, the particle volume fraction should not exceed the close-packing limit (which is usually around 0.6 for three-dimensional case). In the Eulerian-Eulerian approach for two-phase flows, this is ensured by force due to the gradient of interparticle stress in the averaged momentum equation for the particle phase (Gidaspow 1986; Gidaspow 1994). Same model was used in Eulerian-Lagrangian approach by Andrews & O'Rourke (1996), Patankar & Joseph (2001b), Snider *et al.* (1998), and Snider (2001). Accordingly, the expression for acceleration of particles due to collision ($\mathbf{A}_{cp}$) is

$$\mathbf{A}_{cp} = -\frac{1}{\Theta_p \rho_p} \bigtriangledown \tau \tag{2.14}$$

where τ is the interparticle stress that provides a pressure type force that prevents packing of particles beyond the close-packing limit. Expression for τ is given as (from Snider *et al.* (1998))

$$\tau = \frac{P_s \Theta_p^{\beta}}{\Theta_{cp} - \Theta_p} \tag{2.15}$$

where P_s has units of pressure, Θ_{cp} is the particle volume fraction at close packing and β is a constant. The values for P_s and β are obtained from Snider *et al.* (1998). In this model, the inter-particle acceleration due to particle collision is assumed to be independent of its size and velocity. This model is least expensive in terms of computational cost as particle binary pairs are not formed and the collision force is directly obtained by interpolation from equation (2.14). This model, however, couldn't completely prevent the particle volume fraction to exceed the close packing limit and some numerical instabilities were experienced in the present unstructured code. Further research on this model will be conducted to eliminate this problem. An alternative but expensive collision scheme based on the distinct element method (DEM) of Cundall & Strack (1979). This scheme can be readily applied to parcel techniques used in Lagrangian spray simulations. A parcel represents a number (N_p) of droplets/particles of same size, velocity, and other properties. The effective radius (R_{par}) of a parcel based on its total volume is then given

by

$$R_{par} = \left(\frac{3N_pV_p}{4\pi}\right)^{1/3} \tag{2.16}$$

In this method, the interaction among particles and between wall and particles is taken into account separately to ensure that $\Theta_p \leq \Theta_{cp}$. The force F_{pj}^{P-P} on parcel p due to collision with parcel j is given by

$$\begin{aligned}
F_{pj}^{P-P} &= 0 \quad for \quad d_{pj} \geq (R_{par},p + R_{par},j + \alpha) \\
&= \left(k_c\delta_{pj}^{3/2} - \eta_c(\mathbf{u}_p - \mathbf{u}_j)\cdot\mathbf{n}_{pj}\right)\mathbf{n}_{pj} \quad for \quad d_{pj} < (R_{par},p + R_{par},j + \alpha) \\
\delta_{pj} &= (R_{par},p + R_{par},j + \alpha) - d_{pj} \\
F_{jp}^{P-P} &= -F_{pj}^{P-P}
\end{aligned}$$

where d_{pj} is the distance between the center of the p^{th} and j^{th} parcels, $\mathbf{n}_{pj}$ is the unit vector from the center of parcel j to that of parcel p, α is the force range, k_c the stiffness parameter, and η_c the damping parameter. Tsuji *et al.* (1993) used the following expressions to compute the damping parameter

$$\begin{aligned}
\eta_c &= 2\alpha\sqrt{\frac{m_pk_c}{1+\alpha^2}} \\
\alpha &= -\ln(e/\pi)
\end{aligned}$$

where e is the coefficient of restitution. Similarly, the parcel-wall force (Fi_{pw}^{P-W}) on parcel p due to collision with wall w is

$$\begin{aligned}
F_{pw}^{P-W} &= 0 \quad for \quad d_{pw} \geq (R_{par},p + \alpha) \\
&= \left(k_c\delta_{pw}^{3/2} - \eta_c(\mathbf{u}_p)\cdot\mathbf{n}_{pw}\right)\mathbf{n}_{pw} \quad for \quad d_{pw} < (R_{par},p + \alpha) \\
\delta_{pw} &= (R_{par},p + \alpha) - d_{pw}
\end{aligned}$$

where d_{pw} is the distance between the parcel and the wall, and $\mathbf{n}_{pw}$ is the unit vector from the wall to the center of the parcel. The total collision force is obtained by looping over all particles and walls. The corresponding particle acceleration is obtained by dividing the collision force by parcel mass ($m_p = N_p\rho_pV_p$).

3. Numerical Method

The collocated, finite-volume numerical scheme on unstructured grids developed by Mahesh *et al.* (2003) is modified to take into account the gas-phase volume fraction. In addition, the particle centroids are tracked using the Lagrangian framework developed by Apte *et al.* (2003b). The important feature of the numerical scheme is the computation of Θ_f and Θ_p on the unstructured grids. As the particles in the simulations performed do not move out of the domain or are destroyed, the total volume occupied by the particles remains constant from mass-conservation. As a particle crosses a particular control volume, its contribution to the particle volume fraction on neighboring cells must provide global mass-conservation. In addition, it was observed that the Eulerian volume fraction field should also be smooth in order to avoid numerical instabilities encountered due to changes in Θ as the particles move from one grid cell to another. A strategy similar

Computational domain, $0.2 \times 0.6 \times 0.0275m$	Grid, $10 \times 30 \times 5$
Fluid density, $1.254kg/m^3$	Particle Density, $2500kg/m^3$
Numer of Parcels, 2880	Particles per parcel, 3375
Diameter of particles, $500\mu m$	Initial particle concentration, 0.4

TABLE 1. Parameter description for the gravity-dominated sedimentation case.

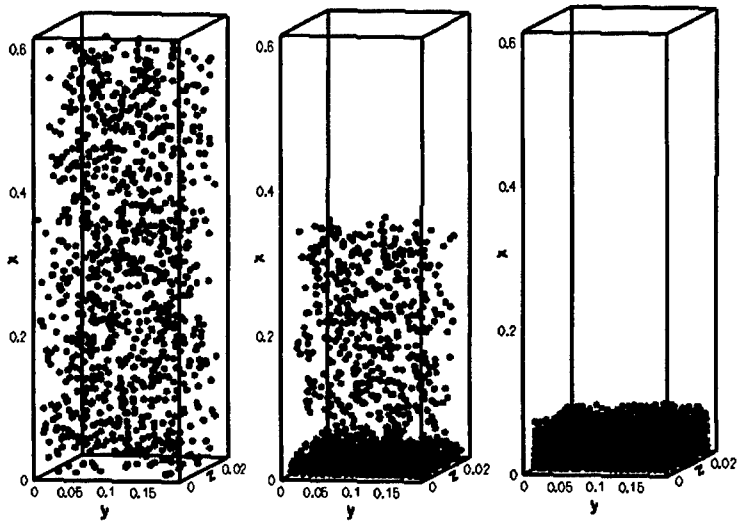


FIGURE 2. Temporal evolution particle distribution during gravity-dominated sedimentation. Initially the particles are randomly distributed over the box rectangular box.

to the two-way coupling methodology by Maxey & Patel (2001) is used to compute the volume fraction. The interphase momentum transport terms are also treated in a similar way.

The particle equations are integrated using third-order Runge-Kutta schemes for *ode*-solvers. At each Runge-Kutta step, the particles were located and the collision force was re-computed. This was found necessary to ensure that the close-packing limit for particle-volume fraction is not exceeeded.

4. Results

We first simulated sedimentation of solid particles under gravity in a rectangular box. Details of this case are given in Table 1. The initial parcel positions are generated randomly in the top half of the box, $0.3 \leq y \leq 0.6$. These particles are then allowed to settle

Computational domain, $0.2 \times 0.6 \times 0.0275m$	Grid, $10 \times 30 \times 5$
Gas jet velocity, $9m/s$	Jet diameter, $0.04m$
Fluid density, $1.254kg/m^3$	Particle Density, $2500kg/m^3$
Numer of Parcels, 2880	Particles per parcel, 3375
Diameter of particles, $500\mu m$	Initial particle concentration, 0.4

TABLE 2. Parameter description for the simulation of fluidization by a gas jet.

through the gas-medium under gravity. The collision model is important here near the bottom wall after the initial group of parcels hit and bounce back from the bottom wall. This prevents particle volume fraction to exceed the close-pack limit. The upper mixture interface between the particles and the fluid is closely approximated by $h = gt^2/2$ similar to that obtained by Snider (2001). The particles eventually settle down with close-packing near the bottom wall. Snider (2001) and Patankar & Joseph (2001a) did sedimentation under gravity, in an inclined pipe with large number of parcels and used the particle stress model for collision force. This allowed them to use large number of parcels as the computational cost for this collision model is negligible. We plan to use this model to do similar validation test cases using the unstructed LES code. One difficulty at the time of writing was that this model didn't always prevent the particle volume fraction from exceeding the close-pack limit. Further investigations on this matter will be performed.

4.1. *Gas-Solid Fluidization*

We consider the problem of fluidization of solid particles arranged in an array at the bottom of a rectangular box. Fluidization is achieved by a jet of gas issuing from the bottom of the box. The flow parameters are given in Table 2. The choice of collision parameters is based on the recent computations by Patankar & Joseph (2001b). The particle motion is mostly dominated by the hydrodynamic drag force and collision model should not affect the overall particle motion. The collision model, however, is important in governing the particle behavior near the walls and helps prevent the volume fraction from exceeding the close-pack limit.

Figure 3 shows the position of parcels at different times during bubbling fluidization. Parcel diameters are drawn to scale. The jet issuing from the bottom wall pushes the particles away from the center region and creates a gas-bubble in the center. The particles collide with each other and the wall and are pushed back towards the central jet along the bottom wall. They are then entrained by the jet and are levitated. This eventually divides the central bubble and two bubbles are trapped. The particles tend to move upwards and collide with the upper wall and remain levitated during future times. The computational results are in good agreement with the simulations of Patankar & Joseph (2001b) as well as in qualitative agreement with experiments on jet fluidization. Similar results are reported using Eulerian-Eulerian approach in two-dimensions by Ding & Gidaspow (1990).

4.2. *Fluidization by Lift of Spherical Particles*

The transport of particles by fluids in coal-water slurries, hydraulically fractured rocks in oil-bearing reservoirs, bedload transport in rivers and canals and their overall effect on the river bed erosion etc., are important scientific and industrial issues in particulate flows. In order to understand fluidization/sedimentation in such conduits, (Choi & Joseph 2001) performed a DNS study of fluidization of circular cylinders (300 particles) arranged

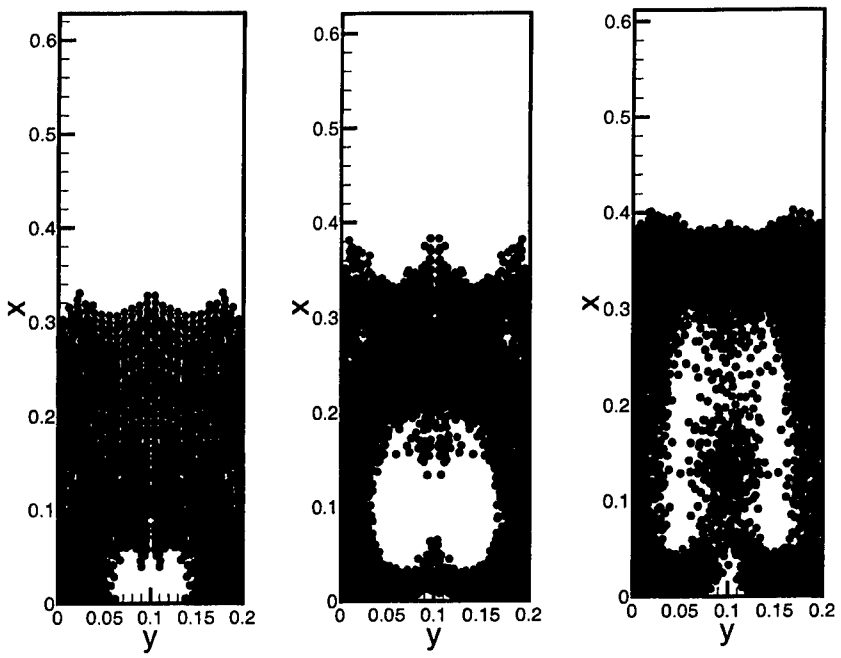


FIGURE 3. Temporal evolution of particle distribution during fluidization by a gas jet. Initially all the particles are uniformly arranged in layers at the bottom of the rectangular box. Air is injected through a rectangular slot at the bottom wall. Air bubbles are trapped within the particles and the growth and pattern of these bubbles are in agreement with experimental observations.

Computational domain, $63 \times 12 \times 12cm$	Grid, $20 \times 11 \times 10$
Gas jet velocity, $9m/s$	Jet diameter, $0.04m$
Fluid density, $1g/cm^3$	Fluid viscosity, $1poise$
Particle Density, $1.01g/cm^3$	Diameter of particles, $0.95cm$
Numer of Parcels, 3780	Particles per parcel, 1
Initial array height, $4.75cm$,	Initial centerline velocity, $360cm/s$
Pressure gradient, $20dyne/cm^3$	

TABLE 3. Parameter description for the simulation of fluidization of spherical particles in a plane Poiseuille flow.

at the bottom of a channel in plane Poiseuille flow. They observed that with sufficient pressure gradient across the channel, the particles initially at rest in the lower half of the channel start moving and roll over the wall. Particle rotation in a shear flow generates lift and the channel is fluidized after some time. We attempt to capture this phenomenon by our Eulerian-Lagrangian model. The flow parameters are given in Table 3. As opposed to Choi & Joseph (2001), we are performing three-dimensional simulations and our particles are spheres. As shown in Fig.4 we observe that the effect of volume displacement due

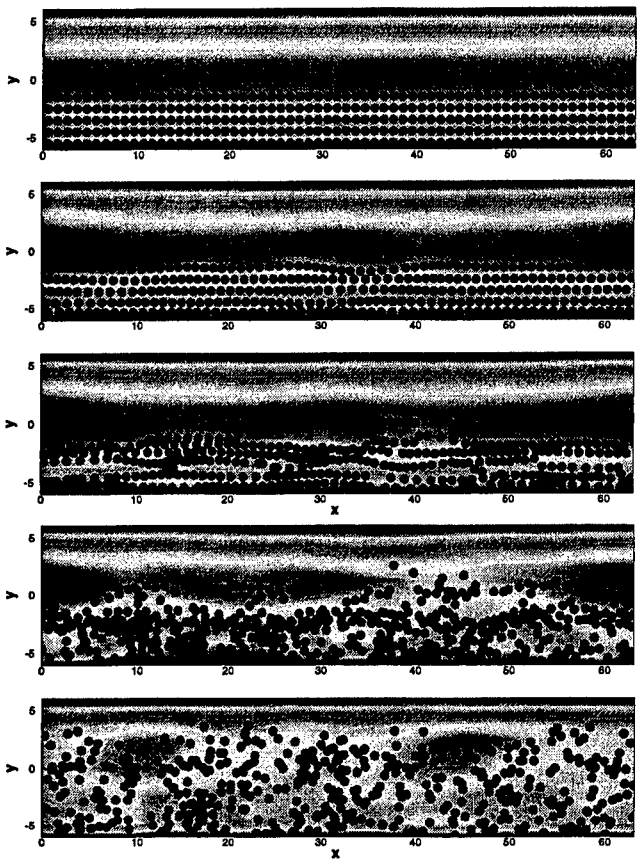


FIGURE 4. Temporal evolution of particle distribution during fluidization by lift in a plane Poiseuille flow. Also shown are contours of axial gas-phase velocity. Initially all particles are arranged at the bottom of the channel.

to particles is to set up Kelvin-Helmholtz type waves between the fluid and particle layers.. A vertical pressure gradient is created and gives vertical velocity to the particles and the channel gets fluidized. We also did several test cases, with higher grid resolution, increased density ratios to obtain similar results. With increased particle density, the two-way coupling between the particle and fluid momentum equation, decelerates the fluid in the bottom half of a channel and an inflection point is created in the axial velocity profile. This eventually cause lift and particle dispersal. In liquid-fuel combustor applications, we believe that similar mechanism can be observed in the dense-spray regime near the injector and will allow us to capture the important features of primary atomization.

5. Summary

We have developed a numerical scheme which accounts for the displacement of the fluid by particles and is applicable to dense particulate flows and spray regimes close to the nozzle injector. This scheme has been implemented into the unstructured LES code. We performed various numerical simulations of fluidization and particulate flows to validate our scheme. It was shown through simulation of channel flow with layers of spherical

particles at the bottom wall that the effect of particle volume fraction is to displace the fluid in a control volume and create vertical pressure gradient through two-way coupling between the particles and fluid. This gives Kelvin-Helmholtz type instability waves which result in dispersal and lift-off of particles. This liftoff of dense-particles cannot be observed without explicit modeling of lift-forces on particles by using the standard point-particle approximation in Lagrangian-Eulerian framework. Similar K-H waves are present in the dense spray regime near the injector nozzle which may affect the overall spray dynamics and breakup in practical combustors. We plan to apply this model coupled with secondary breakup model to perform simulations of spray atomization. We also plan to perform several validation studies of this methodology for dense particulate/granular flows to address some issues related to collision scheme, efficient and consistent computation of particle volume fraction on multiple domain-decomposition.

6. Acknowledgement

Support for this work was provided by the United States Department of Energy under the Accelerated Strategic Computing Initiative (ASCI) program. We also thank Prof. Parviz Moin and Dr. Nagi Mansour for useful discussions as well as for providing support to perform this work.

REFERENCES

ANDREWS, M. J., & O'ROURKE, P. 1996 The multiphase particle-in-cell (MP-PIC) method for dense particle flow. *Int. J. Mult. Flow* **22**, 379-402.

APTE, S. V., GOROKHOVSKI, M. & MOIN, P. 2003a LES of atomizing spray with stochastic modeling of secondary breakup *Int. J. Mult. Flow* **29**, 1503-1522.

APTE, S. V., MAHESH, K., MOIN, P., & OEFELEIN, J.C. 2003b Large-eddy simulation of swirling particle-laden flows in a coaxial-jet combustor. *Int. J. Mult. Flow* **29**, 1311-1331.

CHOI, H.G., & JOESPH, D.D. 2001 Fluidization by lift of 300 circular particles in plane Poiseuille flow by direct numerical simulation. *J. Fluid. Mech.* **438**, 101-128.

CUNDALL P.A., & STRACK, O.D.L. 1979 A discrete numerical model for granular assemblies. *Geotechnique* **29**, 47-65.

DING, J. & GIDASPOW, D. 1990 A bubbling fluidization model using kinetic theory of granular flow. *AIChE* **36**, 523-537.

DUKOWICZ, J. K. 1980 A particle-fluid numrical model for liquid sprays. *J. Comput. Phys.* **35**, 229-253.

GIDASPOW, D. 1986 Hydrodynamics of fluidization and heat transfer supercomputer modeling *Appl. Mech. Rev.* **39**, 1.

GIDASPOW, D. 1994 Multiphase flow and fluidization continuum and kinetic descriptions. Academic Press, Boston, MA.

HERRMANN, M. 2003 Modeling primary breakup: A three-dimensional Eulerian level set/vortex sheet method for two-phase interface dynamics. *Annual Research Briefs*, Center for Turbulence Research.

JOSEPH, D.D., & LUNDGREN, T. 1990 Ensemble averaged and mixture theory equations for incompressible fluid-particle suspensions. *Int. J. Mult. Flow* **16**, 35-42.

MAHESH, K., CONSTANTINESCU, G.,& MOIN, P. 2003 A new time-accurate finite-

volume fractional-step algorithm for prediction of turbulent flows on unstructured hybrid meshes. *J. Comput. Phys.*, to appear.

MAXEY, M.R., & PATEL, B.K. 2001. Localized force representations for particles sedimenting in Stokes flow. *Int. J. Mult. Flow.* **27**, 1603-1626.

PATANKAR, N. A., & JOSEPH, D. D. 2001a Modeling and numerical simulation of particulate flows by the Eulerian-Lagrangian approach. *Int. J. Multi. Flow* **27**, 1659-1684.

PATANKAR, N. A., & JOSEPH, D. D. 2001b Lagrangian numerical simulation of particulate flows. *Int. J. Multi. Flow* **27**, 1685-1706.

SNIDER, D. M. 2001 An incompressible three-dimensional multiphase particle-in-cell model for dense particulate flows. *J. Comput. Phys.* **170**, 523-549.

SNIDER, D. M. 1998 Sediment flow in inclined vessels calculated using multiphase particle-in-cell model for dense particle flow. *Int. J. Mult. Flow.* **24**, 1359.

SUSSMAN, M., SMEREKA, P. & OSHER, S. 1994 A level set approach for computing solutions to incompressible two-phase flow. *J. Comput. Phys.* **114**, 146-159.

THOMAS, D.G. 1965 Transport characteristics of suspension: VIII. A note on the viscosity of Newtonian suspensions of uniform spherical particles. *J. Colliod. Sco.* **20**, 267-277.

TRYGGVASON, G., BUNNER, B. ESMAEELI, A., JURIC, D., AL-RAWAHI, N., TAUBER, W., HAN, J., NAS, S. & JAN, Y.-J. 2001 A Front-Tracking Method for the Computations of Multiphase Flow *J. Comput. Phys.* **169**, 708-759.

TSUJI, Y., KAWAGUCHI, T., & TANAKA, T. 1993 Discrete particle simulation of 2-dimensional fluidized-bed. *Powder Technology* **77**, pp. 79-87.

New type of the interface evolution in the Richtmyer-Meshkov instability

By S. I. Abarzhi and M. Herrmann

1. Motivation and objectives

When a shock wave passes an interface between two fluids with different values of the acoustic impedance, the misalignment of the pressure and density gradients results in a growth of the interface perturbations and causes the development of the Richtmyer-Meshkov instability (RMI) (Richtmyer 1960; Meshkov 1969). The instability produces with time the turbulent mixing of the fluids, which controls many physical and technological processes, such as inertial confinement fusion, supernova explosion, and impact dynamics of liquids (Kull 1991). Reliable description of the turbulent mixing is the basic objective of studies of RMI (Kull 1991; Schneider *et al.* 1998).

Observations report the following evolution of the Richtmyer-Meshkov instability. In the linear regime, the light fluid accelerates impulsively the heavy fluid, and a small amplitude perturbation of the fluid interface grows linearly with time (Richtmyer 1960; Meshkov 1969). The acceleration value is determined by the shock-interface interaction, which is essentially non-local and results in a baroclinic production of vorticity (Haan 1991; Velikovich & Dimonte 1996; Vandenboomgaerde *et al.* 1998; Wouchuk 2001). In the non-linear regime, a structure of bubbles and spikes appear (Pavlenko *et al.* 2000; Chebotareva *et al.* 1999; Jacobs & Sheeley 1996; Bonazza & Sturtevant 1996). The light (heavy) fluid penetrates the heavy (light) fluid in bubbles (spikes). The bubbles decelerate and the spikes move steadily. Small-scale structures appear on the side of evolving spikes due to shear, and the direct cascade of the fluid energy may occur (Matsuoka *et al.* 2003). For a finite-amplitude perturbation, the fluid energy may be transferred also to larger scales (Alon *et al.* 1995; Oron *et al.* 2001). Eventually, a mixing zone develops. In the chaotic regime, the bubbles and spikes decelerate, and their positions are described by power-law time-dependencies with exponents determined by the density ratio (Schneider *et al.* 1998; Dimonte 2000).

The dynamics of the Richtmyer-Meshkov instability is far from being completely understood. For a long time, the theoretical models and numerical simulations failed to predict the growth-rate in the linear RMI observed in experiments (Holmes *et al.* 1999). Only recently, a rigorous theory has accounted for the non-local character of the interface dynamics in the case of strong and weak shocks and provided therefore for impulsive models the correct value of the acceleration (Wouchuk 2001). To describe the nonlinear RMI, several models have applied a single-mode approximation, which presumed locality of the bubble (spike) dynamics (Alon *et al.* 1995; Goncharov 2002). Some other models have used an empiric equation with adjustable parameters to balance "drag" and "inertia" in the flow (Oron *et al.* 2001; Dimonte 2000). All these models however cannot explain the observations and remain subjects for controversy (Dimonte 2000). There is a strong need in a formal theoretical approach and in experiments and simulations with systematic variation of parameters and improved diagnostics. In this work we suggest analytical and numerical solutions describing the nonlinear coherent dynamics

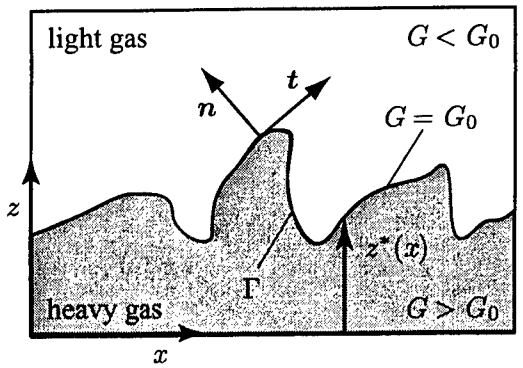


FIGURE 1. Interface definition.

of two-dimensional Richtmyer-Meshkov instability for fluids with a finite density ratio. Our results predict new properties of the nonlinear evolution of RMI, explain existing experiments, and identify new sensitive diagnostic parameters.

2. Governing equations

The dynamics of the Richtmyer-Meshkov instability are governed by a system of conservation laws, which are compressible two-dimensional Navier-Stokes with the initial conditions and the boundary conditions at the fluid interface,

$$\frac{\partial \rho}{\partial t} + \nabla \cdot (\rho \boldsymbol{v}) = 0 \tag{2.1}$$

$$\frac{\partial \rho \boldsymbol{v}}{\partial t} + \nabla \cdot (\rho \boldsymbol{v}\boldsymbol{v}) + \nabla p + \nabla \cdot \overline{\overline{\tau}} = 0 \tag{2.2}$$

$$\frac{\partial \rho E}{\partial t} + \nabla \cdot ([\rho E + p]\, \boldsymbol{v}) + \nabla \cdot \boldsymbol{q} + \overline{\overline{\tau}} : \nabla \boldsymbol{v} = 0\,. \tag{2.3}$$

Here, ρ denotes the density, $\boldsymbol{v}$ the velocity vector, p the pressure, $\overline{\overline{\tau}}$ the stress tensor, E the total energy, and $\boldsymbol{q}$ the heat flux vector. All quantities are either in the heavy gas, denoted by the subscript h in the following, or in the light gas, denoted by the subscript l. The above system of equations is closed by the ideal gas law,

$$p = \rho \Phi T\,, \tag{2.4}$$

with Φ the gas constant and T the temperature.

The interface Γ located at $z^*(x,t)$ separating heavy from light gas, is described by a level set scalar G, see Fig. 1. Defining

$$G(\boldsymbol{x},t)\Big|_{\Gamma} = G_0 = \text{const}\,, \tag{2.5}$$

with $G(\boldsymbol{x},t) < G_0$ in the light gas and $G(\boldsymbol{x},t) > G_0$ in the heavy gas, compare Fig. 1, an evolution equation for the scalar G can be derived by simply differentiating Eq. (2.5) with respect to time,

$$\frac{\partial G}{\partial t} + \boldsymbol{v} \cdot \nabla G = 0\,. \tag{2.6}$$

This equation is called the level set equation (Osher & Sethian 1988). It is easy to see that Eq. (2.6) is independent of the choice of G away from the interface. However, to

facilitate the numerical solution of Eq. (2.6), G is chosen to be a distance function away from the interface,

$$|\nabla G|\Big|_{G\neq G_0} = 1\,. \tag{2.7}$$

Using the level set scalar, geometrical properties of the interface, like its normal vector $\boldsymbol{n}$ or curvature ζ, can be easily calculated,

$$\boldsymbol{n} = \frac{\nabla G}{|\nabla G|}\,, \qquad \kappa = \nabla\cdot\boldsymbol{n}\,. \tag{2.8}$$

There is no mass flow across the moving interface, and the normal component of velocity, pressure and temperature are continuous at the fluid interface:

$$\boldsymbol{v}_{n,h}\big|_\Gamma = \boldsymbol{v}_{n,l}\big|_\Gamma \tag{2.9}$$

$$\boldsymbol{v}_{t,h}\big|_\Gamma = \boldsymbol{v}_{t,l}\big|_\Gamma \tag{2.10}$$

$$p_h\big|_\Gamma = p_l\big|_\Gamma \tag{2.11}$$

$$T_h\big|_\Gamma = T_l\big|_\Gamma\,. \tag{2.12}$$

The flow has no mass sources, and the boundary conditions at the infinity close the set of the governing equations

$$\boldsymbol{v}_h\big|_{z=+\infty} = \boldsymbol{v}_l\big|_{z=-\infty} = 0\,. \tag{2.13}$$

Initially, the fluid interface is slightly disturbed with a small amplitude co-sinusoidal perturbation, $z^*(x,t=0) \sim (1/k)\cos(kx)$, where $k = 2\pi/\lambda$ is the wave-vector, and λ is the spatial period in the x-direction. The perturbation should be symmetric, in order a stable coherent structure of the bubbles and spikes to occur. The density ratio or the Atwood number $A = (\rho_h - \rho_l)/(\rho_h + \rho_l)$ is a determining factor of RMI dynamics.

3. Non-local theoretical solutions

Based on the observations, we divide the fluid interface into active regions (small scales) with intensive vorticity, and passive regions (large scales) which are simply advected. If the energy cascades are not extensive (i.e., the fluid densities are not very similar, the perturbation amplitude is small, and the initial shock is weak), then, a considerable part of the fluid energy concentrates in the large-scale coherent motion with $\nabla\cdot\boldsymbol{v}_{h(l)} = 0$ and $\nabla\times\boldsymbol{v}_{h(l)} = 0$. To find the nonlinear solutions, describing the dynamics of the bubble front in a vicinity of its tip, we reduce the Eqs. (2.1), (2.2), (2.9), and (2.11) to a local dynamical system. All calculations are performed in the frame of reference moving with velocity $v(t)$ in the z-direction, where $v(t)$ is the velocity at the bubble tip in the laboratory frame of reference. For the large-scale motion $\boldsymbol{v}_{h(l)} = \nabla\Phi_{h(l)}$, and we expand the potential $\Phi_{h(l)}$ as a Fourier series,

$$\Phi_h = \sum_{m=1}^{\infty}\Phi_m(t)\big(\cos(mkx)\exp(-mkz)/mk + z\big) \tag{3.1}$$

$$\Phi_l = \sum_{m=1}^{\infty}\tilde{\Phi}_m(t)\big(\cos(mkx)\exp(mkz)/m - z\big) \tag{3.2}$$

For $x \approx 0$ the interface has the form $z^* = \sum_{N=1}^{\infty}\zeta_N(t)x^{2N}$, where $\zeta_1(t) < 1$ is the

principal curvature at the bubble tip, and N is the order of approximation. Substituting these expressions in the governing equations, taking the first integral of Eq. (2.2), and re-expanding Eqs. (2.9) and (2.11) for $x \approx 0$, we derive a system of ordinary differential equations for the surface variables $\zeta_N(t)$, and the moments $M_n(t) = \sum_{m=1}^{\infty} \Phi_m(t)(km)^n$ and $\tilde{M}_n(t) = \sum_{m=1}^{\infty} \tilde{\Phi}_m(t)(km)^n$ where n is integer. For $N = 1$, one has from Eqs. (2.9)-(2.13) respectively

$$\dot{\zeta}_1 = 3\zeta_1 M_1 + M_2/2 = 3\zeta_1 \tilde{M}_1 - \tilde{M}_2/2, \tag{3.3}$$

$$(\dot{M}_1/2 + \zeta_1 \dot{M}_0 - M_1^2/2 - \zeta_1)\rho_h = (\dot{\tilde{M}}_1/2 - \zeta_1 \dot{\tilde{M}}_0 - \tilde{M}_1^2/2 - \zeta_1)\rho_l, \tag{3.4}$$

$$M_0(t) = -\tilde{M}_0(t) = -v(t)\,. \tag{3.5}$$

The system (3.3)-(3.5) describes the local dynamics of the bubble as long as the period of the structure is invariable, and the energy cascades are not extensive. The presentation in terms of moments allows one to account for the effect of higher-order correlations. The time-scale in Eqs. (3.3)-(3.5) is $\tau = 1/kv_0$, where v_0 is the absolute value of the initial velocity. For $t/\tau \ll 1$, the dynamical system (3.3)-(3.5) has regular asymptotic solutions with time independent surface variables ζ_N and with velocity v and moments M_n, $\tilde{M}_n$ decaying as $1/t$.

It is easy to see that the local system (3.3)-(3.5) cannot be satisfied in a single-mode approximation. One may derive, for example, a single-mode solution of the Layzer-type, which conserve mass, momentum and has no mass sources. For this bubble $\zeta_1 = \zeta_L = -Ak/6$ and velocity $v = v_L = (1 - A^2/3)/Ak$, however the solution does not satisfy Eqs. (2.9) and (3.3) and requires mass flux across the interface. To reproduce the parameters of the drag model (Oron *et al.* 2001) with $\zeta_1 = \zeta_D = -k/6$ and $v = v_D = (1 + A/3)/k(1 + A)$, one should violate Eqs. (2.13) and (3.5) and introduce a source of mass of the light fluid (Goncharov 2002). Obviously, these solutions are unphysical, because they violate the conservation laws.

To obtain regular asymptotic solutions describing the nonlinear dynamics of the bubble front, one should account for the non-local properties of the flow that has singularities. The singularities determine the interplay of harmonics in the global flow and the local dynamical system, and affect therefore the shape of the regular bubble. We find a continuous family of regular asymptotic solutions for Eqs. (3.3)-(3.5), parameterized by the principal curvature at the bubble tip, and choose the fastest solution in the family as the physically significant one. For $N = 1$ the bubble velocity as the function of the bubble curvature is

$$v = \frac{3}{2kt} \frac{(1 + A(\zeta_1/k) - 12A(\zeta_1/k)^3)}{(A - 4(\zeta_1/k) + 4A(\zeta_1/k)^2)} (1 - 4(\zeta_1/k)^2), \tag{3.6}$$

where $\zeta_{cr} < \zeta < 0$. For the family solutions (3.6), the interplay of harmonics is well captured, the higher order corrections for the velocity and lowest-order amplitudes are small, the solutions converge, yet, most of them are unstable. The fastest stable solution in the family (3.6) is the solution with

$$\zeta_1 = \zeta_A, = 0 \quad v = v_A = 3/2Akt \tag{3.7}$$

The foregoing theoretical results suggest the following evolution of the bubble front in the Richtmyer-Meshkov instability. In the linear regime of RMI, the bubble curvature and velocity change as $\sim t$; in the weakly non-linear regime, the curvature reaches an extreme value, dependent on the initial conditions and the Atwood number; asymptotically, the

bubble flattens and decelerates. For $A < 1$ the bubbles move faster than those for $A = 1$, and for all A the bubbles flatten asymptotically. The flattening of the bubble front is a distinct feature of RMI universal for all A. It follows from the fact that RM bubbles decelerate. As $A \sim 0$, the velocity $v \sim \infty$ and this suggests that for fluids with similar densities the bubble velocity has a much faster time-dependence, such as t^a where $-1 < a < 0$, in a qualitative agreement with experiments of Jacobs & Sheeley (1996), where for $A \sim 0$ the dependence $1/t$ was shown to underestimate the velocity data.

4. Numerical method

In our numerical simulations, the Navier-Stokes equations (2.1)-(2.3) are solved using a hybrid capturing-tracking scheme, originally proposed by Smiljanovski *et al.* (1997) for deflagration waves. When applying this scheme to the RMI, its key idea is to explicitly track the location and motion of the interface between the light and the heavy gas by the level set equation (2.6), whereas all other fluid phenomena like shocks and expansion fans are captured. The main advantage of this approach is that while the simplicity and robustness of standard capturing schemes can be retained, the interfacial processes are described with accuracy comparable to standard tracking schemes. In the following two sections, the hybrid capturing-tracking scheme is summarized briefly. The interested reader is referred to Smiljanovski *et al.* (1997) for a more detailed description.

4.1. *In-cell-reconstruction*

In finite volume schemes, the cell value of a conserved quantity $\boldsymbol{U}^{i,j}$ is defined as the volume average of that quantity,

$$\boldsymbol{U}^{i,j} = \frac{1}{V^{i,j}} \int_{V^{i,j}} \boldsymbol{U}(\boldsymbol{x}')d\boldsymbol{x}', \tag{4.1}$$

averaged over the cell volume $V^{i,j}$. Assuming piecewise constant distributions of $\boldsymbol{U}$ for each fluid within each cell, Eq. (4.1) reduces to

$$\boldsymbol{U}^{i,j} = \alpha \boldsymbol{U}_h^{i,j} + (1-\alpha)\boldsymbol{U}_l^{i,j}, \tag{4.2}$$

where α is the heavy gas cell volume fraction that can easily be calculated from the level set scalar G,

$$\alpha = \frac{1}{V^{i,j}} \int_{V^{i,j}} H(G(\boldsymbol{x}') - G_0)d\boldsymbol{x}', \tag{4.3}$$

with H the Heavyside function.

The key idea of the in-cell-reconstruction scheme is to reconstruct both $\boldsymbol{U}_h^{i,j}$ and $\boldsymbol{U}_l^{i,j}$ from $\boldsymbol{U}^{i,j}$, see Fig. 2, and to use only the reconstructed two states to calculate cell face fluxes in cells containing part of the interface. Combining the jump conditions of $\boldsymbol{U}$ across the interface, Eqs. (2.9) - (2.12), with (4.2) and Eqs. (4.3), the cell values $\boldsymbol{U}_h^{i,j}$ and $\boldsymbol{U}_l^{i,j}$ in each cell containing part of the interface can be reconstructed from $\boldsymbol{U}^{i,j}$.

4.2. *Cell update*

The numerical solution is evolved in time using an operator splitting technique (Strang 1967),

$$\boldsymbol{U}^{n+1} = \mathcal{C}^x_{\Delta t/2}\mathcal{C}^z_{\Delta t/2}\mathcal{D}_{\Delta t}\mathcal{C}^z_{\Delta t/2}\mathcal{C}^x_{\Delta t/2}\boldsymbol{U}^n, \tag{4.4}$$

where $\mathcal{C}$ denotes the convection operator, $\mathcal{D}$ the diffusion operator, $\boldsymbol{U}^n$ the cell volume averaged solution at time t^n, and $\boldsymbol{U}^{n+1}$ the cell volume averaged solution at $t^{n+1} =$

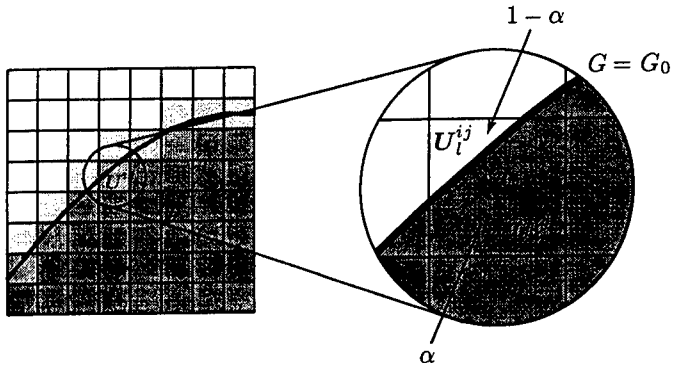


FIGURE 2. In-cell-reconstruction.

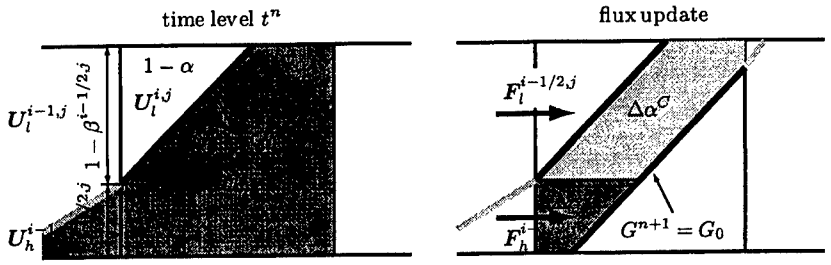


FIGURE 3. Flux update in cells containing part of the interface.

$t^n + \Delta t$. In order to calculate the correct update, all gradients in the individual operator steps must be calculated using only cell values of the same fluid type.

In the diffusion operator $\mathcal{D}$, we calculate all gradients using 2nd order central differences. The corresponding stencils across the interface thus involve the reconstructed cell values $\boldsymbol{U}_h$ respectively $\boldsymbol{U}_l$ plus one additional adjacent cell value on the opposite side of the interface. This cell has to be first transformed into the corresponding matching state using Eqs. (2.9)-(2.12) before the gradients are evaluated. In this operation, our method resembles the ghost fluid approach (Fedkiw *et al.* 1999).

Since the convection operator $\mathcal{C}$ is split into each spatial direction, we will only focus on the x-direction operator in the following. If a cell (i, j) and its directly adjacent neighbors do not contain part of the interface, $\boldsymbol{U}^{n,i,j}$ is advanced in time by

$$\boldsymbol{U}^{n+1,i,j} = \boldsymbol{U}^{n,i,j} + \frac{\Delta t}{\Delta x}\left(\boldsymbol{F}^{i-1/2,j} - \boldsymbol{F}^{i+1/2,j}\right). \tag{4.5}$$

In our numerical method we solve cell face Riemann problems using a 2nd order wave distribution algorithm due to LeVeque (1990) and formally recast the individual wave contributions in the form of cell face fluxes $\boldsymbol{F}^{i-1/2,j}$ and $\boldsymbol{F}^{i+1/2,j}$. However, special care must be taken, if (i, j) contains part of the interface at t^n or t^{n+1}, as shown in Fig. 3.

To ensure the correct flux calculation, individual cell face fluxes for both the heavy and the light gas must be calculated using only (reconstructed) quantities of the respective fluid,

$$\boldsymbol{F}_h^{i-1/2,j} = \boldsymbol{F}_h^{i-1/2,j}\left(\boldsymbol{U}_{h-}^{i-1/2,j}, \boldsymbol{U}_{h+}^{i-1/2,j}\right) \tag{4.6}$$

$$\boldsymbol{F}_l^{i-1/2,j} = \boldsymbol{F}_l^{i-1/2,j}\left(\boldsymbol{U}_{l-}^{i-1/2,j}, \boldsymbol{U}_{l+}^{i-1/2,j}\right). \tag{4.7}$$

Here, the subscripts $-$ and $+$ denote the left-hand side respectively right-hand side approximation of $\boldsymbol{U}_{h,l}^{i-1/2,j}$. Then, the average cell face flux $\boldsymbol{F}^{i-1/2,j}$ is

$$\boldsymbol{F}^{i-1/2,j} = \beta^{i-1/2,j}\boldsymbol{F}_h^{i-1/2,j} + (1-\beta^{i-1/2,j})\boldsymbol{F}_l^{i-1/2,j}\,, \tag{4.8}$$

with β the heavy gas cell face fraction, see Fig. 3. Note that because our convection operator is based upon a wave distribution scheme, $\boldsymbol{F}^{i-1/2,j}$ only takes those wave contributions into account that arise from the cell face Riemann problem. Since the interface itself constitutes a separate wave, its contribution to the change of $\boldsymbol{U}^{i,j}$ has to be taken into account additionally,

$$\begin{aligned}\Delta\boldsymbol{U}^{i,j} = {} & \Delta\alpha^C\left(\boldsymbol{U}_h^{i,j} - \boldsymbol{U}_l^{i,j}\right) + \\ & \Delta\alpha^L\left(\boldsymbol{U}_h^{i-1,j} - \boldsymbol{U}_l^{i-1,j}\right) + \Delta\alpha^R\left(\boldsymbol{U}_h^{i+1,j} - \boldsymbol{U}_l^{i+1,j}\right)\,.\end{aligned} \tag{4.9}$$

Here, $\Delta\alpha^C$ is the change of the heavy gas cell volume fraction due to the movement of the interface within the cell (i,j) itself, and $\Delta\alpha^L$ and $\Delta\alpha^R$ are the contributions due to movement from adjacent cells to the left respectively right, see Fig. 3. Note that Eq. (4.9) implies that the global conservation property of the numerical scheme is now dependent on the accuracy with which the individual $\Delta\alpha$ are calculated and hence relies on the accuracy of the level set method.

Finally, combining Eq. (4.8) and Eq. (4.9) yields the update for $\boldsymbol{U}^{i,j}$ in cells that contain part of the interface

$$\begin{aligned}\boldsymbol{U}^{n+1,i,j} = \boldsymbol{U}^{n,i,j} + \frac{\Delta t}{\Delta x}\ \Big\{ & \left(\beta^{i-1/2,j}\boldsymbol{F}_h^{i-1/2,j} + (1-\beta^{i-1/2,j})\boldsymbol{F}_l^{i-1/2,j}\right) - \\ & \left(\beta^{i+1/2,j}\boldsymbol{F}_h^{i+1/2,j} + (1-\beta^{i+1/2,j})\boldsymbol{F}_l^{i+1/2,j}\right) + \\ & \Delta\alpha^C\left(\boldsymbol{U}_h^{i,j} - \boldsymbol{U}_l^{i,j}\right) + \Delta\alpha^L\left(\boldsymbol{U}_h^{i-1,j} - \boldsymbol{U}_l^{i-1,j}\right) + \\ & \Delta\alpha^R\left(\boldsymbol{U}_h^{i+1,j} - \boldsymbol{U}_l^{i+1,j}\right)\Big\}\end{aligned} \tag{4.10}$$

One of the major advantages of using Eq. (4.10) is the fact that the CFL-condition can be based on the grid size Δx of the underlying grid, because cell updates are performed only on the cell volume averaged quantities.

5. Results

We present the numerical results of the RMI calculated for a shock Mach number of Ma $= 1.2$ and two different Atwood and Reynolds numbers. The fist case corresponds to the SF_6/Air experiment of Benjamin *et al.* (1993) with $A = 0.67$ and Re $= 11442$, whereas in the second case $A = 0.9$ and Re $= 6977$. The Reynolds numbers are calculated using the bubble velocity V in the laboratory frame of reference and the wave length λ. The initial interface of wave length $\lambda = 0.0375\,\mathrm{m}$ and amplitude $a_0 = 0.0024\,\mathrm{m}$ is located at $z = 0\,\mathrm{m}$. All simulations are performed in a $[-1.1\,\mathrm{m}, 0.3\,\mathrm{m}] \times [-0.01875\,\mathrm{m}, 0.01875\,\mathrm{m}]$ box resolved by 2352×63 equidistant cartesian grid cells.

Figure 4 depicts the temporal evolution of the interface shape for $A = 0.67$, whereas Fig. 5 shows the interface shapes for $A = 0.9$. In both cases, a spike of heavy gas is formed that penetrates ever further into the light gas. In the $A = 0.67$ case, the spike takes on the typical mushroom-like shape, whereas in the $A = 0.9$ the spike simply bulges

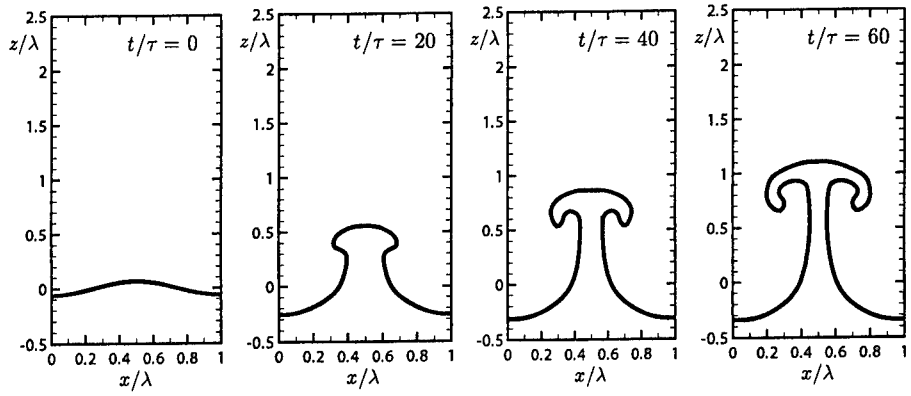


FIGURE 4. Temporal evolution of the interface for A=0.67.

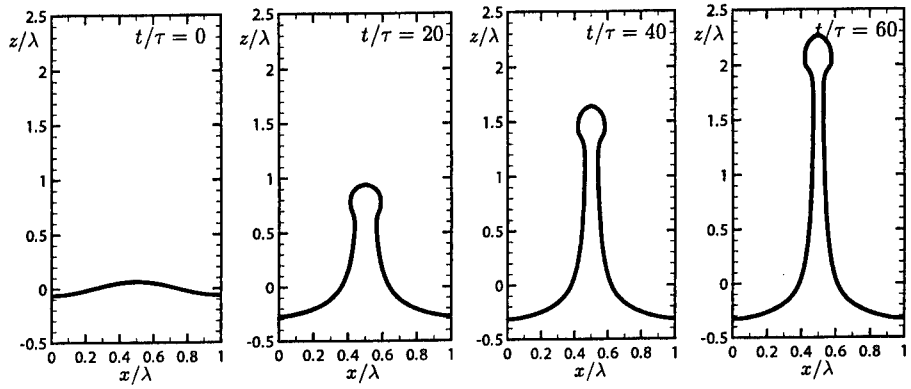


FIGURE 5. Temporal evolution of the interface for A=0.9.

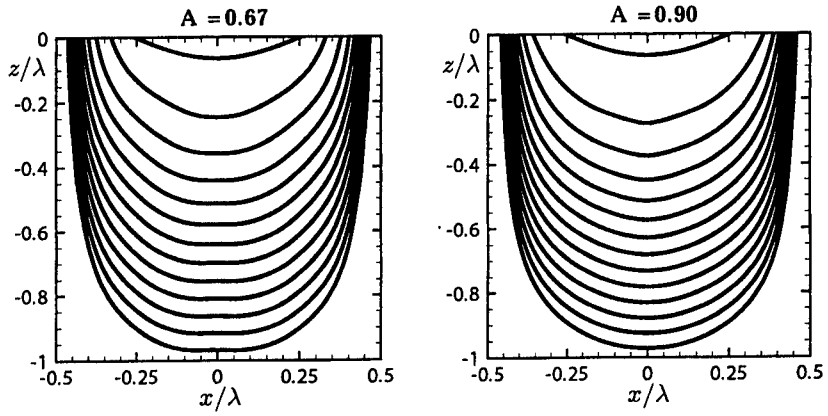


FIGURE 6. Shape of the bubble front for A=0.67 (left) and A=0.9 (right) plotted every $\Delta t/\tau = 10$. Each interface is shifted by $\Delta z = -0.05$.

at the end. This difference is most likely due to the employed numerical resolution that is not sufficient to resolve the apparently smaller scale spike mushroom structure in the $A = 0.9$ case.

Figure 6 shows the temporal evolution of the bubble front for both cases. The flattening

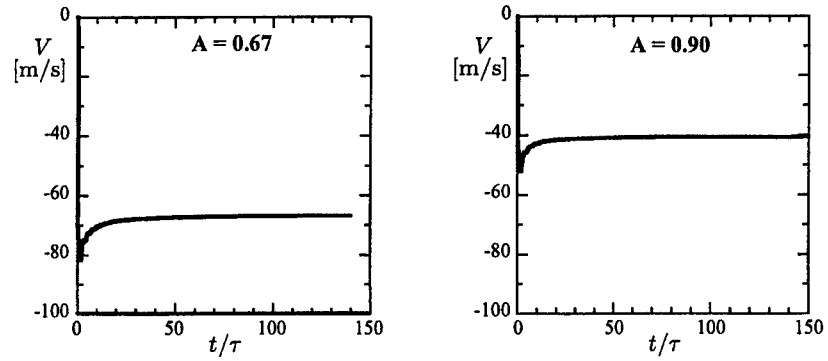


FIGURE 7. Bubble velocity V in the laboratory frame of reference for $A = 0.67$ (left) and $A = 0.9$ (right).

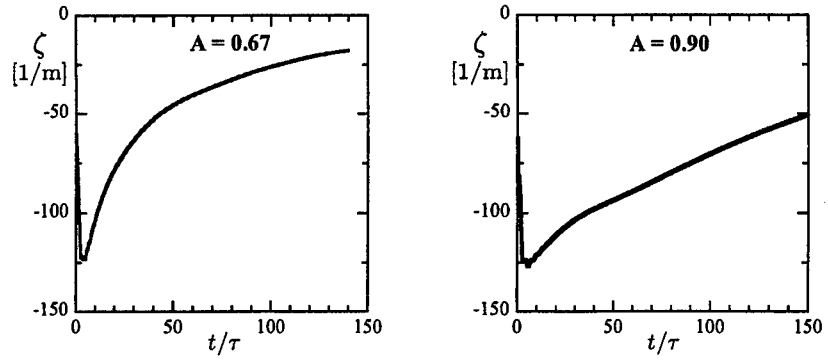


FIGURE 8. Bubble curvature ζ for $A = 0.67$ (left) and $A = 0.9$ (right).

of the bubble front that is predicted by non-local theory is clearly visible in both cases, but is more pronounced in the $A = 0.67$ case. Also, the $A = 0.67$ case exhibits some tiny oscillations of the bubble front at later times that are not visible in the $A = 0.9$ case.

The bubble velocity V in the laboratory frame of reference is depicted in Fig. 7. Initially being at rest, both bubbles are impulsively accelerated by the passing shock. As predicted by non-local theoretical analysis, the bubble velocity reaches a local maximum in the weakly non-linear regime and then asymptotically decelerates to a constant velocity. In the laboratory frame of reference the asymptotic bubble velocity is $V = 66.8$ m/s for $A = 0.67$ and $V = 40.7$ m/s for $A = 0.9$.

Figure 8 shows the evolution of the bubble curvature ζ. Here, ζ is calculated using a least squares fit of a circle of radius $1/|\zeta|$ to all intersection points of the interface with the cell face within $|x|/\lambda \leq 0.12$. As predicted by non-local theoretical analysis, in the linear regime, the bubble curvature changes linear with time. Then, in the weakly non-linear regime, the curvature reaches an extremum followed by an asymptotic flattening of the bubble, i.e. a decrease in curvature for both values of A.

Finally, Figure 9 depicts the calculated bubble velocity v as a function of the absolute bubble curvature $|\zeta|$. Initially, the bubble exhibits an abrupt acceleration that is due to the interaction with the passing shock, whereas the curvature remains roughly unchanged. In the linear regime, the bubble curvature increases with only gradual changes in the bubble velocity. This result is consistent with linear theory, Eqs. (3.3)-(3.5). In

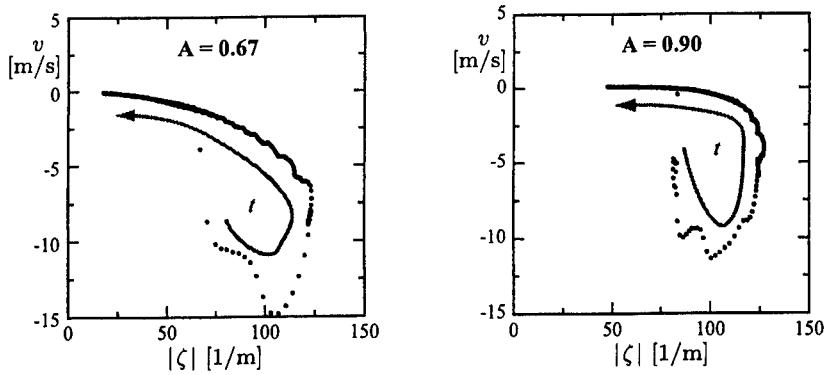


FIGURE 9. Bubble velocity v as function of absolute bubble curvature $|\zeta|$ for $A = 0.67$ (left) and $A = 0.9$ (right).

the weakly non-linear regime, the bubble velocity reaches a local maximum and then starts to decrease with almost constant curvature. Finally, the bubble curvature asymptotically tends to zero while the bubble continues to decelerate, as predicted by non-local theory. However, depending on the case, a slightly different bubble behavior is evident. For $A = 0.67$, the bubble both flattens and decelerates simultaneously. For $A = 0.9$, the bubble deceleration occurs prior to any significant decrease of ζ, thus leading to a flattening of the bubble front with only gradual changes in the bubble velocity.

In summary, these numerical results affirm the bubble behavior predicted by the non-local theory.

6. Conclusion

We performed systematic theoretical and numerical studies of the nonlinear large-scale coherent dynamics in the Richtmyer-Meshkov instability for fluids with contrast densities. Our simulations modeled the interface dynamics for compressible and viscous fluids. For a two-fluid system we observed that in the nonlinear regime of the instability the bubble velocity decays and its surface flattens, and the flattening is accompanied by slight oscillations. We found the theoretical solution for the system of conservation laws, describing the principal influence of the density ratio on the motion of the nonlinear bubble. The solution has no adjustable parameters, and shows that the flattening of the bubble front is a distinct property universal for all values of the density ratio. This property follows from the fact that the RM bubbles decelerate. The theoretical and numerical results validate each other, describe the new type of the bubble front evolution in RMI, and identify the bubble curvature as important and sensitive diagnostic parameter.

REFERENCES

ALON, U., HECHT, J., OFFER, D. & SHVARTS, D. 1995 Power laws and similarity of rayleigh-taylor and richtmyer-meshkov mixing fronts at all density ratios. *Phys. Rev. Lett.* **74**, 534–537.

BENJAMIN, R., BESNARD, D. & HAAS, J. 1993 Shock and reshock of an unstable interface. *Tech. Rep.* LANL Report No. LA-UR 92-1185. Los Alamos National Laboratory.

BONAZZA, R. & STURTEVANT, B. 1996 X-ray measurements of growth rates at a gas interface accelerated by shock waves. *Phys. Fluids* **8**, 2496–2512.

CHEBOTAREVA, E. I., ALESHIN, A. N., ZAYTSEV, S. G. & SERGEEV, S. V. 1999 Investigation of interaction between reflected shocks and growing perturbation on an interface. *Shock waves* **9** (2), 81–86.

DIMONTE, G. 2000 Spanwise homogeneous buoyancy-drag model for rayleightaylor mixing and experimental evaluation. *Phys. Plasmas* **7**, 2255–2269.

FEDKIW, R., ASLAM, T., MERRIMAN, B. & OSHER, S. 1999 A non-oscillatory Eulerian approach to interfaces in multimaterial flows (the ghost fluid method). *J. Comput. Phys.* **152**, 457–492.

GONCHAROV, V. N. 2002 Analytical model of nonlinear, single-mode, classical rayleigh-taylor instability at arbitrary atwood numbers. *Phys. Rev. Lett.* **88**.

HAAN, S. W. 1991 Weakly nonlinear hydrodynamic instabilities in inertial fusion. *Phys. Fluids B* **3** (8), 2349–2355.

HOLMES, R. L., DIMONTE, G., FRYXELL, B., GITTINGS, M. L., GROVE, J. W., SCHNEIDER, M., SHARP, D. H., VELKOVITCH, A. L., WEAVER, R. P. & ZHANG, Q. 1999 Richtmyermeshkov instability growth: experiment, simulation and theory. *J. Fluid Mech.* **389**, 55–79.

JACOBS, J. & SHEELEY, J. 1996 Experimental study of incompressible richtmyer-meshkov instability. *Phys. Fluids* **8**, 405–415.

KULL, F. 1991 *Physics Reports* .

LEVEQUE, R. 1990 *Numerical Methods for Conservation Laws*. Basel: Birkhäuser.

MATSUOKA, C., NISHIHARA, K. & FUKUDA, Y. 2003 Erratum: Nonlinear evolution of an interface in the richtmyer-meshkov instability [phys. rev. e 67, 036301 (2003)]. *Phys. Rev. E* **67** (029902), 1.

MESHKOV, E. 1969 *Sov. Fluid Dyn.* **4**, 101.

ORON, D., ALON, U., OFFER, D. & SHVARTS, D. 2001 Dimensionality dependence of the rayleightaylor and richtmyermeshkov instability late-time scaling laws. *Phys. Plasmas* **8**, 2883–2889.

OSHER, S. & SETHIAN, J. A. 1988 Fronts propagating with curvature-dependent speed: Algorithms based on Hamilton-Jacobi formulations. *J. Comput. Phys.* **79**, 12–49.

PAVLENKO, A. V., BAISHEV, A. I., KUCHERENKO, Y. A., LITVIN, A. T. & SOROKATYI, N. N. 2000 Experimental investigation into the interaction of the stationary shock wave with the turbulent layer. *Laser Part. Beams* **18** (2), 171–174.

RICHTMYER, R. 1960 *Commun. Pure & Appl. Math.* **13**, 297.

SCHNEIDER, M., DIMONTE, G. & REMINGTON, B. 1998 Large and small scale structure in rayleigh-taylor mixing. *Phys. Rev. Lett.* **80**, 3507–3510.

SMILJANOVSKI, V., MOSER, V. & KLEIN, R. 1997 A capture-tracking hybrid scheme for deflagration discontinuities. *Combust. Theory Modelling* **1**, 183–215.

STRANG, G. 1967 On the construction and comparison of difference schemes. *SIAM J. Num. Anal.* **5**, 506–517.

VANDENBOOMGAERDE, M., MUGLER, C. & GAUTHIER, S. 1998 Impulsive model for the richtmyer-meshkov instability. *Phys. Rev. E* **58**, 1874–1882.

VELIKOVICH, A. & DIMONTE, G. 1996 Nonlinear perturbation theory of the incompressible richtmyer-meshkov instability. *Phys. Rev. Lett.* **76**, 3112–3115.

WOUCHUK, J. 2001 Growth rate of the linear richtmyer-meshkov instability when a shock is reflected. *Phys. Rev. E* **63** (056303), 1–13.

Modeling primary breakup: A three-dimensional Eulerian level set/vortex sheet method for two-phase interface dynamics

By M. Herrmann

1. Motivation and objectives

Atomization processes play an important role in a wide variety of technical applications and natural phenomena, ranging from inkjet printers, gas turbines, direct injection IC-engines, and cryogenic rocket engines to ocean wave breaking and hydrothermal features. The atomization process of liquid jets and sheets is usually divided into two consecutive steps: the primary and the secondary breakup. During primary breakup, the liquid jet or sheet exhibits large scale coherent structures that interact with the gas-phase and break up into both large and small scale drops. During secondary breakup, these drops break up into ever smaller drops that finally may evaporate.

Usually, the atomization process occurs in a turbulent environment, involving a wide range of time and length scales. Given today's computational resources, the direct numerical simulation (DNS) of the turbulent breakup process as a whole, resolving all physical processes, is impossible, except for some very simple configurations. Instead, models describing the physics of the atomization process have to be employed.

Various models have already been developed for the secondary breakup process. There, it can be assumed that the characteristic length scale ℓ of the drops is much smaller than the available grid resolution Δx and that the liquid volume fraction in each grid cell Θ_l is small, see Fig. 1. Furthermore, assuming simple geometrical shapes of the individual drops, like spheres or ellipsoids, the interaction between these drops and the surrounding fluid can be taken into account. Statistical models describing the secondary breakup process in turbulent environments can thus be derived (O'Rourke 1981; O'Rourke & Amsden 1987; Reitz 1987; Reitz & Diwakar 1987; Tanner 1997).

However, the above assumptions do not hold true for the primary breakup process. Here, the turbulent liquid fluid interacts with the surrounding turbulent gas-phase on scales larger than Δx, resulting in highly complex interface dynamics and individual grid cells that can be fully immersed in the liquid phase, compare Fig. 1. An explicit treatment of the phase interface and its dynamics is therefore required. To this end, we propose to follow in essence a Large Eddy Simulation (LES) type approach: all interface dynamics and physical processes occurring on scales larger than the available grid resolution Δx shall be fully resolved and all dynamics and processes occurring on subgrid scales shall be modeled. The resulting approach is called Large Surface Structure (LSS) model.

In order to develop such a LSS model for the turbulent primary breakup process, one potential approach is to start off from a fully resolved description of the interface dynamics using the Navier-Stokes equations and include an additional source term in the momentum equation due to surface tension forces (Brackbill *et al.* 1992). In order to track the location, motion, and topology of the phase interface, the Navier-Stokes equations are then coupled to one of various possible tracking methods, for example marker particles

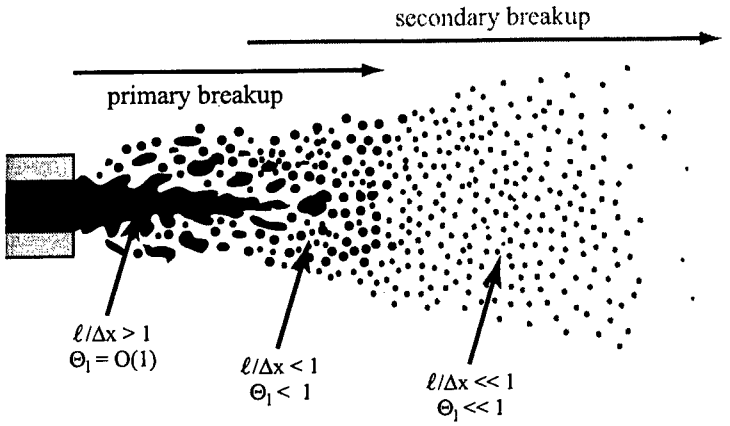


FIGURE 1. Breakup of a liquid jet.

(Brackbill *et al.* 1988; Rider & Kothe 1995; Unverdi & Tryggvason 1992), the Volume-of-Fluid method (Noh & Woodward 1976; Kothe & Rider 1994; Gueyffier *et al.* 1999), or the level set method (Osher & Sethian 1988; Sussman *et al.* 1994, 1998). Then, introducing ensemble averaging or spatial filtering results in unclosed terms that require modeling (Brocchini & Peregrine 2001*a*,*b*). Unfortunately, the derivation of such closure models is not straightforward and, hence, has not been achieved yet. This is in part due to the fact that, with the exception of the surface tension term, all other physical processes occurring at the phase interface itself, like for example stretching, are not described by explicit source terms. Instead, they are hidden within the interdependence between the Navier-Stokes equations and the respective interface tracking equation. Thus, a formulation containing the source terms explicitly could greatly facilitate any attempt to derive the appropriate closure models.

To this end, a novel three-dimensional Eulerian level set/vortex sheet method is proposed. Its advantage is the fact that it contains explicit source terms for each individual physical process that occurs at the phase interface. It thus constitutes a promising framework for the derivation of the LSS subgrid closure models.

This paper is divided into four parts. First, the level set/vortex sheet method for three-dimensional two-phase interface dynamics is presented. Second, the LSS model for the primary breakup of turbulent liquid jets and sheets is outlined and all terms requiring subgrid modeling are identified. Then, preliminary three-dimensional results of the level set/vortex sheet method are presented and discussed. Finally, conclusions are drawn and an outlook to future work is given.

2. The level set/vortex sheet method

The aim of the level set/vortex sheet method is to describe the dynamics of the phase interface Γ between two inviscid, incompressible fluids 1 and 2, as shown in Fig. 2. In this case, the velocity $\boldsymbol{u}_i$ on either side i of the interface Γ is determined by the incompressible Euler equations, given here in dimensionless form,

$$\nabla \cdot \boldsymbol{u}_i = 0\,, \tag{2.1}$$

$$\frac{\partial \boldsymbol{u}_i}{\partial t} + (\boldsymbol{u}_i \cdot \nabla)\,\boldsymbol{u}_i = -\frac{1}{\rho_i}\nabla p\,, \tag{2.2}$$

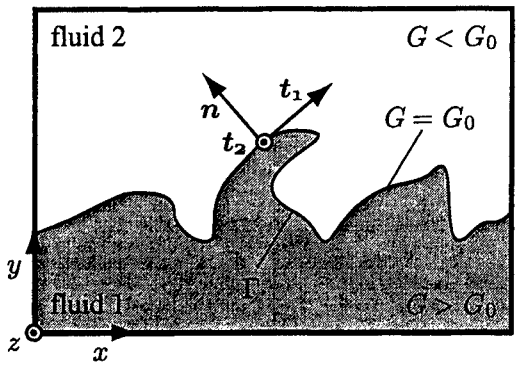


FIGURE 2. Phase interface definition.

subjected to the boundary conditions at the interface Γ,

$$[(\boldsymbol{u}_1 - \boldsymbol{u}_2) \cdot \boldsymbol{n}]\Big|_\Gamma = 0 \tag{2.3}$$

$$[\boldsymbol{n} \times (\boldsymbol{u}_2 - \boldsymbol{u}_1)]\Big|_\Gamma = \boldsymbol{\eta} \tag{2.4}$$

$$[p_2 - p_1]\Big|_\Gamma = \frac{1}{\mathrm{We}}\kappa \tag{2.5}$$

and at infinity,

$$\lim_{y \to \pm\infty} \boldsymbol{u}_i = \pm \boldsymbol{u}_\infty \,. \tag{2.6}$$

Here, $\boldsymbol{n}$ is the interface normal vector, $\boldsymbol{\eta}$ is the vortex sheet strength, and κ is the local curvature of Γ. The Weber number is defined as

$$\mathrm{We} = \rho_{\mathrm{ref}} u_{\mathrm{ref}}^2 / \Sigma L_{\mathrm{ref}} \,, \tag{2.7}$$

where Σ is the surface tension coefficient and ρ_{ref}, u_{ref}, and L_{ref} are the reference density, velocity, and length, respectively. An interface subjected to the above boundary conditions is called a vortex sheet (Saffman & Baker 1979).

The partial differential equation describing the evolution of the vortex sheet strength $\boldsymbol{\eta}$ can be derived by combining the Euler equations, Eqs. (2.1) and (2.2), with the boundary conditions at the interface, Eqs. (2.3)-(2.5), resulting in (Pozrikidis 2000)

$$\begin{aligned}\frac{\partial \boldsymbol{\eta}}{\partial t} + \boldsymbol{u} \cdot \nabla \boldsymbol{\eta} = &-\boldsymbol{n} \times [(\boldsymbol{\eta} \times \boldsymbol{n}) \cdot \nabla \boldsymbol{u}] + \boldsymbol{n}\,[(\nabla \boldsymbol{u} \cdot \boldsymbol{n}) \cdot \boldsymbol{\eta}] \\ &+ \frac{2(A+1)}{\mathrm{We}} (\boldsymbol{n} \times \nabla \kappa) + 2A \boldsymbol{n} \times \boldsymbol{a} \,. \end{aligned} \tag{2.8}$$

Here, $A = (\rho_1 - \rho_2)/(\rho_1 + \rho_2)$ is the Atwood number and $\boldsymbol{a}$ is the average acceleration of fluid 1 and fluid 2 at the interface. The major advantage of Eq. (2.8), as compared to a formulation based on the Euler equations, is the fact that Eq. (2.8) contains explicit local individual source terms on the right-hand side describing the physical processes at the interface. These are, from left to right, two stretching terms, a surface tension term $\boldsymbol{T}_\sigma$, and a density difference term.

In addition to the evolution of the local vortex sheet strength, Eq. (2.8), the location and motion of the phase interface itself has to be known. To this end, vortex sheets are typically solved by a boundary integral method within a Lagrangian framework where the phase interface is tracked by marker particles (Baker *et al.* 1982; Pullin 1982; Hou

et al. 1997, 2001; Rangel & Sirignano 1988). Marker particles allow for highly accurate tracking of the phase interface motion in a DNS. However, the introduction of ensemble averaging and spatial filtering of the interface topology is not straightforward and hence a strategy for the derivation of appropriate LSS subgrid closure models is not directly apparent.

Level sets, on the other hand, have been successfully applied to the derivation of closure models in the field of premixed turbulent combustion (Peters 1999, 2000). Thus, instead of using marker particles to describe the location and motion of the phase interface, here, the interface is represented by an iso-surface of the level set scalar field $G(\boldsymbol{x},t)$, as shown in Fig. 2. Setting

$$G(\boldsymbol{x},t)|_\Gamma = G_0 = \text{const}\,, \tag{2.9}$$

$G(\boldsymbol{x},t) > G_0$ in fluid 1, and $G(\boldsymbol{x},t) < G_0$ in fluid 2, an evolution equation for the scalar G can be derived by simply differentiating Eq. (2.9) with respect to time,

$$\frac{\partial G}{\partial t} + \boldsymbol{u}\cdot\nabla G = 0\,. \tag{2.10}$$

This equation is called the level set equation (Osher & Sethian 1988). Using the level set scalar, geometrical properties of the interface, like its normal vector and curvature, can be easily expressed as

$$\boldsymbol{n} = \frac{\nabla G}{|\nabla G|}\,, \quad \kappa = \nabla\cdot\boldsymbol{n}\,. \tag{2.11}$$

Strictly speaking, Eqs. (2.8) and (2.10) are valid only at the location of the interface itself. However, to facilitate the numerical solution of both equations in the whole computational domain, $\boldsymbol{\eta}$ is set constant in the interface normal direction,

$$\nabla\boldsymbol{\eta}\cdot\nabla G = \boldsymbol{0}\,, \tag{2.12}$$

and G is chosen to be a distance function away from the interface,

$$|\nabla G|\Big|_{G\neq G_0} = 1\,. \tag{2.13}$$

Equations (2.8) and (2.10) are coupled by the self-induced velocity $\boldsymbol{u}$ of the vortex sheet. To calculate $\boldsymbol{u}$, the vector potential $\boldsymbol{\psi}$ is introduced,

$$\Delta\boldsymbol{\psi} = \boldsymbol{\omega}\,. \tag{2.14}$$

Here, the vorticity vector $\boldsymbol{\omega}$ is calculated following a vortex-in-cell type approach (Christiansen 1973; Cottet & Koumoutsakos 2000)

$$\boldsymbol{\omega}(\boldsymbol{x}) = \int_V \boldsymbol{\eta}(\boldsymbol{x}')\delta(\boldsymbol{x}-\boldsymbol{x}')\delta\left(G(\boldsymbol{x}')-G_0\right)|\nabla G(\boldsymbol{x}')|d\boldsymbol{x}'\,, \tag{2.15}$$

where δ is the delta-function. Then, $\boldsymbol{u}$ can be calculated from

$$\boldsymbol{u}(\boldsymbol{x}) = \int_V \delta(\boldsymbol{x}-\boldsymbol{x}')\left(\nabla\times\boldsymbol{\psi}\right)d\boldsymbol{x}'\,. \tag{2.16}$$

In summary, Eqs. (2.8), (2.10), and (2.14) - (2.16) describe the three-dimensional two-phase interface dynamics and constitute the level set/vortex sheet method.

2.1. *Numerical methods*

Numerically, Eqs. (2.8) and (2.10) are solved in a narrow band (Peng *et al.* 1999) by a third-order WENO scheme (Jiang & Peng 2000) using a third-order TVD Runge-

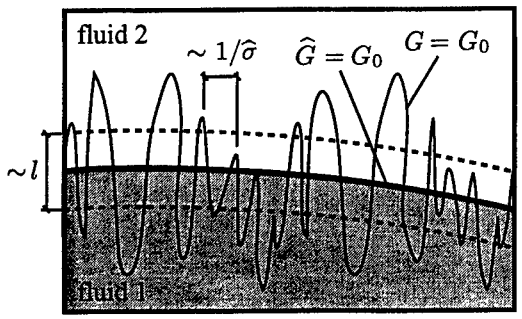


FIGURE 3. LSS interface definitions.

Kutta time discretization (Shu & Osher 1989). The redistribution of η (2.12) is solved by a Fast Marching Method (Sethian 1996; Adalsteinsson & Sethian 1999), whereas the reinitialization of G (2.13) is solved by an iterative procedure (Sussman *et al.* 1994; Peng *et al.* 1999). The interested reader is referred to Herrmann (2002) for a detailed description of the numerical methods employed in the level set/vortex sheet method.

3. The LSS model for turbulent primary breakup

The basic idea of the LSS model is to split the treatment of the primary breakup process into two parts. All phase interface dynamics occurring on scales larger than the local grid size are explicitly resolved and tracked by a level set approach, whereas interface dynamics occurring on subgrid scales are described by an appropriate subgrid model. Furthermore, the LSS subgrid model has to separate out all broken off subgrid scale liquid drops and transfer them to a secondary breakup model.

The level set equation describing the interface location and motion on the resolved scales can be derived by first introducing appropriate interface based filters (Oberlack *et al.* 2001) into the level set equation (2.10), see Fig. 3,

$$\frac{\partial \widehat{G}}{\partial t} + \widehat{\boldsymbol{u}} \cdot \nabla \widehat{G} = 0\,. \tag{3.1}$$

Here, $\widehat{\cdot}$ denotes quantities on the resolved (filter) scale. Furthermore, the mass transfer rate $\dot{m}_p$ into the secondary breakup model has to be taken into account,

$$\dot{m}_p = \rho_1 s_p \widehat{A}_{G_0} = \frac{4}{3}\pi\rho_1 \frac{\partial}{\partial t}\int_0^{\Delta x} P(D) D^3 dD\,, \tag{3.2}$$

where s_p is the subgrid primary breakup velocity, $\widehat{A}_{G_0}$ is the local surface area of the resolved interface, and $P(D)$ is the droplet diameter number distribution,

$$\int_0^{\infty} P(D) = N\,, \tag{3.3}$$

where N is the total number of drops. Then, the resolved scale level set equation reads

$$\frac{\partial \widehat{G}}{\partial t} + (\widehat{\boldsymbol{u}} + s_p \widehat{\boldsymbol{n}}) \cdot \nabla \widehat{G} = 0\,, \tag{3.4}$$

where $\widehat{\boldsymbol{n}}$ is the normal vector of the resolved scale interface,

$$\widehat{\boldsymbol{n}} = \frac{\nabla \widehat{G}}{|\nabla \widehat{G}|} \,. \tag{3.5}$$

To describe the phase interface dynamics on the resolved scale, their effect on the flow field has to be taken into account by an additional source term $\boldsymbol{T}$ in the momentum equation,

$$\boldsymbol{T} = \Sigma \widehat{\kappa} \delta (\widehat{G} - G_0) \widehat{\boldsymbol{n}} + \boldsymbol{T}_{\mathrm{SGS}} \,. \tag{3.6}$$

Here, the first term on the right-hand side describes the effect of surface tension forces due to the local curvature $\widehat{\kappa}$ of the resolved scale interface, whereas the second term, $\boldsymbol{T}_{\mathrm{SGS}}$, accounts for the effect of the subgrid scale surface tension forces on the resolved scale flow field.

Thus, the yet unclosed subgrid terms of the LSS model requiring modeling are the subgrid primary breakup velocity s_p, the droplet diameter number distribution $P(D)$, and the subgrid scale surface tension effect $\boldsymbol{T}_{\mathrm{SGS}}$. As previously indicated, these subgrid terms are to be derived from the level set/vortex sheet method. Performing DNS of the primary breakup of liquid surfaces and sheets in turbulent environments will help to identify characteristic regimes of the turbulent primary breakup and their dominant physical processes. These can then be quantified using the explicit source terms in the η-equation (2.8), thus providing guidelines for the derivation of appropriate LSS subgrid models.

4. Results

In order to both validate the three-dimensional level set/vortex sheet method and to demonstrate its ability to perform DNS of the primary breakup process, the results of two different cases are presented. First, the calculated oscillation periods of liquid columns and spheres are compared to theoretical results. Then, the breakups of a randomly perturbed liquid surface and sheet are presented.

4.1. *Oscillating columns and spheres*

To validate the proposed level set/vortex sheet method, the calculated oscillation periods T of liquid columns and spheres of mean radius $R = 0.25$, center $\boldsymbol{x}_c = (0.5, 0.5, 0.5)$, amplitude $\epsilon = 0.05R$, and Atwood number $A = 0$ are compared to theoretical results (Lamb 1945). The initial vortex sheet strength in both cases is set to

$$\boldsymbol{\eta}(\boldsymbol{x}, t = 0) = \boldsymbol{0} \,. \tag{4.1}$$

All calculations are performed in a unit sized box resolved by an equidistant cartesian grid of 128×128 and $128 \times 128 \times 128$ nodes, respectively.

Figure 4 shows the distribution of the surface tension term $\boldsymbol{T}_\sigma$ of the $\boldsymbol{\eta}$-equation (2.8) in the x-, y-, and z-direction,

$$\boldsymbol{T}_\sigma = \frac{2(A+1)}{\mathrm{We}} (\boldsymbol{n} \times \nabla \kappa) \,, \tag{4.2}$$

for the oscillating sphere of mode number $n = 5$ and Weber number $\mathrm{We} = 10$ calculated at $t = 0$. As the shape of the sphere indicates, $\boldsymbol{T}_\sigma$ in the x-direction is a factor of roughly four higher than $\boldsymbol{T}_\sigma$ in the other two directions, leading to the predominant oscillation in the y-z-plane.

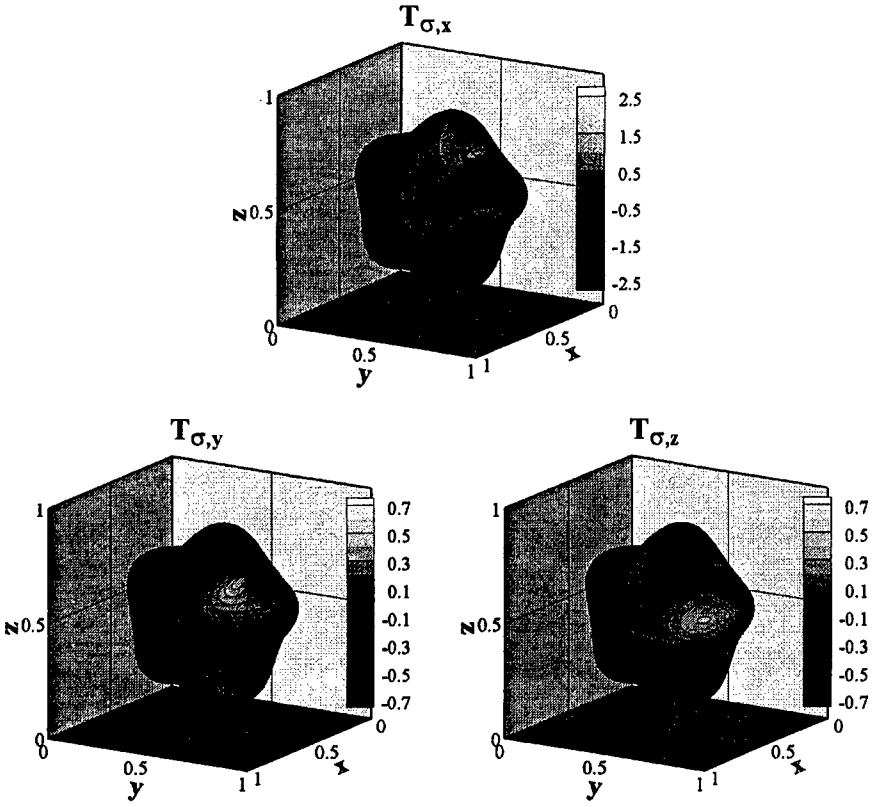


FIGURE 4. Distribution of the surface tension term $\boldsymbol{T}_\sigma$ in the x-direction (top), y-direction (left), and z-direction (right) for the mode $n = 5$ oscillating sphere at $t = 0$ and We $= 10$.

Figure 5 depicts the comparison of the oscillation period for the oscillating columns on the left-hand side and the oscillating spheres on the right-hand side for two different Weber numbers. As can be clearly seen, agreement between simulation and theory is very good.

4.2. *Liquid surface and sheet breakup*

To demonstrate the capability of the proposed level set/vortex sheet method to simulate the primary breakup process, the temporal evolution of both a randomly perturbed liquid surface and sheet are simulated. In the case of the liquid surface, the on average flat interface located at $z = 0$ is perturbed in the z-direction by a Fourier series of 64 sinusoidal waves in both the x- and y-direction with random amplitude $0 < \epsilon < 0.01$ and random phase shift. In the case of the liquid sheet, the two on average flat interfaces are located at $z = -B/2$ and $z = +B/2$ and are again perturbed by two Fourier series of 64 sinusoidal waves. The thickness of the liquid sheet is set to $B = 0.1$.

The initial vortex sheet strength for the liquid surface is set to

$$\eta(\boldsymbol{x}, t = 0) = (-1, 0, 0) \tag{4.3}$$

and to

$$\eta(\boldsymbol{x}, t = 0) = \begin{cases} (-1, 0, 0) & : \quad z > 0 \\ (\ 1, 0, 0) & : \quad z \leq 0\,, \end{cases} \tag{4.4}$$

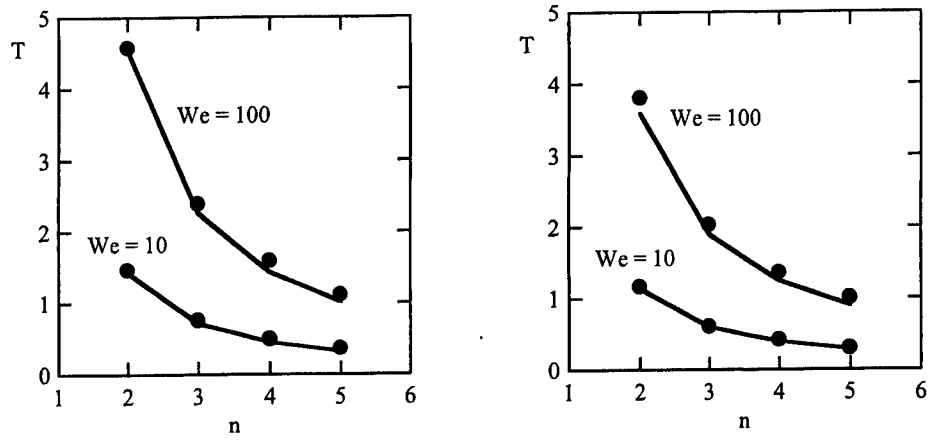


FIGURE 5. Oscillation period T of liquid columns (left) and spheres (right) as a function of mode number n for varying Weber numbers We. Lines denote theoretical and symbols computational results.

in the liquid sheet case. Both, the surface and the sheet simulation were performed in a x- and y-direction periodic box of size $[0,1] \times [0,1] \times [-1,1]$ resolved by a cartesian grid of $64 \times 64 \times 128$ equidistant nodes. In both simulations, the Atwood number is $A = 0$. The Weber number in the surface simulation is $\mathrm{We} = 500$ and the Weber number in the sheet simulation based on the sheet thickness is $\mathrm{We}_B = 100$.

As depicted in Fig. 6, the surface shows an initial growth of two-dimensional Kelvin-Helmholtz instabilities ($t = 1$). These continue to grow ($t = 3$) and form three-dimensional structures ($t = 5$) resulting in elongated fingers ($t = 6.5$) that finally initiate breakup ($t = 8.0$).

The liquid sheet, depicted in Fig. 7, also exhibits the initial formation of two-dimensional Kelvin-Helmholtz instabilities ($t = 1$) that continue to grow ($t = 3$) until the liquid film gets too thin and ruptures ($t = 5$). Individual fingers are formed that extend mostly in the transverse direction ($t = 8$) and continue to break up into individual drops of varying sizes ($t = 12$).

5. Conclusions and future work

A Eulerian level set/vortex sheet method has been presented that allows for the three-dimensional calculation of the phase interface dynamics between two inviscid and incompressible fluids. Results obtained with the proposed method for oscillating columns and spheres show very good agreement with theoretical predictions. Furthermore, the applicability of the method to the primary breakup process has been demonstrated by simulations of the breakup of both a liquid surface and a liquid sheet.

In addition, the LSS model for turbulent primary breakup has been outlined, and all terms requiring subgrid modeling have been identified. The proposed level set/vortex sheet method has the advantage that it allows for the detailed study of each individual physical process occurring at the phase interface. It thus provides a promising framework for the derivation of the LSS subgrid models.

Future work will focus on including the effect of non-zero Atwood numbers and on coupling of the level set/vortex sheet method to an outside turbulent flow field. Also, the level set/vortex sheet method will be parallelized making use of the new domain decom-

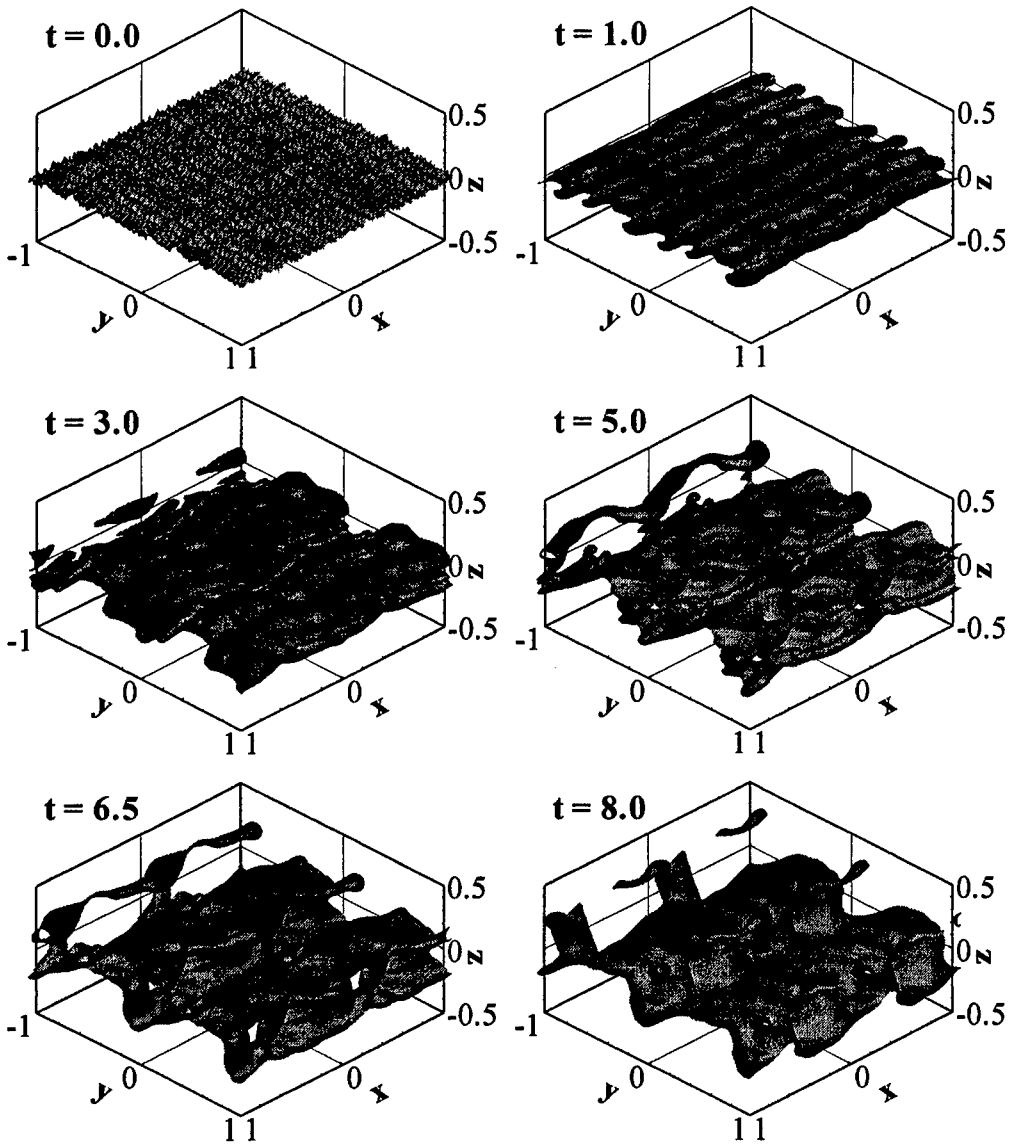


FIGURE 6. Temporal evolution of the three-dimensional liquid surface breakup, $A = 0$, $\mathrm{We} = 500$.

position parallelization of the Fast Marching Method presented in Herrmann (2003). This will allow for efficient DNS of the primary breakup process to help identify the different regimes of turbulent primary breakup and their dominant physical processes, facilitating the derivation of the LSS subgrid models. Finally, combining the LSS model to spray models describing the secondary breakup will allow for the first LES of the turbulent atomization process as a whole.

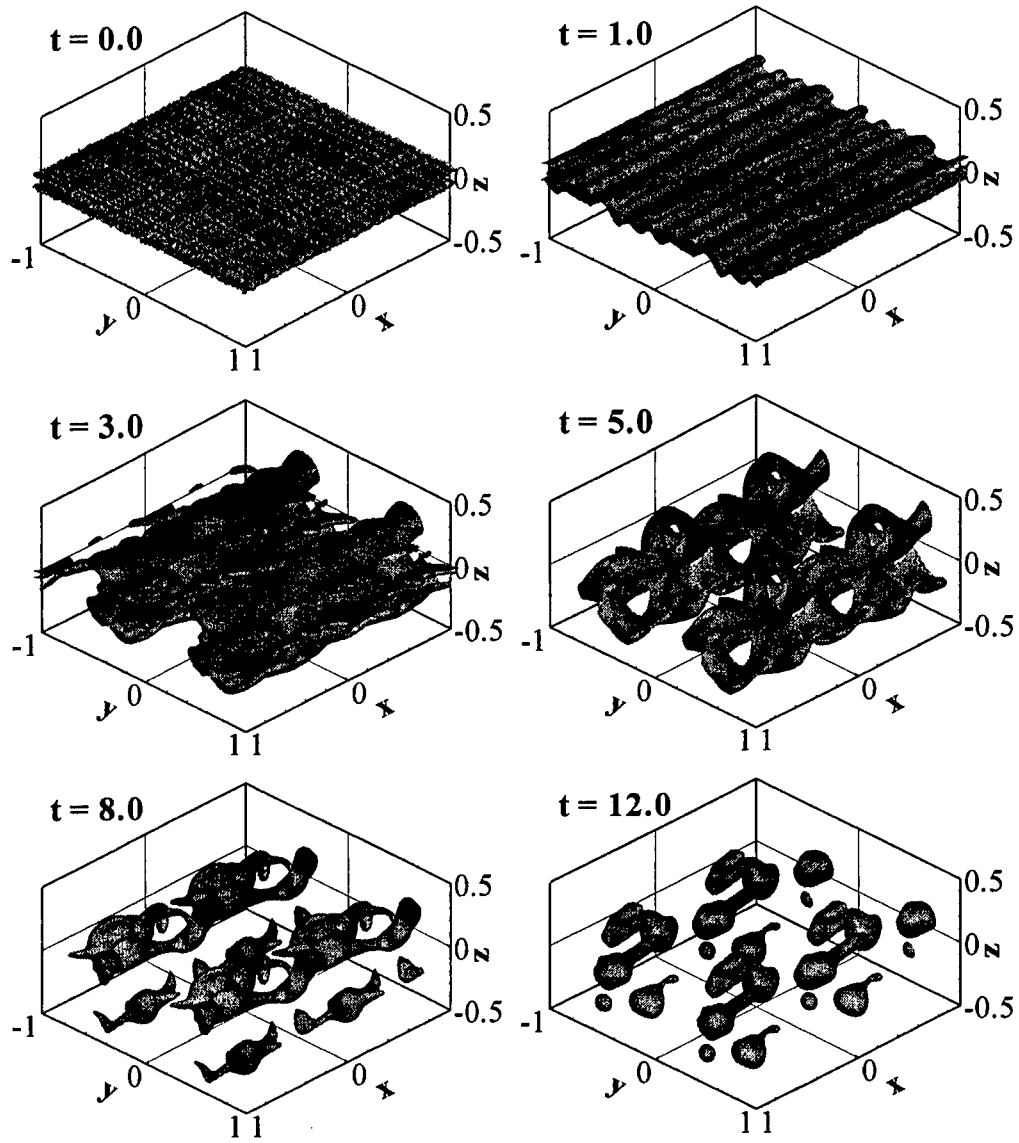


FIGURE 7. Temporal evolution of the three-dimensional liquid sheet breakup, $A = 0$, $We_B = 100$.

Acknowledgments

The support of the German Research Foundation (DFG) is gratefully acknowledged.

REFERENCES

ADALSTEINSSON, D. & SETHIAN, J. A. 1999 The fast construction of extension velocities in level set methods. *J. Comput. Phys.* **148**, 2–22.

BAKER, G. R., MEIRON, D. I. & ORSZAG, S. A. 1982 Generalized vortex methods for free-surface flow problems. *J. Fluid Mech.* **123**, 477–501.

BRACKBILL, J. U., KOTHE, D. B. & RUPPEL, H. M. 1988 FLIP: A low dissipation, particle-in-cell method for fluid flow. *Comput. Phys. Commun.* **48**, 25–38.

BRACKBILL, J. U., KOTHE, D. B. & ZEMACH, C. 1992 A continuum method for modeling surface tension. *J. Comput. Phys.* **100**, 335–354.

BROCCHINI, M. & PEREGRINE, D. H. 2001*a* The dynamics of strong turbulence at free surfaces. Part 2. Free-surface boundary conditions. *J. Fluid Mech.* **449**, 255–290.

BROCCHINI, M. & PEREGRINE, D. H. 2001*b* The dynamics of turbulent free surfaces. Part 1. Description. *J. Fluid Mech.* **449**, 225–254.

CHRISTIANSEN, J. P. 1973 Numerical simulation of hydrodynamics by the method of point vortices. *J. Comput. Phys.* **13**, 363–379.

COTTET, G.-H. & KOUMOUTSAKOS, P. D. 2000 *Vortex Methods*. Cambridge: Cambridge University Press.

GUEYFFIER, D., LI, J., NADIM, A., SCARDOVELLI, S. & ZALESKI, S. 1999 Volume of Fluid interface tracking with smoothed surface stress methods for three-dimensional flows. *J. Comput. Phys.* **152**, 423–456.

HERRMANN, M. 2002 An Eulerian level set/vortex sheet method for two-phase interface dynamics. In *Annual Research Briefs* (ed. P. Bradshaw), pp. 103–114. Stanford: Center for Turbulence Research.

HERRMANN, M. 2003 A domain decomposition parallelization of the Fast Marching Method. In *Annual Research Briefs*. Stanford: Center for Turbulence Research.

HOU, T. Y., LOWENGRUB, J. S. & SHELLEY, M. J. 1997 The long-time motion of vortex sheets with surface tension. *Phys. Fluids* **9** (7), 1933–1954.

HOU, T. Y., LOWENGRUB, J. S. & SHELLEY, M. J. 2001 Boundary integral methods for multicomponent fluids and multiphase materials. *J. Comput. Phys.* **169**, 302–362.

JIANG, G.-S. & PENG, D. 2000 Weighted ENO schemes for Hamilton-Jacobi equations. *SIAM J. Sci. Comput.* **21** (6), 2126–2143.

KOTHE, D. B. & RIDER, W. J. 1994 Comments on modelling interfacial flows with Volume-of-Fluid methods. *Tech. Rep.* LA-UR-3384. Los Alamos National Laboratory.

LAMB, H. 1945 *Hydrodynamics*. New York: Dover Publications.

NOH, W. F. & WOODWARD, P. 1976 SLIC (Simple Line Interface Calculation). In *Lecture Notes in Physics Vol. 59, Proceedings of the Fifth International Conference on Numerical Methods in Fluid Dynamics* (ed. A. I. V. D. Vooren & P. J. Zandenbergen), pp. 330–340. Berlin: Springer.

OBERLACK, M., WENZEL, H. & PETERS, N. 2001 On symmetries and averaging of the G-equation for premixed combustion. *Combust. Theory Modelling* **5**, 363–383.

O'ROURKE, P. J. 1981 Collective drop effects on vaporizing liquid sprays. PhD thesis, Princeton University, 1532-T.

O'ROURKE, P. J. & AMSDEN, A. A. 1987 The TAB method for numerical calculations of spray droplet breakup. *Tech. Rep.* 872089. SAE Technical Paper.

OSHER, S. & SETHIAN, J. A. 1988 Fronts propagating with curvature-dependent speed: Algorithms based on Hamilton-Jacobi formulations. *J. Comput. Phys.* **79**, 12–49.

PENG, D., MERRIMAN, B., OSHER, S., ZHAO, H. & KANG, M. 1999 A PDE-based fast local level set method. *J. Comput. Phys.* **155**, 410–438.

PETERS, N. 1999 The turbulent burning velocity for large-scale and small-scale turbulence. *J. Fluid Mech.* **384**, 107–132.

PETERS, N. 2000 *Turbulent Combustion*. Cambridge, UK: Cambridge University Press.

POZRIKIDIS, C. 2000 Theoretical and computational aspects of the self-induced motion of three-dimensional vortex sheets. *J. Fluid Mech,* **425**, 335–366.

PULLIN, D. I. 1982 Numerical studies of surface-tension effects in nonlinear Kelvin-Helmholtz and Rayleigh-Taylor instability. *J. Fluid Mech.* **119**, 507–532.

RANGEL, R. H. & SIRIGNANO, W. A. 1988 Nonlinear growth of Kelvin-Helmholtz instability: Effect of surface tension and density ratio. *Phys. Fluids* **31** (7), 1845–1855.

REITZ, R. D. 1987 Modeling atomization processes in high-pressure vaporizing sprays. *Atom. Spray Tech.* **3**, 309–337.

REITZ, R. D. & DIWAKAR, R. 1987 Structure of high pressure fuel sprays. *Tech. Rep.* 870598. SAE Technical Paper.

RIDER, W. J. & KOTHE, D. B. 1995 Stretching and tearing interface tracking methods. AIAA Paper 95-1717.

SAFFMAN, P. G. & BAKER, G. R. 1979 Vortex interactions. *Annu. Rev. Fluid Mech.* **11**, 95.

SETHIAN, J. A. 1996 A fast marching level set method for monotonically advancing fronts. *Proc. Natl. Acad. Sci. USA* **93**, 1591–1595.

SHU, C.-W. & OSHER, S. 1989 Efficient implementation of essentially non-oscillatory shock-capturing schemes. *J. Comput. Phys.* **77**, 439–471.

SUSSMAN, M., FATEMI, E., SMEREKA, P. & OSHER, S. 1998 An improved level set method for incompressible two-phase flows. *Comp. Fluids* **27** (5-6), 663–680.

SUSSMAN, M., SMEREKA, P. & OSHER, S. 1994 A level set method for computing solutions to incompressible two-phase flow. *J. Comput. Phys.* **119**, 146.

TANNER, F. X. 1997 Liquid jet atomization and droplet breakup modeling of non-evaporating Diesel fuel sprays. *SAE Transactions: J. of Engines* **106** (3), 127–140.

UNVERDI, S. O. & TRYGGVASON, G. 1992 A front-tracking method for viscous, incompressible, multi-fluid flows. *J. Comput. Phys.* **100**, 25–37.

Fragmentation under the scaling symmetry and turbulent cascade with intermittency

By M. Gorokhovski †

1. Motivation and objectives

Fragmentation plays an important role in a variety of physical, chemical, and geological processes. Examples include atomization in sprays, crushing of rocks, explosion and impact of solids, polymer degradation, etc. Although each individual action of fragmentation is a complex process, the number of these elementary actions is large. It is natural to abstract a simple 'effective' scenario of fragmentation and to represent its essential features. One of the models is the fragmentation under the scaling symmetry: each breakup action reduces the typical length of fragments, $r \Rightarrow \alpha r$, by an independent random multiplier $\alpha\,(0 < \alpha < 1)$, which is governed by the fragmentation intensity spectrum $q(\alpha)$, $\int_0^1 q(\alpha)d\alpha = 1$. This scenario has been proposed by Kolmogorov (1941), when he considered the breakup of solid carbon particle. Describing the breakup as a random discrete process, Kolmogorov stated that at latest times, such a process leads to the log-normal distribution. In Gorokhovski & Saveliev (2003), the fragmentation under the scaling symmetry has been reviewed as a continuous evolution process with new features established.

The objective of this paper is twofold. First, the paper synthesizes and completes theoretical part of Gorokhovski & Saveliev (2003). Second, the paper shows a new application of the fragmentation theory under the scale invariance. This application concerns the turbulent cascade with intermittency. We formulate here a model describing the evolution of the velocity increment distribution along the progressively decreasing length scale. The model shows that when the turbulent length scale gets smaller, the velocity increment distribution has central growing peak and develops stretched tails. The intermittency in turbulence is manifested in the same way: large fluctuations of velocity provoke highest strain in narrow (dissipative) regions of flow.

2. Universalities of fragmentation under the scaling symmetry

2.1. *The evolution equation for normalized distribution of fragments and its steady-state solution*

The population balance in the case of fragmentation under the scaling symmetry evolves according to the following integro-differential equation (see, for example, Gorokhovski & Saveliev (2003)):

$$\frac{\partial f}{\partial t} = (\widehat{I}_+ - 1)\nu f \tag{2.1}$$

† University of Rouen

where $f(r,t)$ is the normalized distribution of size, ν is constant breakup frequency, $\int_0^\infty f(r)dr = 1$ and

$$\widehat{I}_+ f = \int_0^1 f\left(\frac{r}{\alpha}\right) q(\alpha)\frac{d\alpha}{\alpha} \tag{2.2}$$

is the operator of fragmentation. To fulfill the evolution of distribution with time, we consider $q(\alpha)$ to be different from delta function. The ultimate steady-state solution of equation (2.1) is delta function:

$$f(r) = \delta(r) \tag{2.3}$$

To get (2.3), remark that $\widehat{I}_+\delta(r) = \int_0^1 \frac{d\alpha}{\alpha} q(\alpha)\delta\left(\frac{r}{\alpha}\right) = \delta(r)$, and then from $\left(\widehat{I}_+ - 1\right) f = 0$, it follows that $\widehat{I}_+\delta(r) - \delta(r) = 0$. The question is: How does the distribution $f(r,t)$ evolve to the ultimate steady-state solution (2.3)? This question can not be completely answered since the solution of the evolution equation (2.1) requires knowledge of the spectrum $q(\alpha)$, which is principally unknown function. At the same time, the operator $\widehat{I}_+$ in equation (2.1) is invariant under the group of scaling transformations ($r \to \alpha r$). Due to this symmetry, the evolution of the distribution $f(r,t)$ to the ultimate steady-state solution (2.3) goes at least, through two intermediate asymptotics. Evaluating these intermediate asymptotics does not require knowledge of entire function $q(\alpha)$ - only its first two logarithmic moments, and further only the ratio of these moments in the long-time limit, determine the behavior of the solution to equation (2.1). These two universalities are shown as follows.

2.2. *First and second universalities*

The asymptotic solution of (2.1) is (Gorokhovski & Saveliev 2003):

$$f(r, t\to\infty) = \frac{1}{R}\frac{1}{\sqrt{2\pi\left\langle \ln^2\alpha\right\rangle \nu t}}\exp\left(-\frac{\left\langle \ln\alpha\right\rangle^2}{2\left\langle \ln^2\alpha\right\rangle}\nu t\right)\times$$
$$\times\exp\left(-\frac{\left\langle \ln(r/R)\right\rangle^2}{2\left\langle \ln^2\alpha\right\rangle \nu t}\right)\left(\frac{R}{r}\right)^{1-\left\langle \ln\alpha\right\rangle/\left\langle \ln^2\alpha\right\rangle} \tag{2.4}$$

where R denotes the initial length scale. The expression (2.4) confirms the main result of Kolmogorov (1941): the long-time limit distribution is log-normal (*first universality* with two parameters, which are the first and the second logarithmic moments of the fragmentation intensity spectrum). At the same time, it is seen from (2.4), that the second multiplier tends to unity as time progresses. This implies that *only one universal parameter*, $\frac{\left\langle \ln\alpha\right\rangle}{\left\langle \ln^2\alpha\right\rangle}$, controls the last stage of the fragmentation process (*second universality*):

$$f(r,t) \propto \left(\frac{1}{r}\right)^{1-\frac{\left\langle \ln\alpha\right\rangle}{\left\langle \ln^2\alpha\right\rangle}} \tag{2.5}$$

2.3. *First universality and Fokker-Planck equation*

The emerging corollary from the first universality is as follows: changing of higher moments $\left\langle \ln^k\alpha\right\rangle$, $k > 2$ in equation (2.1) does not affect its solution at times sufficiently larger than the life time of the breaking fragment. Then the moments $\left\langle \ln^k\alpha\right\rangle$, $k > 2$ can be simply equated to zero (rather than making the broadly-used assumption about the smallness of latest). Consequently, by expanding $\frac{1}{\alpha}f\left(\frac{r}{\alpha}\right)$ on powers of $\ln\alpha$ in (2.1), and

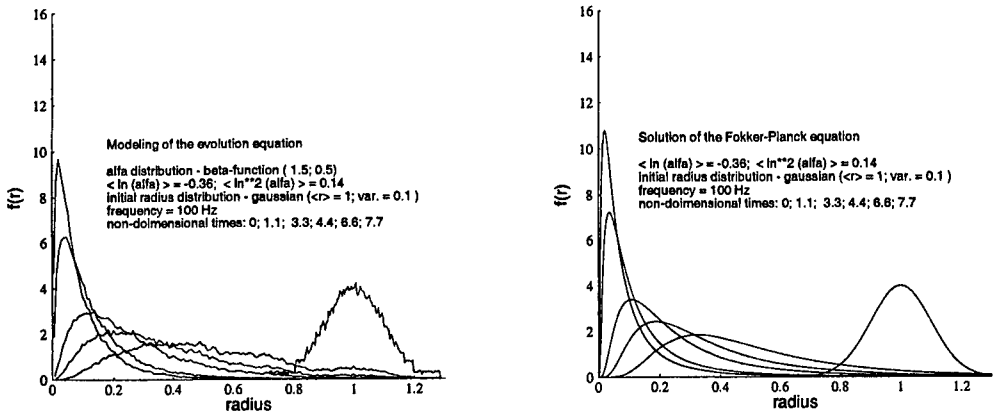


FIGURE 1. Size distributions computed by direct modeling of the evolution equation with presumed Gaussian spectrum of breakup intensity, $q(\alpha)$, (on the left-side) and by analitical solution of Fokker-Planck equation with $\langle \ln \alpha \rangle$ and $\langle \ln^2 \alpha \rangle$ taken from presumed $q(\alpha)$.

by setting to zero the third and all higher logarithmic moments, the evolution equation (2.1) reduces *exactly* to the Fokker-Planck equation (Gorokhovski & Saveliev 2003):

$$\frac{\partial f(r)}{\partial t} = \left[-\frac{\partial}{\partial r} r \langle \ln \alpha \rangle + \frac{1}{2!} \frac{\partial}{\partial r} r \frac{\partial}{\partial r} r \langle \ln^2 \alpha \rangle \right] \nu f(r) \tag{2.6}$$

or in terms of logarithm of size distribution $\Phi(x = \ln r)$, one yields:

$$\frac{\partial \Phi(x)}{\partial t} = \left[-\frac{\partial}{\partial x} \langle \ln \alpha \rangle + \frac{1}{2!} \frac{\partial^2}{\partial x^2} \langle \ln^2 \alpha \rangle \right] \nu \Phi(x) \tag{2.7}$$

The solution of (2.6) verifies to be:

$$f(r,t) = \frac{1}{r} \int_0^\infty \frac{1}{\sqrt{2\pi \langle \ln^2 \alpha \rangle \nu t}} \exp \left[-\frac{\left(\ln \frac{r_0}{r} + \langle \ln \alpha \rangle \nu t \right)^2}{2 \langle \ln^2 \alpha \rangle \nu t} \right] f_0(r_0) dr_0 \tag{2.8}$$

where $f_0(r_0)$ is the initial distribution.

If $q(\alpha)$ is presumed, we can compare the Monte-Carlo simulation of the evolution equation (2.1) with analytical solution (2.8), where $\langle \ln \alpha \rangle$ and $\langle \ln^2 \alpha \rangle$ are calculated from the presumed $q(\alpha)$. In Fig.1, on the left hand-side, we show the distribution from Monte Carlo computation of (2.1) at different non-dimensional time νt, with $q(\alpha)$ presumed as Gaussian; $\langle \ln \alpha \rangle = -0.36$ and $\langle \ln^2 \alpha \rangle = 0.14$. The same moments have been prescribed in (2.8) to compute the evolution of distribution by Fokker-Planck equation (right hand-side of Fig.1). It is seen that at $\nu t = 1.1$ and later, the Monte Carlo simulation of (2.1) and analytical solution of Fokker-Planck equation (2.8) match each other. We performed such a comparison using different shapes of $q(\alpha)$ and the emerging picture shows that after a certain time (the weaker the spectrum of breakup intensity is, the larger this time is), the Monte Carlo solution of the evolution equation and the analytical solution of Fokker-Planck equation were practically the same.

2.4. *Second universality, fractals and Boltzman distribution. Identification of* $\frac{\langle \ln^2 \alpha \rangle}{\langle \ln \alpha \rangle}$

The power distribution (2.5) implies the fractal properties of formed fragments in the long-time limit. The dimension of such a fractal object is defined by the ratio $\frac{\langle \ln \alpha \rangle}{\langle \ln^2 \alpha \rangle}$. Setting in (2.5) $x = \ln r$, one yields:

$$\Phi(x) = r \cdot f(r,t) \;\propto\; e^{-\frac{x}{h}} \tag{2.9}$$

where

$$h = -\frac{\langle \ln^2 \alpha \rangle}{\langle \ln \alpha \rangle} \tag{2.10}$$

From (2.9), one can see that in the fragmentation process, the asymptotic power distribution (2.5) plays the same role as the Boltzmann distribution in problems of statistical physics. This gives an idea for the choice of $\frac{\langle \ln \alpha \rangle}{\langle \ln^2 \alpha \rangle}$ by making use of the theory of Einstein on the Brownian motion. In this theory, the coefficient of diffusion in the Fokker-Planck equation is represented by the product *mobility*×*energy*, while the drift velocity is given by the product *mobility*×*force*. The ratio characterizes the typical length scale. In this spirit, making analogy with (2.7), one gives for the normalized typical length scale r_*:

$$\frac{\langle \ln^2 \alpha \rangle}{\langle \ln \alpha \rangle} = \ln\left(\frac{r_*}{r_0}\right) \tag{2.11}$$

This scale may characterize the dominant mechanism of the cascade fragmentation (an example of r_* can be found in Gorokhovski (2001)).

3. Application to the turbulent cascade with intermittency

The cascade in isotropic turbulence with intermittency in the velocity field may also be viewed in the framework of fragmentation under the scaling symmetry. Here, the energy of larger unstable eddies is transferred to smaller one at a fluctuating rate. It is clear that controlling of each elementary breakup of eddy is useless and impossible task, since the number of degrees of freedom to produce each turbulent structure is very large. The very simple way is again, to assume that at each repetitive step of cascade, the probability to find the velocity scale of a 'daughter' eddy is independent of the velocity scale of its 'mother' eddy; *i.e.* when the turbulent length scale r gets smaller, the velocity increment, $\triangle_r \mathbf{v}(x) = |\mathbf{v}(x+r) - \mathbf{v}(x)|$, is changed by independent positive random multiplier:

$$\triangle_r \mathbf{v} = \alpha \, \triangle_l \, \mathbf{v}, \;\text{ with } r \leq l \tag{3.1}$$

The formulation (3.1) is similar to Castaign *et al.* (1990), Castaign *et al.* (1993), Castaign (1996), Kahalerras *et al.* (1997), Naert *et al.* (1998). In these papers, the measurements of statistics of the velocity increment at the progressively reduced length scale showed distributions with stretched tails and sharp central peak, *i.e.* at small length scales, the small amplitude events alternate with events of strong velocity variation. This provokes effect of intermittency: highest strain in narrow regions of flow. By Taylor's hypothesis of 'frozen turbulence', it is traditional to evaluate the velocity increment by one-point measurement of the velocity time increment. Consequently, the penetration towards smaller scale in the turbulent cascade may be viewed as evolution 'in time' by: $\tau_i = \ln(L_{int}/l_i)$ (Friedrich & Peinke 1997), where L_{int} is integral length scale and l_i is the eddy scale. Then we may compare equation (2.8) with measured distribution of the velocity increment for different length scales. Another way, is to compare equations (2.8) and (2.11)

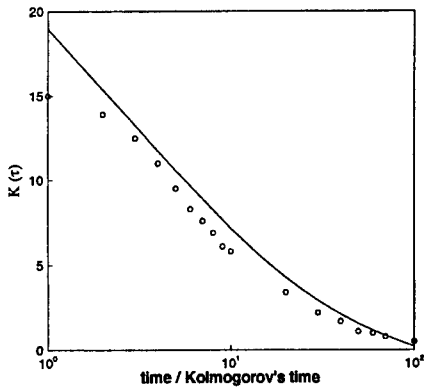


FIGURE 2. Evolution of the flatness factor $K(\tau) = \left\langle (\triangle_\tau \mathbf{v})^4 \right\rangle / \left\langle (\triangle_\tau \mathbf{v})^2 \right\rangle^2 - 3$ for the PDF of the time velocity increment (continuous line: model; symbol: Mordant *et al.* (2001)).

directly with Lagrangian velocity statistics measured by Mordant *et al.* (2001) in fully developed turbulence. Assuming that at integral time scale, the distribution of the velocity increment is Gaussian (see, for example, Obukhov's (1959) Lagrangian theory of isotropic turbulence), the expression (2.8) can be written as:

$$f(\triangle_\tau \mathbf{v}, \tau_*) = \frac{1}{\triangle_\tau \mathbf{v}} \times$$
$$\int_0^\infty \frac{1}{\sqrt{2\pi \left\langle \ln^2 \alpha \right\rangle \tau_*}} \exp\left[-\frac{\left(\ln \frac{\triangle \mathbf{V}}{\triangle_\tau \mathbf{v}} + \left\langle \ln \alpha \right\rangle \tau_* \right)^2}{2 \left\langle \ln^2 \alpha \right\rangle \tau_*} \right] Gauss(\triangle \mathbf{V}) d(\triangle \mathbf{V}) \qquad (3.2)$$

where τ_* is assumed here to be $\ln(T_{int}/\tau_i)$ (T_{int} is integral time scale and τ_i is eddy turbulent time scale). The crucial problem in (3.2) concerns definition of $\left\langle \ln^2 \alpha \right\rangle$ and $\left\langle \ln \alpha \right\rangle$. It has been recognized in two recent papers of Lundgren (2002) and Gange *et al.* (2003), that the typical turbulent length scale, at which Kolmogorov's scaling takes place at finite large Reynolds number, is close to Taylor micro-scale, λ. In this spirit, the expression (2.11) is formulated here as: $\left\langle \ln^2 \alpha \right\rangle / \left\langle \ln \alpha \right\rangle = \ln(\lambda/L_{int})$ and further $\left\langle \ln \alpha \right\rangle = const \cdot \ln(\lambda/L_{int})$. In Fig. 3, the computed PDF's of the velocity increment are shown against measurements of Mordant *et al.* (2001) for $Re_\lambda = 740$; $\mathbf{v}_{rms} = 0.98\ m/s$; $T_{int} = 23\ ms$; $\tau_\eta = 0.2\ ms$ (variations have been normalized to unit variance in order to emphasize changes in the functional form). Without special fit to each experimental profile (computation requires only one constant giving a good fit to the experimental evolution of the flatness parameter, Fig. 2), it is seen that expression (3.2) is in agreement with the measured PDF. The computed PDF's reproduce the progressive non-Gaussianity with development of stretched tails as time increment becomes smaller.

4. Conclusion and future work

The main result in this paper concerns formulation of the turbulent cascade with intermittency in the framework of the fragmentation theory with scale invariance. The model of evolution of the velocity increment distribution along the progressively decreasing length scale is proposed. The Monte Carlo simulation of the evolution equation with

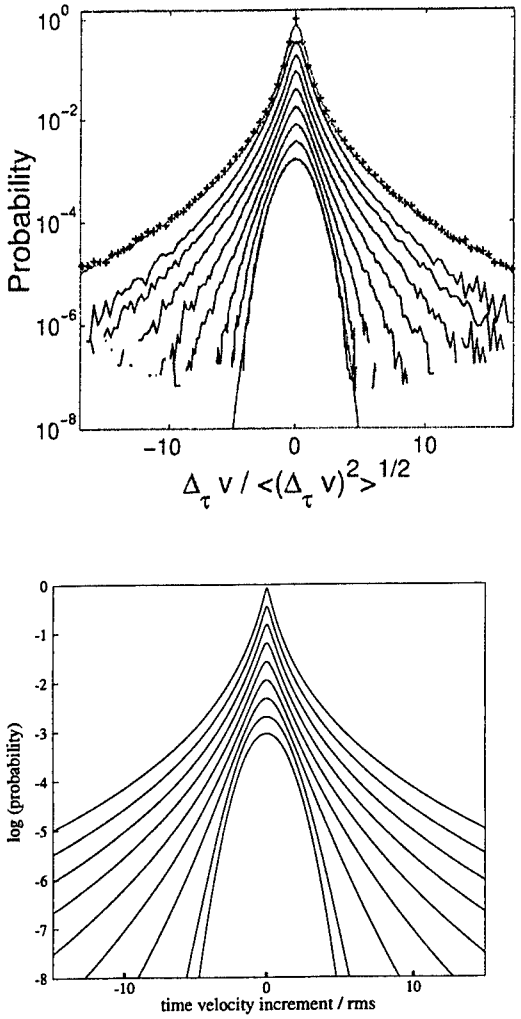


FIGURE 3. Experimental from Mordant *et al.* (2001) (upper part) and corresponding modeled (bottom part) PDF of the normalized increment $\Delta_\tau \mathbf{v} / \left\langle (\Delta_\tau \mathbf{v})^2 \right\rangle^{1/2}$ at $Re_\lambda = 740$. The curves are shifted for clarity. From top to bottom: $\tau = 0.15; 0.3; 0.6; 1.2; 2.5; 5; 10; 20; 23\, ms$..

presumed fragmentation spectrum showed that the solution matches the Fokker-Planck approximation. We showed that the long-time evolution towards fractals is similar to the Boltzmann distribution in the statistical physics. This allowed to represent the ratio of two first logarithmic moments of the fragmentation intensity spectrum as a typical scale, at which the cascade fragmentation is manifested. The distribution of velocity increment showed that when the turbulent length scale gets smaller, this distribution has central growing peak and develops stretched tails. This is similar to what we know on the intermittency in turbulence from papers of Castaign *et al.* (1990, 1993, 1996, 1997, 1998). In addition, the model proposed can be readily applied in LES computation of turbulent intermittent flow with dispersed particles. In such computation we often need to predict the flow properties at scales substantially smaller than the grid size. The knowledge of the

velocity increment at these scales may improve simulation of light particles dispersion, droplet evaporation involving blowing effects, and sub-grid vapor/air mixing.

REFERENCES

KOLMOGOROV, A. N. 1941 On the log-normal distribution of particles sizes during break-up process. *Dokl. Akad. Nauk. SSSR XXXI* **2**, 99-101.

GOROKHOVSKI, A. M. & SAVELIEV, V. 2003 Analyses of Kolmogorov's model of breakup. *Phys. Fluids* **15**, 184-192.

GOROKHOVSKI, A. M. 2001 The Stochastic Sub-Grid-Scale Approach for Spray Atomization. *J.Atomization and Sprays* **11**, 505-519.

CASTAIGN, B., GANGE, Y. & HOPFINGER, E. J. 1990 Velocity probability density functions of high Reynolds number tirbilence. *Physica D* **46**, 177-200.

CASTAIGN, B., GANGE, Y. & MARCHAND, M. 1993 Log-similarity for turbulent flows? *Physica D* **68**, 387-400.

CASTAIGN, B. 1996 The temperature of turbulent flows. *J. Phys. II France* **6**, 105-114.

KAHALERRAS, H., MALECOT, Y., GANGE, Y. & CASTAIGN, B. 1997 Intermittency and Reynolds number. *Phys. Fluids* **10**, 910-921.

NAERT, A., CASTAIGN, B., CHABAUD, B., HEBRAL, B. & PEINKE, J. 1998 Conditional statistics of velocity fluctuations in turbulence. *Physica D* **113**, 73-78.

FRIEDRICH, R. & PEINKE, J. 1997 Description of a turbulent cascade by a Fokker-Planck equation. *Phys. Rev. Lett.* **78**.

MORDANT, N., METZ, P., MICHEL. O. & PINTON, J.-F. 2001 Measurement of Lagrangian velocity in fully developed turbulence. *Phys. Rev. Lett.* **87**.

OBUKHOV, A. M. 1959 Description of turbulence in terms of Lagrangian variables. *Adv. in Geophysics (Atmospheric Diffusion and Air Polution)* **6**, 113-115.

LUNDGREN, T. S. 2002 Kolmogorov two-thirds law by matched asymptotic expansion. *Phys. Fluids* **14**, 638-642.

GANGE, Y., CASTAIGN, B., BAUDET, CH. & MALECOT, Y. 2003 Reynolds log-similarity of third-order velocity structure functions. to be published in *Phys. Fluids.*

"Hypothetical" heavy particles dynamics in LES of turbulent dispersed two-phase channel flow

By M. Gorokhovski AND A. Chtab †

1. Motivation and objectives

The extensive experimental study of dispersed two-phase turbulent flow in a vertical channel has been performed in Eaton's research group in the Mechanical Engineering Department at Stanford University (see Kulick *et al.* (1994) and Fessler *et al.* (1994)). In Wang & Squires (1996), this study motivated the validation of LES approach with Lagrangian tracking of round particles governed by drag forces. While the computed velocity of the flow have been predicted relatively well, the computed particle velocity differed strongly from the measured one. Using Monte Carlo simulation of inter-particle collisions, the computation of Yamamoto *et al.* (2001) was specifically performed to model Eaton's experiment. The results of Yamamoto *et al.* (2001) improved the particle velocity distribution. At the same time, Vance & Squires (2002) mentioned that the stochastic simualtion of inter-particle collisions is too expensive, requiring significantly more CPU resources than one needs for the gas flow computation. Therefore, the need comes to account for the inter-particle collisions in a simpler and still effective way. To present such a model in the framework of LES/Lagrangian particle approach, and to compare the calculated results with Eaton's measurement and modeling of Yamamoto is the main objective of the present paper.

2. Equation for the particle motion along smoothed trajectory

In the high-Reynolds number flows, three random forces act on the motion of solid particles: (i) particle-small scale turbulence interaction (affecting mostly light particle dynamics); (ii) inter-particle collisions (important for relatively heavy particle motion; this randomness motivated the present work); (iii) particle-wall interaction (due to the wall roughness). Accounting for all details of this randomness in LES is formidable. The problem is how to describe effectively the random Lagrangian motion of solid particles. One of the possibilities is as follows: By analogy with kinetic theory, we may introduce a 'hypothetical' particle, which is moving along the smoothed trajectory averaged over random collision trajectories. The smoothed acceleration of such solid particle changes the local momentum in the gas phase, thereby affecting the acceleration of neighboring solid particles. To derive the equation of such a smoothed motion, let us consider the dispersed two-phase turbulent flow as a time evolution of a system of interacting stochastic fluid (Pope 2000) and solid particles. The kinetic description is then specified by the distribution function of particles with position $\vec{\mathbf{r}}(x_1, x_2, x_3)$ and velocity $\vec{\mathbf{v}}(\mathrm{v}_1, \mathrm{v}_2, \mathrm{v}_3)$, $f(\vec{\mathbf{r}}, \vec{\mathbf{v}}, t)$, in the six-dimensional space, for solid particles, $f_p(\vec{\mathbf{r}}_p, \vec{\mathbf{v}}_p, t)$ and fluid particles, $f_g(\vec{\mathbf{r}}_g, \vec{\mathbf{v}}_g, t)$. For solid particles, the Boltzman equation can be written in the

† University of Rouen

following form:

$$\frac{\partial f_p}{\partial t} + \vec{\mathbf{v}}_p \cdot \frac{\partial f_p}{\partial \vec{\mathbf{r}}_p} = I(f_p, f_p) + I(f_p, f_g) \tag{2.1}$$

where $I(f_p, f_p)$ and $I(f_p, f_g)$ are operators for solid-solid and solid-liquid particle collisions, respectively. The first collision operator in (2.1) is usually modeled assuming pair hard sphere collisions with prescribed efficiency (see Vance & Squires (2002), Lavelieville *et al.* (1997), Simonin *et al.* (2002), Sommerfeld (2001), Wang *et al.* (2000), Mei & Hu (1999), Sigurgeirsson *et al.* (2001)). The form of the second operator is principally unknown. The total number of solid particles does not change due to any collisions, as well as the total momentum of solid particles is unchanged due to solid-solid collisions,*i.e.*:

$$\int d^3\mathbf{v}_p I(f_p, f_p) = 0 \tag{2.2}$$

$$\int d^3\mathbf{v}_p I(f_p, f_g) = 0 \tag{2.3}$$

$$\int d^3\mathbf{v}_p I(f_p, f_p)\mathbf{v}_p = 0 \tag{2.4}$$

However

$$\int d^3\mathbf{v}_p I(f_p, f_g)\mathbf{v}_p \neq 0 \tag{2.5}$$

Introducing the solid particles density, n_p (in usual terms of kinetic approach) and the particle velocity averaged by f_p, $\langle \mathbf{v}_p \rangle_{f_p} = \frac{1}{n_p}\int d^3\mathbf{v}_p f_p \mathbf{v}_p$, let us assume that the solid-solid particle collision occurs frequently such that the correlation of fluctuations of solid particle velocities can be identified with the particle temperature of ordinary statistical mechanics, T_p:

$$\left\langle \mathbf{v}'_{p,\alpha}\mathbf{v}'_{p,\beta} \right\rangle_{f_p} = \frac{1}{3}\left\langle \mathbf{v}'^2_p \right\rangle_{f_M} \delta_{\alpha\beta} = \frac{T_p}{m_p} \tag{2.6}$$

Here f_M is Maxwellian distribution, m_p is the mass of the considered solid particle and $\delta_{\alpha\beta}$ is the Kronecker delta. Multiplying (2.1) by the velocity of particle, integrating over all these velocities and using (2.6), one yields:

$$\frac{d\langle \mathbf{v}_{p,\beta} \rangle_{f_p}}{dt} = -\frac{1}{n_p}\frac{\partial}{\partial x_\beta}\left(\frac{n_p T_p}{m_p}\right) + \frac{1}{n_p}\int \mathbf{v}_{p,\beta} I(f_p, f_g) d^3\mathbf{v}_{p,\beta} \tag{2.7}$$

where the first term implies the change of the 'particle pressure' along the smoothed trajectory of the particle and the second term is the mean rate of the particle velocity change due to particle-turbulence interaction. These two terms have to be modeled. The first term is modeled as follows. We introduce the 'temperature' of stochastic fluid particles, $T_{tur,g}$. According to its kinetic definition, one writes:

$$T_{tur,g} = \frac{2}{3}\rho_g VOL_L \langle \mathbf{v}'^2_g \rangle / 2 \tag{2.8}$$

where ρ_g is the gas density, VOL_L may be viewed as a volume over integral spatial scale and $\langle \mathbf{v}'^2_g \rangle / 2$ is the kinetic energy of turbulence in gas flow. Assuming a relaxation of the statistical temperature of solid particle to the statistical temperature of liquid one, one writes:

$$\frac{dT_p}{dt} = \beta(T_{tur,g} - T_p) \tag{2.9}$$

where β is an exchange frequency parameter. If β is very large, the statistical temperature

of particle may be assumed to be locally in a 'thermodynamic' equilibrium with the surrounding turbulence:

$$T_p = T_{tur,g} \tag{2.10}$$

Concerning the second term in (2.7), for heavy particles, it can be presented by the draft force:

$$\left(\langle \mathbf{v}_{g,\beta} \rangle_{f_g} - \langle \mathbf{v}_{p,\beta} \rangle_{f_p}\right) / \tau_p \tag{2.11}$$

where τ_p is the Stokes time. With the particle Reynolds dependency from Clift *et al.* (1978), it writes:

$$\tau_p = \frac{\rho_p d_p^2}{18 \rho_g \nu_g} \frac{1}{1 + 0.15 Re_p^{0.687}} \tag{2.12}$$

In this formulation, the equation (2.7) without the first term represents usual LES/ particle tracking procedure.

3. Computation procedure

LES of particle-laden flow is performed for conditions corresponding to the Eaton's experiment. In this experiment, a set of measurements has been performed on a vertical fully-developed air-channel flow laden with spherical particles of different mass loading. From this measurement, we chose the case with particles of copper (density $\rho_p = 8800\, kg/m^3$, diameter $d_p = 70\, \mu m$ and 20% of mass loading). The numerical code developed at CTR, Stanford University by Pierce & Moin (2001), was adapted in this paper for IBM PC. In this code, the sub-grid momentum transport term was modeled by dynamic approach of Germano *et al.* (1990). In the present work, this code has been coupled in 'two-ways' with Lagrangian particle solver, according to (2.7)-(2.11). The second order Runge-Kutta scheme has been used for computation of the particle motion.

To define the local statistical temperature of turbulence in (2.8), the volume was associated with the control volume of the finite-difference mesh. Two different expressions for the 'temperature' of turbulence have been used to calculate (2.8):

$$T_{turb,g} = \frac{2}{3} \rho_g \Delta_x \Delta_y \Delta_z \sum_{\alpha} (\mathbf{v}_{g,\alpha} - \overline{\mathbf{v}}_{g,\alpha})^2 / 2 \tag{3.1}$$

and for the mean one

$$\langle T_{turb,g} \rangle = \frac{2}{3} \rho_g \Delta_x \Delta_y \Delta_z \sum_{\alpha} \left\langle (\mathbf{v}_{g,\alpha} - \overline{\mathbf{v}}_{g,\alpha})^2 \right\rangle / 2 \tag{3.2}$$

The numerical algorithm of two-way momentum coupling was implemented. The particle equations have been solved using the second order Runge-Kutta method. For the gas velocity at a particle position, the linear interpolation scheme has been used. The implementation of higher order schemes of interpolation did not give an explicit advantage, requiring at the same time a substantial computational effort. The computations were performed at Reynolds number based on friction velocity and channel half-width of 644 (corresponding to Reynolds numbers of 13800 based on centerline velocity and channel half-width). Parameters of the computation have been chosen similar to Wang & Squires (1996) with $64 \times 65 \times 64$ grid points for the flow resolution in the x, y and z directions, respectively, that covered the computational domain $5\pi\delta/2 \times 2\delta \times \pi\delta/2$. In the streamwise and spanwise directions, uniform grid was used. In the direction normal to the wall, the non-uniform stretched grid has been used with first velocity position at

$y^+ = 0.88$. Periodic boundary conditions were used for gas phase and for particles at free boundaries.

4. Results

For unladen and laden turbulent flow with different mass loading, Fig.1a shows the mean stream-wise gas-velocity obtained in Eaton's experiment and in the present computation. It has been noted in the experiment that particles do not change practically the mean velocity profile of gas. As it is seen from Fig.1a, the computed mean gas velocity field is also not influenced by the presence of particles. Fig.1b and 1c show the turbulence intensity in stream-wise and wall-normal directions. The Eaton's experiment predicted an attenuation of the turbulence by particles. This is also seen from computation in Fig.1b and 1c. To demonstrate the strong effect of the turbulence attenuation, the centreline experimental and computed values of kinetic energy and viscous dissipation are presented in Fig.2. versus different mass loading. In Fig.3, the profiles of mean particle velocity and of its variance are shown. Fig.3a gives the particle mean streamwise velocity. It is clearly seen that similar to measurements and computations of Yamamoto *et al.* (2001), the present computation gives the flattened profile. In Fig.3b, the computed r.m.s. streamwise particle velocity is compared with the measurements. The computation is in agreement with experiment except near the channel centre. At the same time, it is seen from Fig.3c, that computed r.m.s. of wall-normal velocity is overestimated against the measured values (the data from Yamamoto *et al.* (2001) show an underestimation of measurements).

5. Conclusion and future work

The recent LES computation of particle-laden turbulent flow showed that the particle velocity distribution can be predicted relatively well, if the inter-particle collisions are included in the simulation. However the Monte Carlo simulation of inter-particle collisions, which is used in those computations, is too expensive for practical applications. In this paper, a simplified approach of two-phase flow simulation is proposed. By analogy with kinetic theory, we introduced a 'hypothetical' particle, which is moving along the smoothed trajectory averaged over random collision trajectories. An equation of such a smoothed motion has been derived, using hypothesis of a 'thermodynamic' equilibrium between the statistical temperature of the particle and the surrounding turbulence. The Lagrangian tracking of 'hypothetical' particles was performed along LES computation of a vertical fully-developed air-channel flow (experiment in Eaton's research group). It has been shown that our computation is in agreement with Eaton's experiment and computation, where the inter-particle interaction has been simulated by hard-sphere collisions with prescribed efficiency. At the same time, to account for inter-particle interactions, the presented model does not require additional CPU time. Our future work concerns the further development of this approach for interaction between particles & rough wall.

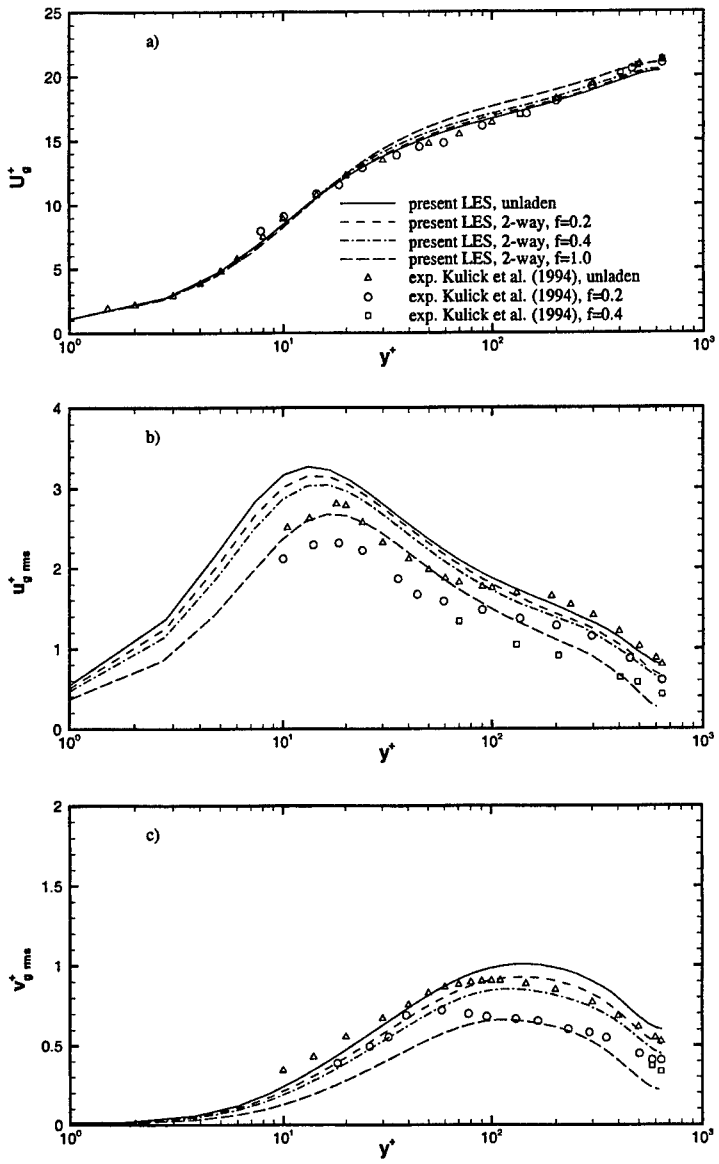


FIGURE 1. Comparison of computed gas velocity profiles with measurements of Kulick *et al.* (1994) at different mass loading: a) streamwise mean velocity; b) r.m.s. of streamwise velocity; c) r.m.s. of wall-normal velocity.

REFERENCES

KULICK, D., FESSLER, J. R. & EATON, J. K. 1994 Particle response and turbulence modification in fully developed channel flow. *J. Fluid Mech.* **277**, 190-134.

FESSLER, J. R., KULICK, J. D. & EATON, J. K. 1994 Preferential concentration of heavy particles in a turbulent channel flow. *Phys. Fluids* **6**, 3742-3749.

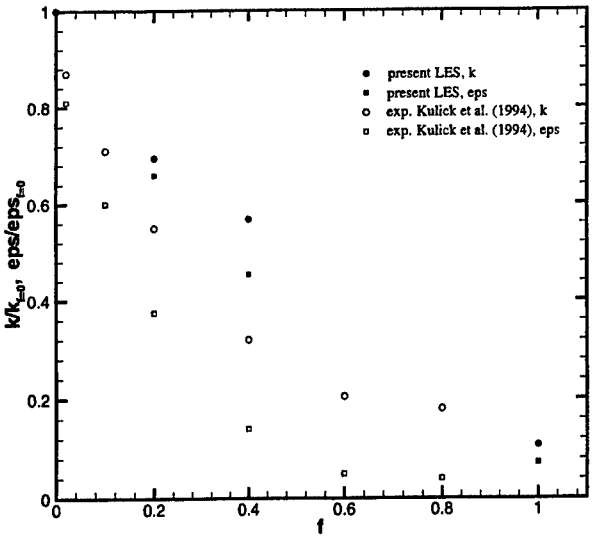


FIGURE 2. Attenuation of gas-phase turbulent kinetic energy and dissipation with particle mass loading: filled symboles - computation; empty symbols - measurement.

WANG, Q. & SQUIRES, K. 1996 Large eddy simulation of particle-laden turbulent channel flow. *Phys. Fluids* **8**, 1207-1223.

VANCE, M. W. & SQUIRES, K. D. 2002 An approach to parallel computing in an Eulerian-Lagrangian two-phase flow model. *ASME* 14-18 July, Monreal, Canada. FEDSM2002-31225.

LAVELIEVILLE, J., SIMONIN, O., BERLEMENT, A. & CHANG, Z. 1997 Validation of inter-particle collision models based on Large eddy simulation in gas-solid turbulent homogeneous shear flow. *Proc. 7th Int. Symp. on Gas-Particle Flows* ASME FEDSM97-3623.

SIMONIN, O., FEVRIER, P. & LAVELIEVILLE, J. 2002 On the spatial distribution of heavy-particle velocities in turbulent flow: from continuous field to particulate chaos. *J. of Turbulence*,30-40.

SIGURGEIRSSON, H., STUART, A. & WAN. W.-L. 2001 Algorithm for particle field simulations with collisions. *J. Comput. Phys.* **172**, 766-807.

YAMAMOTO, Y., POTTHOFF, M., TANAKA, T., KAJISHIMA, T. & TSUJI, Y. 2001 Large-eddy simulation of turbulent gas-particle flow in a vertical channel: effect of considering interparticle collisions. *J. Fluid Mech.* **442**, 303-334.

POPE, S. 2000 *Turbulent flows.* Cambridge University Press.

SOMMERFELD, M. 2001 Validation of a stochastic Lagrangian modeling approach for inter-particle collisions in homogeneous turbulence. *Int. J. Multiphase Flow* **27**, 1829-1858.

WANG, L.-P., WEXLER, A. S. & ZHOU, Y. 2000 Statistical description and modelling of turbulent collision of inertial particles. *J. Fluid. Mech.* **415**, 117-153.

MEI, R. & HU, K. C. 1999 On the collision rate of small particles in turbulent flows. *J. Fluid. Mech.* **391**, 67-89.

CLIFT, R., GRACE, J. R., WEBER, M. 1978 *Bubbles, Drops and Particles.* Academic Press.

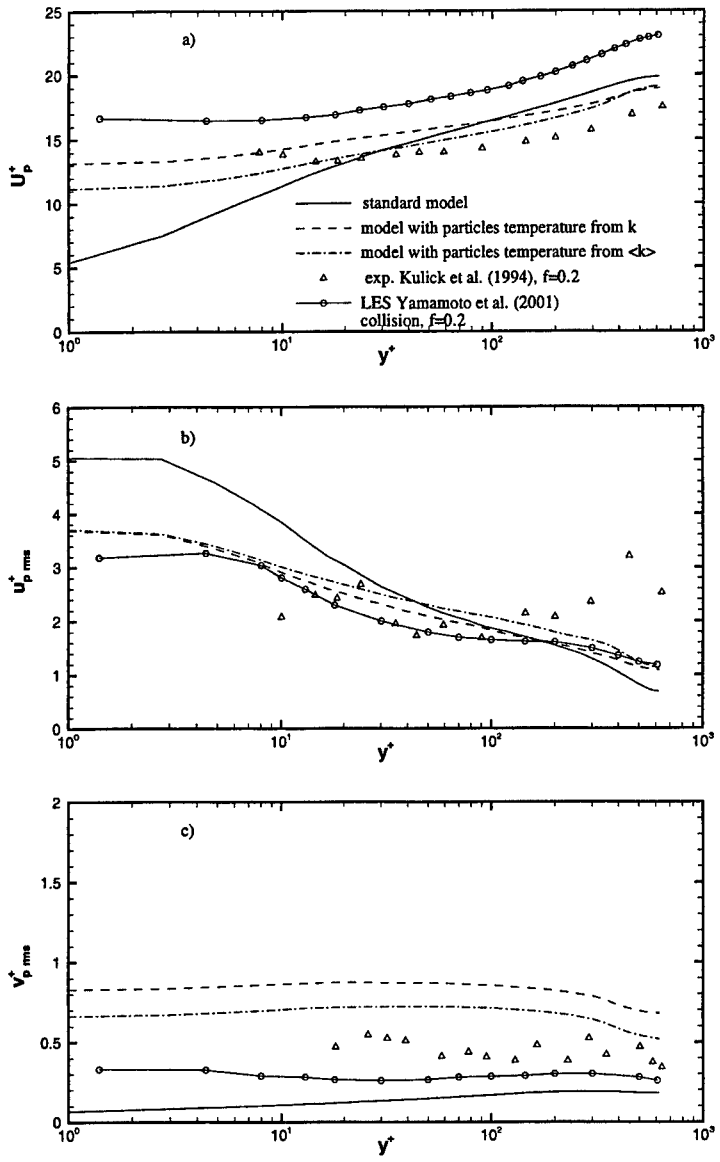


FIGURE 3. Comparison of computed particle velocity profiles with measurements of Kulick *et al.* (1994) and results from Yamamoto *et al.* (2001) with inter-particle collisions: a) streamwise mean velocity; b) r.m.s. of streamwise velocity; c) r.m.s. of wall-normal velocity.

PIERCE, C. D. & MOIN, P. 2001 Progress-variable approach for large eddy simulation of turbulent combustion *Stanford University Report* **TF-80**, Flow Physics and Computational Division, Dept. of Mech. Engineering.

GERMANO, M., PIOMELLY, U., MOIN, P. & CABOT, W. H. 1990 A dynamic subgrid scale eddy viscosity modelProc. Summer Workshop CTR, Stanford CA.

A domain decomposition parallelization of the Fast Marching Method

By M. Herrmann

1. Motivation and objectives

Evolving interfaces play an important role in a multitude of different areas, ranging from fluid mechanics, combustion, and grid generation to material sciences, semiconductor manufacturing, seismic analysis, and control problems [see Sethian (1999*b*) for a detailed overview]. Traditionally, interfaces have been treated in a Lagrangian framework tracking their evolution by, for example, marker particles [see among others Brackbill *et al.* (1988)]. In recent years, however, describing the topology and evolution of interfaces by Eulerian partial differential equations (PDE) has become ever more popular since this approach offers certain theoretical and computational advantages over the Lagrangian formulation (Sethian 1999*b*). Depending on the type of problem, two different solution strategies for the Eulerian approach exist. In the case of an initial value problem, level set methods (Osher & Sethian 1988), or alternatively Volume-of-Fluid methods (Noh & Woodward 1976), can be employed to solve the evolving interface. In the case of a boundary value problem, the Fast Marching Method (Sethian 1996*a*) has emerged as the efficient solution method.

In this paper, we focus on two boundary value problems that typically arise in the numerical implementation of level set methods, namely reinitialization and redistribution. In level set methods, an iso-surface of the level set scalar G,

$$G(\boldsymbol{x},t) = G_0 = \text{const}\,, \tag{1.1}$$

is used to define the location of an arbitrary shaped interface Γ. The transport equation for the scalar G can then be derived from simple kinematic considerations as

$$\frac{\partial G}{\partial t} + \boldsymbol{u}\cdot\nabla G = 0\,. \tag{1.2}$$

Since this so-called level set equation (1.2) is valid only at the location of the interface itself, the choice of G outside the interface, i.e. $G \neq G_0$, is in principle arbitrary. However, for numerical reasons, G is generally chosen to be a distance function,

$$\left|\nabla G\right|\Big|_{G\neq G_0} = 1\,. \tag{1.3}$$

Enforcing this condition is usually called reinitialization.

Furthermore, some quantities S may be defined only at the location of the interface. In order to extend these quantities to the whole computational domain, they are set constant in the interface normal direction,

$$\nabla S\cdot\nabla G = 0\,. \tag{1.4}$$

This procedure is called redistribution, since it redistributes the values of S from the interface into the surrounding domain.

Both, Eqs. (1.3) and (1.4) constitute boundary value problems, since G and S are defined on Γ only. Several different numerical methods exist to solve these equations. Among these are brute force approaches based on calculating the minimum of the geometric distance between each grid node in the computational domain and every point on the interface (Merriman *et al.* 1994), and PDE-based approaches like the iteration scheme by Sussman *et al.* (1994). While the former are computationally very expensive, the latter inadvertently alter both the location of interface and the value of S on the interface due to their iterative nature. In the case of the reinitialization equation (1.3), supplementary fixes addressing this problem relatively successfully have been proposed (Russo & Smereka 2000; Peng *et al.* 1999; Sussman *et al.* 1998; Sussman & Fatemi 1999; Enright *et al.* 2002).

An alternative approach to solving Eqs. (1.3) and (1.4) is the so-called Fast Marching Method (FMM). It was originally proposed by Tsitsiklis (1994, 1995) and applied to the level set formulation by Sethian (1996*a*) and Helmsen *et al.* (1996). The FMM is a non-iterative procedure that explicitly makes use of the way information in Eqs. (1.3) and (1.4) propagates. The FMM is thus theoretically optimal in its operation count. Still, typical problem sizes of state of the art numerical simulations in general require a domain decomposition approach for parallel computing. However, the FMM is highly sequential and hence not straightforward to parallelize in a domain decomposition sense. At least to the knowledge of the author, no domain decomposition parallelization of the Fast Marching Method has been published yet.

This paper is structured as follows: first, the standard, sequential FMM is reviewed. Then, different parallelization strategies are discussed and a domain decomposition parallelization is proposed. Thereafter, some preliminary results concerning the speedup of the proposed method are presented and discussed. Finally, conclusions are drawn and an outlook to future work is given.

2. The sequential Fast Marching Method

In this section, a short overview of the standard Fast Marching Method is given. For further details, the interested reader is referred to Sethian (1996*a*), Adalsteinsson & Sethian (1999), and Sethian (1999*a*).

The idea of the FMM for level sets is to first solve Eq. (1.3) and use its solution to then solve Eq. (1.4) (Adalsteinsson & Sethian 1999). Hence, we will at first focus on the solution of Eq. (1.3).

To solve Eq. (1.3) correctly, the gradient operator has to be approximated by upwind, entropy-satisfying finite differences (Sethian 1999*a*). The approximation most often used is due to Godunov (Rouy & Tourin 1992):

$$\begin{aligned} |\nabla G| \approx \Big[& \max(D^{-x}_{ijk}G, -D^{+x}_{ijk}G, 0)^2 + \\ & \max(D^{-y}_{ijk}G, -D^{+y}_{ijk}G, 0)^2 + \\ & \max(D^{-z}_{ijk}G, -D^{+z}_{ijk}G, 0)^2 \Big]^{1/2} , \end{aligned} \tag{2.1}$$

where $D^{\pm}_{ijk}$ are difference notations. For example, the first order approximation is

$$D^{-x}_{ijk}G = \frac{G_{ijk} - G_{i-1jk}}{\Delta x} , \qquad D^{+x}_{ijk}G = \frac{G_{i+1jk} - G_{ijk}}{\Delta x} . \tag{2.2}$$

(a) Calculate all node values that are directly adjacent to the interface and tag them as *accepted*. Tag all nodes adjacent to these *accepted* nodes as *close* and all others as *far*.

(b) Calculate G of all *close* nodes by Eq. (2.3), treating G in any adjacent *close* or *far* node as ∞. Set the loop index $n = 1$.

(c) Mark as *accepted* the *close* node ijk with the smallest G value, denoted by $G^n = G_{ijk}$.

(d) Mark all *far* nodes adjacent to G_{ijk} as *close*.

(e) Recalculate the G values of all *close* nodes adjacent to G_{ijk} by Eq. (2.3), treating G in any adjacent *close* or *far* node as ∞.

(f) Set $n = n + 1$ and return to step (c) until all nodes are *accepted*.

TABLE 1. The sequential FMM algorithm

Thus, the discretized version of Eq. (1.3) solved in the FMM reads as

$$\begin{aligned}&\Big[\max(D^{-x}_{ijk}G, -D^{+x}_{ijk}G, 0)^2 + \\ &\max(D^{-y}_{ijk}G, -D^{+y}_{ijk}G, 0)^2 + \\ &\max(D^{-z}_{ijk}G, -D^{+z}_{ijk}G, 0)^2\Big]^{1/2} = 1\,.\end{aligned} \tag{2.3}$$

Provided that the G values of all nodes neighboring ijk are given, Eq. (2.3) constitutes a quadratic equation yielding G_{ijk} itself. The simple, albeit inefficient way to solve Eq. (2.3) throughout the whole computational domain is to iteratively update each node in the domain by Eq. (2.3) until a stationary solution is reached (Rouy & Tourin 1992).

However, this approach neglects to take advantage of the fact that, due to the upwind structure of Eq. (2.3), information propagates only from smaller to larger values of G. This yields attribute 1 of the FMM:

ATTRIBUTE 1. *A node value G_{ijk} is determined only by those neighboring nodes of smaller value. It can thus globally depend at most on those nodes in the domain that are of smaller value.*

Attribute 1 implies that a smallest node is fixed and cannot change its value. Hence, given appropriate boundary conditions for G_{ijk} at or adjacent to the interface $G = G_0$, updates of G_{ijk} according to Eq. (2.3) can be confined to a narrow band around the globally smallest values that sweeps outward to ever larger values of G_{ijk}. For details see Sethian (1996*a*), Sethian (1999*a*), and Adalsteinsson & Sethian (1999).

In summary, this leads to the sequential FMM algorithm given in Table 1. The algorithm is executed once for all nodes $G^0_{ijk} < G_0$ and once for all nodes $G^0_{ijk} \geq G_0$, where the superscript 0 denotes the initial values of G at node ijk. Furthermore, the following attribute of the Fast Marching Method can be discerned:

ATTRIBUTE 2. *The sequential loop steps (c)-(f) sort all accepted nodes that are not initially accepted in step (a) in ascending order, i.e. $G^{n+1} \geq G^n$.*

Using a heap sort algorithm with back pointers (Sethian 1996*b*) to locate the smallest value G in step (c) makes the sequential FMM algorithm highly efficient with a theoretical operation count of $O(N \log N)$.

(A_m) Perform steps (a) and (b) of the sequential FMM algorithm.

(B_m) Send all nodes with $G^0_{ijk} < G_0$ to process #0, all nodes with $G^0_{ijk} \geq G_0$ to process #1.

(C_m) Perform sequential FMM algorithm steps (c)-(f).

(E_m) Receive results for nodes $G^0_{ijk} < G_0$ from process #0 and results for nodes $G^0_{ijk} \geq G_0$ from process #1.

TABLE 2. The parallel FMM algorithm $\mathcal{P}_1$

3. Parallelizing the Fast Marching Method

In this section, different strategies to parallelize the FMM are discussed. First, a simple parallelization strategy not based on domain decomposition is given, followed by the discussion of several domain decomposition parallelization approaches.

3.1. *G_0-based parallelization*

The trivial way to parallelize the FMM algorithm described in table 1 is to execute the complete sequential algorithm for all nodes $G^0_{ijk} < G_0$ and for all nodes $G^0_{ijk} \geq G_0$ in parallel, since neither region influences the other. The resulting algorithm $\mathcal{P}_1$ is summarized in Table 2.

This parallelization strategy has two obvious drawbacks. First, the parallelization is limited to two parallel processes, since only two independent regions exist. Secondly, depending on the problem size, memory resource problems arise, because both processes need to work on the whole computational domain.

3.2. *Domain decomposition parallelization*

Domain decomposition parallelization of the sequential FMM algorithm poses two problems. First, the globally smallest *close* value has to be located in step (c). Although this procedure is non-local by definition, it still is easy to parallelize, since each domain can compute its locally smallest value independently, and then simply use these to find a global minimum. Second, a new globally smallest value G^n can be found in step (c) only after steps (d)-(e) of the previous loop step $n-1$ have been executed.

Nevertheless, leaving at first efficiency considerations aside, domain decomposition is straightforward. In order to simplify the notation in the following, we only discuss the domain decomposition into two neighboring domains $\mathcal{D}_m$ and $\mathcal{D}_{m+1}$. All arguments, however, apply analogous to the three-dimensional domain decomposition into an arbitrary number of domains. Figure 1 depicts some naming conventions that are employed in the following. Each domain $\mathcal{D}_m$ is extended by r ghost nodes in the domain boundary normal direction, where r is the spatial order of the difference approximation, Eq. (2.2). Here, only the first order approximation is employed. Hence, each domain is extended as depicted in Fig. 1.

Assuming that each process $m = 0 \ldots N_p$ works only on part $\mathcal{D}_m$ of the whole computational domain, Table 3 summarizes the parallel FMM algorithm $\mathcal{P}_2$. Note that $\mathcal{P}_2$ has to be executed twice on each process, once for all nodes $G^0_{ijk} < G_0$ and once for all nodes $G^0_{ijk} \geq G_0$. In essence, disregarding step (A), algorithm $\mathcal{P}_2$ is a domain decomposed sequential algorithm, because globally only one single node in a single domain is updated per loop step, while all other domains are waiting idle. However, algorithm $\mathcal{P}_2$ introduces a clearly defined inter-domain communication boundary. Recalling that the update of

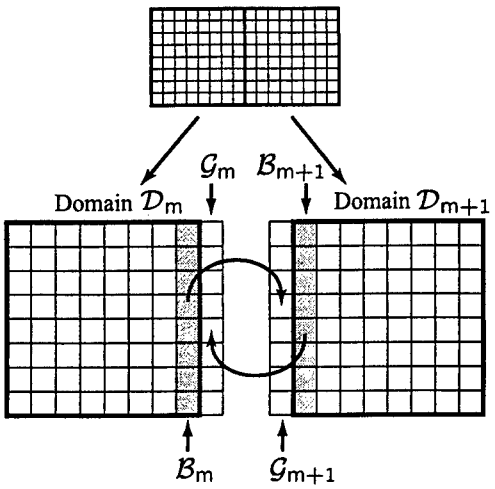


FIGURE 1. Domain naming conventions.

(A) Perform steps (a) and (b) of the sequential FMM algorithm.

(B) Locate the locally smallest *close* G value; denote it as $G_{\mathcal{D}_m}$.

(C) Find the globally smallest *close* G value, $G_G = \min(G_{\mathcal{D}_{0\ldots N_p}})$, and mark it as *accepted*. If $G_G \in \mathcal{D}_m$, go to next step, else go to step (F).

(D) Perform sequential FMM algorithm steps (c)-(e) for G_G.

(E) If any of the *close* nodes, updated in step (e) of the sequential FMM, belong to $\mathcal{B}_m$, communicate them to $\mathcal{G}_{m+1}$ of domain $\mathcal{D}_{m+1}$.

(F) Set $n = n + 1$. Return to step (B) until all local nodes are *accepted*.

TABLE 3. The parallel FMM algorithm $\mathcal{P}_2$

G_{ijk}, Eq. (2.3), using first order approximations, Eq. (2.2), does involve at most the directly adjacent nodes in the $\pm i$, $\pm j$, and $\pm k$ direction, any local node in domain $\mathcal{D}_m$ can be updated correctly, provided that all ghost nodes $\mathcal{G}_m = \mathcal{B}_{m+1}$ are known. Hence, only changes of $\mathcal{B}_{m+1}$ need to be communicated to $\mathcal{G}_m$, as is done in step (E) above.

Taking these arguments into account, one can in fact avoid the strict sequential nature of algorithm $\mathcal{P}_2$. Looking for example at domain $\mathcal{D}_m$, as long as no change in $\mathcal{G}_m$ occurs, the locally smallest *close* value $G_{\mathcal{D}_m}$ can be moved into a local *accepted* group and updates of the nodes adjacent to $G_{\mathcal{D}_m}$ can be performed according to the sequential FMM algorithm steps (d) and (e).

However, special care must be taken whenever a node belonging to $\mathcal{G}_m$, for example G_{ijk}, changes. If G_{ijk} changes to *accepted* status, then, recalling attribute 1, all locally *accepted* nodes belonging to $\mathcal{D}_m$ that are smaller than or equal to G_{ijk} cannot be influenced by this change. Conversely, all locally *accepted* nodes belonging to $\mathcal{D}_m$ larger than G_{ijk} might be wrong, since they could depend on G_{ijk}. Hence, to allow for a consistent algorithm, each domain has to be able to rollback to its state at the beginning of loop step p, where p is such that $G^{p-1} \leq G_{ijk} \leq G^p$. The same argument applies, if G_{ijk} changes from *accepted* to *close* status through a rollback operation in domain $\mathcal{D}_{m+1}$.

(A) Perform steps (a) and (b) of the sequential FMM algorithm.

(B) Check, if any node belonging to $\mathcal{G}_m$ changed status with new value G_B. If so, rollback to state S^p, where p is given by $G^{p-1} \leq G_B \leq G^p$. Mark G_B as *close* and insert it into list $\mathcal{L}_B$. Set $n = p$.

(C) Locate the locally smallest *close* G value (including list $\mathcal{L}_B$); denote it as $G_{\mathcal{D}_m}$.

(D) Perform steps (c)-(e) of the sequential FMM algorithm for $G_{\mathcal{D}_m}$.

(E) If node $G_{\mathcal{D}_m}$ or any of its adjacent nodes updated in step (D) belongs to $\mathcal{B}_m$, communicate them to $\mathcal{G}_{m+1}$ of domain $\mathcal{D}_{m+1}$.

(F) Store the current state as S^n.

(G) Set n=n+1. Return to step (B) until all local nodes are *accepted.*

(H) Wait until all other domains reach step (H) or a node belonging to $\mathcal{G}_m$ changes status. In the latter case, go to step (B).

TABLE 4. The parallel FMM algorithm $\mathcal{P}_3$

These considerations lead to the domain decomposed parallel algorithm $\mathcal{P}_3$ summarized in Table 4.

The drawback of algorithm $\mathcal{P}_3$ is two-fold. First, the complete state of the local domain has to be stored at every loop step in order to allow for a possible rollback to this state. Second, any change in status of a node belonging to $\mathcal{G}_m$ leads to a rollback operation in domain $\mathcal{D}_m$. To overcome these shortcomings, we will make use of the following additional attribute of the FMM:

ATTRIBUTE 3. *Let G^p_{ijk} be the solution to Eq. (2.3) at loop step p. If any single one of the adjacent nodes $i'j'k'$ becomes smaller, i.e. $G^{p'}_{i'j'k'} \leq G^p_{i'j'k'}$ with $p' > p$, then a subsequent update of node ijk by Eq. (2.3) yields $G^{p'}_{ijk} \leq G^p_{ijk}$.*

The proof of attribute 3 is straightforward. Attribute 3 implies that any node which has been locally *accepted* at loop step p and is then rolled back to status *close*, can retain its G^p_{ijk} value, because any subsequent update will either decrease its value or leave it unchanged. Its change back to *accepted* status at a later loop step is thereby uninfluenced. Following the same line of argument, all neighboring *close* nodes can also retain their $G^p_{i'j'k'}$ values. Thus, step (B) of $\mathcal{P}_3$ needs to rollback only the status of the nodes from *accepted* back to *close*, but does not need to rollback their node values. Furthermore, attribute 3 implies that only the change to *accepted* status of a node in $\mathcal{G}_m$ needs to initiate a rollback.

Incorporating attribute 3, the final domain decomposed parallel algorithm $\mathcal{P}_4$ is given in Table 5. Obviously, the efficiency of algorithm $\mathcal{P}_4$ depends on the required amount of inter-domain communication, i.e. how often nodes belonging to $\mathcal{B}_m$ change to *accepted* status, and how many rollback operations are required in step (B). If the solution of Eqs. (1.3) and (1.4) is required only up to a certain distance T away from the $G = G_0$ interface, then, naturally, only those nodes within this band, $|G^0_{ijk} - G_0| \leq T$, need to be considered in the FMM algorithm. Depending on the geometry of the $G = G_0$ interface, this so-called narrow band approach (Peng *et al.* 1999) may drastically reduce the necessary inter-domain communication, as illustrated in Fig. 2. In fact, as long as there are no nodes ijk belonging to $\mathcal{B}_m$ with $|G^0_{ijk} - G_0| \leq T$, no inter-domain communication is

(A) Perform steps (a) and (b) of the sequential FMM algorithm.

(B) Check, if any node belonging to $\mathcal{G}_m$ changed status to *accepted* and decreased its value from a previously *accepted* value to the new value G_B. If so, rollback by marking all nodes $G^{p\ldots n}$ as *close*, where p is given by $G^{p-1} \leq G_B \leq G^p$. Mark G_B as *close* and insert it into list $\mathcal{L}_B$. Set $n = p$.

(C) Locate the locally smallest *close* G value (including list $\mathcal{L}_B$); denote it as $G_{\mathcal{D}_m}$.

(D) Perform steps (c)-(e) of the sequential FMM algorithm for $G_{\mathcal{D}_m}$.

(E) If node $G_{\mathcal{D}_m}$ belongs to $\mathcal{B}_m$, communicate it to $\mathcal{G}_{m+1}$ of domain $\mathcal{D}_{m+1}$.

(F) Set n=n+1. Return to step (B) until all local nodes are *accepted.*

(G) Wait until all other domains reach step (G) or a node belonging to $\mathcal{G}_m$ changes to *accepted* status. In the latter case go to step (B).

TABLE 5. The parallel FMM algorithm $\mathcal{P}_4$

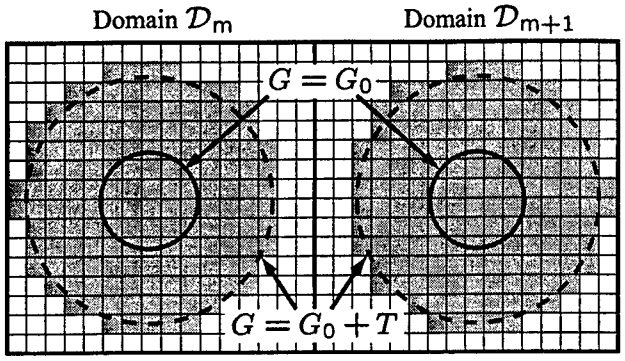


FIGURE 2. Narrow band approach.

required at all and the problem completely decouples. Although in most applications this is not the case, the narrow band approach can still reduce the number of inter-domain communications substantially.

4. Redistribution

The preceding sections dealt exclusively with the solution of the reinitialization equation (1.3) as the prerequisite for solving the redistribution equation (1.4). The basic idea in solving Eq. (1.4) is to again confine its solution to a small band around the globally smallest G_{ijk} values that marches outward to ever larger values of G_{ijk}.

To this end, first, initial values of S have to be calculated at all nodes directly adjacent to the $G = G_0$ interface by either first order approximations (Adalsteinsson & Sethian 1999) or higher order schemes (Chopp 2001). Then, Eq. (1.4) is approximated by

$$\begin{aligned} &A^{-x}\left(D^{-x}_{ijk}G^n \cdot D^{-x}_{ijk}S\right) + A^{+x}\left(D^{+x}_{ijk}G^n \cdot D^{+x}_{ijk}S\right) + \\ &A^{-y}\left(D^{-y}_{ijk}G^n \cdot D^{-y}_{ijk}S\right) + A^{+y}\left(D^{+y}_{ijk}G^n \cdot D^{+y}_{ijk}S\right) + \\ &A^{-z}\left(D^{-z}_{ijk}G^n \cdot D^{-z}_{ijk}S\right) + A^{+z}\left(D^{+z}_{ijk}G^n \cdot D^{+z}_{ijk}S\right) = 0\,. \end{aligned} \tag{4.1}$$

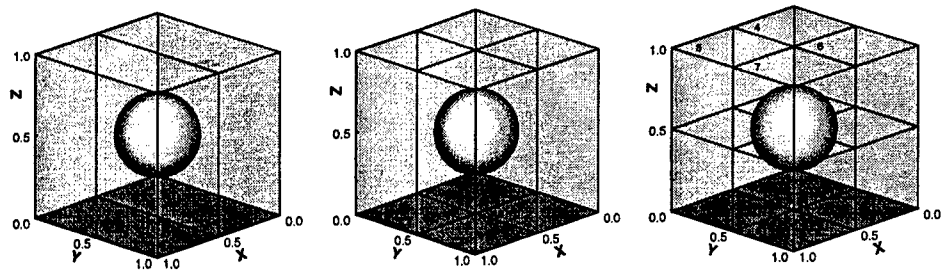


FIGURE 3. Optimal domain decomposition into 2, 4, and 8 domains.

Here, the switch A^{-x} is given by

$$A^{-x} = \begin{cases} 1 & : \quad \max\left(D_{ijk}^{-x}G^n, -D_{ijk}^{+x}G^n, 0\right) = D_{ijk}^{-x}G^n \\ 0 & : \quad \text{otherwise}\,, \end{cases} \tag{4.2}$$

with all other A defined accordingly. The switch A ensures that only those nodes are used to evaluate S_{ijk} in Eq. (4.1) that also contributed to the update of G_{ijk}^n, Eq. (2.3). In every FMM loop step, Eq. (4.1) is only solved for the node that changes status to *accepted* in step (c) of the sequential FMM. If this node belongs to $\mathcal{B}_m$, its new value S^n has to be communicated to the corresponding ghost node in domain $\mathcal{D}_{m+1}$ in step (E) of the parallel FMM algorithm $\mathcal{P}_4$.

5. Results

To evaluate the performance of the proposed parallel FMM algorithm $\mathcal{P}_4$ to solve Eqs. (1.3) and (1.4), the results of four different sets of computations are presented in the following. All four sets are three-dimensional and based upon the same interface geometry, composed of a sphere with radius $R_0 = 0.25$ and center located at $\boldsymbol{x}_c = (0.5, 0.5, 0.5)$. The level set scalar field representing this sphere is given by

$$G(\boldsymbol{x}) = R_0 - |\boldsymbol{x} - \boldsymbol{x}_c|\,. \tag{5.1}$$

The distribution of $\boldsymbol{S}$ on the interface is set to

$$\boldsymbol{S}(\boldsymbol{x}) = \cos\left(\arctan\left(\frac{y - y_c}{z - z_c}\right)\right)\sin\left(\arctan\left(\frac{x - x_c}{\sqrt{(y - y_c)^2 + (z - z_c)^2}}\right)\right)\,. \tag{5.2}$$

All computations are performed on a global domain of size [0,1]x[0,1]x[0,1] discretized by 192x192x192 equidistant cartesian grid nodes.

5.1. *Optimal domain decomposition*

As mentioned in section 1, information in Eqs. (1.3) and (1.4) propagates in the interface normal direction. Hence, a domain decomposition such that all domain boundaries are parallel to the interface normal vectors is optimal in the sense that no information does cross these boundaries. Figure 3 shows such a decomposition into 2, 4, and 8 domains. This domain decomposition is also optimal with regard to load balancing. Since all domains contain the exact same number of nodes $G_{ijk} < G_0$ as well as $G_{ijk} \geq G_0$, the load imbalance factor is $F_l = 0$, see Eq. (5.5) defined later.

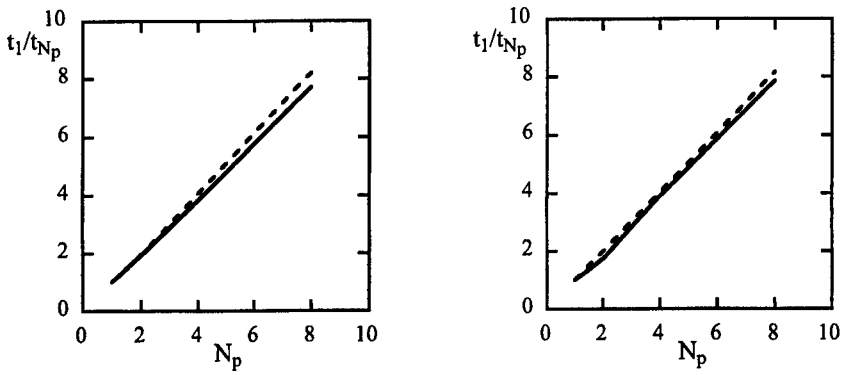


FIGURE 4. Speedup due to parallel FMM employing the narrow band approach (left) and whole domain update (right) with the optimal decomposition into 1, 2, 4, and 8 domains. Dashed line denotes theoretically possible speedup, straight line represents attained speedup.

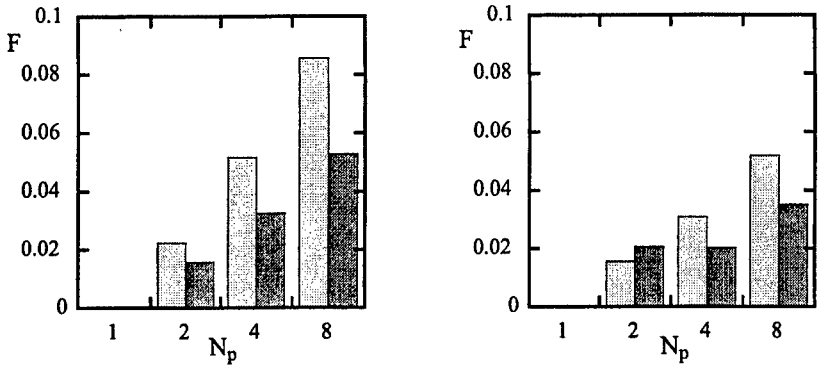


FIGURE 5. Overhead due to parallel FMM employing the narrow band approach (left) and whole domain update (right) with the optimal decomposition into 1, 2, 4, and 8 domains. Shown are communication factor F_c ( ) and rollback factor F_r ( ).

Two different sets of computations were performed. The first set employs the narrow band approach with the width of the band set to $T = 8\Delta x$. The second set performs the FMM throughout the whole computational domain.

Figure 4 shows a comparison of the speedup for both cases to the theoretically possible speedup. The theoretically possible speedup was determined by calculating only domain number 0, see Fig. 3, using Neumann boundary conditions. Note that, since the operation count of the sequential FMM is $O(N \log N)$, slightly hyperlinear speedup is theoretically possible. However, the actual efficiency attained in the parallel computation is approximately 0.96 for the narrow band approach and roughly 0.98 for the whole domain update.

Figure 5 illustrates the overhead due to the parallelization. Depicted are the communication factor F_c, defined as

$$F_c = \frac{\text{total number of communication operations}}{\text{total number of nodes}}, \tag{5.3}$$

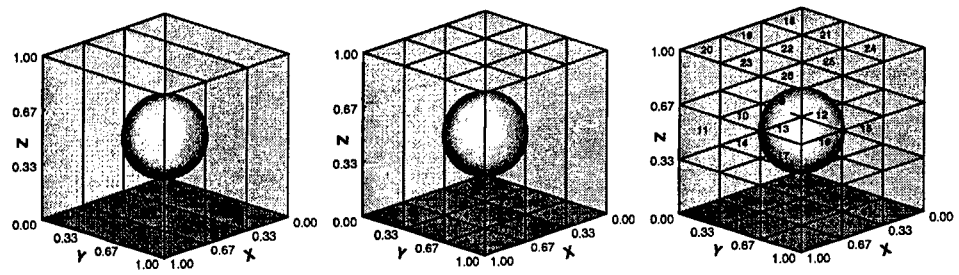


FIGURE 6. Non-optimal domain decomposition into 3, 9, and 27 domains.

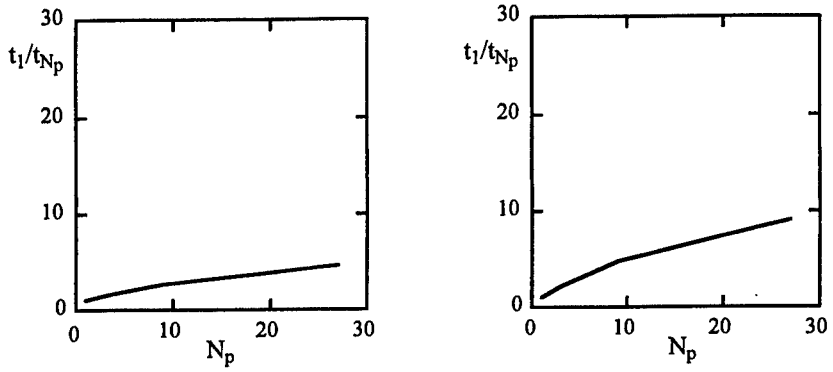


FIGURE 7. Speedup due to parallel FMM employing the narrow band approach (left) and whole domain update (right) with the non-optimal decomposition into 1, 3, 9, and 27 domains.

and the rollback factor F_r, defined as

$$F_r = \frac{\text{total number of rollback operations}}{\text{total number of nodes}}. \tag{5.4}$$

As expected, with optimal domain decomposition, the amount of communication and rollback operations is very small, indicating that the overhead due to parallelization is minimal. This result is consistent with the observed high efficiency.

5.2. *Non-optimal domain decomposition*

When applying the parallel FMM to actual problems, an optimal domain decomposition, as presented in the previous section, is not always viable. In this non-optimal case, three major factors can impact the performance of the parallel algorithm: load imbalancing, communication overhead, and rollback overhead. To illustrate their effect, two sets of computations are performed using a decomposition into 1, 3, 9, and 27 domains as depicted in Fig. 6. The first set again uses the narrow band approach with the width of the band set to $T = 8\Delta x$, whereas the second set calculates the FMM throughout the whole computational domain.

Figure 7 shows the speedup attained for both the narrow band approach on the left and the whole domain update on the right. As can be seen, speedup, and thus efficiency, is significantly lower than the optimal domain decomposition case, see Fig. 4. The efficiency decreases to 0.17 for the narrow band approach and 0.34 for the whole domain update.

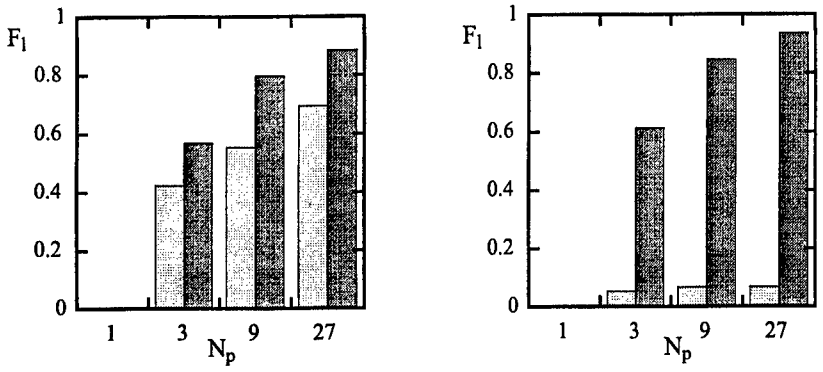


FIGURE 8. Load imbalance factor F_l due to parallel FMM employing the narrow band approach (left) and whole domain update (right) with the non-optimal decomposition into 1, 3, 9, and 27 domains. Shown is F_l for $G_{ijk} < G_0$ (▒) and F_l for $G_{ijk} \geq G_0$ (■).

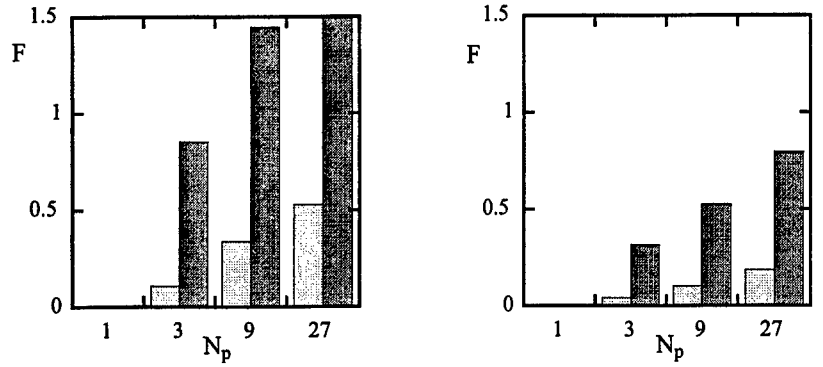


FIGURE 9. Overhead due to parallel FMM employing the narrow band approach (left) and whole domain update (right) with the non-optimal decomposition into 1, 3, 9, and 27 domains. Shown are communication factor F_c (▒) and rollback factor F_r (■).

To further analyze this behavior, the load imbalance factor

$$F_l = 1 - \frac{\text{maximum number of nodes per domain}}{\text{average number of nodes per domain}} \tag{5.5}$$

for each of the four different domain decompositions is depicted in Fig. 8. Since the parallel FMM algorithm is called twice, once for all nodes $G_{ijk} < G_0$ and once for all nodes $G_{ijk} \geq G_0$, F_l is calculated accordingly. Obviously, the load imbalance factors for both sets are relatively large. This explains the significantly reduced efficiency of the non-optimal domain decomposition as compared to the optimal domain decomposition. Otherwise, the load imbalance factors for $G_{ijk} \geq G_0$ are roughly the same for both sets. However, the load imbalance factor for $G_{ijk} < G_0$ is significantly larger in the narrow band approach than in the whole domain update, leading to the lower speedup and efficiency in the narrow band approach as compared to the whole domain update.

Figure 9 exhibits the communication factor F_c and the rollback factor F_r. Compared to the optimal domain decomposition case (Fig. 5) both factors are one order of magnitude larger. Furthermore, F_c and F_r are significantly larger in the narrow band approach as opposed to the whole domain update. This is due to the aforementioned higher load imbalance in the narrow band approach.

6. Conclusions and future work

In this paper, the first domain decomposition parallelization of the Fast Marching Method for level sets has been presented. Parallel speedup has been demonstrated in both the optimal and non-optimal domain decomposition case. The parallel performance of the proposed method is strongly dependent on load balancing separately the number of nodes on each side of the interface. A load imbalance of nodes on either side of the domain leads to an increase in communication and rollback operations. Furthermore, the amount of inter-domain communication can be reduced by aligning the inter-domain boundaries with the interface normal vectors. In the case of optimal load balancing and aligned inter-domain boundaries, the proposed parallel FMM algorithm is highly efficient, reaching efficiency factors of up to 0.98.

Future work will focus on the extension of the proposed parallel algorithm to higher order accuracy. Also, to further enhance parallel performance, the coupling of the domain decomposition parallelization to the G_0-based parallelization will be investigated.

Acknowledgments

The support of the German Research Foundation (DFG) is gratefully acknowledged. The author also would like to thank Frank Ham and Yuan-Nan Young for many helpful discussions.

REFERENCES

ADALSTEINSSON, D. & SETHIAN, J. A. 1999 The fast construction of extension velocities in level set methods. *J. Comput. Phys.* **148**, 2–22.

BRACKBILL, J. U., KOTHE, D. B. & RUPPEL, H. M. 1988 FLIP: A low dissipation, particle-in-cell method for fluid flow. *Comput. Phys. Commun.* **48**, 25–38.

CHOPP, D. L. 2001 Some improvements of the fast marching method. *SIAM J. Sci. Comput.* **23**, 230–244.

ENRIGHT, D., FEDKIW, R., FERZIGER, J. & MITCHELL, I. 2002 A hybrid particle level set method for improved interface capturing. *J. Comp. Phys.* **183**, 83–116.

HELMSEN, J., PUCKETT, E., COLELLA, P. & DORR, M. 1996 Two new methods for simulating photolithography development in 3D. *Proc. SPIE* **2726**, 253–261.

MERRIMAN, B., BENCE, J. & OSHER, S. 1994 Motion of multiple junctions: A level set approach. *J. Comput. Phys.* **112**, 334.

NOH, W. F. & WOODWARD, P. 1976 SLIC (Simple Line Interface Calculation). In *Lecture Notes in Physics Vol. 59, Proceedings of the Fifth International Conference on Numerical Methods in Fluid Dynamics* (ed. A. I. V. D. Vooren & P. J. Zandenbergen), pp. 330–340. Berlin: Springer.

OSHER, S. & SETHIAN, J. A. 1988 Fronts propagating with curvature-dependent speed: Algorithms based on Hamilton-Jacobi formulations. *J. Comput. Phys.* **79**, 12–49.

PENG, D., MERRIMAN, B., OSHER, S., ZHAO, H. & KANG, M. 1999 A PDE-based fast local level set method. *J. Comput. Phys.* **155**, 410–438.

ROUY, E. & TOURIN, A. 1992 A viscosity solution approach to shape-from-shading. *SIAM J. Num. Anal.* **29**, 867–884.

RUSSO, G. & SMEREKA, P. 2000 A remark on computing distance functions. *J. Comput. Phys.* **163**, 51–67.

SETHIAN, J. A. 1996*a* A fast marching level set method for monotonically advancing fronts. *Proc. Natl. Acad. Sci. USA* **93**, 1591–1595.

SETHIAN, J. A. 1996*b* *Level Set Methods: Evolving Interfaces in Geometry, Fluid Mechanics, Computer Vision and Material Science*. Cambridge, UK: Cambridge University Press.

SETHIAN, J. A. 1999*a* Fast marching methods. *SIAM Review* **41** (2), 199–235.

SETHIAN, J. A. 1999*b* *Level Set Methods and Fast Marching Methods*, 2nd edn. Cambridge, UK: Cambridge University Press.

SUSSMAN, M. & FATEMI, E. 1999 An efficient, interface-preserving level set redistancing algorithm and its application to interfacial incompressible fluid flow. *SIAM J. Sci. Comput.* **20** (4), 1165–1191.

SUSSMAN, M., FATEMI, E., SMEREKA, P. & OSHER, S. 1998 An improved level set method for incompressible two-phase flows. *Comp. Fluids* **27** (5-6), 663–680.

SUSSMAN, M., SMEREKA, P. & OSHER, S. 1994 A level set method for computing solutions to incompressible two-phase flow. *J. Comput. Phys.* **119**, 146.

TSITSIKLIS, J. 1994 Efficient algorithms for globally optimal trajectories. In *Proceedings of the 33rd Conference on Decision and Control*, pp. 1368–1373. Lake Buena Vista.

TSITSIKLIS, J. 1995 Efficient algorithms for globally optimal trajectories. *IEEE Transactions on Automatic Control* **40**, 1528–1538.

A Cartesian adaptive level set method for two-phase flows

By F. Ham AND Y.-N. Young

1. Motivation and objectives

Simulations of flows involving free surfaces have become ubiquitous in the literature. The evolution of both simulation methods and computer speed have allowed the investigation of many problems of increasing complexity and engineering relevance. For 2D simulations, it is reasonably common to use grid resolutions of 512×512 or larger. See for example the 2D planar breaking wave simulations of Chen *et al.* (1999), or the axisymmetric drop breakup simulations of Han and Tryggvason (1999a, 1999b). Many such free surface problems are fundamentally three dimensional and the absence of three-dimensional effects such as the pinch-off of stretched filaments by surface tension makes it difficult to make valid physical conclusions or use 2D results to develop models. Achieving similar grid resolution in 3D, however, is outside the computational reach of most research centers.

For many problems of interest, a fine grid is required in only a relatively small portion of the domain (e.g. around regions of high surface curvature) and much coarser grids are sufficient to capture the smoothly evolving velocity fields far from the surface. It is this type of problem that motivates the present Cartesian adaptive method, where the finest resolution in the neighbourhood of the free surface may be of order 512^3 (sometimes called the effective resolution), but the coarsening away from the free surface yields an actual number of control volumes that is less than using the fine grid everywhere by at least an order of magnitude.

A number of adaptive Cartesian methods for freesurface calculations have been proposed in the literature. For example, Haj-Hariri *et al.* (1997) used Cartesian local grid refinement to investigate thermocapillary motion of 3D drops. Their method used an octree-based structure to store the grid heirarchy. More recently Sussman *et al.* (1999) proposed an adaptive levelset method based on the embedded grid approach, where the global computational domain is divided into uniformly refined rectangular patches. This approach has the advantage of allowing a traditional staggered or semi-staggered structured discretization throughout most of the domain, with special interpolations required only at the interface between grid levels. The embedded grid approach may not, however, lead to the smallest Cartesian grids possible because of the restriction that refined regions be rectangular and isotropic. Additionally, embedded grid approaches can be difficult to parallelize and load balance.

In the present contribution we develop a level set method based on local anisotropic Cartesian adaptation as described in Ham *et al.* (2002). Such an approach should allow for the smallest possible Cartesian grid capable of resolving a given flow. The remainder of the paper is organized as follows. In section 2 the level set formulation for free surface calculations is presented and its strengths and weaknesses relative to the other free surface methods reviewed. In section 3 the collocated numerical method is described. In section 4 the method is validated by solving the 2D and 3D drop oscilation problem. In section

5 we present some results from more complex cases including the 3D drop breakup in an impulsively accelerated free stream, and the 3D immiscible Rayleigh-Taylor instability. Conclusions are given in section 6.

2. Mathematical Formulation

For recent reviews of the level set method and its many applications, the interested reader is referred to Osher and Fedkiw (2001) or Sethian (2001). Here we briefly present its formulation for incompressible 2-fluid problems.

The incompressible, immiscible, two-fluid system is treated as a single fluid with strong variations in density and viscosity in the neighborhood of the interface. The continuity and momentum equations for such a flow can be written in conservative form as:

$$\frac{\partial \rho}{\partial t} + \frac{\partial \rho u_j}{\partial x_j} = 0, \tag{2.1}$$

$$\frac{\partial \rho u_i}{\partial t} + \frac{\partial \rho u_j u_i}{\partial x_j} = -\frac{\partial p}{\partial x_i} + \frac{\partial \tau_{ij}}{\partial x_j} + \rho g_i + \sigma \kappa \delta(d) n_i, \tag{2.2}$$

where u_i is the fluid velocity, ρ the fluid density, p the pressure, τ_{ij} the viscous stress tensor, g_i the acceleration due to gravity, σ the surface tension coefficient, κ the local free surface curvature, δ the Dirac delta function evaluated based on d the normal distance to the surface, and n_i the unit normal at the free surface.

It is well known that solving equations 2.1 and 2.2 directly in the presence of the discontinuities at the interface will lead to the excessive smearing of the interface over long time integration, and/or numerical "ringing" in the region of the discontinuities due to dispersive errors in the numerical discretization. In the present work, we capture the interface as the zero-level isosurface of a higher-order function ϕ, the level set function (effectively an additional transported scalar). On either side of the interface, the sign of the level set function can be used to determine which fluid is present. This allows the fluid properties to be written as a function of the level set only, specifically $\rho = \rho(\phi)$. This allows the continuity equation to be written:

$$\frac{d\rho}{d\phi}\left(\frac{\partial \phi}{\partial t} + u_j \frac{\partial \phi}{\partial x_j}\right) + \rho \frac{\partial u_j}{\partial x_j} = 0 \tag{2.3}$$

For the case of constant density except in the neighborhood of the zero level set, which represents the fluid interface, the solution of the continuity equation can thus be decomposed into the solution of the following:

$$\frac{\partial \phi}{\partial t} + u_j \frac{\partial \phi}{\partial x_j} = 0 \Big|_{\phi=0} \tag{2.4}$$

$$\frac{\partial u_j}{\partial x_j} = 0 \tag{2.5}$$

Eq. 2.4 is the standard evolution equation for the level set function, and eq. 2.5 is the incompressible continuity equation. Note that the level set equation need only be solved near the interface, which we have defined as the zero level set. Away from the interface, it is common to make ϕ equal to a signed distance function.

In a similar way, the application of chain rule to the momentum equation allows the

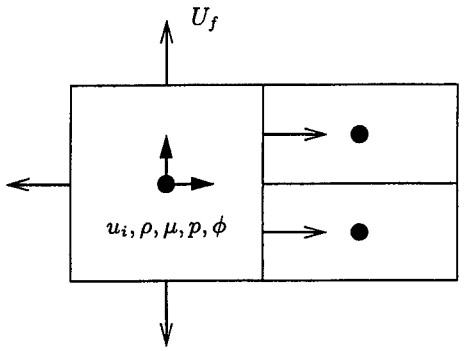


FIGURE 1. Spatial location of variables for collocated discretization.

decomposition of the momentum equation into the solution of the level set equation, eq. 2.4, and the solution of the following momentum equation:

$$\rho\frac{\partial u_i}{\partial t} + \rho\frac{\partial u_j u_i}{\partial x_j} = -\frac{\partial p}{\partial x_i} + \frac{\partial \tau_{ij}}{\partial x_j} + \rho g_i + \sigma\kappa\delta(|\phi|)n_i \tag{2.6}$$

Equations 2.4 – 2.6 comprise our governing system for the present work. Note that the level set formulation results in a system of governing equations that can no longer be written in conservative form. Thus, when the finite volume method is applied to this system, we cannot expect to achieve discrete conservation of mass and momentum (in the region of the interface). It is the hope of the level set formulation that these errors in conservation are mitigated by the more accurate capturing of the interface that is possible with the smoothly-varying level set function.

3. Numerical Method

The governing equations are solved on a Cartesian adaptive grid. The grid arrangement and adaptation are described more completely in Ham *et al.* (2002), and here we only discuss details specific to the simulation of multiphase flows using level set methods on such a grid.

Figure 1 shows the spatial arrangement of variables on the Cartesian adaptive grid. All variables are stored at the control volume (CV) centers with the exception of a face-normal velocity, located at the face centers, and used to enforce the divergence-free constraint in each time step. The variables are staggered in time so that they are located most conveniently for the time advancement scheme. Denoting the time level by a superscript index, the velocities are located at time level t^n and t^{n+1}, and pressure, density, viscosity, and the level set at time levels $t^{n-\frac{1}{2}}$ and $t^{n+\frac{1}{2}}$. The semi-descretization of the governing equations in each time step is then as follows.

Step 1. Advance the level set:

$$\frac{\phi^{n+\frac{1}{2}} - \phi^{n-\frac{1}{2}}}{\Delta t} + u_j^n \frac{1}{2}\frac{\partial}{\partial x_j}\left(\phi^{n-\frac{1}{2}} + \phi^{n+\frac{1}{2}}\right) = 0 \tag{3.1}$$

Here the advantage of time-staggering is evident – i.e. we know the velocity u_i^n from the previous time step, so this equation is decoupled from the other equations, and can be advanced on its own to get the level set value at the mid-point of the new time level, $\phi^{n+\frac{1}{2}}$. Here we have used an implicit Crank-Nicholson time advancement scheme, which requires an iterative solution method. In practice the hyperbolic system is not stiff, and can be quickly converged by a simple iterative scheme such as Gauss-Seidel. The spatial derivatives required in eq. 3.1 are approximated by a 5^{th}-order WENO scheme (Jiang & Peng 2000). While effective at recovering the viscosity solution to the level set equation, the WENO discretization requires that the grid be locally refined in a uniform way in a band about the zero level set, and thus does not take full advantage of the flexibility in the adaptive grid.

Step 2. Reinitialize the level set by solving to steady state:

$$\frac{\partial \phi}{\partial \tau} = sgn\left(\phi\right)\left(1 - |\nabla \phi|\right). \tag{3.2}$$

The reinitialization step is performed every time step, and ensures that the level set is a signed distance function away from $\phi = 0$, without (theoretically) changing the location of the zero-level set. Spatial derivatives required in eq. 3.2 are once again approximated using a 5^{th}-order WENO scheme (Jiang & Peng 2000). For this equation we use explicit third order TVD Runge-Kutta method for time integration. In practice, it is not neccessary to solve to steady state, and we have found that 5 iterations with a pseudo-time step of $\Delta\tau = \Delta x/4$ is sufficient when performed every computational time step.

Step 3. Calculate the new density and viscosity at the midpoint of the time step:

$$\rho^{n+\frac{1}{2}} = \rho_1 H\left(\phi^{n+\frac{1}{2}}\right) + \rho_2\left(1 - H\left(\phi^{n+\frac{1}{2}}\right)\right) \tag{3.3}$$

$$\mu^{n+\frac{1}{2}} = \mu_1 H\left(\phi^{n+\frac{1}{2}}\right) + \mu_2\left(1 - H\left(\phi^{n+\frac{1}{2}}\right)\right) \tag{3.4}$$

where ρ_1, μ_1 are the constant properties of the fluid occupying the region $\phi > 0$, and ρ_2, μ_2 are the constant properties of the fluid occupying the region $\phi \leq 0$, and H is a smoothed Heaviside step function (Sussman *et al.* 1994).

Step 4. Project the momentum equations:

The remaining steps are a variant of the collocated fractional step method described, for example, by Kim and Choi (2000). First, calculate a projected velocity field $\hat{u}_i$ using the momentum equations:

$$\frac{\hat{u}_i - u_i^n}{\Delta t} = -\frac{1}{\rho^{n+\frac{1}{2}}}\left(\frac{\partial p}{\partial x_i}^{n-\frac{1}{2}} + R_i^{n+\frac{1}{2}}\right) \tag{3.5}$$

where R_i contains all other terms in the momentum equation, eq 2.6. We discretize both the convective and viscous terms implicitly using second-order symmetric discretizations, and the surface tension explicitly based on the known level set at the midpoint of the current time step, $\phi^{n+\frac{1}{2}}$. Some care must be taken in the discretization of the surface tension terms when treated as source terms in the momentum equations of a collocated scheme, as described below.

Step 5. Subtract the old pressure gradient:

$$u_i^{*n+1} = \widehat{u}_i^{n+1} + \Delta t \frac{1}{\rho^{n+\frac{1}{2}}} \frac{\delta p}{\delta x_i}^{n-\frac{1}{2}} \tag{3.6}$$

Step 6. Interpolate the starred velocity field to the faces:

$$U_f^{*n+1} = \overline{u_i^{*n+1}}^f - \Delta t \left(\overline{\frac{R_i^{n+\frac{1}{2}}}{\rho^{n+\frac{1}{2}}}}^f - \frac{R_f^{n+\frac{1}{2}}}{\rho_f^{n+\frac{1}{2}}} \right), \tag{3.7}$$

where $\overline{()}^f$ is a second-order interpolation operator that yields a face-normal component from two CV-centered vectors.

Step 7. Solve the variable coefficient Poisson equation for the new pressure:

$$\frac{1}{\Delta t} \sum_f U_f^{*n+1} A_f = \sum_f \frac{1}{\rho_f^{n+\frac{1}{2}}} \frac{\delta p}{\delta n}^{n+\frac{1}{2}} A_f. \tag{3.8}$$

Step 8. Update the face velocities to the new divergence-free field:

$$\frac{U_f^{n+1} - U_f^*}{\Delta t} = -\frac{1}{\rho_f^{n+\frac{1}{2}}} \frac{\partial p}{\partial n}^{n+\frac{1}{2}} \tag{3.9}$$

Step 9. Reconstruct the pressure gradient at the CV centers:

$$\frac{1}{\rho^{n+\frac{1}{2}}} \frac{\partial p}{\partial x_i}^{n+\frac{1}{2}} = \overline{\frac{1}{\rho_f^{n+\frac{1}{2}}} \frac{\partial p}{\partial n}^{n+\frac{1}{2}}}^{x_i} \tag{3.10}$$

where $\overline{()}^{x_i}$ represents a reconstruction operator. In this case we use a face-area weighted least squares reconstruction.

Step 10. Update the CV velocities:

$$\frac{u_i^{n+1} - u_i^*}{\Delta t} = -\frac{1}{\rho^{n+\frac{1}{2}}} \frac{\partial p}{\partial x_i}^{n+\frac{1}{2}} \tag{3.11}$$

By adding eqs. 3.5, 3.6, and 3.11, it is clear that a second-order time advancement of the momentum equation is recovered.

A critical difference between the present formulation and the formulation of Kim and Choi is in the calculation of the starred face-normal velocities (eq. 3.7). Kim and Choi assume that:

$$\overline{\frac{R_i^{n+1/2}}{\rho^{n+1/2}}}^f \approx \frac{R_f^{n+1/2}}{\rho_f^{n+1/2}}. \tag{3.12}$$

This is an $O(\Delta x^2)$ approximation, seemingly consistent with the overall accuracy of the method, and significantly simplifies the calculation of the Poisson equation source term. In the present investigation, however, it was found that when surface tension forces were introduced in the region of the zero level set, this approximation could lead to large non-physical oscillations in the CV-centered velocity field. To solve this problem, the surface tension forces must be calculated at the faces, and then averaged to the CV centers, i.e.:

$$\frac{R_i^\sigma}{\rho} \equiv \frac{\overline{R_f^\sigma}^{x_i}}{\rho_f} \tag{3.13}$$

With this calculation of the surface tension forces, we can no longer make the assumption of eq. 3.12, and the additional terms must be included in the calculation of U_f^* and thus in the Poisson equation source term.

4. Validation

As validation cases for the method, we solve the 2D column and 3D drop oscillation problems.

4.1. *2D column oscillation*

From Lamb (1932), for a 2D column of liquid in the limit of zero viscosity perturbed according to:

$$r = a\left(1 + \varepsilon cos\left(n\theta\right)\right) \tag{4.1}$$

where a is the mean radius, ε a small perturbation, and n the mode, the oscillation frequency will be:

$$\omega^2 = n\left(n^2 - 1\right)\frac{\sigma}{\rho a^3}. \tag{4.2}$$

Figure 2(a) shows the initial condition for a drop oscillation calculation for mode $n = 5$. Here we have exaggerated the perturbation amplitude to $\varepsilon = 0.15$ for illustrative purposes. In the actual computations, $\varepsilon = 0.02$ was used for the initial condition. Figure 2(b) compares the calculated results to the theory (period $T = 2\pi/\omega$), with generally good agreement. For these calculations, we used periodic boundary conditions in a square domain of size $L = 4a$, and set the density of the surrounding fluid to $\rho_2 = 0.001\rho$ to minimize its effect on the oscillations. The fluid viscosity was adjusted to keep the decay in amplitude of the oscillations to less that 5% per cycle.

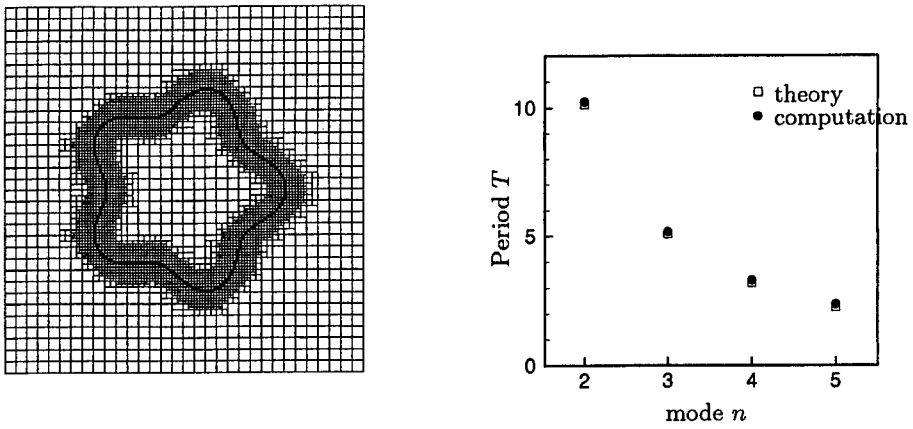
4.2. *3D drop oscillation*

For a 3D drop perturbed according to

$$r = a\left(1 + \epsilon S_n\right) \tag{4.3}$$

where the surface harmonics of order n, S_n, are defined:

$$S_1 = \frac{1}{2}\sqrt{\frac{3}{\pi}}cos\theta \tag{4.4}$$



(a) (b)

FIGURE 2. a) Sample grid and initial zero-level set for 2D drop oscillation problem with $n = 5$. b) Comparison of computed and theoretical 2D drop oscillation periods for modes $n = 2$ through 5.

$$S_2 = \frac{1}{4}\sqrt{\frac{5}{\pi}}\left(3cos^2\theta - 1\right) \tag{4.5}$$

$$S_3 = \frac{1}{4}\sqrt{\frac{7}{\pi}}\left(5cos^3\theta - 3cos\theta\right) \tag{4.6}$$

$$S_4 = \frac{3}{16}\sqrt{\frac{1}{\pi}}\left(35cos^4\theta - 30cos\theta + 3\right) \tag{4.7}$$

$$S_5 = \frac{1}{16}\sqrt{\frac{11}{\pi}}\left(63cos^4\theta - 70cos^2\theta + 15\right) \tag{4.8}$$

the oscillation frequency is given by:

$$\omega^2 = n\left(n-1\right)\left(n+2\right)\frac{\sigma}{\rho a^3}. \tag{4.9}$$

Figure 3 (a) shows the drop surface for the mode $n = 5$. Figure 3 (b) compares the calculated results to the theory, also with good agreement.

5. Results

In the following subsections we present some results from simulations of more complex flows. For the purposes of this paper describing the numerical method, these cases are meant to simply illustrate the potential of the method. Consequently we do not present any analysis of the associated flow physics, which will be the subject of future investigations.

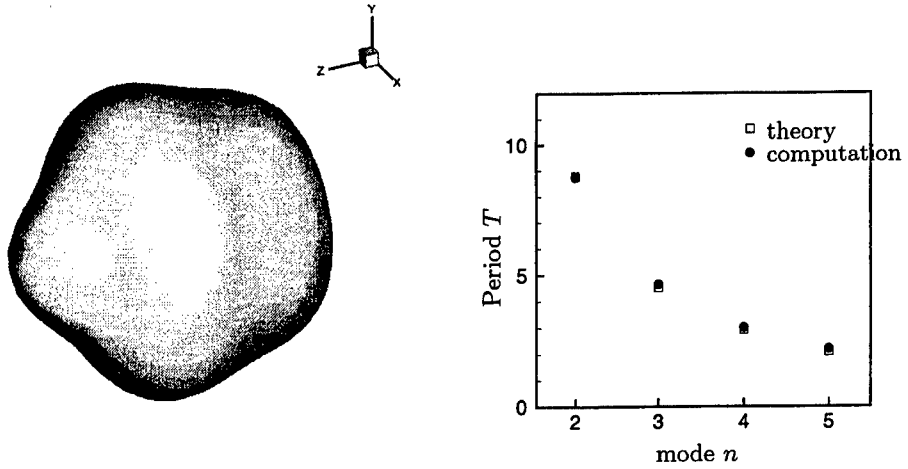


FIGURE 3. a) Initial zero-level set for 3D drop oscillation problem with $n = 5$. b) Comparison of computed and theoretical 3D drop oscillation periods for modes $n = 2$ through 5.

5.1. *Secondary breakup of spherical drops*

The secondary breakup of drops is an important problem in spray atomization, and the subject of the 2D axisymmetric numerical investigation of Han and Tryggvason (1999a, 1999b). We used the present Cartesian adaptive method to calculate 3D drop breakup in an impulsively accelerated free stream. Figure 4 shows the calculated free surface for a case run with equivalent resolution of $128 \times 128 \times 128$ with a domain size of $5D \times 5D \times 5D$.

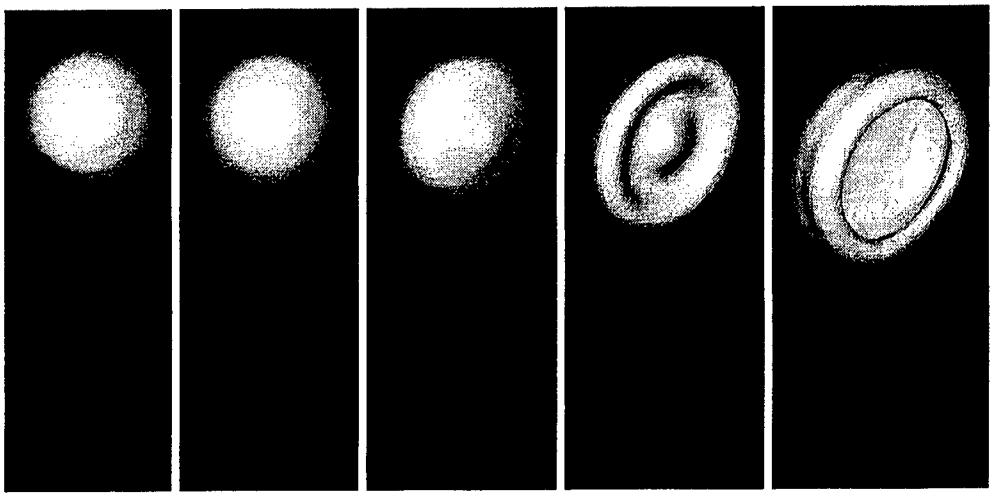
5.2. *Rayleigh-Taylor Problem*

The Rayleigh-Taylor instability refers to the instability of the plane interface between two fluids of different density superimposed one over the other and subject to gravity. When the upper fluid has a density greater than the lower fluid, the interface can be unstable to small perturbations whose amplification is well described by linear theory with dependence on the density ratio, gravity, surface tension coefficient, and viscosity (Chandrasekhar 1961). As the amplification continues and the problem enters the nonlinear regime, the fluid mixing can become chaotic, characterized by bubbles of lighter fluid rising into the heavier fluid, and spikes of heavier fluid falling into the lighter fluid, with regions of high vorticity near the spike/bubble interface. The resulting mixing zone is known experimentally (Schneider *et al.* 1998) to broaden in a way that depends linearly on the gravitational acceleration g and the Atwood number $A = (\rho_1 - \rho_2)/(\rho_1 + \rho_2)$, and quadratically on the time, i.e.

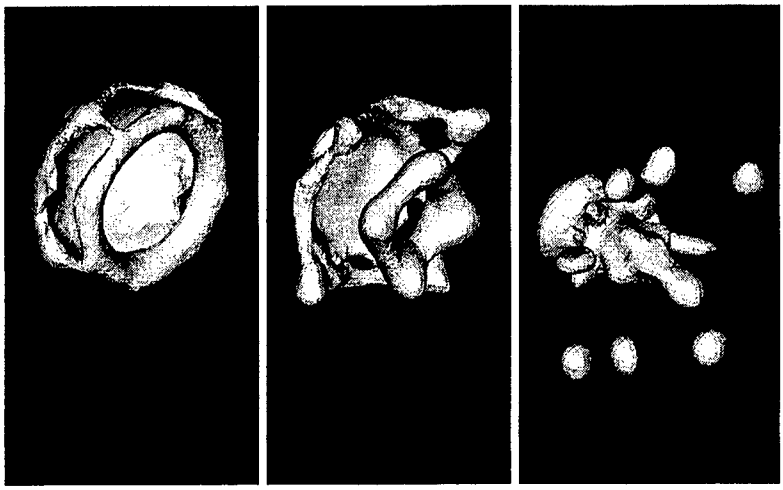
$$h_{b,s} = \alpha_{b,s} A g t^2, \tag{5.1}$$

where h_b or h_s represents the penetration length for bubbles or spikes respectively, and α has been introduced as a constant of proportionality, sometimes called the acceleration constant.

Recently, the miscible Rayleigh-Taylor problem has been investigated numerically by



(a) 0.5 (b) 1.5 (c) 2.5 (d) 3.5 (e) 4.5



(f) 5.5 (g) 6.5 (h) 8.5

FIGURE 4. Breakup of an initially spherical drop in an impulsively accelerated field. The number below each figure indicates the non-dimensional time tU/D. Free stream velocity is from top-left-back to lower-right-front. Properties for this simulation are as follows: $Re = \rho_g DU/\mu_g = 1000$, $We = \rho_g U^2 D/\sigma = 20$, $Oh = \mu_l/\sqrt{\rho_l \sigma D} = 0.007$.

Young *et al.* (2001), who calculate $\alpha_b \approx 0.03$. Experimental results for immiscible fluids yield higher values of $\alpha_b \approx 0.05 - 0.07$. A recent review of experimental and simulation results for the immiscible case is given by Glimm *et al.* (2001).

Figure 5 presents some results from the application of the present Cartesian adaptive method to this problem. These computations were performed in a $2 \times 2 \times 2$ box with the interface perturbed randomly with a maximum amplitude of 0.01. Properties of the simulation were selected to give a wavelength of maximum instability of $\lambda^* = 0.35$. These

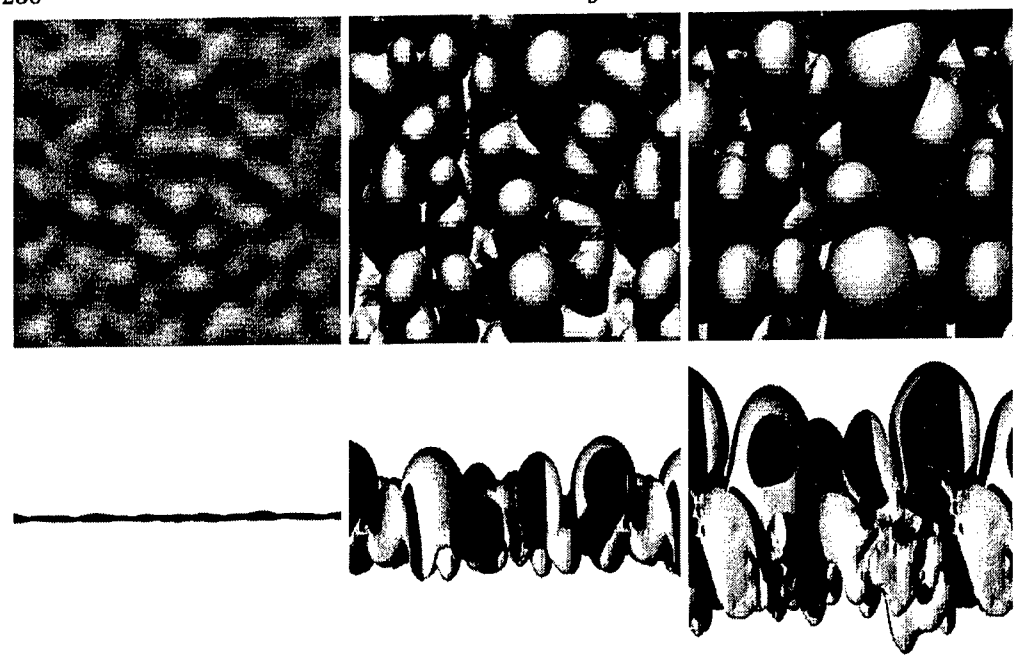


FIGURE 5. Evolution of the interface for the 3D Rayleigh-Taylor problem with multi-mode perturbation: top panels – plan view looking down on interface; bottom panels – elevation view from side.

preliminary simulations were made with the relatively coarse equivalent resolution in the region of the zero-level set of $64 \times 64 \times 64$, or about 10 CVs per wavelength for the most unstable mode. Figure 5 illustrates the evolution of the interface at 3 different times for the Atwood number $A = 0.98$.

6. Conclusions

A simulation tool that integrates Cartesian adaptive grids with the level set method has been developed. The method as described is particularly suited to problems where the smallest scales are associated with the free surface motions, and significant savings can thus be realized by coarsening the grid away from the surface. The method has been validated and its potential demonstrated by solving several test problems, including 2D and 3D drop oscillations, drop breakup in an impulsively accelerated free stream, and the immiscible 3D Rayleigh-Taylor problem.

Our ongoing work is focused on changing the level set solver to the particle level set method of Enright *et al.* (2002). The improved conservation properties of this method may allow us to move away from the higher-order WENO discretizations presently used in the level set advancement and reinitialization equations. With lower-order methods, adaptation can be added in the region of the zero-level set, resulting in a further significant reduction in computational cost.

REFERENCES

CHANDRASEKHAR, S. 1961 Hydrodynamic and Hydromagnetic Stability. *Oxford University Press.*

CHEN, G., KHARIF, C, ZALESKI, S., & LI, J. 1999 Two-dimensional Navier-Stokes simulation of breaking waves. *Phys. Fluids* **11** no. 1, 121-133.

ENRIGHT, D., FEDKIW, R., FERZIGER, J. & MITCHELL, I. 2002 A hybrid particle level set method for improved interface capturing. *J. Comput. Phys.* **183**, 83-116.

GLIMM, J., GROVE, J. W., LI, X. L., OH, W. & SHARP, D. H. 2001 A critical analysis of Rayleigh-Taylor growth rates. *J. Comput. Phys.* **169**, 652-677.

H. HAJ-HARIRI, Q. SHI, AND A. BORHAN 1997 Thermocapillary motion of deformable drops at finite reynolds and marangoni numbers. *Phys. Fluids* **9**, 845.

HAM, F. E., LIEN, F. S. & STRONG, A. B. 2002 A Cartesian grid method with transient anisotropic adaptation. *J. Comput. Phys.* **179**, 469-494.

HAN, J. & TRYGGVASON, G. 1999a Secondary breakup of axisymmetric liquid drops. I. Acceleration by a constant body force. *Phys. Fluids* **11** no. 12, 3651-3667.

HAN, J. & TRYGGVASON, G. 1999b Secondary breakup of axisymmetric liquid drops. II. Impulsive acceleration. *Phys. Fluids* **13** no. 6, 1554-1565.

JIANG, G-.S. & PENG, D. 2000 Weighted ENO schemes for Hamilton-Jacobi equations. *SIAM J. Sci. Comput.* **21** (6), 2126-2143.

KIM, D. & CHOI, H. 2000 A Second-Order Time-Accurate Finite Volume Method for Unsteady Incompressible Flow on Hybrid Unstructured Grids. *J. Comput. Phys.* **162**, 411-428.

LAMB, H. 1932 Hydrodynamics. *Cambridge University Press.*

OSHER, S. & FEDKIW, R. 2001 Level set methods: an overview and some recent results. *J. Comput. Phys.* **169**, 463.

SCHNEIDER, M. B., DIMONTE, G. & REMINGTON, B. 1998 Large and small structure in Rayleigh-Taylor mixing. *Phys. Rev. Lett.* **80**, 3507-3510.

SETHIAN, J. 2001 Evolution, implementation, and application of level set and fast marching methods for advancing fronts. *J. Comput. Phys.* **169**, 503.

SUSSMAN, M., SMEREKA, P. & OSHER, S. 1994 A level set approach for computing solutions to incompressible two-phase flow. *J. Comput. Phys.* **114**, 146-159.

MARK SUSSMAN, ANN S. ALMGREN, JOHN B. BELL, PHILLIP COLELLA, LOUIS H. HOWELL, AND MICHAEL L. WELCOME 1999 An Adaptive Level Set Approach for Incompressible Two-Phase Flows *J. Comput. Phys.* **148**, 81-124.

YOUNG, Y.-N., TUFO, H., DUBEY, A. & ROSNER, R. 2001 On the miscible Rayleigh-Taylor instability: two and three dimensions. *J. Fluid Mech.* **447**, 377-408.

Turbulent mixing of multiphase flow

By Y.-N. Young
J. Ferziger, F. E. Ham and M. Herrmann

1. Motivation and objectives

Mixing of multi-phase fluids is common in diverse research fields, and understanding of such an important phenomenon is useful to a range of engineering applications such as the polymer blender or control and designs of fluid processing. In this paper we adopt the phase-field modeling approach to investigate capillary induced effects on mixing. Phase-field modeling has been applied to simulation of multi-phase flow (Chella & Vinals 1996; Jasnow & Vinals 1996; Jacqmin 1999) due to its attractive aspect of easy numerical implementation. More recently it has also been applied to simulations of solidification of dendritic alloys (Zhao *et al.* 2003) and polymer blenders (Roths *et al.* 2002).

On macroscopic scales, the interface between two fluids is infinitely sharp. In phase-field modeling, the fluid properties are modeled (assumed) to change smoothly over a small layer across the interface on mesoscopic scales (Chella & Vinals 1996; Jasnow & Vinals 1996). Such a diffuse interface of separation is first considered in a liquid near or at its critical point, where the fluid property within the boundary needs to be modeled and resolved (Siggia 1979). However, phase-field modeling is not restricted to liquids at or near the critical point (Chella & Vinals 1996; Jasnow & Vinals 1996; Jacqmin 1999; Young *et al.* 2003). In fact, one can certainly envision that on the time scale of macroscopic fluid motions, the thermodynamic potential may depend on the gradient of the order parameter, which designates the fluid phase (or density). Accordingly, the macroscopic jump in the normal stress across the interface due to surface tension can be modeled as a mesoscopic continuum body force proportional to gradient of surface potential. On the mescoscopic scales, such a continuum surface tension force varies smoothly in the transition region around the interface. Naturally such a smooth continuum model of fluid interface brings great numerical convenience. Recently, phase-field modeling is made exactly energy-conserving by adding a thermodynamical constraint (Jamet *et al.* 2002). We did not include this constraint in this work as the correction is small for our cases of interest.

An interesting finding in multiphase fluids stirred by chaotic mixing flow is the self-similar drop size distribution (Berthier *et al.* 2001; Muzzio *et al.* 1991*b*). After rescaling the drop size distribution with respect to the characteristic size, all the drop size distributions collapse to a universal functional form for various combinations of parameters, such as viscosity, capillary number, and stirring flow strength. Some explanation to the self-similarity is provided in (Muzzio *et al.* 1991*a*,*c*), and it is not obvious if similar collapse of size distribution can also be found in a more general turbulent flow, where the distribution of stretching and stretching rate is randomly distributed. In the case of stochastic mixing (Lacasta *et al.* 1995), the existence of a characteristic domain size is an indication that similar collapse of drop size distribution may be found. However, no report on the self-similar drop size distribution is given in Lacasta *et al.* (1995). Thus we conduct numerical simulations of multiphase fluids stirred by two-dimensional turbulence to assess the possibility of self-similar drop size distribution in turbulence. In our

turbulence simulations, we also explore the non-diffusive limit, where molecular mobility for the interface is vanishing. Special care is needed to transport the non-diffusive interface. Numerically, we use the particle level set method to evolve the interface. Instead of using the usual methods to calculate the surface tension force from the level set function, we reconstruct the interface based on phase-field modeling, and calculate the continuum surface tension forcing from the reconstructed interface.

This paper is organized as follows. In §2 we formulate the coupled Navier-Stokes-Cahn-Hilliard system and present results from direct numerical simulations of the coupled system stirred by turbulent flows. In §3.1 we formulate the multiphase fluid problem combining the particle level set method (for interface tracking) with phase-field modeling (for surface tension force). Numerics for the particle level set method are summarized in §3.2, and validation is provided in §3.3. In §3.4 we present results of drop dynamics from direct numerical simulations, and finally we provide some conclusion in §4.

2. Turbulent mixing in the Navier-Stokes-Cahn-Hilliard system

We generalize the system in Berthier *et al.* (2001) to include the effect of surface tension on stirring flows. The phase-field function C denotes the phase of the fluid: $C = \pm 1$ corresponds to fluid phase 1 and 2, respectively. C is described by the Cahn-Hilliard equation, which is coupled to the incompressible, two-dimensional Navier-Stokes equations in our formulation.

$$\frac{\partial C}{\partial t} + \mathbf{u} \cdot \nabla C = \beta \mathcal{M} \nabla^2 \psi, \tag{2.1}$$

$$\frac{\partial \mathbf{u}}{\partial t} + \mathbf{u} \cdot \nabla \mathbf{u} = -\nabla P + \nu \nabla^2 \mathbf{u} - C \nabla \psi + \mathrm{F} + \mathrm{F}_d, \tag{2.2}$$

$$\nabla \cdot \mathbf{u} = 0, \tag{2.3}$$

where

$$\psi(C) \equiv \frac{\delta F(C)}{\delta C} - \frac{\alpha}{\beta} \nabla^2 C, \quad F(C) = \frac{1}{4}(C^2 - 1)^2. \tag{2.4}$$

In equation 2.2, F is a random forcing at wavenumber k in the range $n_1 \leq k/k_0 \leq n_2$, where $k_0 \equiv 2\pi/l$ and l is the dimension of the computation domain. $\mathrm{F}_d = -\lambda \mathbf{u}$ ($\lambda = 0.1$ in all our simulations) is the drag force dissipating energy at large scales.

The positive, constant coefficient $\mathcal{M}$ is the molecular mobility, ν is the kinematic viscosity, α and β are related to the interfacial properties: The interfacial thickness $\xi \sim \sqrt{\alpha/\beta}$, and the surface tension coefficient $\sigma = \frac{2}{3}\rho_0\sqrt{\alpha\beta} \equiv \sqrt{\alpha\beta}\sigma_0$, where ρ_0 is the uniform fluid density and σ_0 is the surface tension force when $\sqrt{\alpha\beta} = 1$. We can non-dimensionalize the above equations with respect to a characteristic length scale l (of the order of interfacial thickness), a characteristic velocity v_0, and the corresponding time l/v_0. The dimensionless equations are

$$\frac{\partial C}{\partial t} + \mathbf{u} \cdot \nabla C = D \nabla^2 \left[C^3 - C - \nabla^2 C \right], \tag{2.5}$$

$$\frac{\partial \mathbf{u}}{\partial t} + \mathbf{u} \cdot \nabla \mathbf{u} = -\nabla P + \frac{1}{Re} \nabla^2 \mathbf{u} - \frac{\gamma}{Re} C \nabla \left[C^3 - C - \nabla^2 C \right] + \mathrm{F}' + \mathrm{F}'_d, \tag{2.6}$$

$$\nabla \cdot \mathbf{u} = 0. \tag{2.7}$$

The dimensionless coefficient $D \equiv \beta \mathcal{M}/v_0 l$ is the inverse Peclet number, $Re \equiv v_0 l/\nu$ is the Reynolds number, and $\gamma \equiv \sqrt{\alpha\beta}/v_0\nu$ is the capillary number. If the scaling length

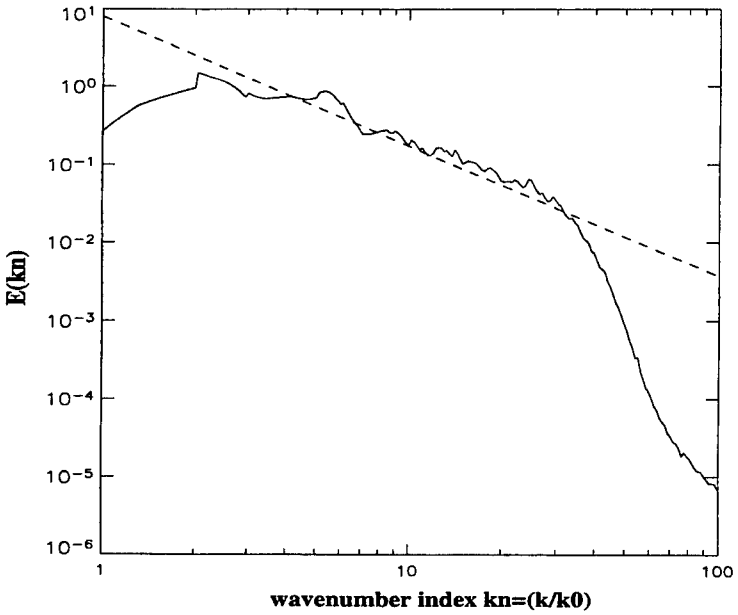


FIGURE 1. Energy spectrum of turbulent velocity (solid line), and the $k^{-5/3}$ inverse cascade scaling is the dashed line. $k_0 = \frac{2\pi}{8\pi} = 1/4$.

scale l is the interfacial thickness ($l \equiv \xi$) and the characteristic velocity is the "diffusion velocity" across the interface ($v_0 \equiv \beta\mathcal{M}/\xi$), then the Reynolds number $Re = \beta\mathcal{M}/\nu$ and the capillary number $\gamma = \alpha/\beta\mathcal{M}\nu$. The time scale for diffusion across the interface is $\tau_C \equiv \xi^2/\beta\mathcal{M}$. The characteristic hydrodynamic time scale is $\tau_S \equiv 1/|\mathbf{S}|$, where $|\mathbf{S}|$ is the velocity strain rate. It is convenient to control the interfacial properties using both α and β, thus in the numerical code the dimensional equations 2.1-2.4 are implemented instead.

For the following simulation results, the domain size of the double-periodic computation box is $8\pi \times 8\pi$, and the numerical resolution is 512^2. The small-scale forcing range is fixed at wavenumbers $5 \leq k/k_0 \leq 15$. At the beginning of each simulation, an initially circular interface of radius 1.5π is placed at the center of a two-dimensional turbulent flow, and the volume average of the concentration is $\langle C \rangle = 0.41 > 0$. The energy spectrum of the turbulent flow is the inverse cascade with a slope of $-5/3$ as shown in figure 1. Throughout the simulations the energy spectrum is little affected by the surface tension force from the interface.

A numerical challenge in turbulent simulations of NS-CH system is that the diffusion coefficient has to be small to avoid phase homogenization. If the diffusion coefficient is too large, or if the surface tension is too small, drops disappear as the order parameter C homogenizes and settles to the phase that is closest to the mean value. Thus, for a given turbulent strength and numerical resolution, we optimize the number of drops by minimizing the diffusion with enough surface tension force so we can collect drops of various sizes. We integrate the turbulent flow over a long duration so the number of drops fluctuates many times around the mean value. The area distributions collected from three simulations with resolution 512^2, after rescaled with respect to the average drop area, are shown in figure 2(a). The three rescaled area distributions collapse reasonably well in the

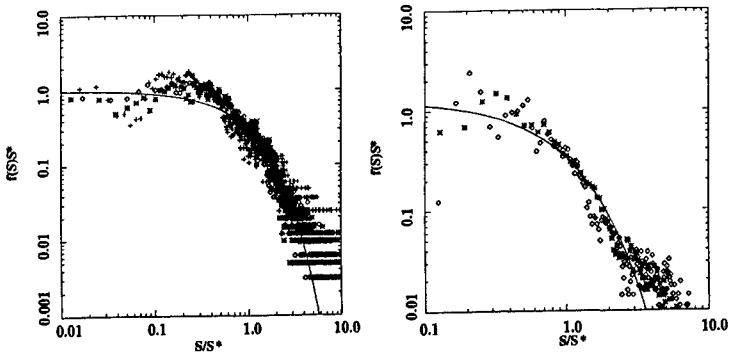


FIGURE 2. Size distribution for simulations of turbulent NS-CH flows. Panel (a): Diamonds are for $\alpha = 2$, $\beta = 200$ and $\mathcal{M} = 10^{-6}$. Crosses are for $\alpha = 2$, $\beta = 200$ and $\mathcal{M} = 5 \times 10^{-7}$. Asterisks are for $\alpha = 3$, $\beta = 300$ and $\mathcal{M} = 10^{-6}$. The numerical resolution is 512^2 and $\nu = 0.1$ for all three simulations, and the curve is $\sim \exp -S/S^*$. Panel (b): Diamonds are for $\alpha = 2$, $\beta = 200$ and $\mathcal{M} = 2 \times 10^{-7}$. Asterisks are for $\alpha = 1.5$, $\beta = 150$ and $\mathcal{M} = 2 \times 10^{-7}$. The numerical resolution is 1024^2 and $\nu = 0.1$ for all both cases, and the curve is $\sim \exp -S/S^*$.

range $0.3 \leq S/S^* \leq 20$, despite the poor statistics at both ends of the distribution. The diffusion coefficients (see caption in figure 2) that we used in the numerical simulations are close to the minimum for this numerical resolution (512^2). 1024^2 grid points are used for two simulations as we decrease the mobility to $\mathcal{M} = 2 \times 10^{-7}$, and similar scaling in the distributions is also found as shown in figure 2(b). Despite the limited reliable range in both figure 2, the general trend suggests that similar scaling may also exist in the tubulent mixing case.

3. Phase-field modeling with zero mobility $\mathcal{M} = 0$

In reality the mobility $\mathcal{M}$ for multiphase flow can be very small, and the equation for the phase field concentration C reduces to the advection transport equation. This distinguished limit corresponds to the non-diffusive, immiscible two-fluid flow, where the interfacial thickness is ideally zero and thus requires special numerical treatment in the simulations.

In the case of zero diffusivity, we use the phase-field modeling as a means to reconstruct the interface knowing its location. We use particle level set method to evolve the interface between the two phases. In the level set framework, the zero of the scalar level set function ϕ implies the location of the interface. To retain the structure of the interface, we assume that the Cahn-Hilliard potential ψ governs the interfacial energetics, and reconstruct the interface for a given interfacial thickness $\xi (= \sqrt{\alpha/\beta}$ as in §2). In §3.1 we formulate this system in terms of level set representation of the interface with phase-field modeling for interfacial structure with zero molecular mobility. In §3.2 we briefly discuss the numerics and some validation is given in §3.3. We then present results from direct numerical simulations of multiphase mixing in two-dimensional turbulence in §3.4.

3.1. *Formulation*

Basically the equations are exactly the same as those in §2 except the Cahn-Hilliard equation is now reduced to an advection equation for C:

$$\frac{\partial C}{\partial t} + (\mathbf{u} \cdot \nabla) C = 0. \tag{3.1}$$

In the case of vanishing molecular mobility across the interface, the advection transport equation 3.1 for concentration C is a numerical challenge, and more complication arises in the evaluation of the surface tension force. Our remedy is that, despite the non-diffusiveness of the phase field, we assume that the interfacial thickness is finite based on the free energy ψ. Naturally, if we adopt the Cahn-Hilliard surface free energy for ψ, we expect the concentration C to behave as $C \sim \tanh(\sqrt{\beta/\alpha}|r - r_0|)$, where $|\mathbf{r} - \mathbf{r}_0|$ is the distance between the point $\mathbf{r}$ and the interface (located at $\mathbf{r}_0$). A great advantage of this approach is that the surface tension force can be calculated directly from the phase-field modeling as a continuum force $-C\nabla\psi$, which peaks at the interface.

Thus instead of solving equation 3.1 over the whole computation domain for C, we solve the same equation for a level set function ϕ only at the interface (where $\phi = 0$), and re-initialize the level set function ϕ to a signed distance function away from $\phi = 0$. We replace equation 3.1 with the level set equation valid only at the fluid interface $\phi = 0$:

$$\partial_t \phi + \mathbf{u} \cdot \nabla \phi = 0\big|_{\phi=0}. \tag{3.2}$$

Away from $\phi = 0$, inside a band of width $\sim 6dx$ around $\phi = 0$, we re-initialize ϕ to a signed distance function. To achieve this we have to re-initialize the level set function at each time step by solving the following equation to a stationary state

$$\partial_\tau \phi + sgn(\phi_0)(|\nabla \phi| - 1) = 0, \tag{3.3}$$

where $sgn(\phi_0)$ is the sign of $\phi(\mathbf{x}, t = t_0)$ defined as

$$sgn(\phi_0) = \frac{\phi_0}{\sqrt{\phi_0^2 + |\nabla \phi_0|^2 dx^2}}, \tag{3.4}$$

for a given grid spacing dx. The normal vector and the mean curvature can be calculated in terms of the level set function ϕ: $\hat{\mathbf{n}} \equiv \nabla\phi/|\nabla\phi|$ and $\kappa \equiv \nabla \cdot \hat{\mathbf{n}}$. The concentration phase-field C is then reconstructed from the level set function (ξ, as previously defined, is the interfacial thickness):

$$C = \tanh(\frac{\phi}{\xi}) \ \ if \ \ |\phi| \leq a\xi, \tag{3.5}$$

$$C = \frac{\phi}{|\phi|} \ \ if \ \ |\phi| > a\xi,$$

where a is a constant in the range $2 \leq a \leq 5$ so that the concentration C transitions smoothly from $|C| < 1$ to $|C| = 1$ at the edge of the band around the interface. From our fully-resolved simulations of drop dynamics presented here, we conclude that the volume integral of C remains constant at all time provided that the level set is accurately capturing the interface.

Numerically there are various ways to calculate the surface tension force from the level set function. Physically the surface tension force leads to a pressure jump across the interface. In our one-fluid formulation the surface tension is formulated as a body force F_σ ($= -C\nabla\psi$ in the phase field modeling). Ideally, in the limit of zero interfacial thickness, the surface tension force is non-zero only at the interface: $\mathrm{F}_\sigma = (\sigma\kappa\hat{\mathbf{n}} + \partial_s\sigma\hat{\mathbf{s}})\delta(\phi)$, where $\partial_s\sigma$ is the Marangoni force, with s the arclength and $\hat{\mathbf{s}}$ the unit vectors along the

tangential direction. On a discrete numerical grid, however, the surface tension force F_σ has to be smoothed over several grid spacings to avoid un-controllable numerical oscillation. The usual cosine-delta function used to calculate F_σ on a uniform grid (Sussman *et al.* 1994) leads to artificial broadening of the interface, which in turn leads to large unphysical parasitic currents around the numerically smoothed interface. In our phase field modeling, we assume an interfacial structure based on the the Cahn-Hilliard surface free energy. A continuum surface tension force is then derived based on the surface free energy. As shown in (Jacqmin 1999), this continuum surface tension force gives very small parasitic currents compared with that from the cosine-delta construction of the interface. Recently a numerical scheme has been developed to minimize the parasitic currents (Enright *et al.* 2002). In our approach, the parasitic currents are small but not as minimized as in Enright *et al.* (2002). The turbulent flow in our resolved simulations of drop dynamics is much larger than the parasitic currents, and thus we expect the constraint in Enright *et al.* (2002) to have little effects on the dynamics and drop area distributions presented in §3.4. The formulation we proposed for reconstructing the interface from the phase-field modeling through level set function (equations 3.2-3.5) is somehow similar to the splitting of particle advection from particle diffusion in the random walk particle method (Ghoniem & Sherman 1985). In random walk particle methods, particles can be first transported by the velocity field at their positions, and then perform random walks to account for diffusion. Such a numerical scheme is commonly used in particle tracking when the particle diffusion is very small. Similarly in our formulation we first evolve the interface by solving the advection equation only near the interface using the hybrid particle level set method. Once the location of the interface is advanced and the level set is re-initialized as a signed distance function, we construct the phase-field C based on the steady state solution to equation 2.1 without advecting flow,

$$C(C^2 - 1) - \frac{\alpha}{\beta}\nabla^2 C = 0. \tag{3.6}$$

Assuming that the interfacial structure is only a function of the signed distance to the interface, we then express C in terms of the level set function ϕ in equation 3.5.

In summary, the system of iso-density, iso-viscosity fluid with an interface separating the two phases is described by equations 2.2, 2.3, and 3.2 with the surface tension force $-C\nabla\psi$, where ψ is the Cahn-Hilliard free energy and the concentration C is calculated from equation 3.5.

3.2. *Numerics*

The level set equation (3.2) is solved using the hybrid particle level set method (Enright *et al.* 2002). We use WENO 5th order scheme to calculate the flux in equation 3.2, and the TVD-3rd order RK scheme to advance the level set in time. Following Enright *et al.* (2002), Lagrangian particles are added inside a narrow band (Γ_p) around the interface and are transported using the same RK 3rd order scheme. Before and after re-initialization (equation 3.3), particle correction (for detail see Enright *et al.* (2002)) is conducted to ensure that the zero level is not shifted numerically. This hybrid level set method is at most volume-conserving as long as particle density along the zero level is sufficient. In all our simulations, we use at least 4^2 particles for each cell within the (Γ_p) band. Re-seeding of particles is conducted if the average particle density is found to be below 75% of the initial particle density. We re-initialize the level set within a second band (Γ_r) enclosing the particle band (Γ_p). We refer readers to Enright *et al.* (2002) for detail of the algorithm. Standard tests have been performed (Young *et al.* 2002) and

results are identical to those in the original paper (Enright *et al.* 2002). To couple the level set equation(s) to the fluid solver, we advance both the level set ϕ and the fluid velocity $\mathbf{u}$ using the 3-rd order explicit scheme. The diffusion part in the momentum equation is incorporated as integrating factors in spectral space. The surface tension force is calculated from the interface at the previous time step, and we use the same velocity fields from the previous time step to advect the velocity, interface, and particles.

3.3. *Linear capillary waves*

To demonstrate that the surface tension force is properly captured in the phase-field modeling, we compute the oscillatory frequency of the capillary waves for a two-dimensional drop. The initial condition for ϕ is the signed distance function perturbed by a sinusoid with a small amplitude and a wavenumber n

$$\phi(\mathbf{x}, t=0) = r - r_0(1 + 0.02\sin(n\theta)), \tag{3.7}$$

where r_0 is the drop radius, $r \equiv |\mathbf{x}-\mathbf{x}_0|$ is the distance between $\mathbf{x}$ and the drop center $\mathbf{x}_0$, and $\theta \equiv \tan^{-1}((y-y_0)/(x-x_0))$. Analytically (following Rayleigh (1892)), the oscillation frequency of capillary waves on the interface separating fluids of the same density and zero viscosity ($1/Re = 0$) can be expressed in terms of surface tension coefficient σ, drop radius r_0, and wavenumber n of the perturbation

$$\omega = \sqrt{\frac{n(n^2-1)\sigma}{2r_0^3}}. \tag{3.8}$$

We obtain the linear solutions from simulating the full system (described in section 3.1) with small non-linearity: starting from the initial condition $\mathbf{u} = 0$ and ϕ given in equation 3.7, the non-linearity remains small at all time because the small disturbance is damped by viscosity. In all our simulations in this section, the viscosity ν is fixed at $\nu = 0.1$, and the perturbation amplitude decays exponentially at rate λ with a capillary oscillation of frequency ω. We compute the capillary frequency ω numerically by extracting the oscillation from the decaying amplitude.

We first calibrate the relationship between σ and (α, β). From §2 the surface tension σ is proportional to $\sqrt{\alpha\beta}$. With the ratio β/α fixed (the interface thickness is thus fixed at $\sim$ 8 grid spacings), we expect the surface tension σ to be linearly proportional to α (or β). Table 3.3 shows the computed oscillation frequency from simulations and the corresponding surface tension coefficient σ from equation 3.8. We find that the surface tension σ (computed from ω in our case via equation 3.8) indeed varies linearly with $\sqrt{\alpha\beta}$.

For $1 \leq n \leq 6$ we compute the oscillation frequency ω from the simulations with $\alpha = 0.9817$ and $\beta = 89.1875$ ($\sigma = 94.32\sigma_0$ from table 3.3). As shown in figure 3, excellent agreement is found between the computed and analytical values of ω for all $1 \leq n \leq 6$. In addition we also remark that the parasitic currents are as small as 10^{-6} with a numerical resolution 128^2 in a square box of size $2\pi \times 2\pi$.

3.4. *Drop dynamics in two-dimensional turbulence*

Drop dynamics and the drop break-up in simple flow configurations has been extensively investigated both numerically (Zaleski *et al.* 1995; Cristini *et al.* 1998; Tauber *et al.* 2002) and experimentally (Muzzio *et al.* 1991*b*). Results from experiments (Muzzio *et al.* 1991*b*) and modeling (Berthier *et al.* 2001) on passive chaotic mixing of immiscible fluids show that the statistics of drop size collapse due to the self-similar breakup and coalescence

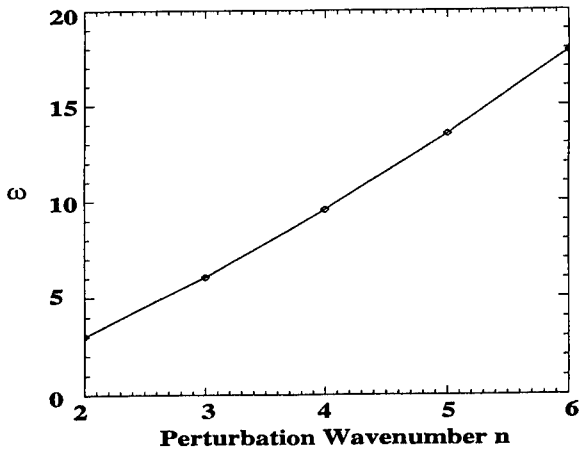


FIGURE 3. Capillary oscillation frequency ω as a function of n. Symbols are simulation data, and line is from analytical result for $\sigma = 94.32\sigma_0$ and $r_0 = \pi$.

TABLE 1. Parameters α and β used in the linear simulations, and the capillary frequency ω computed from the time-varying perturbation amplitude. $n = 2$, $\nu = 0.1$, and numerical resolution is 128^2.

	α	β	ω	σ/σ_0
Case 1	0.98	89.18	3.02	94.32
Case 2	1.96	178.37	4.24	188.64
Case 3	2.94	267.56	5.22	282.96
Case 4	3.92	356.75	6.04	377.28

processes. However, there are only a few recent direct numerical simulations on drop dynamics in turbulent flows (Tryggvason *et al.* 2001). Due to the difficulty in tracking the interface accurately while conserving fluid mass, it is a great numerical task to capture the statistics of drop size distribution after a series of breakups and coalescence in numerical simulations.

Due to numerical diffusion, it is in general a great numerical challenge to conserve total volume for each fluid using level set methods. The hybrid particle level set method conserves volume almost perfectly in standard tests (Enright *et al.* 2002), and is the only level set method that can both track the interface accurately and minimize the mass loss in a controllable fashion. The particle level set method, in combination with the phase field modeling of the surface tension force, is a good tool for tracking interface accurately with minimum mass loss. Provided that enough Lagrangian particles are used in tracking the interface, the mass loss can be reduced to a tolerable level. Thus we are able to accurately evolve the dynamics of drops in a turbulent flow, and our main goal is to examine the statistics collected from DNS dataset. In our simulations, less than 1% of maximum volume loss is found for all cases presented here. For the following simulation results, the combination of α and β is chosen so that the interface thickness is fixed ($\sim 6dx$ at least). The double-periodic computation domain is of size $8\pi \times 8\pi$, and the numerical resolution is 512^2.

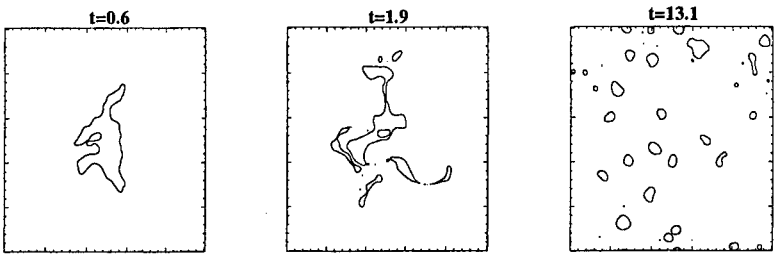


FIGURE 4. Drop deformation and break-up in two-dimensional turbulence. $\alpha = 2.95$, $\beta = 118.92$, $\nu = 0.2$ and $\lambda = 0.1$. (a) $t = 0.6$ (b) $t = 1.9$ and (c) $t = 13.1$.

We fixed the range of small-scale forcing at wavenumbers $5 \leq k/k_0 \leq 15$, and the large scale friction $\mathrm{F}_f = -0.1\mathbf{u}$. At the beginning of each simulation, an initially circular interface of radius π is placed at the center of a two-dimensional turbulent flow. The energy spectrum of the turbulent flow is the inverse cascade with a slope of $-5/3$ as shown in figure 1. Throughout the simulations the energy spectrum is little affected by the surface tension force from the interface. The well-known effect of bubbles/drops on the turbulent energy spectra (Mazzitelli *et al.* 2003) is also absent here because there is no buoyancy/density contrast in our simulations.

In figure 4 we demonstrate how the initial drop gets deformed, stretched, and finally breaks up into smaller drops: In figure 4(a) ($t = 0.6$) the interface is highly distorted, and in figure 4(b) ($t = 1.9$) several break-ups lead to smaller children drops. At late times ($t > 10$) the drops are small and the surface tension force is sufficient to overcome the stretching to prevent further break-ups, and a statistical equilibrium is reached as shown in figure 4(c) ($t = 13.1$), where there are a lot of small drops of irregular shapes and various sizes.

We can easily calculate the total length of the interface from the level set as

$$\begin{aligned} \mathrm{Length}\{\phi = 0\} &= \int_\Omega |\nabla H(\phi(\mathbf{x}))| dxdy \\ &= \int_\Omega \delta(\phi(\mathbf{x}))|\nabla\phi| dxdy, \end{aligned} \tag{3.9}$$

where

$$H(\phi) = \frac{1}{2}\left[1 + \frac{\phi}{\pi} + \frac{1}{\pi}\sin(\frac{\pi\phi}{\epsilon})\right], \tag{3.10}$$

$$\delta(\phi) = \frac{d}{d\phi}H(\phi), \tag{3.11}$$

with $\epsilon = 3 \sim 4dx$ as in Sussman *et al.* (1994). Panel (a) in figure 5 shows the evolution of the arclength (scaled to the initial length), and panel (b) is the time-history of kinetic energy. We find that the early growth in the length is accompanied by a similar growth of the total number of drops as several break-up processes have occurred during ($0 \leq t \leq 3$). After $t \sim 10$ (about 2.5 eddy turnover times) the amplification in length saturates and fluctuates throughout the simulations. We integrate to at least 15 eddy turnover times to attain statistically equilibrium states. The interfacial thickness is fixed at $\sim 6.4dx$ for all three curves in figures 5. With the same small scale random forcing F, large scale dissipation F_d and viscous dissipation $\nu = 0.2$, the only difference between the three

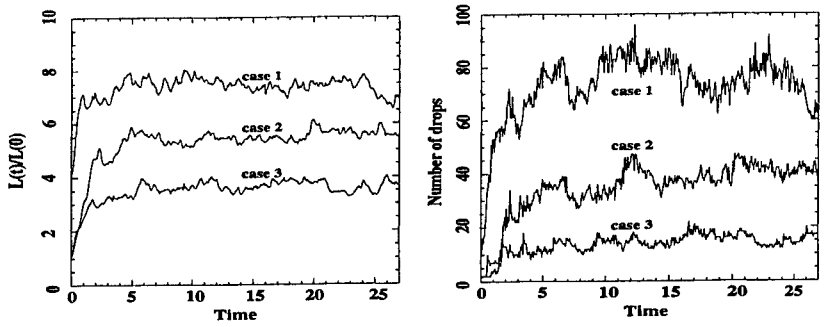


FIGURE 5. (a) Evolution of total arclength scaled to the initial value. (b) Corresponding evolution of number of drops.

TABLE 2. Averaged number of drops and arclengths for the three simulations.

	α	β	σ/σ_0	L/L_0	N
Case 1	1.47	59.45	9.35	7.51	79.98
Case 2	2.94	119.91	18.71	5.50	39.69
Case 3	5.89	239.83	37.42	3.66	15.18

simulations is the surface tension coefficient: $\sigma = 9.36\sigma_0$, $\sigma = 18.71\sigma_0$, and $\sigma = 37.43\sigma_0$ for curves 1, 2, and 3, respectively. (As defined earlier σ_0 is the surface tension coefficient when $\sqrt{\alpha\beta} = 1$.) The balance between stabilizing surface tension force and stirring turbulent flow results in a critical length scale (Lacasta *et al.* 1995)

$$\lambda_c^2 \sim \frac{\pi^2}{2}\frac{\sigma}{\bar{u}}, \tag{3.12}$$

where $\bar{u}$ is the turbulence characteristic velocity. Since the total area (volume) of each fluid phase has to conserve in two (three)-dimensions, we can estimate the dependence of average number of drops (N) on the surface tension. For a given characteristic turbulence velocity, in two-dimensions,

$$N\lambda_c^2 \sim \text{ total area of fluid phase 1 } = \text{ constant } \rightarrow N \sim \sigma^{-1}. \tag{3.13}$$

Similarly in three-dimensions,

$$N\lambda_c^3 \sim \text{ total volume of fluid phase 1 } = \text{ constant } \rightarrow N \sim \sigma^{-3/2}. \tag{3.14}$$

From equations 3.13 and 3.14, the total circumference (area or arclength in two and three-dimensions, respectively) is inversely proportional to the square root of surface tension: $N\lambda_c$ in two-dimensions and $N\lambda_c^2$ in three-dimensions both lead to $\sim 1/\sqrt{\sigma}$. These scaling results in two-dimensions are consistent with the time-averaged values of our simulation data in figures 5. In table 3.4 we list the time-averaged N and total arclength for all three simulations.

In the statistically equilibrium state the number of drops fluctuates around the mean value, we collect enough statistics for the drop area distribution by integrating over a long period of time. Following Berthier *et al.* (2001) and Muzzio *et al.* (1991*b*), we rescale the drop area distribution by the mean area (calculate by taking moments of the area

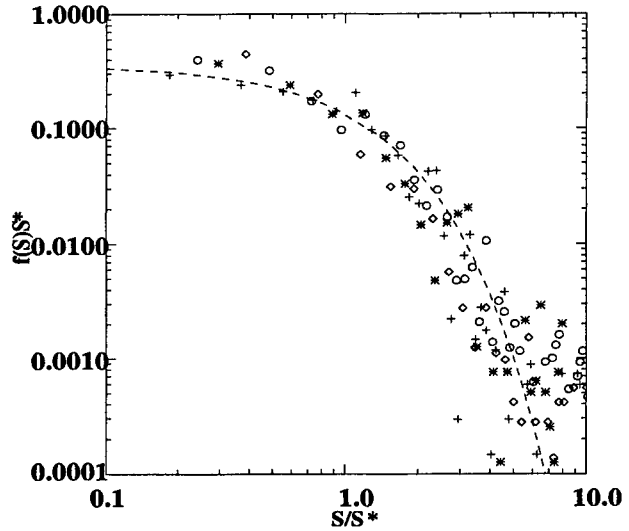


FIGURE 6. Size distribution for the three cases. Diamonds are for case 1, asterisks are for case 2 and crosses are for case 3. Open circles are for a different forcing function but same parameters as in case 1. The dashed line is $\sim \exp -(S/S^*)$.

distribution functions as in Muzzio *et al.* (1991*b*)). Since the effective diffusion coefficient is assumed to be zero in our turbulence simulations, we cannot calculate the mean area based on the scaling of the characteristic domain size L^* and D^* as in Berthier *et al.* (2001). The rescaled area distributions collapse as shown in figure 6. One additional simulation data set (open circles) with a different interfacial thickness and turbulent random forcing is added in figure 6. For this additional simulation, the surface tension $\sigma = 18.71\sigma_0$ and the interfacial thickness $\xi = 5.0dx$ and the turbulent random forcing is at wavenumbers $5 \leq k/k_0 \leq 7.5$, narrower than the other three simulations. However, it seems that the collapse works reasonably well regardless of the differences between the simulations.

4. Conclusion

We have extended the phase-field modeling to the non-diffusive case. Surface free energy from the phase-field modeling is used to calculate the surface tension force based on the reconstructed interface using the level set function. Numerically the non-diffusive, infinitely sharp interface has to be smoothed over a few grid points. Some interfacial structure is always assumed in the numerics, and the resultant surface tension force inherits the modeled structures. One popular way to reconstruct interface in level set method is the cosine-delta function. However, no physical meaning can be related to such a construction, and as a result, the parasitic currents are undesirably large. We replace the cosine-delta function with the smooth interfacial structure from the stationary solution in phase-field modeling, and we calculate the surface tension force from the corresponding surface free energy. The only assumption we make in this approach is that the reconstructed interface is a function of the signed distance to the interface. We assume that "some" molecular dynamics acts on such a fast time scale that the interfacial thickness remains the same, even when the flow is vigorously acting on and around the interface. The collapse of drop area distribution in our two-dimensional turbulence

simulation confirms our conjecture that the self-similar drop area distribution exists for more general velocity fields.

The particle level set method, combined with phase-field modeling, has great promise for large scale, three-dimensional numerical simulations of multiphase flow. One of our future goals is to generalize our simulations of two-dimensional drop dynamics to three dimensions. We also plan to include density and viscosity contrast for multi-fluid using the phase-field modeling. Finally, we are also investigating how the phase-field modeling can be applied in simulating micro-fluidic multiphase flows carried out in experiments (Truesdell *et al.* 2003).

REFERENCES

Berthier, L., Barrat, J. & Kurchan, J. 2001 *Phys. Rev. Lett.* **86**, 2014.

Chella, R. & Vinals, J. 1996 *Phys. Rev. E* **53**, 3832.

Cristini, V., Blawzdziewicz, J. & Loewenberg, M. 1998 *Phys. Fluids* **10**, 1781.

Enright, D., Fedkiw, R., Ferziger, J. & Mitchell, J. 2002 *J. Comp. Phys.* **183**, 83.

Ghoniem, A. F. & Sherman, F. S. 1985 *J. Comput. Phys.* **61**, 1.

Jacqmin, D. 1999 *J. Fluid Mech.* **155**, 96.

Jamet, D., Torres, D. & Brackbill, J. 2002 *J. Comp. Phys.* **182**, 262.

Jasnow, D. & Vinals, J. 1996 *Phys. Fluids* **8**, 660.

Lacasta, A., Sancho, J. & Sagues, F. 1995 *Phys. Rev. Lett.* **75**, 1791.

Mazzitelli, I. M., Lohse, D. & Toschi, F. 2003 *Phys. Fluids* **15**, L5.

Muzzio, F., Swanson, P. & Ottino, J. 1991*a* *Phys. Fluids* **3**, 822.

Muzzio, F., Tjahjadi, M. & Ottino, J. 1991*b* *Phys. Rev. Lett.* **67**, 54.

Muzzio, F. J., Meneveau, C., Swanson, P. D. & Ottino, J. M. 1991*c* *Phys. Fluids* **4**, 1439.

Rayleigh, L. 1892 *Phil. Mag. Science* **34**, 145.

Roths, T., Friedrich, C., Marth, M. & Honerkamp, J. 2002 *Rheol. Acta* **41**, 211.

Siggia, E. D. 1979 *Phys. Rev. A* **20**, 595.

Sussman, M., Smereka, P. & Osher, S. 1994 *J. Comp. Phys.* **114**, 146.

Tauber, W., Unverdi, S. O. & Tryggvason, G. 2002 *Phys. Fluids* **14**, 2871.

Truesdell, R. A., Vorobieff, P. V., Sklar, L. A. & Mammoli, A. A. 2003 *Phys. Rev. E* **67**, 066304.

Tryggvason, G., Bunner, B., Esmaeeli, A., Juric, D., Al-Rawahi, N., Tauber, W., Han, J., Nas, S. & Jan, Y. J. 2001 *J. Comp. Phys.* **169**, 708.

Young, Y.-N., Ferziger, J., Mansour, N., Ham, F. & Herrmann, M. 2003 *Phys. Fluids* **submitted**.

Young, Y.-N., Ham, F., Mansour, N. & Herrmann, M. 2002 *CTR Annual Research Briefs* .

Zaleski, S., Li, J. & Succi, S. 1995 *Phys. Rev. Lett.* **75**, 244.

Zhao, P., Venere, M., Heinrich, J. C. & Poirier, D. R. 2003 *J. Comp. Phys.* **188**, 434.

The effect of the density ratio on the nonlinear dynamics of the unstable fluid interface

By S.I. Abarzhi

1. Motivation and objectives

When a light fluid accelerates a heavy fluid, the misalignment of the pressure and density gradients gives rise to the instability of the interface, and produces eventually the turbulent mixing of the fluids (Rayleigh 1892; Davies & Taylor 1950; Richtmyer 1960; Meshkov 1969). This phenomenon is called the Rayleigh-Taylor instability (RTI) if the acceleration is sustained, and the Richtmyer-Meshkov instability (RMI) if the acceleration is driven by a shock or if it is impulsive. The RT/RM turbulent mixing is of extreme importance in astrophysics, inertial confinement fusion, and many other applications (Sharp 1984). To obtain a reliable description of the mixing process, the evolution of a large-scale coherent structure, the dynamics of small-scale structures, and the cascades of energy should be understood.

The large-scale coherent structure is an array of bubbles and spikes periodic in the plane normal to the direction of gravity or the initial shock (Rayleigh 1892; Davies & Taylor 1950; Meshkov 1969; Schneider *et al.* 1998). It appears in the nonlinear regime of RTI and RMI and has a spatial period determined by the mode of fastest growth (Chandrasekhar 1961). The light (heavy) fluid penetrates the heavy (light) fluid in bubbles (spikes). The density ratio is a determining factor of the instability dynamics (Sharp 1984; Schneider *et al.* 1998). Singular aspects of the interface evolution (such as the generation of vorticity and secondary instabilities, resulting in the direct and inverse cascades of energy, a finite contrast of the fluid densities and the non-linearity of the dynamics) cause theoretical difficulties and preclude elementary methods of solution (Dalziel *et al.* 1999; He *et al.* 1999; Gardner *et al.* 1988; Jacobs & Sheeley 1996; Kucherenko *et al.* 2000; Holmes *et al.* 1999; Volkov *et al.* 2001).

For fluids with highly contrasting densities (fluid-vacuum), the effect of singularities on the interplay of harmonics and on the nonlinear motion in RTI/RMI has been studied intensively over the decades (Layzer 1955; Garabedian 1957; Tanveer 1993). A new approach based on group theory has been developed recently by Abarzhi (1998, 2002). The asymptotic theories of Layzer (1955); Garabedian (1957); Abarzhi (1998, 2002) agreed with experiments and simulations. For fluids with a finite density contrast, the influence of singularities on the cascades of energy and the large-scale coherent dynamics in RTI/RMI has yet to be elucidated (Baker *et al.* 1982; Moore 1979; Hou *et al.* 1997; Cowley *et al.* 1999; Matsuoka *et al.* 2003). The empiric models proposed by Sharp (1984) and Oron *et al.* (2001) could not explain observations completely and were a subject for controversy. These models disregarded the conservation of mass and introduced adjustable parameters to balance drag, buoyancy, and inertia in the flow, (Dimonte 2000). In a recent attempt of Goncharov (2002) to reproduce the results of the drag model of Oron *et al.* (2001) in a single-mode approximation, a complete set of the boundary conditions were not satisfied (see below), and the conservation laws were thus violated.

Here we report multiple harmonic theoretical solutions for a complete system of conser-

vation laws, which describe the large-scale coherent dynamics in RTI and RMI for fluids with a finite density ratio in the general three-dimensional case. The analysis yields new properties of the bubble front dynamics. In either RTI or RMI, the obtained dependencies of the bubble velocity and curvature on the density ratio differ qualitatively and quantitatively from those suggested by the models of Sharp (1984), Oron *et al.* (2001), and Goncharov (2002). We show explicitly that these models violate the conservation laws. For the first time, our theory reveals an important qualitative distinction between the dynamics of the RT and RM bubbles. Asymptotically, the RT bubble is curved, and its curvature has a strong dependence on the density ratio, while the RM bubble flattens independently of the density ratio. The velocity of the RT bubble depends has a power-law dependence on the bubble curvature with exponent 3/2 and a universal coefficient independent of the density ratio, while the RM bubble decelerates. The bubble curvature and velocity depend mutually on one another, as do the differences between the RM and RT cases for these quantities. Our theory explains existing data, formulates the universal properties of the RT and RM nonlinear dynamics, and identifies sensitive diagnostic parameter for future observations.

2. Governing equations

Let t be time, (x, y, z) be the Cartesian coordinates, and $\theta(x, y, z, t)$ be the scalar function with $\theta = 0$ at the fluid interface. Locally, $\theta = z^*(x, y, t) - z$ where $z^*(x, y, t)$ is the position of the fluid interface. The fluid density and velocity have the form $\rho = \rho_h H(-\theta) + \rho_l H(\theta)$, and $\boldsymbol{v} = \boldsymbol{v}_h H(-\theta) + \boldsymbol{v}_l H(\theta)$, where H is the Heaviside step-function, and $\rho_{h(l)}$ and $\boldsymbol{v}_{h(l)}$ are the density and velocity of the heavy (light) fluid located in the region $\theta < 0$ ($\theta > 0$). For incompressible fluids, $\nabla \cdot \boldsymbol{v} = 0$, and the values of $\rho_{h(l)}$ are independent of the coordinates and time. The equation of continuity is reduced then to

$$(\dot{\theta} + \boldsymbol{v}_h \cdot \nabla\theta)\rho_h\big|_{\theta=0} = (\dot{\theta} + \boldsymbol{v}_l \cdot \nabla\theta)\rho_l\big|_{\theta=0} \tag{2.1}$$

where the dot indicates a partial time-derivative. If there is no mass flux across the moving interface, the normal component of velocity is continuous at the interface and

$$\boldsymbol{v}_h \cdot \nabla\theta\big|_{\theta=0} = \boldsymbol{v}_l \cdot \nabla\theta\big|_{\theta=0} = -\dot{\theta}\big|_{\theta=0}. \tag{2.2}$$

With neglected terms for viscous stress and surface tension, the momentum equation is transformed into the conditions

$$\rho_h\,(\dot{\boldsymbol{v}}_h + (\boldsymbol{v}_h \cdot \nabla)\boldsymbol{v}_h + \boldsymbol{g}) + \nabla p_h\big|_{\theta<0} = 0\,, \tag{2.3}$$

$$\rho_l\,(\dot{\boldsymbol{v}}_l + (\boldsymbol{v}_l \cdot \nabla)\boldsymbol{v}_l + \boldsymbol{g}) + \nabla p_l\big|_{\theta>0} = 0, \tag{2.4}$$

$$p_h - p_l\big|_{\theta=0} = 0, \tag{2.5}$$

where $p_{h(l)}$ is the pressure of the heavy (light) fluid, and $\boldsymbol{g}$ is the gravity directed from the heavy fluid to the light fluid with $|\boldsymbol{g}| = g$. There are mass sources in the flow, and the boundary conditions at the infinity close the set of the governing equations

$$\boldsymbol{v}_h\big|_{\theta=-\infty} = \boldsymbol{v}_l\big|_{\theta=+\infty} = 0. \tag{2.6}$$

The spatial period, the time-scale, and the symmetry of the motion in (2.1-2.6) are determined from the initial conditions. We choose the spatial period λ in a vicinity of

the wavelength of the mode of fastest growth, $\lambda \sim \lambda_{max}$, where λ_{max} is set by surface tension and viscosity (Chandrasekhar 1961). For RTI, the time-scale is $\tau_{RT} \sim \sqrt{\lambda/Ag}$, where $A = (\rho_h - \rho_l)/(\rho_h + \rho_l)$ is the Atwood number with $0 \leq A \leq 1$. For RMI, $g = 0$ and $\tau_{RM} \sim \lambda/v_0$, where v_0 is the initial velocity value. Based on the experimental observations, we separate scales and divide the fluid interface into active and passive regions, similarly to Aref & Tryggvason (1989). In the active regions (scales $\ll \lambda$) the vorticity is intensive, while the passive regions (scales $\sim \lambda$) are simply advected. In order to be stable under modulations with scales $\gg \lambda$, the large-scale coherent motion must be invariant under one of symmorphic groups with inversion in the plane (Abarzhi 1998, 2002).

To describe the dynamics of the nonlinear bubble, we reduce (2.1-2.6) to a local dynamical system. All calculations are performed in the frame of reference moving with velocity in the z-direction, where $v(t)$ is the velocity at the bubble tip in the laboratory frame of references. For the large-scale coherent motion, $\boldsymbol{v}_{h(l)} = \nabla\Phi_{h(l)}$, and in the case of a 3D flow with hexagonal symmetry

$$\Phi_h = \sum_{m=1}^{\infty} \Phi_m(t)\big(z + \big(\exp(-mkz)/3mk\big)\sum_{i=1}^{3}\cos(m\boldsymbol{k}_i\boldsymbol{r})\big) + \text{cross terms} + f_h(t), \quad (2.7)$$

$$\Phi_l = \sum_{m=1}^{\infty} \tilde{\Phi}_m(t)\big(-z\big(\exp(-mkz)/3mk\big)\sum_{i=1}^{3}\cos(m\boldsymbol{k}_i\boldsymbol{r})\big) + \text{cross terms} + f_l(t), \quad (2.8)$$

where $\boldsymbol{k}_i$ are the vectors of the reciprocal lattice, $\boldsymbol{r} = (x, y)$, and $f_{h(l)}$ are time-dependent functions. For $x \approx 0$ and $y \approx 0$ the interface can be expanded as a power series, $z^* = \sum_{N=1}^{\infty} \zeta_N(t)(x^{2N} + y^{2N})$ + cross terms, where $\zeta_1(t)$ is the principal curvature at the bubble tip, and $\zeta_1(t) < 0$.

Substituting these expressions in (2.1-2.6), taking the first integral of (2.5), and re-expanding (2.1-2.6) $x, y \approx 0$, we derive a dynamical system of ordinary differential equations for the variables ζ_N and the moments $M_n(t) = \sum_{m=1}^{\infty} \Phi_m(t)(km)^n$+cross terms and $\tilde{M}_n(t) = \sum_{m=1}^{\infty} \tilde{\Phi}_m(t)(km)^n$+cross terms, where n is an integer. The moments are correlations functions by their physical meaning. For $N = 1$, the conditions in (2.2-2.6) take respectively the form

$$\dot{\zeta}_1 = 2\zeta_1 M_1 + M_2/4 = 2\zeta_1\tilde{M}_1 - \tilde{M}_2/4, \quad (2.9)$$

$$\big(\dot{M}_1/4 + \zeta_1\dot{M}_0 - M_1^2/8 - \zeta_1 g\big)\rho_h = \big(\dot{\tilde{M}}_1/4 - \zeta_1\dot{\tilde{M}}_0 - \tilde{M}_1^2/8 - \zeta_1 g\big)\rho_l, \quad (2.10)$$

$$M_0(t) = -\tilde{M}_0(t) = -v(t)\ . \quad (2.11)$$

The local dynamical system (2.11) describes the dynamics of the bubble in a vicinity of its tip as long as the spatial period λ of the coherent structure is invariable. The presentation in terms of moments M_n and $\tilde{M}_n$ allows one to perform a multiple harmonic analysis and find the regular asymptotic solutions with a desired accuracy.

3. Regular asymptotic solutions

Retaining only the first order amplitudes in the expressions for the moments, we derive a nonlinear solution of the Layzer-type, which conserves mass, momentum, and has no mass sources. In RTI, for $t/\tau_{RT} \gg 1$ the curvature and velocity of the Layzer-type

bubble are $\zeta_1 = \zeta_L = -Ak/8$, and $v = v_{L,RT} = \sqrt{Ag/k}$, in agreement with the empiric approach of Sharp (1984). In RMI, for $t/\tau \gg 1$, the curvature and velocity are $\zeta_1 = \zeta_L = -Ak/8$, and $v = v_{L,RM} = (2 - A^2)/Akt$. These single-mode solutions however do not satisfy (2.2) and (2.9) and permits mass flux across the interface. To avoid this difficulty Goncharov (2002) has violated the boundary conditions in (2.6) and (2.11), and introduced an artificial time-dependent mass flux of the light fluid in the flow. For the solutions of Goncharov (2002), $\zeta_1 = \zeta_D = -k/8$, and $v = v_{D,RT} = \sqrt{2Ag/(1+A)k}$ in RTI, and $\zeta_1 = \zeta_D = -k/8$, and $v = v_{D,RM} = 2/(1+a)kt$ in RMI, in agreement with drag model of Oron *et al.* (2001). We conclude that Layzer-type approach (either in our version or in the models Oron *et al.* (2001) and Goncharov (2002)) does not satisfy the complete set of the conservation laws, and the single-mode solutions are not therefore physical. The reason for this difficulty lies in a non-local character of the non-linearity in (2.1-2.6) and (2.9-2.11).

To find regular asymptotic solutions, describing the nonlinear evolution of the bubble front in RTI or RMI, one should account for non-local properties of the flow that has singularities (Abarzhi *et al.* 2003). The singularities determine the interplay of harmonics in the global flow as well as in the local dynamics system. They transfer the fluid energy to smaller and larger scales and generate higher order harmonics. If the energy transports are not extensive, so the symmetry and the spatial period of the coherent structure do not change, the singularities affect the shape and velocity of the regular bubble. Assuming the bubble shape, parameterized by the principal curvature(s) at its tip, is free, we find a continuous family of regular asymptotic solutions for the local system. The family involves all solutions allows by the symmetry of the global flow. For the regular asymptotic solutions the interplay of harmonics is well captured. We perform a stability analysis and choose the fastest stable solution in the family as being physically significant. The reader is referred to Abarzhi *et al.* (2003) for more details.

For the Rayleigh-Taylor instability, the bubble velocity is the function on the bubble curvature and density ratio, $v = v(\sqrt{g/k}, A, (\zeta_1/k))$. In the interval $\zeta_{cr} < \zeta \leq 0$, the Fourier amplitudes Φ_m and $\tilde{\Phi}_m$ decay exponentially with increase in their m, the lowest-order amplitudes are dominant, and higher order corrections for family solutions are small. For $\zeta \sim \zeta_{cr}$ the convergence is broken, where $\zeta_{cr} \approx -k/6$ for $A \approx 1$ and $\zeta_{cr} \approx 0$ for $A \approx 0$. For fluids with highly contrasting densities, $A \sim 1$, the magnitudes of the Fourier amplitudes of the light fluids are much larger that those of the heavy fluid, so $|\Phi_m| \sim |\tilde{\Phi}_{m+1}|$. For fluids with similar densities, $A \sim 0$, this difference is insignificant, and $|\Phi_m| \sim |\tilde{\Phi}_m|$.

The fastest solution in the family has the curvature and velocity

$$\zeta_1 = \zeta_{A,RT}, \quad v = v_{A,RT} \tag{3.1}$$

Explicit analytical expressions for $\zeta_{A,RT}$ and $v_{A,RT}$ are cumbersome and not presented here. Remarkably, the bubble velocity and the curvature obey a universal dependence

$$v_{A,RT} = \sqrt{g/k}(8|\zeta_{A,RT}|/k)^{3/2}. \tag{3.2}$$

In the limiting case of fluids with highly contrasting densities, $A \approx 1$, the solution (3.1) takes the form

$$\zeta_{A,RT} \approx -(k/8)\big(1 - (1-A)/8\big), \quad v_{A,RT} \approx \sqrt{g/k}\big(1 - 3(1-A)/16\big). \tag{3.3}$$

In the other limiting case, $A \approx 0$, it can be expanded as

$$\zeta_{A,RT} \approx -(k/2)A^{1/3}, \quad v_{A,RT} \approx (3/2)^{3/2}\sqrt{Ag/3k}, \tag{3.4}$$

Stability analysis shows that solutions with $\zeta \sim \zeta_{cr}$ and $\zeta \sim 0$ are unstable, while solutions with $\zeta \sim \zeta_{A,RT}$ are stable. Therefore, the physically significant solution in the RT family is the solution (3.1).

For the Richtmyer-Meshkov instability, the multiple harmonic regular asymptotic solutions in (2.9-2.11) with $M_n \sim 1/t$, $\tilde{M}_n \sim 1/t$ and $v \sim 1/t$, and time-independent ζ_N are found in a similar way. The RM and RT families have a number of common properties such as the dominance of the lowest order amplitudes, convergence, and critical solutions. However the asymptotic dynamics of the bubble front in RMI appears quite different from that in RTI. In the RM family, the fastest solution corresponds to a bubble with a flattened shape:

$$\zeta_1 = \zeta_{A,RM}, = 0 \quad v = v_{A,RM} = 3/Akt \tag{3.5}$$

Higher order corrections for the solution (3.5) are reasonably small. The stability analysis shows that solutions with a finite curvature $\zeta \sim 1/\lambda$ are unstable, while flattened bubbles with $\zeta = \zeta_{A,RM}$ are stable. Therefore, the physically significant solution in the RM family is the solution (3.5).

The foregoing analysis can be applied for 3D flows with other symmetries. In either RTI or RMI, the nonlinear dynamics of 3D highly symmetric flows (Abarzhi 1998, 2002)) coincide except for the difference in the normalization factor k. A nearly isotropic shape of the bubble is the reason of this universality. The 3D and 2D results are similar qualitatively. In main order, in RTI $v_{A,RT,3D}/v_{A,RT,2D} \sim \sqrt{3}$ and $\zeta_{A,RT,3D}/\zeta_{A,RT,2D} \sim 3/4$, while in RMI $v_{A,RM,3D}/v_{A,RM,2D} \sim 2$ and $\zeta_{A,RM,3D}/\zeta_{A,RM,2D} \sim 1$, similarly to Abarzhi (1998) and Abarzhi (2002) for $A = 1$. For 3D low-symmetric flows, the asymptotic analysis shows a tendency of 3D bubbles to conserve isotropy in the plane, and a discontinuity of the 3D-2D dimensional crossover.

4. Discussion

Based on the foregoing results, we expect the following dynamics of the bubble front in the Rayleigh-Taylor and Richtmyer-Meshkov instabilities for fluids with finite density differences in the case of a small initial perturbation. In RTI, the bubble curvature ζ_1 and velocity v grow as $\sim \exp(t/\tau_{RT})$ in the linear regime, $t/\tau_{RT} \ll 1$, and reach finite values $\zeta_1 \approx \zeta_{A,RT}$ and $v \approx v_{A,RT}$ asymptotically for $t/\tau_{RT} \gg 1$. The parameters $\zeta_{A,RT}$ and $v_{A,RT}$ depend strongly on the Atwood number. However, the value $v_{A,RT}^2/\zeta_{A,RT}^3$ is a parameter universal for all A. This universality suggests that the bubble front evolution in RTI is quite complicated and cannot be approximated by the motion of a spherical bubble, in contrast to suggestions of the drag models of Oron *et al.* (2001) and Goncharov (2002). For $A < 1$ the bubbles are slower and less curved compared to the case of $A = 1$; for $A \approx 0$ the bubbles flatten and their velocity approaches zero.

In RMI, the bubble curvature and velocity change as $\zeta_1 \sim -kt/\tau_{RM}$ and $v(t) - v_0 \sim -v_0 t/\tau_{RM}$ in the linear regime, $t/\tau_{RM} \ll 1$; for $t \sim \tau_{RM}$ the curvature ζ_1 reaches an extreme value, dependent on the initial conditions; as $t/\tau_{RM} \gg 1$ the bubble flattens, $\zeta_1 \sim \zeta_{A,RM}$ and decelerates $v \sim v_{A,RM}$. For $A < 1$ the bubbles move faster than those for $A = 1$, and for $A \leq 1$ the bubbles are flat. The flattening of the bubble front is a

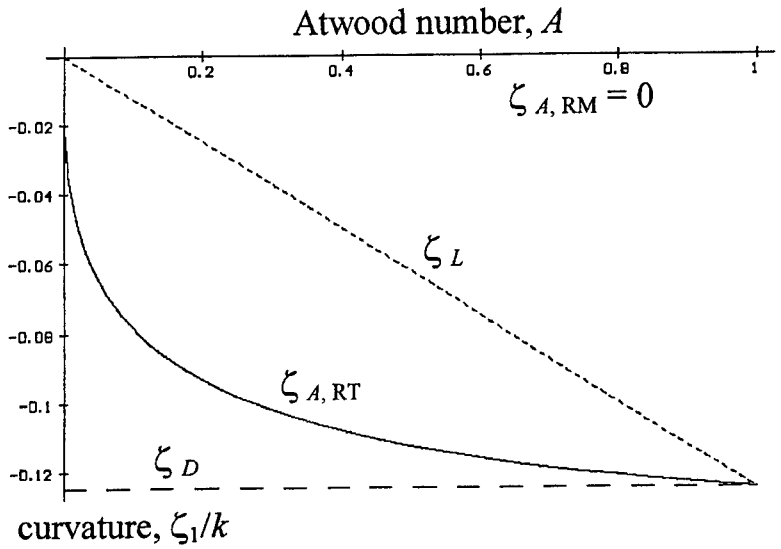


FIGURE 1. Dependence of the bubble curvature on the Atwood number A for 3D highly symmetric flows in the Rayleigh-Taylor and Richtmyer-Meshkov instabilities; k is the wavevector, $\zeta_L = -Ak/8$ is the Layzer-type solution, $\zeta_D = -k/8$ is given by the drag models, $\zeta_{A,RT}$ and $\zeta_{A,RM}$ are given by the non-local multiple harmonic solutions in RTI and RMI respectively.

distinct feature of RMI universal for all A. It follows from the fact that RM bubbles decelerate. The equation (3.5) suggests that for for fluids with very similar densities, $A \sim 0$, the bubble velocity has a much faster time-dependence, as t^a with $-1 < a < 0$, in a qualitative agreement with experiments of Jacobs & Sheeley (1996).

Figures 1, 2 and 3 compare our multiple harmonic non-local solutions with the models of Oron *et al.* (2001) and Goncharov (2002), and with the Layzer-type solution, which agrees with Sharp (1984). For $0 < A \leq 1$ the asymptotic dynamics is different in RTI and RMI: the bubble velocity reaches a constant value in RTI and decreases with time in RMI. Therefore the distribution of pressure around the bubble is distinct in RTI and RMI. This should lead to a different shape for the bubble front. Our theory adequately describes the fact that in RTI the curvature $\zeta_{A,RT}$ has a strong dependence on the Atwood number, while in RMI $\zeta_{A,RM} = 0$ for all A, Figure 1. The models of Sharp (1984), Oron *et al.* (2001), and Goncharov (2002) do not predict any difference between the shape of the RT and RM bubbles. In RTI, for $A = 1$ the values of $\zeta_{A,RT} = \zeta_L = \zeta_D$. However, for finite A the difference among the values $\zeta_{A,RT}$, ζ_L and ζ_D is significant, Fig. 1; in the limit $A \to 0$, $\zeta_{A,RT}/\zeta_D \to 0$, while $\zeta_{A,RT}/\zeta_L \to \infty$. We emphasize that for $A = 0$ the RT instability does not develop and the bubble curvature should remain zero for all t, in agreement with (3.4). In RMI, the bubble in (3.5) flattens asymptotically for all A, while the models of Oron *et al.* (2001) and Goncharov (2002) suggest an A-independent finite value of the bubble curvature $\zeta_D = \zeta_L\big|_{A=1}$, Fig. 1.

We conclude that in either RTI or RMI the bubble curvature is sensitive diagnostic parameter, which tracks the conservation of mass in the flow. The value $\lambda|\zeta_1|$ defines how flat or narrow the bubble is for a given lengths scale λ. This dimensionless shape parameter is related to the bubble velocity and determines the flow drag. The value of the drag force is still a subject for controversy in the chaotic RTI and RMI (Dimonte

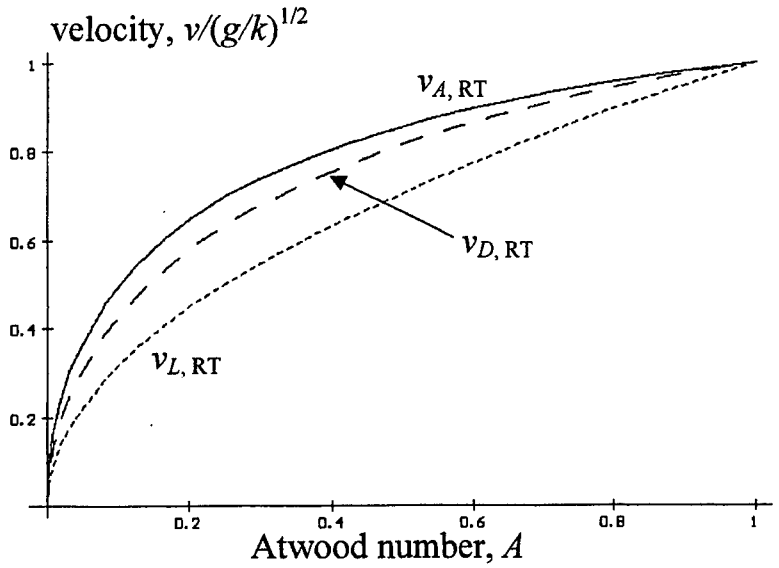


FIGURE 2. Dependence of bubble velocity v on the Atwood number A for 3D highly symmetric flows in the Rayleigh-Taylor instability; k is the wavevector and g is gravity, $v_{L,RT} = \sqrt{Ag/k}$ is the Layzer-type solution, $v_{D,RT} = \sqrt{2Ag/(1+A)k}$ is given by the drag models, and $v_{A,RT}$ is given by the RT multiple harmonic non-local solution.

2000). Our theory resolves this issue for highly nonlinear Rayleigh-Taylor and Richtmyer-Meshkov instabilities. The foregoing analysis suggests that the empiric models of Sharp (1984), Oron *et al.* (2001) and Goncharov (2002) may not be applicable in RTI and RMI.

Our results are in good agreement with available data (Kucherenko *et al.* 2000; He *et al.* 1999; Gardner *et al.* 1988; Jacobs & Sheeley 1996; Holmes *et al.* 1995; Schneider *et al.* 1998; Holmes *et al.* 1999; Dimonte 2000; Volkov *et al.* 2001). However, in most of existing experiments, the measurement of the bubble curvature requires an improvement of diagnostics of the interface dynamics. The major issues to check by future observations are the following: Does the curvature of the RT bubble have a strong dependence on the Atwood number or reach an A-independent value? Does the curvature of the RM bubble vanish asymptotically or approach a finite value?

For the bubble velocity, in the case of $A \sim 1$ the experiments and simulations have been in a reasonable agreement with the dependencies $v_{L,RT}$ and $v_{D,RT}$ in RTI, and with the dependence $v_{D,RM}$ in RMI. On the other hand, as evinced in the foregoing, the single-mode solutions $v_{L,RT}$ and $v_{D,RT}$ as well as $v_{L,RM}$ and $v_{D,RM}$ violate the conservation laws. This apparent paradox is easily explained. Figure 2 shows that in RTI for finite A and for $\zeta_1 \sim 1/\lambda$, the bubble velocity is relatively insensitive to details of the interface dynamics, and the quantitative distinction among the values of $v_{A,RT}$, $v_{D,RT}$ and $v_{L,RT}$ is $10-20\%$. In RMI, the velocities $v_{L,RM}$ and $v_{D,RM}$ differ significantly from $v_{A,RM}$, Figure 3. The difference is however hard to distinguish in experiments. Since the velocity decays as $1/t$, the bubble displacement, $\sim C\log(t/\tau_{RM})/k$, is comparable with an experimental error, and the coefficient C is in this dependence is impossible to evaluate. In contrast, the bubble curvature is a reliable diagnostic parameter as discussed in the foregoing.

Our theory describes the principal influence of the density ratio on the large-scale

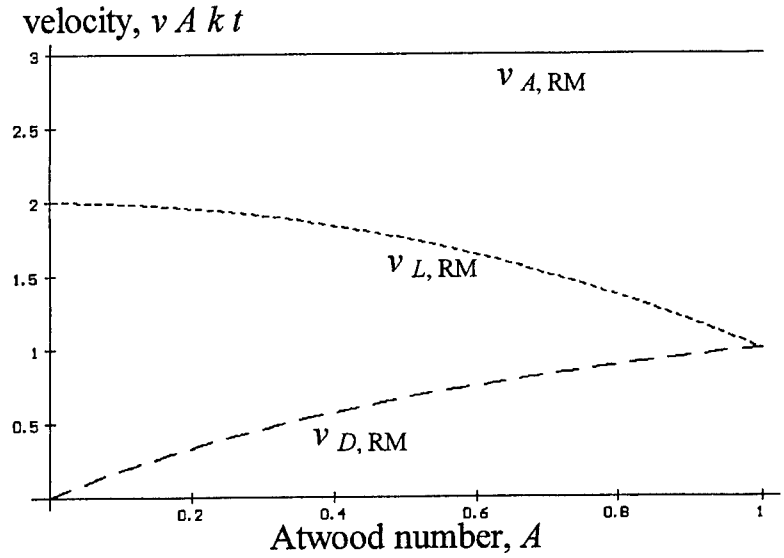


FIGURE 3. Dependence of the bubble velocity v on the Atwood number A for 3D highly symmetric flows in the Richtmyer-Meshkov instability; k is the wavevector, t is time, $v_{L,RM} = (2 - A^2)/Akt$ is the Layzer-type solution, $v_{D,RM} = 2/(1 + A)kt$ is given by the drag models, $v_{A,RM} = 3/Akt$ is given by the RM multiple harmonic non-local solution.

nonlinear dynamics of the RT and RM bubbles. The analysis is based on the assumptions that the flow dynamics is governed by a dominant mode, the transfers of energy to smaller or larger scales are not extensive, and the vorticity does not change the time-dependence of the large-scale coherent motion. If these conditions are broken (for example, for fluids with similar densities, $A \approx 0$), the potential approximation may not give a correct time-dependence for the asymptotic bubble motion. We address these issues in the future.

5. Conclusion

We have found a multiple harmonic solution for a complete system of conservation laws describing the large-scale coherent dynamics in RTI/RMI in general three-dimensional case. The theory yields new dependencies of the bubble curvature and velocity on the density ratio, formulates the universal properties of the nonlinear dynamics in RTI and RMI, reveals an important difference between the dynamics of RT and RM bubbles, and shows the significance of mass conservation for the buoyancy-drag balance.

REFERENCES

ABARZHI, S. I. 1998 Stable steady flows in Rayleigh-Taylor instability. *Phys. Rev. Lett.* **81** (2), 337–340.

ABARZHI, S. I. 2002 A new type of the evolution of the bubble front in the Richtmyer-Meshkov instability. *Physics Letters A* **294** (2), 95–100.

ABARZHI, S. I., NISHIHARA, K. & GLIMM, J. 2003 Rayleigh-Taylor and Richtmyer-Meshkov instabilities for fluids with a finite density ratio. *Phys Letters A* **317**, 470–476.

AREF, H. & TRYGGVASON, G. 1989 Model of Rayleigh-Taylor instability. *Phys. Rev. Lett.* **62**, 749–752.

BAKER, G. R., MEIRON, D. I. & ORSZAG, S. A. 1982 Generalized vortex methods for free-surface flow problems. *J. Fluid Mech.* **123**, 477–501.

CHANDRASEKHAR, S. 1961 *Hydrodynamic and Hydromagnetic Stability*. London: Oxford University Press.

COWLEY, S., BAKER, G. & TANVEER, S. 1999 On the formation of Moore curvature singularities in vortex sheets. *J. Fluid Mech.* **378**, 233–267.

DALZIEL, S., LINDEN, P. & YOUNGS, D. 1999 Self-similarity and internal structure of turbulence induced by the Rayleigh-Taylor instability. *J. Fluid Mech.* **399**, 1–48.

DAVIES, R. & TAYLOR, G. 1950 The mechanics of large bubble rising through extended liquids and through liquids in tubes. *Proc. Roy Soc. A London* **200**, 375–390.

DIMONTE, G. 2000 Spanwise homogeneous buoyancy-drag model for Rayleigh-Taylor mixing and experimental evaluation. *Phys. Plasmas* **7**, 2255–2269.

GARABEDIAN, P. 1957 *Proc. Roy. Soc. London A* **241**, 423–430.

GARDNER, C., GLIMM, J. & MCBRYAN, O. 1988 The dynamics of bubble growth for Rayleigh-Taylor instability. *Phys. Fluids* **31**, 447–465.

GONCHAROV, V. N. 2002 Analytical model of nonlinear, single-mode, classical Rayleigh-Taylor instability at arbitrary Atwood numbers. *Phys. Rev. Lett.* **88**.

HE, X., XHANG, R., CHEN, S. & DOOLEN, G. 1999 On three-dimensional Rayleigh-Taylor instability. *Phys. Fluids* **11**, 1143–1152.

HOLMES, R., GROVE, J. & SHARP, D. 1995 *J. Fluid Mech.* **301**, 51.

HOLMES, R. L., DIMONTE, G., FRYXELL, B., GITTINGS, M. L., GROVE, J. W., SCHNEIDER, M., SHARP, D. H., VELKOVICH, A. L., WEAVER, R. P. & ZHANG, Q. 1999 Richtmyer-Meshkov instability growth: experiment, simulation and theory. *J. Fluid Mech.* **389**, 55–79.

HOU, T. Y., LOWENGRUB, J. S. & SHELLEY, M. J. 1997 The long-time motion of vortex sheets with surface tension. *Phys. Fluids* **9** (7), 1933–1954.

JACOBS, J. & SHEELEY, J. 1996 Experimental study of incompressible Richtmyer- .

KUCHERENKO, Y. A., PYLAEV, A., BALABIN, S., MURZAKOV, V., ARDASHOVA, R., POPOV, V., KOMAROV, O., SAVEL'EV, V., KOZELKOV, O., ROMANOV, I., R, R. C. & HAAS, J. 2000 Behavior of turbulized mixtures at the stage of inertial motion for different Atwood numbers. *Laser Part. Beams* **18**, 163–169.

LAYZER, D. 1955 *Astrophys. Jour.* **122**, 1.

MATSUOKA, C., NISHIHARA, K. & FUKUDA, Y. 2003 Nonlinear evolution of an interface in the Richtmyer-Meshkov instability. *Phys. Rev. E* **67** (art. 036301), 1–12.

MESHKOV, E. 1969 *Sov. Fluid Dyn.* **4**, 101–104.

MOORE, D. 1979 Spontaneous appearance of a singularity in the shape of an evolving vortex sheet. *Proc. Roy. Soc. London A* **365**, 105–119.

ORON, D., ALON, U., OFFER, D. & SHVARTS, D. 2001 Dimensionality dependence of the Rayleigh-Taylor and Richtmyer-Meshkov instability late-time scaling laws. *Phys. Plasmas* **8**, 2883–2889.

RAYLEIGH, L. 1892 On the instability of a cylinder of viscous liquid under capillary force. *Pilos. Mag.* **34**, 145.

RICHTMYER, R. 1960 Taylor instability in shock acceleration of compressible fluids. *Commun. Pure Appl. Math.* **13**, 297–319.

SCHNEIDER, M., DIMONTE, G. & REMINGTON, B. 1998 Large and small scale structure in Rayleigh-Taylor mixing. *Phys. Rev. Lett.* **80**, 3507–3510.

SHARP 1984 An overview of the Rayleigh-Taylor instability. *Physica D* **12**, 3–18.

TANVEER, S. 1993 Singularities in the classical Rayleigh-Taylor flow - formation and subsequent motion. *Proc. Roy. Soc. London A* **441**, 501–525.

VOLKOV, N. V., MAIER, A. E. & YALOVETS, A. P. 2001 The nonlinear dynamics of the interface between media possessing different densities and symmetries. *Tech. Phys. Lett.* **27**, 20–24.

Quadrature moments method for the simulation of turbulent reactive flows

By Venkatramanan Raman, Heinz Pitsch and Rodney O. Fox †

1. Motivation and Objectives

In recent years, computational fluid mechanics has become one of the primary tools for design and optimization of chemical reactors. With stringent environmental constraints, close control of product selectivity and an estimate of by-products are essential in successfully operating chemical plants. The fast throughput and enhanced mixing conditions offered by turbulent flows are increasingly exploited in chemical reactors. Viable simulation methods for such flows should be able to model the complex interaction of reaction and turbulent flow. All known reaction models used in these simulations follow a segregated approach where different techniques are used to solve the momentum and scalar transport equations. It is assumed that reaction affects fluid flow only through the change in density. Usually a variable density flow solver is utilized that accepts the density field from the scalar handler to correct the flow field. The scalar transport scheme uses the flow properties to evaluate the local density and this iterative procedure is used to advance the solution in time. The Eulerian solution technique that is commonly used in solving scalar transport equations inherently does not contain information about sub-grid level processes. The adverse effect of neglecting sub-grid scalar fluctuations in cases where the scalar evolves through non-linear rate expressions is well known. In combustion processes which are characterized by fast chemistry, use of flamelet model (Pitsch & Steiner 2000) or conditional moment closure (CMC) (Bilger 1993) based on a conserved scalar is known to be quite accurate in making qualitative as well as quantitative predictions. Such a method obviates the need for solving multiple scalar transport equations and is not restricted by the time-scale of individual reactions in the chemistry mechanism. The flamelet model, like all other reaction models, requires the specification of a scalar dissipation rate and assumes the shape of the PDF at the sub-grid level. The first-order CMC method models the conditional mean of the reacting scalars as a function of mixture fraction and local flow conditions. But the model ignores any fluctuations about the conditional mean and may not be viable in slow chemistry regimes. Both the CMC and flamelet model assume that all the reactive scalars can be parameterized by a single conserved scalar. On the other end of the spectrum, the transported-PDF scheme computes the sub-grid scalar-PDF in terms of a set of delta-functions. This method can be used in tandem with a flow solver like those based on the Reynolds-Averaged Navier Stokes (RANS) equation or Large-Eddy Simulation (LES) scheme to model reaction (Muradoglu *et al.* 1999; Haworth & El Tahry 1991). Such a formulation computes the profiles of all the species involved in the flow and leads to a closed form for the reaction source term. However, a mixing model is needed to describe the sub-grid mixing process and has been the focus of study in PDF methods (Subramaniam & Pope 1999; Valino 1995; Tsai & Fox

† Department of Chemical Engineering, Iowa State University

1998). The fact that no convincing mixing model exists is one of the important drawbacks of the method.

The transported-PDF still is an attractive scheme in that the reaction source term appears closed. The inhomogeneous transport equation for the sub-grid PDF is multi-dimensional and cannot be solved using Eulerian grid techniques. Particle based Monte-Carlo schemes used with realistic chemistry show good agreement with experimental results (Xu & Pope 2000; Masri & Pope 1990; Roekaerts 1991; Raman *et al.* 2003*a*). However, the handling of a large number of Lagrangian particles along with detailed chemistry can be computationally expensive. When using LES as the flow solver, such schemes can be outright intractable in practical flow configurations. In this work, an equivalent Eulerian version of the transported-PDF method is formulated for LES of reactive flows.

2. Filtered Quadrature Scheme for Variable Density Flows

For use in LES of reactive flows, a filtered density function (FDF) is defined (Gao & O'Brien 1993) that prescribes the sub-filter joint composition density function of the scalars.

$$F_L(\psi;\mathbf{x},t) = \int_{-\infty}^{+\infty} \rho(\mathbf{x}',t)\delta[\psi - \phi(\mathbf{x}',t)]G(\mathbf{x}'-\mathbf{x})d\mathbf{x}', \tag{2.1}$$

where F_L is the mass density function. This definition implies that in variable density flows, the FDF is the mass weighted and spatially filtered fine-grain density (Jaberi *et al.* 1999).

$$\int_{-\infty}^{+\infty} F_L(\psi;\mathbf{x},t)d\psi = \overline{\rho}, \tag{2.2}$$

where $\overline{\rho}$ is the filtered density. Using the scalar transport equation, the FDF is shown to evolve in multi-dimensional space as:

$$\frac{\partial F_L}{\partial t} + \frac{\partial\left[\overline{u}_i F_L\right]}{\partial x_i} = \frac{\partial}{\partial x_i}\left[(\gamma+\gamma_t)\frac{\partial\left(F_L/\overline{\rho}\right)}{\partial x_i}\right] + \frac{\partial}{\partial\psi_\alpha}\left[\Omega_m\left(\psi_\alpha - \overline{\phi}_\alpha\right)F_L\right] - \frac{\partial\left[S_\alpha F_L\right]}{\partial\psi_\alpha}, \tag{2.3}$$

where $\overline{u}_i$ is the Favre filtered velocity component, ψ is the composition array and $\overline{\phi}$ is the Favre filtered mean composition array. The molecular and turbulent diffusivities are denoted by γ and γ_t respectively. The mixing frequency is modeled as $\Omega_m = C_\Omega(\gamma+\gamma_t)/\left(\langle\rho\rangle_l \Delta_G^2\right)$, where Δ_G is the filter width. This high- dimensional equation is traditionally solved using Monte-Carlo schemes (Colucci *et al.* 1998; Raman *et al.* 2003*b*). As mentioned before, the particle based Monte-Carlo schemes are computationally expensive for large grids and hence become intractable even for simple chemistry. The Direct Quadrature Method of Moments (DQMOM) (Marchisio & Fox 2003; Wang & Fox 2003) is introduced here in the context of LES to provide an alternate tractable scheme.

Figure 1 shows the fine-grained PDF composed of a set of delta-functions approximating an arbitrary shaped PDF at a given point in the flow. Any particle based solution to the FDF equation will yield such an approximation. The FDF plot can be considered as a plot of normalized weights of particles in the computational cell. The accuracy of the approximation depends, among other factors, on the number of approximating delta functions. The N_α delta-functions are characterized by their positions ($\phi_{\alpha i}$) and their heights ($w_{\alpha i}$). The FDF is considered solved if for a given number of delta functions, the

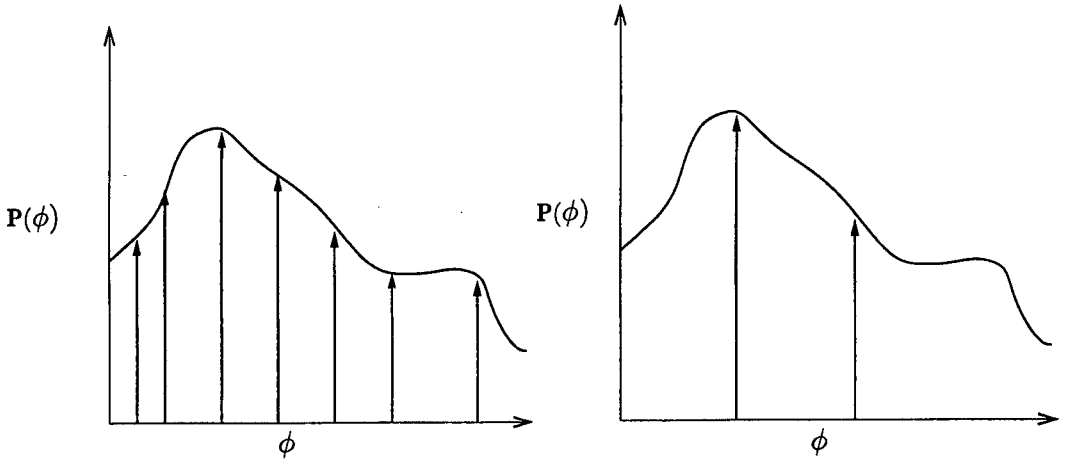


FIGURE 1. Approximation of a PDF using a finite number of delta functions. (Left) Transported PDF method and (Right) DQMOM method.

values of $\phi_{\alpha i}$ and $w_{\alpha i}$ are known. The DQMOM model formulates transport equations for these quantities based on pre-determined number of so-called environments, where each environment corresponds to a single delta-peak. The source terms involved in these equations ensure that the DQMOM equations match the moment equations of the scalar.

In the multi-environment DQMOM model, the FDF is assumed to be of the form:

$$F_L = \overline{\rho} \sum_{i=1}^{N} w_i \delta\left(\psi - \overline{\phi}_i\right). \tag{2.4}$$

The individual transport equations for the weights and locations of the delta-functions can be derived by substituting Eq. 2.4 into Eq. 2.3 (Fox 2003). For a single scalar case, this leads to

$$\begin{aligned}
&\sum_{i=1}^{N} \delta\left(\psi - \overline{\phi}_i\right) \left[\frac{\partial \overline{\rho} w_i}{\partial t} + \nabla \overline{\rho \mathbf{u}} w_i - \nabla \cdot (\Gamma + \Gamma_T) \nabla w_i\right] \\
&- \sum_{i=1}^{N} \delta^{(1)}\left(\psi - \overline{\phi}_i\right) \left\{\frac{\partial \overline{\rho} \overline{G}_i}{\partial t} + \nabla \overline{\rho \mathbf{u}} \overline{G}_i - \nabla \cdot (\Gamma + \Gamma_T) \nabla \overline{G}_i \right. \\
&\qquad \left. - \overline{\phi}_i \left[\frac{\partial \overline{\rho} w_i}{\partial t} + \nabla \overline{\rho \mathbf{u}} w_i - \nabla \cdot (\Gamma + \Gamma_T) \nabla w_i\right]\right\} \\
&- \sum_{i=1}^{N} \delta^{(2)}\left(\psi - \overline{\phi}_i\right) w_i (\Gamma + \Gamma_T) \nabla \cdot \nabla \overline{\phi}_i = R(\psi; \mathbf{x}, t),
\end{aligned} \tag{2.5}$$

where $\overline{G}_i = w_i \overline{\phi}_i$ and $R(\psi; \mathbf{x}, t)$ contains the mixing and reaction terms. $\delta^{(m)}$ indicates the m-th derivative of the delta function. The properties of δ function are used in rewriting the derivatives in terms of the filtered quantities (Pope 2000).

$$\frac{\partial \delta\left(\psi - \overline{\phi}\right)}{\partial t} = -\delta^{(1)}\left(\psi - \overline{\phi}\right) \frac{\partial \overline{\phi}}{\partial t} \tag{2.6}$$

and

$$\frac{\partial^2 \delta\left(\psi-\overline{\phi}\right)}{\partial x_j^2} = \delta^{(2)}\left(\psi-\overline{\phi}\right)\frac{\partial^2 \overline{\phi}}{\partial x_j^2}. \tag{2.7}$$

Following Fox (2003), Eq. 2.5 can be rewritten in terms of the transport equations for w_i and G_i, using a_i and b_i to denote the respective equations.

$$\sum_{i=1}^{N}\left[\delta\left(\psi-\overline{\phi}\right)+\overline{\phi}_i\delta^{(1)}\left(\psi-\overline{\phi}\right)\right]a_i - \sum_{i=1}^{N}\delta^{(1)}\left(\psi-\overline{\phi}\right)b_i = \sum_{i=1}^{N}\delta^{(2)}\left(\psi-\overline{\phi}\right)w_i c_i + R(\psi;\mathbf{x},t), \tag{2.8}$$

where $c_i = (\Gamma+\Gamma_t)(\nabla\overline{\phi}_i)^2$. In deriving these equations, the only assumption made so far is that the shape of the PDF is approximated by a finite-set of delta functions. For a N-environment model, $2N$ source terms need to be specified. It should be noted that if the number of scalars is more than one, several cross moments can also be specified. For details on the feasibility and choice of moments refer to Fox (2003) and Marchisio & Fox (2003). Here, only the pure moments, namely the mean and variance of a scalar are used in fixing the source terms. Multiplying Eq. 2.8 by ψ^m and integrating over the composition space yields:

$$(1-m)\sum_{i=1}^{N}\overline{\phi}^{m}{}_i a_i + m\sum_{i=1}^{N}\overline{\phi}^{m-1}{}_i b_i = m(m-1)\sum_{i=1}^{N}\overline{\phi}^{m-2}{}_i w_i c_i + R_m. \tag{2.9}$$

Similarly the reaction and mixing terms can be integrated to yield:

$$\begin{aligned} R_m &= \int_{-\infty}^{+\infty}\psi^m R(\psi;\mathbf{x},t) \\ &= -\int_{-\infty}^{+\infty}\psi^m\frac{\partial}{\partial\psi}\left\{\left[\Omega_m\left(\overline{\phi}-\psi\right)+S(\psi)\right]f_\phi\right\}d\psi \\ &= -m\int_{-\infty}^{+\infty}\psi^{m-1}\left\{\left[\Omega_m\left(\overline{\phi}-\psi\right)+S(\psi)\right]\sum_{i=1}^{N}\overline{\rho}w_i\delta\left(\psi-\overline{\phi}\right)\right\}d\psi \\ &= m\sum_{i=1}^{N}\overline{\rho}w_i\overline{\phi}_i^{m-1}\left\{\Omega_m\left(\overline{\phi}-\overline{\phi}_i\right)+S(\overline{\phi}_i)\right\}. \end{aligned} \tag{2.10}$$

Using Eqs 2.9 and 2.10 we can obtain the source terms a_i and b_i by solving a set of non-linear algberaic equations. In this work, N is set to two for all simulations. To further simplify the equations, we can arbitrarily set a_i to zero (Fox 2003). We then use $m = 1, 2$ to obtain the other source terms. Using the above moment equations, the non-linear system for b_i reduces to:

$$\begin{bmatrix}1 & 1\\ \phi_1 & \phi_2\end{bmatrix}\begin{bmatrix}b_1\\ b_2\end{bmatrix} = \begin{bmatrix}R_1\\ 2\left(w_1c_1+w_2c_2\right)+R_2\end{bmatrix}. \tag{2.11}$$

From the above set of equations, the source terms are determined to be:

$$a_1 = a_2 = 0, \tag{2.12}$$

$$b_1 = \frac{1}{\overline{\phi}_1 - \overline{\phi}_2} \sum_{i=1}^{2} w_i \Gamma_t (\nabla \overline{\phi}_i)^2 + \Omega_m \left(w_1 G_2 - w_2 G_1\right) + w_1 S(\phi_1), \tag{2.13}$$

and

$$b_2 = \frac{-1}{\overline{\phi}_1 - \overline{\phi}_2} \sum_{i=1}^{2} w_i \Gamma_t (\nabla \overline{\phi}_i)^2 - \Omega_m \left(w_1 G_2 - w_2 G_1\right) + w_2 S(\phi_2). \tag{2.14}$$

As discussed earlier, the number of environments can be considered to be equivalent to the particle number density used in a Lagrangian simulation. This implies that as the number of environments is increased, the accuracy of the scheme should increase (Wang & Fox 2003). The single scalar DQMOM can be extended to a multi-variate case using similar derivation technique (Fox 2003). In determining the source terms, one of the important criteria is that the pre-multiplier of the b vector in Eq. 2.11 is invertible. It should also be noted that a_i need not be set to zero and can be determined through a set of extended non-linear equations (Marchisio & Fox 2003).

3. Numerics

The numerical implementation for reactive flow simulations consists of two parts - the flow solver and the scalar handler. Here, we use a LES flow solver along with three different implementations of the scalar transport equation. The first method solves for the mean mixture fraction and reaction progress variable along with the variance of the mixture fraction using Eulerian transport equations for these quantities. The second method uses a Lagrangian Monte-Carlo scheme to solve the FDF of the mixture-fraction and reaction progress variable. The third implementation uses the DQMOM based 2-environment model to obtain the first and second moments of the scalars. In all these cases, the density field is obtained from the scalar handler and fed to the flow solver which corrects the flow according to reaction. To first establish the viability of the DQMOM model, we only consider reactions with no heat release in constant density incompressible flows and thus do not use the feedback loop. The flow solver provides the one-way transfer of velocity and turbulence fields to the scalar handler. The following subsections briefly explain the numerical implementations of each of the components.

3.1. *LES solver*

The second order LES scheme uses an energy conserving formulation for the momentum equations (Pierce 2001). The eddy viscosity and diffusivity are computed using dynamic Smagorinsky model (Moin *et al.* 1991). The LES scheme also solves for the scalar transport equation using a semi-implicit scheme. In the current work, scalar equations are solved for the mixture fraction Z and the reaction progress variable Y. The numerical implementation uses an upwind based QUICK scheme that is designed to reduce numerical oscillations but also leads to some amount of numerical dissipation.

For the sake of comparison, the mixture fraction variance transport equation is also simulated using production and dissipation terms consistent with the FDF formulation. Since sub-grid variance is a very small quantity in LES simulations, numerical dissipation can further increase the errors in the computation. To overcome this problem, a $\overline{Z} - \overline{Z^2}$ system is solved rather than the variance transport equation. The scalar equations are

obtained by integrating the FDF equation over mixture fraction space after multiplying by Z and Z^2.

$$\frac{\partial \overline{\rho}\overline{Z}}{\partial t} + \nabla \overline{\rho}\overline{\mathbf{U}}\overline{Z} = \nabla \left(\Gamma + \Gamma_T\right) \nabla \overline{Z} \tag{3.1}$$

$$\frac{\partial \overline{\rho}\overline{Z^2}}{\partial t} + \nabla \overline{\rho}\overline{\mathbf{U}}\overline{Z^2} = \nabla \left(\Gamma + \Gamma_T\right) \nabla \overline{Z^2} - \Omega_m \left(\overline{Z^2} - \overline{Z}\overline{Z}\right), \tag{3.2}$$

with Ω_m defined as before providing the time scale for scalar dissipation. This formulation ensures that in the limit of zero dissipation, the sub-grid variance is identical to the analytical solution:

$$\overline{Z'^2} = \overline{Z^2} - \overline{Z} = \overline{Z}\left(1 - \overline{Z}\right). \tag{3.3}$$

The inlet and boundary conditions for $\overline{Z^2}$ are identical to the filtered mixture fraction equation. This ensures that the sub-grid variance is zero at both the inlet and any boundaries in the domain. The chemical source term for the progress-variable equation is modeled based on the filtered means of the scalars and neglecting any sub-grid fluctuations. This "laminar" assumption leads to the following transport equation for the reactive scalar:

$$\frac{\partial \overline{\rho}\overline{Y}}{\partial t} + \nabla \overline{\rho}\overline{\mathbf{U}}\overline{Y} = \nabla \left(\Gamma + \Gamma_T\right) \nabla \overline{Y} + \overline{\rho} S(\overline{Y}). \tag{3.4}$$

The LES solution of the mixture fraction mean and variance equation provides an independent way of checking the transported PDF and DQMOM methods.

3.2. *Transported PDF solver*

In the Lagrangian implementation, the FDF transport equation is solved using an ensemble of notional particles. The hybrid composition-PDF scheme used here uses the flow fields from the LES solver (that was described in the previous section) to evolve stochastic particles that are evenly distributed in the entire computational domain. The evolution equations for the particles are obtained from Eq. 2.3 by using techniques similar to the RANS based hybrid method (Pope 1985; Colucci *et al.* 1998). The SDE's are solved for a system of particles which represents the FDF in composition space. The particles move in physical space according to:

$$d\mathbf{x}^* = \left(\overline{\mathbf{u}} + \frac{1}{\overline{\rho}}\nabla(\Gamma + \Gamma_t)\right) dt + \sqrt{2\frac{(\Gamma + \Gamma_T)}{\overline{\rho}}} dW, \tag{3.5}$$

where $\mathbf{x}^*$ is the instantaneous position of the particle and dW represents the Wiener diffusion term. The motion in composition space is due to mixing and reaction.

$$d\boldsymbol{\phi}^* = \left[\Omega_m \left(\overline{\boldsymbol{\phi}} - \boldsymbol{\phi}^*\right) + \mathbf{S}(\boldsymbol{\phi})\right] dt, \tag{3.6}$$

where $\boldsymbol{\phi}^*$ is the notional particle composition. Here the composition vector $\boldsymbol{\phi} = [Z, Y]$ evolves using reaction source terms $S(\boldsymbol{\phi}) = [0, S(Z, Y)]$. The use of the IEM model with the appropriate dissipation rate ensures that the variance dissipation is consistent with the LES solver. Since typical LES simulation use millions of computational cells, even a particle number density of 10-20 particles per cell will be computationally expensive. To ensure tractability, several novel computational algorithms are implemented. A pointer-based storage structure is used for handling the particles. Conventional algorithms use sorting procedures to keep the particles in order but are not feasible for such large numbers. Here an integer numbering procedure is used that uses pointer based linking of

particles to cells. Cells store only the index of the particles in their domain. Ownership of particles is transferred to the destination cell when particles move across faces. Such integer operations are inexpensive, even though they tend to loose some efficiency with iterations as the particles occupy discontinuous locations in memory. Particle motion is handled using an element-to-element tracking procedure (Subramaniam & Haworth 2000; Raman *et al.* 2003*a*). This algorithm splits the motion into a sequence of sub-steps that move individual particles from face-to-face with intermediate re-interpolation of particle velocity. Reflective boundaries can then be handled directly. In all the simulations carried out here, a nominal number density of 30 particles per cell is used. Particle splitting and merging is utilized to minimize the fluctuations in the number density. The details of the implementation and some preliminary results can be found in Raman *et al.* (2003*b*).

3.3. *DQMOM implementation*

The two-environment version of the model solves for the scalars w_1 ($w_2 = 1 - w_1$), $\overline{G}_{11}$, $\overline{G}_{12}$, $\overline{G}_{21}$, $\overline{G}_{22}$. The working set of equations can be written as

$$\frac{\partial \overline{\rho} w_1}{\partial t} + \nabla \overline{\rho \mathbf{u}} w_1 = \nabla \left(\Gamma + \Gamma_T\right) \nabla w_1. \tag{3.7}$$

$$\frac{\partial \overline{\rho} \overline{G}_{\alpha i}}{\partial t} + \nabla \overline{\rho \mathbf{u}} \overline{G}_{\alpha i} = \nabla \left(\Gamma + \Gamma_T\right) \nabla \overline{G}_{\alpha i} + S_{\alpha i}. \tag{3.8}$$

It can be seen that the evolution equation for the environment (Eq. 3.7) is identical to the mixture-fraction equation with no source term. The weighted scalar equations (Eq. 3.8) contain source terms that can be decomposed into mixing, reaction and correction components. These terms can be specified by first determining the location of the delta-functions in composition space in a given computational cell.

$$\overline{\phi}_{\alpha i} = \frac{\overline{G}_{\alpha i}}{w_i}. \tag{3.9}$$

The mixing source term takes the form:

$$S^m_{\alpha 1} = -S^m_{\alpha 1} = \Omega_m \left(w_{\alpha 1} \overline{G}_{\alpha 2} - w_{\alpha 2} \overline{G}_{\alpha 1}\right). \tag{3.10}$$

The correction term is obtained using the location of the delta peaks as

$$S^c_{\alpha 1} = -S^c_{\alpha 2} = \frac{1}{\overline{\phi}_{\alpha 1} - \overline{\phi}_{\alpha 2}} \sum_{i=1}^{2} (\Gamma_T + \Gamma) \left(\nabla \overline{\phi}_{\alpha i}\right)^2. \tag{3.11}$$

The reaction source term is computed based on the composition vector $\boldsymbol{\phi}_i$ in each environment as

$$S^r_{\alpha i} = S_\alpha \left(\overline{\boldsymbol{\phi}}_i\right). \tag{3.12}$$

The source term for the scalar equation $G\alpha i$ is then given by

$$S_{\alpha i} = S^m_{\alpha i} + S^c_{\alpha i} + w_i S^r_{\alpha i}, \tag{3.13}$$

where the reaction source term is multiplied by the weight in order to be consistent with the formulation.

The main implementation issue comes for the correction term. The correction term, $S^c_{\alpha 1}$, compensates for the excess moment source term arising from the finite-peak representation of the FDF. As seen above, this source term involves the inverse of the separation distance of the delta-peaks composition space. In regions of near-complete mixing,

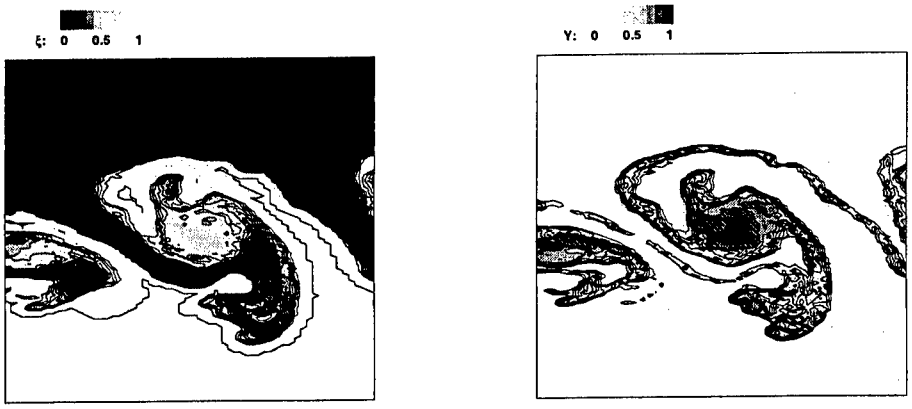


FIGURE 2. Instantaneous mixture fraction (left) and progress variable (right) contours simulated using the FDF scheme.

this term will approach zero leading to very large correction terms. Several alternatives have been suggested (Wang & Fox 2003) but in this work, an ad-hoc limit is used such that for all points where the difference $\phi_{\alpha 1} - \phi_{\alpha 2}$ is less than ϵ, this term is set to ϵ. Such an implementation using $\epsilon = 10^{-4}$ was found to be stable for all the cases studied.

Another important aspect to note is that the scalar solver does not maintain the bounds on the scalars. This might lead to peak locations outside the accessible range for the scalars. It was found that any attempt to limit these values led to a sharp decrease in the estimate of the variance. To counter this problem, for all grid cells that contain peaks outside the natural limits, the source terms were set to zero. The presence of reaction source terms with stiff kinetics was found to adversely affect this occurrence. Smaller time-steps that are determined based on reaction-time scale were found to alleviate this problem.

4. Simulations

The shear flow geometry of Mungal & Dimotakis (1984) is used to test the new scheme. The configuration consists of a planar shear layer formed by two streams entering at 8.8 m/s and 22 m/s velocity. Though the experiment involves a low heat-release fast chemistry, in this work we have not implemented this mechanism. Since the purpose is to compare different reaction models, a simple first order mechanism of the type $A+B \rightarrow P$ is used for modeling reaction. The rate expression is simplified using a mixture fraction-progress variable approach. Three different rate expressions that commonly occur in reacting flows are tested. The transported PDF scheme is also simulated for the same flow conditions and the results are compared with the DQMOM and LES simulations. A 256 $\times$ 128 grid spanning $80D$ in the axial direction and $40D$ in the cross-stream direction is used. Here D is set such that the observation point in the experiment is around $50D$. The inlet velocity profiles are assumed to be laminar with flat profiles. A development region corresponding to $10D$ extends into the domain where the two streams are separated by a splitter plate.

In all the simulations, the rate expression for the progress variable is of the form

$$r_Y = K\left(\frac{Z}{Z_{st}} - Y\right)\left(\frac{1-Z}{1-Z_{st}} - Y\right). \tag{4.1}$$

The rate constant K is varied to study the effect of non-linearity on DQMOM predictions. In the first case, the rate constant is set to a value of $K = 2$. Figure 2 shows the instantaneous mixture fraction and progress variable contours near the center of the domain. It shows the vortex like structure common to shear flows and the presence of highly mixed reactants at the center of such vortices. The peak in source term and mean progress variable are observed near the centerline. The vortices were found to stretch to a maximum of 10D in the cross-stream direction. It was found that the DQMOM model exhibits similar high reaction-rate zones. However, the LES simulations show a thick reaction zone with maximum allowable reaction rate at each location. In order to compare the steady-state trends, mean and variance of all scalars were time-averaged for at least one flow through time. Figure 3 shows the cross-stream profiles of the mixture fraction and sub-grid variance computed from all three schemes. Theoretically, the sub-grid variance obtained from all these methods should be identical. However, the differences in the implementation cause some discrepancy. Nevertheless, the time-averaged filtered mixture fraction and sub-grid variance predicted by all the schemes are in good agreement, thereby validating both the DQMOM and transported-PDF implementation.

The time-averaged mean and sub-grid variance of the reaction progress-variable obtained from the different schemes show some interesting features (Fig. 4). The sub-grid variance is non-zero only for the DQMOM and transported-PDF schemes and is set to zero for the LES scheme. In this context the LES solver can be considered as a one-environment model with complete sub-filter mixing. If the transported-PDF scheme is considered as a multi-environment DQMOM model, the particle scheme with a nominal number density of N represents an N-environment decomposition of the FDF. The cross stream profiles of the mean show that the DQMOM method provides a vast improvement over the one-environment solution. The mean profile shows that in spite of the simple rate expression, second moment terms cannot be neglected. The differences between the LES and DQMOM models are highest in the initial section where the effect of unmixed reactants will be very important. Since the inflow is laminar, the mixing layer itself does not become turbulent until about $X = 7.5$. However, the LES solver predicts very high reaction rates in even these laminar regions where low mixing should essentially keep the reaction rates to a very low value. This "early-ignition" is observed in the profiles at $X = 20$ where the mean value predicted by the LES solver is atleast 50% higher than that predicted by the DQMOM model. Surprisingly, the sub-grid variance profile from the DQMOM scheme also shows very good agreement with the PDF scheme. This essentially implies that the third and higher moments of the reactive scalar can be neglected for this chemistry scheme.

In the next case, a more complex rate expression is implemented. Reaction rates appearing in combustion have a strong dependence on temperature. Most source terms have an exponential dependence on local temperature. To simulate such a condition, the reaction rate constant was set to

$$K = 1000\exp\left(-\frac{b(1-Y)}{1-0.88(1-Y)}\right), \tag{4.2}$$

where b denotes the degree of dependence on temperature. For practical combustion

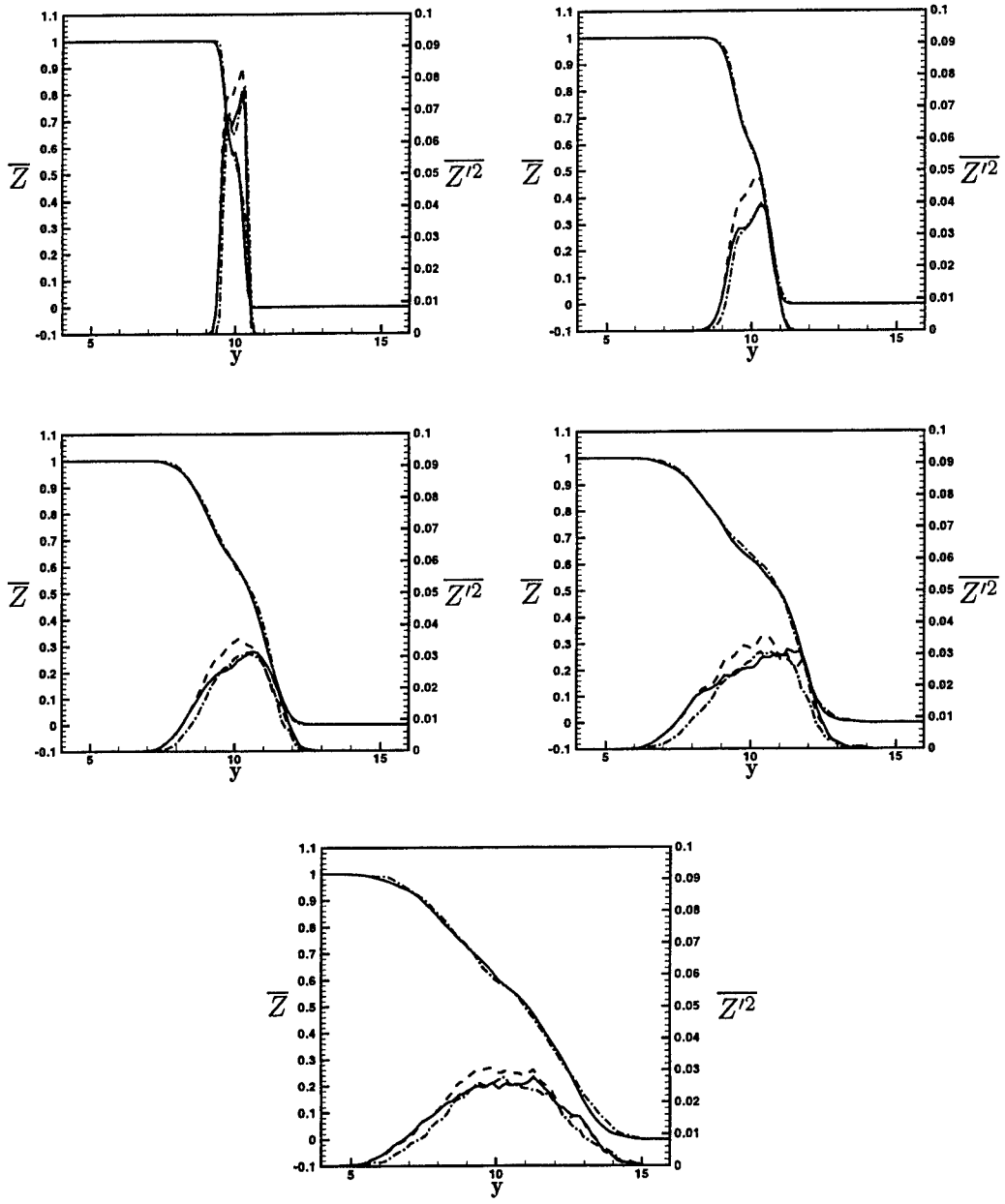


FIGURE 3. Comparison of time-averaged mean and variance of mixture fraction using a constant at different axial locations. (———) DQMOM, (----) LES and (—-—) PDF.

applications, b is usually set to values between 5 and 6. However, such high values lead to extinction for the present flow configuration. Instead, a lower value of 1 is chosen so that the reaction zone can be anchored near the splitter plate. This implies a weaker dependence on temperature but nevertheless makes the rate expression non-linear. Fig. 5 shows the cross-stream profiles of reaction progress variable. Here again, it can be seen

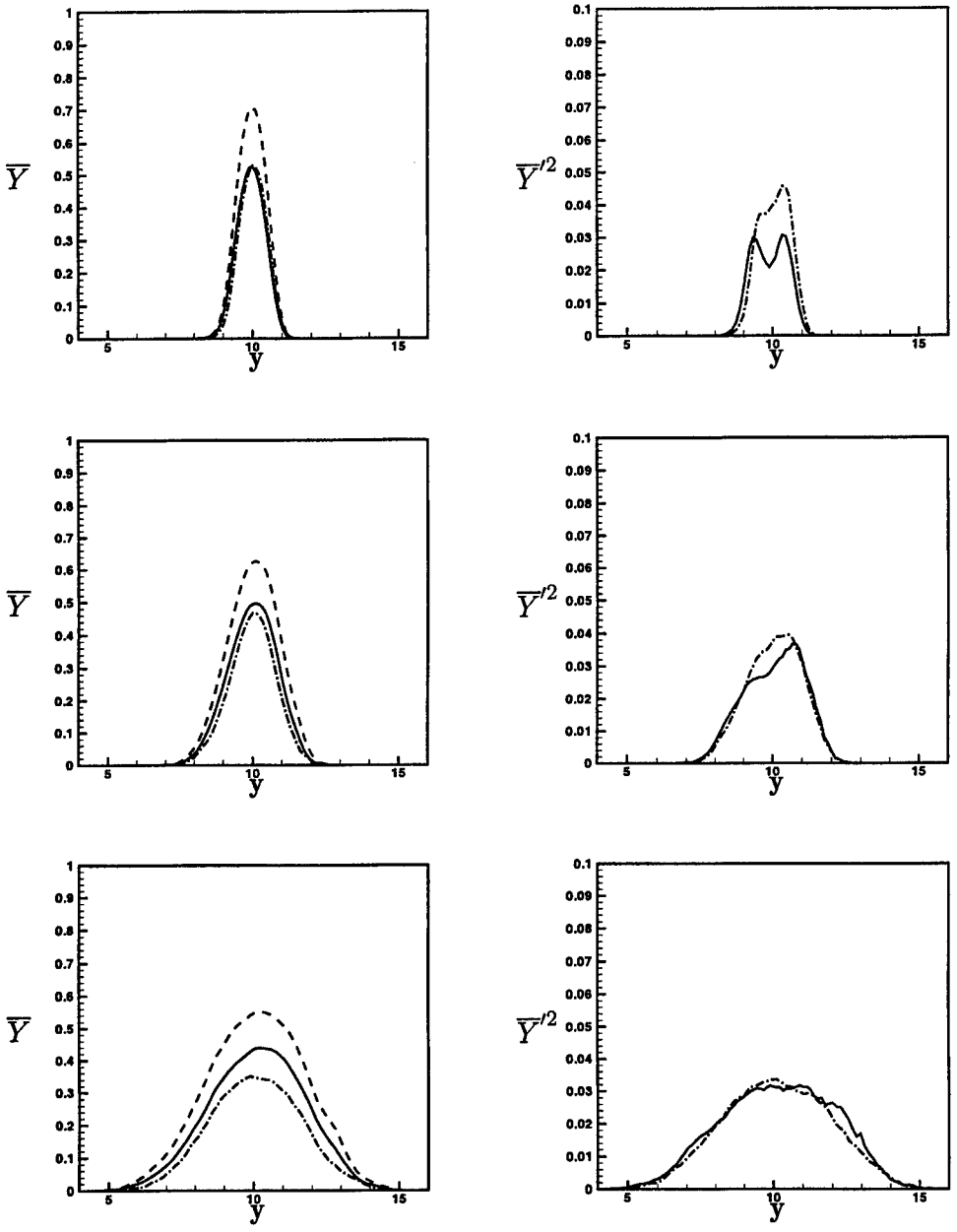


FIGURE 4. Comparison of time-averaged (left) mean and (right) variance of reaction progress variable using a constant rate constant at (top) X=20, (middle) X=30 and (bottom) X=50. (———) DQMOM, (- - - -) LES and (— - —) PDF.

that the DQMOM predictions of both the mean and the variance of the reactive scalar are in good agreement with the transported-PDF results. The LES predictions show fast rates consistent with the laminar assumption. It should be noted that depending on the reaction rates, the complete mixing assumption can also lead to quenching.

The third and final case uses a polynomial rate function which is common to chemical engineering assumptions. Reduced chemical mechanisms like the chloromethane reactions (West *et al.* 1999) may even involve non-integer moments of the scalar variable. Here, the rate is defined as

$$r_Y = 1000\frac{0.0001 + Y^2}{1.0 + Y}. \tag{4.3}$$

This expression ensures that the reaction proceeds without the need for an ignition source. The predicted mean and variance (Fig. 6) indicate good agreement with the transported-PDF scheme. This clearly shows that the DQMOM model with just two environments is able to drastically improve the single-environment predictions obtained from the LES solver.

In terms of computational requirements, the particle based transported-PDF solver was nearly 5 times slower than the DQMOM scheme even for such simple geometries. For complex configurations, the memory requirements of a large ensemble of particles can further slow down the simulation. However, the DQMOM scheme it not without limitations. In particular, the time-scale limitations of a stiff-chemistry source term can reduce the time-step used in the DQMOM model while the robust chemistry solvers (e.g ISAT (Pope 1997)) can increase the computational speed of the transported-PDF model. In addition, detailed chemistry mechanisms will require a large number of scalar transport equations and may eventually diminish the advantages over the particle scheme. In spite of these observations, present study shows that the DQMOM scheme is a viable altrernative to the Monte-Carlo based transported-PDF model and needs to be further explored for multi-species systems.

5. Conclusions and Future Work

A sub-filter model for reactive flows, namely the DQMOM model, was formulated for LES using the filtered mass density function. Transport equations required to determine the location and size of the delta-peaks were then formulated for a 2-peak decomposition of the FDF. The DQMOM scheme was implemented in an existing structured-grid LES solver. Simulations of scalar shear layer using an experimental configuration showed that the first and second moments of both reactive and inert scalars are in good agreement with a conventional Lagrangian scheme that evolves the same FDF. Comparisons with LES simulations performed using laminar chemistry assumption for the reactive scalar show that the new method provides vast improvements at minimal computational cost.

Currently, the DQMOM model is being implemented for use with the progress variable/mixture fraction model of Pierce (2001). Comparisons with experimental results and LES simulations using a single-environment for the progress-variable are planned. Future studies will aim at understanding the effect of increase in environments on predictions.

REFERENCES

BILGER, R. W. 1993 Conditional moment closure for turbulent reacting flow. *Physics of Fluids* **5** (2), 436–444.

COLUCCI, P. J., JABERI, F. A. & GIVI, P. 1998 Filtered density function for large eddy simulation of turbulent reacting flows. *Physics of Fluids* **10** (2), 499–515.

FOX, R. O. 2003 Computational Models for Turbulent Reactive Flows. Cambridge University Press, To be published.

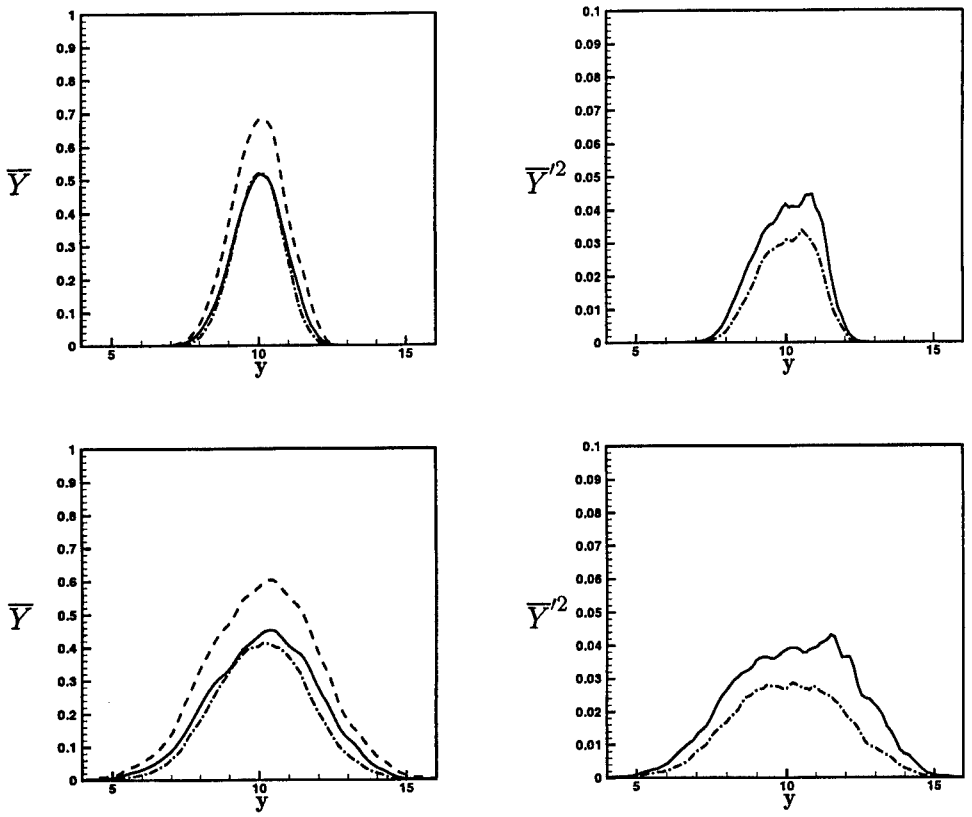


FIGURE 5. Comparison of time-averaged (left) mean and (right) variance of reaction progress variable for exponential reaction rate at (top) X=30 and (bottom) X=50. (———) DQMOM, (----) LES and (—-—) PDF.

GAO, F. & O'BRIEN, E. E. 1993 A large-eddy simulation scheme for turbulent reacting flows. *Physics of Fluids* **5** (6), 1282.

HAWORTH, D. C. & EL TAHRY, S. H. 1991 Probability density function approach for multidimensional turbulent flow calculations with application to in-cylinder flows in reciprocating engines. *AIAA Journal* **29** (2), 208–218.

JABERI, F. A., COLUCCI, P. J., JAMES, S., GIVI, P. & POPE, S. B. 1999 Filtered mass density function for large-eddy simulation of turbulent reacting flows. *Journal of Fluid Mechanics* **401**, 85–121.

MARCHISIO, D. L. & FOX, R. O. 2003 Direct quadrature method of moments: Derivation, analysis and applications. *Submitted to Journal of Computational Physics.*

MASRI, A. R. & POPE, S. B. 1990 Pdf calculations of piloted turbulent nonpremixed flames of methane. *Combustion and Flame* **81** (1), 13–29.

MOIN, P., SQUIRES, K., CABOT, W. & LEE, S. 1991 A dynamic subgrid-scale model for compressible turbulence and scalar transport. *Physics of Fluids A* **3**, 2746–2757.

MUNGAL, M. & DIMOTAKIS, P. E. 1984 Mixing and combustion with low heat release in a turbulent mixing layer. *Journal of Fluid Mechanics* **148**, 349–382.

MURADOGLU, M., JENNY, P., POPE, S. B. & CAUGHEY, D. A. 1999 A consistent

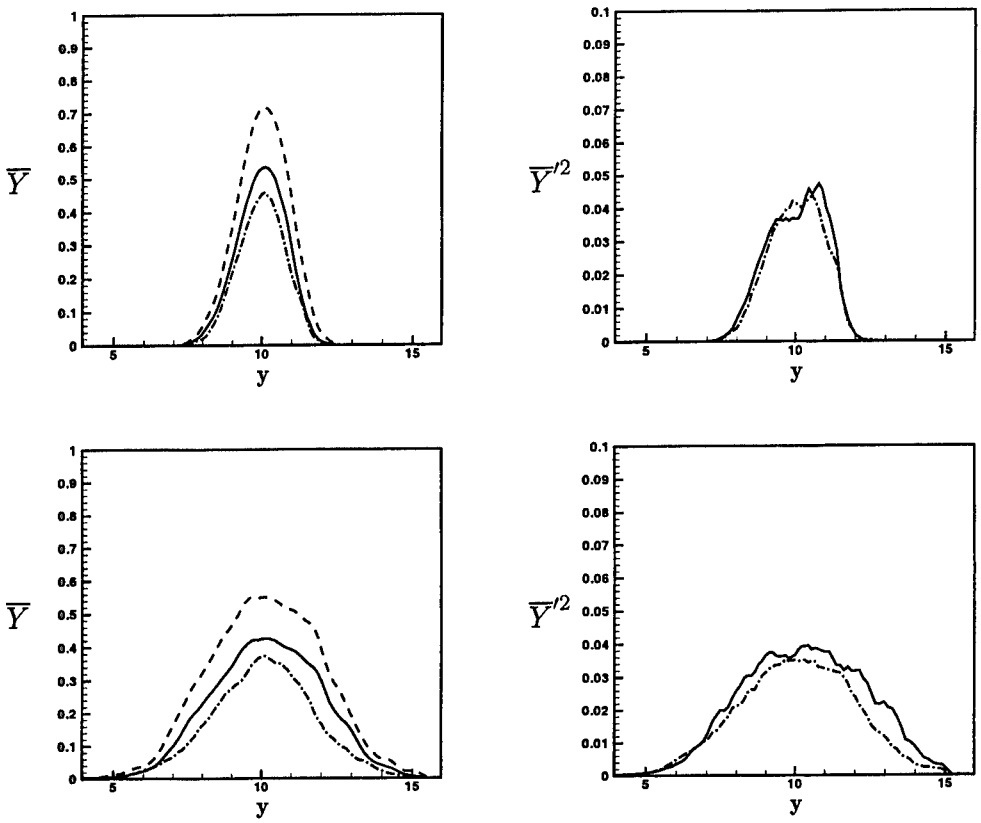


FIGURE 6. Comparison of time-averaged (left) mean and (right) variance of reaction progress variable for polynomial reaction rate at (top) X=30 and (bottom) X=50. (———) DQMOM, (----) LES and (—-—) PDF.

hybrid finite-volume/particle method for the PDF equations of turbulent reactive flows. *Journal of Computational Physics* **154**, 342–371.

PIERCE, C. D. 2001 Progress-variable approach for large-eddy simulation of turbulence combustion. PhD thesis, Stanford University.

PITSCH, H. & STEINER, H. 2000 Large-eddy simulation of a turbulent piloted methane/air diffusion flame (sandia flame D). *Physics of Fluids* **12** (10), 2541–2554.

POPE, S. B. 1985 PDF methods for turbulent reactive flows. *Progress in Energy and Combustion Science* **11**, 119.

POPE, S. B. 1997 Computationally efficient implementation of combustion chemistry using in-situ adaptive tabulation. *Combustion Theory Modelling* **1**, 41.

POPE, S. B. 2000 *Turbulent Flows*. Cambridge University Press.

RAMAN, V., FOX, R. O., HARVEY, A. D. & WEST, D. H. 2003*a* Effect of feed-stream configuration on gas-phase chlorination reactor performance. *Industrial and Engineering Chemistry Research* **42**, 2544–2557.

RAMAN, V., PITSCH, H. & FOX, R. O. 2003*b* Hybrid LES-PDF methods for the simulation of turbulent reactive flows. *To appear in Proceedings of the Topical Conference on Computers at Work, AIChE Annual Meeting, San Francisco, 2003*

ROEKAERTS, D. 1991 Use of a Monte Carlo PDF method in a study of the influence of turbulent fluctuations on selectivity in a jet-stirred reactor. *Applied Scientific Research* **48**, 271.

SUBRAMANIAM, S. & HAWORTH, D. 2000 A PDF method for turbulent mixing and combustion on three-dimensional unstructured deforming meshes. *International Journal of Engine Research* **1**, 171–190.

SUBRAMANIAM, S. & POPE, S. B. 1999 Comparison of mixing model performance for non-premixed turbulent reactive flow. *Combustion and Flame* **117**, 732.

TSAI, K. & FOX, R. O. 1998 The BMC/GIEM model for micromixing in non-premixed turbulent reacting flows. *Industrial Engineering Chemistry Research* **37** (6), 2131–2141.

VALINO, L. 1995 Multiscalar mapping closure for mixing in homogeneous turbulence. *Physics of Fluids* **7**, 144.

WANG, L. & FOX, R. O. 2003 Comparison of micromixing models for CFD simulation of nanoparticle formation by reactive precipitation. *Submitted to AIChE Journal.*

WEST, D. H., HEBERT, L. A. & PIVIDAL, K. A. 1999 Detection of quenching and instability in industrial chlorination reactors. In *Fall AIChE Annual Meeting*. Dallas.

XU, J. & POPE, S. B. 2000 Pdf calculations of turbulent nonpremixed flames with local extinction. *Combustion and Flame* **123**, 281–307.

A self-contained mapping closure approximation for scalar mixing

By Guo-Wei He † AND Zi-Fan Zhang ‡

1. Objective and motivation

Scalar turbulence exhibits interplays of coherent structures and random fluctuations over a broad range of spatial and temporal scales. This feature necessitates a probabilistic description of the scalar dynamics, which can be achieved comprehensively by using probability density functions (PDFs). Therefore, the challenge is to obtain the scalar PDFs (Lundgren 1967; Dopazo 1979). Generally, the evolution of a scalar is governed by three dynamical processes: advection, diffusion and reaction. In a PDF approach (Pope 1985), the advection and reaction can be treated exactly but the effect of molecular diffusion has to be modeled. It has been shown (Pope 1985) that the effect of molecular diffusion can be expressed as conditional dissipation rates or conditional diffusions. The currently used models for the conditional dissipation rates and conditional diffusions (Pope 1991) have resisted deduction from the fundamental equations and are unable to yield satisfactory results for the basic test cases of decaying scalars in isotropic turbulence, although they have achieved some success in a variety of individual cases. The recently developed mapping closure approach (Pope 1991; Chen, Chen & Kraichnan 1989; Kraichnan 1990; Klimenko & Pope 2003) provides a deductive method for conditional dissipation rates and conditional diffusions, and the models obtained can successfully describe the shape relaxation of the scalar PDF from an initial double delta distribution to a Gaussian one. However, the mapping closure approach is not able to provide the rate at which the scalar evolves. The evolution rate has to be modeled. Therefore, the mapping closure approach is not closed. In this Letter, we will address this problem.

The evolution rate of scalar is a key quantity in modeling turbulent mixing for both conserve and reactive scalars (Cha & Trouillet 2003). It specifies the characteristic time scale of scalar evolution. It has been shown that the decay rate of scalar depends on the relative length scale ratio of the initial scalar and velocity fields (Warhaft & Lumley 1978; Sreenivasan, Tavoularis, Henry & Corrsin 1980; Durbin 1982; Eswaran & Pope 1988; Mell, Kosály & Riley 1991), and recently, the asymptotic decay of scalar turbulence has been extensively studied (Eyink & Xin 2000; Chaves, Eyink, Frisch & Vergassola 2001; Chertkov & Lebedev 2003). Nearly all existing models for scalar mixing, ranging from the simple (conditional) moment approaches to the full PDF approaches, require information on the time scales. These models are mainly based on the assumption of a direct proportionality between the scalar time scales and the turbulence time scales (Fox 1995). Moreover, they exclude the effects of chemical reaction on the time scales of scalar evolution. The mapping closure approach of time-dependent reference fields (Girimaji 1992) can provide the time scale externally, which highlights an attack line to this problem.

† Permanent address: LNM, Institute of Mechanics, Chinese Academy of Sciences, Beijing, 100080, China; Email: hgw@lnm.imech.ac.cn
‡ LNM, Institute of Mechanics, Chinese Academy of Sciences.

We develop here a mapping closure approximation (MCA) approach for the time scale of scalar evolution. The MCA approach is based on multi-point joint PDFs. In the mapping closure approach (Pope 1991; Chen, Chen & Kraichnan 1989), an unknown random field is mapped from a known random Gaussian field so that the evolution of the unknown random field can be described by the mapping function. The mapping function is obtained from the transport equation for the unknown random field and the Gaussian closure. Since the mapping function is constructed at the level of one-point PDFs, it is not able to provide the information on two-point statistics, such as the time scales (He, Rubinstein & Wang 2002). In the MCA approach, the mapping functions are constructed at the levels of multi-point joint PDFs. The mapping function based on the two-point joint PDFs could provide the correct information on time scales.

2. Main results

We consider the simple case of a reactive scalar advected by a stochastic velocity field:

$$\frac{\partial \varphi}{\partial t} + \mathbf{u} \cdot \nabla \varphi = \Gamma \nabla^2 \varphi + Q(\varphi), \tag{2.1}$$

where the velocity field $\mathbf{u}$ obeys $\nabla \cdot \mathbf{u} = 0$ and is independent of the scalar field. Without the loss of generality, it may be prescribed as a known homogeneous and isotropic Gaussian field. Γ is a molecular diffusivity, $Q(\varphi)$ mimics a one-species chemical reaction.

In the MCA approach, the scalar field is mapped from a known random field by a mapping function

$$\varphi(\mathbf{x}, t) = X(\theta(\mathbf{x}, t), t). \tag{2.2}$$

Here, the known random field $\theta(\mathbf{x}, t)$ is taken as a Gaussian reference field. Its one-point and two-point joint PDFs are defined by

$$g_1(\eta) = \frac{1}{\sqrt{2\pi}} \exp\left[-\frac{\eta^2}{2}\right], \tag{2.3}$$

$$g_2(\eta_1, \eta_2, r, t) \equiv g(\eta_1, \eta_2, \rho(r, t)) = \frac{1}{2\pi\sqrt{1-\rho^2}} \exp\left[-\frac{\eta_1^2 + \eta_2^2 - 2\rho\eta_1\eta_2}{2(1-\rho^2)}\right], \tag{2.4}$$

where

$$\rho(r, t) = \frac{\langle \theta(\mathbf{x}, t)\theta(\mathbf{x}+\mathbf{r}, t\rangle}{\langle \theta^2(\mathbf{x}, t)\rangle}. \tag{2.5}$$

Here r is the magnitude of separation vector $\mathbf{r}$. The mapping function is required to represent the one-point and two-point joint PDFs of the scalar φ via the following equations

$$f_1(\psi, t) = g_1(\eta)\left[\frac{\partial X(\eta, t)}{\partial \eta}\right]^{-1}, \tag{2.6}$$

$$f_2(\psi_1, \psi_2, r, t) = g_2(\eta_1, \eta_2, r, t)\left[\frac{\partial X(\eta_1, t)}{\partial \eta_1}\frac{\partial X(\eta_2, t)}{\partial \eta_2}\right]^{-1}. \tag{2.7}$$

In the classic mapping closure approach (Pope 1991; Chen, Chen & Kraichnan 1989),

the mapping function X is only required to represent the one-point PDF of the scalar φ via equation (2.6). Differentiating equation (2.6) with respect to t yields

$$\frac{\partial f_1}{\partial t} + \frac{\partial}{\partial \psi}\left[f_1 \frac{\partial X}{\partial t}\right] = 0. \tag{2.8}$$

Meanwhile, the transport equation for the one-point PDF, $f_1(\psi, t)$, can be derived by the test function method (Gotoh & Kraichnan 1993; Kimura & Kraichnan 1993) as

$$\frac{\partial f_1}{\partial t} + \frac{\partial}{\partial \psi}\left[f_1 \left\langle \Gamma \nabla^2 \varphi + Q(\varphi) \mid \psi \right\rangle\right] = 0. \tag{2.9}$$

Thus, comparing the two equations (2.8) and (2.9) with the substitution of (2.2), we obtain the exact result

$$\frac{\partial X}{\partial t} = \Gamma \left\langle \nabla^2 \varphi \mid \varphi = X(\eta, t) \right\rangle + Q(\varphi). \tag{2.10}$$

The conditional moment in (2.10) can be evaluated from the mapping function (2.2) and the Gaussianity (2.3) and (2.4) of the reference field θ (Panchev 1971)

$$\Gamma \left\langle \nabla^2 \varphi \mid \varphi = X(\eta, t) \right\rangle = -C\rho''(0,t)\Gamma \left[\frac{\partial^2 X}{\partial \eta^2} - \eta \frac{\partial X}{\partial \eta}\right], \tag{2.11}$$

where the prime denotes the derivative with respect to separation r. As a result, the transport equation for the mapping function (2.2) becomes

$$\frac{\partial X}{\partial t} = -C\rho''(0,t)\Gamma \left[\frac{\partial^2 X}{\partial \eta^2} - \eta \frac{\partial X}{\partial \eta}\right] + Q(X). \tag{2.12}$$

It is easily shown from the Gaussianity (2.3) and (2.4) that $\langle (\nabla\theta)^2 \rangle = -C\rho''(0,t)$, where $C = 2$ for a two-dimensional physical space and $C = 3$ for a three-dimensional physical space. Equation (2.12) has been obtained in (Chen, Chen & Kraichnan 1989), where $-C\rho''(0,t)$ is represented by the variance $\langle (\nabla\theta)^2 \rangle$. However, the correlation $\rho(r,t)$ in equation (2.12) still remains to be unknown and has to be input externally. For example, it is set using the results from direct numerical simulation in (Chen, Chen & Kraichnan 1989). Therefore, equation (2.12) is unclosed.

The two-point correlation $\rho(r,t)$ cannot be obtained from the one-point PDF $g_1(\eta)$. Rather, it has to be calculated from the two-point joint PDF $g_2(\eta_1, \eta_2, r, t)$. Hence, we propose to invoke the two-point joint PDF (2.4), which is not used in the classic mapping closure approach. By differentiating (2.7) with respect to t, we obtain

$$\frac{\partial f_2}{\partial t} + \frac{\partial}{\partial \psi_1}\left[f_2 \frac{\partial X_1}{\partial t}\right] + \frac{\partial}{\partial \psi_2}\left[f_2 \frac{\partial X_2}{\partial t}\right] = \frac{f_2}{g_2}\frac{\partial g_2}{\partial t}. \tag{2.13}$$

The transport equation for the two-point joint PDF f_2 derived from the test function method (Gotoh & Kraichnan 1993; Kimura & Kraichnan 1993) has the form

$$\begin{aligned} &\frac{\partial f_2}{\partial t} + \nabla_{\mathbf{r}} \cdot [f_2 \langle (\mathbf{u}_2 - \mathbf{u}_1) \mid \psi_1, \psi_2 \rangle] = \\ &-\frac{\partial}{\partial \psi_1}[f_2 \langle \Gamma \nabla^2 \varphi_1 + Q(\varphi_1) | \psi_1, \psi_2 \rangle] - \frac{\partial}{\partial \psi_2}[f_2 \langle \Gamma \nabla^2 \varphi_2 + Q(\varphi_2) | \psi_1, \psi_2 \rangle]. \end{aligned} \tag{2.14}$$

Subtracting (2.13) from (2.14) leads to

$$\frac{f_2}{g_2}\frac{\partial g_2}{\partial t} + \nabla_{\mathbf{r}} \cdot [f_2 \langle (\mathbf{u}_2 - \mathbf{u}_1) \mid \psi_1, \psi_2 \rangle] = \frac{\partial}{\partial \psi_1}[f_2 H_1] + \frac{\partial}{\partial \psi_2}[f_2 H_2], \tag{2.15}$$

where

$$H_k = \Gamma \langle \nabla^2 \varphi_k \mid \psi_k \rangle - \Gamma \langle \nabla^2 \varphi_k \mid \psi_1, \psi_2 \rangle. \tag{2.16}$$

The first term in (2.16) is the conditional diffusion on a single given scalar and is calculated in equation (2.11). The second term is the conditional diffusion on two given scalars at two different locations and, again, can be evaluated using the mapping function (2.2) and the Gaussianity (2.3) and (2.4) of the reference field θ (Panchev 1971)

$$\begin{aligned}
&\langle \nabla^2 \varphi_k | \psi_1, \psi_2 \rangle = \frac{\partial^2 X_k}{\partial \eta_k^2} \left\langle (\nabla \theta_k)^2 \middle| \eta_1, \eta_2 \right\rangle + \frac{\partial X_k}{\partial \eta_k} \left\langle \nabla^2 \theta_k \middle| \eta_1, \eta_2 \right\rangle \\
&= \frac{\partial^2 X_k}{\partial \eta_k^2} \left\{ -C\rho''(0,t) + \frac{\rho'^2(r,t)}{(1-\rho^2(r,t))^2} + \left[(\eta_l - \rho(r,t)\eta_k)^2 - 1 + \rho^2(r,t) \right] \right\} + \\
&\frac{\partial X_k}{\partial \eta_k} \frac{1}{1-\rho^2(r,t)} \left[\left(\rho''(r,t) + \frac{\rho'(r,t)}{r} \right) (\eta_l - \rho(r,t)\eta_k) + C\rho''(0,t)(\eta_k - \rho(r,t)\eta_l) \right]
\end{aligned} \tag{2.17}$$

where $l = 1$ for $k = 2$ and $l = 2$ for $k = 1$. Multiplying (2.15) by ψ_1 and ψ_2 and then taking the mean with substitution of (2.2), (2.4), (2.7) and (2.17), we obtain the transport equation for $\rho(r,t)$ as follows

$$\begin{aligned}
&\frac{\partial \rho(r,t)}{\partial t} + \nabla_{\mathbf{r}} \cdot \langle (\mathbf{u}_1 - \mathbf{u}_2) X_1 X_2 \rangle \left\langle \frac{\partial X_1}{\partial \eta_1} \frac{\partial X_2}{\partial \eta_2} \right\rangle^{-1} = 2\Gamma \cdot \\
&\left[\rho''(r,t) + \frac{\rho'(r,t)}{r} - C\rho(r,t)\rho''(0,t) + \rho'^2(r,t) \left\langle \frac{\partial^2 X_1}{\partial \eta_1^2} \frac{\partial^2 X_2}{\partial \eta_2^2} \right\rangle \left\langle \frac{\partial X_1}{\partial \eta_1} \frac{\partial X_2}{\partial \eta_2} \right\rangle^{-1} \right]
\end{aligned} \tag{2.18}$$

Equations (2.12) and (2.18) form a closed system for the mapping function, where equation (2.12) describes the evolution of the shape of the mapping function and (2.18) specifies the rate at which the mapping function evolves. In equation (2.18), the second term on the left-hand side corresponds to advection, the first three terms on the right-hand side correspond to diffusion and the last term on the right-hand side corresponds to the effect of nonlinear mapping. The last term vanishes if the mapping function is linear. We note that $\rho(r,t)$ is the correlation function of the reference field and is dependent on the mapping function.

The realizability condition of equation (2.18) is $|\rho(r,t)| \leq 1$. For the pure diffusion processes with the initial Gaussian distributions of positive correlations, the diffusion term $\rho''(r,t) + \rho'(r,t)/r$ and the damping term $-C\rho''(0,t)\rho(r,t)$ decrease the amplitudes of the correlation $\rho(r,t)$, so that the solution of equation (2.18) is realizable.

The mapping equation (2.12) is closed using the two-point joint PDF constraint (2.7), from which the correlation equation (2.18) is derived. Another possibility for the closure is to use the constraint of the joint PDF for the scalar and its derivative (Chen, Chen & Kraichnan 1989), which leads to an unclosed equation for $\rho(0,t)$ and its spatial derivatives. It points to another direction to go beyond the one-point mapping (2.2) for different purpose.

The performance of the MCA models (2.12) and (2.18) are evaluated against direct nu-

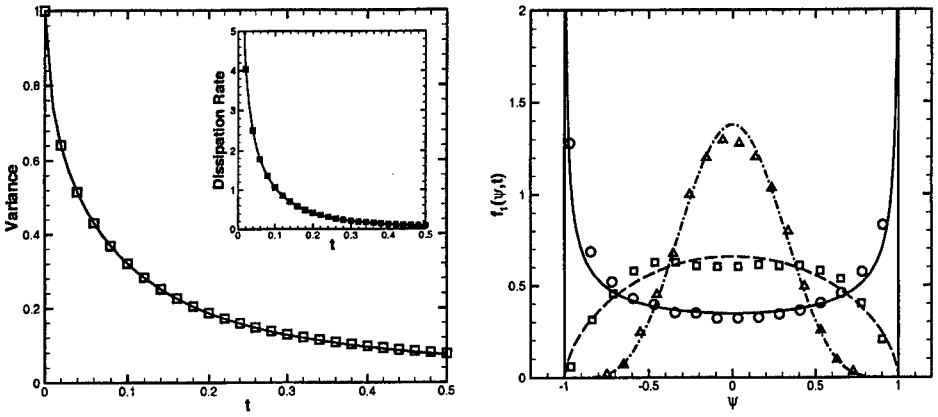


FIGURE 1. Pure diffusion for the conserved scalar with a double-delta initial field. The left: variance and dissipation vs time. Solid lines for MCA and squares for DNS; The right: probability density function. Solid, dashed and dash-dotted lines for MCA at time 0.05, 0.15 and 0.5, and circles, squares and deltas for DNS at the same time, respectively.

merical simulation. The scalar equation (2.1) and the MCA modeled system of equations (2.12) and (2.18) are numerically solved in a cyclic square of side 2π, using second-order Adams-Bashforth scheme in time and fourth-order central finite-difference scheme in space. In all the cases, the non-dimensional molecular diffusivity $\Gamma = 0.01$. Boundary conditions are periodic in space, except that the ones in the direction of the reference field are obtained by extrapolation. The initial fields for (2.1) are double-delta distributions or isotropic Gaussian distributions with their energy spectra $E_\varphi(k) \propto k^{-17/3}$. Thus, the initial mapping for (2.12) and the initial correlation for (2.18) can be calculated from their definitions.

The velocity field is a given homogeneous isotropic Gaussian process with spectrum of the form $E(k) \propto k^{-5/3}$. We will here present the results for the rapidly changed velocity. That is, the velocity fields are set to change at each time step (Kimura & Kraichnan 1993). In order to isolate the effects of the MCA models on diffusivity and reaction, the advection term in equation (2.18) are calculated directly from the DNS without invoking any models. The analytical treatment on this term can be found in (Kimura & Kraichnan 1993).

Figure 1 compares the evolutions of the variance $\langle \varphi^2(\mathbf{x}, t) \rangle$ and the PDF $f_1(\psi, t)$ obtained by DNS of equation (2.1) with an integration of the MCA models (2.12) and (2.18) for the case of pure diffusion: $\mathbf{u} = 0$ and $Q = 0$. The initial condition is set as a double delta distribution. The results illustrate that the MCA models represent the relaxation of the double delta PDF to the Gaussian PDF not only in its shape but also at the correct rate of evolutions.

In Fig. 2, the same plots are made for the diffusion-reaction equation: $\mathbf{u} = 0$ and $Q(\varphi) = -20\varphi|\varphi|$, with the initial Gaussian distribution. The MCA models are also in agreement with the DNS results. It shows that the MCA models can represent the effects of both diffusion and reactions.

Further comparisons are made in Fig. 3 for the advection-diffusion equation with the same initial condition as used in Fig. 2, where the Péclet number is about 101. Evidently the MCA models are in good agreement with the decay rate of the scalar.

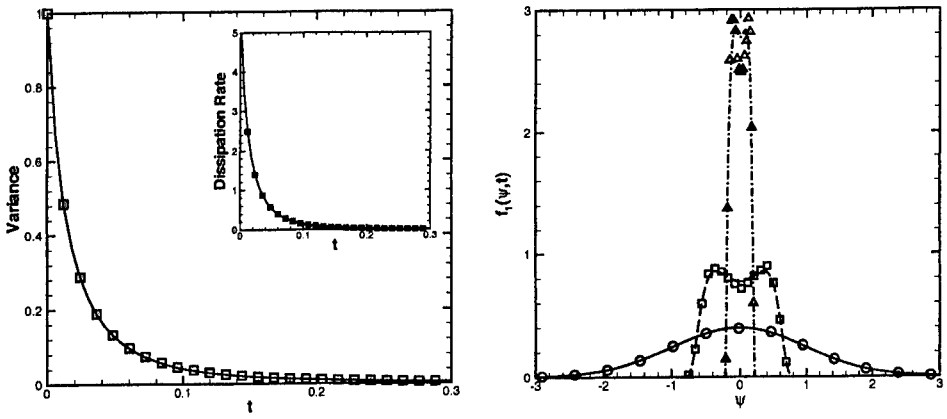


FIGURE 2. Reaction-diffusion for the initial Gaussian scalar. The left: variance and dissipation vs time. Solid lines for MCA and squares for DNS; The right: probability density function. Solid, dashed and dash-dotted lines for MCA at time 0.0, 0.05 and 0.2, and circles, squares and deltas for DNS at the same time, respectively.

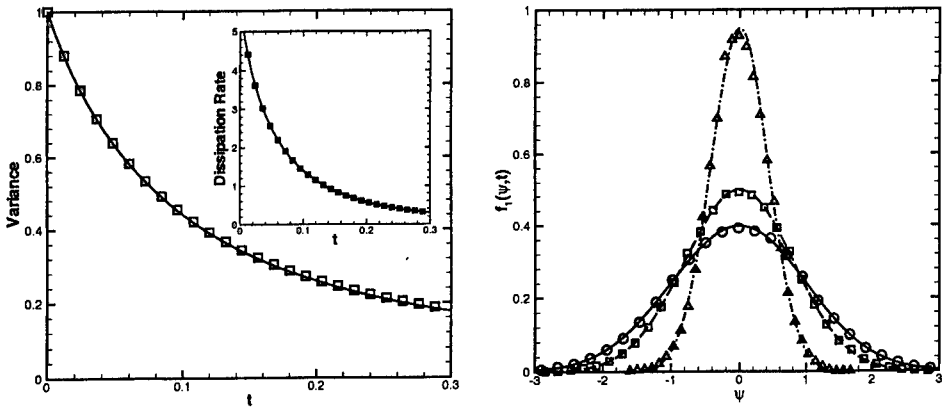


FIGURE 3. Advection-diffusion for the initial Gaussian scalar. The left: variance and dissipation vs time. Solid lines for MCA and squares for DNS; The right: probability density function. Solid, dashed and dash-dotted lines for MCA at time 0.0, 0.05 and 0.3, and circles, squares and deltas for DNS at the same time, respectively.

In this Letter, the two-point joint PDF is represented by a known two-point joint Gaussian PDF and a mapping function. The correlation of the joint Gaussian PDF and the mapping function evolve under their dynamics. Therefore, the representation of the two-point joint PDF evolves with the dynamics of equation (2.1) via the correlation and mapping function. If it happens that $\rho(r,t) = 0$, equation (2.7) is simplified to $f_2(\psi_1, \psi_2, t) = f_1(\psi_1, t) f_1(\psi_2, t)$. This is the stochastic ansatz in the BBGKY hierarchy in statistical mechanics (Balescu 1975), where the correlations are specified a priori and then fixed. The MCA approach does not invoke this kind of a priori assumption. Moreover, a general N-point ($N > 2$) joint PDF can also be obtained using the known two-point joint Gaussian PDF and the mapping function (2.2), since it can be similarly represented

by the mapping function (2.2) and the N-point joint Gaussian PDF. The latter is fully determined by its two-point joint PDF. In this sense, the MCA approach is self-contained.

3. Conclusion and future work

A self-contained MCA approach is developed for modeling scalar mixing in a stochastic velocity field. It differs from the classic mapping closure approach in that the MCA approach makes use of two-point PDFs to represent the time-evolving correlations of the reference fields and thus the scalar fields. Unlike usual treatments in the BBGKY hierarchy (Balescu 1975), where the representations are specified a priori, the representations in the MCA approach are allowed to evolve in coordinate with the dynamics of scalar mixing. The results obtained using the new approach are in good agreement with the DNS results for the three cases of pure diffusion, diffusion-reaction and advection-diffusion. The approach is under further development for more complex situations including multi-scalar mixing and inhomogeneous scalar fields, using time-evolving Gaussian or non-Gaussian reference fields.

G.-W. He thanks R. H. Kraichnan for thoughtful comments and stimulating discussions on the manuscript, G. Kosály for the discussions on time scales, M. Wang for his help on the manuscript preparation, Y. L. Bai, P. Durbin, R. Rubinstein, M. F. Xia and J. B. Zhang for helpful discussions. This work was supported by the Special Funds for Major Basic Research Project G. 2000077305, P. R. China.

REFERENCES

BALESCU, R. 1975 *Equilibrium and Nonequilibrium Statistical Mechanics* John Wiley & Sons Inc, New York.

CHA, C. M. & TROUILLET, P. 2003 A model for the mixing time scale of a turbulent reacting scalar *Phys. Fluids* **15**, 1375–1380.

CHAVES, M., EYINK, G. L., FRISCH, U. & VERGASSOLA, M. 2001 Universal decay of scalar turbulence *Phys. Rev. Lett.* **86**, 2305-2308.

CHEN, H., CHEN, S. & KRAICHNAN, R. H. 1989 Probability distribution of a stochastically advected scalar field. Phys. Rev. Letter **63**, 2657– 2660.

CHERTKOV, M. & LEBEDEV, V. 2003 Decay of scalar turbulence revisited *Phys. Rev. Lett.* **90**, 034501-1–4.

DOPAZO, C. 1979 Relaxation of initial probability density functions in the turbulent convection of scalar fields. *Phys. Fluids* **22**, 20–30.

DURBIN, P. A. 1982 Analysis of the decay of temperature fluctuations in isotropic turbulence *Phys. Fluids* **25**, 1328–1332.

ESWARAN, V. & POPE, S. B. 1988 Direct numerical simulations of the turbulent mixing of a passive scalar *Phys. Fluids* **31**, 506–520.

EYINK, G. L. & XIN, J. 2000 Self-similar decay in the Kraichnan model of a passive scalar *J. Stat. Phys.* **100**, 679–741.

FOX, R. O. 1995 The spectral relaxation of the scalar dissipation rate in homogeneous turbulence *Phys. Fluids* **7**, 1082–1094.

GIRIMAJI, S. S. 1992 A mapping closure for turbulent scalar mixing using a time-evolving reference field *Phys. Fluids A* **4**, 2875–2886.

GOTOH, T. & KRAICHNAN, R. H. 1993 Statistics of decaying Burgers turbulence *Phys. Fluids A* **5**, 445–457.

HE, G.-W., RUBINSTEIN, R. & WANG L. P. 2002 Effects of subgrid-scale modeling on time correlations in large eddy simulation *Phys. Fluids* **14**, 2186–2193.

KIMURA, Y. & KRAICHNAN, R. H. 1993 Statistics of an advected passive scalar *Phys. Fluids A* **5**, 2264–2277.

KLIMENKO, A. Y. & POPE, S. B. 2003 The modeling of turbulent reactive flows based on multiple mapping conditioning *Phys. Fluids* **15** 1907–1925.

KRAICHNAN, R. H. 1990 Models of intermittency in hydrodynamic turbulence. *Phys. Rev. Letter* **65** 575–578.

LUNDGREN, T. S. 1967 Distribution functions in the statistical theory of turbulence. *Phys. Fluids* **10**, 969–975.

MELL, W. E., KOSÁLY, G. & RILEY, J. J. 1991 The length-scale dependence of scalar mixing *Phys. Fluids A* **3**, 2474–2476.

PANCHEV, S. 1971 *Random Functions and Turbulence* Pergamon Press, Oxford.

POPE, S. B. 1985 Pdf methods for turbulent reactive flows. *Prog. Energy Combust. Sci.* **11**, 119–192.

POPE, S. B. 1991 Mapping closures for turbulent mixing and reaction. *Theoret. Comput. Fluid Dynamics* **2**, 255–270.

SREENIVASAN, K. R., TAVOULARIS, S., HENRY, R. & CORRSIN, S. 1980 Temperature fluctuations and scales in grid-generated turbulence *J. Fluid Mech.* **100**, 597–621.

WARHAFT, Z. & LUMLEY, J. L. 1978 An experimental study of the decay of temperature fluctuations in grid-generated turbulence *J. Fluid Mech.* **88**, 659–684.

Stochastic mixing model with power law decay of variance

By S. Fedotov, M. Ihme and H. Pitsch

1. Motivation and objectives

The mixing of a conserved scalar $c = c(t, \boldsymbol{x})$, advected by a turbulent flow, remains a problem of both fundamental and practical interest. One of the basic characteristics of the mixing process is the rate at which the scalar variance $\sigma_c^2(t) = \langle (c-\mu)^2 \rangle$ decays with time. Here μ is the mean value, and the angular brackets $\langle \cdot \rangle$ denote an averaging procedure. One of the simplest and widely used mixing models is the interaction by exchange with the mean (IEM) (Villermaux & Devillon 1972) or linear mean square estimate model (LMSE) (Dopazo & O'Brien 1974, Sabel'nikov & Gorokhovski 2001). In this model, the scalar relaxes toward its mean μ according to the equation

$$\frac{\mathrm{d}c}{\mathrm{d}t} = -\frac{1}{\tau}(c-\mu)\,. \tag{1.1}$$

In the coalescence-dispersion model (CD) (Curl 1963), mixing of two particle volumes is described by (1) a coalescence and (2) dispersion process during one time step Δt. After that time, both particles have the same scalar value, which is equal to the mean of the two values before the mixing. The pdf relaxes to a bell-shaped distribution but deviates from the Gaussian shape primarily in the tails of the distribution (Peters 2000). Both models introduce a time scale τ which is commonly approximated by a turbulent time scale. Other mixing models are based on mapping closure, Fokker-Planck model, euclidean minimum spanning trees (EMST), or Langevin model. Reviews of these can be found in Peters (2000) and Pope (2000).

There are two different laws governing the decay rate of a passive scalar:

(*i*) the exponential law

$$\sigma_c^2(t) \propto \exp\{-t/\tau\} \tag{1.2}$$

with the characteristic time τ and

(*ii*) the power law

$$\sigma_c^2(t) \propto t^{-\alpha} \tag{1.3}$$

without any characteristic time scale (Lesieur 1997).

Most theoretical models introduce a characteristic time scale and assume implicitly or explicitly the exponential decay rate (1.2) which is only appropriate for stationary turbulence.

The main purpose of this paper is to study the mixing process following the power law (1.3) that is typical for decaying turbulence. Experimental results show that the decay of the variance strongly depends on the initial ratio of the velocity and scalar length-scales and that there is no universal decay exponent (Durbin 1982).

It is well known that the decay exponent α depends on the low wavenumber part of the scalar and velocity spectrum, $E_c(k,t)$ and $E(k,t)$ (Lesieur 1997). One can expand both spectra into a Taylor series: $E_c(k,t) = 2\pi k^2(C_0 + C_2 k^2 + \mathcal{O}(k^4))$ and $E(k,t) =$

$2\pi k^2(B_0 + B_2k^2 + \mathcal{O}(k^4))$ (Chasnov 1994). For high Reynolds and Peclet numbers, the scalar variance can be considered as a function of C_0, B_0 and t alone and dimensional arguments lead to

$$\sigma_c^2(t) \propto C_0 B_0^{-3/5} t^{-6/5} \tag{1.4}$$

with $\alpha = 1.2$. For C_0, B_0 equal to zero, the scaling argument results in different approximate decay laws with α equals to $6/7, 10/7$ or 2 (Lesieur 1997).

Here we present a simple stochastic mixing model based on the law of large numbers (LLN) (Feller 1966). The reason why the LLN is involved in our formulation of the mixing problem is that the random conserved scalar $c = c(t, \boldsymbol{x}(t))$ appears to behave as a sample mean. It converges to the mean value μ, while the variance $\sigma_c^2(t)$ decays approximately as t^{-1}. Since the variance of the scalar decays faster than a sample mean (typically α is greater than unity), we will introduce some non-linear modifications into the corresponding pdf-equation (see Eq. (2.28) below). The main idea is to develop a robust model which is independent from restrictive assumptions about the shape of the pdf. Here we exploit the similarity of the behavior of a scalar c to that of the sample mean

$$c_n = \frac{1}{n} \sum_{k=1}^{n} \zeta_k, \tag{1.5}$$

where $\zeta_1, \ldots, \zeta_n$ is a sequence of mutually independent random variables, each having a mean μ and standard deviation σ_ξ^2. The LLN tells us that the random sum c_n tends to the mean value μ with probability one, while the variance $\sigma_{c_n}^2 = \langle (c_n - \mu)^2 \rangle$ decays as σ_ξ^2/n. Then, any arbitrary initial pdf $p(n_0, c)$ tends to a δ-distribution $\delta(c-\mu)$ as $n \to \infty$. In the present paper the discrete increment n can be understood as the time variable t.

The main result of this paper is the derivation of the time-discrete non-linear integral equation for the pdf of c

$$p(t+1,c) = \int_0^1 \int_{-1}^{\frac{1+t}{\lambda}-1} \frac{t+1}{1+t-\lambda(1+\varepsilon)} p\left(t, \frac{(t+1)(c-\mu) - \lambda(1+\varepsilon)(\widetilde{\eta}-\mu)}{1+t-\lambda(1+\varepsilon)}\right) \times \tag{1.6}$$

$$p(t,\widetilde{\eta})\psi(t,\varepsilon)\, \mathrm{d}\varepsilon\, \mathrm{d}\widetilde{\eta}\,,$$

for $t = 1, 2, 3, \ldots$. Here $\psi(t, \varepsilon)$ is the pdf for the exchange rate and λ is the mixing intensity (see below). The main property of this equation is that it describes the relaxation from an arbitrary initial distribution to a δ-function

$$p(t, c) \to \delta(c - \mu) \qquad \text{as} \qquad t \to \infty \tag{1.7}$$

and the decay of the variance, $\sigma_c^2(t) = \langle (c(t) - \mu)^2 \rangle$, is of the form $t^{-\alpha}$. The case $\alpha = 1$ corresponds to the law of large numbers.

The remainder of this paper is organized as follows. In Section 2 we derive the integral equation from a stochastic difference equation describing the evolution of the pdf of a passive scalar in time. The stochastic difference equation introduces an exchange rate γ_n which we model in a first step as a deterministic function. In a second step, we generalize γ_n as a stochastic variable taking fluctuations in the inhomogeneous environment into account. In Section 3 we solve the non-linear integral equation numerically and analyze the influence of the different parameters on the decay rate. The paper finishes with a conclusion.

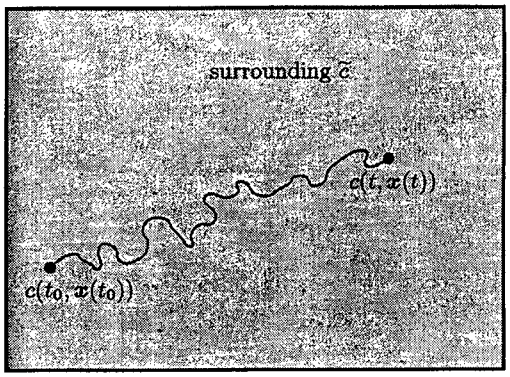


FIGURE 1. Mixing problem along Lagrangian path way.

2. Mixing model

2.1. *Problem statement*

The evolution of a passive scalar $c = c(t, \boldsymbol{x})$ is governed by the stochastic PDE

$$\frac{\partial c}{\partial t} + \boldsymbol{v}(t, \boldsymbol{x})\nabla c = D\nabla^2 c, \tag{2.1}$$

where $\boldsymbol{v}(t, \boldsymbol{x})$ is the random velocity field and D is the molecular (or thermal) diffusivity. The classical problem is to derive a closed equation for the Euler one-point probability density function (pdf) $p = p(c; t, \boldsymbol{x}) = \langle \delta(c - c(t, \boldsymbol{x})) \rangle$. A detailed discussion of this, still unsolved, problem can be found in Pope (2000). In the present paper we consider the mixing problem in the Lagrangian framework by introducing a passive scalar $c(t) = c(t, \boldsymbol{x}(t))$ of a particle volume moving with the velocity $\boldsymbol{v}(t, \boldsymbol{x}(t))$ (see Fig. 1).

2.2. *Stochastic difference equation*

The equation for the scalar $c(t) = c(t, \boldsymbol{x}(t))$ of the particle volume moving with the random velocity $\boldsymbol{v}(t, \boldsymbol{x}(t))$ can be approximated by the stochastic equation

$$\frac{\mathrm{d}c}{\mathrm{d}t} = -\gamma(t)(c - \widetilde{c}(t)) \,, \tag{2.2}$$

where the exchange rate $\gamma(t)$ and the ambient concentration $\widetilde{c}(t)$ are random processes. For the constant values of γ and $\widetilde{c}$, we obtain the IEM model (1.1) with the exponential decay:

$$\frac{c(t) - \widetilde{c}}{c(0) - \widetilde{c}} = \exp\{-\gamma t\} \,. \tag{2.3}$$

The key feature of the present model is that $\widetilde{c}(t)$ is a random process and functional of $c(t)$ itself. The crucial assumption that relates Eq. (2.2) to the law of large numbers is that the mean value $\langle \gamma(t) \rangle$ behaves as t^{-1} for large t. One can show that for a Gaussian scalar field $c = c(t, \boldsymbol{x})$, the mean value $\langle \gamma(t) \rangle$ is proportional to the ratio χ/σ_c^2, where χ is the mean scalar dissipation rate, $\chi = 2D\langle(\nabla c)^2\rangle$ (Pope 2000). It follows from

$$\frac{\mathrm{d}\sigma_c^2}{\mathrm{d}t} = -\chi \,, \tag{2.4}$$

that if $\sigma_c^2(t) \propto t^{-\alpha}$ then χ decays as $t^{-(1+\alpha)}$, and therefore $\langle\gamma(t)\rangle \propto t^{-1}$. The appearance of the power law decay can be understood if we assume that $\gamma = \lambda(t_0+t)^{-1}$

$$\frac{\mathrm{d}c}{\mathrm{d}t} = -\frac{\lambda}{t_0+t}(c-\widetilde{c})\,. \tag{2.5}$$

The solution to this simplified equation is

$$\frac{c(t)-\widetilde{c}}{c(0)-\widetilde{c}} = \left(\frac{t_0}{t_0+t}\right)^{\lambda}\,. \tag{2.6}$$

Since our aim here is to relate the mixing problem to the law of large numbers, it is more convenient to rewrite Eq. (2.2) as a stochastic difference equation

$$c_{n+1}-c_n = -\gamma_n(c_n-\widetilde{c}_{n+1})\,, \qquad 0\le c_n\le 1\,, \qquad \text{for } n=1,2,3,\ldots \tag{2.7}$$

where γ_n and $\widetilde{c}_n$ are assumed to be sequences of mutually independent random variables with the densities

$$\omega(n,\gamma) = \frac{\mathrm{d}}{\mathrm{d}\gamma}P\{\gamma_n<\gamma\}\,, \qquad \phi(n,\widetilde{c}) = \frac{\mathrm{d}}{\mathrm{d}\widetilde{c}}P\{\widetilde{c}_n<\widetilde{c}\} \tag{2.8}$$

and the first moments

$$\langle\gamma_n\rangle = \int_0^1 \gamma\omega(n,\gamma)\mathrm{d}\gamma = \frac{\lambda}{1+n}, \qquad \langle\widetilde{c}_n\rangle = \int_0^1 \widetilde{c}\,\phi(n,\widetilde{c})\mathrm{d}\widetilde{c} = \mu\,. \tag{2.9}$$

Here the mean exchange parameter $\langle\gamma_n\rangle$ has been chosen in such a way that it is equal to $\lambda/2$ at time $n=1$. The parameter λ can be regarded as a measure of the mixing intensity. Since $0\le c_n\le 1$, γ_n obeys the inequality $0\le\gamma_n\le 1$. By introducing the deviations from the mean μ for the concentration of the particle and its surrounding, respectively,

$$u_n = c_n-\mu\,, \tag{2.10}$$

$$\xi_n = \widetilde{c}_n-\mu \tag{2.11}$$

we can rewrite Eq. (2.7) as

$$u_{n+1} = u_n-\gamma_n(u_n-\xi_{n+1})\,, \qquad -\mu\le u_n\le 1-\mu\,, \qquad n=1,2,3,\ldots\,, \tag{2.12}$$

where ξ_n is a sequence of zero mean, independent random variables with the density $\phi(n,\xi)$ and $-\mu\le\xi\le 1-\mu$.

2.3. *Law of large numbers and forward Kolmogorov equation*

To illustrate the connection between the mixing problem and the law of large numbers, consider the case when the sequence ξ_n is stationary, that is $\varphi(\xi)$ is independent of n, and the exchange parameter γ_n is a deterministic sequence of the form

$$\gamma_n = \frac{1}{1+n} \tag{2.13}$$

with $\lambda=1$. If we assume $u_1=\xi_1$, it follows from Eq. (2.12) that $u_2=(\xi_1+\xi_2)/2, u_3=(\xi_1+\xi_2+\xi_3)/3$ and so on. Therefore, the solution of the equation (2.12) can be written as a sample mean

$$u_n = \frac{1}{n}\sum_{k=1}^{n}\xi_k \tag{2.14}$$

which tends to the mean μ as $n \to \infty$ while the variance $\langle u_n^2 \rangle \propto n^{-1}$.

The advantage of having an equation (2.12) is that we can easily derive an equation for the probability density function

$$p(n,u) = \frac{\mathrm{d}}{\mathrm{d}u} P\{u_n < u\}\,, \qquad n = 1,2,3,\ldots\,. \tag{2.15}$$

It follows from Eqs. (2.12) and (2.13) that u_n is a discrete Markov processes and the pdf for this process satisfies the forward Kolmogorov equation (Feller 1966)

$$p(n+1,u) = \frac{n+1}{n} \int_{-\mu}^{1-\mu} p\left(n, \frac{(n+1)u-\xi}{n}\right) \varphi(\xi)\mathrm{d}\xi\,, \qquad n = 1,2,3,\ldots\,. \tag{2.16}$$

Here we used the inverse equation

$$u_n = n^{-1}\left[(1+n)u_{n+1} - \xi_{n+1}\right]. \tag{2.17}$$

The main properties of the solution of the Kolmogorov equation (2.16) with the arbitrary initial condition $p(1,u)$ are

$$p(n,u) \to \delta(u) \qquad \text{as} \qquad n \to \infty \tag{2.18}$$

and

$$\int_{-\mu}^{1-\mu} u^2 p(n,u)\mathrm{d}u \to n^{-1} \qquad \text{as} \qquad n \to \infty\,. \tag{2.19}$$

The asymptotic behavior of $p(n,u)$ for large n is quite universal. It can be written as

$$p(n,u) \propto \sqrt{n}\exp\{-nS(u)\} \qquad \text{for} \qquad n \gg 1\,, \tag{2.20}$$

where the function $S(u)$ depends on the particular choice of the density $\varphi(\xi)$ for the random sequence ξ_k. One can show that $S(u)$ obeys the equation (Knessl *et al.* 1985)

$$u\frac{\mathrm{d}S}{\mathrm{d}u} - S = \ln M\left(\frac{\mathrm{d}S}{\mathrm{d}u}\right)\,, \qquad M(x) = \int_{-\mu}^{1-\mu} \exp\{x\,\xi\}\,\varphi(\xi)\mathrm{d}\xi\,. \tag{2.21}$$

2.4. *General case: random exchange rate and non-linear equation for the pdf*

To account for the entire spectrum of time scales we now assume that the exchange parameter γ_n is a stochastic variable. It is convenient to write

$$\gamma_n = \frac{\lambda}{1+n}(1+\varepsilon_n)\,, \tag{2.22}$$

where ε_n is the sequence of zero mean, independent random variables. Since $0 \le \gamma_n \le 1$, it follows from Eq. (2.22) that

$$-1 \le \varepsilon_n \le \frac{1+n}{\lambda} - 1\,. \tag{2.23}$$

The decay of the variance of the exchange rate, $\sigma_\gamma^2(n)$, can be determined as

$$\sigma_\gamma^2(n) = \langle(\gamma_n - \langle\gamma_n\rangle)^2\rangle = \frac{\lambda^2\langle\varepsilon_n^2\rangle}{(1+n)^2}\,. \tag{2.24}$$

When both ε_n and ξ_n are random variables, we have to specify the joint probability density for ε and ξ. If we denote it by $\Psi(n,\varepsilon,\xi)$, then the forward Kolmogorov equation for $p(n,u)$ takes the form

$$p(n+1,u)=\int_{-\mu}^{1-\mu}\int_{-1}^{\frac{1+n}{\lambda}-1}\frac{n+1}{1+n-\lambda(1+\varepsilon)}p\left(n,\frac{(n+1)u-\lambda(1+\varepsilon)\xi}{1+n-\lambda(1+\varepsilon)}\right)\Psi(n,\varepsilon,\xi)\mathrm{d}\varepsilon\mathrm{d}\xi\,, \tag{2.25}$$

This equation follows from the stochastic difference equation for the Markov jump process

$$u_{n+1}=u_n-\frac{\lambda}{1+n}(1+\varepsilon_n)(u_n-\xi_{n+1})\qquad\text{for}\qquad -\mu\le u_n\le 1-\mu \tag{2.26}$$

and its inverse function

$$u_n=\frac{(n+1)u_{n+1}-\lambda(1+\varepsilon)\xi_{n+1}}{1+n-\lambda(1+\varepsilon)}. \tag{2.27}$$

Since γ_n is determined by the random scalar dissipation rate, it is natural to assume that γ_n and ξ_n are independent. Moreover, the density for ξ_n must be related to $p(n,u)$. The simplest choice would be to assume $p(n,\xi)$ which gives $\Psi(n,\varepsilon,\xi)=p(n,\xi)\psi(n,\varepsilon)$ and the generalized non-linear integral equation for $p(n,u)$ can be written as

$$p(n+1,u)=\int_{-\mu}^{1-\mu}\int_{-1}^{\frac{1+n}{\lambda}-1}\frac{n+1}{1+n-\lambda(1+\varepsilon)}p\left(n,\frac{(n+1)u-\lambda(1+\varepsilon)\xi}{1+n-\lambda(1+\varepsilon)}\right)p(n,\xi)\psi(n,\varepsilon)\mathrm{d}\varepsilon\mathrm{d}\xi \tag{2.28}$$

for $n=1,2,3,\ldots$. It follows from Eq. (2.24) that the variance of the exchange rate $\sigma_\gamma^2(n)$ decays as n^{-2}. In the subsequent sections we assume for simplicity that the variance $\sigma_\varepsilon^2=\langle\varepsilon_n^2\rangle$ is constant.

We expect that the variance of a passive scalar $\sigma_c^2(n)=\langle(c_n-\mu)^2\rangle=\langle u_n^2\rangle$ behaves as $n^{-\alpha}$ for large n. Taking the analytical solution of the simplified model (2.5) into account, we anticipate a strong dependence of α on the mixing intensity λ.

3. Results

The integral equation (2.28) describes the relaxation of an arbitrary initial density distribution of a conserved scalar c to a δ-distribution for large n. Because of the non-linearity in c and $\widetilde{c}$, the equation needs to be solved numerically for non-trivial initial conditions.

The trivial case $\lambda=0$ describes the motion of an inert particle (*e.g.* dye) in its surround and Eq. (2.12) has the simple solution $u_n=u_1$ for all n. However, if λ is close to its upper limit, the Lagrangian particle volume experiences strong interactions with its surrounding and intuitively, it can be expected that the mixing intensity λ has a distinct influence on the decay of σ_u^2 (see solution (2.6) to simplified equation).

The stochastic variable ε influences the exchange rate γ_n and the effect of its distribution on the decay exponent α is desirable to understand. Formally, we can express α as a non-explicit available function of the form $\alpha=\alpha(\lambda,\psi(n,\varepsilon))$ where $\lambda=\lambda(\ell_u/\ell_c,\mathrm{Pe}\text{ or }\mathrm{Re})$. In the subsequent sections the behavior of Eq. (2.28) for different parameters and initial conditions is analyzed.

3.1. *Numerical issues*

In order to advance the density $p(n+1,u)$ in time, Eq. (2.28) must be integrated over the ξ- and ε-space which results in the overall-complexity $\mathcal{O}(N_u \times N_\xi \times N_\varepsilon)$ for each time step. Here, N_ζ denotes the number of grid points in the ζ-direction. This makes the computation rather time-consuming. However, a computer code can be easily parallelized along the u-coordinate.

The initial density of u relaxes to a δ-distribution with steep gradients around $u = 0$. An adaptive grid using the equidistribution principle is employed in u- and ξ-space in order to resolve the shape of the pdf properly. In the equidistribution principle (Liseikin 1999), an initially given number of grid points is distributed in such a way that the condition $\int_{u_i}^{u_{i+1}} w(u)\mathrm{d}u = (N_u - 1)^{-1} \int_{-\mu}^{1-\mu} w(u)\mathrm{d}u$ is satisfied. The weight function $w(u)$ is a positive function measuring the variation of the solution.

3.2. *Parameters and initial conditions*

From experiments and DNS studies it is shown that the density distribution of a passive scalar can be reasonably approximated by a β-distribution. The β-distribution has non-zero probability in the interval $[u_{\min}, u_{\max}]$ and has the form

$$\beta(u; \langle u\rangle, \sigma_u^2) = \frac{\Gamma(a+b)}{\Gamma(a)\Gamma(b)} (u_{\max} - u_{\min})^{1-a-b} (u - u_{\min})^{a-1} (u_{\max} - u)^{b-1} \,. \tag{3.1}$$

It is fully described by two parameters, which are functions of $\langle u\rangle$ and σ_u^2

$$a = \frac{\langle u\rangle - u_{\min}}{u_{\max} - u_{\min}} \left[\frac{(\langle u\rangle - u_{\min})(u_{\max} - \langle u\rangle)}{\sigma_u^2} - 1 \right] , \tag{3.2}$$

$$b = \frac{u_{\max} - \langle u\rangle}{u_{\max} - u_{\min}} \left[\frac{(\langle u\rangle - u_{\min})(u_{\max} - \langle u\rangle)}{\sigma_u^2} - 1 \right] . \tag{3.3}$$

The β-distribution adopts a wide range of shapes: for the maximum variance $\sigma_u^2 = \mu(1-\mu)$ and zero mean a double δ-distribution at $u_{\min}$ and $u_{\max}$ is approached and for small σ_u^2 a Gaussian distribution around $\langle u\rangle$ is obtained. Throughout the following simulations, this distribution is used as initial condition for $p(1,u)$.

In order to solve Eq. (2.28) we have to provide an appropriate density distribution for the random fluctuation ε. The time-dependent distribution of ε is certainly problem-dependent and unknown in the present consideration. Therefore we assume for simplicity that ε has a statistically stationary distribution. A reasonable choice would be to assume that ε is distributed following Eq. (3.1). A particular case is obtained if $\psi(\varepsilon)$ has a δ-distribution. For the following test cases we use both distributions as prescribed probabilities. The constant parameters for all simulations of Eq. (2.28) are summarized in Table 1.

3.3. *Influence of initial distribution in $p(1,u)$*

In the first numerical experiment the dependence of the decay exponent α on the initial conditions in u and ε is investigated. Therefore, prescribed distributions with different initial variance for $\sigma_u^2(1)$ and σ_ε^2 are used (see Table 2 and Fig. 2). For this simulation λ is chosen to be unity and ε is in the range $-1 \le \varepsilon \le (1+n)/\lambda - 1$. The maximum possible value for ε is then found for $n = 1$.

The decay rate of σ_u^2 and the decay exponent α are evaluated and plotted in Fig. 3. In the left column, the four different combinations with initial variance $\sigma_u^2(1) = 0.20$ are plotted, the middle column shows the decay rate for the cases with $\sigma_u^2(1) = 0.15$. In the

Parameter	Description	Value
$nEnd$	number of time steps	100,000
μ	mean value	0.5
N_u	dimension of u	101
N_ξ	dimension of ξ	101
N_ε	dimension of ε	101

TABLE 1. Fixed parameters used for the numerical simulation.

Run	$p(1,u)$	$\psi(1,\varepsilon)=\psi(\varepsilon)$
BB1	$\beta(0.20)$	$\beta(0.500)$
BB2	$\beta(0.20)$	$\beta(0.250)$
BB3	$\beta(0.20)$	$\beta(0.125)$
BB4	$\beta(0.15)$	$\beta(0.500)$
BB5	$\beta(0.15)$	$\beta(0.250)$
BB6	$\beta(0.15)$	$\beta(0.125)$

Run	$p(1,u)$	$\psi(1,\varepsilon)=\psi(\varepsilon)$
BB7	$\beta(0.05)$	$\beta(0.500)$
BB8	$\beta(0.05)$	$\beta(0.250)$
BB9	$\beta(0.05)$	$\beta(0.125)$
BD1	$\beta(0.20)$	$\delta(\varepsilon)$
BD2	$\beta(0.15)$	$\delta(\varepsilon)$
BD3	$\beta(0.05)$	$\delta(\varepsilon)$

TABLE 2. Combinations of initial distributions used for the parameter study: $\beta(\sigma_\zeta^2)$ - β-distribution with prescribed variance σ_ζ^2; $\delta(\zeta)$ - Dirac δ-function for ζ.

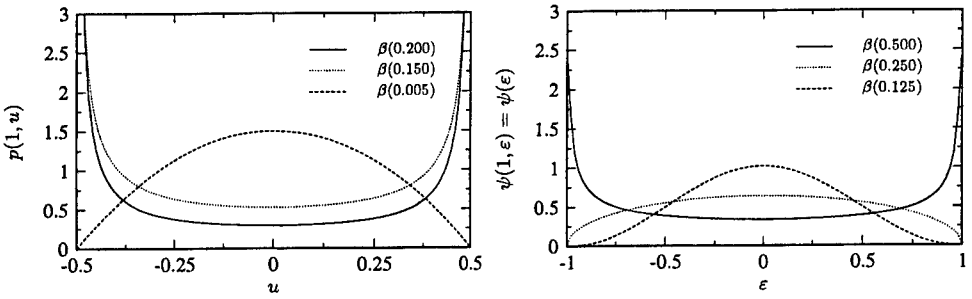


FIGURE 2. Initial conditions for $p(1,u)$ and $\psi(1,\varepsilon)=\psi(\varepsilon)$; $\lambda=1.0$.

right column, the evolution of $p(n,u)$ is shown for the mono-modal initial β-distribution with $\sigma_u^2(1)=0.05$. From the bottom row of Fig. 3 it can be seen that $p(n,u)$ experiences strong dynamics over the initial interval, say for $n \leq 10$. Over this interval the variance does not follow the power law decay. Furthermore it can be deduced that the stochastic perturbation ε reduces the decay rate of σ_u^2 if σ_ε^2 is close to $\sigma_{\varepsilon,\max}^2$ (see solid curves).

The influence of the initial distribution of ε on the evolution of $p(n,u)$ and consequently on $\sigma_u^2(n)$ vanish for large n. This is most pronounced for the cases BB7-BB9 and BD3 (right column). Here the decay exponents for all of these cases collapse to a single curve, independent of $\psi(\varepsilon)$.

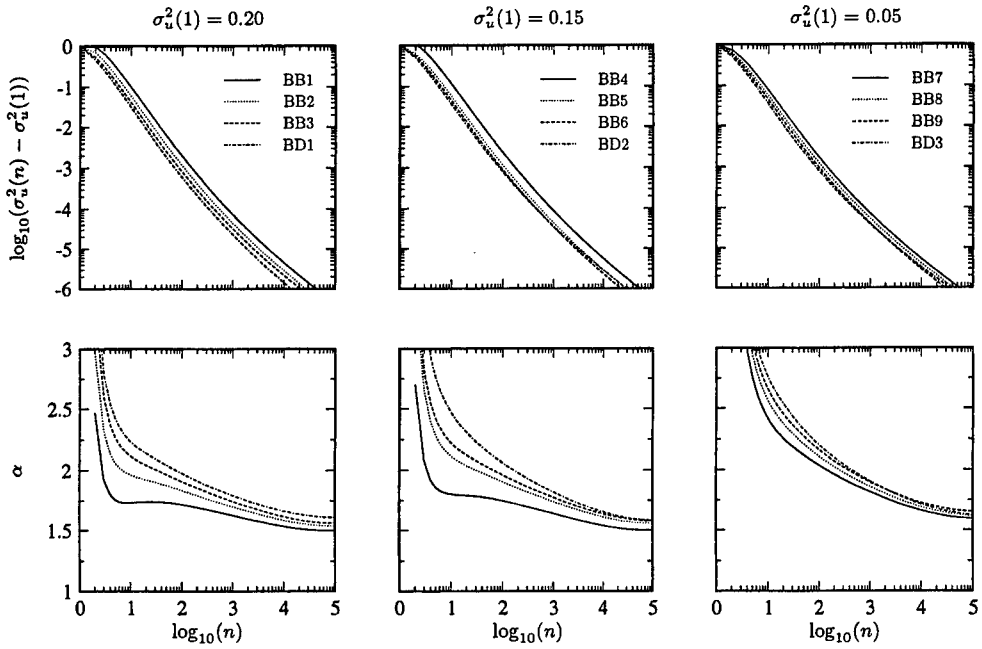


FIGURE 3. Evolution of σ_u^2 and decay exponent α for the initial β-distribution in u.

Run	$p(1,u)$	$\psi(\varepsilon)$
Dyn1	$[\delta(\mu+u)+\delta(1-\mu-u)]/2$	$\delta(\varepsilon)$
Dyn2	$\beta(0.15)$	$\beta(0.50)$

TABLE 3. Combinations used to study dynamic behavior of $p(n,u)$ for $\lambda = 0.75$.

From this simulation it can be concluded that the initially assumed distribution for ε has only marginal influence on the decay exponent α for large n. During the simulation the value for α never reaches a steady state. The final convergence rate for $n = 100,000$ is $|d\alpha/dn| < 1.0 \times 10^{-6}$ so that α is in the range $1.50 \leq \alpha \leq 1.65$ for all test cases used in the present section.

3.4. *Dynamic behavior of* $p(n,u)$

In the present section we are interested in the influence of $\psi(\varepsilon)$ on the dynamics of $p(n,u)$. The transitional behavior of σ_u^2 can be retarded if the mixing intensity λ is small. This effect was already discussed previously. In the present section the mixing intensity $\lambda = 0.75$ is used.

In order to obtain insight into the transitional behavior we use a double δ-distribution and a bimodal β-distribution as initial condition for u, $p(1,u) = [\delta(\mu+u)+\delta(1-\mu-u)]/2$ and $p(1,u) = \beta(0.15)$. For $\psi(\varepsilon) = \delta(\varepsilon)$ a simple analytical solution to Eq. (2.28) can be found for the first time step $n = 1$. For clarity the different combinations used here are summarized in Table 3. At $n = 1$ the initial distribution for the case Dyn1 splits up into

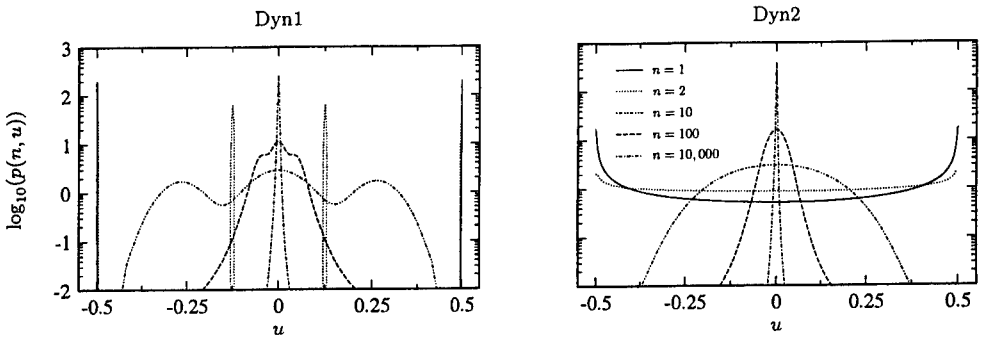


FIGURE 4. Transitional behavior of $p(n,u)$ for different initial conditions and mixing intensity.

Run	λ	$p(1,u)$	$\psi(\varepsilon)$	$[\varepsilon_{\min}, \varepsilon_{\max}]$
LA1	1.50	$\beta(0.15)$	$\beta(0.20)$	$[-1, 1/3]$
LA2	1.00	$\beta(0.15)$	$\beta(0.20)$	$[-1, 1]$
LA3	0.75	$\beta(0.15)$	$\beta(0.20)$	$[-1, 5/3]$
LA4	0.50	$\beta(0.15)$	$\beta(0.20)$	$[-1, 3]$
LA5	0.25	$\beta(0.15)$	$\beta(0.20)$	$[-1, 7]$

TABLE 4. Combinations used to study the influence of the mixing intensity λ on the evolution of the variance.

four peaks at positions $u = \lambda(\xi - \gamma)/2 + \gamma$ with $\gamma = \{-\mu, 1-\mu\}$ and $\xi = \{-\mu, 1-\mu\}$. In the succeeding time those peaks move toward the center $u = 0$ whereas the tails flatten.

An entirely different dynamic behavior is obtained for the case Dyn2. The initially smooth density function $p(1,u)$ transits rapidly to a mono-modal distribution and converges to the δ-pdf. With the results of this and the previous section we can summarize that the prescribed distribution of ε influences the transitional dynamics of $p(n,u)$, however its effect on the decay exponent α for large n is insignificant.

3.5. *Mixing intensity* λ

From experiments and DNS studies it is well-known that the decay rate strongly depends on the initial ratio of the velocity and scalar length-scales, ℓ_u and ℓ_c. The free parameter λ is introduced in the exchange rate (2.22) in order to link the present model to physical processes. It needs to be emphasized that we did not attempt to reproduce any experimental or numerical data, amply and in great diversity available in the literature. Presently, we are only interested in understanding the general behavior of Eq. (2.28). It was concluded previously that the presumed form of $\psi(\varepsilon)$ has only insignificant influence on the decay rate. However, the dynamic behavior of $p(n,u)$ in the transitional range is influenced by the stochastic variable ε. In anticipation of the overall weak influence of $\psi(\varepsilon)$ on the decay exponent we chose arbitrarily $\psi(\varepsilon) = \beta(0.20)$ whereas $\psi(\varepsilon)$ has non-zero probability only in the interval $-1 \leq \varepsilon \leq 2/\lambda - 1$. The parameters used for the five different test cases are summarized in Table 4.

Figure 5 shows the distinct dependence of the mixing intensity on the decay of σ_u^2.

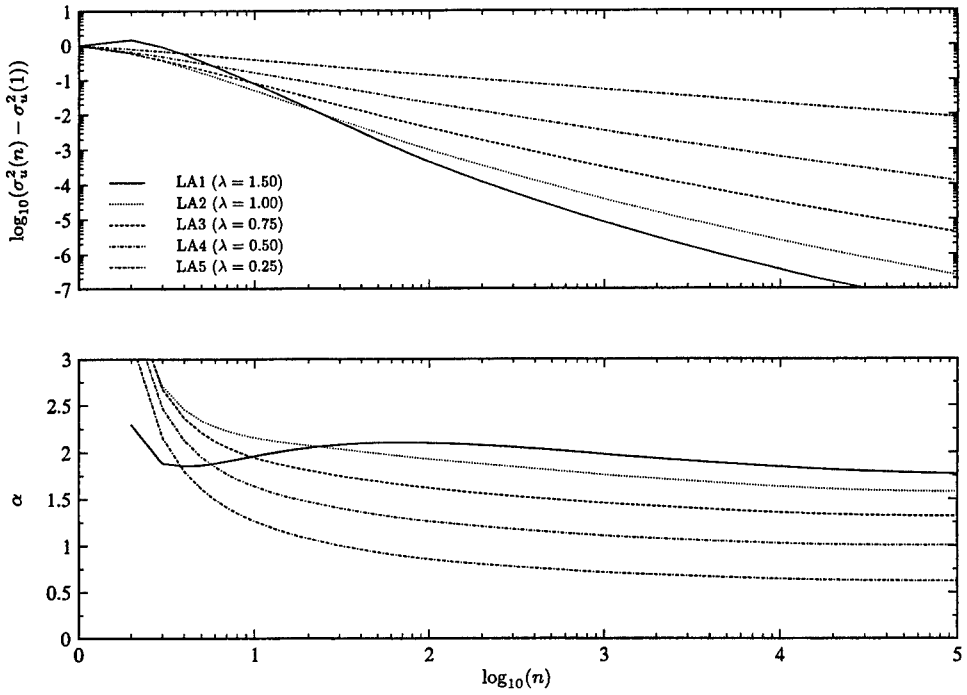


FIGURE 5. Decay of σ_u^2 for different mixing intensities λ.

Experiments on turbulent mixing show that the variance σ_u^2 decreases faster with increasing ratio ℓ_u/ℓ_c, until about $\ell_u/\ell_c \sim 5$. For ratios greater than that value the dependence is negligible. This tendency can be resembled by changing the mixing intensity λ. The power law exponent α is approximately 1.77 for high mixing intensity and decreases to about 0.62 for $\lambda = 0.25$ which corresponds to an indolent mixing process. From the present findings it is difficult to specify the exact functional relation between λ and initial conditions used in experiments. Therefore we express the mixing intensity formally as $\lambda = \lambda(\ell_u/\ell_c, \text{Re or Pe})$.

4. Conclusion

In the present paper we presented a robust mixing model based on the law of large numbers. The exchange rate decays as t^{-1} and links the mixing model to the law of large numbers. By adding stochastic fluctuations to the exchange rate, we extend the model to the general case, taking the fluctuations of the surround into account.

The sensitivity of the model is analyzed for different initial conditions and parameters. It was shown that the initial distribution for ε and u has only insignificant influence on the decay rate of the variance. This is to be expected because the initial distribution of the scalar is almost never measured in experiments, assuming implicitly that either the scalar is distributed initially as a double δ-function or generally disregard the dependence of the decay of σ_c^2 on the initial density distribution.

It was shown that with increasing mixing intensity the variance of the passive scalar decreases faster. The connection of our model to physical mixing processes is provided through λ, which can account for initial length-scale dependences ℓ_u/ℓ_c and other physical effects.

REFERENCES

CHASNOV, J. R. 1994 Similarity states of passive scalar transport in isotropic turbulence. *Phys. Fluids* **6**, 1036-1051.

CURL, R. L. 1963 Dispersed phase mixing: I Theory and effects in single reactors. *AIChE journal* **9**, 175-181.

DOPAZO, C. AND O'BRIEN, E. E. 1974 An approach to the autoignition of a turbulent mixture. *Acta Astronautica* **1**, 1239-1266.

DURBIN, P. A. 1982 Analysis of the decay of temperature fluctuations in isotropic turbulence. *Phys. Fluids* **25**, 1328-1332.

FELLER, W. 1966 An Introduction to Probability Theory and its Applications. J. Wiley & Sons.

KNESSL, C., MATKOWSKY, B. J., SCHUSS, A. & TIER, C. 1985 An asymptotic theory of large deviations for Markov jump processes. *SIAM J. Appl. Math.* **46**, 1006-1028.

LESIEUR, M. 1997 *Turbulence in Fluids.* Kluwer Academic Publishers.

LISEIKIN, V. D. 1999 *Grid Generation Methods.* Springer-Verlag.

PETERS, N. 2000 *Turbulent Combustion.* Cambridge University Press.

POPE, S. B. 2000 *Turbulent Flows.* Cambridge University Press.

SABEL'NIKOV, V. A. & GOROKHOVSKI 2001 *Extended LMSE and Langevin models of the scalar mixing in the turbulent flow.* In Second International Symposium on Turbulence and Shear Flow Phenomena. Royal Institute of Technology (KTH), Stockholm, Sweden, June 27-29.

VILLERMAUX, J. & DEVILLON, J. C. 1972 Représentation de la coalescence et de la redispersion des domaines de ségrégation dans un fluide par un modèle d'interaction phénoménologique. in *Proceedings of the Second International Symposium on Chemical Reaction Engineering*, 1-13.

Large-eddy simulation of conductive flows at low magnetic Reynolds number

By B. Knaepen AND P. Moin

1. Introduction

In large-eddy simulations (LES), only the large-scale structures of the flow are simulated directly while the small-scale structures are taken into account through a model, referred to as the subgrid-scale (SGS) model. This results in significant reduction in computational requirements. The trade-off comes in the extra modelling effort that has to be produced in order to adequately take into account the discarded small scales structures. In the computational fluid mechanics community, the most widely used SGS model is the Smagorinsky eddy viscosity model (Smagorinsky 1963). This model has gained an even bigger practical interest following the work of Germano *et al.* (1991) in which the dynamic procedure was introduced. The dynamic procedure enables optimization "on the fly" of the arbitrary scaling factor that is inherently present in the original Smagorinsky model (more details below) and thus allows the model to automatically adapt to the flow being studied.

In this paper we study the LES method with dynamic procedure in the context of conductive flows subject to an applied external magnetic field at low magnetic Reynolds number R_m. These kind of flows are encountered in many industrial applications. For example, in the steel industry, applied magnetic fields can be used to damp turbulence in the casting process. In nuclear fusion devices (Tokamaks), liquid-lithium flows are used as coolant blankets and interact with the surrounding magnetic field that drives and confines the fusion plasma. Also, in experimental facilities investigating the dynamo effect, the flow consists of liquid-sodium for which the Prandtl number and, as a consequence, the magnetic Reynolds number is low.

Most of the previous works considering LES in the case of MHD flows have been directed towards flows at high R_m, where the full non-linear MHD equations have to be used, or towards flows in the absence of an external magnetic field: Yoshizawa (1987); Zhou & Vahala (1991); Theobald *et al.* (1994); Agullo *et al.* (2001); Müller & Carati (2002). To our knowledge, the only attempt to study MHD turbulence at low magnetic Reynolds number from the LES point of view is due to Shimomura (1991). In that work, the author considers the case of magnetohydrodynamic turbulent channel flow and introduces a new SGS model designed to incorporate the effects of the applied uniform magnetic field. However, like the original Smagorinsky model, the model of Shimomura contains constants that have to be adjusted and are thus flow dependent. In the present paper, we show that it is possible to circumvent this problem by the use of the dynamic Smagorinsky model.

Our attention is focused here on the case of homogeneous (initially isotropic) decaying turbulence. The numerical simulations performed mimic the thought experiment described in Moffatt (1967) in which an initially homogeneous isotropic conductive flow is suddenly subjected to an applied magnetic field and freely decays without any forcing. Note that this flow was first studied numerically by Schumann (1976). It is well known

that in that case, extra damping of turbulence occurs due to the Joule effect and that the flow tends to become progressively independent of the coordinate along the direction of the magnetic field. Our comparison of filtered direct numerical simulation (DNS) predictions and LES predictions show that the dynamic Smagorinsky model enables one to capture successfully the flow with LES, and that it automatically incorporates the effect of the magnetic field on the turbulence.

Our paper is organized as follows. In the next section we summarize the LES approach in the case of MHD turbulence at low R_m and recall the definition of the dynamic Smagorinsky model. In Sec. 3 we describe the parameters of the numerical experiments performed and the code used. Section 4 is devoted to the comparison of filtered DNS results and LES results. Conclusions are presented in Sec. 5.

2. LES at low magnetic Reynolds number

For homogeneous flows, the magnetic Reynolds number can be defined through the following relation:

$$R_m = \frac{uL}{\eta}, \tag{2.1}$$

where $u = \sqrt{\langle u_i u_i \rangle / 3}$ is the r.m.s. of the fluctuating velocity u_i, L is the integral length scale of the flow and η is the magnetic diffusivity. R_m represents the relative importance of the non-linear terms and the diffusion term in the magnetic induction equation. In the limit of low R_m, the MHD equations can be simplified considerably Roberts (1967). It is indeed possible to close independently the momentum equation and take into account the effect of the magnetic field through an extra damping term. This approximation is known as the *quasi-static (QS) approximation* and along with the incompressibility condition, $\partial_i u_i = 0$, reads,

$$\partial_t u_i = -\partial_i (p/\rho) - u_j \partial_j u_i - \frac{\left(B_z^{ext}\right)^2}{\eta} \Delta^{-1} \partial_z \partial_z u_i + \nu \Delta u_i, \tag{2.2}$$

where p is the sum of the kinematic and magnetic pressures, ρ is the fluid density, ν the kinematic viscosity, B_z^{ext} is the applied external magnetic field and Δ^{-1} is the inverse of the Laplacian operator. Note that B_z^{ext} has by convention been aligned with the z-direction and expressed in Alfven units.

LES equations are obtained by filtering (2.2). The filtered velocity $\overline{u}_i$ is defined by,

$$\overline{u}_i(\mathbf{x}) = \int G(\mathbf{x}, \mathbf{y}) u_i(\mathbf{y}) d\mathbf{y}, \tag{2.3}$$

where G is a smoothing kernel that eliminates the small scale part of u_i and satisfies the relation,

$$\int G(\mathbf{x}, \mathbf{y}) d\mathbf{y} = 1. \tag{2.4}$$

In terms of the filtered velocity, Eq. 2.2 can be written as,

$$\partial_t \overline{u}_i = -\partial_i (\overline{p}/\rho) - \overline{\overline{u}_j \partial_j \overline{u}_i} - \frac{\left(B_z^{ext}\right)^2}{\eta} \Delta^{-1} \partial_z \partial_z \overline{u}_i + \nu \Delta \overline{u}_i - \partial_j \overline{\tau}_{ij}, \tag{2.5}$$

where,

$$\overline{\tau}_{ij} = \overline{u_i u_j} - \overline{\overline{u}_i \overline{u}_j}, \tag{2.6}$$

is the subgrid-scale stress tensor. In order to close (2.5), $\overline{\tau}_{ij}$ has to be expressed only in terms of the filtered velocity.

Is is interesting to note that $\overline{\tau}_{ij}$ does not depend explicitly on the magnetic field. Indeed, the magnetic contribution, being a linear term in (2.2), does not require an explicit SGS counterpart in the LES equation. In the case of non-conductive flows, the most widely used model for $\overline{\tau}_{ij}$ is the Smagorinsky model:

$$\overline{\tau}_{ij} = -2C_s\overline{\Delta}^2|\overline{S}|\overline{S}_{ij}, \quad \overline{S}_{ij} = \frac{1}{2}(\partial_i\overline{u}_j + \partial_j\overline{u}_i), \quad \overline{S} = \sqrt{2\overline{S}_{ij}\overline{S}_{ij}}, \tag{2.7}$$

where $\overline{\Delta}$ is the width of the filter G and C_s is the Smagorinsky constant. However, as was observed by Shimonura in Shimomura (1991), model (2.7) with C_s optimized for a non-conductive flow, is not adequate in the present context. This is easily understood when one refers to the fact that the applied external magnetic field has the tendency to suppress non-linear transfers in the velocity field. Thus, the effect of the SGS stress tensor needs to be decreased for conductive flows when the external magnetic field is switched on. This should result in a lower optimal value for the Smagorinsky constant.

Contrary to what was done in Shimomura (1991), we will not explicitly modify the Smagorinsky model to incorporate the effect of the magnetic field but rather we will make use of the dynamic procedure (Germano *et al.* 1991) to optimize the value of C_s.

To define the dynamic procedure one introduces a second, coarser filter called the test-filter which we denote by $\widetilde{\cdots}$. Applying this filter in addition to (2.5) yields,

$$\partial_t\widetilde{\overline{u}}_i = -\partial_i(\widetilde{\overline{p}}/\rho) - \widetilde{\overline{\overline{u}}_j\partial_j\overline{u}_i} - \frac{(B_z^{ext})^2}{\eta}\Delta^{-1}\partial_z\partial_z\widetilde{\overline{u}}_i + \nu\Delta\widetilde{\overline{u}}_i - \partial_j\widetilde{\overline{\tau}}_{ij} - \partial_j\widetilde{\overline{L}}_{ij}, \tag{2.8}$$

where $\widetilde{\overline{L}}_{ij} = \widetilde{\overline{u}_i\overline{u}_j} - \widetilde{\overline{\overline{u}}_i\overline{\overline{u}}_j}$ is the Leonard tensor which does not require any modeling since it is expressed in closed form using the filtered velocity $\overline{u}_i$. The sum $\widetilde{\overline{\tau}}_{ij} + \widetilde{\overline{L}}_{ij}$ represents the SGS stress tensor $\widetilde{\overline{T}}_{ij}$ of the combined $\widetilde{\overline{\cdots}}$ filter and we have the well-known Germano identity,

$$\widetilde{\overline{L}}_{ij} = \widetilde{\overline{T}}_{ij} - \widetilde{\overline{\tau}}_{ij}. \tag{2.9}$$

Assuming that $\overline{u}_i$ and $\widetilde{\overline{u}}_i$ are self-similar, a suitable model for $\widetilde{\overline{T}}_{ij}$ should be,

$$\widetilde{\overline{T}}_{ij} = -2C_s\widetilde{\overline{\Delta}}^2|\widetilde{\overline{S}}|\widetilde{\overline{S}}_{ij}, \quad \widetilde{\overline{S}}_{ij} = \frac{1}{2}(\partial_i\widetilde{\overline{u}}_j + \partial_j\widetilde{\overline{u}}_i), \quad \widetilde{\overline{S}} = \sqrt{2\widetilde{\overline{S}}_{ij}\widetilde{\overline{S}}_{ij}}, \tag{2.10}$$

where $\widetilde{\overline{\Delta}}$ is the width of the $\widetilde{\overline{\cdots}}$ filter. When one models $\overline{\tau}_{ij}$ and $\widetilde{\overline{T}}_{ij}$ using (2.7) and (2.10), the Germano identity will undoubtedly be violated. However, the constant C_s can be chosen in such a way as to minimize the difference (in the least square sense) between both sides of (2.9). Assuming homogeneity in all directions, the optimal choice is (Lilly 1992):

$$C_s = \frac{\left\langle \widetilde{\overline{M}}_{ij}\widetilde{\overline{L}}_{ij} \right\rangle}{\left\langle \widetilde{\overline{M}}_{ij}\widetilde{\overline{M}}_{ij} \right\rangle}, \quad \widetilde{\overline{M}}_{ij} = 2\left[\overline{\Delta}^2\widetilde{|\overline{S}|\overline{S}_{ij}} - \widetilde{\overline{\Delta}}^2|\widetilde{\overline{S}}|\widetilde{\overline{S}}_{ij}\right], \tag{2.11}$$

where $\langle \cdots \rangle$ denotes spatial averaging. Thus, although model (2.7) does not explicitly incorporate the magnetic field, the dynamic constant C_s should adjust to an appropriate value if the scale-similarity hypothesis is at all justified.

3. Numerical experiments

To assess the dynamic Smagorinsky model in the present context, we have built a set of DNS databases. Since we restrict our attention to a cubic domain with periodic boundary conditions, a spectral (dealiased) code has been used.

The velocity field can then be initialized in Fourier space. The initial mode amplitudes are computed to match the spectra of the Comte-Bellot & Corrsin (1971) experiment at stage 1 (see Rogallo (1981) for more information on the procedure). Phases are initially random and the flow is left to freely decay until the skewness of the velocity derivative reaches a quasi constant value of $S = -0.4$. At this time (hereafter referred to as t_0) the flow is considered "physical" and used as the initial condition for all of our runs. All the DNS simulations are done in a $(2\pi)^3$ box using a resolution of 512^3 Fourier modes and the viscosity is set to $\nu = 0.006$. Other relevant quantities measured at $t = t_0$ are summarized here:

$$Re = \frac{uL}{\nu} = 380 \quad \text{(integral Reynolds number)}, \tag{3.1}$$

$$R_\lambda = \sqrt{\frac{15}{\epsilon\nu}} u^2 = 84.1 \quad \text{(microscale Reynolds number)}, \tag{3.2}$$

$$\tau_{eddy} = \frac{3}{2}\frac{u^2}{\epsilon} = 0.238 \quad \text{(eddy turnover time)}. \tag{3.3}$$

Three test cases have been considered. The first one corresponds to a decaying flow without the addition of any applied external magnetic field. The other two numerical experiments are distinguished by their characteristic *interaction numbers* at t_0. The interaction number N (also known as the Stuart number) is defined as follows:

$$N = \frac{(B_z^{ext})^2}{\eta}\frac{L}{u}. \tag{3.4}$$

N measures the relative strengths of the magnetic damping term and the non-linear term in (2.2). Two cases are examined here, $N = 1$ and $N = 10$.

To illustrate the effect of the external magnetic field, the time history of the kinetic energy density $E = \frac{1}{V}\int d\mathbf{x}\frac{1}{2}u_i(\mathbf{x})u_i(\mathbf{x})$ of the flow for the three cases is presented in Fig. 1. As in all the following figures, time has been normalized by the initial eddy turnover time and the non-dimensional time is denoted by t^*.

4. LES results

In order to assess the LES method, some DNS snapshots of the flow field have been truncated from the 512^3 resolution to a 32^3 resolution (using a sharp Fourier cut-off). The initial condition for the LES runs has been obtained in the same way by truncating the DNS field at $t = t_0$. As can be easily seen from (2.11), the only free parameter in the subgrid-scale model is the ratio $\bar{\tilde{\Delta}}/\bar{\Delta}$. As is standard practice in LES of non-conductive flows, the value of 2 is adopted here.

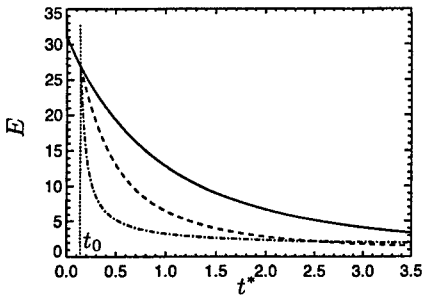


FIGURE 1. Time history of the kinetic energy density E. The solid line represents the flow decay without applied magnetic field, the dashed curve corresponds to the case $N = 1$ and the dash-dot curve corresponds to the case $N = 10$. The dotted line represents the time t_0 at which the magnetic field is switched on.

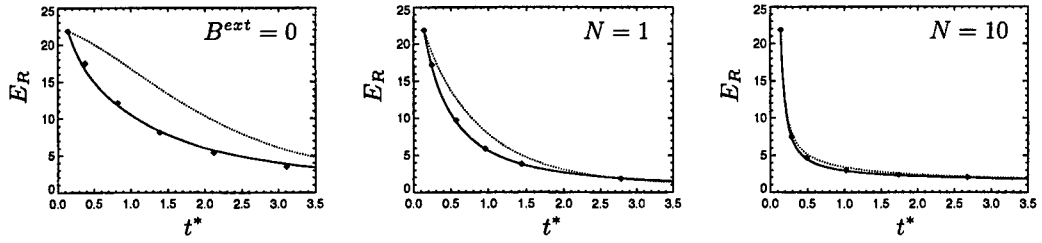


FIGURE 2. Time history of the resolved kinetic energy density: LES vs. filtered DNS. The solid lines represent the predictions of the LES. The diamonds represent the filtered kinetic energy density obtained by truncating the DNS fields to a 32^3 resolution. The dotted lines represent the predictions of the unresolved DNS (performed on the 32^3 mesh) without any subgrid-scale model.

4.1. *Kinetic Energy*

Figure 2 represents the time evolution of the resolved kinetic energy density $E_R = \frac{1}{V}\int d\mathbf{x}\frac{1}{2}\overline{u}_i(\mathbf{x})\overline{u}_i(\mathbf{x})$ predicted by the LES and compared to the filtered DNS. On each plot, a third curve representing a simulation (referred to as 'unresolved DNS') on the 32^3 mesh without SGS modeling is added to stress the action of the subgrid-scale model. The case $B^{ext} = 0$ serves as a benchmark to check that in the case of non-conductive flows, our LES code behaves as expected. In both the cases $N = 1$ and $N = 10$, the LES performs remarkably well. In the case $N = 1$ the difference between LES and unresolved DNS is very clear. In the case $N = 10$ and for this diagnostic, the unresolved DNS does not depart significantly from the filtered DNS and LES.

4.2. *Energy spectra*

The energy spectrum constitutes a finer diagnostic than the kinetic energy density since it retains information about the repartition of energy among the different scales of the flow. Figures 3 and 4 contain respectively kinetic energy spectra for the cases $N = 1$ and $N = 10$ at several instants in the simulation. Agreement between LES and DNS is again excellent. The unresolved DNS exhibits the usual pile up of energy at high wave numbers that results from lack of resolution. Thus, although in terms of global energy the unresolved DNS does perform quite well in the $N = 10$ case, the spectral properties of the flow are poorly predicted and the LES does a much better job.

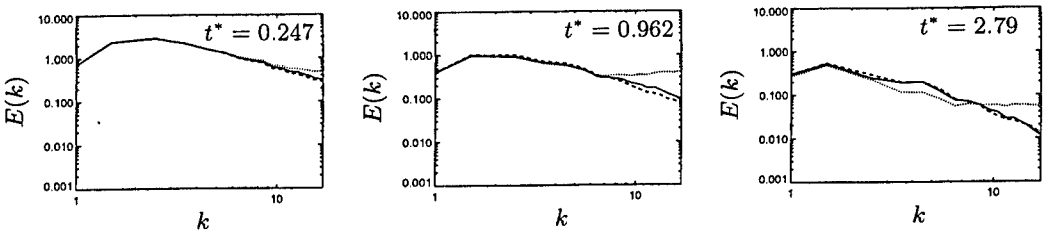


FIGURE 3. Three-dimensional kinetic energy spectra for the case $N = 1$. The solid line represents the filtered DNS, the dashed line represents the LES and the dotted line corresponds to the unresolved DNS. The times at which the spectra are calculated are indicated in the plots.

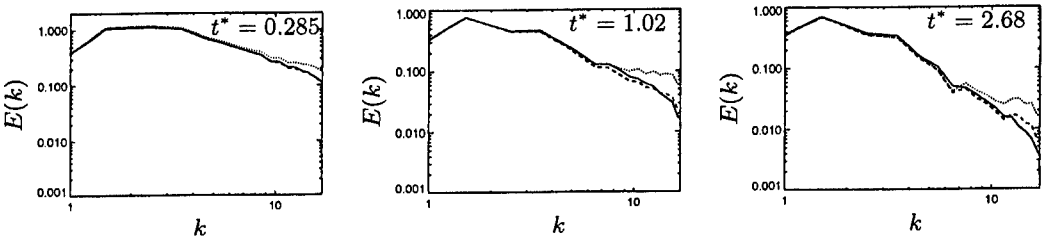


FIGURE 4. Three-dimensional kinetic energy spectra for the case $N = 10$. The solid line represents the filtered DNS, the dashed line represents the LES and the dotted line corresponds to the unresolved DNS. The times at which the spectra are calculated are indicated in the plots.

4.3. *Dissipation rate budget*

The evolution of the resolved kinetic energy density E_R is governed by,

$$\frac{dE_R}{dt} = -\frac{1}{V}\int d\mathbf{x}(\epsilon_\nu + \epsilon_B + \epsilon_{sgs}) \tag{4.1}$$

where,

$$\epsilon_\nu = 2\nu\overline{S}_{ij}\overline{S}_{ij}, \quad \epsilon_B = \frac{(B_z^{ext})^2}{\eta}\overline{u}_i\Delta^{-1}\partial_z\partial_z\overline{u}_i, \quad \epsilon_{sgs} = \overline{\tau}_{ij}\overline{S}_{ij}. \tag{4.2}$$

From Fig. 2 it is clear that the LES predicts the total dissipation rate very well. It is however instructive to know how the different contributions (4.2) are reproduced separately.

In Fig. 5 we present the time evolution of the resolved viscous dissipation rate ϵ_ν for the LES, the filtered DNS and the unresolved DNS. The figures show that the LES reproduces this diagnostic very well, whereas the unresolved DNS systematically overestimates it. This results from the pile-up of energy near the LES cut-off where most of the resolved viscous dissipation occurs.

Figure 6 represents the time evolution of the resolved magnetic dissipation ϵ_B. Again the LES predictions match the filtered DNS results very well. The differences with the unresolved DNS are less severe than for the viscous dissipation. This is to be expected since the magnetic dissipation occurs at every scale in the flow and its overall intensity is thus less contaminated by the pile-up of energy occurring near the LES cut-off for the unresolved DNS. It is also interesting to note that in the case $N = 10$, the magnetic dissipation falls very rapidly with time at the early stages of the decay. This happens because in that case the flow quickly becomes fairly independent of the z-direction which is parallel to the magnetic field (this is illustrated further in Section 4.4).

Finally, in Fig. 7 the evolution of the subgrid-scale transfer rate ϵ_{sgs} is presented. For

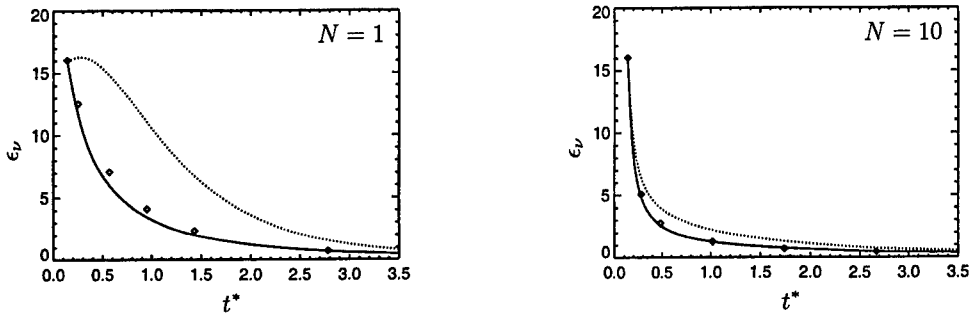


FIGURE 5. Resolved viscous dissipation rate ϵ_ν for the cases $N = 1$ (left) and $N = 10$ (right). In each plot, the solid line represents the LES, the diamonds represent the filtered DNS and the dotted line represents the unresolved DNS.

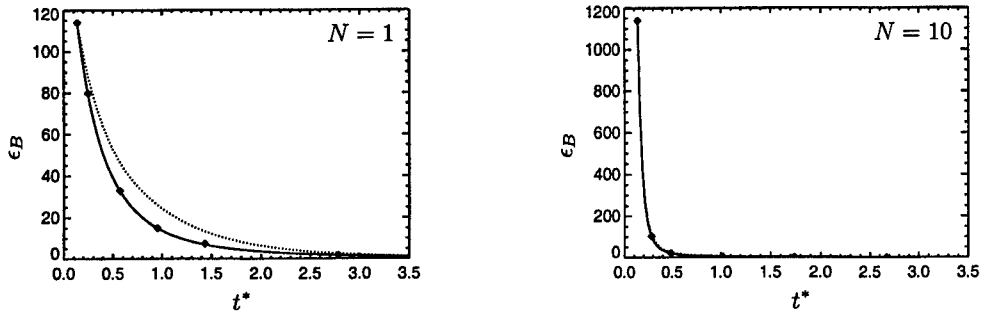


FIGURE 6. Resolved magnetic dissipation rate ϵ_B for the cases $N = 1$ (left) and $N = 10$ (right). In each plot, the solid line represents the LES, the diamonds represent the filtered DNS and the dotted line represents the unresolved DNS.

the LES, ϵ_{sgs} is obtained by substituting the dynamic Smagorsinky in place of $\overline{\tau}_{ij}$ in (4.2). DNS results are obtained by computing the exact $\overline{\tau}_{ij} = \overline{u_i u_j} - \overline{u}_i \overline{u}_j$ from the DNS data fields. Obviously, no (non-zero) results are available for the unresolved DNS. From the plots we see that the subgrid-scale transfer rate is initially overestimated in the LES. This is not a surprise since the dynamic procedure usually needs a little time to settle. Soon after this short transient time, the agreement between LES and DNS predictions is very good.

4.4. *Flow structures*

It is well known that the extra damping term present in the quasi-static approximation (2.2) leads to a progressive suppression of spatial variations in the flow along the direction of the magnetic field. It is thus important to assess how well the LES is able to reproduce this feature. To that end, we have plotted in Figures 8 and 9 the contours of the kinetic energy density at three different times respectively for the filtered DNS and the LES (only the case $N = 10$ is shown because the effect is more pronounced for strong applied magnetic fields). Since the turbulence is decaying with time, the colormap had to be rescaled for each of the single plots. However, the same colormap for the filtered DNS and LES has been used in the plots corresponding to the same times. As is obvious from the plots, the LES reproduces the filtered DNS structures very well. The unresolved DNS also captures the large-scales structures of the flow (no plots shown) but due to the pile

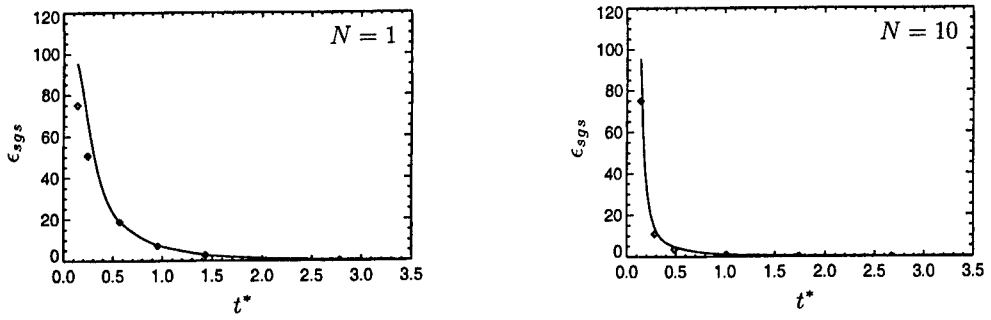


FIGURE 7. Subgrid-scale transfer rate ϵ_{sgs} for the cases $N = 1$ (left) and $N = 10$ (right). In each plot, the solid line represents results obtained from the LES while the diamonds are obtained from the DNS data.

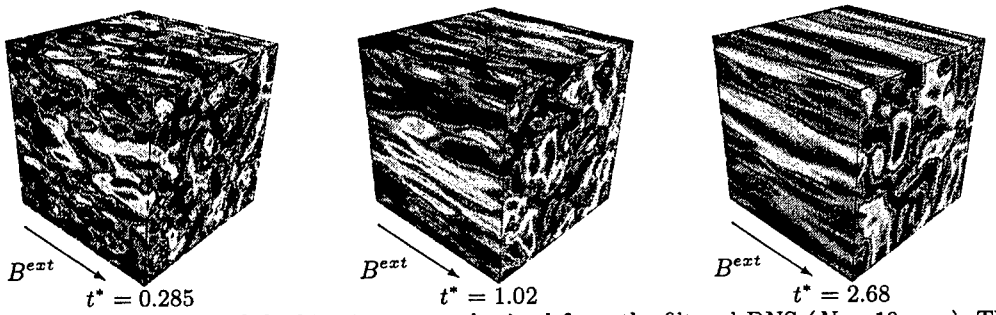


FIGURE 8. Contours of the kinetic energy obtained from the filtered DNS ($N = 10$ case). The different times at which the contours are calculated are indicated under the plots and are the same ones as those used in Fig. 9.

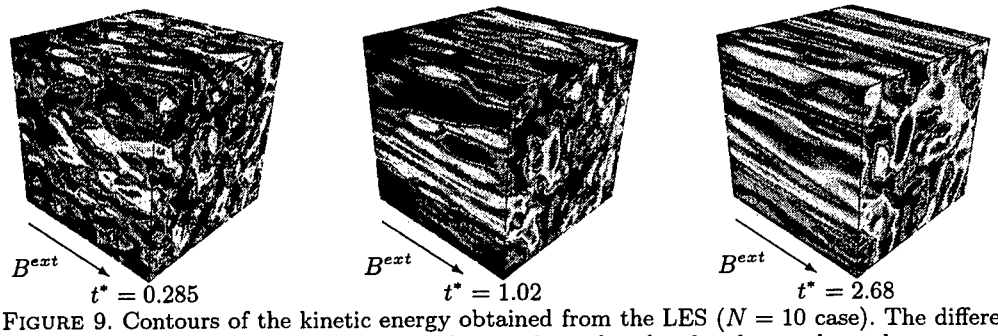


FIGURE 9. Contours of the kinetic energy obtained from the LES ($N = 10$ case). The different times at which the contours are calculated are indicated under the plots and are the same ones as those used in Fig. 8.

up of energy it predicts a significant amount of small scales; the corresponding contour plots contain some excessive 'noise' on top of the large-scales structures.

4.5. *Dynamic Constant*

As recalled in Section 2, the dynamic procedure is designed to optimize the scaling constant C_s present in the Smagorinsky subgrid-scale model. We also mentioned that when an external magnetic field is present, the value of C_s should decrease since non-linear transfers are reduced and the effect of the subgrid-scale model should be damped

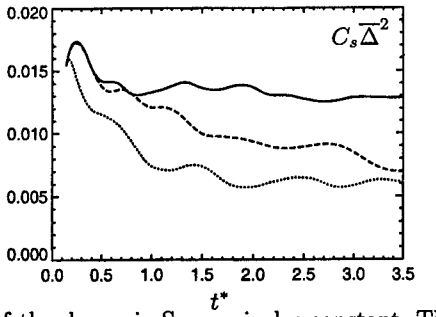


FIGURE 10. Time history of the dynamic Smagorinsky constant. The solid line represents the case with no magnetic field, the dashed line corresponds to the case $N = 1$ and the case $N = 10$ is represented by the dotted line.

accordingly. In Fig. 10 the evolution of $C_s\overline{\Delta}^2$ is plotted. From the figure, it is clear that the expected behavior is observed. As the interaction number is increased, the dynamic procedure automatically adapts the value of the Smagorinsky constant to decrease the effect of the subgrid-scale model.

5. Conclusions

In this article we have shown that the dynamic Smagorinsky model can be used to perform large-eddy simulations of flows subject to an applied external magnetic field at low magnetic Reynolds number, R_m. Although this subgrid-scale model was not designed for this application, its behavior is excellent owing to its adaptation to the flow and the applied magnetic field through the dynamic procedure. The model can be considered robust since it works equally well for interaction (or Stuart) numbers ranging from $N = 0$ (no magnetic field) to $N = 10$ (for which the flow becomes nearly two dimensional). In the future, the same model will be tested in more complex geometries.

6. Acknowledgments

The authors are grateful to O. Debliquy, Y. Dubief, M. Fatica, A. Honein, S. Kassinos for fruitful discussions and to G. Burton for his comments on this manuscript.

REFERENCES

AGULLO, O., MULLER, W.-C., KNAEPEN, B. & CARATI, D. 2001 Large eddy simulation for decaying magnetohydrodynamics turbulence with dynamic subgrid modeling. *Phys. Plasmas* **7**, 3502–3505.

COMTE-BELLOT, G. & CORRSIN, S. 1971 Simple eulerian time correlations of full- and narrow-band velocity signals in grid generated 'isotropic' turbulence. *J. Fluid Mech.* **48**, 273–337.

GERMANO, M., PIOMELLI, U., MOIN, P. & CABOT, W. 1991 A dynamic subgrid-scale eddy-viscosity model. *Phys. Fluids A* **3** (7), 1760–1765.

LILLY, D. 1992 A proposed modification of the germano subgrid-scale closure method. *Phys. Fluids* **4**, 633–635.

MOFFATT, H. K. 1967 On the suppression of turbulence by a uniform magnetic field. *J. Fluid Mech.* **28**, 571–592.

MÜLLER, W.-C. & CARATI, D. 2002 Dynamic gradient-diffusion subgrid models for incompressible magnetohydrodynamic turbulence. *Physics of Plasmas* **9** (3), 824–834.

ROBERTS, P. H. 1967 *An Introduction to Magnetohydrodynamics*. American Elsevier Publishing Company, Inc. New York.

ROGALLO, R. 1981 Numerical experiments in homogeneous turbulence. NASA technical Memorandum 81315. NASA, Ames Research Center.

SCHUMANN, U. 1976 Numerical simulation of the transition from three- to two-dimensional turbulence under a uniform magnetic field. *J. Fluid Mech.* **74**, 31–58.

SHIMOMURA, Y. 1991 Large eddy simulation of magnetohydrodynamic turbulent channel flows under a uniform magnetic field. *Phys. Fluids A* **3** (12), 3098.

SMAGORINSKY, J. 1963 General circulation experiments with the primitive equations: 1. the basic experiment. *Month. Weather Rev.* **91**, 99–164.

THEOBALD, M., FOX, P. & SOFIA, S. 1994 A subgrid-scale resistivity for magnetohydrodynamics. *Phys. Plasmas* **1**, 3016.

YOSHIZAWA, A. 1987 Subgrid modeling for magnetohydrodynamic turbulent shear-flows. *Phys. Fluids* **30** (4), 1089–1095.

ZHOU, Y. & VAHALA, G. 1991 Aspects of subgrid modelling and large-eddy simulation of magnetohydrodynamic turbulence. *J. Plasma Physics* **45**, 239–249.

DNS and LES of a shear-free mixing layer

By B. Knaepen, O. Debliquy† and D. Carati †

1. Introduction

The shear-free mixing layer represents one of the simplest inhomogeneous flows. It consists of two 'distinct' homogeneous regions of different turbulent kinetic energy interacting through a layer of rapid transition. The layer is said to be shear-free since the two homogeneous regions have no relative velocity. While flows encountered in nature or industrial applications are more often not devoid of shear, the study of the shear-free mixing layer is nevertheless useful since it allows the mixing properties of turbulence to be examined in a simplified environment. Indeed, turbulent transport properties in shear flows are more difficult to track since they can be overwhelmed by production sources originating from gradients in the mean velocity.

The shear-free mixing layer has already received attention in the past, both from the experimental and the numerical point of view. The first experimental study of the shear-free mixing layer is due to Glibert (1980). The flow was obtained by forcing a stream through a grid with two different mesh spacings. The two sides of the grid have however equal solidity resulting in an outgoing shear-free flow. In this first experimental study, the author mainly concentrated his attention on the downstream evolution of the spreading-rate parameter, which is a measure of the thickness of the mixing-layer. A more extensive experimental study was later performed by Veeravalli & Warhaft (1987, 1989). Owing to a different experimental setup, the authors achieved a higher ratio between the energies characterizing the two sides of the flow and this resulted in the observation of large-scale intermittency in the flow. The Veeravalli & Warhaft (1989) data will be used here as the main benchmark for the present study since it contains a detailed documentation of the flow characteristics we will be examining. From the numerical point of view, the shear-free mixing layer was studied in Briggs *et al.* (1996) using DNS. In that article the authors also used the data of Veeravalli & Warhaft (1989) as the point of comparison. Their simulations were done using a spectral code with a resolution of 128^3 Fourier modes. The microscale Reynolds numbers reached in the low- and high-energy homogeneous regions were, respectively, 11 and 22.5, which are roughly half of the values reported in the Veeravalli & Warhaft (1989) experiment (note that Briggs *et al.* (1996) use a different definition of the microscale Reynolds number than the one in Veeravalli & Warhaft (1989) and here). However, when properly nondimensionalized, they were able to reproduce satisfactorily the turbulence statistics of the flow.

The purpose of this work is twofold. First, given the computational resources available today, it is possible to reach, using DNS, higher Reynolds numbers than in Briggs *et al.* (1996). In the present study, the microscale Reynolds numbers reached in the low- and high-energy homogeneous regions are, respectively, 32 and 69. The results reported earlier can thus be complemented and their robustness in the presence of increased turbulence studied. The second aim of this work is to perform a detailed and documented LES of

† Universté Libre de Bruxelles, Statistical and Plasma Physics, CP231, Boulevard du Triomphe, Campus Plaine, 1050 Brussels, Belgium

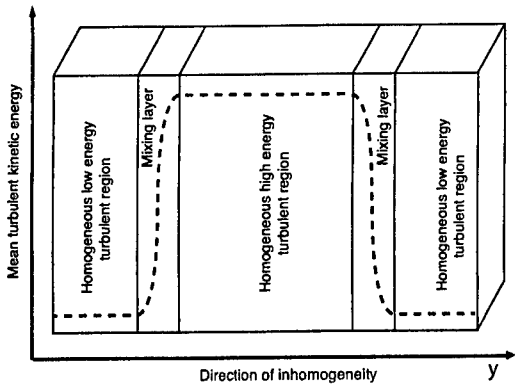


FIGURE 1. Graphical representation of the shear–free mixing layer

the shear-free mixing layer. In that respect, the creation of a DNS database at higher Reynolds number is necessary in order to make meaningful LES assessments. From the point of view of LES, the shear-free mixing-layer is interesting since it allows one to test how traditional LES models perform in the presence of an inhomogeneity without having to deal with difficult numerical issues. Indeed, as argued in Briggs *et al.* (1996), it is possible to use a spectral code to study the shear-free mixing layer and one can thus focus on the accuracy of the modelling while avoiding contamination of the results by commutation errors etc.

This paper is organized as follows. First we detail the initialization procedure used in the simulation. Since the flow is not statistically stationary, this initialization procedure has a fairly strong influence on the evolution. Although we will focus here on the shear-free mixing layer, the method proposed in the present work can easily be used for other flows with one inhomogeneous direction. The next section of the article is devoted to the description of the DNS. All the relevant parameters are listed and comparison with the Veeravalli & Warhaft (1989) experiment is performed. The section on the LES of the shear-free mixing layer follows. A detailed comparison between the filtered DNS data and the LES predictions is presented. It is shown that simple eddy viscosity models perform very well for the present test case, most probably because the flow seems to be almost isotropic in the small-scale range that is not resolved by the LES.

2. Initialization of the flow

From the numerical point of view, one of the most appealing properties of the shear-free mixing layer is the possibility of simulating this flow with a purely spectral three dimensional code. Indeed, periodicity can be enforced by considering a second mixing-layer, which performs the 'reverse' transition compared to the first one. The situation is depicted in Fig. 1. This also has the advantage that results gathered from the two mixing layers can be averaged to improve the statistics. This possibility will be systematically exploited in the presentation of numerical results in the following sections.

Given a 3D spectral code, the non-trivial part of the simulation is then to build a suitable initial condition that mimics the mixing layer. Indeed, because the decaying mixing layer is not statistically stationary, it is not acceptable to wait until the initial condition is forgotten by the flow due to the stochastic nature of turbulence. Indeed, the simulation will remain quite strongly influenced by the initial state of the velocity

field. To proceed, it is necessary to introduce a few definitions and notations. The Fourier modes associated with the velocity field $u_i(x, y, z)$ will be denoted $\tilde{u}_i(k_x, k_y, k_z)$ and are defined by

$$\tilde{u}_i(k_x, k_y, k_z) = \sum_{\mathbf{x}} u_i(x, y, z) e^{-i\mathbf{k}\cdot\mathbf{x}}. \tag{2.1}$$

Since the mixing layer is homogeneous in two directions it is also convenient to consider 2D Fourier transforms. Here we take the y direction as the inhomogeneous direction and define the 2D Fourier modes $\tilde{u}_i(k_x, y, k_z)$ by

$$\tilde{u}_i(k_x, y, k_z) = \sum_{\mathbf{x}_\perp} u_i(x, y, z) e^{-i\mathbf{k}_\perp\cdot\mathbf{x}_\perp}, \tag{2.2}$$

where $\mathbf{x}_\perp = (x, z)$ and $\mathbf{k}_\perp = (k_x, k_z)$. For convenience, we will also adopt the following notations: $u_x \equiv u$, $u_y \equiv v$ and $u_z \equiv w$. When the flow is homogeneous and isotropic, a common way to initialize the modes $\tilde{u}_i(k_x, k_y, k_z)$ is to fix their amplitudes to match a given energy spectra $E(k)$ and assign them random phases in such a way that continuity is enforced (Rogallo 1981). One then has,

$$\langle |\tilde{u}_i(k_x, k_y, k_z)|^2 \rangle = A^2(k), \text{ with } E(k) = 2\pi k^2 A^2(k) \tag{2.3}$$

and $k^2 = k_x^2 + k_y^2 + k_z^2$. For the case at hand, we can adopt a similar strategy but consider instead the 2D spectra in each plane perpendicular to the direction of inhomogeneity. Indeed, in those planes the flow is assumed to be homogeneous and isotropic. We thus initialize our flow by imposing the following constraints on the 2D Fourier modes (the assignment of the random phases and the treatment of continuity will be described below),

$$< |\tilde{u}_i(k_x, y, k_z)|^2 >= B^2(k_\perp, y), \text{ with } E(k_\perp, y) = \pi k_\perp B^2(k_\perp, y) \tag{2.4}$$

and $k_\perp^2 = k_x^2 + k_z^2$. In the above equation, $E(k_\perp, y)$ is the energy spectra of velocity field in (x, z) plane. The arbitrary part remaining is the choice of the function $B^2(k_\perp, y)$. For homogeneous isotropic flows, it is trivial to relate the 2D amplitudes to the 3D amplitudes (using Parseval's theorem):

$$B^2(k_\perp, y) = \int dk_y A^2(k_y^2 + k_\perp^2). \tag{2.5}$$

Note that as expected, $B^2(k_\perp, y)$ is independent of y for homogeneous flows. In the case of the shear–free mixing layer we will choose an amplitude function $A(k)$ for each homogeneous region and compute the corresponding functions $B(k_\perp, y)$ using (2.5). If the 2D amplitudes functions in the high energy and low energy regions are respectively denoted $B_H(k_\perp, y)$ and $B_L(k_\perp, y)$, we then define the complete 2D amplitudes function for the shear-free mixing layer as,

$$B_{ML}(k_\perp, y) = (1 - f(y))B_L(k_\perp, y) + f(y)B_H(k_\perp, y). \tag{2.6}$$

The function $f(y)$ is equal to 0 in the low energy region and equal to 1 in the high energy region; inside the mixing layers it varies smoothly from 0 to 1. The complete initialization procedure is as follows. First we initialize our 3D Fourier modes using the procedure of Rogallo (1981). The 3D energy spectra used here is taken from the high-energy homogeneous region of the mixing layer. This ensures that the Fourier modes $\tilde{u}_i(k_x, k_y, k_z)$ satisfy the continuity equation. The 3D Fourier modes are then transformed to $\tilde{u}_i(k_x, y, k_z)$ using a 1D Fourier transform. At this point their 2D amplitudes are

measured and the modes are rescaled in order to match the prescribed 2D amplitudes given by (2.6):

$$\tilde{u}_i(k_x, y, k_z) \to \tilde{u}'_i(k_x, y, k_z) = \tilde{u}_i(k_x, y, k_z)\sqrt{\frac{B_{ML}(k_\perp, y)}{|\tilde{u}_i(k_x, y, k_z)|^2}}. \tag{2.7}$$

The $\tilde{u}'_i(k_x, y, k_z)$ are then transformed back into 3D Fourier modes, $\tilde{u}'_i(k_x, k_y, k_z)$. By performing the transformation (2.7), one of course destroys the continuity property of the initial field and it has to be recovered by projecting the $\tilde{u}'_i(k_x, k_y, k_z)$ onto a divergence–free field:

$$\tilde{u}'_i(k_x, k_y, k_z) \to \tilde{u}''_i(k_x, k_y, k_z) = \left(\delta_{ij} - \frac{k_i k_j}{k^2}\right)\tilde{u}'_j(k_x, k_y, k_z). \tag{2.8}$$

This in turn partly undoes the prescription of the 2D amplitudes. Fortunately, by iterating the transformations (2.7) and (2.8) one converges to a velocity field that has 2D amplitudes arbitrarily close to $B_{ML}(k_\perp, y)$ and which satisfies continuity. At this stage, the flow still has random phases. In order to correct this problem, we have time evolved the flow until the global skewness of the velocity derivatives reached a converged value. Between each time step, the mixing layer was rebuilt using (2.7) and (2.8) in order to retain the desired 2D amplitudes profile. After that, we stopped the rebuilding procedure and let the flow decay freely.

3. DNS results

3.1. *Parameters of the simulation*

The choice of parameters for the DNS was mainly guided by the following considerations. In order to have an experimental reference to compare with, the parameters of the DNS have been chosen to match as closely as possible those from the Veeravalli & Warhaft (1989) experiment performed using the 3 : 1 perforated plate. Of course, since numerical capabilities are not unlimited, some compromises had to be made. The most important restriction in the present study is the ability to adequately resolve the high-energy region of the flow. Given this constraint, the initial 3D spectra of the homogeneous high-energy region $E_H(k)$ was chosen to match the spectra measured in the Comte-Bellot & Corrsin (1971) experiment at stage 1. This experimental spectra was fitted with the following function,

$$E_H(k) = \frac{ak^4}{(k^4 + q^4)^{1+\alpha}} e^{-bk^\beta} \tag{3.1}$$

which contains several parameters a, q, b, α and β. This fairly complicated function has been chosen because it allows an easy fit of various properties of the energy spectrum. For instance, the parameters b and β can be used for characterizing the viscous range of the spectrum. The parameters q and α determine the energy peak and the transition between the energy containing scales and the viscous range. Finally, a determines the total energy. The function (3.1) does not allow one to derive analytical expressions for the total energy and the total dissipation in terms of the parameters a, q, b, α and β. It is thus not possible to express these parameters in terms of simple global experimental data and we have not found a systematic procedure for prescribing them. It has however been observed that the following set of parameters, $a = 10.6, q = 1.5, b = 0.02, \alpha = 1.233, \beta = 1.1$, allows an almost perfect fit to the Comte-Bellot & Corrsin spectrum. Of course, the value of some

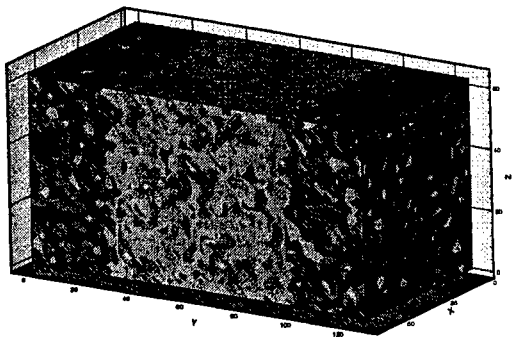


FIGURE 2. 3D contour plot of the energy density for the initial velocity field. The labels indicated on the figure correspond to grid-points. The data field was sampled every four grid-points in order to produce the graph.

of these parameters might depend on the units chosen to perform the simulation. This is not really an issue since the time scale and the length scale can be seen as entirely defined by the computational domain size $l_x = 2\pi, l_y = 4\pi, l_z = 2\pi$ and by the viscosity, chosen here to have the numerical value of 0.006. In the Veeravalli & Warhaft (1989) experiment the ratio of energy between the two homogeneous regions is 6.27 while the ratio of dissipation is 7.28. These two ratios can be reproduced well by choosing the spectra of the low energy homogeneous region to be of the same form as (3.1) but with the following parameters: $a = 2.74, q = 3.33, b = 0.027, \alpha = 1.233, \beta = 1.1$. Furthermore, with the above choices of parameters, the maxima of the two spectra are separated by a ratio that matches the inverse ratio of the initial integral length-scales in the Veeravalli & Warhaft (1989) experiment between the low- and high-energy regions. Accordingly, the differences in typical sizes of the large-scale structures on both sides of the mixing layer are also reproduced. From these definitions it is possible to compute numerically the two functions $B_L(k_\perp, y)$ and $B_H(k_\perp, y)$ needed in (2.6) using (2.5). The initialization procedure is then fully defined if the smoothing function $f(y)$ is prescribed. Here, the following choice has been adopted:

$$f(y) = \begin{cases} 0 & \text{if } 0 < y < 5l_y/24, \\ 1/2(\sin(12\pi\frac{(y-l_y/4)}{l_y}) + 1) & \text{if } 5l_y/24 < y < 7l_y/24, \\ 1 & \text{if } 7l_y/24 < y < 17l_y/24, \\ 1/2(\sin(12\pi\frac{(y-2l_y/3)}{l_y}) + 1) & \text{if } 17l_y/24 < y < 19l_y/24, \\ 0 & \text{if } 19l_y/24 < y < l_y. \end{cases} \tag{3.2}$$

With this smoothing function, the high-energy region and the combined low-energy regions have the same length. Both are five times larger than each of the two mixing layers. As an illustration, the contour plot of the initial energy density is shown in Fig. 2. As far as the numerics are concerned, our DNS was performed using a pseudo-spectral dealiased code. The grid resolution adopted consists of $512 \times 1024 \times 512$ points. The higher resolution dimension being the direction of inhomogeneity, taken here to be y.

3.2. *Kinetic energy diagnostics*

One of the major motivations of this study is to investigate the effect of inhomogeneities on the properties of the turbulence. Since the direction of inhomogeneity is along y, it is convenient to present statistics obtained by averaging over the x and z directions.

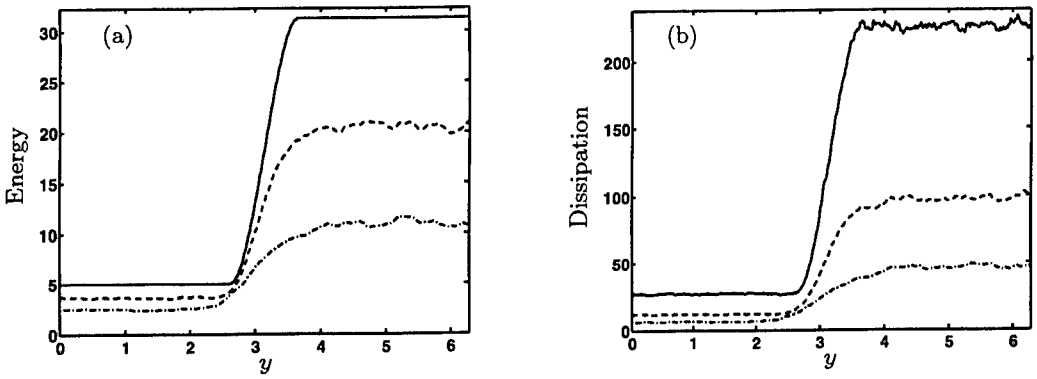


FIGURE 3. (a) Energy and (b) Dissipation rate profiles across the mixing layer calculated from (3.3) and (3.4); ——— : $t^* = 0$; - - - - - - : $t^* = 0.56$; —·—· : $t^* = 1.51$.

For instance, the kinetic energy and dissipation rate profiles are calculated from the expressions:

$$E(y) = \frac{1}{2}\overline{|u_i(\mathbf{x})|^2} = \frac{1}{n_x n_z}\sum_{x,z}\frac{1}{2}|u_i(\mathbf{x})|^2\,, \tag{3.3}$$

$$\epsilon(y) = 2\,\nu\,\overline{S_{ij}(\mathbf{x})S_{ij}(\mathbf{x})}\,, \tag{3.4}$$

where $S_{ij}(\mathbf{x}) = (\partial_i u_j + \partial_j u_i)/2$. Here, and in the rest of this paper, the overbar $\overline{\cdots}$ denotes averaging over the planes perpendicular to the direction of inhomogeneity. Figures 3(a) - 3(b) represent the profiles of the kinetic energy and the dissipation rate at three different times in the simulation. Time has been normalized using the initial eddy turnover time, $t^* = t\epsilon_0/k_0$ where t is the dimensional time, k_0 is the initial average turbulent kinetic energy and ϵ_0 is the initial average dissipation rate. The Figs. 3 demonstrate that as the decay proceeds, the mixing-layer widens but the homogeneous regions remain largely discernible. Fig. 4(a) shows the temporal decay of the average energy in the high-energy and low-energy homogeneous regions. Assuming an asymptotic power-law decay $E(t) \sim t^n$, a decay exponent of $n = -1.3$ is found in the high-energy homogeneous region while in the low-energy region the decay exponent is $n = -1.1$ (the global energy decay has a decay exponent of $n = -1.3$). These decay rates are compatible with the DNS of Briggs *et al.* (1996) for which a k^4 low wave–vector energy spectrum was adopted as in the present simulation. In Fig. 4(b) the 2D spectra defined in (2.4) are presented to confirm that the flow is sufficiently resolved. As was observed in Briggs *et al.* (1996), the energy of the high wave–numbers decays faster with time than the energy of the low wave–numbers. It is noted that for the discretization used and the times considered, the energy peaks remain at a constant wave-vector in the homogeneous regions. The strong influence from the homogeneous layers seems to induce a shift of this energy peak in the mixing layer towards higher wave–vectors, though this effect remains moderate for the times considered.

3.3. *Intermittency*

The skewness and kurtosis of a velocity component u_i are respectively defined as,

$$S_{u_i} = \frac{\overline{u_i^3}}{(\overline{u_i^2})^{\frac{3}{2}}}, \qquad K_{u_i} = \frac{\overline{u_i^4}}{(\overline{u_i^2})^2}. \tag{3.5}$$

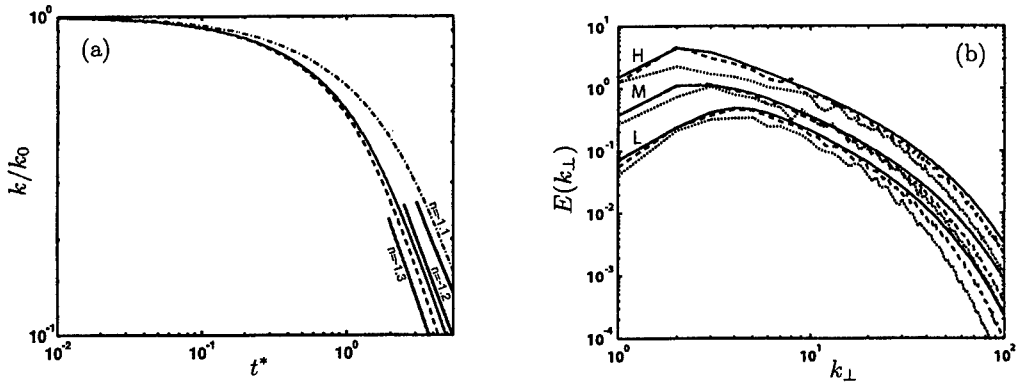


FIGURE 4. (a) Energy decays of the high (------) and low (–·–·) energy homogeneous regions; (———) represents the global energy decay. All curves have been normalized using their initial value of k_0. (b) 2D spectra $E(k_\perp, y)$ (defined by (2.4)) computed inside the high (H) and low (L) homogeneous regions and the mixing-layer (M) for three different times; ——— : $t^* = 0$; ------ : $t^* = 0.56$; –·–· : $t^* = 1.51$.

For homogeneous isotropic turbulence, measures of these quantities show that they are very close to those calculated for a Gaussian signal, i.e., $S = 0$ and $K = 3$.

The skewness profile of v is shown in Fig. 5(a). The y direction has been normalized by the half-width $l_{1/2}$ of the mixing layer and centered around the inflection point of the variance of v. Other skewness and kurtosis diagnostics are normalized in a similar fashion (see Veeravalli & Warhaft (1989) for the details of this normalization procedure). The skewness profile of v exhibits a sharp deviation from the Gaussian value around the location of the mixing layer. As described in Veeravalli & Warhaft (1989), this behaviour is attributed to the intermittent penetration into the low-energy region of structures originating from the high-energy region (a similar penetration of structures from the low-energy region into the high-energy region is certainly also happening but is however a lot less frequent). Agreement with experimental data from Veeravalli & Warhaft (1989) is very good both in terms of the location of the peak and its amplitude. For symmetry reasons, it is expected that the skewness of u and w should remain close to zero. Up to statistical deviations, this is confirmed in our simulation (although not illustrated in this paper). Kurtosis profiles of the velocity components are shown in Fig. 5(b,c,d) and display deviations from the Gaussian value of 3 again around the location of the mixing layer. In the Kurtosis of the u, we observe an unexpectedly high peak in the profile (compared to the experimental data). At this point we attribute this issue to the fact that the profile was computed from a single realization of the flow (although averaging in the (x, z) planes was performed). We also note, however, an initial small peak in this Kurtosis component present in the initial condition (in contrast to the Kurtosis of the other two velocity components) but it is not clear whether or not it was amplified during the evolution of the flow and by what mechanism. The other two Kurtosis profiles agree very well with the experimental data again both in terms of the location of the peaks and their amplitudes. Both the numerical simulation and the experiments indicate that the deviations from the Gaussian values for S and K occur on the low energy side of the inflection points. This supports the idea that these deviations result from the more likely penetration of intermittent structures from the high-energy region into the low-energy region. Finally, it must be stressed that the initialization procedure presented in section 2, though quite sophisticated, does not allow imposition of the initial skewness or the

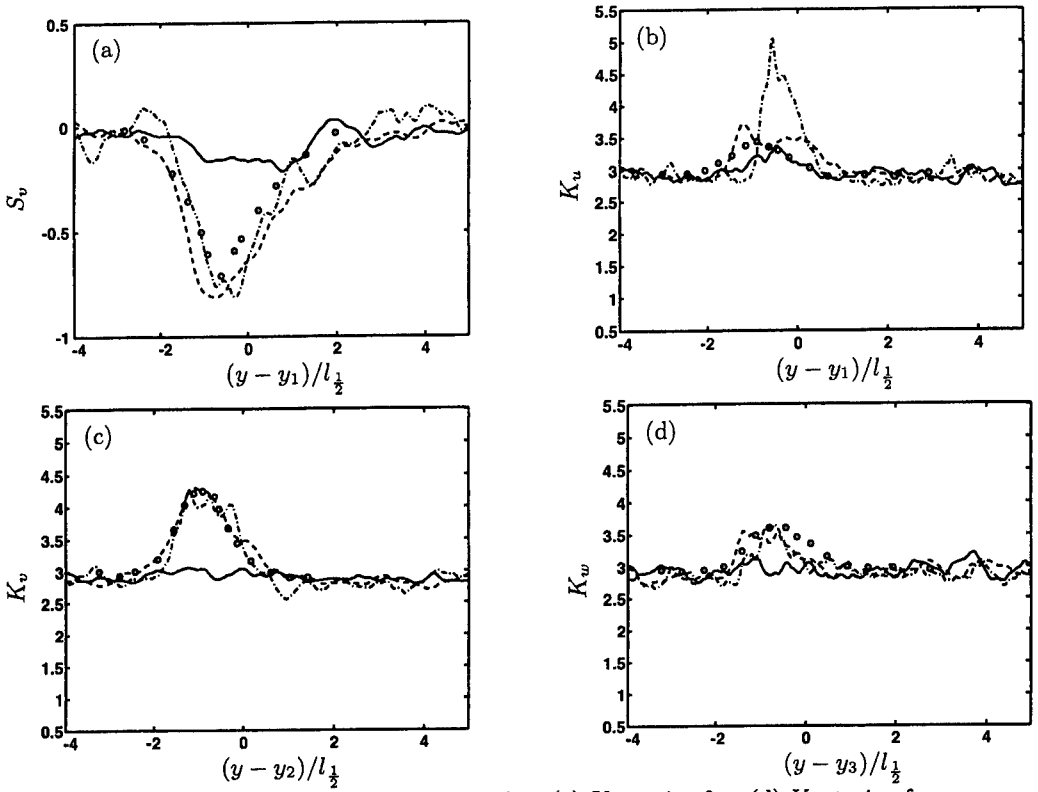


FIGURE 5. (a) Skewness of v; (b) Kurtosis of u; (c) Kurtosis of v; (d) Kurtosis of w; ——— : $t^* = 0$; ------ : $t^* = 0.56$; -·-·- : $t^* = 1.51$; o: experimental data from Veeravalli & Warhaft (1989). At $t^* = 0$ the numerical curves are close to their Gaussian value since the penetration mechanism described in the text has not occurred yet.

kurtosis profiles in the region of the mixing layer (Gaussian values are in fact observed everywhere for the initial profiles as shown in Fig. 5 except for a small deviation for K_u as mentioned above). The fact that the DNS later reproduces the experimental profiles observed in the mixing layer indicate that the transport mechanisms are successfully resolved.

4. LES of the shear-free mixing-layer

4.1. *Notations and conventions - LES model*

Starting from the Navier-Stokes equations, one obtains the LES equations (4.1) by applying a filter, here denoted $\widetilde{\cdots}$ (since our code is spectral, we will only consider spectral cut-offs for the LES filter):

$$\partial_t \tilde{u}_i + \partial_j(\widetilde{\tilde{u}_j \tilde{u}_i}) = -\partial_i \tilde{p} + \nu \triangle \tilde{u}_i - \partial_j \tilde{\tau}_{ij}. \tag{4.1}$$

The unknown subgrid-scale stress (SGS) tensor $\tilde{\tau}_{ij} = \widetilde{u_i u_j} - \widetilde{\tilde{u}_i \tilde{u}_j}$ needs to be modelled in terms of $\tilde{u}_i$ in order to close (4.1). In this work, we will use for τ_{ij} a model proposed in Wong & Lilly (1994) and further studied in Carati *et al.* (1995) and in Dantinne *et al.* (1998). This model, which can be considered as a variant of the dynamic Smagorinski model (Smagorinsky 1963; Germano *et al.* 1991; Lilly 1992; Germano 1992), has been

shown to perform very well in the context of homogeneous isotropic turbulence and its predictions are extremely close to the dynamic Smagorinski model. The advantage of this model rests upon the ease with which its dynamic version can be implemented. The definition of the model is the following:

$$\tilde{\tau}_{ij} - \frac{1}{3}\tilde{\tau}_{kk}\delta_{ij} = -2C\tilde{\Delta}^{\frac{4}{3}}\tilde{S}_{ij}, \tag{4.2}$$

where $\tilde{S}_{ij} = \frac{1}{2}(\partial_i\tilde{u}_j + \partial_j\tilde{u}_i)$ is the resolved strain tensor and $\tilde{\Delta}$ is the LES filter width. The dimensional parameter C is evaluated by introducing a second (coarser) filter $\widehat{\cdots}$ (the test filter) and using the dynamic procedure:

$$C = \frac{1}{2(\tilde{\Delta}^{4/3} - \widehat{\Delta}^{4/3})} \times \frac{< \widehat{L}_{ij}\widehat{S}_{ij} >}{< \widehat{S}_{ij}\widehat{S}_{ij} >} \tag{4.3}$$

where $\widehat{L}_{ij} = \widehat{\tilde{u}_i\tilde{u}_j} - \widehat{\tilde{u}_i}\widehat{\tilde{u}_j}$ is the Leonard tensor (note that we have systematically used the property $\widehat{\widehat{\cdots}} \equiv \widehat{\cdots}$ valid for spectral cut-offs). As in the dynamic Smagorinski model, the only free parameter available is the ratio of the spectral cut-offs: $\tilde{\Delta}/\widehat{\Delta}$. In the following discussion this ratio will be assumed to be equal to 2. For homogeneous isotropic turbulence, the averages $\langle\cdots\rangle$ in (4.3) are obtained by averaging over the whole computational domain. The idea is of course that, since turbulence is homogeneous, the constant C should be statistically independent of the position. For inhomogeneous flows in one direction, like the shear-free mixing layer or the channel flow, dependence on the direction of inhomogeneity is introduced by averaging quantities only over the other two homogeneous directions. This is justified only if the flow is not too inhomogeneous. The dynamic coefficient C then depends explicitly on the inhomogeneous direction: $C = C(y)$. Our LES condition was obtained by filtering (with a sharp spectral cut-off) the initial DNS field down to $32 \times 64 \times 32$ modes. Thus, only $\frac{1}{16}$ of the gridpoints are retained in each direction for the LES, meaning that there is one LES grid point for about 4 000 DNS grid points. The box-size is unchanged and remains $2\pi \times 4\pi \times 2\pi$. In our study we have also included a run obtained at LES resolution but with no subgrid-scale stress model to emphasize the effect of the model in the LES simulation. For comparison we have filtered the DNS fields stored during the simulation down to $32 \times 64 \times 32$ modes.

4.2. *Comparison of the filtered DNS and the LES*

Figure 6(a) represents the temporal evolution of the normalized global kinetic energy E/E_0. From the graph it is clear that the simulation with LES model does a very good job in reproducing this diagnostic, while the run with no model does not. Likewise, Figs. 6(b) and 6(c) show that the 2D spectra with LES modelling are in good agreement with DNS data. 2D spectra gathered from the run with no model exhibit a strong pile up of energy in the high wave–number side of spectra, indicating that the flow is not adequately resolved in that case.

To further illustrate the decay of the kinetic energy, we display in Fig. 7(a) and 7(b) the profiles of the kinetic energy at two different times. This is of course a more sensitive diagnostic since it retains information about the inhomogeneity of the flow. Both figures again reveal a good agreement between the DNS and LES runs and a poor behaviour of the run without modelling. Variance profiles of u, v and w have been examined (not shown) and again the LES matches the DNS very nicely, whereas the no model simulation performs poorly. For our assessment of LES we have retained the same intermittency diagnostics described earlier: the skewness and the kurtosis of the velocity components.

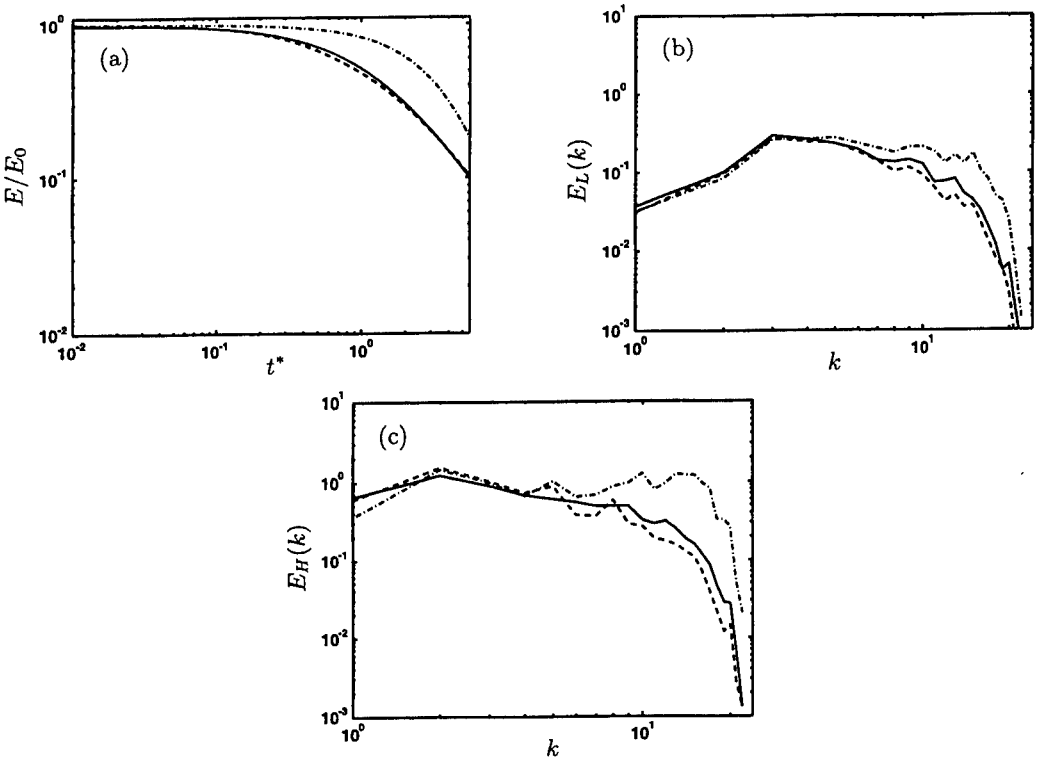


FIGURE 6. (a) Evolution with time of the normalized global kinetic energy E/E_0; (b) and (c) 2D spectra $E(k_\perp, y)$ (defined by (2.4)) computed inside the high (H) and low (L) homogeneous regions for time $t^* = 1.51$. In both figures, ——— : filtered DNS; ------ : LES; –·–· : no model.

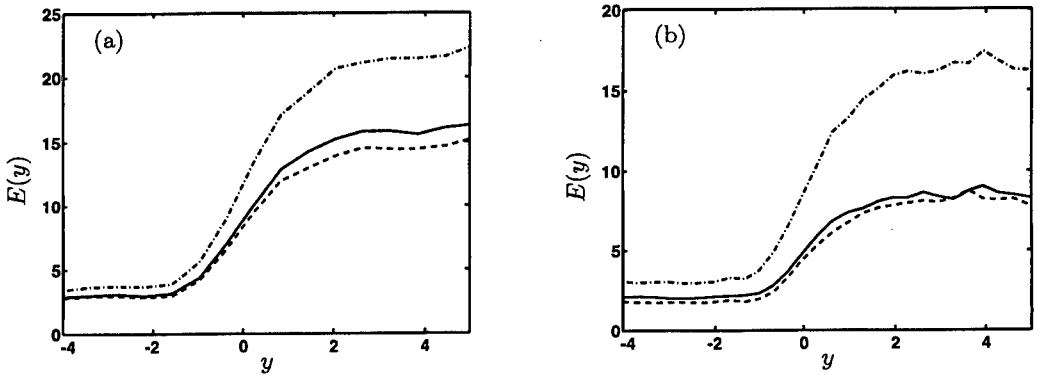


FIGURE 7. Energy profile across the mixing-layer calculated from (3.3) at times (a) $t^* = 0.56$, (b) $t^* = 1.51$. In both figures, ——— : filtered DNS; ------ : LES; –·–· : no model.

A sample of those quantities is displayed in Fig. 8. Once again, the LES run produces results which compare well with the filtered DNS data. Surprising at first, the run without subgrid-scale stress model also performs quite well. However, since the intermittency is attributed to large-scale structures penetrating the low energy region from the high energy region this is to be expected. Indeed, looking at the spectra displayed in Fig. 6(c),

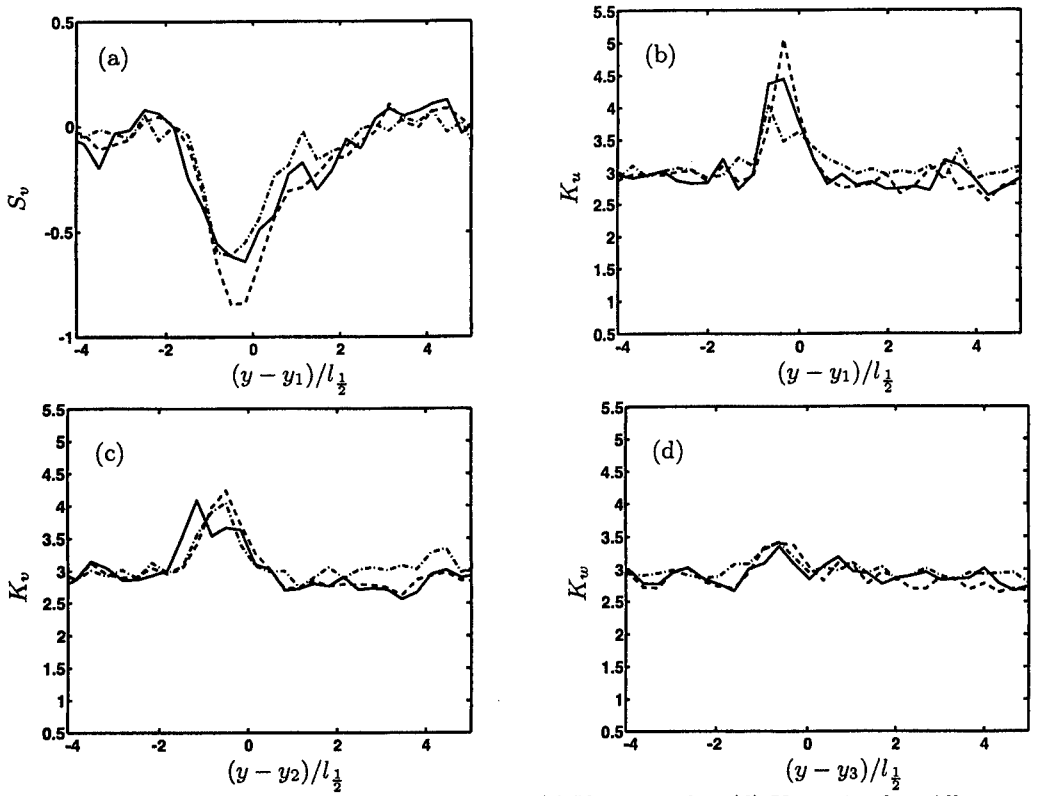


FIGURE 8. (a) Skewness of v; (b) Kurtosis of u; (c) Kurtosis of v; (d) Kurtosis of w. All curves computed at $t^* = 1.51$. ——— : filtered DNS; ------ : LES; –·–· : no model.

we see that the run without subgrid-scale stress model is not ill-behaved for modes at the lowest wave–numbers.

5. Conclusions

This study of the shear-free mixing layer reveals that DNS is capable of reproducing most of the aspects of the experimental database that have been produced by Veeravalli & Warhaft (1989). Energy, dissipation rate and velocity variance profiles are accurately reproduced. Also, departure from Gaussianity inside the mixing layer revealed by the measurement of the skewness and the kurtosis of the velocity field are also in excellent agreement with the experimental observation. This is particularly satisfactory since inside the mixing layer the initial values of these quantities cannot be prescribed by the initialization procedure and are entirely produced at later times by the transfer mechanisms simulated by the DNS. It is also observed that, in the absence of shear, no significant anisotropy is observed in this flow. This is consistent with previous numerical results and strongly supports the use of eddy-viscosity type models for the LES of such flows. As a consequence, it is not surprising that comparisons between the predictions of LES using such eddy-viscosity models and DNS show very good agreement.

Acknowledgements

The authors are very grateful to M. Rogers and G. Burton for their comments on this manuscript. We also thank Dr. S. Veeravalli for providing us some data gathered during the Veeravalli & Warhaft (1989) experiment. B.K. and D.C. are researchers of the Fonds National pour la Recherche Scientifique (Belgium). O.D. is "boursier FRIA" (Belgium). This work has been supported by the Communauté Française de Belgique (ARC 02/07-283) and by the contract of association EURATOM - Belgian state. The content of the publication is the sole responsibility of the authors and it does not necessarily represent the views of the Commission or its services.

REFERENCES

BATCHELOR, G. K. 1953 *The theory of homogeneous turbulence*. Cambridge University Press.

BRIGGS, D., FERZIGER, J., KOSEFF, J. & MONISMITH, S. 1996 Entrainment in a shear–free turbulent mixing layer. *J. Fluid. Mech.* **310**, 215–241.

CARATI, D., JANSEN, K. & LUND, T. 1995 A family of dynamic models for large-eddy simulation. In *Annual Research Briefs - 1995* (ed. P. Moin & W. Reynolds), pp. 35–40. Stanford University and NASA Ames Research Center: Center for Turbulence Research.

COMTE-BELLOT, G. & CORRSIN, S. 1971 Simple eulerian time correlations of full- and narrow-band velocity signals in grid generated 'isotropic' turbulence. *J. Fluid Mech.* **48**, 273–337.

DANTINNE, G., JEANMART, H., WINCKELMANS, G. S., LEGAT, V. & CARATI, D. 1998 Hyperviscosity and vorticity-based models for subgrid scale modeling. *Applied Scientific Research* **59**, 409–420.

GERMANO, M. 1992 Turbulence: the filtering approach. *J. Fluid Mech.* **238**, 325–336.

GERMANO, M., PIOMELLI, U., MOIN, P. & CABOT, W. 1991 A dynamic subgrid-scale eddy-viscosity model. *Phys. Fluids A* **3** (7), 1760–1765.

GLIBERT, B. 1980 Diffusion mixing in grid turbulence. *J. Fluid Mech.* **100**, 349–365.

LILLY, D. 1992 A proposed modification of the germano subgrid-scale closure method. *Phys. Fluids* **4**, 633–635.

ROGALLO, R. 1981 Numerical experiments in homogeneous turbulence. NASA technical Memorandum 81315. NASA, Ames Research Center.

SHEBALIN, J. V., MATTHAEUS, W. H. & MONTGOMERY, D. 1983 Anisotropy in MHD turbulence due to a mean magnetic field. *J. Plasma Phys.* **29** (3), 525–547.

SMAGORINSKY, J. 1963 General circulation experiments with the primitive equations: 1. the basic experiment. *Month. Weather Rev.* **91**, 99–164.

VEERAVALLI, S. & WARHAFT, Z. 1987 The interaction of two distinct turbulent velocity scales in the absence of mean shear. In *Turbulent Shear Flows 5* (ed. L. T. S. Bradbury *et al*), pp. 31–43. Springer.

VEERAVALLI, S. & WARHAFT, Z. 1989 The shearless turbulence mixing layer. *J. Fluid Mech.* **207**, 191–229.

WONG, V. & LILLY, D. 1994 A comparison of two subgrid closure methods for turbulent thermal convection. *Phys. Fluids* **6**, 1016–1023.

On the computation of space-time correlations by large-eddy simulation

By Guo-Wei He†, Meng Wang AND Sanjiva K. Lele

1. Motivation and objectives

Sound radiated by turbulent flow is dependent on the space-time characteristics of the flow field. According to Lighthill's theory (Lighthill 1952; Proudman 1952), acoustic power spectra in the far-fields are determined by the two-time, two-point Eulerian velocity correlations. This has significant implications to the use of large eddy simulation (LES) for aerodynamic noise prediction. The existing subgrid scale (SGS) models are mostly constructed to predict spatial statistics such as energy spectra (Meneveau & Katz 2000). However, it is not clear whether these models can lead to accurate space-time correlations, or frequency contents at individual wavenumbers. The latter information is essential to accurate noise predictions, because for a given frequency, only the spectral element of the source field corresponding to the acoustic wavenumber in a given direction can radiate in that direction (Crighton 1975). This represents a very small fraction of flow energy, and is very susceptible to numerical and modeling errors. Hence, accurate prediction of the space-time correlation is a new requirement imposed on SGS modeling by aeroacoustic applications.

For brevity, we henceforth refer to the two-time, two-point correlation of the velocity field simply as time correlation. It describes the space-time statistics of turbulent flows. The time correlation can be equivalently expressed by a two-time correlation of velocity Fourier modes in spectral space

$$C(k,\tau) = \langle u_i(\mathbf{k},t)u_i(-\mathbf{k},t+\tau)\rangle, \tag{1.1}$$

or its normalized form

$$R(k,\tau) = \frac{\langle u_i(\mathbf{k},t)u_i(-\mathbf{k},t+\tau)\rangle}{\langle u_i(\mathbf{k},t)u_i(-\mathbf{k},t)\rangle}. \tag{1.2}$$

Previous research (He, Rubinstein & Wang 2002) compared the normalized time correlations or correlation coefficients in forced isotropic turbulence calculated by direct numerical simulation (DNS) and LES using a standard spectral eddy viscosity model (Chollet & Lesieur 1981). The comparisons show that the LES overpredicts decorrelation time scales. A following-up study (He, Wang & Lele 2002) made the comparisons in decaying turbulence, using the classic Smagorinsky model (Smagorinsky 1963), the dynamic Smagorinsky model (Germano et al. 1991) and the multiscale LES method (Hughes, Mazzei & Oberai 2001). The overpredictions are still observed. These numerical observations motivated the present analysis to investigate the overpredictions and their influence on sound power spectra. The analysis will be carried out for the un-

† Permanent address: LNM, Institute of Mechanics, Chinese Academy of Sciences, Beijing, 100080, China; Email: hgw@lnm.imech.ac.cn

normalized time correlations, not the normalized ones as before, since the former are the ones actually used in the computation of sound power spectra.

The analysis starts with a generalization of Kraichnan's sweeping hypothesis (Kraichnan 1964) from stationary turbulence to decaying turbulence. This involves replacing a constant convection velocity by a time-dependent one in a simple kinematic model. The solution of the kinematic model defines a time-dependent sweeping velocity. Kraichnan's sweeping hypothesis is the foundation of the turbulence theory on time correlation. Kaneda and Gotoh (1991) and Kaneda (1993) developed the Lagrangian renormalization group theory and the Taylor expansion technique for time correlations. Rubinstein and Zhou (2000) used the sweeping hypothesis to formulate the scaling law of sound power spectra.

The present analysis on time correlations will shed some light on the ability of LES to predict sound power spectra, since the latter can be analytically expressed as an integration of time correlations using the quasi-normal closure assumption. Previous evaluations (e. g. Witkowska, Juvé & Brasseur 1997; Seror et al. 2001) are made directly on acoustic fields. These calculations unavoidably have to cope with the numerical errors caused by the truncation of the source region (Crighton 1993; Wang, Lele & Moin 1996). Instead, we will discuss the influences of the SGS modeling on the accuracy of sound prediction through an analysis of time correlations.

In this paper, we consider decaying homogeneous isotropic turbulence. Unlike stationary turbulence, the time correlations in decaying turbulence are dependent on both time separations and starting time. Therefore, two different starting time will be chosen, one at the energy propagation stage and another at the final decaying stage.

2. Main results

2.1. *Numerical results*

A decaying homogeneous isotropic turbulence in a cubic box of side 2π is simulated by DNS with grid size 256^3 and LES with grid size 64^3. A standard pseudo-spectral method is used, in which spatial differentiation is made by the Fourier spectral method, time advancement is made by a second-order Adams-Bashforth method with the same time steps for both DNS and LES, and molecular viscous effects are accounted for by an exponential integrating factor. All nonlinear terms are dealiased with the two-thirds rule.

The following SGS models are used in the LES:

(1) The spectral eddy viscosity model: we use the Chollet-Lesieur standard form for the spectral eddy viscosity (Chollet & Lesieur 1981), where the cutoff energy is evaluated from the LES.

(2) The Smagorinsky model (Smagorinsky 1963): the Smagorinsky constant is $C_s = 0.22$ and the filter width is set equal to the inverse of the largest effective wave number $k_c = 21$.

(3) The dynamic Smagorinsky model (Germano et al. 1991): the Smagorinsky coefficients are determined by the Germano identity. The grid filter width is k_c^{-1} and the test filter width is taken as $2k_c^{-1}$.

(4) The multi-scale LES method (Hughes et al. 2001): we decompose the filtered Navier-Stokes equations into the large scale equations for the lower one-half Fourier modes and the small scale equations for the remaining half Fourier modes. The dynamic Smagorinsky model is only applied to the small scale equations.

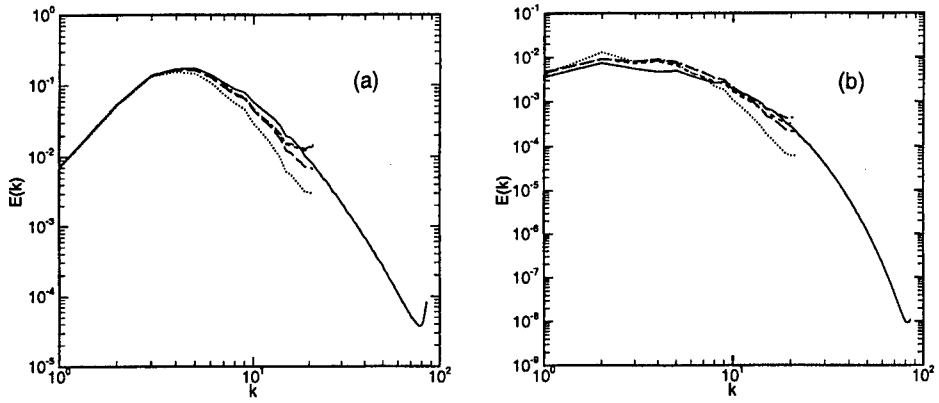


FIGURE 1. Energy spectra at (a) $t = 0.5$ and (b) $t = 4.0$ ——— DNS; - - - - dynamic Smagorinsky model; —·— multiscale LES; ····· Smagorinsky model; — — — spectral eddy viscosity model.

The initial condition for DNS is an isotropic Gaussian field with energy spectrum

$$E(k,0) \propto (k/k_0)^4 \exp[-2(k/k_0)^2], \tag{2.1}$$

where $k_0 = 4.68$ is the wave number corresponding to the peak of the energy spectrum. The shape of the energy spectrum excludes the effects of the box size. The initial Reynolds number based on Taylor's microscale is 127.4. The initial condition for LES is obtained by filtering the initial DNS velocity fields with filtering wavenumber $k_c = 64/3 \approx 21$. Therefore, the initial LES and filtered DNS velocity fields are exactly the same. At early stages, the LES and DNS velocity fields are highly correlated due to the same initial conditions. Therefore, the time correlations of the LES velocity field are nearly the same as those of the DNS field. As time progresses, the LES fields become decorrelated from the DNS fields. The difference in time correlations between the LES and DNS velocity fields are then observed. Therefore, we first advanced the DNS and LES velocities in time to decorrelate them before starting to calculate the time correlations.

The energy spectra at $t = 0.5$ and $t = 4.0$ are presented in Fig. 1. Generally speaking, the LES results are in good agreement with the DNS result at small wavenumbers but drop faster than DNS at large wavenumbers. The decay of the total resolved energy is presented in Fig. 2. The results from LES with all SGS models follow the DNS results with some deviations throughout the entire time range. They exhibit excessive dissipation before the time $t = 1.5$ (the energy propagation range) and insufficient dissipations after $t = 1.5$ (the final decay range). Note that $t = 0$ does not correspond to the start time of the simulation. Rather, it is 0.1 time units after the start, and hence the deviations among DNS and LES results are already significant. In both Figs. 1 and 2, the multiscale LES results are the best of all models and the classic Smagorinsky model results are the worst. The dynamic Smagorinsky model and spectral eddy viscosity model yield results in the middle with small differences.

Figure 3 plots the un-normalized time correlations of the velocity fields from the DNS and LES for wavenumbers $k = 5, 9, 13$, and 17, spanning a range of scales from the integral scale to the lower end of the resolved scale. The starting time is $t = 0.5$. It clearly shows that there exist discrepancies between the LES and DNS results, and that the discrepancies become larger with increasing wavenumbers. Again, the classic Smagorinsky

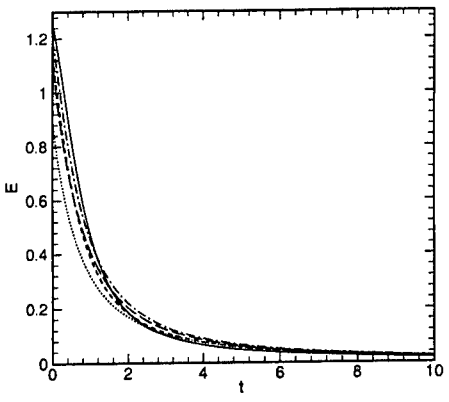


FIGURE 2. Decay of total resolved energy. —— DNS; ---- dynamic Smagorinsky model; —·— multiscale LES; ····· Smagorinsky model; — — — spectral eddy viscosity model.

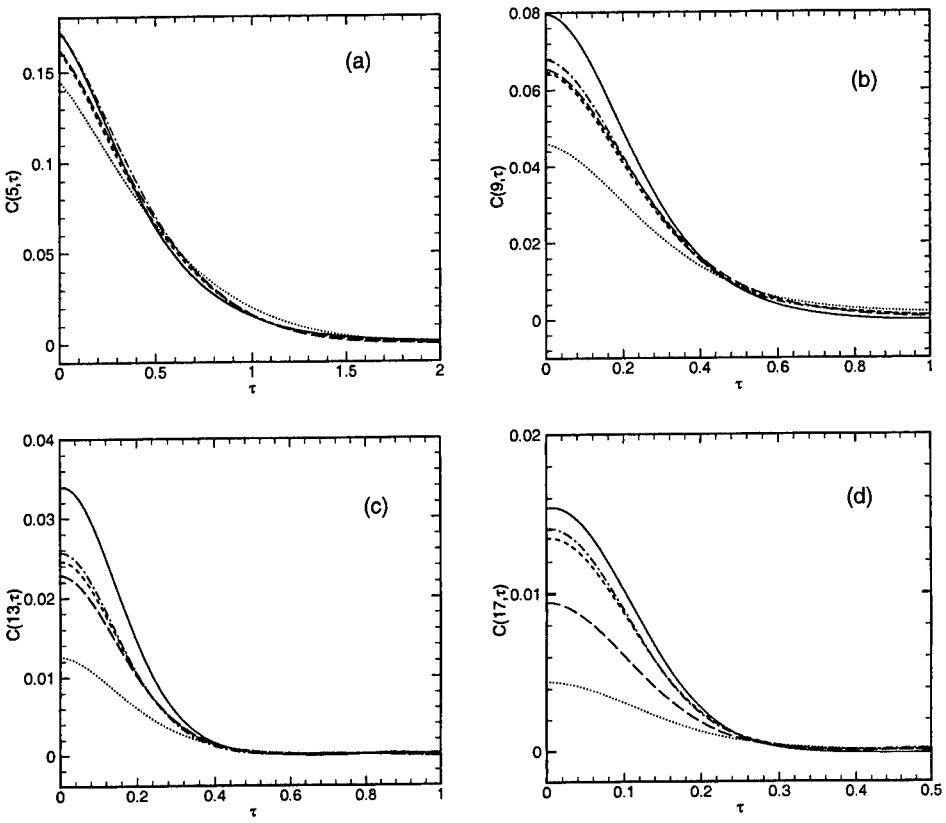


FIGURE 3. Time correlation $C(k,\tau)$ vs time lag τ with starting time $t = 0.5$ for (a) $k = 5$, (b) $k = 9$, (c) $k = 13$, (d) $k = 17$. —— DNS; ---- dynamic Smagorinsky model; —·— multiscale LES; ····· Smagorinsky model; — — — spectral eddy viscosity model.

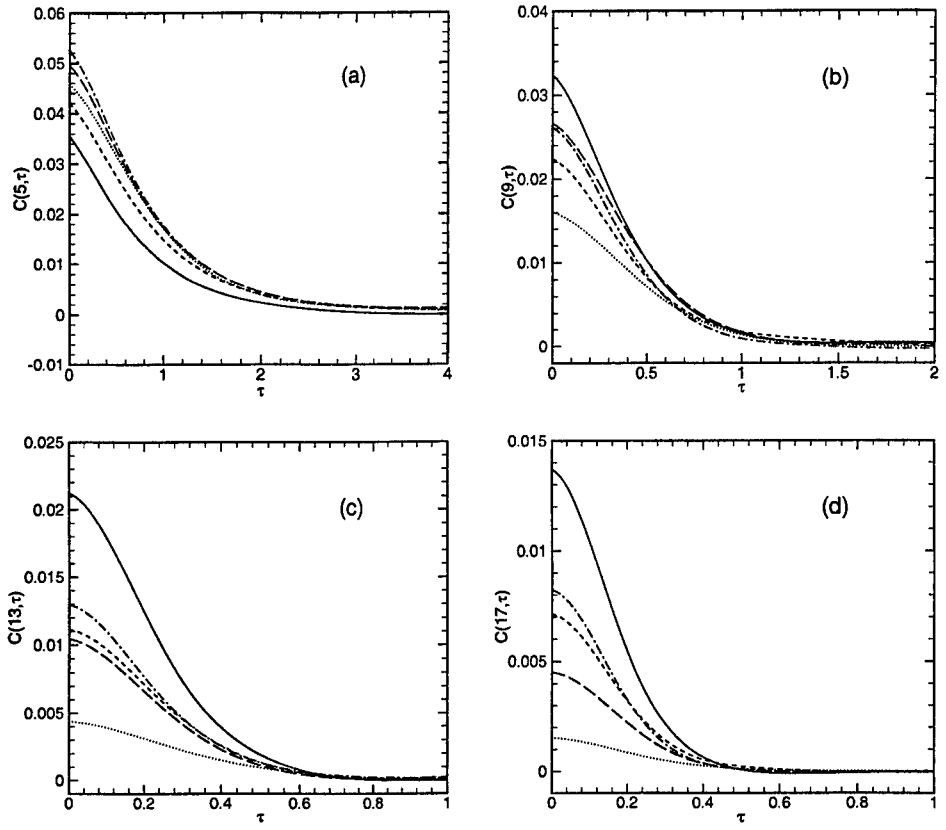


FIGURE 4. Time correlation $C(k,\tau)$ vs time lag τ with starting time $t = 1.5$ for (a) $k = 5$, (b) $k = 9$, (c) $k = 13$, (d) $k = 17$. —— DNS; - - - - dynamic Smagorinsky model; —·— multiscale LES; ····· Smagorinsky model; — — — spectral eddy viscosity model.

model results are the least accurate of all models, the multiscale LES method is the most accurate, and the spectral eddy viscosity model and the dynamic Smagorinsky model lie in between, the latter being slightly better than the former.

Figure 4 plots the same time correlations as in Fig. 3 but with a different starting time $t = 1.5$. The discrepancies observed are qualitatively the same as in the $t = 0.5$ case, which indicates that the SGS modeling errors equally affect the time correlations in the final decay range.

In summary, it is observed in decaying isotropic turbulence that discrepancies exist between the un-normalized time correlations calculated from DNS and those from the LES. These discrepancies will be analysed in the next section.

2.2. *Analysis of the numerical results*

The analysis is based on the generalized sweeping hypothesis for decaying turbulence. In the sweeping hypothesis for stationary isotropic turbulence, the convection velocity is constant (Kraichnan 1964). However, in decaying turbulence, the convection velocity varies with time. A generalization can be made by introducing a time-dependent convection velocity, which evolves slowly relative to the time scales of velocity fluctuations.

Consider a fluctuating velocity Fourier mode $\mathbf{u}(\mathbf{k},t)$ convected by a bulk velocity $\mathbf{v}(t)$. We assume that the wavenumbers $\mathbf{k}$ of the fluctuating velocity are sufficiently large. The flow scales associated with these wavenumbers are small, over which the convection velocity is spatially uniform and relatively large in magnitudes. In this case, the convection effect is dominant. The governing equation for the fluctuating velocity modes is therefore

$$\frac{\partial \mathbf{u}(\mathbf{k},t)}{\partial t} + i[\mathbf{k}\cdot\mathbf{v}(t)]\mathbf{u}(\mathbf{k},t) = 0, \tag{2.2}$$

which yields

$$\mathbf{u}(\mathbf{k},t+\tau) = \mathbf{u}(\mathbf{k},t)\exp\left(-i\int_t^{t+\tau}\mathbf{k}\cdot\mathbf{v}(s)ds\right). \tag{2.3}$$

Then, the time correlation can be expressed by

$$\begin{aligned}&\langle\mathbf{u}(\mathbf{k},t+\tau)\mathbf{u}(-\mathbf{k},t)\rangle\\ &= \langle\mathbf{u}(\mathbf{k},t)\mathbf{u}(-\mathbf{k},t)\rangle\exp\left(-\frac{1}{2}k^2\int_t^{t+\tau}\int_t^{t+\tau}\langle\mathbf{v}(s')\mathbf{v}(s'')\rangle ds'ds''\right).\end{aligned} \tag{2.4}$$

In the derivation of (2.4), the convection velocity $\mathbf{v}(t)$ is assumed to be Gaussian and independent of the velocity $\mathbf{u}(\mathbf{x},t)$ at the starting time t. These assumptions can be justified by the near-Gaussianity of the large-scale velocity and its initial independence of the small-scale velocity. By introducing a sweeping velocity

$$V^2(t,\tau) = \frac{1}{\tau^2}\int_t^{t+\tau}\int_t^{t+\tau}\langle\mathbf{v}(s')\mathbf{v}(s'')\rangle ds'ds'', \tag{2.5}$$

we obtain a general expression of time correlation similar to the one in stationary turbulence

$$\langle\mathbf{u}(\mathbf{k},t+\tau)\mathbf{u}(-\mathbf{k},t)\rangle = \langle\mathbf{u}(\mathbf{k},t)\mathbf{u}(-\mathbf{k},t)\rangle\exp\left(-\frac{1}{2}k^2V^2(t,\tau)\tau^2\right). \tag{2.6}$$

The calculation of the sweeping velocity (2.5) can be further simplified by assuming the following form of the bulk velocity correlation

$$\langle\mathbf{v}(s')\mathbf{v}(s'')\rangle = \langle\mathbf{v}^2(s')\rangle\exp\left(-\lambda|s'-s''|\right), \tag{2.7}$$

where λ^{-1} is a correlation time scale. Substituting (2.7) into (2.5), we find

$$V^2(t,\tau) = \frac{1}{\tau^2}\int_t^{t+\tau}\langle\mathbf{v}^2(s')\rangle\lambda^{-1}\left(2-\exp[-\lambda(s'-t)]-\exp[-\lambda(t+\tau-s')]\right)ds'. \tag{2.8}$$

In isotropic turbulence, the bulk velocity is determined by large scale motions. Hence, its decorrelation time scale λ^{-1} is much larger than those of velocity fluctuation modes considered here. Since the time separation τ of interest is within the decorrelation time scales of the velocity fluctuations, we have $\lambda\tau \ll 1$. Using Taylor series expansion with respect to $\lambda\tau$ and ignoring the second and higher order terms in (2.8), we obtain

$$V^2(t,\tau) = \frac{1}{\tau}\int_t^{t+\tau}\langle\mathbf{v}^2(s')\rangle ds'. \tag{2.9}$$

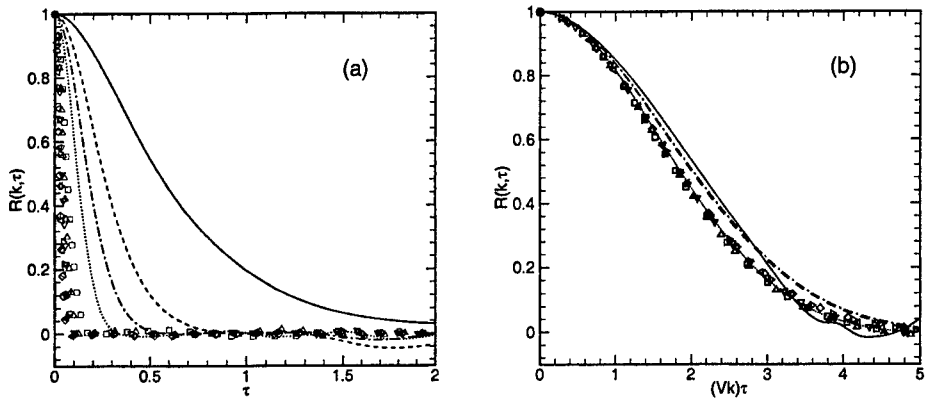


FIGURE 5. Normalized time correlation $R(k,\tau)$ vs (a) un-normalized and (b) normalized time lag for different modes computed using DNS. ——— $k = 5$; - - - - $K = 9$; —·— $k = 13$; ····· $k = 17$; □ $k = 30$; △ $k = 40$; ▽ $k = 50$; ▷ $k = 60$; ◁ $k = 70$; ◇ $k = 80$.

Note that the bulk velocity is associated with the energy-containing motions, and its variance $\langle \mathbf{v}^2(t) \rangle$ is the total energy of the instantaneous velocity field. Since the energy decay is relatively small over the decorrelation time scale, the sweeping velocity can be easily calculated by simple approximations $V^2(t,\tau) \cong \langle \mathbf{v}^2(t+\tau) \rangle$ or $V^2(t,\tau) \cong [\langle \mathbf{v}^2(t) \rangle + \langle \mathbf{v}^2(t+\tau) \rangle]/2$. The former is used in the following discussions.

Figure 5 plots the normalized time correlations $R(k,\tau)$ from DNS for wavenumbers $k = 5, 9, 13, 17, 30, 40, 50, 60, 70$ and 80, where the correlations are normalized by the instantaneous energy spectra. The time separation is un-normalized in Fig. 5(a) and normalized by the scale-dependent similarity variable Vk in Fig. 5(b). The latter figure clearly exhibits that, with time normalization, all curves for different modes collapse. This verifies the validity of the generalized sweeping velocity in decaying turbulence.

Equation (2.6) indicates that the normalized time correlations are solely determined by the sweeping velocities. In the present LES, the sweeping velocities are smaller than that of DNS values because of the reduced total energy. Therefore, the time correlations in LES decay more slowly than the ones in DNS. That is to say, the LES overpredicts the decorrelation time scales compared to DNS. Figure 6 plots the normalized time correlations from the DNS and LES with respect to the un-normalized time for the modes $k = 5, 9, 13, 17$. It confirms that the time correlations from LES decay more slowly than the ones from DNS. Again, the multiscale LES method is the most accurate and the classic Smagorinsky model is the least accurate of the all models tested. The dynamic Smagorinsky model and the spectral eddy viscosity model are in the middle.

Equation (2.6) also indicates that if the time separation is normalized by Vk, the un-normalized time correlations are solely determined by the instantaneous energy spectra. Figure 7 plots the un-normalized correlations vs the normalized time separation. It shows that the LES underestimates the magnitudes of time correlations relative to the DNS results. The underestimation obviously becomes more significant as the wavenumber increases, which is consistent with the more severe drops of the LES energy spectra at high wavenumbers. Again, the relative performance of the SGS models in terms of the magnitudes of time correlations is the same as before.

In conclusion, the discrepancies between the time correlations computed using DNS and LES consist of two parts: the decorrelation time scale and magnitude. The errors in

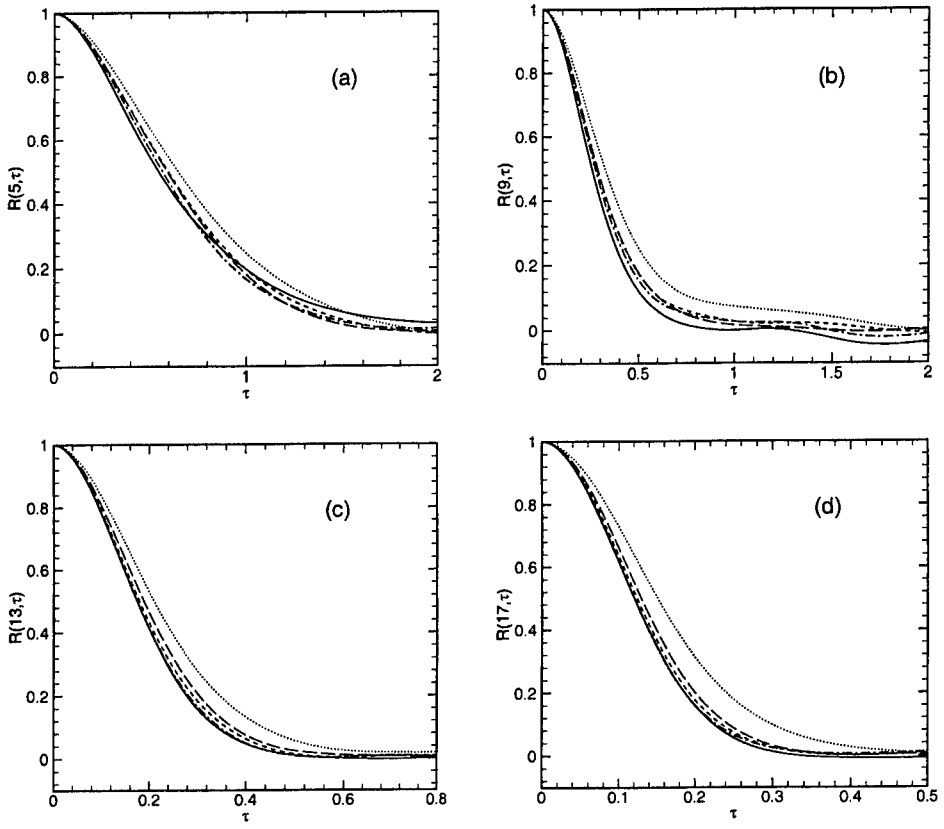


FIGURE 6. Normalized time correlation $R(k,\tau)$ vs time lag τ with starting time $t = 0.5$ for (a) $k = 5$, (b) $k = 9$, (c) $k = 13$, (d) $k = 17$. ——— DNS; - - - - dynamic Smagorinsky model; —·— multiscale LES; ····· Smagorinsky model; — — — spectral eddy viscosity model.

decorrelation scales are induced by the instantaneous sweeping velocity, and the errors in magnitudes are induced by the instantaneous energy spectra. In relative terms, the errors in decorrelation time scales are less significant than those in magnitudes. However, they must not be ignored since the sound power spectra are sensitive to the decorrelation time scale, (see discussions in the next section). Note that the sweeping velocity used in our analysis is the *r.m.s.* of velocity fluctuations, or the square root of the total energy. Thus, an accurate prediction of the instantaneous energy spectra is most critical to the accurate computation of the time correlations.

2.3. *Discussion*

It is difficult to determine the influence of SGS modeling on acoustic power spectra through numerical evaluation in general, since it involves the truncation of the source region (Wang et al. 1996). To avoid this problem, we use an analytical expression of acoustic power spectra based on Lighthill's theory and the quasi-normal closure assumption. The analytical expression is only valid for stationary turbulence. However, reasonable inferences can be drawn for decaying turbulence through this analysis.

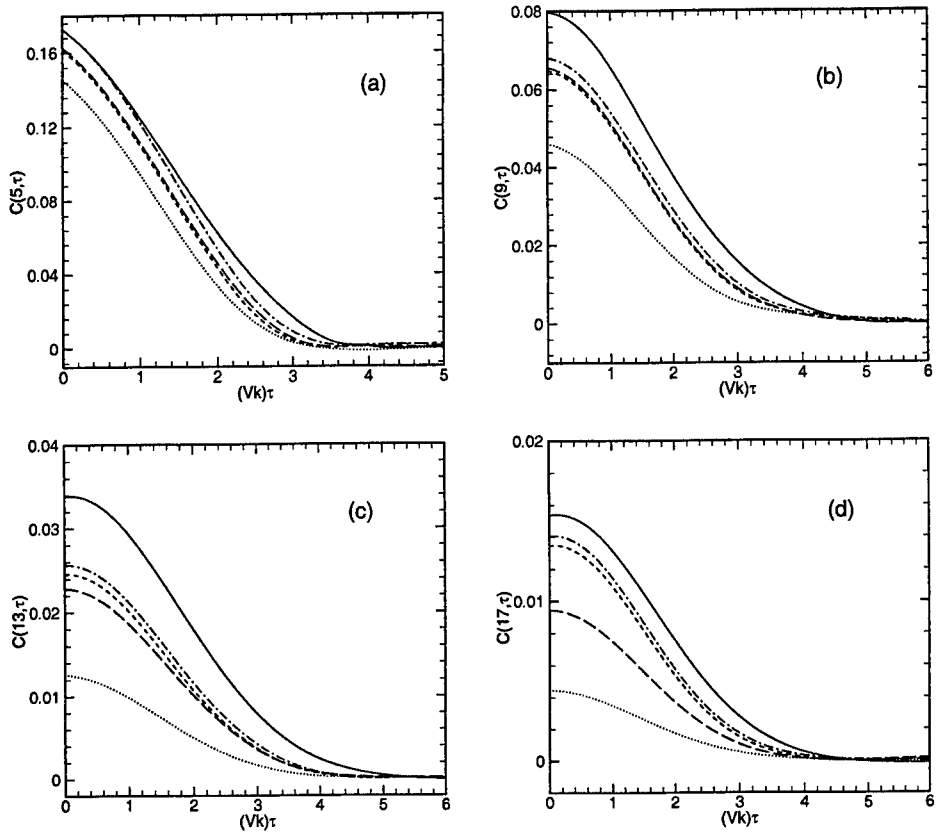


FIGURE 7. Un-normalized time correlation $C(k,\tau)$ vs the normalized time lag τ with starting time $t = 0.5$ for (a) $k = 5$, (b) $k = 9$, (c) $k = 13$, (d) $k = 17$. ——— DNS; - - - - dynamic Smagorinsky model; —·— multiscale LES; ····· Smagorinsky model; — — — spectral eddy viscosity model.

According to Lighthill's theory (Lighthill 1952), the acoustic pressure in a far-field position $\mathbf{x}$ is given by

$$p(\mathbf{x},t) = \frac{1}{4\pi c^2}\frac{x_i x_j}{|\mathbf{x}|^3}\int_\Omega d\mathbf{y}\frac{\partial^2}{\partial t^2}T_{ij}\left(\mathbf{y}, t - \frac{|\mathbf{x}-\mathbf{y}|}{c}\right), \tag{2.10}$$

where $T_{ij}(\mathbf{y},t) = \rho u_i(\mathbf{y},t)u_j(\mathbf{y},t)$ is the Lighthill stress tensor, Ω the source region, ρ the mean far-field density, c the speed of sound in the far-field, and $\mathbf{y}$ a position vector in the source field. Based on this equation, Kraichnan calculated the far-field acoustic power spectral density (Kraichnan 1953)

$$P(\omega) = \pi\frac{\omega^4}{2c^8}\left\langle\left|n_i n_j T_{ij}\left(\frac{\omega\mathbf{n}}{c},\omega\right)\right|^2\right\rangle, \tag{2.11}$$

where $\mathbf{n}$ is the unit vector in the direction of the point $\mathbf{x}$, ω the frequency of the radiated sound, and $T_{ij}(\mathbf{k},\omega)$ the space-time Fourier transformation of the Lighthill stress tensor.

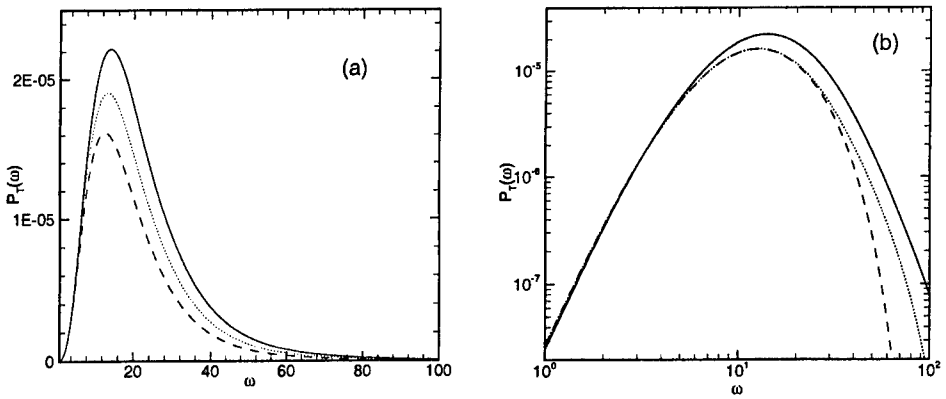


FIGURE 8. Effects of (a) sweeping velocity and (b) unresolved scales on sound power spectra. (a) ——— $V = 1.0$; ····· $V = 0.95$; ---- $V = 0.90$. (b) ——— $V = 1.0$ with full spectra; ····· $V = 0.95$ and $k_c = 25$; ---- $V = 0.95$ and $k_c = 13$.

Using the quasi-normal hypothesis, the acoustic power spectral density function can be written in the form (Rubinstein & Zhou 2002)

$$P(\omega) = \frac{\pi}{2}\rho\frac{\omega^4}{c^5}\frac{32\pi}{15}\int_0^{+\infty} 4\pi k^2 \frac{E^2(k)}{(2\pi k^2)^2}dk \frac{1}{2\pi}\int_{-\infty}^{+\infty} R^2(k,\tau)\exp(-i\omega\tau)d\tau \tag{2.12}$$

In the following discussion, the normalized time correlation $R(k,\tau)$ is taken as the exponential form

$$R(k,\tau) = \exp\left(-\frac{1}{2}k^2V^2\tau^2\right). \tag{2.13}$$

and the energy spectrum $E(k)$ assumes the von Kármán form

$$E(k) = C\epsilon^{2/3}k_0^{-5/3}(k/k_0)^4[1+(k/k_0)^2]^{-17/6}k^{-2}, \tag{2.14}$$

where $k_0 = 5$ defines the peak of energy spectrum. The exponential form and the von Kármán spectrum are the appropriate approximations to the time correlations and the energy spectra, respectively, in our numerical simulations.

With the substitution of (2.13) into (2.12), the non-dimensionalized sound power spectra are given by

$$P_T(\omega) = \frac{2\sqrt{\pi}}{15}\rho M^5\frac{\omega^4}{V}\int_0^{+\infty} k^{-3}E^2(k)\exp\left(-\frac{\omega^2}{4(Vk)^2}\right)dk, \tag{2.15}$$

where $M = V_0/c$ is the Mach number and $V_0 = \omega_0/k_0$. k_0 is the inverse integral length scale and ω_0 the inverse integral time scale.

The influences of the overpredicted decorrelation scales on acoustic power spectra can be seen in Figure 8(a), where the sound power spectra are evaluated according to (2.15) with the sweeping velocities V equal to 1.0, 0.95 and 0.9. The small variations, up to 10%, of the sweeping velocities cause significant reductions of the sound power spectra at higher frequencies. This illustrates the sensitivity of the acoustic power spectra to the sweeping velocities.

The sweeping velocity induced errors can be compounded by the truncation of the energy spectra at high wavenumbers, corresponding to unresolved scales in LES. To test this effect, the energy spectrum is truncated ($E(k)$ set to zero) for either $k > 25$ or $k > 13$. Figure 8(b) plots the acoustic power spectra for the sweeping velocity $V = 0.95$ with the above truncated energy spectra. It shows that the acoustic power spectra drop considerably at moderate to high frequencies, and the spectral peaks are shifted towards left to lower frequencies.

3. Conclusions and future work

Numerical comparisons in decaying isotropic turbulence suggest that there exist discrepancies in time correlations evaluated by DNS and LES using eddy-viscosity-type SGS models. This is consistent with the previous observations in forced isotropic turbulence. Therefore, forcing is not the main cause of the discrepancies. Comparisons among different SGS models in the LES also indicate that the model choice affects the time correlations in the LES. The multi-scale LES method using the dynamic Smagorinsky model on the small scale equation is the most accurate of the all models, the classic Smagorinsky model is the least accurate and the dynamic Smagorinsky model and spectral eddy viscosity model give intermediate results with small differences.

The generalized sweeping hypothesis implies that time correlations in decaying isotropic turbulence are mainly determined by the instantaneous energy spectra and sweeping velocities. The analysis based on the sweeping hypothesis explains the discrepancies in our numerical simulations: the LES overpredicts the decorrelation time scales because the sweeping velocities are smaller than the DNS values, and underpredicts the magnitudes of time correlations because the energy spectrum levels are lower than the DNS ones. Since the sweeping velocity is determined by the energy spectra, one concludes that an accurate prediction of the instantaneous energy spectra guarantees the accuracy of time correlations.

An analytical expression of sound power spectra based on Lighthill's theory and the quasi-normal closure assumption suggests that the sound power spectra are sensitive to errors in time correlations. Small errors in time correlations can cause significant errors in the sound power spectra, which exhibit a sizable drop at moderate to high frequencies accompanied by a shift of the peaks to lower frequencies.

Based on the above analysis, two possible ways to improve the acoustic power spectrum predictions can be considered. The first is to construct better SGS models to improve the LES accuracy for time correlations. The second is to remedy the temporal statistics of the Lighthill stress tensor in order to "recover" the contribution from the unresolved scales in LES to time correlations.

Acknowledgment: We wish to thank Prof. P. Moin, Dr. A. Wray and Dr. R. Rubinstein for helpful discussions. He's work was partly supported by the National Committee of Science and Technology, P. R. China, under the project "Nonlinear Science".

REFERENCES

CHOLLET, J.-P. & LESIEUR, M. 1981 Parameterization of small scales of three-dimensional isotropic turbulence utilizing spectral closure. *J. Atmos. Sci.* **38**, 2747–2757.

CRIGHTON, D. G. 1975 Basic principles of aerodynamic noise generation. *Prog. Aerospace Sci.* **16**, 31-96.

CRIGHTON, D. G. 1993 Computational aeroacoustics for low Mach number flows. *Computational Aeroacoustics*, ICASE/NASA LaRC Series, edited by J. C. Hardin and M. Y. Hussaini, Springer-Verlag, New York, 50-68.

GERMANO, M., PIOMELLI, U., MOIN, P. & CABOT, W. H. 1991 A dynamic subgrid-scale eddy viscosity model. *Phys. Fluids A.* **3**, 1760–1765.

HE, G.-W., RUBINSTEIN, R. & WANG, L.-P. 2002 Effects of subgrid scale modeling on time correlations in large eddy simulation. *Phys. Fluids* **14**, 2186–2193.

HE, G.-W., WANG, M. & LELE, S. K. 2002 Evaluation of subgrid-scale models in terms of time correlations, *Summer Program Proceedings,* Center for Turbulence Research, NASA AmesStanford University, 73-78.

HUGHES, T. J. R., MAZZEI, L. & OBERAI, A. S. 2001 The multiscale formulation of large eddy simulation: decay of homogeneous isotropic turbulence. *Phys. Fluids* **13**, 505–512.

KANEDA, Y. & GOTOH, T. 1991 Lagrangian velocity autocorrelation in isotropic turbulence. *Phys. Fluids A.* **3**, 1924–1933.

KANEDA, Y. 1993 Lagrangian and Eulerian time correlations in turbulence. *Phys. Fluids A.* **5**, 2835–2845.

KRAICHNAN, R. H. 1953 The scattering of sound in a turbulent medium. *J. Acoust. Soc. Am.* **25**, 1096–1104

KRAICHNAN, R. H. 1964 Kolmogorov's hypotheses and Eulerian turbulence theory. *Phys. Fluids* **7**, 1723-1734.

LIGHTHILL, M. J. 1952 On sound generated aerodynamically: I. General theory. *Proc. R. Soc. Lond.* **A211**, 564–587.

MENEVEAU, C. & KATZ, J. 2000 Scale-invariance and turbulence models for large eddy simulation. *Annu. Rev. Fluid Mech.* **32**, 1–32.

PROUDMAN, I. 1952 The generation of sound by isotropic turbulence. *Proc. R. Soc. Lond.* **A214**, 119–132.

RUBINSTEIN, R. & ZHOU, Y. 2000 The frequency spectrum of sound radiated by isotropic turbulence. *Phys. Lett. A* **267**, 379–383.

RUBINSTEIN, R. & ZHOU, Y. 2002 Characterization of sound radiation by unresolved scales of motion in computational aeroacoustics. *Eur. J. Mech. B Fluids* **21**, 105–111.

SEROR, C., SAGAUT, P., BAILLY, C. & JUVÉ, D. 2001 On the radiated noise computed by large-eddy simulation. *Phys. Fluids* **13**, 476–487.

SMAGORINSKY, J. 1963 General circulation experiments with the primitive equations: I. The basic experiment. *Mon. Weather Rev.* **91**, 99–164.

WANG, M., LELE, S. K. & MOIN P. 1996 Computation of quadrapole noise using acoustic analogy. *AIAA. J.* **24**, 2247–2254.

WITKOWSKA, A., JUVÉ, D. & BRASSEUR, J. M. 1997 Numerical study of noise from isotropic turbulence. *J. Comput. Acoust.* **5**, 317–336.

Grid-independent large-eddy simulation in turbulent channel flow using three-dimensional explicit filtering

By Jessica Gullbrand

1. Motivation

The most commonly used Large Eddy Simulation (LES) approach is the implicitly filtered approach. In implicitly filtered LES, the computational grid and the discretization operators are considered as the filtering of the governing equations.Thereby the turbulent flow field is divided into grid resolved and unresolved scales, where the unresolved scales must be modeled.

When explicit filtering is used in LES, the filtering procedure of the governing equations is separated from the grid and discretization operations. The flow field is divided into resolved filtered scale (RFS) motions, and subfilter-scale (SFS) motions. The SFS is itself divided into a resolved part (RSFS) and an unresolved part (USFS) (Zhou *et al.* 2001); see figure 1. The RFS motion is obtained by solving the filtered Navier-Stokes equations. The RSFS motions can be reconstructed from the resolved field and occur due to the use of a smooth (in spectral space) filter function. The USFS motions consist of scales that are not resolved in the simulation and need to be modeled. The explicitly filtered governing equations were recently studied by Carati *et al.* (2001) in forced isotropic turbulence.

The smallest resolved scales are often used to model the turbulence-closure term in LES, and therefore it is important to capture these scales accurately. The accuracy of the LES solution can be increased by using high-order numerical schemes. Although high-order methods treat the important large energy-containing scales more accurately, the small resolved scales would still be contaminated with truncation errors when using non-spectral methods. These errors can be reduced or eliminated by using explicit filtering in LES (Lund 1997). This can be achieved either by using a large ratio of filter width to cell size, or by using a higher-order method, in which case the ratio need not be so large. In recent *a priori* studies by Chow & Moin (2003), a minimum ratio of filter width to cell size was determined to prevent the numerical error from becoming larger than the contribution from the turbulence-closure term. They concluded that with a fourth-order scheme a filter width of at least twice the cell size should be used, and for a second-order scheme the filter width should be at least four times the cell size.

Using explicit filtering and high-order numerical schemes requires the filter functions to be commutative to at least the same order as the numerical scheme. The differentiation and filtering operations must commute, to ensure that the filtered Navier-Stokes equations have nearly the same structure as the unfiltered equations. In general, the operations do not commute when a variable filter width is used, as is needed in inhomogeneous turbulent flows. Ghosal & Moin (1995) showed that the commutation error might overwhelm the contribution from the turbulence-closure term. Therefore, this error must be reduced or eliminated to avoid significant effects on the LES solution. A general

theory for constructing discrete high-order commutative filters was proposed by Vasilyev *et al.* (1998).

Most of the previous studies of LES using explicit filtering in turbulent channel flow have used filtering in two dimensions (the homogeneous directions) and only a few studies have applied filtering in all three dimensions. We limit our discussion to investigations performed using smooth filter functions. Two-dimensional filtering was investigated by Moin & Kim (1982), Piomelli *et al.* (1988), Najjar & Tafti (1996), and Gullbrand & Chow (2002) among others. Studies using three-dimensional filtering were performed by Cabot (1994), Gullbrand (2001), Winckelmans *et al.* (2001), and Stolz *et al.* (2001). However, most of the studies using three-dimensional filtering did not focus on minimizing the effect of the numerical errors. If care is not taken to reduce the numerical errors, they may be larger than the contribution from the turbulence-closure models. Therefore, it will not be possible to separate the numerical effects from the performance of turbulence-closure models. Cabot (1994), for example, used a second-order finite-difference scheme and second-order commutative filter functions with a ratio of two between the local filter width and the local cell size. The error from the second-order scheme is probably larger than the turbulence-closure contribution due to the small ratio of the filter width to cell size used and, in addition, a second-order commutation error is present. Winckelmans *et al.* (2001) used a high-order finite-difference scheme (fourth-order) but applied a second-order commutative filter with a ratio of filter width to cell size of $\sqrt{6}$. The filter functions used introduce a commutation error of second-order into the simulations. A spectral method was used by Stolz *et al.* (2001), together with fourth-order commutative filter functions with a filter-grid ratio of approximately 1.5. The use of spectral methods clearly reduces the numerical errors in the simulation when compared to the studies previously mentioned. However, spectral methods are not considered in this study. Gullbrand (2001) used fourth-order commutative filter functions, with a ratio of two between the local filter width and the local cell size, in a fourth-order finite-difference code. The commutation error is then of the same order as the numerical scheme, which is of higher order than the turbulence-closure contribution. According to the study by Chow & Moin (2003), the filter-grid ratio used ensures that the contribution from the turbulence-closure term is larger than the numerical errors. Thus, a fourth-order scheme using fourth-order commutative filters with a filter width of at least twice the cell size creates a numerically-clean environment where turbulence-closure models can be tested and validated.

In this paper, turbulence-closure models are evaluated using the "true" LES approach in turbulent channel flow. The study is an extension of the work presented by Gullbrand (2001), where fourth-order commutative filter functions are applied in three dimensions in a fourth-order finite-difference code. The true LES solution is the grid-independent solution to the filtered governing equations. The solution is obtained by keeping the filter width constant while the computational grid is refined (figure 2). As the grid is refined, the solution converges towards the true LES solution. The true LES solution will depend on the filter width used, but will be independent of the grid resolution. In traditional LES, because the filter is implicit and directly connected to the grid spacing, the solution converges towards a direct numerical simulation (DNS) as the grid is refined, and not towards the solution of the filtered Navier-Stokes equations. The effect of turbulence-closure models is therefore difficult to determine in traditional LES because, as the grid is refined, more turbulence length scales are resolved and less influence from the models is expected. In contrast, in the true LES formulation, the explicit filter eliminates all scales

that are smaller than the filter cutoff (k_{cg} in figure 2), regardless of the grid resolution. This ensures that the resolved length-scales do not vary as the grid resolution is changed. In true LES, the cell size must be smaller than or equal to the cutoff length scale of the filter function.

The turbulence-closure models investigated are the dynamic Smagorinsky model (DSM), the dynamic mixed model (DMM), and the dynamic reconstruction model (DRM). These turbulence models were previously studied using two-dimensional explicit filtering in turbulent channel flow by Gullbrand & Chow (2002). The DSM by Germano *et al.* (1991) is used as the USFS model in all the simulations. This enables evaluation of different reconstruction models for the RSFS stresses. The DMM (Zang *et al.* 1993) consists of the scale-similarity model (SSM) by Bardina *et al.* (1983), which is an RSFS model, in linear combination with the DSM. In the DRM (Gullbrand & Chow 2002), the RSFS stresses are modeled by using an estimate of the unfiltered velocity in the unclosed term (Stolz *et al.* 2001), while the USFS stresses are modeled by the DSM. The DSM and the DMM are two commonly used turbulence-closure models, while the DRM is a more recent model.

2. Governing equations

The governing equations for an incompressible flow field are the continuity equation together with the Navier-Stokes equations,

$$\frac{\partial u_i}{\partial x_i} = 0\,, \qquad \frac{\partial u_i}{\partial t} + \frac{\partial u_i u_j}{\partial x_j} = -\frac{\partial p}{\partial x_i} + \frac{1}{Re_\tau}\frac{\partial^2 u_i}{\partial x_j \partial x_j}\,. \tag{2.1}$$

Here u_i denotes velocity, p pressure and Re_τ the Reynolds number based upon friction velocity, u_τ, and channel half-width, h. Einstein summation is applied to repeated indices.

In LES, the governing equations are filtered in space. The filtering procedure is applied to the flow-field variables according to

$$\overline{u}_i(x,\Delta,t) = \int_D G(x,x',\Delta)u_i(x',t)dx'\,, \tag{2.2}$$

where G is the filter function and Δ is the filter width.

Hence, the filtered governing equations can be written as

$$\frac{\partial \overline{u}_i}{\partial x_i} = 0\,, \qquad \frac{\partial \overline{u}_i}{\partial t} + \frac{\partial \overline{\overline{u}_i}\overline{\overline{u}_j}}{\partial x_j} = -\frac{\partial \overline{p}}{\partial x_i} + \frac{1}{Re_\tau}\frac{\partial^2 \overline{u}_i}{\partial x_j \partial x_j} - \frac{\partial \overline{\tau}_{ij}}{\partial x_j} \tag{2.3}$$

where the turbulent stresses are defined as $\overline{\tau}_{ij} = \overline{u_i u_j} - \overline{\overline{u}_i \overline{u}_j}$. The filtered equations are not closed because of the nonlinear term $\overline{u_i u_j}$. The approach by Leonard is followed where the instantaneous velocity field is divided into a filtered velocity and a fluctuating part, $u_i = \overline{u}_i + u_i'$, and the unclosed term can be rewritten to $\overline{u_i u_j} = \overline{(\overline{u}_i + u_i')(\overline{u}_j + u_j')} = \overline{\overline{u}_i \overline{u}_j} + \overline{\tau}_{ij}$. The product of the nonlinear terms ($\overline{u}_i \overline{u}_j$) introduces high wavenumbers that are beyond the wavenumber content of the filtered velocity field ($\overline{u}_i$) and beyond the cutoff of the filter function. To prevent these high wavenumbers to influence the resolved wavenumbers, the nonlinear terms are explicitly filtered. A potential drawback of (2.3) is that the resulting equation is not in general Galilean-invariant (Speziale 1985) provided that the SFS models are Galilean-invariant. In a moving coordinate system, the resulting equation contains the additional term $c_j \partial(\overline{\overline{u}}_i - \overline{u}_i)/\partial x_j$, where c_j is the uniform translation velocity. The additional term is proportional to the difference between the

doubly filtered and singly filtered velocity field. This difference will be zero when a sharp cut-off filter is used, but will not vanish in the general case. The error can be minimized by constructing the explicit filter function as close as possible to a sharp cut-off filter. However, the preferable solution is to choose an appropriate turbulence-closure model so the problem can be avoided. Speziale (1985) showed that using the SSM by Bardina *et al.* (1983) with the model coefficient of unity as the turbulence-closure model would solve the problem. However, a drawback of this model is that it generates higher frequencies and the desired effects from the explicit filtering approach is thus destroyed (Lund 1997). The DRM on the other hand has the desired properties and avoids the Galilean-invariance problem. Description of this model and further discussion are found in the next section.

3. Subfilter-scale models

The turbulent flow field is divided into RFS and SFS motions when explicit filtering of the Navier-Stokes equations is applied. In figure 1, a sketch of a typical energy spectrum is shown. The solid line represents the energy captured by a fully resolved DNS, while the dashed line represents the LES energy. The vertical line at k_{cg} shows the filter cutoff in the LES. The filter cutoff is determined by where the filter function goes to zero and stays zero (in spectral space), *i.e.*, no wavenumbers higher than the cutoff wavenumber are resolved in the simulation. The filter cutoff can be seen in figure 2. All wavenumbers smaller than the filter cutoff wavenumber are resolved in the simulations. However, they are damped by the filter function and have to be recovered by an inverse filter operation. This corresponds to the RSFS portion of the energy spectrum. The same terminology for the RSFS and the USFS was previously suggested by Zhou *et al.* (2001). In principle, the RSFS can be exactly recovered, but this is only possible when using spectral methods. If non-spectral methods are applied, there are numerical errors (NE) associated with the high wavenumbers and thus the recovered scales are contaminated with errors.

The unresolved portion of the spectrum (the USFS) consists of wavenumbers that are higher than the filter cutoff wavenumber. The USFS motions need to be modeled. The vertical lines in figure 1 represent the grid cutoff wavenumbers for two grid resolutions. The coarse grid cutoff, k_{cg}, happens to coincide with the filter cutoff, while the fine grid cutoff, k_{fg}, is located in the USFS portion of the spectrum. However, the USFS motions that need to be modeled are the same for the two resolutions, since the filter cutoff determines the wavenumbers resolved.

To recover the RSFS stresses, the iterative method of van Cittert (1931) is used in this study. This method was previously used by Stolz *et al.* (2001) in their approximate deconvolution procedure to reconstruct the unfiltered velocity field u_i from the filtered field $\overline{u}_i$. To fully recover the unfiltered velocity, an infinite number of iterations is needed. However, since this is not practical in numerical simulations, the unfiltered velocity field is approximated by a finite number of iterations. By varying this number, different models can be obtained to model the RSFS stresses.

Here, low-level reconstruction (the SSM) and reconstruction up to level five are used. Further details of the reconstruction used are found in 3.3. In order to compare the different RSFS models, the same USFS model (the DSM) is used in all the simulations. The combinations of RSFS and USFS models used are described below.

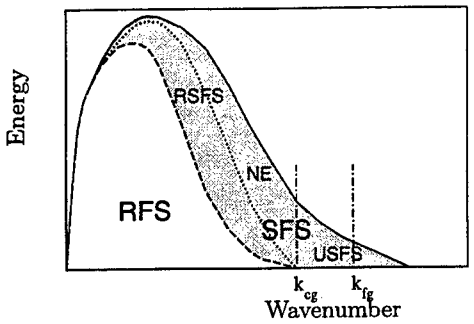


FIGURE 1. Schematic of velocity energy spectrum showing partitioning into resolved filtered scale (RFS), resolved subfilter-scale (RSFS), and unresolved subfilter-scale (USFS) motions. The numerical error (NE) region, denoted by ····· , is a subregion of the RSFS. ——— represents DNS energy, - - - - LES energy, and —·— filter cutoff. The vertical line at k_{cg} represents the filter cutoff wavenumber, which corresponds to the smallest resolved wavenumber for the coarse grid. The vertical line at k_{fg} represents the wavenumber cutoff for the fine grid.

3.1. *Dynamic Smagorinsky Model*

The DSM is a widely-used eddy viscosity USFS model (Smagorinsky 1963):

$$\overline{\tau}_{ij} = -2\overline{\nu_e \overline{S}}_{ij} = -2\overline{(C\Delta)^2|\overline{S}|\overline{S}}_{ij}, \tag{3.1}$$

where ν_e is the eddy viscosity, Δ the filter width, and the strain rate tensor $\overline{S}_{ij} = 0.5(\partial\overline{u}_i/\partial x_j + \partial\overline{u}_j/\partial x_i)$. The model parameter $(C\Delta)^2$ is calculated dynamically (Germano *et al.* 1991) using the least-square approximation of Lilly (1992). The model parameter is averaged in the homogeneous directions and is calculated by the same dynamic procedure as described in the papers previously mentioned. The explicit filtering of the nonlinear terms is not considered when the model parameter is calculated. The filtering enters only when τ_{ij} is introduced into the filtered Navier-Stokes equations. Large magnitudes of negative values of the eddy viscosity are clipped to avoid negative total viscosity in the simulations, $(\nu_e + \nu \geq 0)$, as proposed by Zang *et al.* (1993).

3.2. *Dynamic Mixed Model*

Low-level reconstruction of the RSFS stresses can be performed by using the SSM proposed by Bardina *et al.* (1983). Here the RSFS stress is modeled by the scale-similarity term and the DSM is used as the USFS model:

$$\overline{\tau}_{ij} = (\overline{\overline{u}_i\overline{u}_j} - \overline{\overline{u}}_i\overline{\overline{u}}_j) - 2\overline{(C\Delta)^2|\overline{S}|\overline{S}}_{ij}\,, \tag{3.2}$$

to form the DMM. The SSM term is discretized with the same numerical scheme as the convective terms.

3.3. *Dynamic Reconstruction Model*

High-order reconstruction of the RSFS stress tensor can be achieved by the iterative deconvolution method of van Cittert (1931). The unfiltered quantities can be derived by a series of successive filtering operations (G) applied to the filtered quantities with

$$u_i = \overline{u}_i + (I - G) * \overline{u}_i + (I - G) * ((I - G) * \overline{u}_i) + \cdots \tag{3.3}$$

where I is the identity matrix. The truncation order of the expansion determines the level of deconvolution, as discussed by Stolz *et al.* (2001). If the series includes the terms

explicitly shown in (3.3), it corresponds to reconstruction of level two. An approximate unfiltered velocity ($u_i^\star$) is obtained by the truncated series. $u_i^\star$ is substituted into the unclosed term $\overline{u_i u_j}$, which results in $\overline{u_i^\star u_j^\star}$. The reconstruction of the RSFS stresses are used in linear combination with the DSM,

$$\overline{\tau}_{ij} = \overline{\overline{u_i^\star u_j^\star}} - \overline{\overline{u}_i \overline{u}_j} - 2\overline{(C\Delta)^2 |\overline{S}| \overline{S}}_{ij} \,, \tag{3.4}$$

which is called the dynamic reconstruction model (DRM). In the simulations, the same numerical scheme is used for the convective terms and the RSFS terms. The DRM yields a Galilean-invariant expression of (2.3), since the nonlinear terms $\overline{\overline{u}_i \overline{u}_j}$ on the right-hand side and left-hand side of the equation cancel each other. A reconstruction series of up to level five is used in this study.

4. Filter functions

It is important that the explicit filter and the test filter, which is used in the dynamic procedure of the DSM, have similar shapes, since the dynamic procedure is based upon the scale-similarity assumption in the Germano identity (Germano *et al.* 1991). In the simulations presented here, the same filter function is used in all the simulations. It is only the filter width that is varied between the simulations. The base filter is a fourth-order commutative filter function with filter width $2\Delta_{cg}$, where Δ_{cg} is the grid cell size for the coarse-grid resolution. The computational domain and grid resolutions used in the simulations are discussed in section 6. It is not straightforward to determine the filter width of a high-order filter, and different methods were studied by Lund (1997). Here, one of the methods suggested by Lund is applied. The filter width is defined as the location where the filter function reaches a value of $G(k) = 0.5$. The filter function used in the simulations was developed by Vasilyev *et al.* (1998) and is

$$\overline{\phi}_i = -\frac{1}{32}\phi_{i-3} + \frac{9}{32}\phi_{i-1} + \frac{1}{2}\phi_i + \frac{9}{32}\phi_{i+1} - \frac{1}{32}\phi_{i+3}, \tag{4.1}$$

where the filter weights for $\phi_{i\pm2}$ are zero. The smooth filter function is shown in spectral space in figure 2. In the near-wall region, asymmetric filters are used in the first three grid points for the coarse grid in the wall-normal direction. Since the filter width is held fixed, this corresponds to using asymmetric filters in the first six grid points for the fine grid.

In the simulations, the ratio of the test-filter width to the explicit-filter width is chosen to be two, as proposed by Germano *et al.* (1991) for the DSM. The test filter is used only in the calculation of $(C\Delta)^2$ in the DSM, while the explicit filter function is used to determine the RSFS contribution through either the SSM or reconstruction by the van Cittert (1931) iterative method. The ratio between the explicit-filter width and the cell size for the coarse grid is two and for the fine grid, the ratio is four. This preserves the effective filter width as the grid resolution is increased, as seen in figure 2. The vertical line at low wavenumber represents the grid cutoff (k_{cg}) for the coarse-grid resolution. The filter cutoff wavenumber is the same as the grid cutoff for the coarse grid. For the fine grid, the filter cutoff is held fixed, resulting in a separation between the filter cutoff and grid cutoff (k_{fg}) locations. The grid-cutoff wavenumbers are also shown schematically in figure 1. The ratio of two for the filter width and the cell size for the coarse grid was chosen to prevent the numerical errors from becoming larger than the contribution of the turbulence-closure model (Ghosal 1996; Chow & Moin 2003).

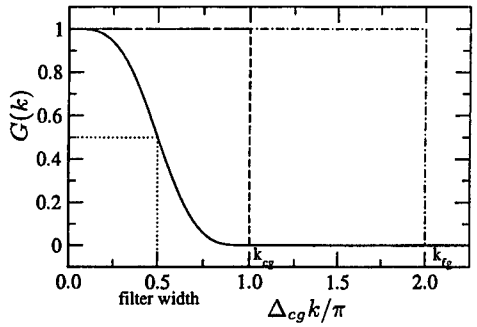


FIGURE 2. The base filter function in spectral space and its relation to the computational grid resolutions. ——— : filter function, ····· : filter width, - - - - : coarse grid resolution, and —·— : fine grid resolution. The wavenumber k_{cg} represents the grid cutoff wavenumber for the coarse grid, while k_{fg} represents the grid cutoff wavenumber for the fine grid.

5. Solution algorithm

In the computational code, the spatial derivatives are discretized using a fourth-order central-difference scheme on a staggered grid. The convective term is discretized in the skew-symmetric form (Morinishi, Lund, Vasilyev & Moin 1998; Vasilyev 2000) to ensure conservation of turbulent kinetic energy. The equations are integrated in time using the third-order Runge-Kutta scheme described by Spalart, Moser & Rogers (1991). The diffusion terms in the wall-normal direction are treated implicitly by the Crank-Nicolson scheme. The splitting method of Dukowicz & Dvinsky (1992) is used to enforce the solenoidal condition. The resulting discrete Poisson equation for the pressure is solved in the wall-normal direction using a penta-diagonal matrix solver. In the homogeneous directions, the Poisson equation is solved using a discrete Fourier transform. Periodic boundary conditions are applied in the streamwise and spanwise homogeneous directions, and no-slip conditions are enforced at the channel walls. A fixed mean pressure gradient is used to drive the flow. The results using the fourth-order computational code is compared to results from a second-order finite-difference code in Gullbrand (2000) and Gullbrand & Chow (2002).

6. Turbulent channel flow simulations

The Reynolds number is $Re_\tau = 395$ and the computational domain is $(2\pi h, 2h, \pi h)$ in (x, y, z), where x is the streamwise direction, y the wall-normal direction, and z the spanwise direction. The computational grid is stretched in the y-direction by a hyperbolic tangent function

$$y(j) = -\frac{\tanh(\gamma(1 - 2j/N_2))}{\tanh(\gamma)} \qquad j = 0, ..., N_2 \tag{6.1}$$

where N_2 is the number of grid points in the wall-normal (j) direction and γ is the stretching parameter, which is set to 2.75. Two computational grids are used for the LES calculations; (64,49,48), which corresponds to one-quarter of the DNS resolution in each spatial direction, and (128,97,96), which is half the number of DNS grid points in each direction. The cell size for the coarser grid resolution is $\Delta x^+ = 39$, $\Delta z^+ = 26$, and $0.4 \leq \Delta y^+ \leq 45$. The finer resolution corresponds to the cell size $\Delta x^+ = 19$, $\Delta z^+ = 13$, and $0.2 \leq \Delta y^+ \leq 23$. The 'plus' values (wall units) are obtained by normalizing the length

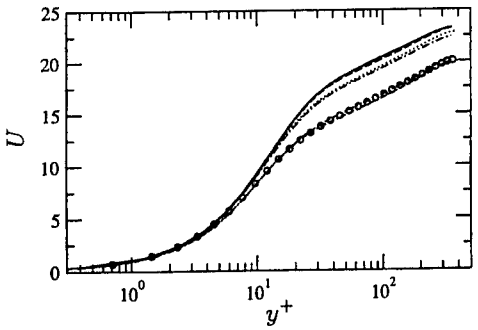


FIGURE 3. Mean velocity profiles using different turbulence-closure models. o: filtered DNS, ——— : DSM (64,49,48), - - - - : DSM (128,97,96), —·— : DMM (64,49,48), ····· : DMM (128,97,96), —··— : DRM (N=5) (64,49,48), and ·——· : DRM (N=5) (128,97,96).

scale with the friction velocity and the kinematic viscosity. A statistically stationary solution is obtained after 30 dimensionless time units, and thereafter statistics were sampled during 15 additional time units. The time is normalized with the friction velocity and channel half-width. The LES results are compared to filtered DNS data, and all the presented results are averaged in the homogeneous directions.

The DNS is performed with the same computational code as used in the LES simulations. The computational grid resolution is (256,193,192) as used by Moser, Kim & Mansour (1999). The DNS data fields are filtered using the commutative filter functions. In the figures, it is only every third grid point in the filtered DNS that are plotted to make the comparison between the LES and DNS clearer.

7. Results

Figure 3 shows mean velocity profiles from simulations using different RSFS models and different grid resolutions. The filter width is fixed, while the grid resolution is increased. The goal is to obtain a grid-independent LES solution so that the behavior of turbulence-closure models can be evaluated. The changes in the predicted mean velocity profiles as the grid resolution is increased are only minor, indicating that the LES solutions are nearly converged. The mean velocities predicted by the DSM are much higher than the filtered DNS results. The DMM improves the results slightly, while the best agreement with the filtered DNS data is predicted by the DRM (N=5). This shows the need for a RSFS model when a smooth explicit filter function is applied.

The streamwise velocity fluctuations in figure 4 show the same trend as the mean velocity profiles. However, the differences in the results as the grid is refined are slightly larger than for the mean velocity. The DSM shows the largest overprediction of the peak streamwise velocity fluctuations. The peak value decreases slightly as the grid is refined. This is also observed for the DMM and the DRM (N=5). It should be noted that the DRM actually predicts a peak value that is lower than the DNS data. This is very unusual in LES, because most models will overpredict the streamwise velocity fluctuations and underpredict the wall-normal and spanwise fluctuations. However, the wall-normal and spanwise velocity fluctuations shown in figure 4 are even further underpredicted when applying DRM (N=5) compared to the other two models.

The modeled shear stresses are shown in figure 5. It is a well-known problem that the

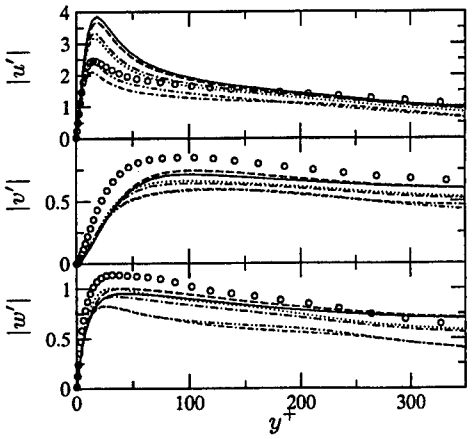


FIGURE 4. Velocity fluctuations in the streamwise $|u'|$, wall-normal $|v'|$, and spanwise $|w'|$ directions. o: filtered DNS, ——— : DSM (64,49,48), - - - - : DSM (128,97,96), —·— : DMM (64,49,48), ····· : DMM (128,97,96), —··— : DRM (N=5) (64,49,48), and ·——· : DRM (N=5) (128,97,96).

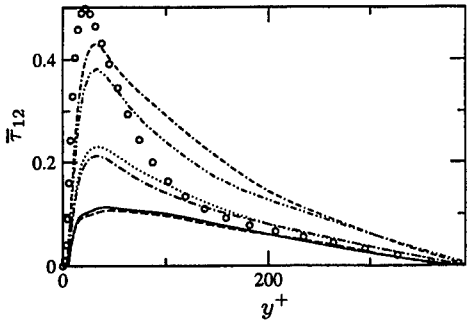


FIGURE 5. Modeled shear stress, $\overline{\tau}_{12}$, using different turbulence-closure models. o: filtered DNS, ——— : DSM (64,49,48), - - - - : DSM (128,97,96), —·— : DMM (64,49,48), ····· : DMM (128,97,96), —··— : DRM (N=5) (64,49,48), and ·——· : DRM (N=5) (128,97,96).

DSM does not predict sufficient shear stress in the near-wall region (Baggett, Jimenez & Kravchenko 1997). As shown in the figure, the DSM predicts the lowest peak values, while the largest are produced by the DRM (N=5). The modeled shear stress increases when the level of reconstruction is increased. However, the contribution from the DSM does not change much between the different simulations; the peak value is approximately the same. The increase of modeled shear stress is therefore almost entirely due to the RSFS model. The peak value of the modeled shear stress is approaching the filtered DNS data as the level of reconstruction is increased. Towards the center of the channel, the high level reconstruction model overpredicts the shear stress when compared to the filtered DNS data.

8. Discussion and conclusions

The true LES approach is investigated in turbulent channel flow using commutative filter functions in all three spatial directions. In the true LES approach, a grid-independent solution to the filtered governing equations is obtained. The LES solution depends upon the explicit filter width used, but is independent of the computational grid. A computational code using an energy-conserving fourth-order finite-difference scheme is applied and fourth-order commutative filters are used. Simulations of turbulent channel flow were performed at $Re_\tau = 395$. The explicit filter width was kept fixed while the computational grid was refined, to obtain a grid-independent solution. The results using two different grid resolutions show only minor differences, indicating that the LES solutions are nearly converged. The explicit filtering also reduces the numerical errors that are associated with the high-wavenumber portion of the spectrum when using non-spectral methods. Therefore, explicit filtering in LES, using high-order commutative filters, results in a numerically-clean environment where turbulence-closure models can be investigated in grid-independent LES solutions. This could not be performed using the traditional LES approach, since the contribution from the SFS models decreases as the computational grid is refined.

The turbulence-closure models investigated are the DSM, DMM and DRM. The models are compared to filtered DNS data for mean velocity profiles, velocity fluctuations, and modeled shear stresses. The mean velocity profiles and the streamwise velocity fluctuations improve as the level of reconstruction increases. The closest agreement between the LES results and the filtered DNS data, in this study, is obtained by the level of reconstruction of five (DRM, N=5).

The poor agreement between the filtered DNS results and the DSM shows the need for RSFS models when using a smooth (in spectral space) explicit filter function. The results predicted by the models investigated show a distinct improvement in the predicted quantities, when compared to filtered DNS results, as the level of reconstruction is increased. These improvements are probably due to the increase of modeled shear stress in the near-wall region. The DSM is known not to predict sufficient shear stress in the near-wall region, and as the level of reconstruction is increased so is the modeled shear stress. The increase is almost entirely due to the RSFS model, since the contribution from the DSM does not change significantly.

Acknowledgments

The author benefited from many helpful discussions with Prof. O. V. Vasilyev. Thanks are also due to F. K. Chow for reading and commenting early drafts of this paper.

REFERENCES

BAGGETT, J., JIMENEZ, J. & KRAVCHENKO, A. G. 1997 Resolution requirements in large-eddy simulations of shear flows. Annual research briefs. Center for Turbulence Research, NASA Ames/Stanford Univ., 51-66.

BARDINA, J., FERZIGER, J. & REYNOLDS, W. 1983 Improved turbulence models based on large eddy simulation of homogeneous, incompressible, turbulent flows. Technical Report TF-19. Department of Mechanical Engineering, Stanford University, Stanford, California.

CABOT, W. 1994 Local dynamic subgrid-scale models in channel flow. Annual research briefs. Center for Turbulence Research, NASA Ames/Stanford Univ., 143-159.

CARATI, D., WINCKELMANS, G. & JEANMART, H. 2001 On the modelling of the subgrid-scale and filtered-scale stress tensors in large-eddy simulation. *Journal of Fluid Mechanics* **441**, 119–138.

CHOW, F. & MOIN, P. 2003 A further study of numerical errors in large-eddy simulations. *Journal of Computational Physics* **184** (2), 366–380.

VAN CITTERT, P. 1931 Zum Einfluß der Spaltbreite auf die Intensitätsverteilung in Spektrallinien II. *Zeitschrift für Physik* **69**, 298–308.

DUKOWICZ, J. & DVINSKY, A. 1992 Approximate factorization as a high-order splitting for the implicit incompressible-flow equations. *Journal of Computational Physics* **102** (2), 336–347.

GERMANO, M., PIOMELLI, U., MOIN, P. & CABOT, W. 1991 A dynamic subgrid-scale eddy viscosity model. *Physics of Fluids* **3** (7), 1760–1765.

GHOSAL, S. 1996 An analysis of numerical errors in large-eddy simulations of turbulence. *Journal of Computational Physics* **125**, 187–206.

GHOSAL, S. & MOIN, P. 1995 The basic equations for the large eddy simulation of turbulent flows in complex geometry. *Journal of Computational Physics* **118**, 24–37.

GULLBRAND, J. 2000 An evaluation of a conservative fourth order DNS code in turbulent channel flow. Annual research briefs. Center for Turbulence Research, NASA Ames/Stanford Univ., 211-218.

GULLBRAND, J. 2001 Explicit filtering and subgrid-scale models in turbulent channel flow. Annual research briefs. Center for Turbulence Research, NASA Ames/Stanford Univ., 31-43.

GULLBRAND, J. & CHOW, F. 2002 Investigation of numerical errors, subfilter-scale models, and subgrid-scale models in turbulent channel flow simulations. Proceedings of the summer program. Center for Turbulence Research, NASA Ames/Stanford Univ., 87-104.

LILLY, D. 1992 A proposed modification of the Germano subgrid-scale closure method. *Physics of Fluids* **4** (3), 633–635.

LUND, T. S. 1997 On the use of discrete filters for large eddy simulation. Annual research briefs. Center for Turbulence Research, NASA Ames/Stanford Univ., 83-95.

MOIN, P. & KIM, J. 1982 On the modelling of the subgrid-scale and filtered-scale stress tensors in large-eddy simulation. *Journal of Fluid Mechanics* **118**, 341–377.

MORINISHI, Y., LUND, T., VASILYEV, O. & MOIN, P. 1998 Fully conservative higher order finite difference schemes for incompressible flow. *Journal of Computational Physics* **143**, 90–124.

MOSER, R., KIM, J. & MANSOUR, N. 1999 Direct numerical simulation of turbulent channel flow up to $Re_\tau = 590$. *Physics of Fluids* **11** (4), 943–945.

NAJJAR, F. & TAFTI, D. 1996 Study of discrete test filters and finite difference approximations for the dynamic subgrid-scale stress model. *Physics of Fluids* **8** (4), 1076–1088.

PIOMELLI, U., MOIN, P. & FERZIGER, J. 1988 Model consistency in large eddy simulation of turbulent channel flows. *Physics of Fluids* **31** (7), 1884–1891.

SMAGORINSKY, J. 1963 General circulation experiments with the primitive equations. *Monthly Weather Review* **91**, 99–152.

SPALART, P., MOSER, R. & ROGERS, M. 1991 Spectral methods for the navier-stokes

equations with one infinite and 2 periodic directions. *Journal of Computational Physics* **96** (2), 297–324.

SPEZIALE, C. 1985 Galilean invariant of subgrid-scale stress models in the large-eddy simulation of turbulence. *Journal of Fluid Mechanics* **156**, 55–62.

STOLZ, S., ADAMS, N. & KLEISER, L. 2001 An approximate deconvolution model for large-eddy simulation with application to incompressible wall-bounded flows. *Physics of Fluids* **13** (4), 997–1015.

VASILYEV, O. 2000 High order finite difference schemes on non-uniform meshes with good conservation properties. *Journal of Computational Physics* **157** (2), 746–761.

VASILYEV, O., LUND, T. & MOIN, P. 1998 A general class of commutative filters for les in complex geometries. *Journal Of Computational Physics* **146** (1), 82–104.

WINCKELMANS, G., WRAY, A., VASILYEV, O. & JEANMART, H. 2001 Explicit-filtering large-eddy simulation using the tensor-diffusivity model supplemented by a dynamic smagorinsky term. *Physics of Fluids* **13** (5), 1385–1403.

ZANG, Y., STREET, R. L. & KOSEFF, J. R. 1993 A dynamic mixed subgrid-scale model and its application to turbulent recirculating flows. *Physics of Fluids* **5** (12), 3186–3196.

ZHOU, Y., BRASSEUR, J. & JUNEJA, A. 2001 A resolvable subfilter-scale model specific to large-eddy simulation of under-resolved turbulence. *Physics of Fluids* **13** (9), 2602–2610.

Advanced signal processing for integrated LES-RANS simulations: Anti-aliasing filters

By J. U. Schlüter

1. Motivation

Currently, a wide variety of flow phenomena are addressed with numerical simulations. Many flow solvers are optimized to simulate a limited spectrum of flow effects effectively, such as single parts of a flow system, but are either inadequate or too expensive to be applied to a very complex problem.

As an example, the flow through a gas turbine can be considered. In the compressor and the turbine section, the flow solver has to be able to handle the moving blades, model the wall turbulence, and predict the pressure and density distribution properly. This can be done by a flow solver based on the Reynolds-Averaged Navier-Stokes (RANS) approach (Davis *et al.* 2002). On the other hand, the flow in the combustion chamber is governed by large scale turbulence, chemical reactions, and the presence of fuel spray. Experience shows that these phenomena require an unsteady approach (Veynante and Poinsot 1996). Hence, for the combustor, the use of a Large Eddy Simulation (LES) flow solver is desirable (Mahesh *et al.* 2001; Constantinescu *et al.* 2003).

While many design problems of a single flow passage can be addressed by separate computations, only the simultaneous computation of all parts can guarantee the proper prediction of multi-component phenomena, such as compressor/combustor instability and combustor/turbine hot-streak migration. Therefore, a promising strategy to perform full aero-thermal simulations of gas-turbine engines is the use of a RANS flow solver for the compressor sections, an LES flow solver for the combustor, and again a RANS flow solver for the turbine section (Fig. 1).

2. Interface Conditions

The simultaneous computation of the flow in all parts of a gas turbine with different flow solvers requires an exchange of information at the interfaces of the computational domains of each part. Previous work has established algorithms, which ensure that two or more simultaneously running flow solvers are able to exchange the information at the interfaces efficiently (Shankaran *et al.* 2001; Schlüter *et al.* 2003d).

The necessity of information exchange in the flow direction from the upstream to the downstream flow solver is obvious: the flow in a passage is strongly dependent on mass flux, velocity vectors, and temperature at the inlet of the domain. However, since the Navier-Stokes equations are elliptic in subsonic flows, the downstream flow conditions can have a substantial influence on the upstream flow development. This can easily be imagined by considering that, for instance, a flow blockage in the turbine section of the gas turbine can determine and even stop the mass flow rate through the entire engine. This means that the information exchange at each interface has to go in both, downstream *and* upstream, directions.

Considering an LES flow solver computing the flow in the combustor, information on

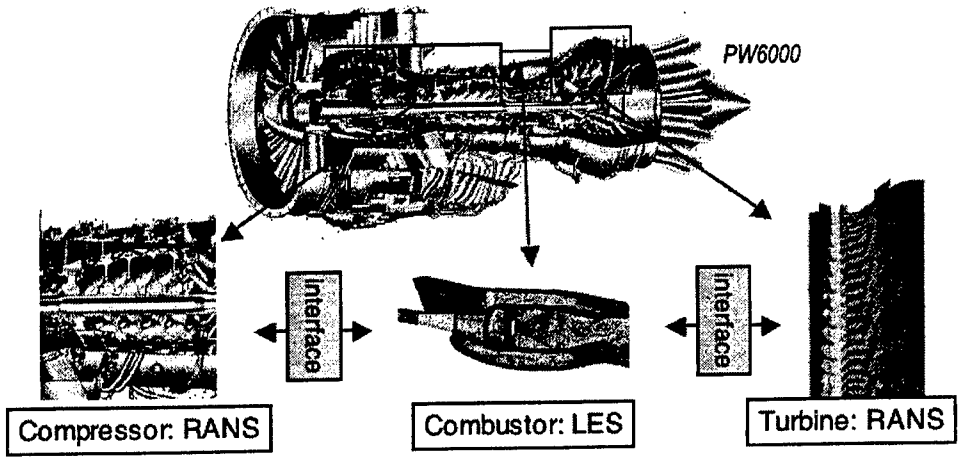


FIGURE 1. Decomposition of gas turbine engine. LES of combustor from Mahesh *et al.* 2001; Constantinescu *et al.* 2003, RANS of turbine section from Davis *et al.* 2002

the flow field has to be provided to the RANS flow solver computing the turbine as well as to the RANS flow solver computing the compressor. At the same time, the LES solver has to obtain flow information from both RANS flow solvers. The coupling can be done using overlapping computational domains for the LES and RANS simulations. For the example of the compressor/combustor interface this would imply that inflow conditions for LES will be determined from the RANS solution at the beginning of the overlap region, and correspondingly the outflow conditions for RANS are determined from the LES solution at the end of the overlap region.

However, the different mathematical approaches of the different flow solvers make the coupling of the flow solvers challenging. Since LES resolves large-scale turbulence in space and time, the time step between two iterations is relatively small. RANS flow solvers average all turbulent motions over time and predict ensemble averages of the flow. Even when a so-called unsteady RANS approach is used, the time step between two ensemble-averages of the RANS flow solver is usually larger by several orders of magnitude than that for an LES flow solver.

The smaller time-step of the LES flow solver results in the necessity of the LES flow solver to average its own LES data over the RANS time-step in order to provide data for the RANS flow solver at the requested times. However, the sampling process may introduce errors in the frequency spectra.

As an analogy, the digitization of an continuous signal during experiments can be seen. Here, the highest frequency recorded without error is the Nyquist frequency, defined as half of the sampling frequency. Low pass filters are used in order to remove high frequency disturbances from the continuous signal before the sampling process. Omitting the filtering would result in aliasing errors, which means that under-resolved frequencies ($f > f_{\text{NYQUIST}}$) are found in the long wave spectrum. Hence, the low-pass filtering *prior* to the digitization is necessary.

For the communication between LES and RANS flow solvers a similar procedure has to be found in order to avoid aliasing of frequencies in the sampling of the LES data. The current study investigates the use of filters to ensure the proper communication of flow variables.

3. Interface Implementation and Flow Solver

For the present study, the information transfer between two flow solvers has been studied. The idea is to periodically excite the flow in the upstream domain and observe the information transfer to the downstream domain. To be able to compare with the true solution of a simulation of the entire domain with a single code, this study has been done by coupling two instances of the same flow solver. Both LES flow solvers exchange information at a time step $\Delta\tau$, which is larger by more than one order of magnitude than the LES time step Δt.

The LES flow solver developed at the Center for Turbulence Research (Pierce & Moin 1998) has been used. The flow solver solves the filtered momentum equations with a low-Mach number assumption on an axi-symmetric structured mesh. A second-order finite-volume scheme on a staggered grid is used (Akselvoll & Moin 1996).

The sub-grid stresses are approximated with an eddy-viscosity approach. The eddy viscosity is determined by a dynamic procedure (Germano *et al.* 1991; Moin *et al.* 1991).

For the real-time exchange of flow variables during the simultaneous computation of both domains, a recently developed interface has been used (Schlüter *et al.* 2002; Schlüter *et al.* 2003d). The interface establishes a communication between the two flow solvers and lets the flow solvers exchange flow variables after a given time-step $\Delta\tau$. Each of the flow solvers obtains a data set of flow variables for each point at the boundary. Then, each flow solver defines its own boundary conditions from the data obtained. At the inlet of the downstream LES flow solver, inflow boundary conditions corresponding to Schlüter *et al.* (2003b) (see also Schlüter *et al.* 2003a; Schlüter 2003) have been employed.

Previous work has shown that at the outflow of the upstream domain outlet boundary conditions have to be employed taking the feedback from the downstream domain into account (Schlüter and Pitsch 2001; Schlüter *et al.* 2002; Schlüter *et al.* 2003c). This can be done by employing a body force near the outlet of the domain, which drives the flow to a solution given by the flow solution of the downstream domain. However, in the current case the feedback was consciously suppressed. This was done to avoid that aliased frequencies received by the downstream domain are given back to the upstream domain and may contaminate the outgoing signal from the upstream domain. This means that if the feedback is not suppressed, the numerical error due to aliasing may even increase. The suppression ensures that all effects of variations of the interface can be associated directly with the filter change. Since there is no feedback from the downstream flow solver, the time-evolving LES solution of the upstream flow solver is identical for all cases reported here.

The inlet boundary condition of the *upstream* domain has been determined by:

$$u_{i,\mathrm{LES}}(t) = \bar{u}_{i,\mathrm{MEAN}}(t) + u'_{i,\mathrm{DB}}(t) \tag{3.1}$$

where t the time using the LES time scale and $u'_{i,\mathrm{DB}}(t)$ is a turbulent motion from a pre-generated data-base. In laminar cases the turbulent fluctuation was set to zero. For turbulent cases, the mean flow-field at the inlet and the data-base for the turbulent motions were determined by a separate LES computation of a weakly swirling periodic pipe flow. The swirl number of this pipe flow was $S = 0.15$ with:

$$S = \frac{1}{D}\frac{\int_0^D r^2 \bar{u}_x \bar{u}_\phi \, dr}{\int_0^D r \bar{u}_x^2 \, dr}, \tag{3.2}$$

where u_x is the axial velocity component, u_ϕ is the azimuthal velocity component, and D is the diameter of the pipe.

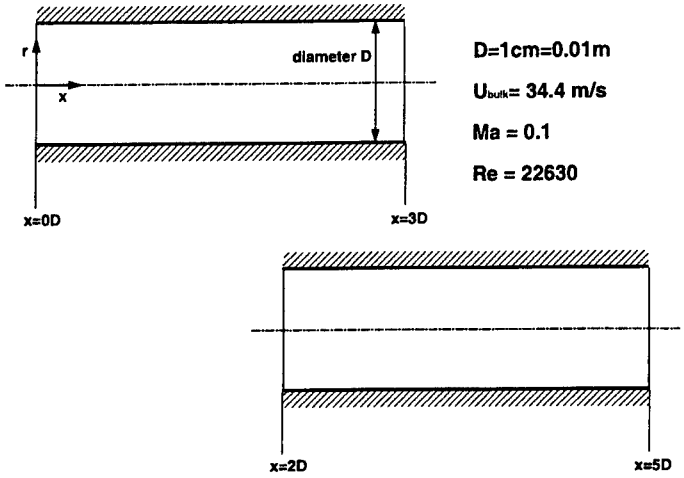


FIGURE 2. Geometry of the test-case.

In order to simulate a convective wave, the azimuthal velocity component has been modulated by:

$$\bar{u}_{\phi,\mathrm{MEAN}}(t) = \bar{u}_{\phi,\mathrm{DB}} \cdot [1.0 + 0.3 \cdot \sin(2\pi \cdot St \cdot t)] \tag{3.3}$$

with $\bar{u}_{\phi,\mathrm{DB}}$ the mean velocity of the data-base.

4. Aliasing Problem

In order to investigate the aliasing problem in integrated LES-RANS computations consider the following case: a pipe is split into an upstream domain computed by one flow solver and a downstream domain computed by another flow solver. Both pipe segments are 3 diameters D long with an overlap of $1D$ (Fig. 2). The upstream flow domain possesses two dominant frequencies, one at a Strouhal number $St = 1.0$ with $St = fD/U_{\mathrm{bulk}}$ and another at $St = 7.5$. The interface frequency is set to $St = 10.0$, which leads to a Nyquist frequency of $St = 5.0$. Hence, the long wave frequency at $St = 1.0$ is well resolved and can be transmitted to the downstream domain. However, the second frequency is under-resolved and will lead to aliasing errors.

To demonstrate this, such a flow calculation was performed under laminar conditions at a Reynolds-number $Re = 1000$. Laminar conditions have been chosen for clarity. A turbulent flow is examined below.

Figure 3 shows the energy spectrum in the upstream domain at a point in the interface plane ($x = 2D$, $r = 0.5R$, $\phi = 0$). The two distinct peaks can be associated with the forcing frequencies. A successful signal processing will transfer the low frequency ($St = 1.0$) with no energy loss, while suppressing the high frequency disturbance ($St = 7.5$).

Figure 4 shows the energy spectrum for the same physical point, but in the downstream domain. Since the flow solver computing the upstream domain has transferred the signal without any treatment, the high frequency perturbation in the upstream domain has been aliased and can now be found as a spurious contribution at a lower frequency of $St = 2.5$.

This may cause considerable problems, since this frequency is resolved by any unsteady RANS flow solver operating at a time-step correspondent to the interface frequency. Since this peak in the long wave spectrum is not present in the upstream domain, this error

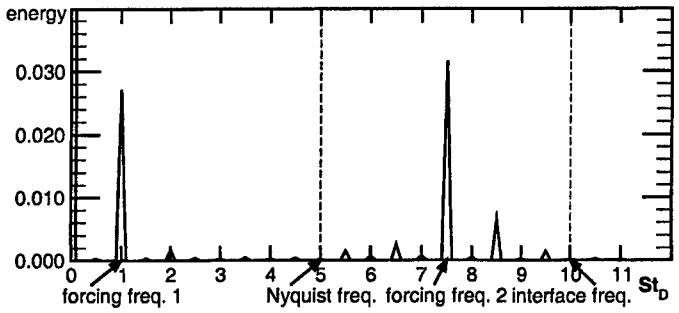


FIGURE 3. Energy spectrum at a point ($x = 2D$, $r = 0.5R$, $\phi = 0$) in the interface plane of the upstream domain.

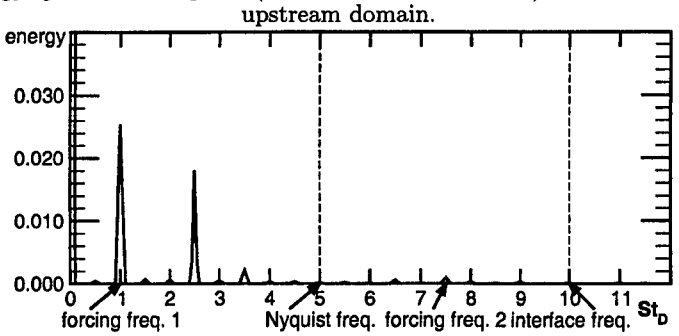


FIGURE 4. Energy spectrum at the interface plane of the downstream domain. Physically identical point as Fig. 3 ($x = 2D$, $r = 0.5R$, $\phi = 0$). No filter used.

has been introduced entirely by the sampling process. Hence, the upstream flow solver has to treat the signal during the sampling process in order to suppress the high frequent perturbation, while keeping the low-frequency oscillation unchanged.

5. Temporal Filters

A common procedure to avoid aliasing errors in experiments is to use low-pass filtering prior to the sampling process. The low-pass filtering suppresses all frequencies above the Nyquist frequency, while passing all lower frequencies unchanged. This filtering process has to be done prior to the sampling process, since otherwise the aliasing error has already taken effect and is indistinguishable from the rest of the long wave spectrum.

To use the same strategy for the sampling of LES data an appropriate digital filter has to be constructed. A digital filter can be defined as:

$$r(t_k) = \sum_{n=0}^{N} b_n s(t_{k-n}) + \sum_{m=1}^{M} a_m r(t_{k-m}) \tag{5.1}$$

with r being the filter response, s the original signal, b_n and a_n the filter constants, and t_k the time. The LES time-step Δt is defined as $t_k - t_{k-1}$. Since in LES computations the time-step is usually not constant, but varies in order to maintain the highest possible time-step satisfying the CFL condition, a pre-sampling process has to be made within. This pre-sampling procedure averages the data with a higher frequency than the actual sampling frequency. In order to avoid aliasing in the pre-sampling process, the frequency of the pre-sampling has to be chosen well within the energy decay, so that the energy of

frequencies higher than the Nyquist frequency are considerably smaller then the energy of the lower frequencies. A filter such as Eq. (5.1) can then be applied.

A filter in the form of Eq. (5.1) uses the history of the signal and the history of prior filter responses. This is a so called infinite response filter (IIR filter), can be used. However, a simplified filter, which uses only the history of the signal, a so called finite response filter (FIR filter) may have advantages:

$$r(t_k) = \sum_{n=0}^{N} b_n s(t_{k-n}) \tag{5.2}$$

First, FIR filters are always stable. Due to the absence of the filter response, no feedback is possible and hence, this kind of filters will cannot amplify errors. Second, FIR filters have a linear phase response. The resulting advantage will be made clear later.

Due to the high number of points at the interface the filter has to be applied to, the order N of the filter is sought to be small, since N determines the number of time-steps that have to be recorded. The determination of the filter constants can be done with any filter design tool such as Matlab (Stearns 2003). The usage of filter design tools allows for the usage of more sophisticated window functions in order to damp the Gibb's phenomenon (Williams 1986), which is most pronounced at filters of low order. For the current investigation, two different filter have been used.

5.1. *Fourier Series Method*

The first filter is designed using the Fourier Series Method (Rorabaugh 1997). The coefficients are defined as:

$$b_n = \frac{1}{2\pi} \int_{2\pi} H(\lambda)[\cos(m\lambda) + j\sin(m\lambda)]d\lambda \tag{5.3}$$

$$\text{with } m = n - \frac{N-1}{2} \tag{5.4}$$

with $H(\lambda)$ being the desired filter response and λ the normalized frequency, which is here normalized to the pre-sampled frequency. The optimal filter response would have a cutoff frequency of $1/2 \cdot f_{\text{Interface}}$. The pre-sampling frequency was chosen here twice the interface frequency, which results in a cutoff frequency $\lambda_{\text{cutoff}} = 1/4$. Equation (5.3) then becomes:

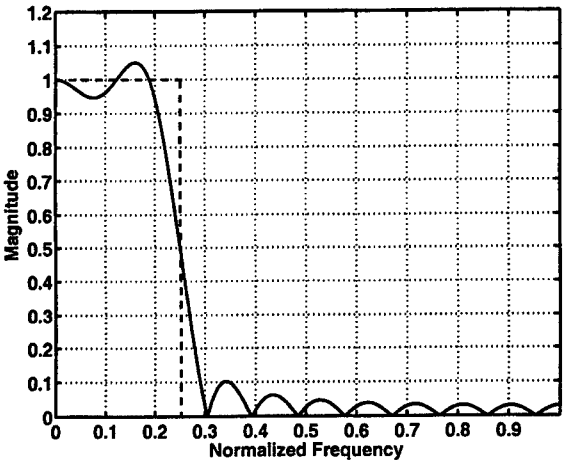
$$b_n = \frac{1}{2\pi} \int_{\frac{\pi}{4}}^{\frac{\pi}{4}} \cos(m\lambda)d\lambda + j\frac{1}{2\pi} \int_{\frac{\pi}{4}}^{\frac{\pi}{4}} \sin(m\lambda)d\lambda \tag{5.5}$$

The second integrant is zero, since the integrant is an odd function and the limits of the integration are symmetric. Equation (5.5) then becomes:

$$b_n = \frac{\sin(m\lambda)}{2m\pi}\Big|_{\lambda=-\frac{\pi}{4}}^{\lambda=\frac{\pi}{4}} = \frac{\sin(m\frac{\pi}{4})}{m\pi} \tag{5.6}$$

Note, that the definition of the filters does not include the knowledge of the actual sampling frequency, but only the cutoff frequency relative to the sampling frequency. This means, if the interface frequency is changed, the filters will adapt automatically.

The filter response of this filter is shown in Fig. 5. The dashed line denotes the ideal filter response: below the cutoff frequency it is unity, above zero. Since only a limited number of filter coefficients are available, here $N = 21$, the actual filter response differs from the ideal filter. Most notably, there is an overshoot right next to the cutoff frequency,



$b_0 =$	$b_{20} =$	0.0311536
$b_1 =$	$b_{19} =$	0.0244766
$b_2 =$	$b_{18} =$	-0.0000006
$b_3 =$	$b_{17} =$	-0.0314696
$b_4 =$	$b_{16} =$	-0.0519226
$b_5 =$	$b_{15} =$	-0.0440576
$b_6 =$	$b_{14} =$	0.0000006
$b_7 =$	$b_{13} =$	0.0734296
$b_8 =$	$b_{12} =$	0.1557666
$b_9 =$	$b_{11} =$	0.2202866
	$b_{10} =$	0.2446776

FIGURE 5. Left: Filter response of filter designed with Fourier Series Method (solid line). $N = 21$. Cutoff frequency: 0.25. Dashed line: Ideal filter response. Right: Filter coefficients

the Gibb's phenomenon. In order to smoothen the filter response a window method has to be employed.

5.2. *Window Method*

The second filter used in this study uses a window method. One of the major shortcomings of the Fourier Series Method is the assumption that the signal is periodic. This creates some problems due to a discontinuity at the end and the beginning of the recorded signal. One possibility to damp this effect is to use window functions:

$$r(t_k) = \sum_{n=0}^{N} b_n w_n s(t_{k-n}) \tag{5.7}$$

with w_n being the window function. Some of the most common window functions are the Hann, Hamming or, Parzen windows. Here, a Kaiser window has been employed (Williams 1986), since this window creates the smoothest filter response (Fig. 6). However, a drawback of window functions is that the slope of the filter response is not as steep as before.

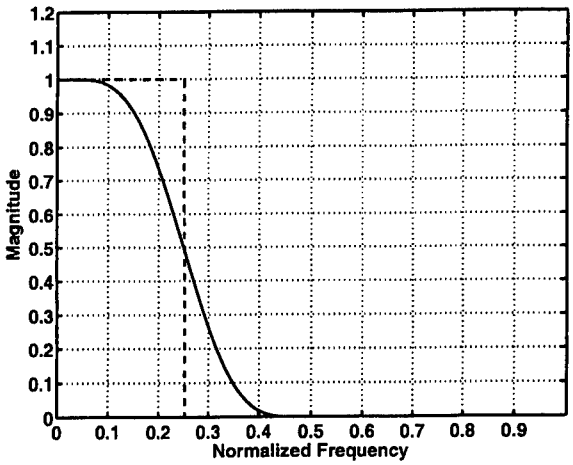
The window function is usually combined with the filter coefficients leading to a new set of coefficients (Fig. 6)

5.3. *Results: Amplitude Response*

In the next step, the filters were applied to the LES computation of the upstream domain. Each filter was applied separately to the LES data in two LES computations. Since the filters have been designed to avoid aliasing, the quality of the signal has been improved.

The signal response of both computations using the two different filters show the desired results (Figs. 7 and 8). The long wave length perturbation at $St = 1.0$, which corresponds to the frequency which is supposed to be transferred, can be found in the downstream domain without a loss of energy. Since the filters have filtered out the high frequency perturbation prior to the actual sampling process, no aliasing can be observed.

These results of both filters show that digital filters are able to suppress aliasing successfully for coupled flow computations. While for the current test case the results of



$b_0 =$	$b_{20} =$	0.0004736
$b_1 =$	$b_{19} =$	0.0013386
$b_2 =$	$b_{18} =$	-0.0000006
$b_3 =$	$b_{17} =$	-0.0069236
$b_4 =$	$b_{16} =$	-0.0179856
$b_5 =$	$b_{15} =$	-0.0217416
$b_6 =$	$b_{14} =$	0.0000006
$b_7 =$	$b_{13} =$	0.0583416
$b_8 =$	$b_{12} =$	0.1425086
$b_9 =$	$b_{11} =$	0.2189896
	$b_{10} =$	0.2500006

FIGURE 6. Left: Filter response of filter designed with Window Method (solid line) using a Kaiser window. $N = 21$. Cutoff frequency: 0.25. Dashed line: Ideal filter response. Right: Filter coefficients

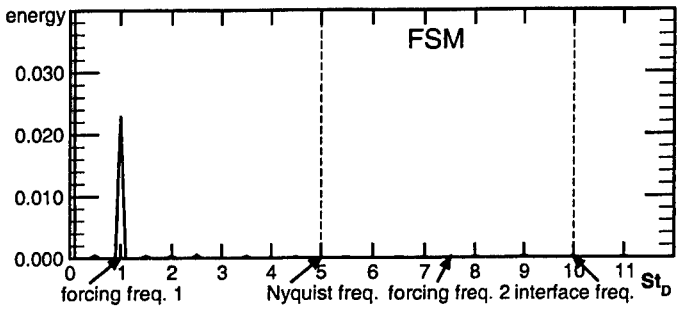


FIGURE 7. Energy spectrum at the interface plane of the downstream domain. Filter designed with FSM (Fig. 5).

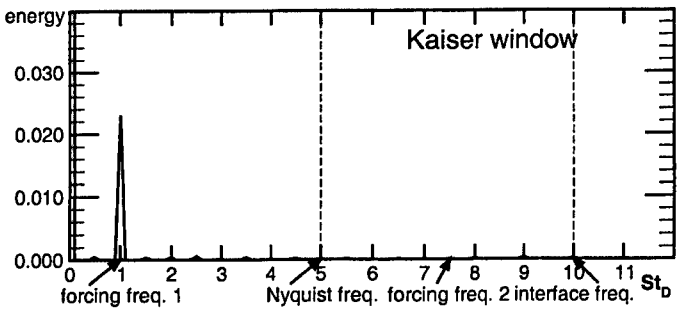


FIGURE 8. Energy spectrum at the interface plane of the downstream domain. Filter designed using Kaiser Window (Fig. 6).

both filters are identical, more complex test-cases may require to choose a filter based on the filter response.

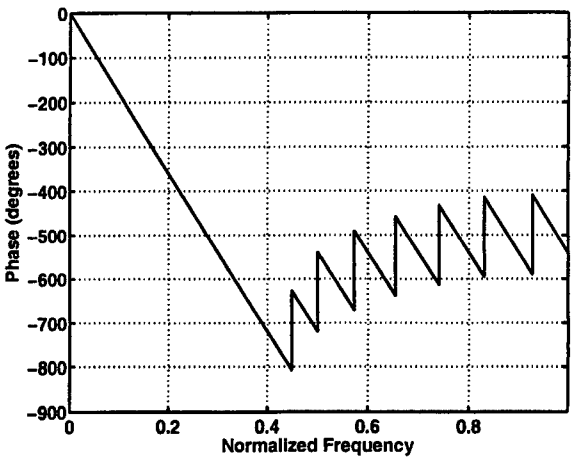


FIGURE 9. Phase response of filter designed with Window Method (solid line) using a Kaiser window. $N = 21$.

5.4. *Results: Phase Response*

Although these filters have shown to efficiently avoid aliasing errors, the application of these filters has a major drawback. Figure 9 shows the phase response of both filters. The phase response is linear in the passing frequency range. This translates to a constant time delay of:

$$\Delta t = \frac{N-1}{2 \cdot f_{\text{sample}}} \tag{5.8}$$

This means that the signal coming from the upstream flow solver arrives with a time delay in the downstream flow solver. The time-delay can be minimized by decreasing the order of the filter. However, it seems that the filters presented here with an order of $N = 21$ are already the minimum order for a filter with an acceptable quality of amplitude response.

If unsteady coupling effects are important, this time delay introduced by the filter is not acceptable.

Since the phase delay is unavoidable using these temporal filters, the application of these filters is limited to the following. Most unsteady RANS flow solvers do not claim to compute a truly unsteady flow, but an ensemble-average or a phase-average. In phase-averaged flows a number of averages of the flow are taken in relation to the phase of a base frequency f_{base}. Assuming that the upstream LES delivers data to a downstream RANS flow solver computing phase-averages, the LES flow solver can compute phase-averages on the basis of the LES data at the interface. Then, a filter is designed which creates the time-delay for one full period of the base frequency. Here, the advantage of a linear phase response of a FIR filter is apparent: the linear phase response translates to a constant time delay, which can be controlled by the order of the filter. The order of the filter is then determined by:

$$N = 2 \cdot \frac{f_{\text{sample}}}{f_{\text{base}}} + 1 \tag{5.9}$$

If the time delay created by the explicit coupling of the flow solvers (Schlüter 2003) can be also corrected in this filter delay, if the order is reduced by 1.

While this procedure might be working for a number of applications, many unsteady LES-RANS computations will neither tolerate the time-delay nor the usage of phase-averages at the interface.

6. Spatial Filters

The major reason why temporal filters are creating a time-delay is the lack of information of the future signal. Since we are interested in single-point time histories, the future development at a given point is given by the flow upstream of this point. Using Taylor's hypothesis:

$$\frac{\partial .}{\partial t} = -u_c \frac{\partial .}{\partial x} \tag{6.1}$$

where u_c is a local convection velocity, time evolutions can be expressed as spatial distributions. The temporal filter then becomes the spatial filter:

$$r(t_k) = \sum_{n=0}^{N} b_n s(x_{k-n}) \tag{6.2}$$

$$\text{with } x_n - x_n - 1 = \frac{u_c}{f_{\text{sample}}} \tag{6.3}$$

Instead of using the time history of the signal, the downstream development is sampled. Unlike the case of the temporal filters, where the time history of the interface points have to be stored, no additional memory is necessary for the spatial form of the filter.

So far, the phase delay is still present, unless the origin of the filter is shifted upstream putting the filter centrally around the desired interface point:

$$x_{0,\text{new}} = x_{0,\text{old}} - \frac{N-1}{2} \frac{u_c}{f_{\text{sample}}} \tag{6.4}$$

Here, the location of the sampling points is defined by the sampling frequency. In many flow solvers, especially when using structured meshes, it may be of advantage to define the sampling frequency according to the mesh spacing. The locations of the sampling points are then defined as points on the mesh and the sampling frequency by the distance of the points:

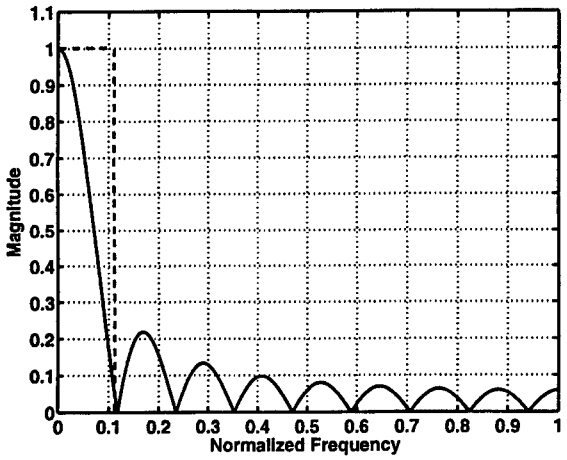
$$f_{\text{sample}} = \frac{u_c}{\Delta x} \tag{6.5}$$

The advantage of this definition is mainly practical nature, since it is easier to retrieve data from these points. Furthermore, no error due to aliasing in the pre-sampling process is introduced, since the sampling points resolve the entire spectrum on the given mesh.

The disadvantage of this definition of the sampling points is the independence of the sampling frequency from the interface frequency. A variation of the RANS time-step, and hence, a variation of the interface frequency, requires a new definition of the filter, since the desired cutoff frequency has changed, while the sampling frequency remains constant.

For the current study, the spacing of mesh points in axial direction is $\Delta x = 3D/128$. With $u_c = U_{\text{bulk}} = 1.0$ this results in a Strouhal number of $St_{\text{sample}} = 42.67$. The cutoff frequency of $St = 5.0$ results in a normalized cutoff frequency $f_{\text{cutoff}} = 0.117$.

The number of sampling points was limited to $N = 17$. A small number of sampling points is desirable, since the Taylor-hypothesis looses validity with increasing distance to the interface point. Furthermore, the extent of the spatial filter is sought to be small for several reasons. First, in geometries more complex than the current pipe flow, the



$b_0 =$	$b_{16} =$	0.0588235
$b_1 =$	$b_{15} =$	0.0588235
$b_2 =$	$b_{14} =$	0.0588235
$b_3 =$	$b_{13} =$	0.0588235
$b_4 =$	$b_{12} =$	0.0588235
$b_5 =$	$b_{11} =$	0.0588235
$b_6 =$	$b_{10} =$	0.0588235
$b_7 =$	$b_9 =$	0.0588235
	$b_8 =$	0.0588235

FIGURE 10. Left: Filter response of spatial filter based on a running average (solid line). Dashed line: Ideal filter response. Right: Filter coefficients

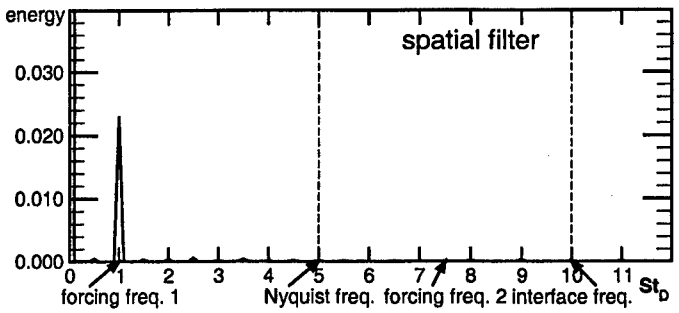


FIGURE 11. Energy spectrum at the interface plane of the downstream domain. Spatial running average filter (Fig. 10).

spatial filter has to be put into an area, where the flow is nearly parallel and has a nearly constant convection velocity over the spatial extend of the filter, which may not be the case over a large portion of the flow. Second, in parallel computations the extend of a spatial filter may be larger than the extend of the flow field computed on a single processor, so that interactions between parallel processors may be necessary.

Since it is rather difficult to design a filter with a low cutoff frequency such as $f_{\text{cutoff}} = 0.117$ on the basis of few sampling points, a running average filter was employed ($b_n = 1/N$). This is the only filter which can ensure that the mean velocity is unchanged. The resulting filter response can be seen in Fig. 10. This filter can still be improved, but seems to be sufficient for the present purposes.

6.1. *Results: Spatial Filter*

The spatial filter was implemented to the upstream LES flow solver computing the pipe flow. The integrated LES-LES computation was performed and the received signal at the inlet of the downstream flow solver examined (Fig. 11). It can be seen that the low frequency perturbation has been transferred correctly. The energy loss due to the filtering is approximately 3%. The high frequency perturbation has been filtered out so that no aliasing errors are present.

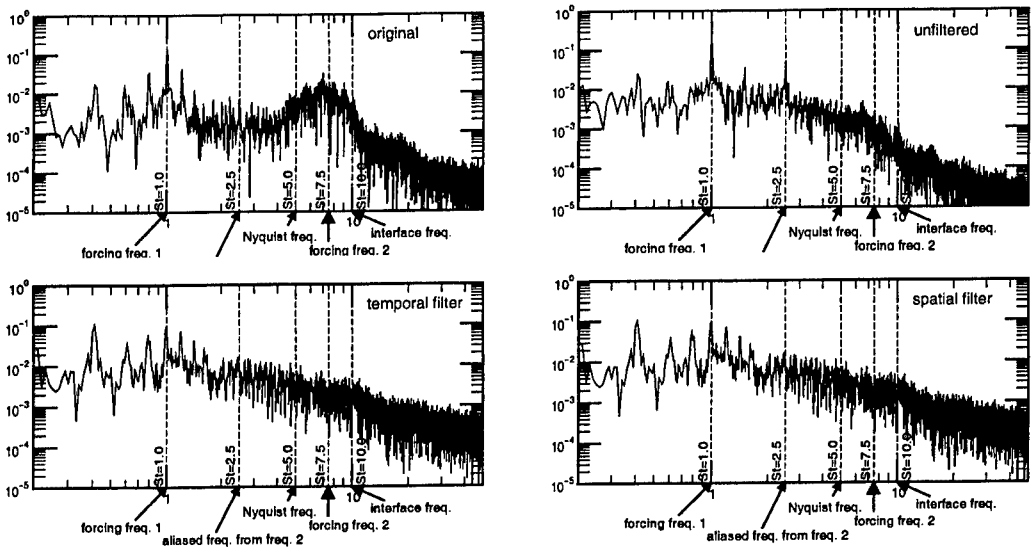


FIGURE 12. Energy spectrum at the interface. Left top: original signal in the upstream domain. Right top: downstream solution without filtering. Left bottom: downstream solution using temporal filter (Kaiser window). Right bottom: downstream solution using spatial filter.

The phase delay of this filter can be expressed as a constant time delay Δt, which is a sum of the filter time-delay and the time correction by the shift of the origin (Eq. (6.4):

$$\Delta t_{\text{total}} = \Delta t_{\text{filter}} + \Delta t_{\text{origin shift}} \tag{6.6}$$

The filter time-delay Δt_{filter} is defined corresponding to Eq. (5.8). The time correction due to the shift of the origin upstream is given by:

$$\Delta t_{\text{origin shift}} = \frac{\Delta x}{u_c} = -\frac{N-1}{2}\frac{u_c}{f_{\text{sample}}}\frac{1}{u_c} \tag{6.7}$$

Equation (6.6) then becomes:

$$\Delta t_{\text{total}} = \frac{N-1}{2 \cdot f_{\text{sample}}} - \frac{N-1}{2}\frac{1}{f_{\text{sample}}} = \mathbf{0} \tag{6.8}$$

The zero time delay results in a true phase transfer of a given perturbation.

This result shows that anti-aliasing with spatial filters is possible, allowing the proper transfer of amplitude *and* phase of a given perturbations resolved by the Nyquist frequency, and hence, allowing a true unsteady coupling between LES and RANS flow solvers.

7. Turbulent Flows

In order to demonstrate the the filtering procedures on turbulent flows, the computations were repeated using a turbulent pipe flow with a Reynolds-number of $Re = 15,000$. Figure 12 shows the resulting energy spectra for these computations. The upstream spectrum shows two distinct peaks, due to the forcing of the flow. The high frequent perturbation is disturbed by turbulence and the peak is less distinct. Yet, the unfiltered solution shows clearly an aliasing error. The computation using the temporal filter and the spatial filter are both able to suppress aliasing errors.

8. Conclusions

In integrated LES-RANS computations, the higher temporal resolution of the flow in the LES domain may lead to aliasing errors when providing data for a RANS flow solver at lower temporal resolution. This problem is similar to the aliasing problem in experiments, where continuous signals are digitally sampled, and where anti-aliasing is achieved with low-pass filtering prior to the sampling.

It has been shown that the application of a digital low pass filter suppresses aliasing successfully. However, the phase delay introduced by the filter limits the application of temporal filters to phase-averaged solutions.

Using Taylor's hypothesis, the digital filter can be expressed in spatial form. Defining the filter centrally around the desired point allows to obtain a filter without phase delay. Despite some drawbacks, the spatial filter has shown to suppress aliasing successfully, while enabling a true unsteady coupling of flow solvers without phase delay.

The identification of the aliasing problem in integrated LES-RANS computations and its solution using spatial filters is another important step towards unsteady coupled computation of gas turbine engines.

9. Acknowledgments

The support by the US Department of Energy under the ASCI program is gratefully acknowledged.

REFERENCES

AKSELVOLL, K., & MOIN, P. 1996 Large-eddy simulation of turbulent confined coannular jets. *J. of Fluid Mech.*, **315**, 387–411.

CONSTANTINESCU, G., MAHESH, K., APTE, S., IACCARINO, G., HAM, F., AND MOIN, P. 2003 A new paradigm for simulation of turbulent combustion in realistic gas turbine combustors using LES. *ASME Turbo Expo 2003*, GT2003-38356, 2003.

DAVIS, R., YAO, J.,CLARK, J. P. , STETSON, G,ALONSO, J. J., JAMESON, A., HALDEMAN, C., AND DUNN, M. 2002 Unsteady interaction between a transsonic turbine stage and downstream components. *ASME Turbo Expo 2002*, GT-2002-30364, 2002.

GERMANO, M., PIOMELLI, U., MOIN, P. & CABOT, W., 1991 A dynamic subgrid-scale eddy viscosity model. *Phys. Fluids* A **(3)**, 1760-1765.

MAHESH, K., CONSTANTINESCU, G., APTE, S., IACCARINO, G. & MOIN, P., 2001 Large-eddy simulation of gas turbine combustors *Annual Research Briefs 2001* Center for Turbulence Research, NASA Ames/Stanford Univ. 3-18.

MOIN, P., SQUIRES, K., CABOT, W. & LEE, S. 1991 A dynamic subgrid-scale model for compressible turbulence and scalar transport. *Phys. Fluids*, A **(3)**, 2746-2757.

PIERCE, C. D. & MOIN, P. 1998 Large eddy simulation of a confined coaxial jet with swirl and heat release. *AIAA Paper* 98-2892.

C. B. RORABAUGH, 1997 *Digital Filter Designer's Handbook.* McGraw-Hill, 2. edition, 1997.

SCHLÜTER, J., PITSCH, H. 2001 Consistent boundary conditions for integrated LES/RANS simulations: LES outflow conditions. *Annual Research Briefs* Center for Turbulence Research, NASA Ames/Stanford Univ. 19–30

SCHLÜTER, J., SHANKARAN, S., KIM, S., PITSCH, H., ALONSO, J. J., 2002 Integration

of LES and RANS flow solvers: Interface validation. *Annual Research Briefs*, 2002. Center for Turbulence Research, NASA Ames/Stanford Univ.

SCHLÜTER, J. U., 2003 Consistent boundary conditions for integrated LES/RANS computations: LES inflow conditions. *AIAA paper*, (AIAA-2003-3971), 2003. 16th AIAA CFD conference 2003.

SCHLÜTER, J. U., PITSCH, H., AND MOIN, P., 2002 Consistent boundary conditions for integrated LES/RANS simulations: LES outflow conditions. *AIAA paper* 2002-3121

SCHLÜTER, J. U., PITSCH, H., AND MOIN, P., 2003a Boundary conditions for LES in coupled simulations. *AIAA paper*, (AIAA-2003-0069), 2003.

SCHLÜTER, J. U., PITSCH, H., AND MOIN, P., 2003b LES inflow boundary conditions for coupled RANS-LES computations. *submitted for publication to AIAA Journal*, 2003.

SCHLÜTER, J. U., PITSCH, H., AND MOIN, P., 2003c LES outflow conditions for integrated LES/RANS simulations. *submitted for publication to AIAA Journal*, 2003.

SCHLÜTER, J., SHANKARAN, S., KIM, S., PITSCH, H., ALONSO, J. J., 2003d Integration of RANS and LES flow solvers for simultaneous flow computations. *AIAA paper*, (AIAA 2003-0085), 2003.

S. SHANKARAN, M.-F. LIOU, N.-S. LIU, AND R. DAVIS ANF J. J. ALONSO 2001 A multi-code-coupling interface for combustor/turbomachinery simulations. *AIAA paper* 2001-0974

STEARNS, S. D., 2003 *Digital signal processing with examples in MATLAB 2003.* CRC Press, 2003.

D. VEYNANTE AND T. POINSOT 1996 Reynolds averaged and large eddy simulation modeling for turbulent combustion. In *New Tools in Turbulence Modelling*, Les edition physique. Springer, pp 105–140

WILLIAMS, C. S. *Designing Digital Filters.* Prentice-Hall, 1986.

Integrated RANS-LES computations of turbomachinery components: Generic compressor/diffuser

By J. U. Schlüter, X. Wu, S. Kim, J. J. Alonso, and H. Pitsch

1. Introduction

The goal of the ASCI project at Stanford is the computation of the entire aero-thermal flow in an aircraft gas turbine engine. As part of the project, high performance flow solvers are developed to address the prediction of the flow in components of the turbine. For the turbomachinery parts, a flow solver based on Reynolds-Averaged Navier-Stokes (RANS) approach is used. This flow solver is validated on a variety of turbomachinery applications (Davis *et al.* 2002; Davis *et al.* 2003) and is scalable to run on a large number of processors in parallel, a feature necessary in light of the enormous task of the final application. For the prediction of the reacting flow in the combustion chamber, a flow solver based on Large Eddy Simulations (LES) is used. The strongly detached flow in the combustor requires that the numerical approach has to resolve the large scale turbulence in time and space in order to predict the flow features accurately. Furthermore, the temporal resolution of the flow is very beneficial for the modeling of the reactive flow. This makes LES much more suitable for this portion of the flow path. An LES flow solver capable of modeling the variety of physical phenomena, such as turbulence, spray and heat release, is currently under development and in the process of validation (Mahesh *et al.* 2001; Constantinescu *et al.* 2003).

In order to predict multi-component phenomena, such as compressor-combustor instability, combustor-turbine hot-streak migration and combustion instabilities, these RANS and LES flow solvers have to run simultaneously, each computing its part of the gas turbine. At the interfaces of the individual domains, the flow solvers have to communicate the flow parameters required to evaluate appropriately defined boundary conditions.

Part of the efforts to integrate these flow solvers is the definition of the interface. The optimization of the communication and the processing of the exchanged data to meaningful boundary conditions are some of the encountered challenges. In previous work interface routines have been established and validated with simple geometries (Shankaran *et al.* 2001; Schlüter *et al.* 2003d; Schlüter *et al.* 2003e). Since the definition of boundary conditions on the LES side requires special attention, LES inflow (Schlüter *et al.* 2003a; Schlüter, 2003; Schlüter *et al.* 2003b) and outflow boundary conditions (Schlüter *et al.* 2002; Schlüter *et al.* 2003c) have been established. While most of this work has been carried out on simple test-cases, the value of coupled RANS-LES computation can only be assessed in the application to industrial problems. The next logical step is to apply the coupled RANS-LES approach to complex geometries of turbomachinery applications.

The goal of the current study is to apply the coupled RANS-LES approach to a compressor-diffuser geometry of a gas turbine. This flow configuration is important, since the outflow of the compressor alters the flow field in the subsequent diffuser (Barker & Carrotte 2001a; Barker & Carrotte 2001b). A detailed knowledge of the flow field in this

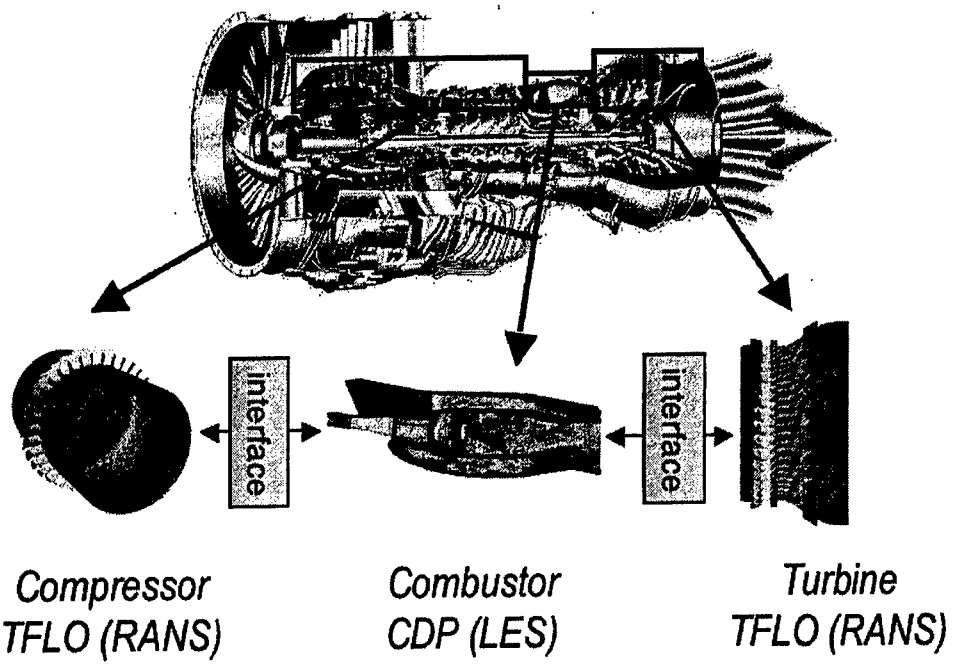


FIGURE 1. Decomposition of gas turbine engine. LES of combustor(Mahesh *et al.* 2001; Constantinescu *et al.* 2003) , RANS of turbine section (Davis *et al.* 2002

section allows to optimize the diffuser design in order to to achieve a decrease of pressure loss.

Here, the NASA stage 35 compressor is coupled with a generic diffuser in order to assess the integrated RANS-LES approach.

2. Interface Description

The interface used for establishing a connection between the flow solvers consists of routines following an identical algorithm in all flow solvers. The message passing interface MPI is used to create communicators, which are used to communicate data directly between the individual processors of the different flow solvers. This means that each processor of one flow solver can communicate directly with all of the processors of the other flow solvers. This requires the interface routines to be part of the source code of all flow solvers. A detailed description of the common algorithms can be found in Schlüter *et al.* (2003d and 2003e).

In a handshake routine, each processor determines whether its domain contains points on the interface. The location of these points are sent to all processors of the other peer flow solvers. The processors of the peer flow solvers then determine and communicate back, whether the received points are within their own domain. During the actual flow computation all processors communicate data for a common point directly with each other.

The approach of embedding the interface into the source code of each flow solver has been chosen for its efficiency in the communication process. Alternative solutions would be to use a third code, which organizes the communication between the flow solvers, or

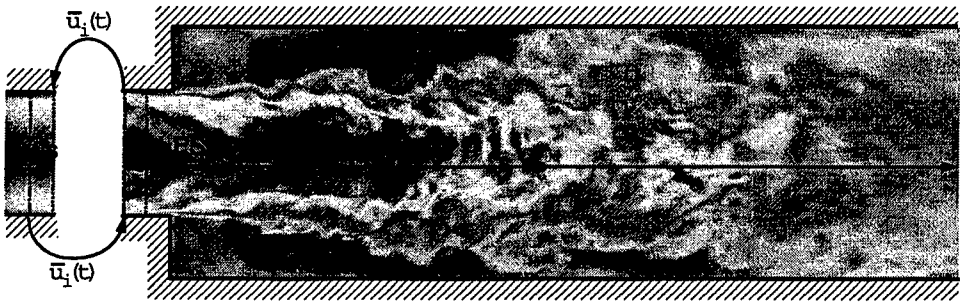


FIGURE 2. Interface validation for CDP-α: Integrated RANS-LES computation of a confined jet.

to limit the peer-to-peer communication to the root processes of each flow solver. While the latter two solutions are usually easier to implement, they cause more communication processes and slow down the computation.

The interface routines are written in a modular approach, where the communication steps are separated from code specific routines. This facilitates the implementation of the interface into other flow solvers.

3. CDP-α Interface Validation

While most of the fundamental issues of integrated RANS-LES computations in previous work were addressed using a structured LES flow solver in order to decrease computational costs, the envisioned increase in complexity of the geometries calls for the use of an unstructured flow solver. Hence, the described interface was implemented into the unstructured LES flow solver CDP-α.

CDP-α has been developed to predict chemically reacting flows in gas turbine combustors. The filtered momentum equations based on a low-Mach number approximation are solved with a 2nd order implicit time-advancement. A dynamic model is used for the turbulent sub-grid stresses.

LES inflow boundary conditions as proposed by Schlüter *et al.* (2003b) have been implemented into CDP-α. Here, the challenge is to prescribe transient turbulent velocity profiles from ensemble-averaged RANS data. Simply adding random fluctuations to the RANS profiles miss the temporal and spatial correlations of real turbulence and are dissipated very quickly. Instead, a data-base of turbulent fluctuations is created by an auxiliary LES computation of a periodic turbulent pipe flow. The LES inflow boundary condition can then be described as:

$$u_{i,\mathrm{LES}}(t) = \underbrace{\overline{u}_{i,\mathrm{RANS}}(t)}_{I} + \underbrace{\left(u_{i,\mathrm{DB}}(t) - \overline{u}_{i,\mathrm{DB}}\right)}_{II} \cdot \underbrace{\frac{\sqrt{\overline{u'^2_{(i)}}_{\mathrm{RANS}}(t)}}{\sqrt{\overline{u'^2_{(i)}}_{\mathrm{DB}}}}}_{III} \tag{3.1}$$

with the sub-script RANS denoting the solution obtained from the RANS computation and quantities with sub-script DB are from the database. Here, t is the time, u_i stands for the velocity components, and $\overline{u}_i$ is the ensemble average of the velocity component u_i.

Term *II* of Eq. (3.1) is the velocity fluctuation of the database. This turbulent fluctu-

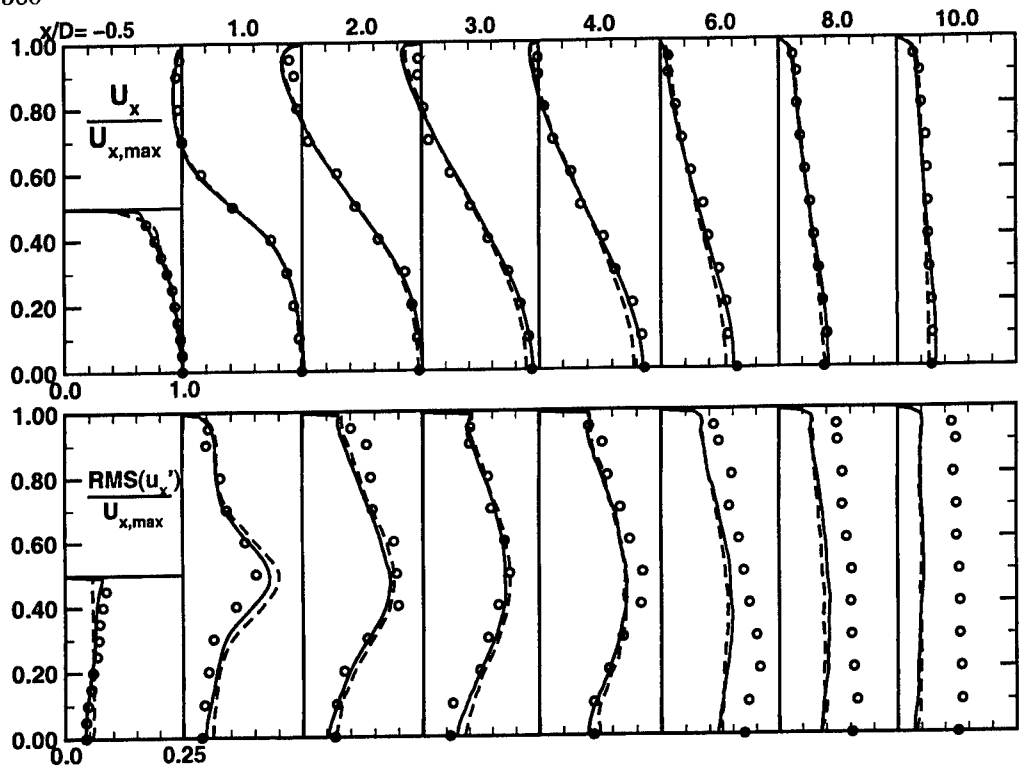


FIGURE 3. Velocity profiles of computation of a confined jet. Circles: experiment, solid line: CDP-α defining inlet from experiments, dashed line: integrated TFLO-CDP computation.

ation is scaled to the desired value by multiplication with term III, which ensures that the correct level of velocity fluctuation is recovered.

As a validation of the interface and the LES inflow boundary condition, a coupled RANS-LES computation of an axisymmetric expansion has been performed. The test-case corresponds to the experimental configuration of Dellenback *et al.* (1988). Here, a part of the flow domain upstream of the expansion is computed with a RANS code (Fig. 2).

The RANS flow solver used for this investigation is the TFLO code developed at the Aerospace Computing Lab (ACL) at Stanford. The flow solver computes the unsteady Reynolds Averaged Navier-Stokes equations using a cell-centered discretization on arbitrary multi-block meshes (Yao *et al.* 2000). The solution procedure is based on efficient explicit modified Runge-Kutta methods with several convergence acceleration techniques such as multi-grid, residual averaging, and local time-stepping. These techniques, multi-grid in particular, provide excellent numerical convergence and fast solution turnaround. Turbulent viscosity is computed from a $k-\omega$ two-equation turbulence model. The dual-time stepping technique (Jameson 1991; Alonso *et al.* 1995; Belov *et al.* 1996) is used for time-accurate simulations that account for the relative motion of moving parts as well as other sources of flow unsteadiness.

The inlet velocity profiles in the RANS section are specified according to the experimental data at this location. The RANS flow solver TFLO computes the flow through the upstream pipe and at its outlet hands over the data to the subsequent LES flow

solver. The RANS domain is relatively short ($0.5D$, with D being the diameter of the pipe upstream of the expansion.)

The LES flow solver CDP obtains its inflow velocity profiles from the RANS flow solver and specifies its LES inflow boundary conditions according to Eq. 3.1.

The results of the integrated computation are then validated against the experimental data and verified against an LES computation using an inflow data-base at the inlet in which the data-base statistics are corresponding to the experimental data at the inlet plane.

The RANS mesh contains 350,000 mesh points and is refined near the wall. The LES mesh contains 1.1 million mesh points with the mesh points concentrated near the spreading region of the jet. The far field of the jet is relatively coarse.

Fig. 3 shows the LES velocity profiles obtained from this computation. The integrated TFLO-CDP computation predicts essentially the same results as the single LES computation and matches the experimental data well. Please note that the far field of the jet is not well resolved and hence, the turbulent fluctuations in the far field are underestimated by both LES computations.

4. Integrated RANS-LES of a Realistic Turbomachinery Geometry

In order to test the applicability of coupled RANS-LES computations in realistic geometries, a turbomachinery case has been investigated. The goal of this study is to test the interface routines for the flow between the compressor and the combustor and to study the influence of possible unsteady interactions of compressor and the combustor inlet diffuser. The test-case consists of a compressor geometry computed by a RANS flow solver and a pre-diffuser, which is a component upstream of the injector to the combustor, computed by an LES flow solver.

The computational study of such cases is relevant and important, since typically these two components are developed in isolation and combined tests are done only in the final prototype assembly. The numerical prediction of this flow configuration would allow to assess the interactions of the components during the design phase of the engine. One of the biggest questions in compressor-prediffuser flows is whether separation in the diffuser takes place. Since the inflow of the pre-diffuser is inhomogeneous and periodically perturbed by blade passings, the integrated computation of this geometry can offer insights on how to modify the geometry in order to develop a more compact, non-separating diffuser.

The drawback of the choice of this configuration is that no experimental data exists to validate the computation. The quality of the computed results can only be guaranteed on the basis of the separate validation process that the component codes have undergone and the detailed testing of the interface routines that has been presented in previous work. Some validation studies of the individual flow solvers are given in Yao *et al.* (2000) and Davis *et al.* (2002 and 2003) for the TFLO code and in Mahesh *et al.* (2001) and Constantinescu *et al.* (2003) for the CDP code. The interface has been developed and tested in detail over the last two years (Shankaran *et al.* 2001; Schlüter *et al.* 2003d; Schlüter *et al.* 2003e). While many of the techniques necessary for coupling these two flow solvers are still under development, all necessary elements, such as the coupling procedure and the boundary conditions on both sides are currently in place for the chosen test-case.

The goal of this computation is to demonstrate the feasibility of integrated RANS-LES

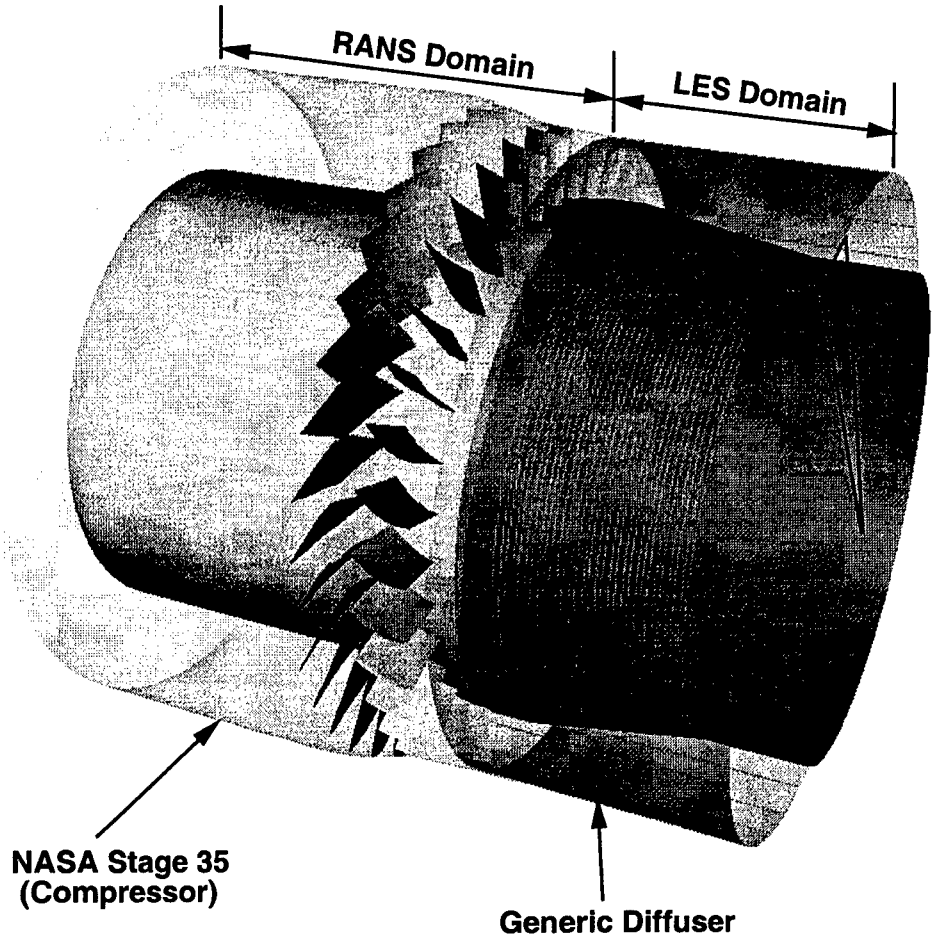


FIGURE 4. Geometry of the coupled NASA stage 35/prediffuser geometry. RANS domain includes one stage of a compressor, consisting of one rotor and one stator. LES domain includes the diffuser. A 10° axi-symmetric sector is computed.

computations in a turbomachinery environment and to identify practical issues involved in these calculations.

4.1. *Geometry*

The compressor geometry for the computed test-case corresponds to that of a modified NASA experimental rig stage 35. The rig consists of a row of 46 rotors and a row of 36 stators. In order to simplify this geometry, the rotor stage has been rescaled to a 36 blade count, which allows us to compute an axisymmetric segment of 10° using periodic boundary conditions at the corresponding azimuthal planes.

For this integrated computation, the rotor tip-gap has been closed in order to decrease the overall computational costs. The inclusion of the tip-gap is addressed in the TFLO flow solver and poses no additional problem from the integration point of view. The RANS time step was chosen to resolve one blade passing with 50 intervals.

The RANS mesh is a structured multi-block mesh consisting of approximately 1.5 million control volumes. The speed of the rotor was set to a relatively low 5000 RPM in

order to keep the flow at the interface within the low-Mach number regime that the LES solver is able to handle. This decrease in rotational speed had to be done for the current case. In a real engine, the compressor consists of a multiple stages resulting in a higher pressure and a higher temperature at the compressor exit. The high temperature of the air in this section of the flow path will ensure that the low-Mach number approximation is not violated, even when the engine is at full load.

For the RANS domain, the flow solver TFLO has been used. On the LES side, computations have been performed with two different LES flow solvers, a structured LES flow solver, which has been used already for many investigations of fundamental issues, and the CDP-α code. Since the structured flow solver is much faster than CDP, finer meshes can be used.

The structured LES flow solver is a code developed at the Center for Turbulence Research at Stanford by Pierce and Moin (1998). The filtered momentum equations with a low-Mach number assumption on an axi-symmetric structured single-block mesh are solved. A second-order finite-volume scheme on a staggered grid is used (Akselvoll & Moin 1996). The subgrid stresses are approximated with an eddy-viscosity approach, where the eddy viscosity is determined by a dynamic procedure (Germano *et al.* 1991; Moin *et al.* 1991)..

The diffuser expands one stator chord length behind the stator. The LES domain starts 1/3 chord behind the stator. The RANS domain reaches 2/3 of the chord length into the LES domain, which essentially means that the RANS outlet plane is just at the expansion of the diffuser.

The diffuser geometry has been chosen with a relatively wide opening such that separation may occur. The diffuser opens towards the centerline of the compressor. Over 3 chord lengths, the diffuser opens up 0.5 chord lengths. The outer wall of the diffuser is straight.

The LES mesh for the structured LES flow solver consists of 3.5 million mesh points. The diverging wall is approximated with a stair-stepping function.

The LES mesh for the CDP flow solver consists of 500,000 control volumes and is concentrated near the walls. LES inflow boundary conditions for both flow solvers were defined corresponding to Eq. 3.1.

In order to initialize the solutions in both domains, separate computations were performed. On the basis of the initial, separate computations, the computational needs for each domain and solver were assessed in order to balance the split of processors for the computation. The load balancing between the two flow solvers has to be done manually, since the current version of MPI does not support a dynamic splitting of the processors using multiple codes.

4.2. *Results*

The computation using TFLO and the structured LES flow solver was carried out using 15 processors for the RANS domain and 3 processors for the LES domain. In total, 6 blade passings were computed. The computation was performed on an SGI Origin 3000 and needed 60 hours of wall-clock time.

The computations using the unstructured LES flow solver CDP-α and TFLO was carried out using 64 processors for TFLO and 64 processors for CDP-α. Here, 8 blade passings were computed in 60 hours of wall clock time using an IBM Power3.

The actual Mach number at the interface was Ma= 0.1 ensuring the validity of the low-Mach number approximation in the LES domain. The mass flux over the interface was conserved with an error of $\approx 0.5\%$.

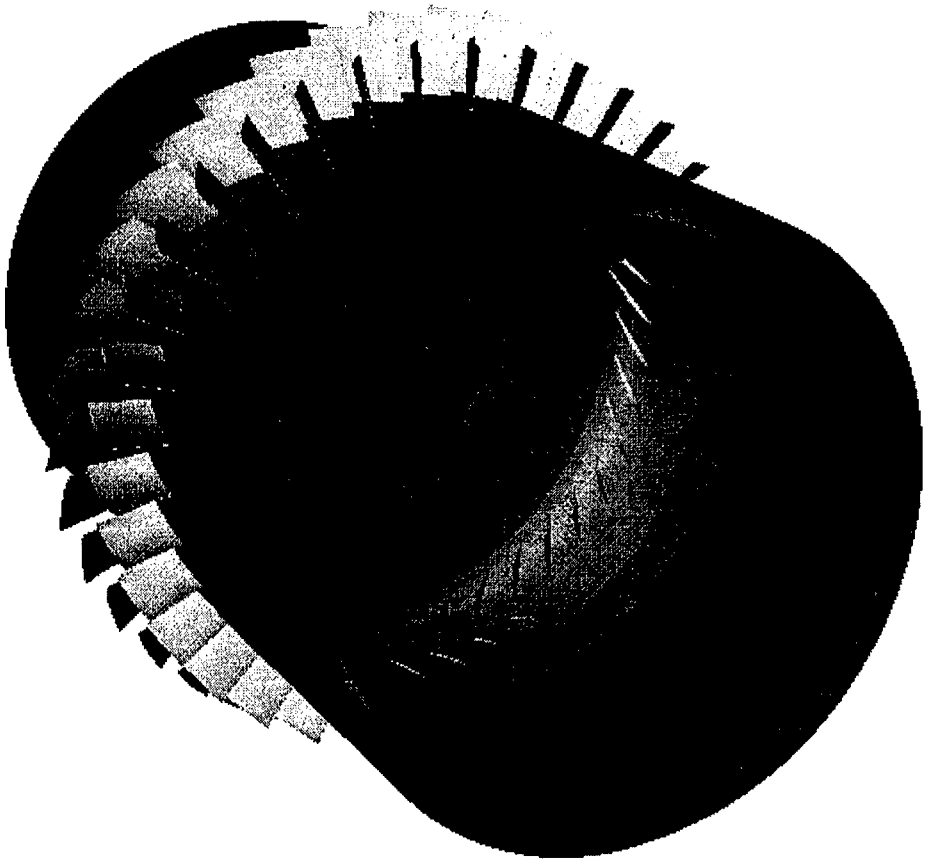


FIGURE 5. Integrated RANS-LES computation: velocity distribution in the NASA stage 35 - prediffuser geometry. The axisymmetric domain is copied and rotated around the circumference for visualization purposes.

The solutions of both LES flow solvers were nearly identical. Since the flow visualization using the structured LES flow solver is simpler, all pictures shown are results from the structured LES flow solver.

Figures 5 and 6 show the axial velocity distributions at 10% span of the compressor blades for an instantaneous snapshot of the computation. The upstream RANS solution corresponds to a phase averaged solution while the downstream LES solution is truly unsteady.

The wakes of the stators can clearly be identified in the RANS domain downstream of the stators. The communication of the flow solvers at the interface ensures that the full 3D flow features are transferred from the upstream flow solver to the downstream domain. The boundary conditions of the LES flow solver are defined according to these data. Hence, the wake of the stator correctly propagates across the interface and can still be found far downstream in the diffuser. It can also be seen that the turbulence, which is resolved in the LES domain, creates a more disturbed velocity distribution.

The differences in the description of turbulence are more apparent in Fig. 7, which shows the vorticity distribution at 10% span of the stator. Here the magnitude of the vorticity is depicted computed according to the unsteady flow field of both domains.

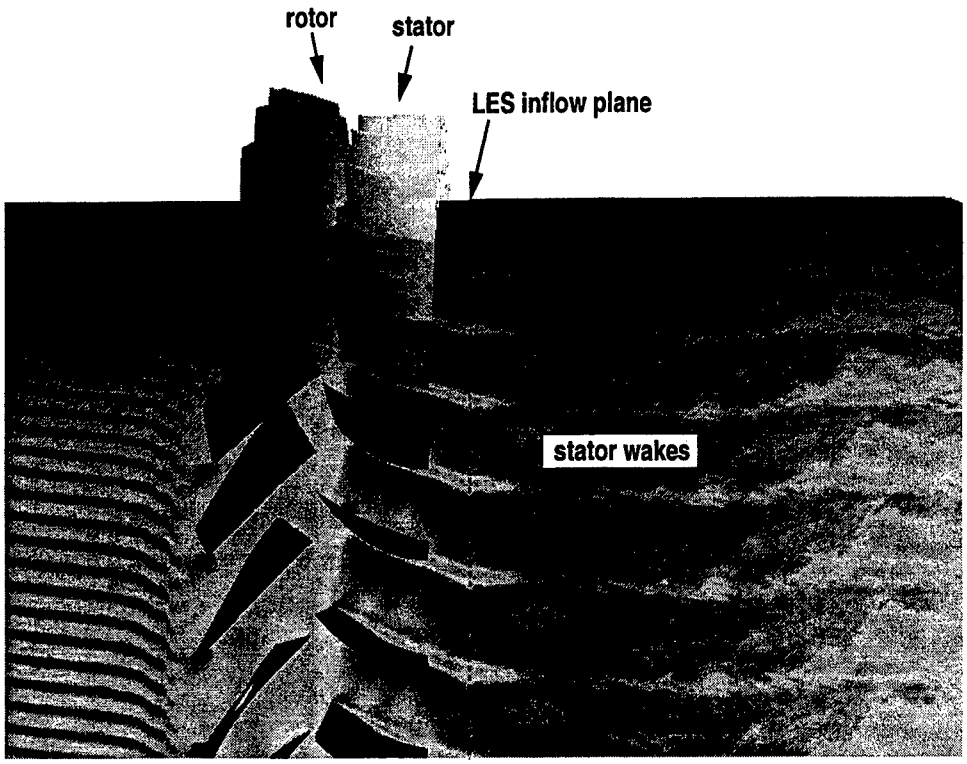


FIGURE 6. Integrated RANS-LES computation: velocity distribution in the NASA stage 35 - prediffuser geometry. Close-up of the interface.

In the RANS domain, the vorticity is mainly created due to the mean flow features, such as wall boundary layers, and secondary flows and vortices. The stator creates two vorticity sheets, one on the extrado, one on the intrado. Both vorticity sheets propagate downstream across the interface.

The vorticity distribution in the LES domain is characterized by small scale turbulence. Turbulence present in the upstream RANS domain and modeled by a RANS turbulence model has to be regenerated. The small scale turbulence has been reconstructed at the interface using the LES inflow boundary condition (Eq. 3.1.) It can be seen that the small-scale turbulence interferes with the stator wakes. The turbulent diffusion of the stator wakes in the RANS domain is modeled with an eddy viscosity model, which gives them a very smooth appearance. In the LES domain, the turbulent transport is given by the resolved turbulence, and hence, vortical turbulent structures can be identified.

Time data recorded on the LES side of the interface did not reveal a predominant frequency such as the blade passing frequency. This could be due to the relatively short computed time-span of six blade passings or due to the low rotational speed of the compressor. Future investigations will study the presence of predominant frequencies in the flow due to blade passings in more detail.

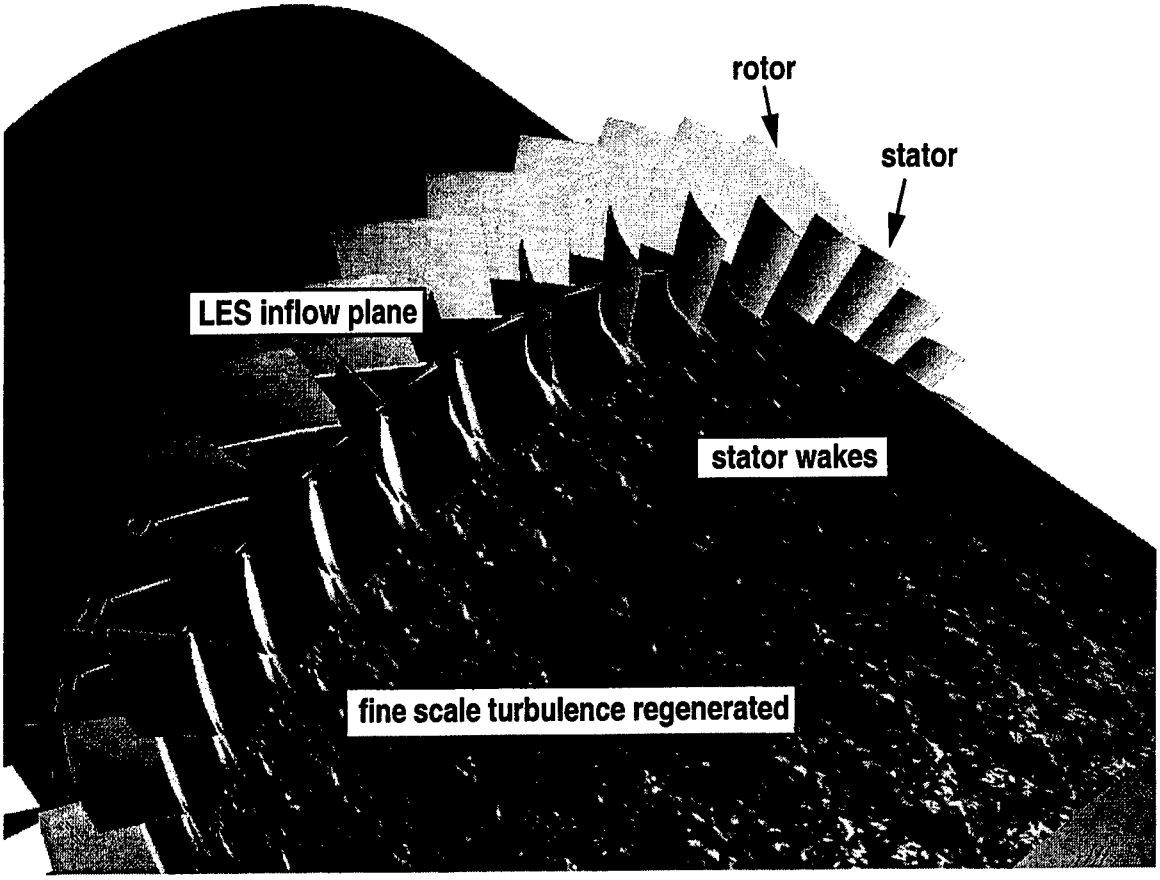


FIGURE 7. Integrated RANS-LES computation: Vorticity magnitude distribution in the coupled NASA stage 35/Prediffuser geometry. Vorticity created by the stator wake can be found in the LES domain.

5. Integrated Simulations: Conclusions

The computation of the coupled NASA stage 35/prediffuser geometry demonstrates the concept of integrated RANS-LES computations in a realistic environment. Future work will use the geometry of a real aircraft engine in order to characterize the flow in the prediffuser.

6. Acknowledgments

The support by the US Department of Energy under the ASCI program is gratefully acknowledged.

REFERENCES

AKSELVOLL, K., & MOIN, P. 1996 Large-eddy simulation of turbulent confined coannular jets. *J. of Fluid Mech.*, **315**, 387–411.

J. J. ALONSO, L. MARTINELLI, AND A. JAMESON 1995 Multigrid unsteady Navier-Stokes calculations with aeroelastic applications. *AIAA Paper* 95-0048

BARKER, A. G., AND CARROTTE, J. F. 2001A Influence of compressor exit conditions on combustor annular diffusers, Part 1: Diffuser performance. *Journal of Propulsion and Power*, **17**, No. 3, 678-686.

BARKER, A. G., AND CARROTTE, J. F. 2001B Influence of compressor exit conditions on combustor annular diffusers, Part 2: Flow redistribution. *Journal of Propulsion and Power*, **17**, No. 3, 687-694.

A. BELOV, L. MARTINELLI, AND A. JAMESON 1996 Three-dimensional computations of time-dependent incompressible flows with an implicit multigrid-driven algorithm on parallel computers. In *Proceedings of the 15th International Conference on Numerical Methods in Fluid Dynamics, Monterey, CA*

CONSTANTINESCU, G., MAHESH, K., APTE, S., IACCARINO, G., HAM, F., AND MOIN, P. 2003 A new paradigm for simulation of turbulent combustion in realistic gas turbine combustors using LES. *ASME Turbo Expo 2003*, GT2003-38356, 2003.

DAVIS, R., YAO, J.,CLARK, J. P. , STETSON, G,ALONSO, J. J., JAMESON, A., HALDEMAN, C., AND DUNN, M. 2002 Unsteady interaction between a transsonic turbine stage and downstream components. *ASME Turbo Expo 2002*, GT-2002-30364.

DAVIS, R., YAO, J.,ALONSO, J. J., PAOLILLO, R., SHARMA, O. P., 2003 Prediction of main/secondary-air system flow interaction in a high pressure turbine. *AIAA Paper* 2003-4833.

DELLENBACK, P. A., METZGER, D. E. & NEITZEL, G. P 1988 Measurements in turbulent swirling flow through an abrupt axisymmetric expansion. *AIAA J.*, **26**, 669-681.

GERMANO, M., PIOMELLI, U., MOIN, P. & CABOT, W., 1991 A dynamic subgrid-scale eddy viscosity model. *Phys. Fluids* A **(3)**, 1760-1765.

JAMESON, A. 1991 Time dependent calculations using multigrid, with applications to unsteady flows past airfoils and wings. *AIAA paper* 91-1596

MAHESH, K., CONSTANTINESCU, G., APTE, S., IACCARINO, G. & MOIN, P., 2001 Large-eddy simulation of gas turbine combustors *Annual Research Briefs 2001* Center for Turbulence Research, NASA Ames/Stanford Univ. 3-18.

MOIN, P., SQUIRES, K., CABOT, W. & LEE, S. 1991 A dynamic subgrid-scale model for compressible turbulence and scalar transport. *Phys. Fluids*, A **(3)**, 2746-2757.

PIERCE, C. D. & MOIN, P. 1998 Large eddy simulation of a confined coaxial jet with swirl and heat release. *AIAA Paper* 98-2892.

SCHLÜTER, J. U., 2003 Consistent boundary conditions for integrated LES/RANS computations: LES inflow conditions. *AIAA paper*, (AIAA-2003-3971), 2003. 16th AIAA CFD conference 2003.

SCHLÜTER, J. U., PITSCH, H., AND MOIN, P., 2002 Consistent boundary conditions for integrated LES/RANS simulations: LES outflow conditions. *AIAA paper* 2002-3121

SCHLÜTER, J. U., PITSCH, H., AND MOIN, P., 2003a Boundary conditions for LES in coupled simulations. *AIAA paper*, (AIAA-2003-0069), 2003.

SCHLÜTER, J. U., PITSCH, H., AND MOIN, P., 2003b LES inflow boundary conditions for coupled RANS-LES computations. *accepted, AIAA Journal*, 2003.

SCHLÜTER, J. U., PITSCH, H., AND MOIN, P., 2003c LES outflow conditions for integrated LES/RANS simulations. *submitted for publication to AIAA Journal*, 2003.

SCHLÜTER, J., SHANKARAN, S., KIM, S., PITSCH, H., ALONSO, J. J., 2003d Inte-

gration of RANS and LES flow solvers for simultaneous flow computations. *AIAA paper*, (AIAA 2003-0085), 2003.

SCHLÜTER, J., SHANKARAN, S., KIM, S., PITSCH, H., ALONSO, J. J., 2003e Towards multi-component analysis of gas turbines by CFD: integration of RANS and LES flow solvers. *ASME paper*, (ASME GT2003-38350), 2003. ASME Turbo Expo 2003, June 16-19, 2003, Atlanta, GA.

S. SHANKARAN, M.-F. LIOU, N.-S. LIU, AND R. DAVIS AND J. J. ALONSO 2001 A multi-code-coupling interface for combustor/turbomachinery simulations. *AIAA paper* 2001-0974

J. YAO, A. JAMESON, J. J. ALONSO, AND F. LIU 2000 Development and validation of a massively parallel flow solver for turbomachinery flows. *AIAA paper* 00-0882

Toward immersed boundary simulation of high Reynolds number flows

By Georgi Kalitzin and Gianluca Iaccarino

1. Motivation and Background

In the immersed boundary (IB) method, the surface of an object is reconstructed with forcing terms in the underlying flow field equations. The surface may split a computational cell removing the constraint of the near wall gridlines to be aligned with the surface. This feature greatly simplifies the grid generation process which is cumbersome and expensive in particular for structured grids and complex geometries.

The IB method is ideally suited for Cartesian flow solvers. The flow equations written in Cartesian coordinates appear in a very simple form and several numerical algorithms can be used for an efficient solution of the equations. In addition, the accuracy of numerical algorithms is dependent on the underlying grid and it usually deteriorates when the grid deviates from a Cartesian mesh.

The challenge for the IB method lies in the representation of the wall boundaries and in providing an adequate near wall flow field resolution. The issue of enforcing no-slip boundary conditions at the immersed surface has been addressed by several authors by imposing a local reconstruction of the solution. Initial work by Verzicco *et al.* (2000) was based on a simple linear, one-dimensional operator and this approach proved to be accurate for boundaries largely aligned with the grid lines. Majumdar *et al.* (2001) used various multidimensional and high order polynomial interpolations schemes. These high order schemes, however, are keen to introduce wiggles and spurious extrema. Iaccarino & Verzicco (2003) and Kalitzin & Iaccarino (2002) proposed a tri-linear reconstruction for the velocity components and the turbulent scalars. A modified implementation that has proven to be more robust is reported in this paper.

The issue of adequate near wall resolution in a Cartesian framework can initially be addressed by using a non-uniform mesh which is stretched near the surface. In this paper, we investigate an unstructured approach for local grid refinement that utilizes Cartesian mesh features.

The computation of high Reynolds number wall bounded flows is particularly challenging as it requires the consideration of thin turbulent boundary layers, i.e. near wall regions with large gradients of the flow field variables. For such flows, the representation of the wall boundary has a large impact on the accuracy of the computation. It is also critical for the robustness and convergence of the flow solver.

2. Numerical Technique

The computational code IBRANS is based on the steady-state incompressible RANS equations closed either with an one-equation turbulence model (Spalart & Allmaras 1994) or a two-equation model (Kalitzin & Iaccarino 2002). A second-order, implicit, cell centered Cartesian discretization is used within a SIMPLE pressure-velocity coupling algorithm with a segregated solution of the field equations (Ferziger & Peric 2002).

The equations are discretized in three-dimensions with a typical 7-point stencil. In this paper, however, we will refer for simplicity to the corresponding two-dimensional equations. For each cell (i,j), the discretized field equation for momentum, turbulent scalar and pressure correction can be written as:

$$a_W^n \phi_W^{n+1} + a_E^n \phi_E^{n+1} + a_S^n \phi_S^{n+1} + a_N^n \phi_N^{n+1} + a_{(i,j)}^n \phi_{(i,j)}^{n+1} = s_{(i,j)}^n \tag{2.1}$$

where the indices E, W, S, N denominate the neighboring cells that have a common face with cell (i,j), e.g. E for cell $(i+1,j)$ etc. The superscript n indicates the iteration. The equation is under-relaxed implicitly to increase the diagonal dominance of the implicit matrix. The Strong Implicit Procedure (SIP) by Stone (1968) is used for the solution of (2.1).

The flow solver is set up as a virtual wind tunnel. The x-direction is the main flow direction with inflow and outflow, the other directions have either the usual wall boundary, symmetry or periodicity conditions. The domain is partitioned in x-direction and the equations are solved in parallel using MPI. An object is placed into the flow domain and the immersed boundaries, described in the next section, are applied to the velocity components and the turbulence variables. There is no special treatment of the pressure at the immersed boundary. The immersed boundaries affect the Poisson equation for the pressure correction only through the source term which represents the divergence of the velocity field. Thus, the Poisson equation is solved in the entire computational domain. A parallel geometric multigrid is being used to accelerate the convergence of the Poisson equation.

The non-uniform computational grid and the IB interpolation stencil is generated automatically and the pre-processing time to start the computation is negligible. The procedure is based on the ray tracing technique that allows one to identify the cells cut by the immersed boundary. An initial coarse (and typically) uniform mesh is specified by the user; a three-steps iterative procedure is employed: (a) tag the grid identifying the cells cut by the immersed boundary, (b) split these cells in the direction that moves the cell center closer to the immersed boundary, (c) regenerate a structured grid by propagating the cell split to the domain boundaries, and restart from (a). This procedure is repeated until a prescribed distance from the wall is achieved for all the interface cells. The geometry definition is based on the StereoLitography format and therefore the CAD model can be used directly.

3. Immersed Boundary Treatment

After the pre-processor detects the computational cells that are cut by the body, the cells are divided in those that are inside and outside of the body as shown in Fig. 1. The cut cells are separated in two type of cells corresponding to the location of their cell center. The cells that have their cell center outside or on the surface are labeled as interface cells. The other cut cells are treated like inside cells.

The flow variable ϕ, which represents a velocity component or a turbulence variable, is set to zero in the inside cells. Note that the turbulence models considered have zero wall boundary conditions for all turbulence variables. At the interface cells, the nearby wall is modeled with an off wall boundary condition which in general consists of an implicit linear interpolation stencil with an explicit (non-linear) correction.

A sketch of the linear interpolation algorithm is shown in Fig. 1a. Like the plotted tangential velocity component, the scalar variable ϕ in the interface cell (i,j) is interpolated

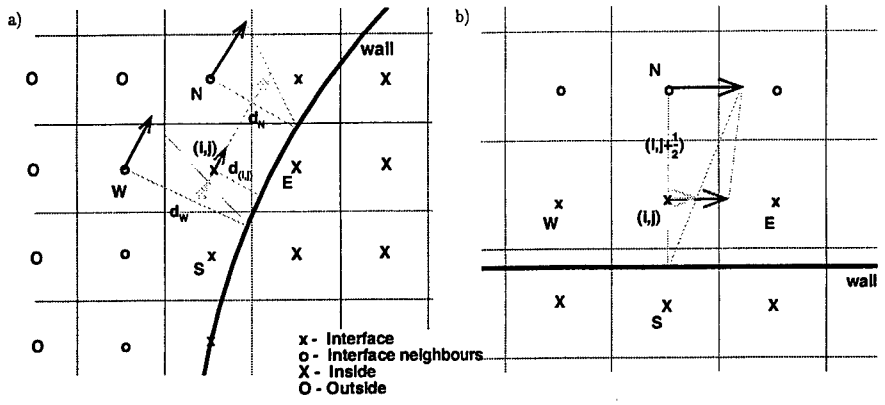


FIGURE 1. Schematic representation of interpolation algorithm for the tangential velocity. General case (left) and wall function approach for a grid aligned case (right). Tangential velocity: ⟶ computed, ⟶ interpolated linearly on intermediate location, ⟶ imposed in interface cell.

using only the neighboring cells that are further away from the body. The interpolation is carried out in two steps. First, for each neighboring cell an interpolation is carried out normal to the wall to an intermediate location that has the same distance to the wall as the interface cell center (i,j). This interpolation might be linear, quadratical or other, depending on the near wall behavior of the considered variable. The second interpolation is on a surface that is parallel to the wall. Here we use the inverse-distance weighted method proposed by Franke (1982) that has the property of preserving local maxima and producing smooth reconstructions. The interpolation of $\phi_{(i,j)}$ in the interface cell is:

$$\phi_{(i,j)} = \sum_m w_m \tilde{\phi}_m / q \text{ with } w_m = \left(\frac{H - h_m}{H h_m}\right)^p, \quad q = \sum_m w_m \text{ and } p = 2 \qquad (3.1)$$

where $\tilde{\phi}_m$ represents the previously interpolated values, h_m is the distance between the location of $\phi_{(i,j)}$ and the location of $\tilde{\phi}_m$ and H represents the maximum of the h_m's. The sum is over all neighboring cells with $m = W, E, S, N$. The weights w_m are zero for all non-qualifying neighbors. For each interface cell the described linear interpolation results in a set of weights β_m which correspond to the effect of the neighboring cells on the interface cell:

$$\phi_{(i,j)} = \beta_W \phi_W + \beta_E \phi_E + \beta_S \phi_S + \beta_N \phi_N \qquad (3.2)$$

By considering only the neighboring cells (W, E, S, N) that have a common face with the interface cell (i,j) the linear interpolation (3.2) can easily be treated implicitly; the implicit matrix of the discretized equation (2.1) can be modified with the weights β_m without introducing new diagonals with non-zero elements. The inclusion of other neighbors such as corner cells in the interpolation stencil (3.2) can be done explicitly. For a non-linear near wall behavior of ϕ an explicit correction $\Delta\phi^{corr}_{(i,j)}$ is added to the right hand side of equation (3.2). This correction is computed as the difference of the non-linear value of $\phi_{(i,j)}$ and the linear interpolated value, both computed with values from the current iteration.

The described interpolation can be applied to the velocity vector $\vec{v}$ without coupling

implicitly the momentum equations for the Cartesian velocity components. For this, the velocity components are transformed into a wall aligned 2-D coordinate system with the axis pointed in the tangential $\vec{t}$ and normal $\vec{n}$ velocity direction: $\vec{v}_n = (\vec{v} \cdot \vec{n})\vec{n}$ and $\vec{v}_t = \vec{v} - \vec{v}_n$, respectively. The normal unit vector is obtained from the wall distance d as: $\vec{n} = \nabla d/|\nabla d|$. Both components v_t and v_n are interpolated according to their physical behavior normal to the wall and using the interpolation (3.1) along the surface. The tangential and normal velocity components in the interface cell are then rotated back into the base Cartesian system. Because of linearity the weights β remain the same for the Cartesian components. As before, the non-linearity is treated as an explicit correction.

For low Reynolds numbers, the near wall behavior of the tangential velocity is linear. As plotted in Fig. 1a, the tangential component on the intermediate location for cell N is: $(\tilde{v}_t)_N = (v_t)_N d_{(i,j)}/d_N$. The corresponding quadratically interpolated normal component is: $(\tilde{v}_n)_N = (v_n)_N d^2_{(i,j)}/d^2_N$. For high Reynolds numbers, the near wall behavior of the tangential velocity is in general non-linear and the value at the intermediate location is determined with a non-linear procedure that utilizes adaptive wall functions.

In Kalitzin *et al.* (2003), an adaptive wall function concept has been developed for body fitted grids and zero pressure gradient flow. These wall functions are independent of the location of the first grid point above the wall. A look-up table provides an explicit dependency of the friction velocity on the local Reynolds number. This look-up table consists of cubic splines that approximate piecewise a solution obtained on a very fine grid for a zero pressure gradient boundary layer flow. This universal law is written in terms of the local Reynolds number Re_y rather than in terms of y^+. The local Reynolds number is defined as $Re_y = U^+ y^+ = Uy/\nu$. The look-up table is turbulence model specific as the universal law varies slightly depending on the turbulence model. Similar look-up tables provide the explicit dependency of the eddy-viscosity and turbulence variables on the local Reynolds number or on the wall distance y^+. The tables also include the derivative of the velocity and turbulence variables.

In this paper, we only consider a high Reynolds number case in which the plate is aligned but not coincident with the grid lines as shown in Fig. 1b. For zero pressure gradient flows, the Navier-Stokes equations simplify near the wall to:

$$(\nu + \nu_t)\frac{dU}{dy} = u_\tau^2 \tag{3.3}$$

In the current approach, the velocity in cell (i,j) is chosen such that the flux at the face $(i, j+\frac{1}{2})$ fulfills equation (3.3). The tangential velocity and the wall distance in cell N define the local Reynolds number Re_y which is related to the friction velocity u_τ via the adaptive wall function table. The friction velocity u_τ and the distance between the face $(i, j+\frac{1}{2})$ and the wall allow to introduce a wall distance y^+ which determines an eddy-viscosity value $(\nu_t)_{(i,j+\frac{1}{2})}$. The discretized equation (3.3) defines the tangential velocity in (i,j):

$$u_{(i,j)} = u_N - \frac{u_\tau^2}{\nu + (\nu_t)_{(i,j+\frac{1}{2})}}(d_N - d_{(i,j)}) \tag{3.4}$$

This approach can not simply be generalized for a situation shown in Fig. 1a as the tangential velocity in (i,j) is not uniquely determined by one single interface flux. For the general non-aligned case we employ therefore a crude approach by simply extrapolating of the tangential velocity component and eddy-viscosity using wall function information about the derivative in cell N.

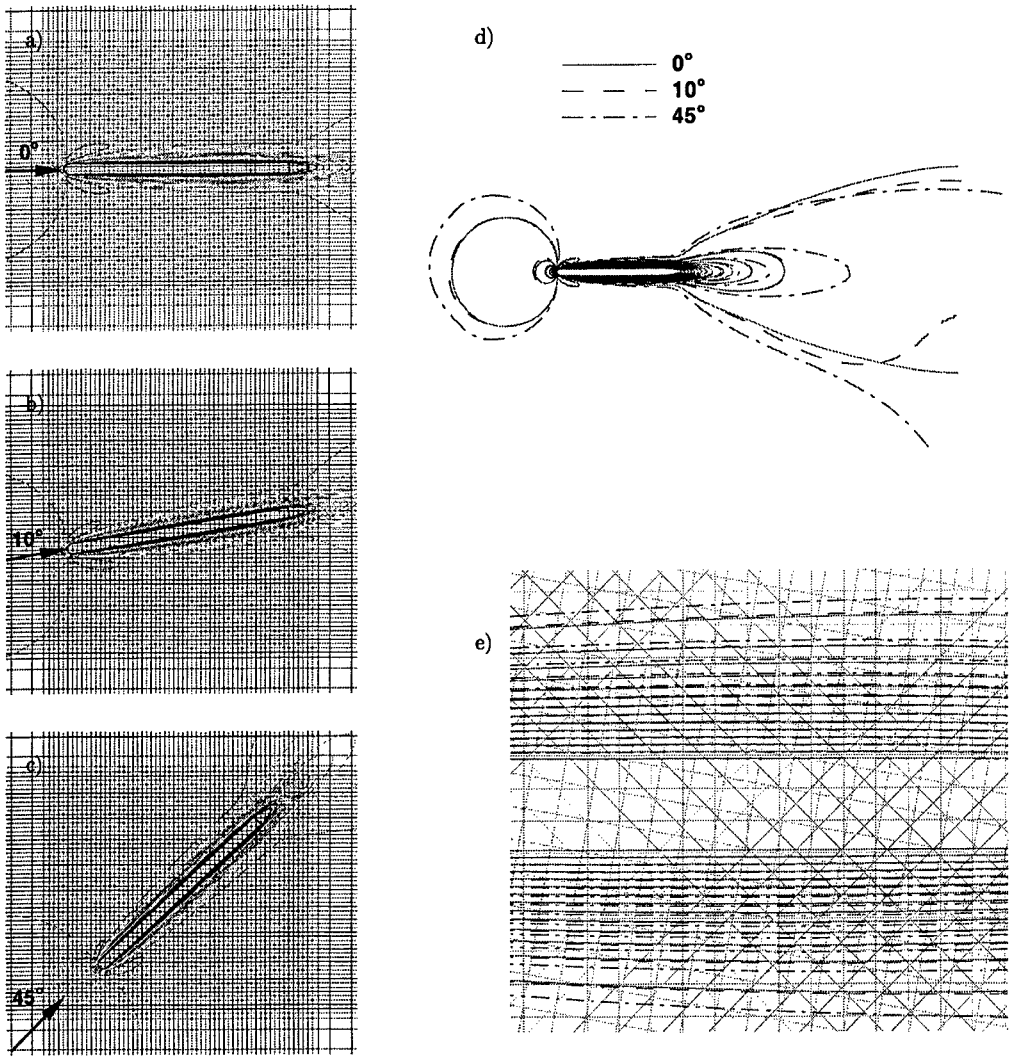


FIGURE 2. Velocity magnitude for immersed boundary layers simulations on non-aligned grids, $Re = 1000$, mesh with every $8th$ line plotted.

Immersed boundary results for a flat plate boundary layer at $Re = 1,000$ are shown in Fig. 2. The three simulations are carried out on uniform, non-aligned grids with a different angle between the plate and the gridlines. The flow is laminar and y^+ of the first cell center is about 0.1. The case of 10° is the most challenging as the wall distance of the first grid point above the wall fluctuates by moving in the streamwise direction along the plate. There are about 30 cells in the boundary layer and 20 cells across the plate resolving the cylindrical leading edge. The solution is nearly independent of the angle between plate and gridlines as shown with the velocity magnitude contours in Fig. 2d

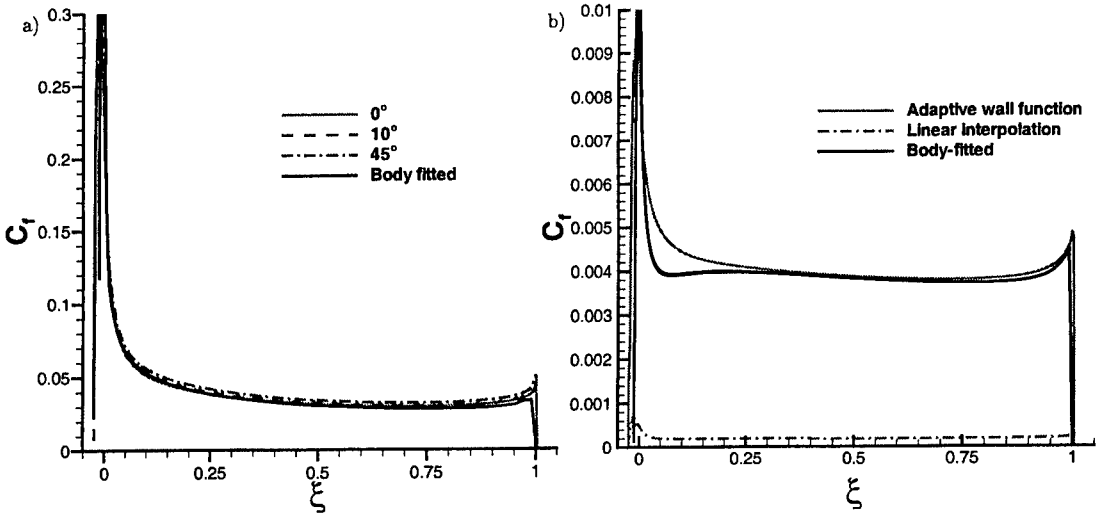


FIGURE 3. Skin friction distribution for immersed boundary layer simulations over a flat plate for various grid alignments for $Re = 1000$ (left) and for grid aligned case for $Re = 10^6$ (right)

and Fig. 2e. The contour lines for larger velocity values deviate slightly for the 45^o what is likely to be a numerical dissipation effect. However, the skin friction along the plate matches remarkably well the body fitted solution shown in Fig. 3a.

In Fig. 3b, skin friction is reported for an immersed boundary simulation of a flat plate boundary layer at $Re = 10^6$. The plate is aligned with the grid and the turbulent flow is computed with the Spalart-Allmaras turbulence model. The wall distance y^+ of the first cell center above the wall is about 25. The results obtained using wall functions are compared to the ones obtained using the simple linear interpolation and to a body fitted solution. The skin friction levels for the linear interpolation are incorrect whereas the wall functions results are in good agreement with the body fitted solution downstream of $\xi = 0.25$. Upstream of this location, the discrepancy between the wall function and body fitted result is related to the grid resolution and wall function implementation. The resolution of the cylindrical leading edge is very coarse for this Reynolds number. The grid is the same as the one used for the simulations in Fig. 2.

4. Local grid refinement

A new version of IBRANS with a local grid refinement capability is in development for an efficient clustering of cells in the boundary layers. The present implementation is an extension of the "classical" adaptive mesh refinement (AMR) technique to allow non-isotropic refinement. It can also be interpreted as a generalization of the procedure used for building coarse grids for geometric multigrid on structured meshes.

The basic idea was introduced in Durbin & Iaccarino (2002) for a finite difference discretization. The AMR grid is considered as a *coarsened* version of an underlying, structured grid; on this underlying grid the cells are defined (in two-dimensions) by a couple of vertices with indices (i, j) and $(i + 1, j + 1)$. On the AMR grid each element

is bounded by the gridlines passing through the vertices (i, j) and $(i + \Delta_i, j + \Delta_j)$. The effective element size in the AMR grid is not constant ($\Delta_i \neq \Delta_j$ and both indices depend on (i, j)). Therefore, the cells are not organized in a structured way with one-to-one neighbors in each Cartesian direction. This requires a modification of the algorithm to deal with *hanging nodes*. In Durbin & Iaccarino (2002) this was simply based on a second-order interpolation. In the current finite volume implementation, flux conservation is enforced and the algorithm resembles the unstructured face-based algorithm described in Ferziger & Peric (2002) and, more closely, the AMR discretization used in Ham *et al.* (2002). Each face-flux is computed using the two adjacent cells and for each cell the fluxes (in general more than four) are collected to build the corresponding diffusive and convective operators. In two dimensions, the implicit discretization yields a sparse matrix with elements not organized in five diagonals as for its structured counterpart. This complexity in the matrix structure prevents the use of the SIP procedure and a Krilov-type algorithm with a simple Jacobi pre-conditioner was implemented. Standard conjugate gradient is used for the pressure equation and the BiCGStab (Van den Vorst 1992) for the momentum and turbulent scalars.

The major advantage of the present approach with respect to classical OCTREE-based (Berger & Aftosmis 1998) and fully-unstructured (Ham *et al.* 2002) schemes lies in the economy and flexibility of storing and retrieving connectivity information due to the underlying grid. In particular, only N cells are effectively defined on a $N_i \times N_j$ underlying grid and they are defined by the two couples (i, j) and $(i + \Delta_i, j + \Delta_j)$. The total storage cost is $4N$ integers. In addition, an array of integers, $ID_{(i,j)}$, is defined on the fine grid to store the correspondence between the underlying cell and the actual AMR element. In other words, all the underlying cells included in the range $(i, i+\Delta_i-1)$ and $(j, j+\Delta_j-1)$ are tagged using the AMR cell number. The total storage required is, therefore, $N_i \times N_j$. The connectivity information for each cell are retrieved consistently to a structured framework by indirectly querying the array $ID_{(i,j)}$. The neighbors of a AMR cell are $ID_{(i-1,k)}$ and $ID_{(i+\Delta_i+1,k)}$ for k ranging between j and $j+\Delta_j-1$, in the positive and negative i-direction respectively. It is evident that the approach handles multiple hanging nodes for each cell and, eventually, allows to reconstruct additional connectivity information without any increase in storage; for example it is straightforward to identify all the vertex-based neighbors.

The generation of AMR grids is carried out by creating the underlying (fine) grid as discussed before and then coarsening it in the region away from the immersed boundary. The advantage of this approach is that all the cell tagging (ray tracing) can be performed on a structured grid taking full advantage of the alignment of the cell centers and the grid nodes. The coarsening and the generation of the connectivity information is the last step of the grid generation process.

An example of the application of this procedure is shown in Fig. 4 where both the underlying and the AMR grids are reported; note that the AMR grid contains only 9% of the underlying cells. A sample calculation has been performed on both grids and it is reported in Fig. 5 in terms of turbulent kinetic energy. The solution on the AMR grid is remarkably smooth and consistent with the one obtained on the structured mesh. It converges significantly faster as reported in Fig. 6. This is mainly due to a reduced aspect ratio of the cells away from the immersed boundary. In terms of computational cost the savings is about 70%.

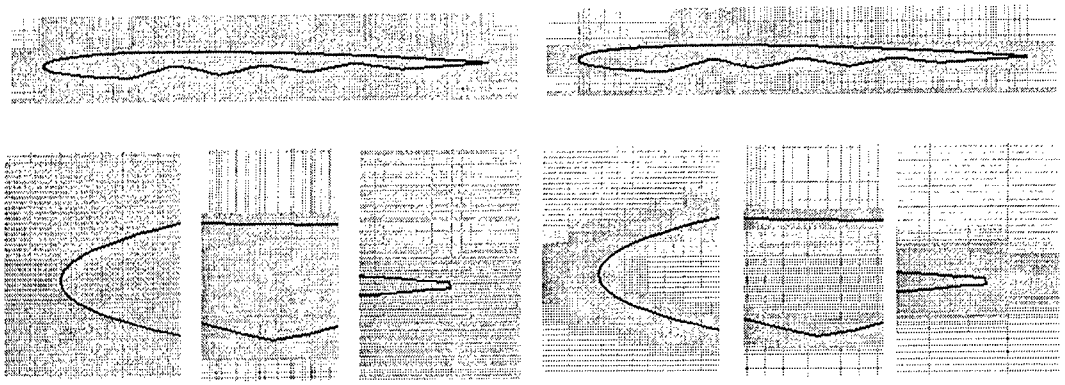


FIGURE 4. Computational grid for the flow around an airfoil. Structured, underlying grid on the left with every second grid line plotted and locally refined grid on the right.

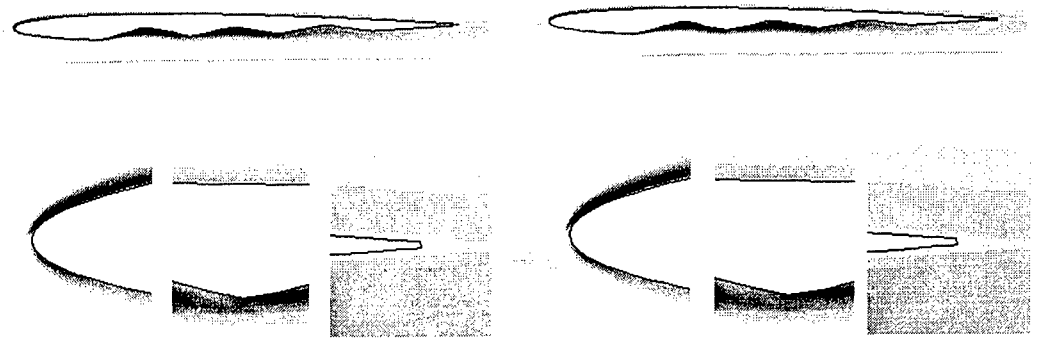


FIGURE 5. Turbulent kinetic energy for structured grid (left) and locally refined grid (right).

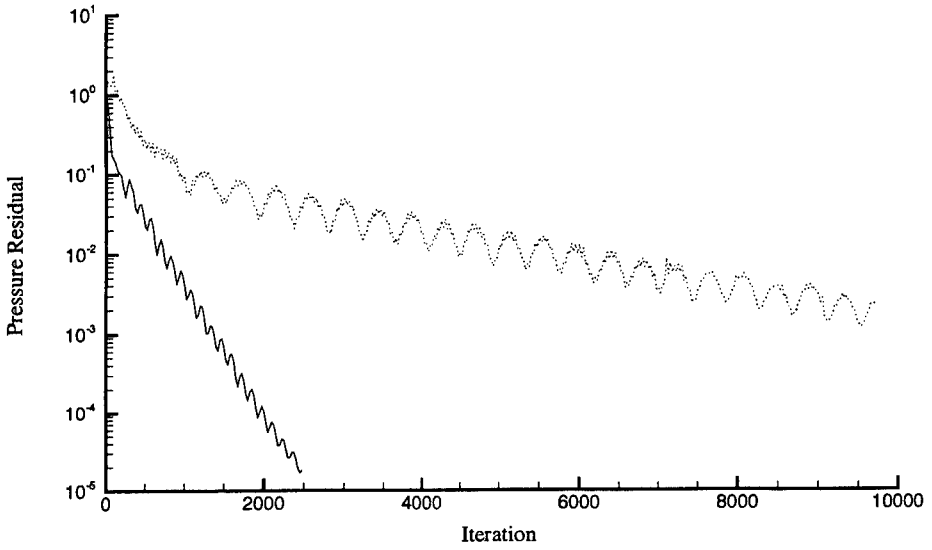


FIGURE 6. Convergence history for structured grid (grey) and a locally refined grid (black).

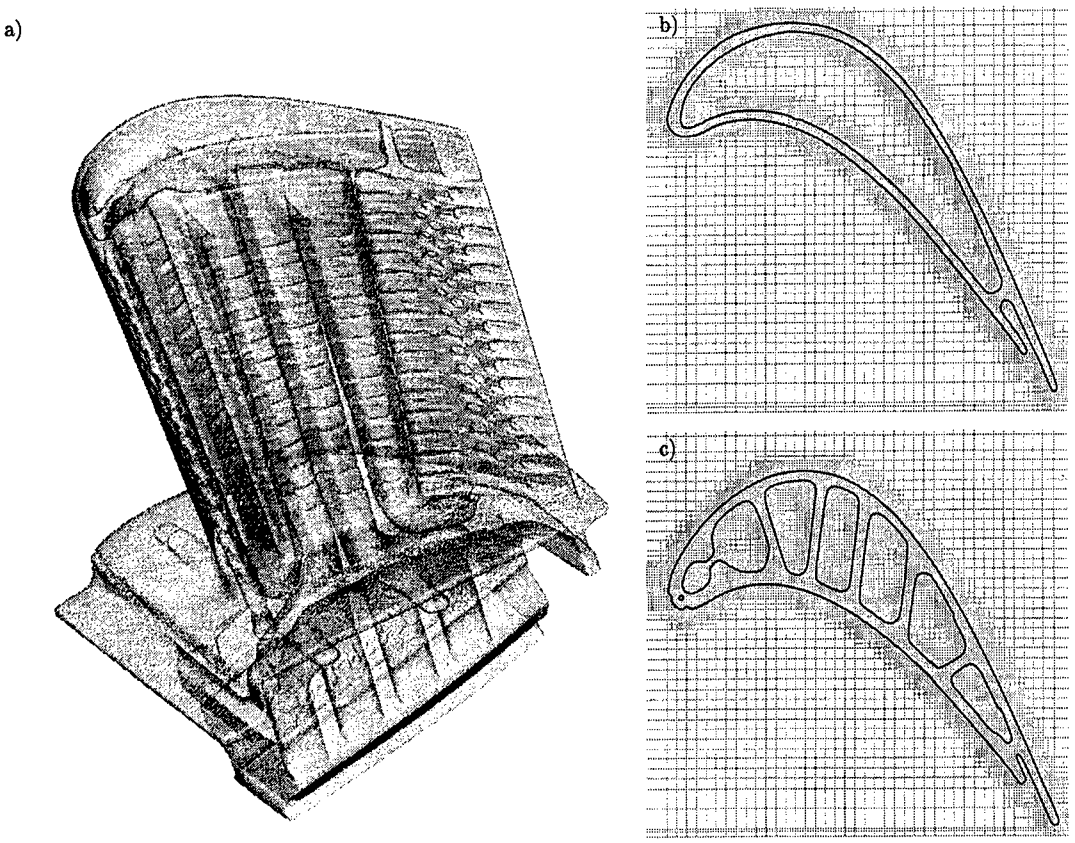


FIGURE 7. Turbine blade with internal cooling passages (a) and planar cuts through locally refined grid: (b) cut near the tip, (c) cut near mid-span

The local grid refinement algorithm has been implemented in three-dimensions and it works well even with very complex geometries as the real turbine blade shown in Fig. 7. The blade is twisted and the internal cooling system of the blade consist of extremely intricate passages with multiple serpentines, ribs, tip ejection holes, film cooling holes, leading edge impingement, etc. Planar cuts through the locally refined grid are shown in the same figure. A comparison between both cuts reveal a remarkable consistent refinement in all internal flow regions. The local grid refinement also follows the twisted outer surface of the blade.

5. Conclusions and future work

The paper presents details of a Cartesian immersed boundary method for RANS flow simulations. It focuses on the IB implementation for mean flow and turbulence variables. The immersed boundary is represented with an implicit, linear, off wall interpolation with an explicit, non-linear correction. An extension of the method with adaptive wall functions is presented for grid aligned cases. The paper also addresses the issue of flow resolution at the immersed boundary and discusses a local grid refinement algorithm.

Skin friction distributions are presented for a boundary layer over a flat plate that is non-aligned with the gridlines at $Re = 1,000$. The results are nearly independent of

the angle between the plate and the gridlines. For the grid aligned case, skin friction is presented for a flat plate boundary layer at $Re = 10^6$.

Future work consists in continuing the development of IBRANS and combining the described technologies into one mature computational code. The code is in the process of being extended for conjugate heat transfer computations. The energy transport equation has been implemented and it needs the development of appropriate heat transfer immersed boundary conditions. The adaptive wall functions for immersed boundaries need to be extended for general grids and heat transfer problems. It is planned to parallelize and adapt the multigrid procedure for the flow solver with local grid refinement.

6. Acknowledgment

The authors would like to acknowledge Gorazd Medic (Stanford University) for his contribution to the adaptive wall function formulation for boundary fitted grids.

REFERENCES

BERGER M. & AFTOSMIS M., 1998 Aspects (and aspect ratios) of Cartesian mesh methods. *16th Int. Conf. on Numerical Methods in Fluid Dynamics.*

DURBIN, P. A. & IACCARINO, G., 2002 An Approach to Local Refinement of Structured Grids. *J. of Comput. Phy*, **181**, 639–653.

FERZIGER, J. H. & PERIC, M., 2002 Computational Methods for Fluid Dynamics. *Springer-Verlag*, third-edition.

FRANKE, R., 1982 Scattered data interpolation: Tests of some methods. *Math. Comput.*, **38**, 181–200.

IACCARINO, G. & VERZICCO, R., 2003 Immersed Boundary Technique for Turbulent Flow Simulations. *Appl. Mech. Rev.*, **56**, 331–347.

HAM, F. E., LIEN, F. S., & STRONG, A. B., 2002 A Cartesian grid method with transient anisotropic adaptation. *J. Comput. Phys.* **179**, 469-494.

KALITZIN, G., MEDIC, G., & IACCARINO, G., 2003 On wall functions for RANS. In preparation.

KALITZIN, G. & IACCARINO, G., 2002 Turbulence Modeling in an Immersed Boundary RANS Method. *Annual Research Briefs*, Center for Turbulence Research, 415–426.

MAJUMDAR, S., IACCARINO, G. & DURBIN, P. A., 2001 RANS solver with adaptive structured boundary non-conforming grids. *Annual Research Briefs*, Center for Turbulence Research, 353–366.

SPALART, P. R. & ALLMARAS, S. R., 1994 A One-Equation Turbulence Model for Aerodynamic Flows. *La Recherche Aerospatiale*, **1**, 1–23.

STONE, H. L., 1968 Iterative solution of implicit approximations of multidimensional partial differential equations. *SIAM J. Numer. Anal.*, **5**, 530–558.

VAN DEN VORST, H. A., 1992 BI-CGSTAB: a fast and smoothly converging variant of BI-CG for the solution of non-symmetric linear systems. *SIAM J. Sci. Stat. Comput.*, **13**, 631–644.

VERZICCO, R., MOHD-YUSOF, J., ORLANDI, P. & HAWORTH D., 2000 LES in complex geometries using boundary body forces. *AIAA J.*, **38**, 427–433.

Numerical and experimental investigation of the turbulent flow in a ribbed serpentine passage

By Gianluca Iaccarino, Georgi Kalitzin† and Christopher J. Elkins‡

1. Introduction and motivations

Modern gas turbine engines operate at high combustor outlet temperatures to achieve higher thermal efficiency and thrust. Turbine blades are exposed to these high-temperature gases and undergo severe thermal stress and fatigue. The design of highly efficient cooling systems for turbine blades has an enormous potential impact on engine development. Cooling devices are based on a secondary flow system built into each blade, as illustrated in Fig. 1. The secondary flow passages are extremely complicated consisting of one or multiple legs with turbulators (rib-roughened serpentines), holes connecting the secondary path to the external surface of the blade (film cooling), tube bundles, slots, etc. The geometrical complexity of these passages, however, is extremely challenging for the use of advanced simulation tools based on state-of-the-art three-dimensional CFD solvers. The generation of a computational grid (even using unstructured mesh technology) requires a considerable amount of time. As a result, the analysis of the cooling performance of the system is largely based on isolated sub-component simulations, simplified one-dimensional models and experimental correlations.

A large amount of research has been devoted to the analysis of the flow characteristics (in particular turbulence statistics) and heat transfer in channels with ribs. The effects of rib shape, pitch, height and inclination with respect to the incoming flow have been quantified from an experimental point of view. Numerical predictions of these flows are complicated because of the increased turbulence intensity near the ribs and its effect on the flow. In Reynolds-Averaged Navier-Stokes (RANS) approaches the turbulence intensity is strongly affected by the choice of the turbulence closure. RANS eddy viscosity models based on the linear Boussinesq relationship between Reynolds stresses and velocity gradients are the *de facto* standard in industrial numerical simulations. Previous investigations (Ooi *et. al.* 2002a; Iacovides & Raisee 1999) have illustrated the predictive capabilities of such models in turbomachinery cooling systems components: smooth channels, channels with ribs, 180 degrees turns (U-bends), etc. In particular, it has been shown that the flow is strongly three-dimensional and the presence of oblique ribs generates strong coherent vortices in the domain (Ooi *et. al.* 2002b). It must be noted that most of these simulations are performed under the assumption that the flow is periodic in the streamwise direction and, therefore, only a small section of the passage is effectively simulated.

Several experimental datasets are available to evaluate the accuracy of these simulations (Han *et. al.* 1985; Rau *et. al.* 1998); typically the measurements are taken in devices that include many ribs in between duct U-bends and the data are collected at different locations to verify that periodicity conditions are indeed applicable. Although these comparisons between experiments and computations are invaluable in improving

† CITS
‡ Mechanical Engineering Dept., Stanford University

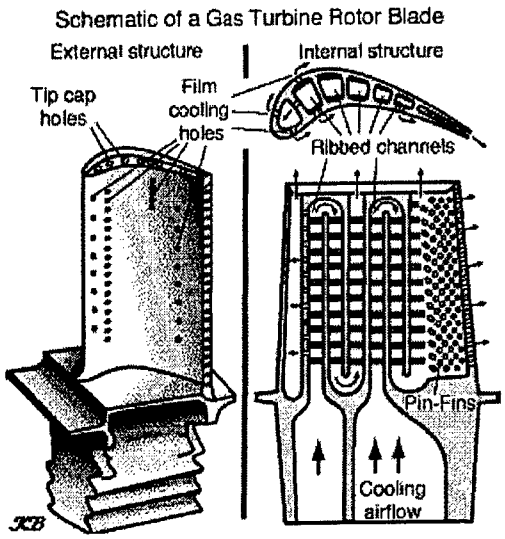


FIGURE 1. Sketch of the Cooling System of a Turbine Blade (Cumpsty 1997).

the understanding of the physics and in providing accurate model validation, they do not represent the wealth of complexity and interactions present in more realistic configurations, like a multiple-leg serpentine.

Unfortunately the computational cost of such simulations becomes substantial. For a single three-dimensional rib-roughened passage it might be necessary to generate a grid with half million cells (Ooi *et. al.* 2002b) to completely resolve the flow structures. In a serpentine with thirty ribs and two 180 degree turns, the mesh size should be in the order of 30 million cells. In addition, it is necessary to obtain extensive experimental datasets to quantify clearly the accuracy of the simulations.

It is clear that a novel numerical and experimental technique for investigating flows in complex geometries would be extremely beneficial to the development and improvement of the predictive tools used in the design.

In this paper, the turbulent flow in a serpentine with oblique ribs is investigated experimentally and by numerical simulations. The measurements are carried out by using Magnetic Resonance Velocimetry (MRV) (Elkins *et. al.* 2003) and the simulations using the Immersed Boundary (IB) technique (Iaccarino & Verzicco 2003; Kalitzin & Iaccarino 2002). A brief description of these two approaches is reported in following sections. The results are reported in terms of velocity distributions in various planes in the serpentine; differences between measurements and simulations are presented qualitatively and quantitatively. The study of the discrepancy allows us to identify areas of needed improvements in the turbulence modeling.

2. Ribbed serpentine

The serpentine used in this study is represented in Fig. 2; the model was drawn in AutoCAD and fabricated using a 3D System 250-50 SLA machine. The serpentine has a square cross section of height $H = 20mm$ and ten staggered oblique ribs on the top and bottom walls. The rib height is $0.1H$ and the pitch (distance between two successive ribs) is $0.6H$; the rib angle is 45 degrees. A fully developed pipe flow enters the first leg of the

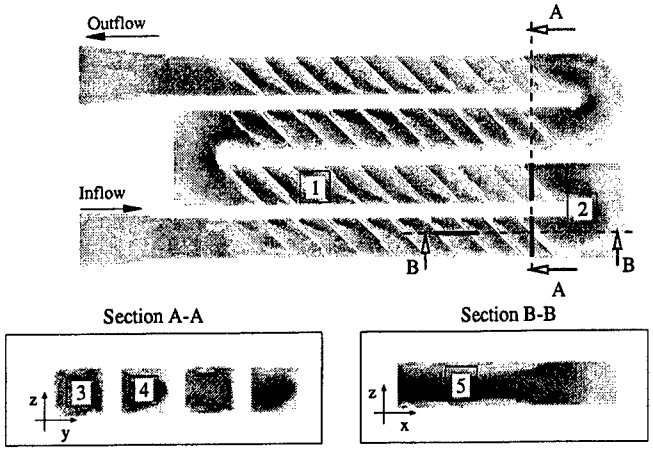


FIGURE 2. Sketch of the cooling passage investigated and the region where the experiments and computations have been compared.

serpentine through a converging section yielding a uniform velocity profile. Two Reynolds numbers have been investigated, 8,000 and 50,000 based on the serpentine height and the bulk velocity; in the present paper only the results at the low Reynolds number are reported.

3. Experimental technique

Magnetic Resonance Velocimetry, MRV, has been used to measure the mean velocity components in the entire serpentine. A massive amount of data, corresponding to about 2 million locations with $1mm$ resolution ($0.05H$) has been collected. The measurement technique is described in detail in Elkins *et. al.* (2003) where a simple pipe flow and a serpentine similar to the one studied here (Fig. 2) are investigated.

The MRV technique is a non-invasive experimental method for measuring mean velocities and is implemented in medical magnetic resonance imaging systems. MRV has been used for many low-Reynolds number investigations (Fukushima 1999), such as physiologic, multiphase, and porous media flows. It has also been used in a few simple turbulent flows such as pipe and jet flow. Our current focus is in high Reynolds number turbulent flows in complex internal geometries with the objective of measuring the time-averaged three-component velocity field in order to provide physical insights and an extensive database for CFD validation. It should be mentioned that the MRV technique is compatible with the rapid prototyping processes of stereolithography and fused deposition machining. Utilizing current RP technology highly complex flow models can be designed and manufactured in only a few days, and the MRV measurements, typically producing over 1 million velocity vectors, can be completed in 30 minutes.

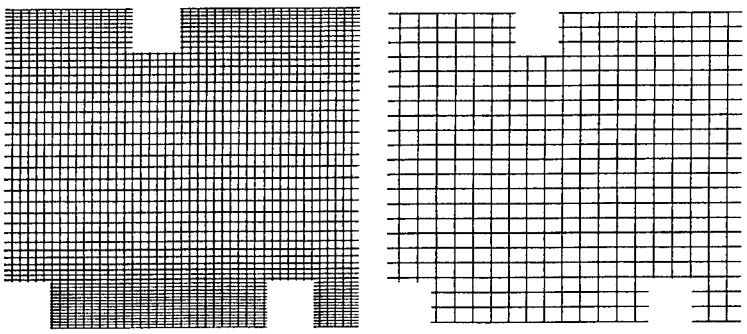


FIGURE 3. Resolution used in the coarse grid simulations (left) and experiments (right) in the region 5 (see Fig. 2).

4. Numerical technique

The numerical simulations presented in this work are based on the Immersed Boundary (IB) technique. The method is presented in detail in Iaccarino & Verzicco (2003) and Kalitzin & Iaccarino (2002); only a brief description is reported herein.

In the IB method Cartesian non-uniform meshes are used and forcing terms are added to the governing equations to enforce boundary conditions (no slip velocity, for example) on surfaces not aligned with the grid lines. The computational code used is based on the steady-state incompressible RANS equations closed with either a one-equation (Spalart & Allmaras 1994) or a two-equation model (Kalitzin & Iaccarino 2002). A second-order implicit discretization is used within a SIMPLE pressure-velocity coupling algorithm; the turbulence equations are solved in a segregated manner. Multigrid is used to accelerate the convergence. The IB forcing is based on a tri-linear reconstruction (Iaccarino & Verzicco 2003) for the velocity components and the turbulent scalars.

The geometry definition is based on the STL file format and, therefore, the same AutoCAD model used to build the experimental configuration has been used to obtain a simplified CFD computational model. The computational grid and the IB interpolation stencil is generated automatically and the pre-processing time to start the computation is negligible.

5. Results and discussion

The geometrical configuration is shown in Fig. 2. The CFD domain includes *only* the first three legs of the serpentine. The simulations have been performed using computational grids ranging from half million to forty millions elements. An example of the coarse grid resolution of the CFD mesh is shown in Fig. 3. The underlying grid for the MRV experiments is shown in the same figure.

The fine grid simulations are compared to the experimental data in the areas indicated in the sketch of Fig. 2. In Fig. 4 and 5 two horizontal planes are reported midway through the ribs and halfway through the passage, respectively. In Fig. 7 and 8 two vertical sections are reported with the streamwise direction pointing away from the page and toward it, respectively. Finally, in Fig. 6 a vertical longitudinal plane showing the streamwise flow (from left to right) is reported.

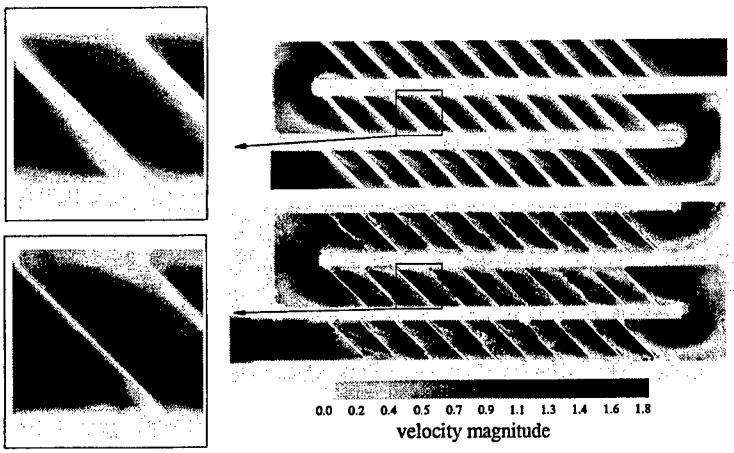


FIGURE 4. Comparison between simulations (top) and experiments (bottom) in region 1 (see Fig. 2): horizontal plane corresponding to a cut through the ribs.

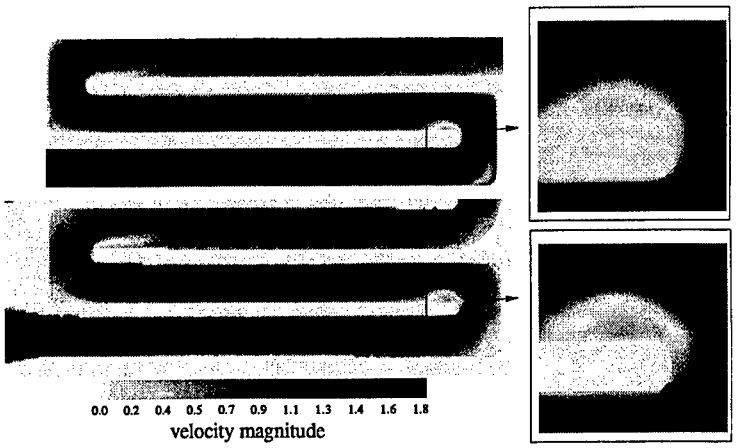


FIGURE 5. Comparison between simulations (top) and experiments (bottom) in region 2 (see Fig. 2):. horizontal plane corresponding to a cut at the mid height of the passage.

The general qualitative agreement between experiments and simulations is remarkable. In particular, the secondary flows in between the ribs described in Ooi *et. al.* (2002b) are well represented. The flow in between the U-bends shows a repeating patterns after about three or four ribs demonstrating the importance of the complete simulation as opposed to a periodic-rib channel study.

The simulations capture the most dominant effects illustrated in the experiments:

(*a*) A strong three-dimensionality, as indicated by the mid-height plane. High velocity regions oblique to the direction of the flow (and orthogonal to the rib orientations) indicate the presence of strong streamwise vortices;

(*b*) Recirculation bubbles in the downstream region of the 180 degree bends; in particular these features are in remarkable good agreement (in terms of length and maximum reverse velocity) with the measurements;

(*c*) A massive separation behind each rib, Fig. 7. Again the length and the velocity

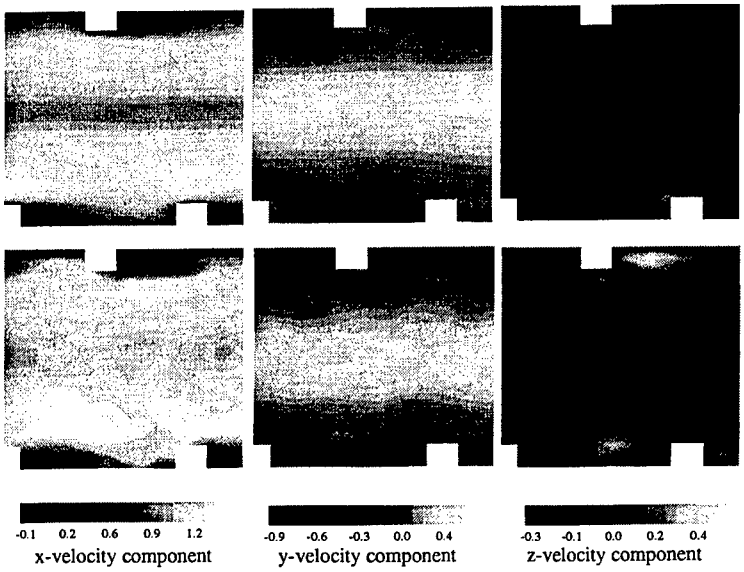


FIGURE 6. Comparison between simulations (top) and experiments (bottom) in region 5 (see Fig. 2): vertical plane corresponding to a longitudinal section before the U-bend.

magnitude are in good agreement, even if the resolution in the experiments is limited (cfn. Fig. 3).

(*d*) High speed regions atop of each rib with high shear and turbulence (not reported).

In addition, they clearly indicate that the flow in the straight sections is accurately represented and the largest discrepancies are around the U-bend regions. This is a well known limitation of the (linear) eddy viscosity models used in the RANS simulations and it does not appear to be linked to the Cartesian nature of the flow solver.

The wealth of information provided by the MRV technique allows a clear identification of the accuracy of the simulation. In particular, it can be used to demonstrate the limitation imposed by the turbulence model. The three components of velocity are reported for various flow regions in Fig. 6, 7 and 8. Region 5 and 3 are located before the U-bend. The flow is here fully developed and the streamwise component in the cross section shows a typical inverted C shape, with larger velocities near the left wall. This combined with the plot of the cross-flow component (y-velocity, cfn, Fig. 2) shows the presence of two fairly symmetric (with respect to the channel mid-height) longitudinal vortices. On the other hand, Fig. 8 shows the same cross-section after the U-bend, and in this case the vortical structures are not yet formed and the flow is substantially affected by the bend. In this section the difference between experiments and simulations appears to be larger, suggesting a limitation in modeling turbulence in the bend region.

Finally, the error in the computed velocities is reported in Fig. 9 for a vertical section before the U-bend. The CFD results are interpolated on the experimental locations and the differences in the three velocities components (normalized by the experimental values) are plotted. The largest error is about 5% and, most importantly, has a unorganized pattern, showing that the same flow features (streamwise vortices and secondary rib structures) are present.

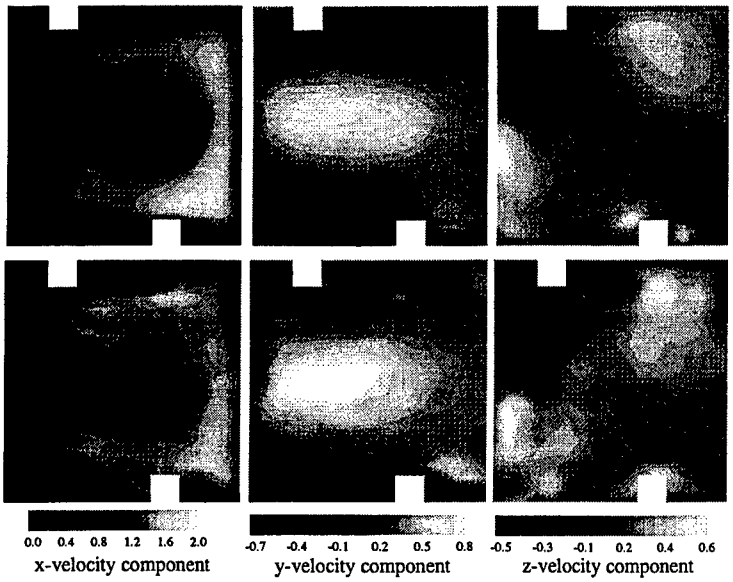


FIGURE 7. Comparison between simulations (top) and experiments (bottom) in region 3 (see Fig. 2): vertical plane corresponding to a cross-section before the U-bend.

Results obtained on coarse grids show the same main features and agree fairly well with the experiments.

6. Conclusions and future work

A numerical and experimental investigation of the turbulent flow inside a multiple-leg serpentine with oblique ribs is presented. Both the simulations and the measurements are based on the use of novel techniques: the immersed boundary approach for the numerical predictions and the magnetic resonance velocimetry for the experiments. Both technique are very fast. Once the experimental stand is setup, large amount of data can be measured in very short time for a CAD model that fits into the measuring section. The same CAD model is used to set up the computations without extra cost in time.

Extremely detailed comparisons are reported due to the high resolution of the two approaches considered: up to 40 million grid cells are used in the simulations and about 2 million point measurements are available. The results show an overall satisfactory agreement and the turbulence model used (two-equation model) seems to perform quite well for the straight parts of the passage capturing the three-dimensional flow structures accurately. The major discrepancies are present in the U-bend and in the immediate downstream areas where the linear eddy viscosity approaches used cannot account for the strong turbulence anisotropy (Iacovides & Raisee 1999).

Additional simulations and experiments have been carried out at a larger Reynolds number and the results show again an encouraging agreement. Future work will be devoted to perform similar comparisons between these two techniques in different complex configurations; in particular, in the cardiovascular system.

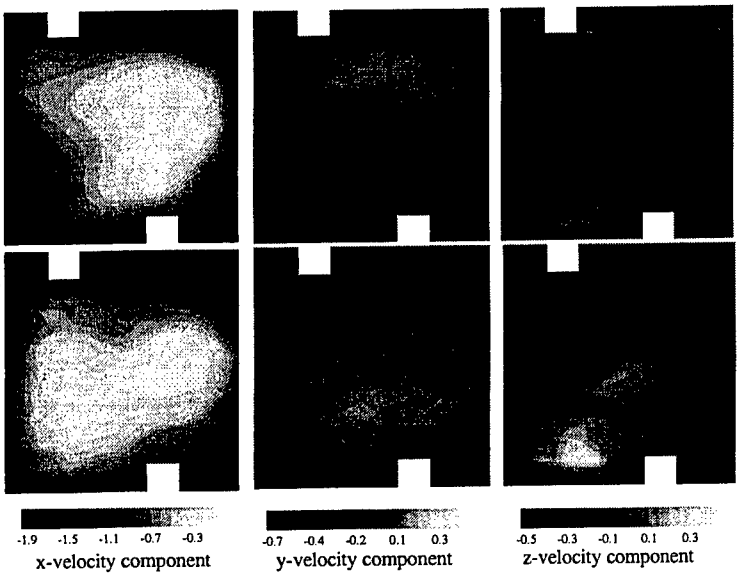


FIGURE 8. Comparison between simulations (top) and experiments (bottom) in region 4 (see Fig. 2): vertical plane corresponding to a cross-section after the U-bend.

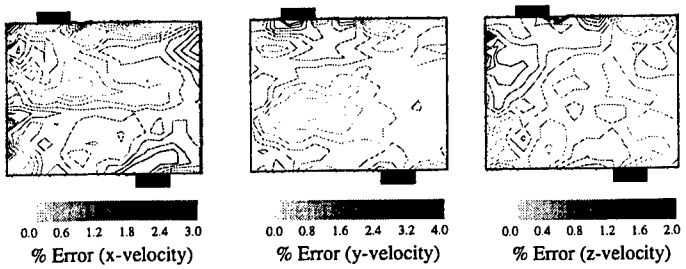


FIGURE 9. Differences between computations and experiments in region 3 (see Fig. 2): vertical plane corresponding to a cross-section before the U-bend.

Acknowledgements

The authors gratefully acknowledge Mr. Chuck Booten of Stanford University for designing the internal passage and Prof. Ryan Wicker and Mr. Francisco Medina at the Unversity of Texas at El Paso for manufacturing it.

REFERENCES

CUMPSTY, N., 1997 *Jet propulsion.* Cambridge University Press, Cambridge UK.

ELKINS, C. S., MARKL, M., PELC, N. & EATON, J.K., 2003 4D magnetic resonance velocimetry for mean flow measurements in complex turbulent flows. *Exp. Fluids* **34** 494–503.

FUKUSHIMA, E. 1999 Nuclear magnetic resonance as a tool to study flow. *Ann. Rev. Fluid. Mech.* **31** 95–123.

HAN, J. C., PARK, J. S. & LEI, C. K., 1985 Heat transfer enhancement in channels with turbulence promoters. *J. of Engr. for Gas Turbines and Power*, **107**, 628-635.

KALITZIN, G. & IACCARINO, G., 2002 Turbulence modeling in an immersed boundary RANS method. *Annual Research Briefs*, Center for Turbulence Research, 415–426.

IACCARINO, G. & VERZICCO, R., 2003 Immersed boundary technique for turbulent flow simulations. *Appl. Mech. Rev.* **56** 331–347.

IACCARINO, G., OOI, A., DURBIN, P. A. & BEHNIA, M., 2002 Conjugate heat transfer predictions in two-dimensional ribbed passages. *Int. J. Heat and Fluid Flow*, **23**, 340–346.

IACOVIDES, H. & RAISEE, M., 1999 Recent progress in the computation of flow and heat transfer in internal cooling passages of turbine blades. *Int. J. Heat and Fluid Flow*, **20**, 320-328.

OOI, A., IACCARINO, G., DURBIN, P. A. & BEHNIA, M., 2002 Reynolds averaged simulations of flow and heat transfer in ribbed ducts. *Int. J. Heat and Fluid Flow*, **23**, 750–757.

OOI, A., PETTERSON REIF, B. A., IACCARINO, G. & DURBIN, P. A. 2002 RANS calculations of secondary flow structures in ribbed ducts. *Proc. of the 2002 Summer Program*, Center for Turbulence Research, 43–53.

RAU, G., CAKAN, M., MOELLER, D. & ARTS, T., 1998 The effect of Periodic ribs on the local aerodynamic and heat transfer performance of a straight cooling channel. *J. Turbomachinery*, **120**, 368-375.

SPALART, P. R. & ALLMARAS S. R., 1994 A one-equation turbulence model for aerodynamic flows. *La Recherche Aerospatiale*, **1**, 1–23.

RANS simulation of the separated flow over a bump with active control

By Gianluca Iaccarino, Claudio Marongiu†,
Pietro Catalano†, Marcello Amato†

1. Introduction and motivations

Active Flow Control (AFC) is an attractive technique to increase the aerodynamic efficiency of lifting and control surfaces. The working principle is to use localized suction or injection to modify the characteristics of the boundary layer flow near regions of separation, thus limiting the associated losses. The effect of steady suction or blowing has been studied in great detail in the past (see Braslow (1999) for a comprehensive review), especially with reference to high-lift configurations. The major limitation to the applicability of conventional AFC devices is the need to provide or discharge a constant supply of flow for blowing or suction, respectively, which requires complicated piping, additional energy supply, and causes efficiency losses. In the last decade, a new AFC device, namely the synthetic jet actuator, has been introduced, which eliminates most of these drawbacks. In this system the net mass flow is zero, because a membrane within a small cavity produces blowing and suction alternatively. The performance of synthetic jets appear to be extremely encouraging, but most of the experimental analysis and numerical studies are performed at low Reynolds number. The current focus is on the application of such devices to turbulent flows especially in the aeronautical industry.

The fluid mechanics of synthetic jets at low Reynolds numbers is well understood (Glezer & Amitay 2002) and their difference with respect to conventional (continuous) jet has been elucidated experimentally (Smith & Swift 2003). In particular, it has been shown that the vortex shedding behind a circular cylinder can be completely suppressed in the laminar regime (Glezer & Amitay 2002) and substantial drag reductions can be obtained at moderate Reynolds numbers (Amitay *et al.* 1997; Catalano *et al.* 2002).

The objective of this paper is to investigate the accuracy of Reynolds-Averaged Navier-Stokes (RANS) techniques in predicting the effect of steady and unsteady flow control devices. This is part of a larger effort in applying numerical simulation tools to investigate of the performance of synthetic jets in high Reynolds number turbulent flows. RANS techniques have been successful in predicting isolated synthetic jets as reported by Kral *et al.* (1997). Nevertheless, due to the complex, and inherently unsteady nature of the interaction between the synthetic jet and the external boundary layer flow, it is not clear whether RANS models can represent the turbulence statistics correctly.

An extensive computational and experimental investigation of turbulent flow with active control is ongoing at NASA Langley. A workshop, CFDVAL2004, will be held in March 2004 under joint sponsorship by NASA and ERCOFTAC with the objective of providing benchmarks for CFD validation (see `cfdval2004.larc.nasa.gov`). The present work is directed towards participation in this workshop.

† CIRA, Italian Center for Aerospace Research

2. Numerical techniques

2.1. *U-ZEN*

The CIRA U-ZEN code solves the compressible RANS equations around complex aeronautical configurations using multiblock structured grids. The numerical discretization is based on a second-order cell-centered finite-volume method with explicitly added (fourth-order) artificial dissipation. The unsteady solution procedure is based on the dual time stepping method where a pseudo steady-state problem is solved at each time step. Conventional convergence accelerators, including geometrical multigrid and residual smoothing, are used. Several turbulence models are available in U-ZEN: for the numerical simulations presented in this paper only the one-equation Spalart-Allmarass (SA) model (Spalart & Allmaras 1994) and the two-equation k-ω (KW) model (Wilcox 1993) have been used.

2.2. *FLUENT*

FLUENT is a commercial CFD code that solves the RANS equations on hybrid unstructured grids. It uses a second-order upwind discretization based on the SIMPLE pressure-velocity coupling and the formulation can accommodate compressible flows. Dual time stepping is used to obtain time accurate simulations and an algebraic multigrid technique is used to accelerate convergence within each time step. A multitude of turbulence models and variants are available in Fluent. In this work the SA model and Durbin's V2F four-equation model (Durbin 1995) are used. The latter model was implemented in FLUENT using the User Subroutines (Iaccarino 2001).

3. Preliminary validation

As a preliminary step toward applying the two codes to AFC problems, flows around bluff bodies at low Reynolds number are considered. In particular, FLUENT has been successfully applied to compute the vortex shedding in two- and three-dimensional flows (Ooi *et. al.* 2002); the same problems have been carried out using U-ZEN. Only a few results are reported for the flow around the circular cylinder at two Reynolds numbers ($Re_D = 100$ and $Re_D = 3,900$) corresponding to unsteady laminar and turbulent flows. The results are summarized in the Table I.

	U-ZEN	FLUENT	Exp.[1]
St	0.164	0.143	0.165
C_D	1.373	1.377	1.340
C_L	0.292	0.340	0.325
L_R	1.450	1.380	1.460
U_{min}	-0.180	-0.185	-0.180

$Re_D = 100$
[1] Zdravkovich 1997

	U-ZEN	FLUENT	LES[1]	Exp.[2]
St	0.208	0.233	0.203	0.215
C_D	0.865	1.050	1.000	0.980
L_R	1.620	1.360	1.360	1.330
U_{min}	-0.180	-0.185	-0.180	-0.180

$Re_D = 3,900$
[1] Beaudan & Moin 1994,[2] Zdravkovich 1997

Table I. Computational results for the flow around the circular cylinder. St is the Strouhal number, C_D and C_L are the maximum aerodynamic forces during a shedding cycle, L_R the length of the recirculation bubble, and U_{min} the minimum velocity on the wake centerline.

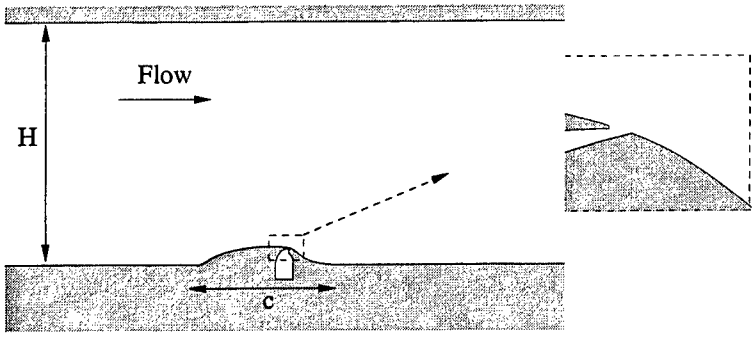


FIGURE 1. Sketch of the bump studied experimentally by Seifert & Pack (2002)

U-ZEN and FLUENT are in good agreement with each other and with the experimental data. Additional simulations were carried out for the flow over a square cylinder, and similar agreement was obtained.

4. Turbulent flow over a bump

Three problems have been proposed for the CFDVAL2004 Workshop: the first two are related to simple synthetic jet flows with and without crossflow. The third concerns the study of a hump model with various steady and unsteady separation controls. Our preliminary work has been focused on the analysis of this test problem.

The geometry with a detailed view of the flow control slot is sketched in Fig. 1. The hump thickness is 20% and the chord of the hump relative to to the height of the channel is $c/H = 2/3$ and, therefore, substantial blockage effects are expected.

Experiments were carried out in the NASA Langley Transonic Cryogenic Tunnel (Seifert & Pack 2002) for Reynolds numbers ranging from 2.4 to 26 millions and Mach number of 0.25. Due to discrepancies observed with previous CFD analysis of this model (see Viken *et. al.* 2003) a new set of measurements will be collected and made available at the workshop. In this work we will the original set of experimental data for an initial assessment of the predictive capabilities of the RANS tools employed.

Structured and unstructured computational grids have been generated. The unstructured grid (Fig. 2) is built using 24 layers of quadrilaterals in the boundary layers and paving in the rest of the domain. Three meshes were considered to evaluate the grid sensitivity of the solution; their sizes range from 12,000 to 70,000 elements. Note that the cavity region is included in the mesh (using triangular paving) to study its effect on the solution. The structured grid is shown in Fig. 3. It contains 16,000 cells, and two additional coarser versions have been considered to evaluate grid dependence. In this case the cavity is not included and the jet control is modeled through a boundary condition to be discussed later.

The first set of simulations is aimed at establishing the accuracy of the two RANS codes used (UZEN and FLUENT) for a case without flow control. Calculations are carried out at Reynolds number of 12 million and Mach 0.25. In Fig. 4 pressure coefficient distributions along the bump are reported using various turbulence models and by considering different heights of the channel to study the effect of the blockage. The agreement is reasonable when the SA and KW models are used in FLUENT and UZEN, respectively. When the same turbulence model (SA) is used the comparison is not satisfactory, with UZEN predicting a substantially lower pressure. The cause seems to be related to the

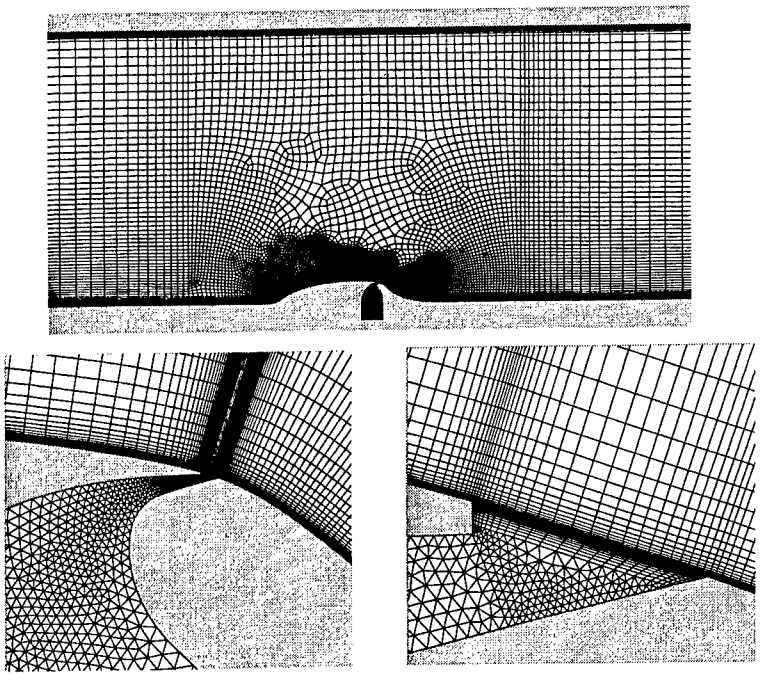


FIGURE 2. Unstructured computational grid with details of the slot region.

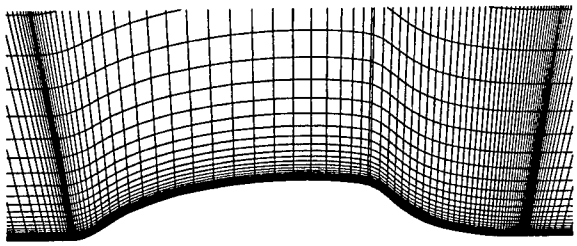


FIGURE 3. Structured computational grid. Note that the cavity is not included but is modeled as a boundary condition.

incoming boundary layer (note the peak at $x/c = 0$ in Fig. 4(a)) which appears to be of different thickness in the various calculations. This was also acknowledged as a crucial aspect of the simulations reported in Viken *et. al.* (2003).

The effect of the blockage plotted in Fig. 4(b) shows that the separation bubble (from $x/c \approx 0.6$) is strongly affected by the height of the channel; however, the simulations fail to capture the level of the pressure in the separated region. This is consistent with the finding in Viken *et. al.* (2003) which has motivated the new experimental study.

In Fig. 5 the streamlines are reported for the cases without control and with a steady suction corresponding to a momentum coefficient $C_\mu = -1.4\%$ (where C_μ is defined as the ratio of jet momentum to free-stream momentum). The recirculation bubble in Fig. 5(a), estimated using the skin friction coefficient (not reported), is $\Delta/c = 0.59$ whereas it is reduced to $\Delta/c = 0.14$ with the control (Fig. 5(c)). The experimental bubble length

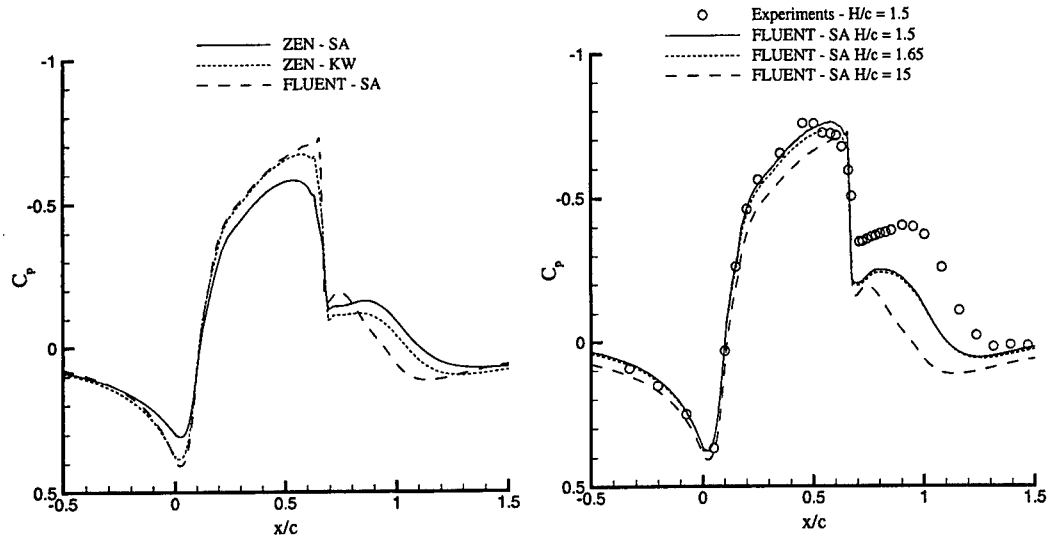


FIGURE 4. Pressure coefficient distribution over the bump; Re = 16 million, Ma = 0.25. Comparison between U-ZEN and FLUENT (left); effect of the height of the tunnel (right), cfn. Fig. 1.

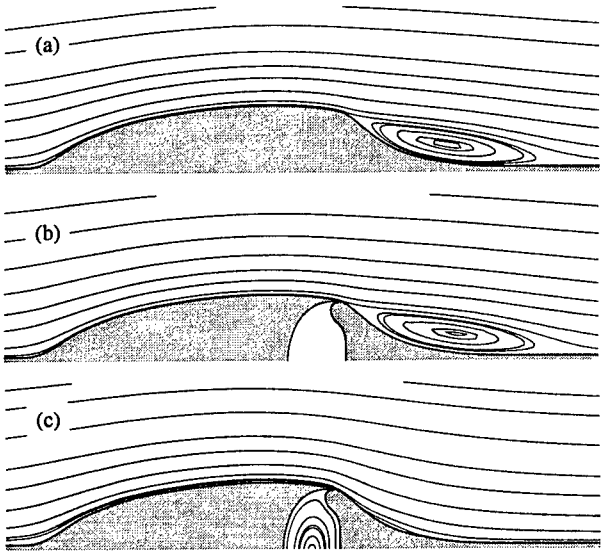


FIGURE 5. Computed streamlines: Re = 16 million, Ma = 0.25. No control (left); no control but model with the cavity (center), steady suction: $C_\mu = -1.4\%$ (right).

is estimated to be $\Delta/c = 0.56$ for the case without control. No information is given for the case with control in Seifert & Pack (2002). In Fig. 5(b) an additional simulation is reported for the case without control but with the cavity to evaluate its effect on the solution.

One important aspect of the present work is to establish the suitability of representing the control jets using boundary conditions instead of explicitly simulating the flow in the

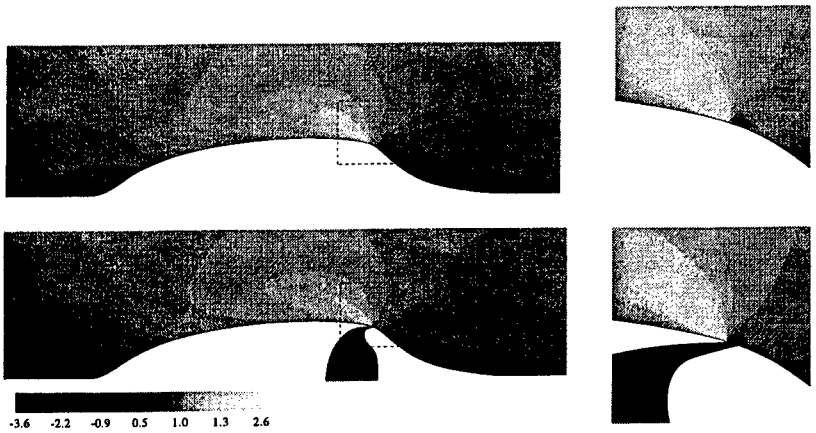


FIGURE 6. Computed streamwise velocity contours. Steady suction modeled as a boundary condition (top) and steady suction applied through the cavity (bottom).

cavity. This is extremely important for synthetic jets generated by a deforming membrane which would require an extremely complicated and time-consuming moving-mesh calculation. In Fig. 6 two simulations of the steady suction control case (reported earlier) are compared. In one case the suction is modeled as a boundary condition whereas in the other the cavity is included in the simulation. From an experimental point of view the momentum ratio C_μ is known together with the total mass flow rate through the slot:

$$C_\mu = \frac{\rho_j V_j^2 H}{1/2 \rho_\infty V_\infty^2 c}$$
$$M_j = \frac{\rho_j V_j H}{\rho_\infty V_\infty c}$$

where the subscripts j and ∞ refer to jet and inflow conditions, respectively, and M_j is the measured mass flow through the slot. These two conditions allow the jet conditions to be determined:

$$\frac{V_j}{V_\infty} = \frac{C_\mu}{2M_j}$$
$$\frac{\rho_j}{\rho_\infty} = \frac{V_\infty}{V_j}\frac{M_f c}{H}$$

The suction boundary condition is formulated by assuming a constant density and velocity (given by the expressions above) and by assuming a zero pressure gradient. The results are presented in Fig. 6 in terms of velocity contours on the bump and in the vicinity of the suction slot. The agreement between the two simulations (with the cavity or with the suction boundary condition) is very good. Another option that has been tested for the specification of the boundary condition is to use a zero gradient condition for the velocity corresponding to an extrapolation from the inside (instead of a direct enforcement). This condition will not guarantee the correct specification of the mass flow and, therefore, the velocity has to be properly scaled. The advantage of this approach is that the velocity is not constant in the slot region but has a variation that accounts

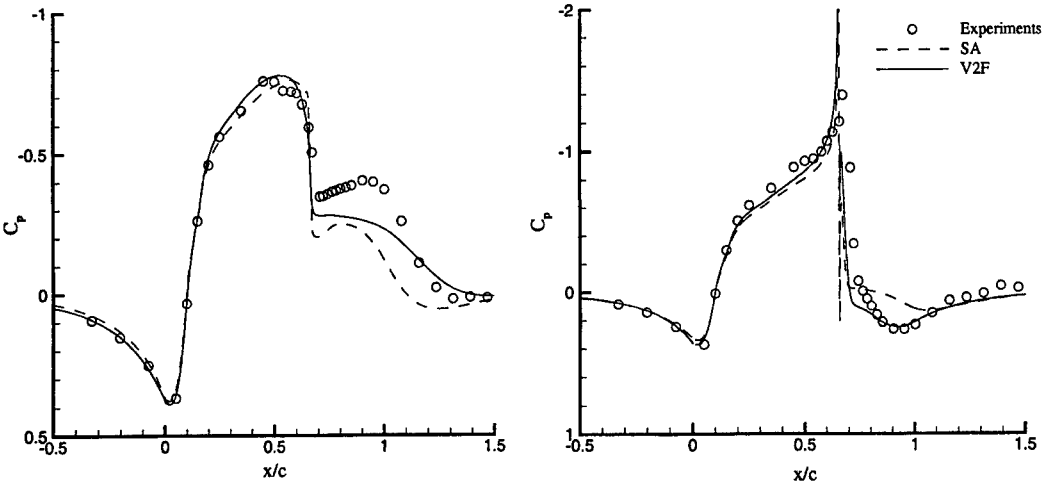


FIGURE 7. Pressure coefficient distribution over the bump: Re = 16 million, Ma = 0.25. No control (left); steady suction: $C_\mu = -1.4\%$ (right).

for the external flow even if the correct suction integral parameters are specified. The difference between the two boundary conditions described was found to be minimal in the present problem.

In Fig. 7 the pressure distributions on the bump with and without (steady) control are reported. Results obtained using two turbulence models are compared with the experimental data. The V2F model appears to be superior to the SA model in predicting the pressure level in the recirculation bubble and in the successive recovery region (as expected, see Iaccarino 2001). In particular, it is interesting to note that the agreement is somewhat better in the controlled case.

Finally, in Fig. 8, results for an unsteady control case are reported. They correspond to an average momentum coefficient $< C_\mu >= 0.95\%$ and a non-dimensional frequency $F^+ = 1.6$ (normalized by free stream velocity and half chord). In this case experimental data are not available for comparison, but the present data are is agreement with the CFD results reported in Viken *et. al.* (2003). It is interesting to note that the envelope (the maximum and minimum within a cycle) shows a large variation of the friction coefficient in the region downstream of the slot with a very small area of recirculating flow.

5. Conclusions and future work

This report presents some preliminary results of steady and unsteady RANS simulations of flows with active control. The main objective is to establish the accuracy of the predictions with particular emphasis on (a) turbulence modeling, and (b) control enforcement (boundary condition).

Calculations are carried out using an unstructured commercial CFD code, FLUENT, and a multiblock structured aeronautical CFD code, UZEN. Several turbulence model have been used, ranging from a one-equation model to a four-equation model. An explicit description of the control device (a cavity with a contoured slot) and its modeling by a velocity boundary condition have been considered and results have been compared.

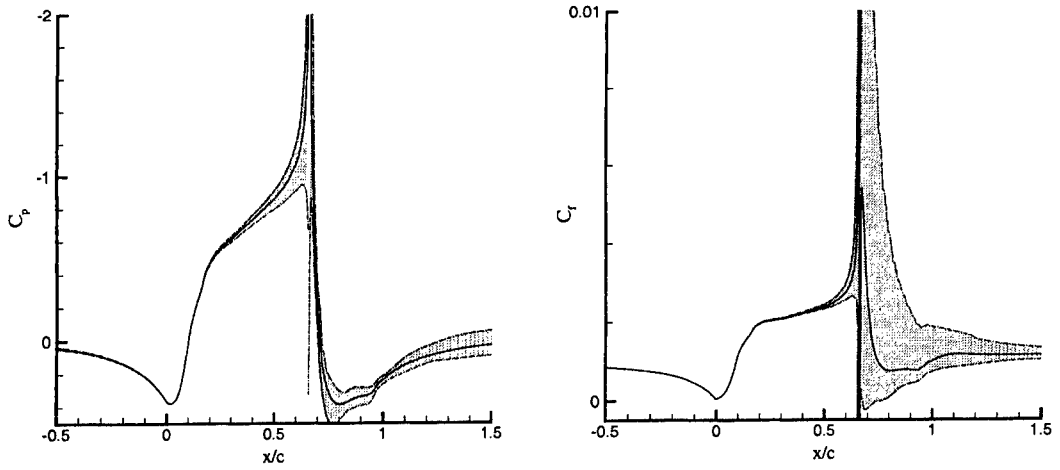


FIGURE 8. Pressure coefficient distribution (left) and skin friction (right) over the bump in the unsteady control case: Re = 16 million, Ma = 0.25. Solid line represent time averaged results; the grey area represents the unsteady envelope. These results are obtained with the full configuration (including the cavity).

The preliminary conclusion is that turbulence modeling plays a crucial role in the accuracy of the results and, at least for a steady suction control, the control device can be reasonably modeled by a boundary condition.

Future work will be focused on the comparison of the present calculation (and additional simulations in different conditions) to the new set of experimental data being provided at the CFDVAL2004 workshop and on the assessment of the suitability of modeling unsteady control (synthetic jet) by boundary conditions.

REFERENCES

AMITAY, M., SMITH, B.L. & GLEZER, A. 1997 Modification of the aerodynamic characteristics of bluff bodies using fluidic actuators. *AIAA Paper 97-2004* .

BEAUDAN, P. & MOIN, P. 1994 Numerical experiments of the flow past a circular cylinder at subcritical Reynolds number. *Rept. No. TF-62, Dept. Mech. Eng.* Stanford University.

BRASLOW, A. L. 1999 *A history of suction-type laminar flow control with emphasis on flight research.* NASA Monographs **13.**

CATALANO, P., WANG, M., IACCARINO, G., SBALZARINI, L. & KOUMOUTSAHOS, P. 2002 Optimization of cylinder flow control via actuators with zero-mass flux. *Proc. of the 2002 Summer Program*, Center for Turbulence Research, 297–304.

DURBIN, P. A., 1995 Separated flow computations with the $k-\epsilon-v^2$ model. *AIAA J.*, **33**, 659–664.

GLEZER, A. & AMITAY, M., 2002 Synthetic jets. *Ann. Rev. Fluid. Mech.* **34** 503–529.

IACCARINO, G., 2001 Predictions of a turbulent separated flow using commercial CFD codes. *J. Fluids Eng.* **123** 819–828.

KRAL, L. D. , DONOVAN, J. F., CAIN, A. B. & CARY, A. W. 1997 Numerical simulation of synthetic jet actuators. *AIAA Paper 97-1824* .

OOI, A., IACCARINO, G., DURBIN, P. A. & BEHNIA, M., 2002 Reynolds averaged simulations of flow and heat transfer in ribbed ducts. *Int. J. Heat and Fluid Flow*, **23**, 750–757.

SEIFERT, A. & PACK, L. G., 2003 Active flow control on wall-mounted hump at high Reynolds numbers. *AIAA J.* **40** 1363–1372.

SMITH, B. L. & SWIFT, G. W., 2003 A comparison between synthetic jets and continuous jets. *Exp. Fluids* . **34** 467–472.

SPALART, P. R. & ALLMARASS S. R., 1994 A one-equation turbulence model for aerodynamic flows. *La Recherche Aerospatiale*, **1**, 1–23.

VIKEN, S. A., VATSA, V. N., RUMSEY, C. L. & CARPENTER, M. H., 2003 Flow control analysis of the hump model with RANS tools. *AIAA Paper 2003-218*

WILCOX D.C. 1993 *Turbulence modeling for CFD.* DCW Industries Inc., USA.

ZDRAVKOVICH, M. M. 1997 *Flow Around Circular Cylinders. Fundamentals.* Oxford University Press, Oxford, UK.

Constrained aeroacoustic shape optimization using the surrogate management framework

By Alison L. Marsden, Meng Wang, and John E. Dennis, Jr.

1. Motivation and objectives

Reduction of noise generated by turbulent flow past the trailing-edge of a lifting surface is a challenge in many aeronautical and naval applications. Numerical predictions of trailing-edge noise necessitate the use of advanced simulation techniques such as large-eddy simulation (LES) in order to capture a wide range of turbulence scales which are the source of broadband noise. Aeroacoustic calculations of the flow over a model airfoil trailing edge using LES and aeroacoustic theory have been presented in Wang & Moin (2000) and were shown to agree favorably with experiments. The goal of the present work is to apply shape optimization to the trailing edge flow previously studied, in order to control aerodynamic noise.

There are several considerations in choosing a tractable optimization method for the trailing-edge problem. The primary concern is the computational expense of the function evaluations, and additional considerations include availability of gradient information and robustness of the optimization method. Although adjoint solvers have been successfully applied for gradient-based optimization in aeronautics problems (for example in Jameson *et al.* (1998)), they present difficulties with implementation, portability, and data storage for unsteady problems. Approximation modeling was used for trailing-edge optimization in Marsden *et al.* (2002), and results showed significant reduction in acoustic power with reasonable computational cost. In these methods, optimization is performed not on the expensive actual function, but on a surrogate function, which is cheap to evaluate. Although the approximation method presented in Marsden *et al.* (2002) was effective, it lacks rigorous convergence properties.

The surrogate management framework (SMF), developed by Booker *et al.* (1999), incorporates the use of surrogate functions into a pattern search framework, hence providing a theoretical basis for convergence. The convergence of pattern search methods has been studied extensively by Audet & Dennis (2003, 2000). Use of the SMF method has been demonstrated, among others, by Booker *et al.* (1999), where the method was successfully applied to a helicopter rotor blade design problem with 31 design variables.

The SMF method provides a robust and efficient alternative to traditional gradient-based optimization methods. In this work, the SMF method is applied for trailing-edge optimization in a time-dependent laminar flow problem with and without constraints on lift and drag. Several interesting optimal shapes have been identified, all of which result in significant reduction of trailing-edge noise. In particular, the development of a trailing-edge bump in the constrained case is an unexpected result which illustrates the trade-off between noise reduction and loss of lift.

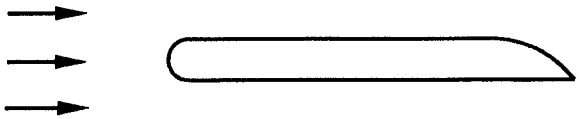


FIGURE 1. Blake airfoil used in model problem. Right half section of upper surface is allowed to deform

2. Problem formulation and cost function

The general optimization problem may be formulated with bound constraints as follows

$$\begin{aligned} &\text{minimize} \quad J(x) \\ &\text{subject to} \quad x \in \Omega. \end{aligned} \tag{2.1}$$

In the above problem statement, $J : \mathbb{R}^n \rightarrow \mathbb{R}$ is the cost function, and x is the vector of design parameters. The bounds on the parameter space are defined by $\Omega = \{x \in \mathbb{R}^n | l \leq x \leq u\}$ where $l \in \mathbb{R}^n$ is a vector of lower bounds on x and $u \in \mathbb{R}^n$ is a vector of upper bounds on x.

In this work, the surrogate management framework is implemented and validated for optimization of a time-dependent flow problem. The airfoil geometry for the model problem is shown in Figure 1 and is a shortened version of the airfoil used in experiments of Blake (1975). The airfoil chord is 10 times its thickness, and the right half of the upper surface is allowed to deform. The flow is from left to right and results presented in this work are at a chord Reynolds number of $Re = 10,000$.

The cost function is defined in terms of noise radiation from an acoustically compact airfoil, calculated using Curle's extension to the Lighthill theory (Curle 1955). The compactness assumption is valid for unsteady laminar flow past an airfoil at low Mach number since the acoustic wavelength associated with the vortex shedding is typically long relative to the airfoil chord. Details of the cost function derivation are given in Marsden *et al.* (2003), and the final cost function expression is

$$\bar{J} = \overline{\left(\frac{\partial}{\partial t}\int_S n_j p_{1j}(\mathbf{y},t)d^2\mathbf{y}\right)^2} + \overline{\left(\frac{\partial}{\partial t}\int_S n_j p_{2j}(\mathbf{y},t)d^2\mathbf{y}\right)^2}, \tag{2.2}$$

which is directly proportional to the radiated acoustic power.

The cost function, $\bar{J}$, depends on control parameters for the airfoil surface deformation. Each parameter corresponds to a deformation point on the airfoil surface, and its value must be within prescribed allowable bounds. The value of each parameter is defined as the displacement of the control point relative to the original airfoil shape, in the direction normal to the surface. A positive parameter value corresponds to displacement in the outward normal direction, and a negative value corresponds to the inward normal direction. A spline connects all the deformation points to the trailing edge point and the left (un-deformed) region to give a continuous airfoil surface. Both ends of the spline are fixed. While the surface must be continuous and smooth on the left side, the trailing edge angle is free to change.

For a given set of parameter values, there is a unique corresponding airfoil shape. To calculate the cost function value for a given shape, a mesh is generated and the flow simulation is performed until the solution is statistically converged. A finite difference code discussed in Wang & Moin (2000) is used to solve the time-dependent incompressible two-dimensional Navier-Stokes equations in generalized curvilinear coordinates. Because

the flow has unsteady vortex shedding, the cost function is oscillatory. In the optimization procedure, the mean cost function $\bar{J}$ (cf. (2.2)) is used, which is obtained by averaging in time until convergence. With each shape modification, the flow field is allowed to evolve for sufficiently long time to establish a new quasi-steady state before the time averaging is taken.

3. Outline of the surrogate management framework

In this section, we outline the steps used for trailing-edge shape optimization with the surrogate management framework. The SMF, introduced in Booker *et al.* (1999), is a pattern search method which incorporates surrogate functions to make the optimization cost effective. The main idea behind the SMF method is to use a surrogate function as a predictive tool, while retaining the robust convergence properties of pattern search methods. Like pattern search methods, SMF is a mesh based algorithm, so that all points evaluated are restricted to lie on a mesh.

The first step in the optimization is to choose a set of initial data. Latin hypercube sampling (LHS) McKay *et al.* (1979), is commonly used to find a well distributed set of initial data in the parameter space. Latin hypercube sampling ensures that each input variable has all portions of its range represented in the chosen data set. Once the initial data set, $x_1 \dots x_m$, has been chosen, the cost function, $J(x)$ is evaluated at these points, and an initial surrogate model is constructed.

A Kriging surrogate model is used to interpolate the data, and to predict the value of the function at a particular location in the parameter space. As the optimization progresses, the surrogate model should be updated to include new data. Kriging, also called DACE, is a statistical method based on the use of spatial correlation functions. It is easily extended to multiple dimensions, making it attractive for optimization problems with several parameters. A detailed derivation of the Kriging approximation is given in Marsden *et al.* (2003), following Lophaven *et al.* (2002). After constructing an initial surrogate, all points subsequently evaluated by the algorithm are restricted to lie on a mesh in the parameter space. The mesh definition is flexible so long as the vectors connecting a point x to any $2n$ points adjacent to x form a positive basis for $\mathbb{R}^n$. The mesh may be refined or rotated during the optimization as long as it satisfies this definition.

The SMF algorithm consists of two steps, SEARCH and POLL. The exploratory SEARCH step uses the surrogate to aid in the selection of points which are likely to improve the cost function. The SEARCH step provides means for local and global exploration of the parameter space, but is not strictly required for convergence. Because the SEARCH step is not integral to convergence, it affords the user a great deal of flexibility and may be adapted to a particular engineering problem.

Convergence of the SMF algorithm is guaranteed by a POLL step, in which points neighboring the current best point on the mesh are evaluated to check whether the current best point is a mesh local optimizer. A set of POLL points are required to generate an $n+1$ positive basis. An example of such a basis is constructed in $\mathbb{R}^n$ as follows. We let V be the matrix whose columns are the basis elements. Then construct $D = [V, -V \cdot e]$, where e is the vector of ones and $-V \cdot e$ is the negative sum of the columns of V. The columns of D form an $n+1$ positive basis for $\mathbb{R}^n$. For example, in three dimensions such a basis could be given by $(1,0,0), (0,1,0), (0,0,1), (-1,-1,-1)$.

Following evaluation of the initial data, the first step in the optimization is a SEARCH step. In the SEARCH step, optimization is performed on the surrogate in order to predict

the location of one or more minimum points, and the function is evaluated at these points. If an improved cost function value is found, the search is considered successful, the surrogate is updated, and another search step is performed. If the SEARCH fails to find an improved point, then it is considered unsuccessful and a POLL step is performed, in which the set of POLL points are evaluated. If the POLL produces an improved point, then a SEARCH step is performed on the current mesh. Otherwise, if no improved points are found, then the current best point is a local minimum of the function on the mesh. For greater accuracy, the mesh may be refined, at which point the algorithm continues with a SEARCH. Convergence is reached when a local minimum on the mesh is found, and the mesh has been refined to the desired accuracy. Each time new data points are found in a SEARCH or POLL step, the data is added to the surrogate model and the surrogate is updated. The steps in the algorithm are summarized below, where the set of points in the initial mesh is M_0, the mesh at iteration k is M_k, and the current best point is x_k.

1. SEARCH

(a) Identify finite set of trial points T_k on the mesh M_k.

(b) Evaluate $J(x_{trial})$ for trial points $T_k \in M_k$.

(c) If for any point in T_k, $J(x_{trial}) < J(x_k)$, a lower cost function value has been found, the *SEARCH is successful.* Increment k and go back to SEARCH.

(d) Else if none of T_k improves the cost function, *SEARCH is unsuccessful.* Increment k and go to POLL.

2. POLL

(a) Find a set of poll points X_k around x_k which are neighboring mesh points that generate a positive basis.

(b) If for any point in X_k , $J(x_{poll}) < J(x_k)$, a lower cost function has been found and the *POLL is successful.* Increment k and go to SEARCH.

(c) Else if none of X_k improves the cost function, *POLL is unsuccessful.*

(a) If convergence criteria are satisfied, a converged solution has been found. STOP.

(b) Else if convergence criteria are not met, refine mesh. Increment k and go to SEARCH.

Because the method has distinct SEARCH and POLL steps, convergence theory for the SMF method reduces to convergence of pattern search methods. Convergence of the SMF method is discussed at length by Booker *et al.* (1999). Pattern search convergence theory is presented by Audet & Dennis (2003).

4. Unconstrained two parameter results

In this section, the full SMF method is validated using two shape parameters. The control points, a and b, are evenly distributed on the upper surface of the airfoil. For each set of parameters, the airfoil surface is interpolated using a hermite spline. The lower bound on the parameters is chosen to correspond to a straight line connecting the left edge of the deformation region and the trailing edge, and the upper bound is an equal deformation in the outward normal direction.

To give a basis for comparison, results using two parameters without the POLL step are presented in Table 1. We term this method the "strawman method." The case shown produces a cost function reduction of 54% with 18 function evaluations. The optimal shape obtained in this case is shown on the left of Figure 2. The corresponding normalized cost function reduction is given on the right of Figure 2, and the initial and final Kriging surrogates are shown in Figure 3. To make the "strawman" case consistent with cases

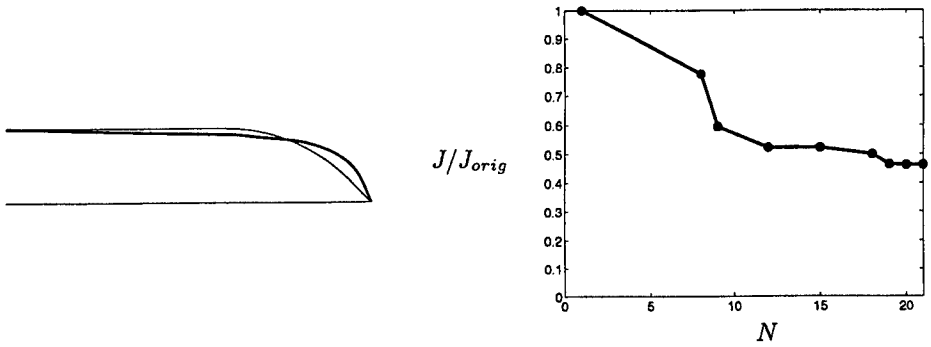


FIGURE 2. Left: initial (thin line) and final (thick line) airfoil shapes using two parameters with no poll step ("strawman method"). Right: normalized cost function (acoustic power) vs. total function evaluations

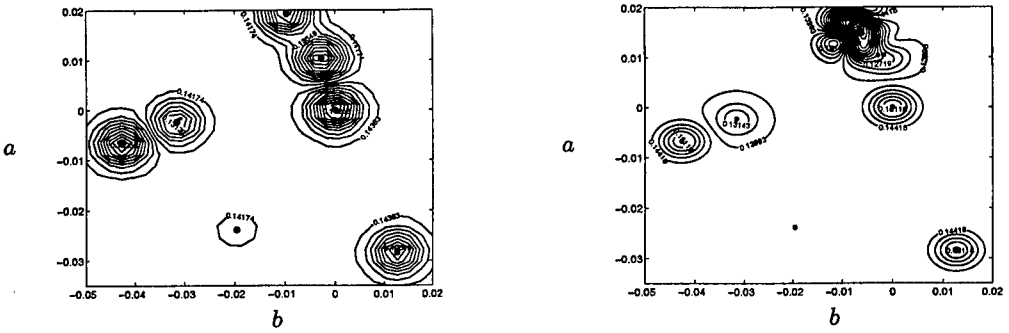


FIGURE 3. Initial and final Kriging surrogate functions for "strawman" case. Left plot shows initial data obtained with latin hypercube sampling; right side shows final surrogate fit.

using the SMF method, all points evaluated were restricted to lie on a mesh of the same size, and the mesh was refined twice. Convergence was reached when surrogate minimum point was the same as the previous iteration.

For purpose of comparison, all full SMF method cases use the same set of LHS initial data (7 points) as the "strawman" case shown on the left side of Figure 3. The two-parameter results obtained using the full SMF method are given in Table 1. The table lists the total number of function evaluations as well as the number of iterations, where one iteration is a complete SEARCH or POLL step. In all cases, the number of function evaluations includes the number of initial data points.

The second line of table 1 shows a case in which one point, the surrogate minimum on the mesh, is evaluated in each SEARCH step. With two mesh refinements, the total cost function reduction is 72%. Comparing with the "strawman" case, the POLL step adds some computational expense, but also results in a significantly lower cost function value. As discussed in Section 3, the POLL step ensures convergence to a local minimum on the mesh in the parameter space.

Lines three and four in Table 1 explore the effect of using multiple points in the SEARCH step of the algorithm. In each case, one SEARCH point is found by a direct search for the minimum of the surrogate function on the mesh. Additional "space-filling" points are added in an effort to keep the data set well distributed and prevent degradation of surrogate accuracy. The addition of "space-filling" points does not necessarily increase the overall cost since the SEARCH points may be evaluated in parallel. Results using two

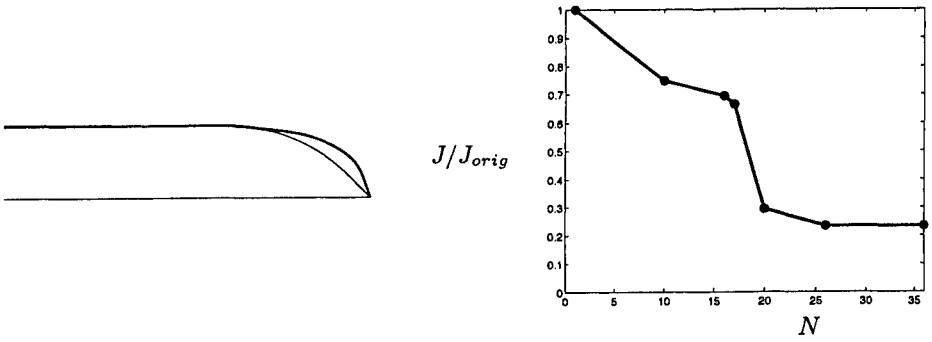


FIGURE 4. Left: initial (thin line) and final (thick line) airfoil shapes using two parameters with SMF method. Right: normalized cost function (acoustic power) vs. total function evaluations. Each SEARCH step used three function evaluations.

optimization method	parameters	search points	% reduction	evaluations	iterations
strawman	2	1	54%	18	11
SMF	2	1	72%	33	15
SMF	2	2	72%	42	15
SMF	2	3	77%	46	13

TABLE 1. Two parameter SMF - Comparison of cases using one, two, and three search points.

points (the surrogate minimum and one "space-filling" point) in each SEARCH step are given in line three of Table 1. The cost function reduction and the optimal shape are identical to the case with only one search point. In both cases, 15 iterations were required using two mesh refinements, a slight increase in cost over the "strawman" case.

Using three SEARCH points (one surrogate minimizer and two 'space-filling' points) a larger cost function reduction of 77% was achieved, as shown in line four of Table 1. Figure 4 shows the optimized airfoil shape (left) and the cost function reduction (right) for this case. Comparing with the other cases in Table 1, the case with three search points required fewer iterations. This savings is explained by a higher surrogate quality in the final iterations, resulting in fewer polling steps. A comparison of surrogate quality is made by evaluating the mean squared error.

We have shown that efforts to reduce surrogate degradation can pay off, resulting in a lower cost function solution. In addition, the two parameter cases, shown in Figures 2 and 4, resulted in airfoil shapes with a blunt trailing-edge, which was at first sight counter-intuitive. Figure 5 illustrates the time-dependent nature of the problem and compares cost function vs. time for the original airfoil, the "strawman" case, and the best SMF case. The magnitude of acoustic power has decreased significantly for the optimized shapes compared to the original. However, with the 77% acoustic power reduction in the best two parameter case, the optimized airfoil has 20% lower lift than the original, which is often not allowed in engineering practice. This emphasizes the need for addition of constraints on lift and drag, which is addressed in Section 5.1.

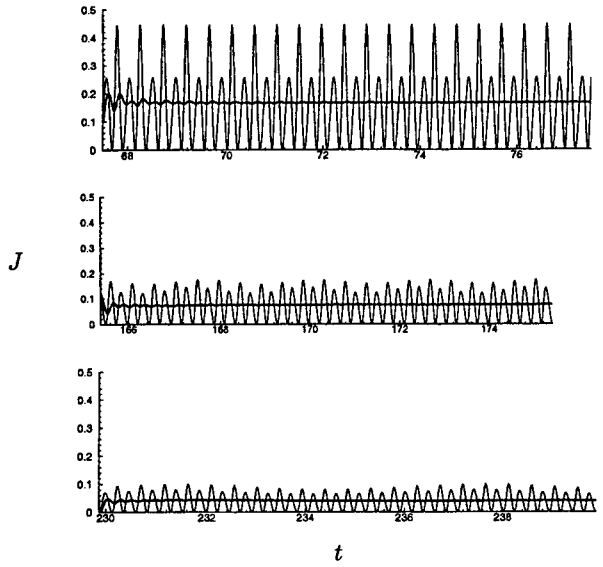


FIGURE 5. Comparison of cost functions for original airfoil (upper plot), "strawman" with 54% reduction (middle plot) and SMF with 77% reduction (lower plot). Thin line is instantaneous cost function (acoustic power), and thick line is averaged cost function (acoustic power).

5. Constrained optimization with multiple parameters

5.1. *Filtering method for constrained optimization*

Lift and drag constraints can be enforced using the filtering method of Audet & Dennis (2000) and Audet *et al.* (2000), an extension of the pattern search method, and hence of the SMF method. We consider the general constrained optimization problem

$$\begin{aligned} &\text{minimize} \quad J(x), \\ &\text{subject to} \quad x \in \Omega, \;\; C(x) \leq 0. \end{aligned} \tag{5.1}$$

In the above problem statement, $J : \mathbb{R}^n \rightarrow \mathbb{R}$ is the cost function, and x is the vector of parameters. The constraints are given by m functions contained in $C(x)$ so that $C = (c_1(x) \ldots c_m(x))^T$. The bounds on the parameter space are defined by a polyhedron in $\mathbb{R}^n$ denoted by Ω.

We begin by defining a constraint violation function, H, the value of which indicates how closely the problem constraints are being met. With multiple constraints, H may be the sum of several constraint functions which are weighted according to relative importance. The goal of the optimization problem is to find solutions which have a small cost function value, together with a small (or zero) value of H.

The feasible region in a plot of J vs. H is defined as the set of points that exactly satisfy $H(x) = 0$. Thus, a point x is infeasible if $H(x) > 0$. A point x' is considered filtered, or dominated, if there is a point x belonging to the filter for which $H(x) \leq H(x')$ and $J(x) \leq J(x')$. A filter, $\mathcal{F}$, is defined here to be the finite set of non-dominated points found so far. The above concepts are exemplified in figure 8, which depicts the final filter corresponding to the constrained trailing-edge optimization (to be discussed later). The points in the filter are connected with vertical and horizontal lines to form a dividing line between filtered and unfiltered regions. The best feasible point, marked with a square, is the point with the lowest cost function value, which exactly satisfies the constraint

(i.e. $H = 0$). The least infeasible point, marked with a triangle, is the filter point with the lowest non-zero constraint function value. Other points in the filter are marked with circles.

The steps in the filtering optimization algorithm fit within the framework of the SMF method, and the basic structure is the same as presented in Section 3. The differences in implementation between unconstrained SMF and the filter method lie in the criteria which make SEARCH and POLL steps successful or unsuccessful. In this implementation of the filter method, a SEARCH step is formally considered successful if it improves the filter, which means that a new non-dominated point was identified. A POLL step is considered successful if it improves either the the best feasible point or the least infeasible point. Convergence theory of this method is also based on pattern search theory, and is discussed at length in Audet & Dennis (2000). The set of points in the initial mesh is M_0, the mesh at iteration k is M_k, the current least infeasible point is LF_k and the current best feasible point is BF_k. The SEARCH and POLL steps are as follows:

1. SEARCH

(a) Identify finite set of trial points T_k on the mesh M_k.

(b) Evaluate $J(x_{trial})$ and $H(x_{trial})$ for trial points $T_k \in M_k$.

(c) If any point in T_k, is an unfiltered point, the *SEARCH is successful.* Increment k and go back to SEARCH.

(d) Else if none of T_k is an unfiltered point, *SEARCH is unsuccessful.* Increment k and go to POLL.

2. POLL

(a) Find a set of POLL points X_k around LF_k or BF_k, which are neighboring mesh points that form a positive basis.

(b) If any point in X_k dominates LF_k or BF_k, the *POLL is successful.* Increment k and go to SEARCH.

(c) Else if none of X_k dominates LF_k or BF_k, the *POLL is unsuccessful.*

(a) If convergence criteria are satisfied, a converged solution has been found. STOP.

(b) Else if convergence criteria are not met, refine mesh. Increment k and go to SEARCH.

5.2. *Incorporation of a penalty function*

Many optimization methods rely on the use of a penalty function to enforce constraints. Penalty functions are attractive due to ease of implementation into existing optimization frameworks. Challenges usually involve the choice of arbitrary weighting of the constraint function relative to the cost function. Penalty functions can be easily incorporated into the SMF filtering method, and can be extremely useful in aiding the selection of SEARCH points. Here, we present a systematic approach for choosing the penalty constant by making use of the filtering framework.

In this approach, a penalty is added to the cost function as follows,

$$\hat{J} = J_{orig} + \alpha H. \tag{5.2}$$

A surrogate is constructed to model the function $\hat{J}$, so that it is used to predict areas of the function which satisfy the constraint. The minimum of the modified surrogate function can then be evaluated in the SEARCH step.

The parameter α is chosen based on the current set of filter points (including the best feasible point). We wish to choose α so as to bias the surrogate towards points with low values of H, which will improve the filter. Let us first consider a filter with two points,

a and b, for which $H(a) < H(b)$ and $J(a) > J(b)$. We wish to choose α so that point a is favored by the surrogate model because it has a smaller constraint violation. We therefore require

$$J(a) + \alpha H(a) < J(b) + \alpha H(b).$$

For this pair of points, α must be at least as large as the slope of the line connecting them. When considering the set of points making up a filter, α should be at least as large as the slope of the steepest line connecting any two points in the filter. This choice guarantees domination of the point with the smallest value of H in the filter. Since the filtered points are not of interest in the optimization, they need not be considered in the choice of α. If there are less than two points in the filter set, $\alpha = 0$. As points are evaluated in the optimization, the filter evolves and the value of α is updated in each iteration. Values of J and H for all data points should be saved so that previous data points may be updated in the surrogate model as the value of α changes.

5.3. *Issues with multiple parameters*

The constrained optimization is performed using five design parameters. An increase in the number of parameters gives greater flexibility in the airfoil geometry and will also demonstrate feasibility and cost of the SMF method for more realistic applications. Increasing the number of parameters also presents challenges for searching on the surrogate model, and these are first discussed briefly.

Thickness constraints are defined by drawing a straight line from the left side of the upper surface deformation region to the trailing-edge point. The maximum airfoil thickness is defined by an equal displacement from the surface in the outward normal direction. Use of a hermite cubic spline as the interpolating function for the airfoil surface guarantees that no point on the surface will be displaced more than the maximum allowable displacement distance. This method can be easily generalized for any prescribed function which defines the thickness constraint.

Using a surrogate of multiple dimensions requires use of an optimization method to search for the surrogate minimum. To search the surrogate in the five parameter cases, a standard covariance matrix adaptation evolutionary strategy, or CMA-ES (Hansen & Ostermeier 1996) is employed. Accuracy is increased by running the CMA-ES optimization several times and taking the minimum value.

Based on experience with two parameters, three points are used in each SEARCH step for the five-parameter cases. In this case, the three SEARCH points are chosen to meet three goals: (1) global search, (2) local search around current best point and (3) model improvement.

The first point is chosen using the surrogate function as a predictor. The minimum of the surrogate is found using the CMA-ES, and the nearest mesh point is evaluated in the SEARCH. The second SEARCH point takes advantage of the surrogate to do a local search around the current best point. In order to pre-empt the need for a POLL step, the surrogate is used to predict the values of the POLL points neighboring the current best point. In the constrained case, the current best point may be either the best feasible point or the least infeasible point. The POLL point with the smallest surrogate value is then evaluated. In the event that the SEARCH step fails, one of the POLL points has already been evaluated, reducing the cost of a POLL step to N evaluations. The third point is for both model improvement and global search. The CMA-ES is used to search the Kriging surrogate for the point of maximum mean squared error (MSE), and the nearest mesh

parameters	constraints	% reduction	%change lift	% change drag	evaluations	iterations
5	no	77%	-17%	-12%	88	22
5	yes	43%	+0.2%	-9%	92	22

TABLE 2. Five parameter cases with SMF method. The first line is unconstrained and the second line is with constraints on lift and drag.

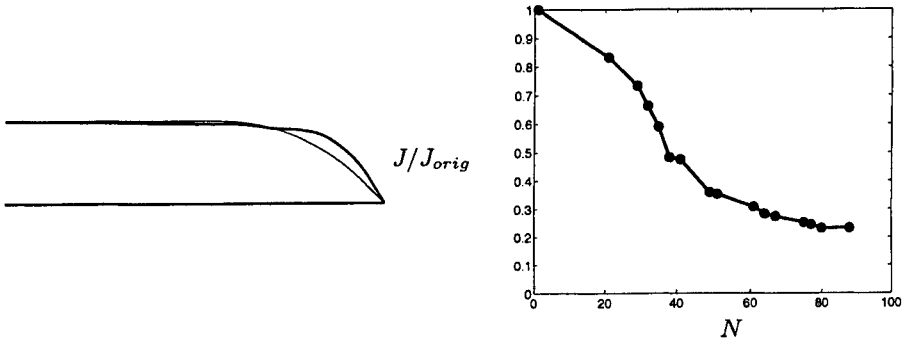


FIGURE 6. Left: initial (thin line) and final (thick line) airfoil shape with 5 shape parameters, unconstrained case. Right: corresponding normalized cost function reduction vs. number of function evaluations.

point is used in the SEARCH. This is done in an attempt to find areas with the fewest data points, as well as mitigate surrogate degradation.

5.4. *Comparison of constrained and unconstrained results*

Unconstrained results using five shape parameters are shown in the first line of Table 2. The number of evaluations in the table includes the initial data set of 15 points, found with LHS. The number of iterations includes all search and poll steps after one mesh refinement. The converged airfoil shape for the unconstrained case is shown on the left side of Figure 6, and the cost function reduction for this case is shown on the right. The blunt trailing-edge shape is qualitatively similar to the shapes obtained with the two parameter optimization, confirming robustness of the SMF method. The maximum cost function reduction for this case is 77% using 22 iterations after one mesh refinement, which agrees with the two parameter results. As in the two parameter case, the blunt trailing-edge results in a significant (nearly 20%) loss in lift. We observe that the blunt trailing-edge reduces the surface area affected by the separation region at the trailing-edge, and that pressure fluctuations are reduced in this region due to the smaller separation area. This in turn results in less vorticity generation, and a smaller vorticity magnitude in the wake.

Results for the constrained case are presented in the second line of Table 2. The surrogate for this case is constructed with an L_1 constraint violation function, aimed at keeping lift and drag at desirable levels:

$$H = max\left(0, \frac{L^* - L}{L^*}\right) + max\left(0, \frac{D - D^*}{D^*}\right), \tag{5.3}$$

where L^* and D^* are the original airfoil lift and drag. The surrogate is constructed using

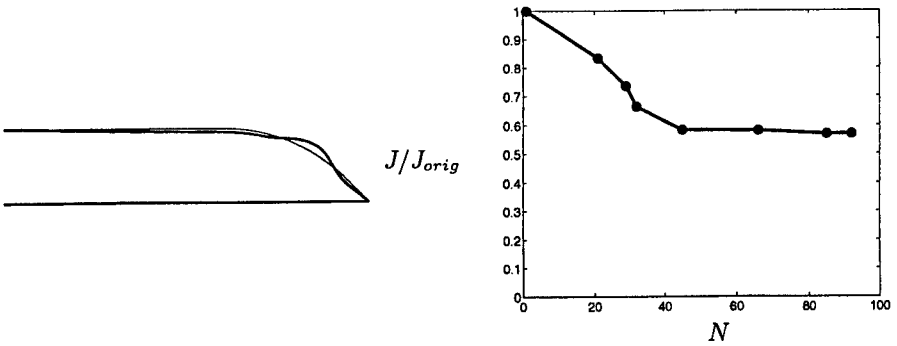


FIGURE 7. Left: initial (thin line) and final (thick line) airfoil shape with 5 shape parameters, and constraints on lift and drag. Right: corresponding normalized cost function reduction vs. number of function evaluations.

equation (5.2), so that a penalty is added if *either* the lift decreases or the drag increases. In this way, we allow the lift to increase and/or the drag to decrease.

The optimized airfoil shape for the constrained case is shown on the left side of Figure 7. The constraints are effective in keeping the lift at the target value, and the drag for this case has fortuitously decreased by 9%. The cost function reduction for this case is 43%, requiring 22 iterations for convergence on a once-refined mesh. The bump near the trailing-edge reduces the magnitude of the unsteady vortex shedding by reducing the size of the separation region. However, when compared to the unconstrained case, the bump size has been compromised to maintain lift, and the trailing-edge shape is closer to a cusp. Comparison of the shapes for the constrained and unconstrained cases also illustrates the sensitivity of the flow to very small changes in the shape of the airfoil.

The final filter is shown in Figure 8. The left side shows the entire filter domain, and the right side shows a magnified view of the filter region. The filter shows the trade-off between cost function reduction and constraint violation. The cluster of points around the filter, and on the $H = 0$ axis verifies that the algorithm is expending much effort in the relevant region of the function. For comparison, the rightmost filter point corresponds to a shape with a 64% cost function reduction and a 13% loss in lift. The other filter points show the range of possible airfoil designs between this point and the optimal point.

Reduction in acoustic power can be caused by reduction in the amplitude, or a decrease in frequency of lift and drag oscillations (see (2.2)). Results do not show a change in frequency when comparing optimized cases with the original, and the influence of the unsteady drag was found to be small. The reduction of unsteady lift amplitude can be illustrated by closer examination of the flow field. Instantaneous vorticity contours are shown in Figure 9 for the original (upper), unconstrained (middle) and constrained (lower) cases. In this plot, we verify that the magnitude of vortex shedding has decreased for both optimized shapes compared to the original. In addition, we observe that vortices are shed much closer to the trailing-edge in the original case compared with the optimized cases. Movement of the unsteady region away from the trailing-edge results in smaller pressure fluctuations on the airfoil surface in this region, and explains the reduction in unsteady lift, and therefore of acoustic power.

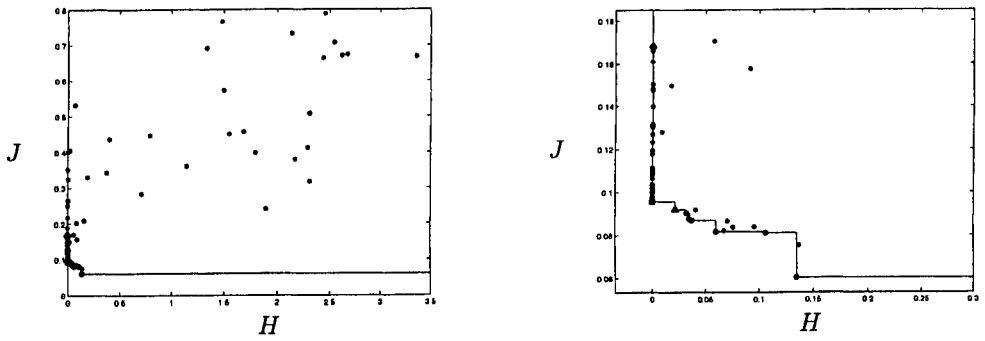


FIGURE 8. Final filter for constrained 5 parameter optimization problem. Cost function J vs. constraint violation function H. The best feasible point is the square, the least infeasible point is the triangle, the filter points are the circles, and filtered points are stars. The original airfoil cost function is marked with a diamond. Right figure is close-up of filter region in left figure.

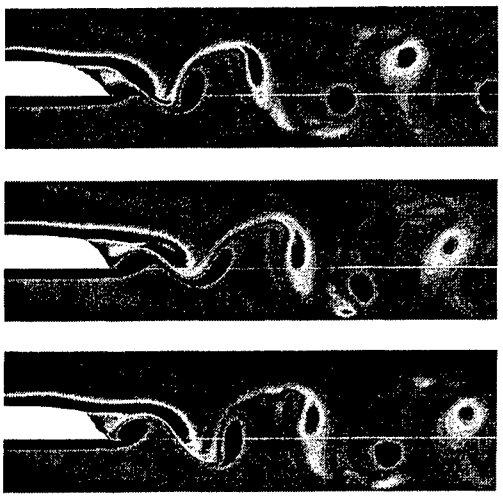


FIGURE 9. Comparison of vorticity contours for original (upper), unconstrained (middle) and constrained (lower) optimal shapes. Each plot shows instantaneous vorticity contours with minimum -25, maximum 25 and 20 contour levels.

6. Summary and future work

Application of the SMF method to optimize a model airfoil trailing-edge with laminar vortex shedding has resulted in significant reduction in acoustic power, as well as several interesting and previously unexpected airfoil shapes. The SMF method is robust and efficient for several design parameters with and without constraints. A filtering method has been applied to enforce constraints on airfoil lift and drag. It was implemented to include use of a penalty function, and a systematic method for choosing the penalty parameter. Comparison between the constrained and unconstrained cases using five parameters clearly showed a trade-off between noise reduction and loss of lift.

Theoretical analysis of trailing-edge noise for the Blake airfoil geometry in turbulent flow is presented by Howe (1988). Results from this work show that the lift dipole is much more significant in contributing to the noise spectra than the thickness (drag)

dipole, which was confirmed by our simulations. Although Howe's work is an analysis of turbulent trailing-edge flow, it is worth noting that his analysis predicted a decrease in trailing-edge noise with an increase in trailing-edge angle. This result agrees qualitatively with the blunt shapes found by the optimization method in the two and five parameter cases, both of which resulted in a dramatic reduction in trailing-edge noise.

The similarity between optimal shapes obtained in the unconstrained two and five parameter cases demonstrates the robustness of the SMF method. Comparison of the full SMF method with the "strawman" approach showed that the POLL step can lead to a greater cost function reduction with minimal additional cost. In general, the number of iterations required by the SMF method was modest. However, it may be possible to further reduce the cost of the method through surrogate quality improvement. The use of a second Gaussian process in Kriging, as in Audet *et al.* (2000), can prevent surrogate degradation and has been shown to reduce the number of POLL steps in several test cases. This is an area for future study.

In this work, we have demonstrated successful use of the SMF method for an expensive, time-dependent cost function. The methodology described here is not restricted to the laminar flow problem, but can be applied to a wide range of fluids problems with complex geometries, unsteadiness and turbulence. Because of the portability of the method, it can be coupled to turbulent flow solvers based on LES, unsteady RANS, or DES (detatched-eddy simulation) for high Reynolds number flows. Use of the SMF method for time-dependent fluid dynamics problems avoids significant difficulties with the addition of constraints, implementation and data storage that arise with adjoint solvers. Even in problems in which gradients are available, the SMF method has many desirable properties. Using only the sign of the gradient, polling directions can be 'pruned' to reduce cost as in Abramson *et al.* (2003). The SMF method has proven to reduce the risk of quickly converging to a shallow local minimum, as is often the case in standard gradient methods.

Constrained optimization of both the upper and lower surfaces of the trailing-edge in laminar flow is currently underway, and initial results are very promising. Deformation of both sides of the airfoil allows for greater flexibility in the trailing-edge shape. In this case, the airfoil thickness is used as an optimization parameter, and the trailing-edge point is free to move in the vertical direction.

In future work, the SMF method will be applied for constrained optimization of the upper and lower surface of trailing-edge in fully turbulent flow using LES. Considerations of computational expense may lead us to incorporate a wall model (Wang & Moin 2002). In the turbulent case, the airfoil is not acoustically compact for all the frequencies of interest, and the cost function may need to be reconsidered. Alternatively, an approximation of the cost function can be used so long as it is well correlated with the true acoustic source function.

Acknowledgments

This work was supported by the Office of Naval Research under grant N00014-01-1-0423. Computer time was provided by the DoD's HPCMP through NRL-DC and ARL/MSRC. John Dennis was supported by the Institute for Mathematics and its Applications (IMA), the National Science Foundation and the Ordway Endowment at the University of Minnesota. The authors also wish to thank the IMA for providing a fo-

rum for collaboration, as well as Charles Audet and Petros Koumoutsakos for valuable discussions.

REFERENCES

ABRAMSON, M. A., AUDET, C. & DENNIS, JR., J. E. 2003 Generalized pattern searches with derivative information. *Tech. Rep.* TR02-10. Department of Computational and Applied Mathematics, Rice University, Houston, TX, to appear in *Mathematical Programming Series B.*

AUDET, C. & DENNIS, JR., J. E. 2000 A pattern search filter method for nonlinear programming without derivatives. *Tech. Rep.* TR00-09. Department of Computational and Applied Mathematics, Rice University, Houston TX.

AUDET, C. & DENNIS, JR., J. E. 2003 Analysis of generalized pattern searches. *SIAM Journal on Optimization* **13**, 889–903.

AUDET, C., DENNIS, JR., J. E. & MOORE, D. W. 2000 A surrogate-model-based method for constrained optimization. *AIAA Paper* 00-4891.

BLAKE, W. K. 1975 A statistical description of pressure and velocity fields at the trailing edge of a flat strut. DTNSRDC Report 4241. David Taylor Naval Ship R & D Center, Bethesda, Maryland.

BOOKER, A. J., DENNIS, JR., J. E., FRANK, P. D., SERAFINI, D. B., TORCZON, V. & TROSSET, M. W. 1999 A rigorous framework for optimization of expensive functions by surrogates. *Structural Optimization* **17**, 1–13.

CURLE, N. 1955 The influence of solid boundary upon aerodynmaic sound. *Proc. Royal Soc. Lond. A* **231**, 505–514.

HANSEN, N. & OSTERMEIER, A. 1996 Adapting arbitrary normal mutation distributions in evolution strategies: the covariance matrix adaptation. *Proc. of the 1996 IEEE Int'l. Conf. on Evolutionary Computation* pp. 312–317.

HOWE, M. S. 1988 The influence of surface rounding on trailing edge noise. *J. Sound & Vib.* **126**, 503–523.

JAMESON, A., MARTINELLI, L. & PIERCE, N. A. 1998 Optimum aerodynamic design using the navier-stokes equations. *Theoret. Comp. Fluid Dynamics* **10**, 213–237.

LOPHAVEN, S. N., NIELSEN, H. B. & SONDERGAARD, J. 2002 Dace: A MATLAB kriging toolbox version 2.0. *Tech. Rep.* IMM-TR-2002-12. Technical University of Denmark, Copenhagen.

MARSDEN, A. L., WANG, M., DENNIS, JR., J. E. & MOIN, P. 2003 Optimal aeroacoustic shape design using the surrogate management framework. Submitted for review.

MARSDEN, A. L., WANG, M. & KOUMOUTSAKOS, P. 2002 Optimal aeroacoustic shape design using approximation modeling. Annual Research Briefs-2001, Center for Turbulence Research,Stanford Univ./NASA Ames.

MCKAY, M. D., CONOVER, W. J. & BECKMAN, R. J. 1979 A comparison of three methods for selecting values of input variables in the analysis of output from a computer code. *Technometrics* **21**, 239–245.

WANG, M. & MOIN, P. 2000 Computation of trailing-edge flow and noise using large-eddy simulation. *AIAA J.* **38**, 2201–2209.

WANG, M. & MOIN, P. 2002 Dynamic wall modeling for large-eddy simulation of complex turbulent flows. *Physics of Fluids* **14**, 2043–2051.

Rough-wall channel analysis using suboptimal control theory

By O. Flores†, J. Jiménez ‡ AND J. Templeton

1. Introduction

The original aim of this work was to shed some light on the physics of turbulence over rough walls using large-eddy simulations and the suboptimal-control wall boundary conditions introduced by Nicoud *et al.* (2001). It was hoped that, if that algorithm was used to fit the mean velocity profile of the simulations to that of a rough-walled channel, instead of to a smooth one, the wall stresses introduced by the control algorithm would give some indication of what aspects of rough walls are most responsible for the modification of the flow in real turbulence. It was similarly expected that the structure of the resulting velocity fluctuations would share some of the characteristics of rough-walled flows, thus again suggesting what is intrinsic and what is accidental in the effect of geometric wall roughness.

A secondary goal was to study the effect of 'unphysical' boundary conditions on the outside flow by observing how a relatively major change of the target velocity profile, and therefore presumably of the applied wall stresses, modifies properties such as the dominant length scales of the velocity fluctuations away from the wall.

As will be seen below, this secondary goal grew more important during the course of the study, which was carried out during a short summer visit of the first two authors to the CTR. It became clear that there are open questions about the way in which the control algorithm models the boundary conditions, even for smooth walls, and that these questions make the physical interpretation of the results difficult. Considerable more work in that area seems to be needed before even relatively advanced large-eddy simulations, such as these, can be used to draw conclusions about the physics of wall-bounded turbulent flows.

The numerical method is the same as in Nicoud *et al.* (2001). The modifications introduced in the original code are briefly described in §2, but the original paper should be consulted for a full description of the algorithm. The results are presented in §3 and summarized in §4. The elementary properties of turbulence over rough walls which are used in the text have been taken from recent reviews such as Raupach *et al.* (1991) or Jiménez (to appear in 2004).

2. Simulations

Turbulent channel flow has been simulated using the code presented by Nicoud *et al.* (2001) with $Re_\tau = u_\tau h/\nu = 1000$, where u_τ is the friction velocity and h is the channel half-width. The coordinates used are x, y and z, indicating streamwise, wall-normal and spanwise directions. The streamwise and spanwise periodicity lengths are $L_x = 2\pi$ and $L_z = 2\pi/3$ for all the cases presented here. Except when explicitly noted to the contrary,

† School of Aeronautics, Universidad Politécnica, 28040 Madrid, Spain
‡ Also School of Aeronautics, Universidad Politécnica, 28040 Madrid, Spain

	Re_τ	Δx^+	Δy^+	Δz^+	L_x/h	L_z/h	$N_x \times N_y \times N_z$	α^+	ΔU^+
S1	1000	196	61	65	2π	$2\pi/3$	$32 \times 33 \times 32$	6×10^{-2}	0
S2	1000	196	61	65	2π	$2\pi/3$	$32 \times 33 \times 32$	1.5×10^{-2}	0
R1	1000	196	61	65	2π	$2\pi/3$	$32 \times 33 \times 32$	6×10^{-2}	9

TABLE 1. Test cases. The subindices x, y and z indicate the streamwise, wall-normal and spanwise directions. The N's are the number of grid points in each direction, the Δ's are the corresponding grid spaces and the L's are box lengths. ΔU^+ is the roughness function, defined in (3.7), and α^+ is the parameter in equation (2.1).

all the variables are normalized with u_τ and h. The superindex $^+$ is used for variables expressed in wall units.

The characteristics of the three main simulations used in this paper are summarized in table 1. The letter **S** indicates smooth channels, and **R** is used for rough ones. The reference velocity profile used for **S1** and **S2** is obtained from a direct simulation by del Álamo *et al.* (2003) with $Re_\tau = 950$. The rough-wall profile is described in the next section.

The LES code uses a standard dynamic Smagorinsky subgrid-scale stress model without explicit grid filtering. The spatial discretization is a second-order finite-difference scheme on a staggered grid, and the time integration is third-order Runge-Kutta with an implicit scheme for the wall-normal viscous terms. The flow is driven by a constant mean pressure gradient that balances the wall stresses, $\overline{\partial_x p}^+ = -1$. The overbar stands for averaging over wall-parallel planes, while $\langle\,\rangle$ will be reserved for temporal averaging. With the single exception described at the end of §3.1, the time step Δt is constant.

The boundary conditions in the streamwise and spanwise directions are periodic, and the impermeability condition is imposed at the walls. The two other boundary conditions are the total shear stresses τ_{xy} and τ_{zy} at each point of each wall. They are adjusted at each time step to minimize a cost function $\mathcal{J}$, which measures the difference between the plane-averaged velocity and a given mean velocity profile U_{ref}.

$$\mathcal{J}(\phi_u, \phi_w) = \int_0^{2h} \left[(\overline{u} - U_{ref})^2 + \overline{w}^2\right] dy + \alpha \left(\overline{\phi_u'^2} + \overline{\phi_w'^2}\right), \tag{2.1}$$

where the control variables are vectors of size $2 \times N_x \times N_z$

$$\phi_u = (\tau_{xy}^w\,|_{y=2h}, -\tau_{xy}^w\,|_{y=0}), \qquad \phi_w = (\tau_{zy}^w\,|_{y=2h}, -\tau_{zy}^w\,|_{y=0}), \tag{2.2}$$

and α is a parameter with dimensions $[\alpha] = L/U^2$ that will be discussed in the next section. Primed variables refer to fluctuations with respect to the plane average, so that $\phi' = \phi - \overline{\phi}$. Note that the global conservation of momentum ensures that $\overline{\phi}$ satisfies

$$\langle\overline{\tau_{xy}^w}\rangle\,|_{y=2h} - \langle\overline{\tau_{xy}^w}\rangle\,|_{y=0} = 1, \tag{2.3}$$

and

$$\langle\overline{\tau_{xy}^w}\rangle\,|_{y=2h} - \langle\overline{\tau_{xy}^w}\rangle\,|_{y=0} = 0, \tag{2.4}$$

but that the instantaneous mean stresses at each wall may oscillate in time.

The minimization of $\mathcal{J}$ implies an iterative scheme in which an adjoint problem is solved in order to compute an estimation for the gradient of the cost function. The

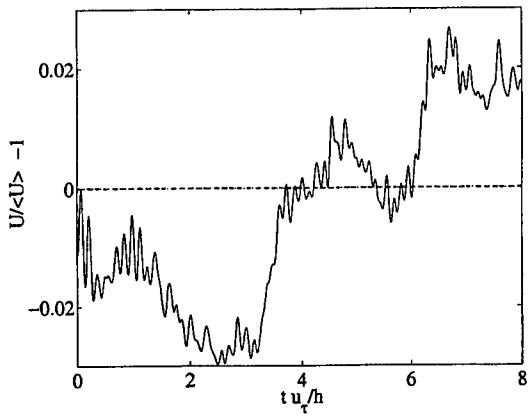


FIGURE 1. Convergence history of the mean velocity at the first plane off the wall, for a smooth-walled channel. ——— , Using the correction (2.5); ---- , without the correction.

algorithm is suboptimal in the sense that, instead of minimizing the averaged value of $\mathcal{J}$ over a long period of time, the optimization is computed over each individual time step.

Several modifications were introduced in the code during preliminary attempts to match smooth-wall velocity profiles at different Reynolds numbers. The most important was probably the use of the more efficient Brent's method for the optimization scheme (Press *et al.* 1993), instead of the simpler relaxation used by Nicoud *et al.* (2001). This allowed the stable utilization of the algorithm over a wider range of parameters.

Another modification involves the recalculation of the mean wall stress. In the original code, the value of $\overline{\tau_{xy}^w}^+ = u_*^{+2}$ was adjusted at each time step so that the mean velocity in the first plane off the wall satisfied the desired logarithmic law,

$$\frac{\overline{u_{j=1}^+}}{u_*^+} - \frac{1}{\kappa}\log(y_{j=1}^+ u_*^+) - A = 0. \tag{2.5}$$

The idea was that the mean stress is directly determined by the averaged momentum balance, and does not have to be controlled. In each time step the optimum wall stresses were computed using the control algorithm, and their mean value was later corrected to the u_*^2 obtained from (2.5). Notice that $u_*^+ = 1$ satisfies (2.5) whenever $u_{j=1}^+$ is given by the desired logarithmic law. While the general argument is sound in a timed-averaged sense, this procedure 'second-guesses' the control algorithm, since the integrated momentum equation is already incorporated in the code, and its effect was found to be pernicious. The convergence of the original code was oscillatory and the time history of most variables suggested a poorly-damped instability of the control algorithm. Removing the correction step suppressed the oscillations and the instability. Two typical convergence histories, with and without the stress correction, are shown in figure 1. All the results below are obtained without using (2.5).

3. Results

3.1. *The cost function*

A point that needs some discussion is the form of the cost function (2.1). The second term on the right-hand side of (2.1) represents the energy of the control variables ϕ_u and

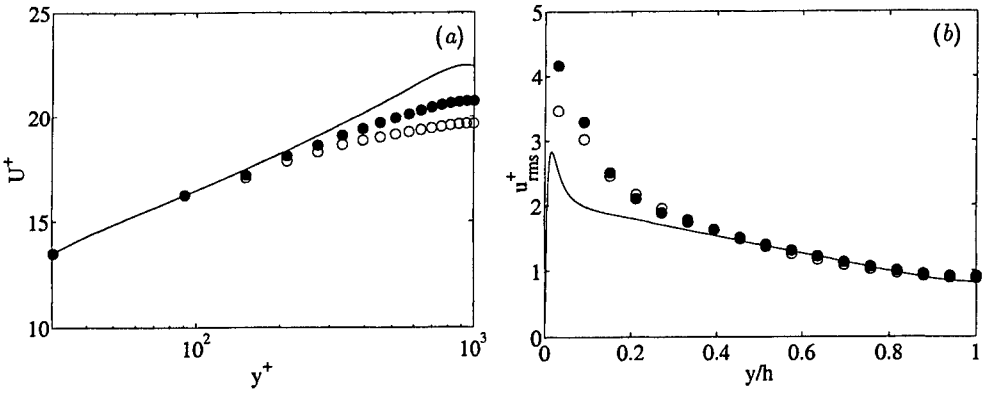


FIGURE 2. Profiles of (a) the mean velocities and (b) the streamwise velocity fluctuations for a smooth-walled channel at $Re_\tau \approx 1000$, using different cost functions. o , case **S1**; • , case **S2**; ——— , direct simulation (del Álamo *et al.*2003).

ϕ_w, and is introduced to ensure numerical stability. The proportionality coefficient α is essentially arbitrary from a physical point of view.

The value of α used here for the cases **S1** and **R1** is the one given by Nicoud *et al.* (2001) as being the smallest one that kept their simulation stable. The effect of a larger α should be to lower the variance of τ^w, weakening the strength of the control, and therefore presumably degrading the quality of the resulting mean profile. It is nevertheless possible to 'overcontrol' a system, in the sense that some properties which are not taken into account in the cost function may be contaminated by the control itself. It was noted by Nicoud *et al.* (2001) that the velocity fluctuations in the simulated channels are stronger than those in direct simulations or in experiments, especially near the wall. Since those fluctuations are driven by the wall stresses, which are in turn influenced by α, it is conceivable that the reason for the high fluctuations is that α was chosen too small.

A measure of the strength of the control is the temporal variability of $\overline{u}$, compared with its 'expected' variation. If the velocities are considered to be uncorrelated random variables, which is probably not too far from the truth for a coarse LES, the expected variance of $\overline{u}$ would be

$$\sigma_P^2 = (N_x N_z)^{-1} \overline{u'^2}, \tag{3.1}$$

which has to be compared with the actual measured value

$$\sigma^2 = \langle (\overline{u} - \langle \overline{u} \rangle)^2 \rangle. \tag{3.2}$$

The ratio σ/σ_P should be of order unity in a natural flow, and its deviation from unity is a measure of the strength of the control.

It is not clear which is the right normalization for α, but the observation in Nicoud *et al.* (2001) that the effect of the control is mainly felt on the velocities near the wall suggests that h is not a relevant length scale, and that a more natural normalization would be wall units. The value recommended by Nicoud *et al.* (2001) is then $\alpha^+ \approx 6 \times 10^{-2}$, and results in $\sigma/\sigma_P \approx 2 \times 10^{-3}$. Both the small magnitude of the dimensionless α and of the ratio of the standard deviations strongly suggest that the system is overcontrolled.

A detailed analysis of the effect of α is beyond the scope of this work, and it was not attempted, but a simple approximation of the cost function can be used to estimate the relevant trends. Assume that the velocity u near the wall is essentially a (random) function of the local wall stresses, $u = f(\tau^w)$, where all the equations in the following

argument have to be understood as being applied at a given x and z. We can then approximate the cost function as,

$$\mathcal{J} \approx 2\delta(\overline{u} - U_{ref})^2 + 2\alpha\overline{(\tau^{w\prime})^2}, \tag{3.3}$$

where δ is a measure of the height over which the velocity is modified by the control, and u is taken at some representative distance from the wall of order δ. The factor of two reflects the contribution from both walls. The minimization of $\mathcal{J}$ requires that its derivative with respect to all the τ^w should vanish, giving for each grid point

$$\frac{\partial \mathcal{J}}{\partial \tau^w} = 4\delta \frac{\overline{u} - U_{ref}}{N_x N_z} \frac{df}{d\tau^w} + 4\alpha \frac{\tau^{w\prime}}{N_x N_z} = 0, \tag{3.4}$$

where we have assumed that $\overline{\tau^w}$ does not depend of the control. Assuming that $f(\tau^w)$ can be linearized around $\overline{\tau^w}$ and expressing $\overline{u}$ in terms of $f(\tau^w)$, we obtain after some algebra that

$$\tau^{w\prime} = [U_{ref} - \overline{f(\overline{\tau^w})}] \frac{\delta f_\tau/\alpha}{1 + \delta \overline{f_\tau^2}/\alpha}, \tag{3.5}$$

where f_τ is $\mathrm{d}f/\mathrm{d}\tau^w$ evaluated at $\overline{\tau^w}$. This is an interesting expression because it captures the tendency of τ'^w to increase with decreasing α, but saturates to some finite value when $\alpha \to 0$. In that limit the cost function becomes $\overline{u} - U_{ref} \propto \alpha$.

This has the simple interpretation that, if there is a solution to the unconstrained control problem, i.e. if there is a τ^w such that the first term in (2.1) vanishes, the control algorithm approximately identifies it for some small value of α, and any further decrease in α does not change that solution appreciably. If such solution does not exist, τ'^w and u' would diverge as α^{-1} when $\alpha \to 0$, and the cost function would saturate to some non-zero minimum value. This would appear in our simple model as $\overline{f_\tau^2} = 0$.

We tested this behavior by running case **S2**, in which α was divided by four with respect to the two other cases. The new value of α decreases σ/σ_P, as expected, while the mean velocity profile improves everywhere (figure 2*a*), and the intensity of the velocity fluctuations near the wall increases (figure 2*b*). All this is in qualitative agreement with the previous analysis. The ratio between the standard deviations of the wall stresses in cases **S2** and **S1** is 2:1, which is smaller than the ratio of 4:1 which would correspond to an α^{-1} behavior, and suggests some degree of saturation towards an exact solution.

To test whether such a solution exists, a second experiment was run with $\alpha = 0$. The velocity fluctuations grew still further, apparently without bound, leading to numerical instability for any given constant time step. When the code was modified to run at a constant CFL, we were able to trace the growth of the fluctuating velocities in the first plane off the wall to values of the order of $u'^+ \approx 600$, implying that the suboptimal boundary conditions, at least in their present form, are not able to drive the LES to full agreement with the desired profile. The errors in figure 2(*a*) suggest that the difficulty is not with the behavior of the near-wall region, but with the center of the channel. It is an interesting, although unresolved, question whether this is a limitation of the LES model itself, which cannot reproduce the phenomena responsible for the wake component, or of the boundary conditions.

3.2. *Rough walls*

The most important effect of roughness on the mean velocity above the buffer zone is a constant velocity decrement, ΔU^+ (Raupach *et al.* 1991; Jiménez, to appear 2004). A second effect is a shift Δy in the wall-normal coordinate, due to the uncertainty in

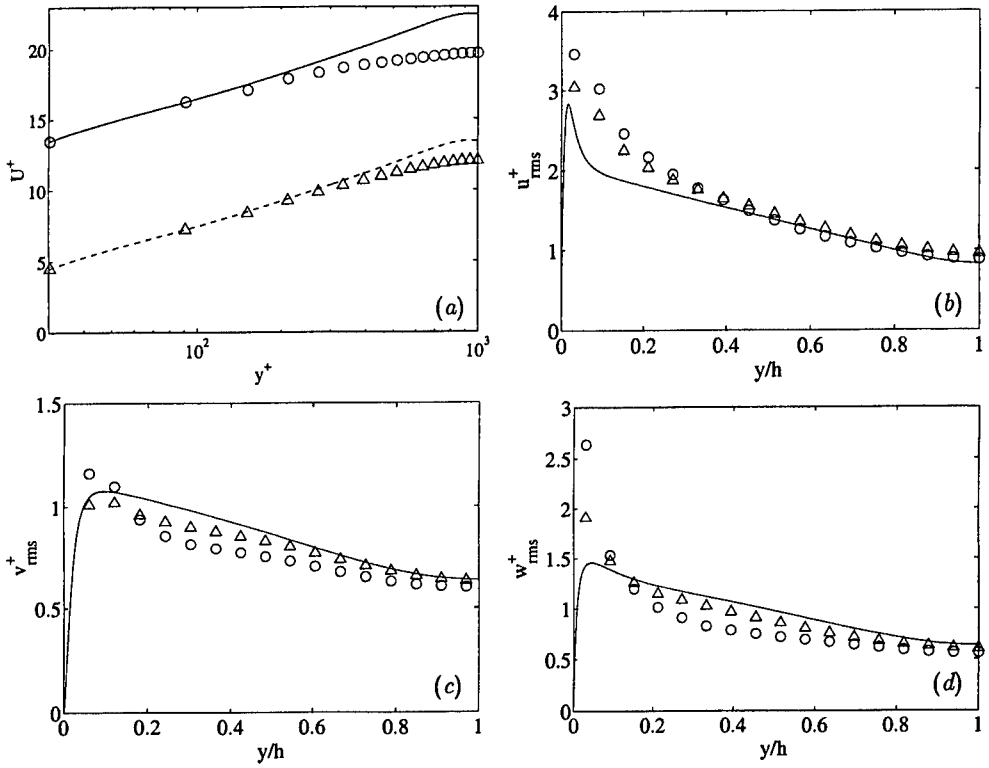


FIGURE 3. (*a*) Mean velocity profiles. (*b*) Streamwise velocity fluctuations. (*c*) Wall-normal velocity fluctuations. (*d*) Spanwise velocity fluctuations. ——— , smooth wall DNS, $Re_\tau = 950$; ---- , reference velocity profile for the rough case; ○ , case **S1**; △ , case **R1**.

the position of the wall. In our case, in which the velocity is only computed at fairly large values of y^+, the wall-normal shift is negligible and the mean velocity profile can be written as

$$U^+(y^+) = \frac{1}{\kappa}\log(y^+) + 8.5 - \frac{1}{\kappa}\log(k_s^+) + \frac{1}{\kappa}\Pi(y/h), \tag{3.6}$$

or

$$U^+(y^+) = \frac{1}{\kappa}\log(y^+) + 5.1 - \Delta U^+ + \frac{1}{\kappa}\Pi(y/h), \tag{3.7}$$

were Π is the wake function, and either ΔU^+ or k_s^+ characterize the effect of roughness on the mean velocity profile.

Using equation (3.7) we construct our rough mean velocity profile for case **R1** just subtracting a constant $\Delta U^+ = 9^+$ from the smooth mean velocity profiles in del Álamo *et al.* (2003). This corresponds to a fully-rough flow with an equivalent sand roughness $k_s^+ \approx 140$.

3.3. *Statistics*

Figure 3 shows the mean velocity and the velocity fluctuations profiles for cases **S1** and **R1**. The mean velocities share some characteristics with those obtained by Nicoud *et al.* (2001), even though the latter used as reference profile a logarithmic law without a wake function. The error between the mean velocity and U_{ref} is given in figure 4 for the three cases computed. It is quite small near the wall, but grows to $O(1)$ at the

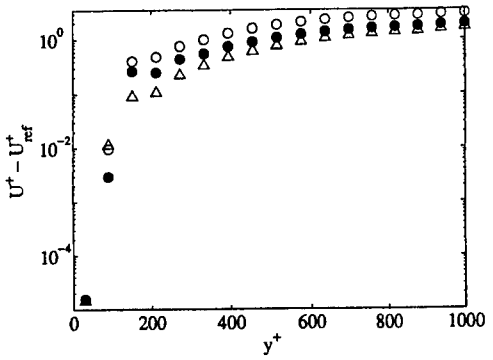


FIGURE 4. Error in the mean velocity profiles with respect to their references. ○ , case **S1**; ● , case **S2**; △ , case **R1**.

center of the channel. Between the second and the third grid point there is a weak discontinuity that changes the intercept of the logarithmic law. Its origin is probably the spatial discretization, because it appears at the same grid point in Nicoud *et al.* (2001) even if their resolution is coarser than ours by a factor of four.

The root-mean-squared velocity fluctuations are presented in figures 3(b), 3(c) and 3(d). The streamwise and spanwise fluctuations near the wall are higher in all the large-eddy simulations than in the direct simulation, although the agreement is quite good in the core region for the streamwise direction. The wall-normal and spanwise fluctuations are slightly underpredicted by the suboptimal code in the core region. The high values for the streamwise velocity fluctuations near the wall and the velocity fluctuations in the core region agree with the results of Nicoud *et al.* (2001), but the exceptionally high values of the spanwise velocity fluctuations near the wall shown in figure 3(d) do not.

The lower values of the velocity fluctuations near the wall in case **R1** with respect to **S1** are consistent with the effect of roughness on physical turbulence. This is often interpreted as the interference of the roughness elements with the smooth-wall self-sustaining turbulence cycle (Jiménez & Moin 1991), as explained by Jiménez (to appear in 2004). This interpretation is unlikely in the present case because the resolution is too coarse in all three directions to capture the scales associated with the regeneration cycle, and the most likely explanation is that the decrease of the fluctuations is due to the lower turbulence production near the wall due to the weaker velocity gradients across the first grid element of the rough reference profile.

The wall stresses τ^w_{xy} and τ^w_{zy} provided by the control algorithm are studied using their probability density functions (p.d.f.), which are shown in figure 5. They are compared at $y^+ = 60$ with the p.d.f.'s of the shear stresses in a DNS channel with $Re_\tau = 550$ (del Álamo *et al.* 2003), after box-averaging the latter to the LES grid ($\Delta_x \times \Delta_z = 196^+ \times 65^+$). Although it was not possible to post-process the shear stresses from the $Re_\tau = 950$ in time for this report, there is probably little differences between them an those at $Re_\tau = 550$, because this part of the flow scales approximately in wall units.

It is clear from figure 5(a) that the τ^w_{xy} in the suboptimal simulations are different from the DNS one, especially in that the former are not able to reproduce the asymmetry of the p.d.f. and try to reproduce the mean value of the shear stresses by displacing their modes to positive values. As expected, the standard deviations behave in the same way as the velocity fluctuations, **R1** < **S1** < **S2**. Figure 5(c) and 5(d) show the p.d.f.'s of the three cases when the stresses are normalized with theirs mean value $\langle\tau\rangle$ and standard

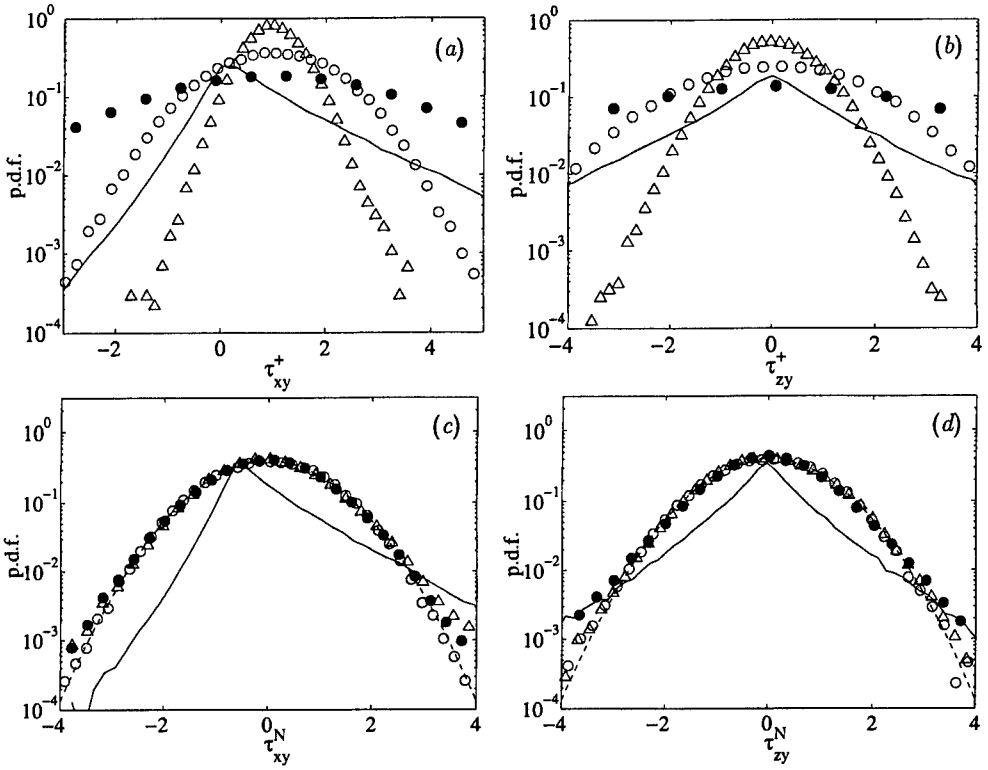


FIGURE 5. Probability density functions (p.d.f.) of the shear stresses at the wall. The shear stresses in figures (*a*) and (*b*) are expressed in wall units, while in figures (*c*) and (*d*) they are normalized as in equation (3.8). ——— , DNS (see text for details); ---- , Gaussian; ○ , case **S1**; • , case **S2**; △ , case **R1**.

deviation σ_τ,

$$\tau^N = \frac{\tau - \langle\tau\rangle}{\sigma_\tau}. \tag{3.8}$$

The collapse of the three curves on the Gaussian distribution, and the differences with the DNS results, suggest that there is little physical information on the shear stresses given by the control algorithm.

Another way of characterizing the shear stresses given by the control is the study of their spectral distribution. We can define the spectrum E_{ij}

$$E_{ij}(k_x, k_z) = \langle \widehat{\tau}_{ij} \widehat{\tau}^*_{ij} \rangle, \tag{3.9}$$

where $\widehat{\tau}_{ij}(k_x, k_z)$ are the Fourier coefficients of the two-dimensional Fourier transform of the wall stresses τ^w_{ij}. The asterisk * indicates complex conjugation and k_x,k_z are the wave numbers.

Figure 6 shows these premultiplied spectra for the cases **S1** and **R1**, as functions of the wavelengths $\lambda_x = 2\pi/k_x$ and $\lambda_z = 2\pi/k_z$. Because each spectrum is normalized with its maximum, it only contains information about the wavelengths. There is very little differences between the two cases.

It is important to notice that the most energetic modes are located in the large-wavelength end of the spectra, specially as regards their widths. The 'infinitely wide'

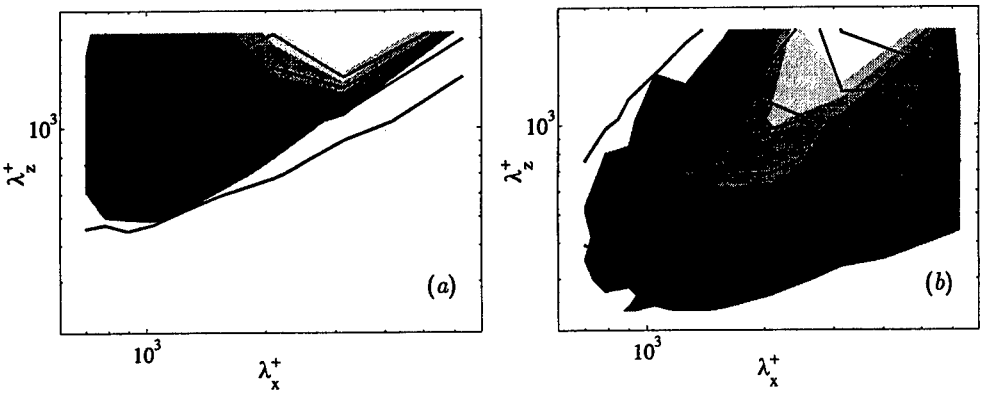


FIGURE 6. Two-dimensional premultiplied spectra of the stresses at the wall as functions of the streamwise and spanwise wavelengths. (*a*) E_{xy}, (*b*) E_{zy}. Shaded contours are from the **S1** case and lines are from **R1**. Each spectrum is normalized with its maximum.

$(\alpha, 0)$ modes for the τ_{xy}^w spectrum sums up to 26% of the energy in the smooth case and to 35% in the rough one, but the energy in the 'infinitely long' $(0, \beta)$ modes is below 1% of the total in both cases. On the other hand, for the τ_{zy}^w spectrum the energy contained in the $(\alpha, 0)$ modes is negligible, while the energy contained in the $(0, \beta)$ modes sums 7% of the total energy in the smooth case and 9% in the rough case. That suggests that the spectrum of τ_{xy}^w is wider, but not too much longer than the simulation box, while the τ_{zy}^w spectrum almost fits in it. The behavior of this quantity in the DNS is not known.

It is interesting to analyze how the control variable characteristics affect flow variables such as the velocities. In order to do that, we have studied the energy spectrum of the velocity components, E_{uu}, E_{vv} and E_{ww}, defined as

$$E_{uu}(k_x, k_z) = \langle \hat{u}_{kx,kz} \hat{u}^*_{kx,kz} \rangle_T \tag{3.10}$$

The corresponding one-dimensional spectra are obtained adding equation (3.10) over a certain direction in Fourier space.

Figures 7(*a*) and 7(*b*) show the one-dimensional premultiplied spectrum of the streamwise velocity components at $y^+ = 30$, which is the first grid point in the mesh. Although the gradient of this variable is determined directly by the control, the agreement between the suboptimal cases and the DNS results is reasonable good, at least as much as can be expected from the coarse grid being used. The same happens for the wall-normal velocity component (not shown here), but not for the spanwise component, whose spectrum is shown in figures 7(*c*) and 7(*d*). The spanwise velocity has a very energetic mode which spans the full width of the box and almost all of its length. When the instantaneous velocity fields are examined, we observe fairly regular diagonal bands of positive or negative spanwise velocity. This is reminiscent of the instabilities observed by Jiménez *et al.* (2001) in a channel with a porous wall, where they were traced to a coupling between a weakly-damped mode of the impermeable channel and the porous-wall condition. In that case the result was a series of spanwise rollers spanning the full height and width of the channel, and it is conceivable that a similar coupling might result in the present structures.

The spurious perturbation of the spanwise velocity disappears as we move a few grid points away from the wall, as can be observed in the spectra in figures 8. This relatively fast relaxation away from the wall of the defects of the wall layer, which recalls the similar

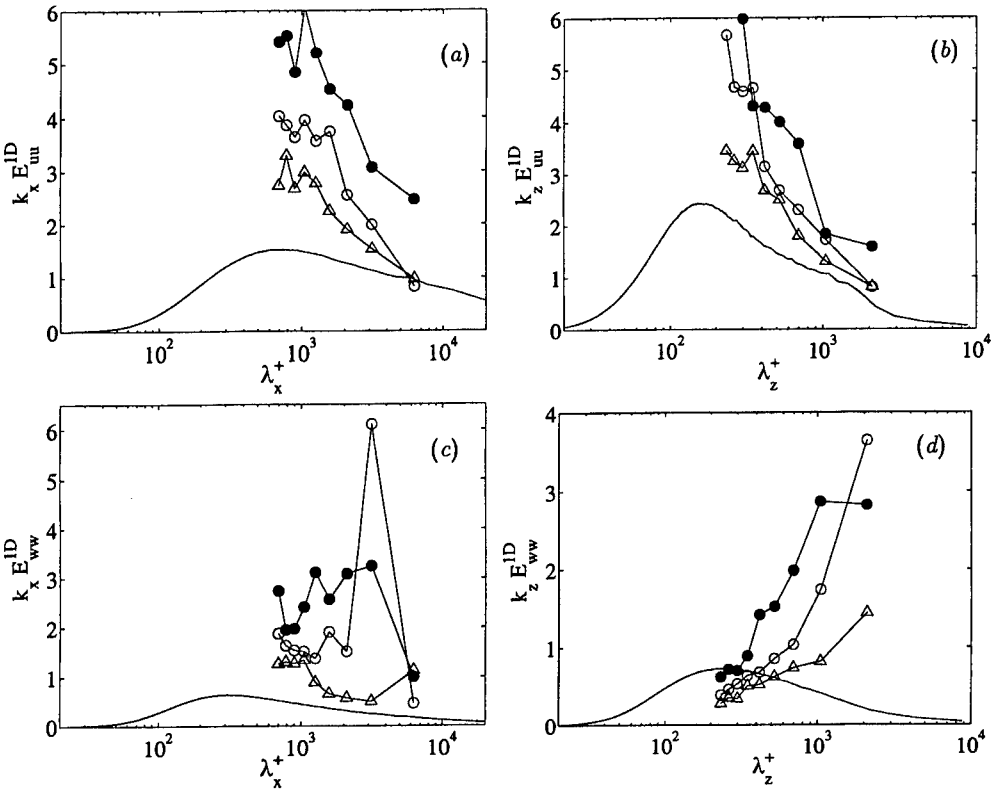


FIGURE 7. One-dimensional premultiplied velocities spectra at $y^+ = 30$, normalized in wall units and plotted as functions of the wavelengths λ_x (a, c) and λ_z (b, d). (a) and (b), streamwise component; (c) and (d) spanwise component. ——— , DNS; ○ , case **S1**; • , case **S2**; △ , case **R1**.

relaxation of the fluctuation intensities in figures 2(b) and 3(b), suggests that the effect of the wall is relatively local to small values of y, and that the main role of the boundary conditions is to provide a correct intercept for the mean velocity.

4. Conclusions

In this work we have simulated three channel flows using the suboptimal-control code developed by Nicoud *et al.* (2001), after some modifications to improve its performance. We have seen that the suboptimal control code is not able to reproduce the wake component of the mean velocity profile of real channels. The magnitude of the error depends on the parameter α which weights the energy of the control in the cost function. Decreasing this parameter decreases the error in the wake, but degrades the agreement of the velocity fluctuation intensities near the wall. A simplified analysis of two numerical experiments with different values of α suggests that the problem with the velocity profile near the channel centerline is intrinsic to the simulation procedure, and not a consequence of the boundary condition algorithm. This result, together with the reorganization of the flow structures away from the wall, raises the question of whether it is possible to control the whole flow just by acting on the wall.

There are also open questions about the effects of α on the mean velocity profile and

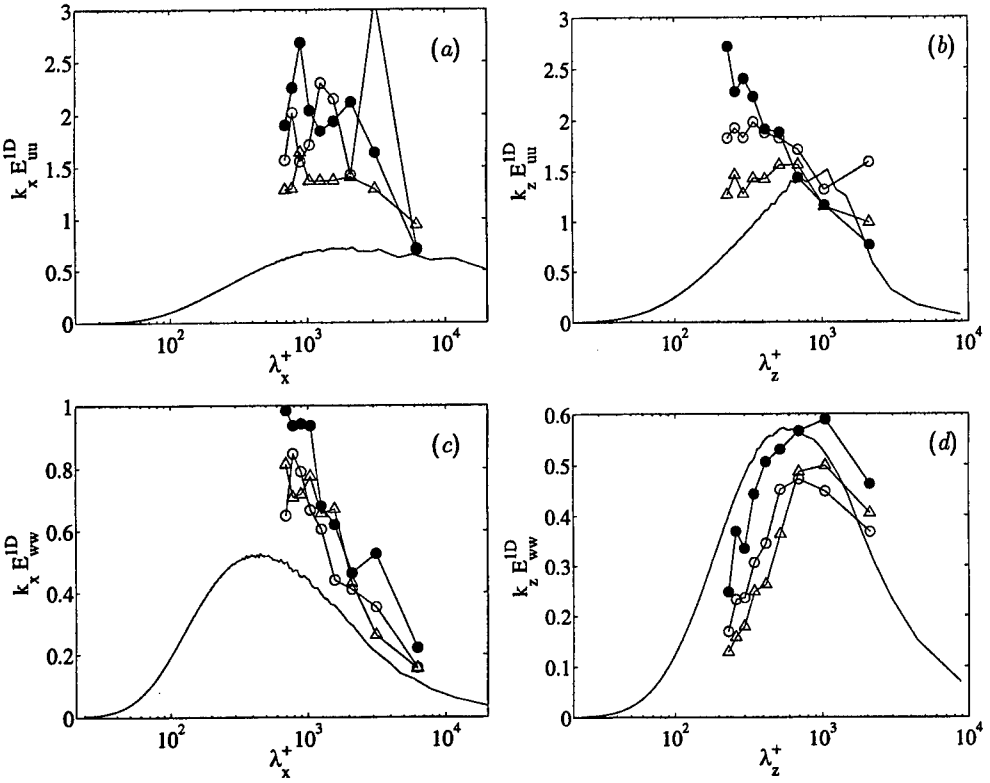


FIGURE 8. One-dimensional premultiplied velocities spectra at $y^+ = 150$, normalized in wall units and plotted as functions of the wavelengths λ_x (*a*, *c*) and λ_z (*b*, *d*). (*a*) and (*b*), streamwise component; (*c*) and (*d*) spanwise component. ——— , DNS; ○ , case **S1**; • , case **S2**; △ , case **R1**.

on the root mean squared velocity fluctuations, where the influence of this parameter seems to be more important. More work is needed in that direction.

We have shown that the suboptimal code is able to match a synthetic profile for a rough turbulent channel, and that the trend of the changes in the root-mean-squared velocity fluctuation profiles agrees with the expected results. It is not clear whether this agreement is due to a change in the physics of the wall, or just a secondary effect of a lower mean velocity gradient. However, the information gathered from the spectra and from the p.d.f.'s point to the latter explanation, as there are no clear differences between the structures near the wall in the smooth and the rough cases, except for the intensities. The structure of the wall stresses introduced by the control algorithm bear little resemblance to the corresponding physical quantities.

There are in all the present simulations a spurious organization of the near-wall spanwise velocity into large diagonal modes, which is most likely due to some instability of the control procedure, but which also disappears a few grid points away from the wall. Its analysis also requires further work.

5. Acknowledgments

This work was supported in part by the Spanish Comisión Interministerial de Ciencia y Tecnología, under grant BFM2000-1468, and by the Center for Turbulence Research.

The computational resources provided by the Centro de Investigaciones Energiéticas, Medioambientales y Tecnológicas in Madrid are gratefully acknowledged. We thank Dr. Meng Wang for his careful reading of a first version of this manuscript.

REFERENCES

DEL ÁLAMO, J.C., JIMÉNEZ, J., ZANDONADE, P. & MOSER, R.D. 2003 Scaling of the energy spectra of turbulent channels. Submitted *J. Fluid Mech.*

JIMÉNEZ, J. 2004 Turbulent Flows over Rough Walls. *Ann. Rev. Fluid Mech.* **36**

JIMÉNEZ, J. & MOIN, P. 1991 The minimal flow unit in near wall turbulence. *J. Fluid Mech.* **225**, 221-240

JIMÉNEZ, J., UHLMANN, M., PINELLI, A. & KAWAHARA, G. 2001 Turbulent shear flow over active and passive porous surfaces. *J. Fluid Mech.* **442**, 89-117

NICOUD, F., BAGGETT J. S., MOIN, P. & CABOT, W. 2001 Large eddy simulation wall-modeling based on suboptimal control theory and linear stochastic estimation. *Phys. fluids.* **13**, 2968-2984

PRESS, W. H., FLANNERY, B. P., TUKOLSKY, S. A. & VETTERLING, W. T. 1993 *Numerical Recipes in FORTRAN 77: The Art of Scientific Computing.* Cambridge University Press.

RAUPACH M.R., ANTONIA R.A., & RAJAGOPALAN S. 1991 Rough-wall turbulent boundary layers. *Appl. Mech. Rev.* **44**, 1-25

Unfolding of proteins : Thermal and mechanical unfolding

By Joe S. Hur & Eric Darve

1. Motivation and Objectives

Over the past few decades, researchers have sequenced the human genome which is a blueprint for proteins. However, given only the information of the sequence we cannot yet accurately predict specific structural information such as the secondary and tertiary structure of a given protein, let alone its functionality in biological processes. Recent theoretical and experimental findings have shown that the topology or conformation of the native structure of small proteins plays a critical role in determining its biological function (Baker 2000; Alm & Baker 1999). In order to carry out their biological function properly, proteins must assume a shape, assembling themselves into an ordered structure. It is now well known that depending on the topology of proteins, for example, when proteins do not fold correctly, there can be serious medical complications, such as Parkinson's disease, Alzheimers to name a few. Furthermore, more biophysical manifestations of protein-protein interactions are reflected in processes related to phase equilibria such as crystallization, and in the marked dependence of the diffusion coefficients of macromolecules on their concentration (Price *et al.* 1999). The latter aspect is currently becoming of much interest to biologists and chemists with advances in techniques for monitoring protein diffusion in the crowded cellular environment (Dayel *et al.* 1999).

With ever increasing areas of interest in biomedical applications as mentioned above, much effort has been put into understanding the mechanism of protein folding. However, at present, there exists neither a simple and universally applicable theoretical framework nor an efficient and accurate computational framework that can account for many experimental findings. Current theories resort to mathematics that vary greatly in complexity and analytic tractablity in order to solve technical difficulties inherent in the problem or start from a phenomenological model (Wolynes *et al.* 1995; Clementi *et al.* 2000). On the computation frontier, with advances in computational resources, we are now equipped with better tools to tackle complex problems that are numerically expensive. However, for example, there is much controversy over the correct form of potential in the force field in molecular dynamics (Baker 2000) and folding proteins using Monte-Carlo simulation is still expensive to be applied to bigger proteins - the folding time scales for these proteins lie between a few milliseconds to minutes. Solving for the stable structures of the isolated proteins should not be the final aim for computer simulations. After all, proteins perform their biological function by interacting with other macromolecules through, for example, electrostatic and non-polar interactions, and thus a clear physical understanding of such phenomena is needed.

Our goal is to understand the mechanisms of protein folding-unfolding in the presence of an external force field - e.g. mechanical, and electrostatic fields - and to investigate the differences in the pathways of force-induced unfolding and thermally or denaturant-induced unfolding. For example, mechanical stability is very important for proteins that form muscle fibres, like myosin and kinesin, and for those that have to withstand forces

like cell-adhesion molecules that stabilize and form the contact between cells in tissues. Having a clear understanding of the mechanisms of unfolding will provide us with a means to design proteins to carry out specific functions as well as to tackle more complex problems that remain unsolved. A few examples of the latter include understanding how a substrate may be attracted to the active site of an enzyme by electrostatic interactions and how the local and global structures of proteins change upon ligand docking.

Recently, relevant to this work, researchers have used atomic force microscopy (AFM) and optical tweezers for dynamic measurement of mechanical unfolding of individual Titin immunoglobulin domains at the single molecule level (Rief *et al.* 1997; Kellermayer *et al.* 1997; Tskhovrebova *et al.* 1997). The widely studied protein Titin is a giant 3 MDalton muscle protein and a major constituent of the sarcomere in vertebrate striated muscle. It is a multi-domain protein which forms filaments approximately 1 μm in length spanning half a sarcomere and has a number of functions including the control of assembly of muscle thick filaments, a role in muscle elasticity and the generation of passive tension. Of the two regions - the I-band and the A-band - we are interested in the I-band of Titin because it plays an important role in muscle elasticity. The I-band is composed of a head to tail linear array of immunoglobulin domains interrupted at intervals by less highly structured linker sequences. All of the immunoglobulin domains are predicted to have the same basic structure. The notation 'I27' is used to represent the 27th domain of the Titin I-band. The wild type Titin protein is far too large for its thermodynamic and kinetic properties to be studied in detail using current techniques, however its multi-domain structure allows investigation of its properties by characterization of the constituent domains in isolation. This approach is frequently used for proteins where, to a first approximation, the domains behave independently.

An interesting aspect of the recent studies of Titin concerns the highly cooperative manner in which the domains break. However, the structural changes under mechanical forces could only be inferred from the force-extension curves in the experiment and for example, the stability of the individual beta-sheets could not be examined. To support the experimental findings using Titin, steered molecular dynamics (SMD) simulations showed that the force-induced unfolding of Titin domains is an all-or-none event, lacking stable intermediates (Lu *et al.* 1998). However, a more recent study by Paci *et al.* showed in their simulation a more complex behavior of force-induced unfolding in contrast to the simple sawtooth profile observed in the unfolding experiments and claimed that in those experiments only the onset of the unfolding of individual domains in multi-domain proteins was revealed (Paci & Karplus 2000).

Even though the experimental and theoretical investigations up to date have given us valuable information on force-induced unfolding of small proteins, the tools to probe multiple kinetic pathways, more complex structures and stability of domains in bigger proteins that carry out biological functions upon docking (where they have to assume a particular partially unfolded shape) are yet to be developed. In this article, we present a Hamiltonian model which builds on the important interactions of the native-state topology. We make a Gaussian approximation within the model such that the contact probabilities are determined self-consistently, in a spirit similar to a local mean-field approximation.

The paper is organized as follows. In §2, we describe our mathematical formulation. The Hamiltonian is defined and the self-consistent Gaussian approximation is introduced in calculating the contact pair probabilities. In §3.1 we present results for the equilibrium properties of several globular proteins and the immunoglobulin domain of Titin. Both

structural and thermodynamic quantities are examined. In §3.2 the thermal denaturation of the immunoglobulin domain of Titin is investigated. In particular, the stability of the six sheet interactions are examined. In §3.3 the results for pulling the ends with constant mechanical forces of a single immunoglobulin domain of Titin are presented and compared to the experimental findings as well as the results in §3.2. We conclude with a brief summary in §4.

2. Method

In our formulation, the Hamiltonian for a given protein of N residues consists of three energy contributions as shown in eqn.(2.1). The first term refers to the energy fluctuations of adjacent residues with respect to the native state. The second term denotes pairwise interactions between non-adjacent (non-consecutive) residue pairs and the last term is the imposed external force field which is assumed to be linear for direct comparison to experiment by Rief *et al.* (1997); Kellermayer *et al.* (1997); Tskhovrebova *et al.* (1997).

$$H = \frac{k_B \cdot \max(T, T_{min})}{2} \sum_{i=1}^{N-1} K(\vec{t_{i+1}} - \vec{t_i})^2 - \sum_{i,j} \frac{\Delta_{ij}}{2} [R^2 - (\vec{t_i} - \vec{t_j})^2] \Theta[R^2 - (\vec{t_i} - \vec{t_j})^2] + F^T t \tag{2.1}$$

In eqn.(2.1), $\vec{t_i}$ denotes the position vector of residue i relative to its native state. Δ_{ij} is the contact matrix of all residues in the native state and Θ is the Heaviside step function, which is defined as :

$$\Theta(x) = \begin{cases} 0 & \text{if } x \leq 0, \\ 1 & \text{if } x > 0. \end{cases} \tag{2.2}$$

We determine Δ_{ij} from the native state structures of proteins from the Protein Data Bank (PDB). We assign a value of 1 to residue pairs whose α-carbons(C_α) are separated by less than 6.5$\mathring{A}$ and 0 otherwise.

In our formulation, pairwise interactions that are separated beyond a cut-off radius of R do not contribute the total energy of the system. We set R to 3$\mathring{A}$ in all calculations. Note that the distance between two adjacent α-carbons is 3.78$\mathring{A}$ and 3.63$\mathring{A}$ in a trans and cis configuration respectively. On the other hand, pairwise interactions within the cut-off radius are modelled to vary quadratically with Δ_{ij}, the contact matrix, given as the weight factor. The requirement for a minimum cut-off temperature, T_{min}, is to ensure that at low temperatures the ratio between the energies arising from the fluctuations of adjacent residues and other energy contributions is finite. Note that in our formulation without specifying a cut-off temperature, C_p diverges as temperature approaches zero. We determine T_{min} from the mimina ($\frac{\partial C_v}{\partial T} = 0$) in the heat capacity constant C_v - temperature curves (C_v versus T) for each protein. We calculate the heat capacity from the following relation,

$$C_v = -T \frac{\partial^2 F}{\partial T^2}, \tag{2.3}$$

where F is the total free energy. The second derivative is calculated using a fourth order finite difference scheme.

Due to the symmetry of the Hamiltonian, the corresponding partition function Z is

singular.

$$Z = \int \Pi_i d\vec{r_i} \exp(-\beta H(\vec{r})) \tag{2.4}$$

By adding an additional spring to the first term in eqn. (2.1), one can break the symmetry in the Hamiltonian and easily decouple the extra energy contribution in the total free energy, where the free energy is related to the partition function Z as :

$$F = -T\ln(Z) = -T\ln\left(\int \Pi_i d\vec{r_i} \exp(-\beta H(\vec{r}))\right). \tag{2.5}$$

The modified Hamiltonian is given by,

$$\begin{aligned} H = & \frac{k_B \cdot \max(T, T_{min})}{2}[\sum_{i=1}^{N-1} K(\vec{t_{i+1}} - \vec{t_i})^2 + K_s t_N^2] \\ & - \sum_{i,j} \frac{\Delta_{ij}}{2}[R^2 - (\vec{t_i} - \vec{t_j})^2]\Theta[R^2 - (\vec{t_i} - \vec{t_j})^2] + F^T t \end{aligned} \tag{2.6}$$

where K_s is the spring constant for the artificially added spring t_N^2. By making use of the self-consistent Gaussian approximation,

$$p_{ij} = < \Theta[R^2 - (\vec{t_i} - \vec{t_j})^2] >, \tag{2.7}$$

Eqn.(2.6) can be rewritten in a compact matrix form as follows:

$$\beta H = \frac{1}{2}(t - \beta MF)^T M^{-1}(t - \beta MF) - \frac{1}{2}\beta^2 F^T MF. \tag{2.8}$$

β is the inverse temperature $(1/k_B T)$ where k_B is set to unity for convenience and the inverse of matrix M is defined as :

$$\begin{aligned} M^{-1} = & \delta_{ij}(K(2 - \delta_{i1} - (1 + \frac{K_s}{K})\delta_{iN}) + \frac{2}{T}\sum_k \Delta_{ik} p_{ik}) \\ & + (1 - \delta_{ij})(\frac{-2}{T} p_{ij}\Delta_{ij} + K(\delta_{i,j-1} - \delta_{i,j+1})). \end{aligned} \tag{2.9}$$

In eqn.(2.9), δ_{ij} is the Kronecker delta and p_{ij} denotes the contact probability of the residue pair i and j. The probability density function of $\vec{t}$ is then given by,

$$P(\vec{t}) = (2\pi)^{-\frac{3N}{2}}(\det M)^{-\frac{3}{2}} \exp(-\frac{1}{2}(t - \beta MF)^T M^{-1}(t - \beta MF)). \tag{2.10}$$

Previously, Micheletti et al. have proposed a self-consistent pair probability approximation for examining equilibrium properties of proteins, and we will follow the same methodology (Micheletti *et al.* 2001). First the contact pair probability is given by

$$p_{ij} = (2\pi)^{-\frac{3N}{2}}(\det M)^{-\frac{3}{2}} \int_{|t_i - t_j| < R} \Pi_k du_k \exp(-\frac{1}{2}(t - \beta MF)^T M^{-1}(t - \beta MF)). \tag{2.11}$$

Physically, p_{ij} corresponds to the pair contact probability of residue i and j that are separated by less than $R = 3\mathring{A}$, and thus is a measure of the structural and conformational deviation from the native state. By making a self-consistent Gaussian approximation for p_{ij} with the given Hamiltonian in eqn.(2.6), we can calculate p_{ij} in an iterative manner.

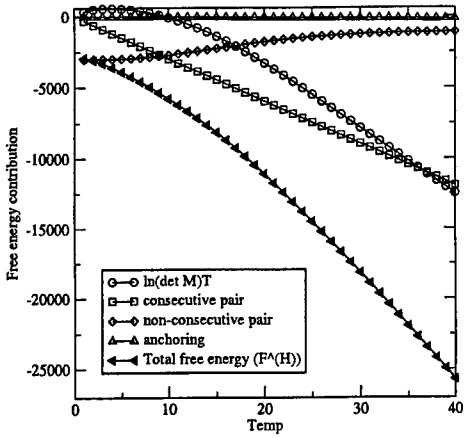


FIGURE 1. Free energy (F^H) versus temperature. Each free energy contribution is also plotted.

First, we transform eqn.(2.11) into spherical coordinates,

$$p_{ij} = \left(\frac{1}{2\pi G_{ij}}\right)^{\frac{3}{2}} \int \Theta(R^2 - |\vec{r} + \vec{L_{ij}}|^2) \exp^{-\frac{r^2}{2G_{ij}}} d\vec{r}. \tag{2.12}$$

In eqn.(2.12), G_{ij} is defined in terms of the matrix M_{ij},

$$G_{ij} = M_{ii} + M_{jj} - 2M_{ij}, \tag{2.13}$$

and $\vec{L}_{ij}$ is the imposed force field defined as

$$\vec{L_{ij}} = \frac{\vec{F}}{T}(M_{i1} - M_{iN} - M_{j1} + M_{jN}) \tag{2.14}$$

for the case of pulling the ends of a protein equally with a force vector $\vec{F}$. By utilizing the isotropicity of spherical coordinates, eqn.(2.12) can be further simplified and expressed as a series of Incomplete Gamma function of order $\frac{1}{2}$ i.e., $P_{\frac{1}{2}}(x)$ which is defined as :

$$P_{\frac{1}{2}}(x) = \frac{1}{\sqrt{\pi}} \int_0^x \exp^{-t} t^{-\frac{1}{2}} dt, \tag{2.15}$$

and p_{ij} is given by :

$$\begin{aligned} p_{ij} = & \frac{\sqrt{G_{ij}}}{\sqrt{2\pi}||L|} \left[\exp^{-\frac{(R+|L|)^2}{2G_{ij}}} - \exp^{-\frac{(R-|L|)^2}{2G_{ij}}}\right] \\ & + \frac{1}{2}\left[P_{\frac{1}{2}}\left(\frac{(R-|L|)^2}{2G_{ij}}\right) + P_{\frac{1}{2}}\left(\frac{(R+|L|)^2}{2G_{ij}}\right) - 2P_{\frac{1}{2}}\left(\frac{|L|^2}{2G_{ij}}\right)\right] \end{aligned} \tag{2.16}$$

In the case of no applied force, eqn.(2.16) reduces to

$$p_{ij} = \frac{2}{\sqrt{\pi}} P_{\frac{3}{2}}\left[\frac{R^2}{2G_{ij}}\right], \tag{2.17}$$

where $P_{\frac{3}{2}}$ is the incomplete Gamma function of order $\frac{3}{2}$.

We first start each calculation by initializing all p_{ij}'s to 0.5. Two different initial values of 0.25 and 0.75 were used to ensure that the results are independent of initial conditions. The matrix M_{ij}^{-1} is then constructed using the initial values of p_{ij}'s and the contact

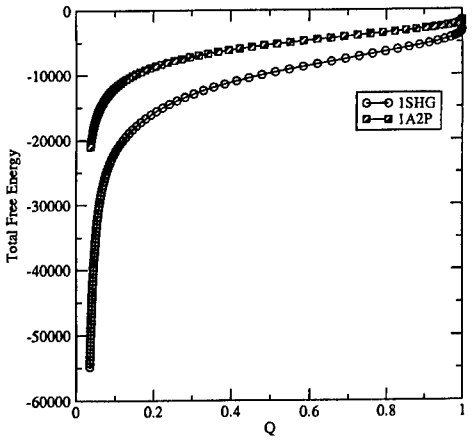


FIGURE 2. Total free energy (F^T) versus the fraction of native contacts (Q) for protein 1SHG and 1A2P.

matrix Δ_{ij}. The native state structure for each protein was taken from the Brookhaven Protein Data Bank (PDB) and was first analyzed in a separate subroutine where the types of amino-acid were identified and the distance between all pair residues was calculated and recorded to construct the contact matrix Δ_{ij}. We have employed a more refined discrete scheme of constructing the contact matrix - where depending on the type of amino-acid and distance between two residues, discrete leveled amino-acid interactions are taken into account - but only minor quantitative differences were observed between the two schemes. LU decomposition is employed to invert the symmetric matrix M_{ij}^{-1}(Press *et al.* 1992). The new p_{ij}'s are then calculated using eqn.(2.16) with the inverted matrix M_{ij} where the incomplete Gamma functions are evaluated using two different schemes, i.e. a fast converging series expansion and 50-point Gaussian quadrature (Press *et al.* 1992) to check numerical accuracy. The iteration continues until the differences between the previous and current values for *all* p_{ij}'s are below a prescribed tolerance δ. We used $\delta = 10^{-6}$ for equilibrium and thermal unfolding, and 10^{-5} for mechanical unfolding calculations and convergence was achieved within a dozen $(10 - 40)$ iterations.

3. Results

In this section, we apply the model to examine the equilibrium and non-equilibrium properties of several proteins. First, the equilibrium properties - both structural and thermodynamic - are presented. We determine the folding temperature in a systematic way as outlined in the previous section and calculate each free energy contributions arising from the Hamiltonian model. By varying the temperature, we further investigate the thermal denaturation of the immunoglobin (Ig) domains of Titin (1TIT). Finally the ends of the Ig domains are pulled mechanically and the unfolding mechanism as well as the stability of six key β-strands are studied.

3.1. *Equilibrium*

Following the steps in §2, we examine the equilibrium properties of the globular protein 2CI2, 1SHG and barnase (1A2P) and the immunoglobulin domain of Titin (1TIT). The remaining parameters we have to set in the Hamiltonian in eqn.(2.6) is the strength of the peptide strength K and K_s for the artificially added spring. Physically, a larger K

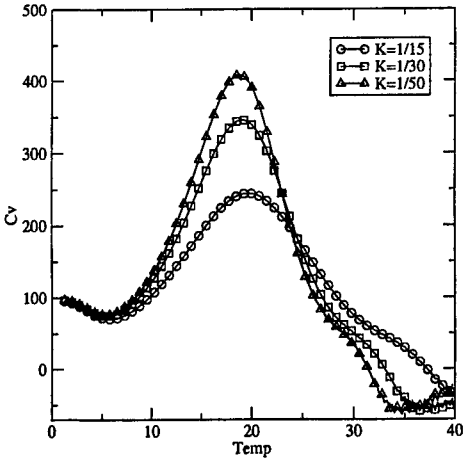


FIGURE 3. Heat capacity versus temperature for 2ci2 with varying peptide strength parameter K.

corresponds to a more rigid rod-like bond. The parameter K_s for the artificially added spring can be set to any non-zero value. The extra free energy due to this spring is F_A:

$$F^A = -T\ln(Z) = -T\ln\left[\frac{2\pi T}{K_s}\right]^{\frac{3}{2}}. \tag{3.1}$$

In all our calculations the total free energy F^T is calculated by subtracting the extra free energy F^A :

$$F^T = F^H - F^A, \tag{3.2}$$

where F^H is the corresponding total free energy to the Hamiltonian in eqn.(2.6) given by,

$$F^H = -\frac{3N}{2}\ln(2\pi)T - \frac{3}{2}\ln(\det M)T - \frac{R^2}{2}\sum_{i,j}\Delta_{ij}p_{ij} - T\ln\left[\frac{2\pi T}{K_s}\right]^{\frac{3}{2}}. \tag{3.3}$$

The free energy (F^H) and the individual energy terms in eqn.(3.3) for the protein 1A2P are shown in Fig.(1). Given our Hamiltonian, there are free energies associated with the consecutive pair interactions (the first term in eqn.(3.3)), and those arising from the non-consecutive pairwise interactions (the second and the third term) as well as those due to the artificial anchoring (the last term). In Fig.(2), the total free energy (F^T) is plotted versus the fraction of native contacts Q for the protein 1SHG and 1A2P, where Q is defined as :

$$Q = \frac{\Sigma'_{i,j}\Delta_{ij}p_{ij}}{\Sigma'_{i,j}\Delta_{ij}}. \tag{3.4}$$

In eqn.(3.4) the prime denotes that sum is carried out over only non-consecutive pairs. Previously, Micheletti *et al.* have used used a value of $K = \frac{1}{15}$ by inspecting the behavior of the fraction of native contacts (Q) as defined in eqn.(3.4)(Micheletti *et al.* 2001). In this work, three values of K were used - $\frac{1}{15}$, $\frac{1}{30}$ and $\frac{1}{50}$. In Fig.(3), we plot the heat capacity as a function of temperature with varying peptide strength parameter K for the protein 2CI2. The maximum of the heat capacity corresponds to the folding temperature which is defined as the temperature at which a protein is equally likely to be either in a

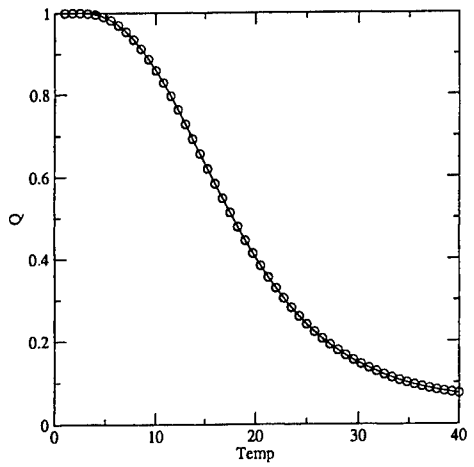


FIGURE 4. The fraction of native contacts (Q) versus temperature for the protein 1A2P.

folded or unfolded state. At the folding temperature the fraction of native contacts was shown to be around 0.5 in previous studies (Clementi *et al.* 2000; Micheletti *et al.* 2001; Plaxco *et al.* 1998; Chan & Dill 1998). To verify if the chosen range of the K parameter yielded consistent results with previous observations, we calculate the fraction of native contacts Q for 1A2P whose folding temperature was $T = 16.25$ for $K = \frac{1}{15}$. At the folding temperature Q is 0.56 as shown in Fig.(4). Note that the folding temperature is not a sensitive function of the peptide strength parameter K as the location of the maxima in heat capacity in Fig.(3) did not shift with different values of K. Next we calculate the equilibrium properties of the immunoglobulin domain of the protein Titin. The folding temperature was determined as above from the C_v-T plot and in Fig.(4) the fraction of native contacts Q is plotted versus temperature. Whereas Q is a global ordering parameter that measures the deviation of an entire folded protein domain from the native state, a more relevant local ordering parameter that monitors the deviation of each residue in the protein from its native state is P_i defined as :

$$P_i = \frac{\Sigma_j' \Delta_{ij} p_{ij}}{\Sigma_j' \Delta_{ij}} \tag{3.5}$$

The local ordering parameter P_i is shown at the folding temperature in Fig.(5). Note that the eight β strands are (in the order of first residue number - last residue number in the strand for each strand and in the parenthesis the type of amino acid) : 4(VAL)-7(PRO), 11(VAL)-15(VAL), 18(THR)-25(LEU), 32(GLY)-36(LEU), 47(CYS)-52(ASP), 55(LYS)-61(HIS), 69((GLY)-75(ALA) and 78(ALA)-88(GLU). We can clearly see that each strand exhibits different degrees of ordering at the folding temperature. In the next section, we examine the thermal denaturation of the same domain of Titin (1TIT).

3.2. *Thermal Unfolding*

The eight β-strands in the immunoglobulin domain of Titin are stabilized via hydrogen bonding. The six interacting residue pairs are : 6-24, 11-85, 19-60, 35-72, 48-59 and 69-84. The corresponding strand-strand or sheet interactions are denoted as : AB, A'G, BE, CF, DE and FG. First we vary the temperature to examine both the global (Q) and local (P_i) ordering. As shown in Fig.(6) as the temperature increases, the global ordering is slowly destroyed and at about twice the folding temperature ($T_f = 17.75$), the protein

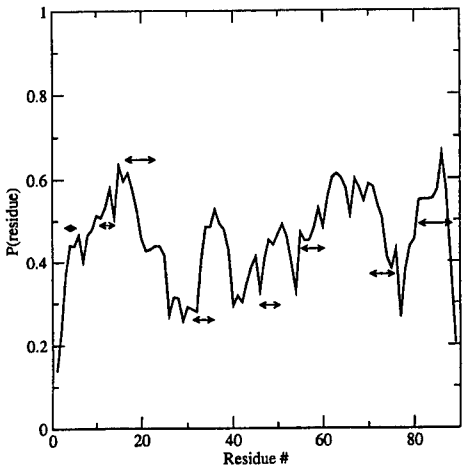


FIGURE 5. Local ordering parameter P_i for 1TIT at the folding temperature. The arrows denote the location of the eight β-strands.

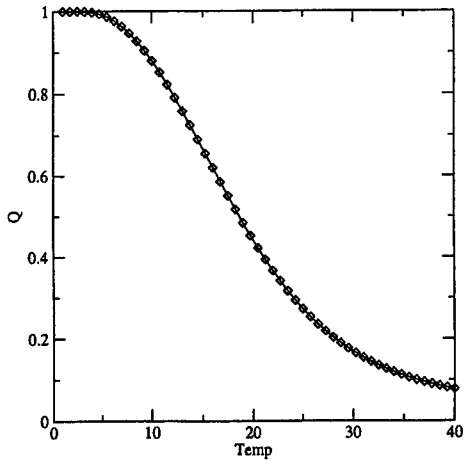


FIGURE 6. The fraction of native contacts (Q) versus temperature for the protein 1TIT.

has almost denatured. The individual residues which are in the ordered state at low temperatures (for example at $0.35T_f = 6.21$) slowly denature from the native state with varying degrees of ordering at high temperatures. Another global parameter to monitor the denaturation process is the size of the domain as a function of temperature which can be calculated by the following relation,

$$S^2(T) = 3G_{1N}(T) + S_o^2 \tag{3.6}$$

where S^2 is the mean square of the end-to-end distance of the protein and the subscript o denotes the native state, and G_{1N} is the component $(1, N)$ of the matrix G_{ij} as defined in eqn.(2.13). In Fig.(8), the extension versus temperature is shown and we see a smooth growth of the domain with increasing temperature. Note that at $2T_f = 35.5$, the domain size has increased only by 5% compared to $T_f = 17.75$. The six sheet interactions represented by the six individual pair interactions are shown in Fig.(9). The sheet interaction FG (69-84) is the most stable interaction over the entire temperature range and A'G is

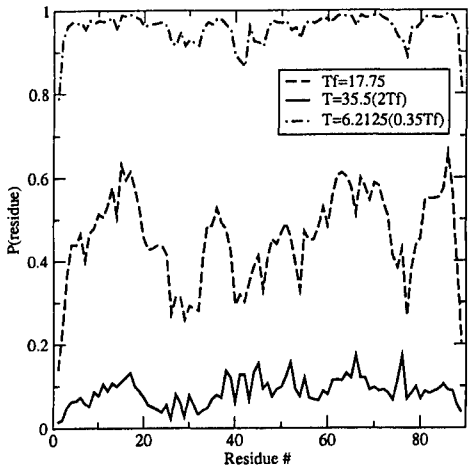


FIGURE 7. Local ordering parameter P_i for 1TIT with varying temperature near the folding temperature.

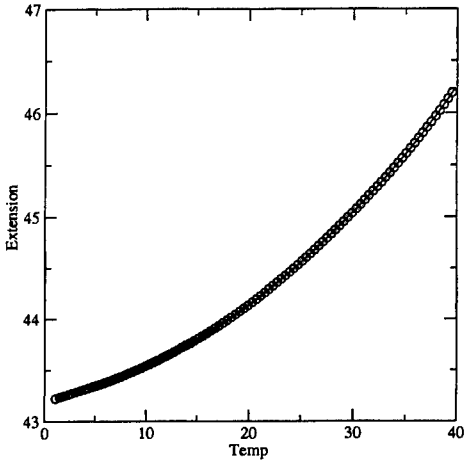


FIGURE 8. Domain size as a function of temperature for 1TIT.

the least stable interaction at low temperatures. Near the folding temperature all five interactions except for FG are comparable in strength.

3.3. *Mechanical Unfolding*

In this section we apply mechanical forces to the immunoglobulin domain of Titin. The experiments mentioned in §1 used two different tools to probe the unfolding pathways of the same molecule. Pulling the ends of it showed that the series of individual immunoglobulin domains open one by one. Also the protein domains were shown to resist a mechanical force of the order of a few hundreds of piconewtons (pN) after which one domain unfolds causing a reduction in the applied force. Further extension gradually increases the applied force until another domain unfolds. This stepwise single domain unfolding results in a so called saw-tooth pattern. The six sheet pair contact probabilities are shown in Fig.(10). The interaction A'G is the most unstable one below $F = 3.7$, which corresponds to a dimensional force of $150pN$. The interaction AB is lost at $F \approx 150pN$,

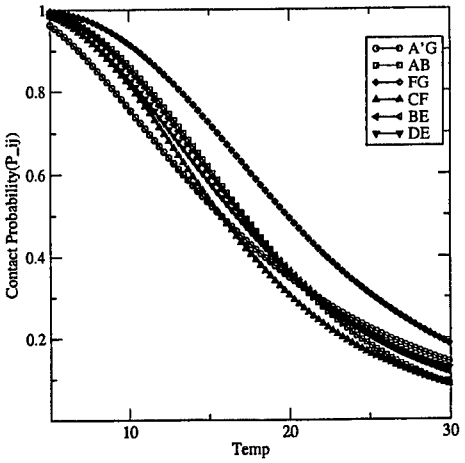


FIGURE 9. Six sheet contact probabilities as a function of temperature for 1TIT.

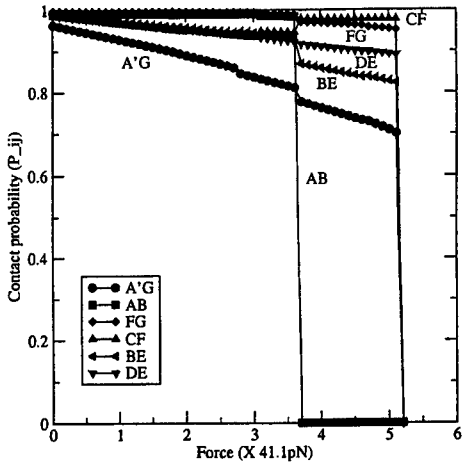


FIGURE 10. Six sheet contact probabilities as a function of pulling force for 1TIT.

suggesting the two β-strands A and B are no longer in contact. At $F = 5.16(212pN)$ the entire immunoglobulin domain is unfolded as seen from the vanishingly small contact pair probabilities for all six sheet interactions. This finding that the sheet interaction A'G and AB are the least stable ones is consistent with the results obtained from steered molecular dynamics by (Lu *et al.* 1998). The fraction of native contacts (Q) as larger forces are applied is shown in Fig. (11). Compared to Fig. (6), we see discrete jumps in the total nativeness of the protein domain.

To directly compare to previous experimental findings (Rief *et al.* 1997; Kellermayer *et al.* 1997; Tskhovrebova *et al.* 1997), we calculate the mean square end-to-end distance in the case of a constant pulling force $\vec{F}$ at the ends of a protein, which is given by,

$$S^2(T) = 3G_{1N}(T) + |\vec{S_o} + \vec{L_{1N}}|^2 \tag{3.7}$$

where $\vec{L}$ is defined in eqn.(2.14). In Fig.(12), the end-to-end distance is plotted as a function of the applied pulling force. We observe similar stalls in the plot where the domain size increases but the force remains constant. Related to the stability of each

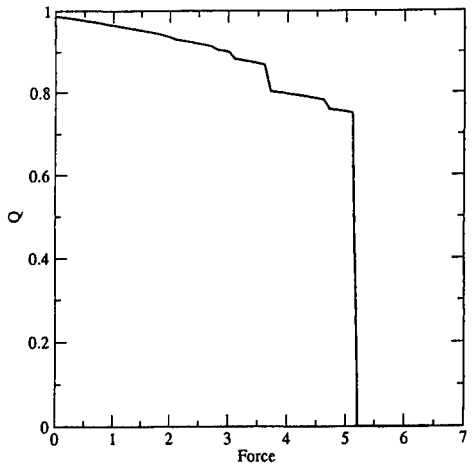


FIGURE 11. The fraction of native contacts (Q) versus pulling force for the protein 1TIT.

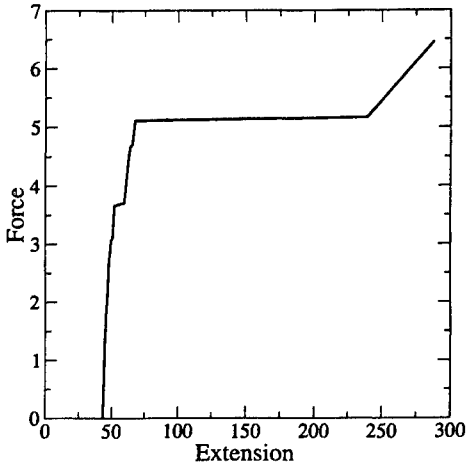


FIGURE 12. Force-extension plot for 1TIT.

sheet interaction, we conclude that the first force stall in Fig.(12) is due to the breakage of the hydrogen bonding pair in the AB sheet (residue pair 6-24). The AB sheet completely breaks at $F = 3.7$ and at $F = 5.16(210pN)$, the six sheet interactions are destabilized and the entire immunoglobulin domain is open. After the critical force of $F = 5.16$, the linear growth in extension isintrinsically due to the quadratic potential of the residues as given by the Hamiltonian (see eqn.(2.6)).

4. Conclusions

We have employed a Hamiltonian model based on a self-consistent Gaussian appoximation to examine the unfolding process of proteins in external - both mechanical and thermal - force fields. The motivation was to investigate the unfolding pathways of proteins by including only the essence of the important interactions of the native-state topology. Furthermore, if such a model can indeed correctly predict the physics of protein unfolding, it can complement more computationally expensive simulations and theoretical

work. The self-consistent Gaussian approximation by Micheletti et al. has been incorporated in our model to make the model mathematically tractable by significantly reducing the computational cost. All thermodynamic properties and pair contact probabilities are calculated by simply evaluating the values of a series of Incomplete Gamma functions in an iterative manner. We have compared our results to previous molecular dynamics simulation and experimental data for the mechanical unfolding of the giant muscle protein Titin (1TIT). Our model, especially in light of its simplicity and excellent agreement with experiment and simulation, demonstrates the basic physical elements necessary to capture the mechanism of protein unfolding in an external force field.

5. Acknowledgments

J. S. Hur would like to thank the Center for Turbulence Research at Stanford University for its support and Dr. Yves Dubief for helpful suggestions on the manuscript. E. Darve would like to thank the center for computational astrobiology at NASA Ames research center.

REFERENCES

ALM, E. & BAKER, D. 1999 Matching theory and experiment in protein folding. *Curr. Opin. Struc. Biol.* **9**, 189–196.

BAKER, D. 2000 A surprising simplicity to protein folding. *Nature* **405**, 39–42.

CHAN, H. S. & DILL, K. A. 1998 Protein folding in the landscape perspective : Chevron plots and non-arrhenius kinetics. *Proteins* **30**, 2–33.

CLEMENTI, C., NYMEYER, H. & ONUCHIC, J. N. 2000 Topological and energetic factors : What determines the structural details of the transition state ensemble and "en-route" intermediates for protein folding : An investigation for small globular proteins. *J. Mol. Biol.* **298**, 937–953.

DAYEL, M. J., HOM, E. F. Y. & VERKMAN, A. S. 1999 Diffusion of green fluorescent protein in the aqueous-phase lumen of endoplasmic reticulum. *Biophys. J.* **76**, 2843–2851.

KELLERMAYER, M. S. Z., SMITH, S. B., GRANZIER, H. L. & BUSTAMANTE, C. 1997 Folding-unfolding transitions in single titin molecules characterized with laser tweezers. *Science* **276**, 1112–1116.

LU, H., ISRALEWITZ, B., KRAMMER, A., VOGEL, V. & SCHULTEN, K. 1998 Unfolding of titin immunoglobulin domains by steered molecular dynamics simulation. *Biophys. J.* **75**, 662–671.

MICHELETTI, C., BANAVAR, J. R. & MARITAN, A. 2001 Conformations of proteins in equilibrium. *Phys. Rev. Lett.* **87**, 88102–88102.

PACI, E. & KARPLUS, M. 2000 Unfolding proteins by external forces and temperature : The importance of topology and energetics. *Proc. Natl. Acad. Sci.* **97**, 6521–6526.

PLAXCO, K. W., SIMONS, K. T. & BAKER, D. 1998 Contact order, transition state placement and the refolding rates of single domain proteins. *J. Mol. Biol.* **277**, 985–994.

PRESS, W. H., TEUKOLSKY, S. A., VETTERLING, W. T. & FLANNERY, B. P. 1992 *Numerical Recipes in Fortan*, 2nd edn., , vol. 1. Cambridge: Cambridge Press.

PRICE, W. S., TSUCHIYA, F. & ARATA, Y. 1999 Lysozyme aggregation and solution

properties studied using pgse nmrdiffusion measurements. *J. Am. Chem, Soc.* **121**, 11503–11512.

RIEF, M., GAUTEL, M., OESTERHELT, F., FERNANDEZ, J. M. & GAUB, H. E. 1997 Reversible unfolding of individual titin immunoglobulin domains by afm. *Science* **276**, 1109–1112.

TSKHOVREBOVA, L., TRINICK, J., SLEEP, J. A. & SIMMONS, R. M. 1997 Elasticity and unfolding of single molecules of the giant muscle protein titin. *Nature* **387**, 308–312.

WOLYNES, P. G., ONUCHIC, J. N. & THIRUMALAI, D. 1995 Navigating the folding routes. *Science* **267**, 1619–1620.

Numerical simulation of high drag reduction in a turbulent channel flow with polymer additives

By Yves Dubief

1. Introduction

The addition of small amounts of long chain polymer molecules to wall-bounded flows can lead to dramatic drag reduction. Although this phenomenon has been known for about fifty years, the action of the polymers and its effect on turbulent structures are still unclear. Detailed experiments have characterized two distinct regimes (Warholic *et al.* 1999), which are referred to as low drag reduction (LDR) and high drag reduction (HDR). The first regime exhibits similar statistical trends as Newtonian flow: the log-law region of the mean velocity profile remains parallel to that of the Newtonian flow but its lower bound moves away from the wall and the upward shift of the log-region is a function of drag reduction, DR. Although streamwise fluctuations are increased and transverse ones are reduced, the shape of the rms velocity profiles is not qualitatively modified. At higher drag reductions, of the order of 40-50%, the flow enters the HDR regime for which the slope of the log-law is dramatically augmented and the Reynolds shear stress is small (Warholic *et al.* 1999; Ptasinski *et al.* 2001). The drag reduction is eventually bounded by a maximum drag reduction (MDR) (Virk & Mickley 1970) which is a function of the Reynolds number. While several experiments report mean velocity profiles very close to the empirical profile of Virk & Mickley (1970) for MDR conditions, the observations regarding the structure of turbulence can differ significantly. For instance, Warholic *et al.* (1999) measured a near-zero Reynolds shear stress, whereas a recent experiment (Ptasinski *et al.* 2001) shows evidence of non-negligible Reynolds stress in their MDR flow. To the knowledge of the authors, only the LDR regime has been documented in numerical simulations (Sureshkumar *et al.* 1997; Dimitropoulos *et al.* 1998; Min *et al.* 2001; Dubief & Lele 2001; Sibilla & Baron 2002). This paper discusses the simulation of polymer drag reduced channel flow at HDR using the FENE-P (Finite Elastic non-linear extensibility-Peterlin) model which was used for the first LDR simulation by Sureshkumar *et al.* (1997). Flow and polymer parameters are close to realistic polymer drag reducing conditions. High drag reductions are achieved by using finite differences and a robust time stepping technique. A minimal channel flow is also used as a numerical experiment to investigate the effect of the outer region turbulent structures on the overall drag at HDR. The drag reducing action of the model is finally studied through the structure of energy transfers from the polymers to the velocity components. This investigation sheds some light on the details of polymer drag reduction.

2. Governing equations and numerical method

The formalism of the constitutive equations for viscoelastic flows typically includes the assumption of uniform concentration of the polymer solution, and the momentum

equations thus become:

$$\partial_t u_i = -u_j\partial_j u_i - \partial_i p + \frac{\beta}{Re}\partial_j\partial_j u_i + \underbrace{\frac{1-\beta}{Re}\partial_j\tau_{ij}}_{f_i}\,, \tag{2.1}$$

where β is the ratio of the solvent viscosity ν to the total viscosity and effectively controls the concentration of polymers. The Reynolds number is defined as $Re = Uh/\nu$, where the velocity, U, and length, h, scale are defined in the next section. Note the addition of the viscoelastic stress which is later referred to as f_i. The viscoelastic tensor τ_{ij} in f_i is obtained by solving the FENE-P equation,

$$\boldsymbol{\tau} : \partial_t c_{ij} = -\underbrace{u_k\partial_k c_{ij}}_{\text{advection}} + \underbrace{c_{kj}\partial_k u_i + c_{ik}\partial_k u_j}_{\text{stretching}} - \underbrace{\frac{1}{We}\left(\frac{c_{ij}}{1-\frac{c_{kk}}{L^2}} - \delta_{ij}\right)}_{=\tau_{ij}:\text{relaxation}} + \kappa D(c_{ij})\,, \tag{2.2}$$

where the conformation tensor, c_{ij}, is the phase average of q_iq_j, q_i being the component of the end-to-end vector of each individual polymer which has a maximum dimensionless extensibility, L. The Weissenberg number We is the ratio of the largest polymer relaxation time λ to the flow time scales, such that $We = \lambda U/h$. The numerical method is essentially that of Min *et al.* (2001) modified to simulate very elastic and long polymer molecules. The successful modification, consisting of a novel time advancement scheme for Eq. (2.2), is described and validated in Dubief *et al.* (2003). In the present paper only a brief outline of the method is given. The momentum equations are solved on a staggered grid with second-order central finite differences. The divergence of the polymer stress (Eq. 2.1) and the spatial derivatives of c_{ij} are computed using a fourth order compact scheme and a third order upwind compact scheme, respectively. Time advancement of Eqs. (2.1) and (2.2) is performed by the classical semi-implicit second-order Crank-Nicolson/third-order Runge-Kutta scheme. In the momentum equation, the Newtonian viscous stress are treated implicitly in the wall-normal direction. Eq. (2.2) is solved with a new semi-implicit time scheme which guarantees the trace of the c_{ij} remains upper bounded ($c_{kk} < L^2$).

In turbulent flows, Eq. (2.2) proves to be fairly stiff and therefore delicate to solve. Originally, Sureshkumar *et al.* (1997) added a diffusive term to the FENE-P ($D(c_{ij}) = \partial_k\partial_k c_{ij}$) and used a fairly significant diffusivity coefficient κ. Min *et al.* (2001) later pointed out that the addition of a diffusivity everywhere in the flow causes the smearing of polymer stress gradients and suggested a local approach. The Local Artificial Dissipation (LAD) is a second-order numerical error ($D(c_{ij}) = \Delta_k^2\partial_k^2 c_{ij}$, Δ_k denoting the local grid size) which is applied only to nodes for which the positiveness of the conformation tensor is not satisfied. Min *et al.* designed the LAD as an-extra diffusion of the scheme used for the advection of c_{ij}.

As discussed in Dubief *et al.* (2003), the advection term in Eq. (2.2) creates small scales similar to the ones observed for a passive scalar at high-Schmidt number, *i.e.* a few orders of magnitude smaller than the dissipative flow scale, the Kolmogorov scale. The LAD allows the polymer field to develop sharper gradients than a global diffusivity approach, however the quality of the simulation depends strongly on the resolution of the smallest turbulent scales. When the drag is very close to its Newtonian value, direct numerical simulations can only resolved up to Kolmogorov which is then the cutoff scale for the advection of c_{ij}. At HDR, the turbulence is so reduced that the simulation of

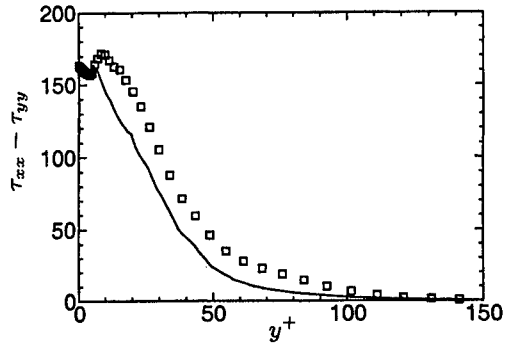


FIGURE 1. *Left*: Normal stress profiles of the viscoelastic simulation L100W120MC, □ , compared to the Brownian dynamic simulation ,——— .

smaller scales for the conformation tensor becomes possible. The quality of a FENE-P simulation is assessed by comparing the polymer stress obtained by Eq. (2.2) and the one obtained with a Brownian dynamic simulation (Terrapon *et al.* 2003). Since the Brownian simulation is only a one-way coupling from the flow to polymers, the comparison is achieved by using the velocity field computed from the viscoelastic simulation. In the case of HDR (Fig. 1) the agreement is within 10% which is considered satisfactory.

Finally, as in any simulation involving dramatic reduction of drag, particular attention to the dimensions of the computational domain must be paid. Here, simulations are performed in a channel flow, where periodicity is enforced in the homogeneous direction, x and z, and no-slip is prescribed on the walls. Periodicity is a very satisfactory boundary condition providing that the energy-containing turbulent structures are smaller than the dimensions of the computational domain. In the case of polymer drag reduction, a coarsening of the streaks is observed (White *et al.* 2003), suggesting that all turbulent scales in the near-wall region are likely to grow with increasing drag reduction. As demonstrated by Jiménez & Moin (1991) in their numerical experiment of the minimal flow unit capable of sustaining turbulence, turbulence vanishes when the computational domain is smaller than 1000 by 100 wall units in the streamwise and spanwise directions, respectively. The wall unit is defined the ratio of the kinematic viscosity ν to the friction velocity $u_\tau = \sqrt{\nu(dU/dy)_{wall}}$. Based on the Newtonian friction velocity, the length and width of the computational domain have been varied from 1000 to 6000 and from 300 to 1200, respectively for a drag reduction of $DR = 60\%$. While velocity correlations in the streamwise direction do not go exactly to zero, even for $L_x^+ = 6000$, the difference in drag reduction is less than 1% for a domain 4000×1200 compared with 6000×1200. In the spanwise direction, correlations drop to zero for $L_z^+ = 1200$, which has led us to choose the intermediate domain $4000 \times 600 \times 1200$ or $4\pi h \times 2h \times 4h$ in integral units, as shown in Table 1. In the course of the study of the channel dimensions, it was noticed that turbulence never disappears in the smallest domain, in spite of its sub-critical dimension in drag reduction mode with $L_x^+ \simeq 600$ and $L_z^+ \simeq 150$ (based on the reduced skin-friction). Results obtained with this domain are also discussed as a numerical experiment.

Simulations are performed in a channel flow at an intermediate Reynolds number, $Re = 7500$ based on the half-width h of the channel and the centerline velocity of the initial Poiseuille profile. The bulk Reynolds number is $Re_M = 5000$. Conservation of the mass flow is imposed which gives $h^+ = hu_\tau/\nu = 300$. The resolution is $\Delta x^+ = 9$, $\Delta y^+ = 0.1-5$ and $\Delta z^+ = 6$, when normalized by the skin friction at $DR = 0\%$. Statistics

Name	Line/symbol	Dimensions	L	$We_{\tau 0}$	β	DR
L60W84LC	•	$4\pi h \times 2h \times 4h$	60	84	0.9	47%
L60W84MC	○	$\pi h \times 2h \times h$	60	84	0.9	67%
L100W120LC	▪	$4\pi h \times 2h \times 4h$	100	120	0.9	60%
L100W120MC	□	$\pi h \times 2h \times h$	100	120	0.9	72%

TABLE 1. Polymer parameters used for the viscoelastic simulations. The Weissenberg number $We_{\tau 0}$ is normalized the wall-shear stress for the Newtonian simulation ($DR = 0\%$). For clarity, data from simulation L60W84MC appear only on the mean velocity profile plot (Fig 2).

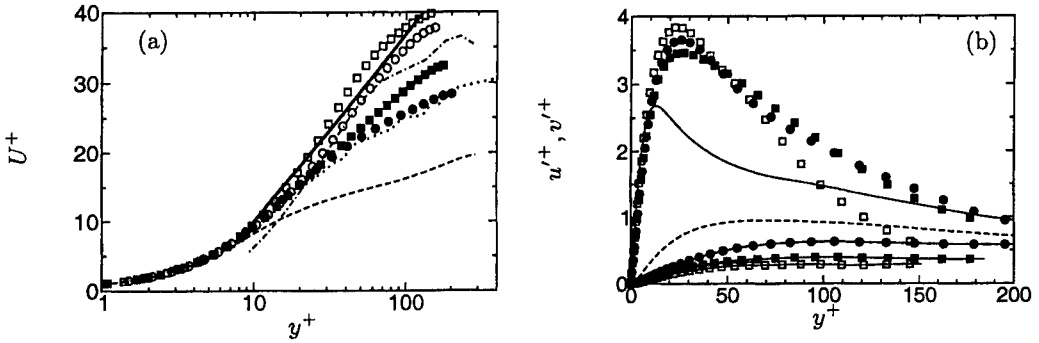


FIGURE 2. *Left*: Mean velocity profiles scaled with inner variables. ---- : Newtonian simulation ($DR = 0\%$); ——— : MDR asymptote, $U^+ = 11.7 \ln y^+ + 17$. Experimental data (White *et al.* 2003): ····· , $DR = 45\%$; —·— , $DR = 67\%$. Other symbols and lines are defined in Table 1. *Right*: RMS of velocity fluctuations scaled with inner variables. Newtonian simulation ($DR = 0\%$): ——— , u'^+; ---- , v'^+. For the viscoelastic simulations, symbols are defined in Table 1, u'^+ is denoted by symbols only; v'^+ is indicated by symbols connected by ——— .

are collected over 300 to 400 convection times h/U, starting after the transient period, typically $200h/U$.

3. Results

In the following, the simulations are referred as to by LxxWyyCD, where xx, yy and CD designate respectively the dimensionless maximum extensibility L, yy the Weissenberg number normalized the Newtonian wall-shear and CD the computational domain, MC for minimal channel, LC for large channel (see Table 1).

Two observations can readily be made from table 1. First the FENE-P model requires fairly high Weissenberg numbers to achieve HDR with long-chain type polymers, while HDR has experimentally been measured for We ranging from unity to 100. The need for high We can be attributed to the underestimation of polymer stress by the model in the case of low extension, and therefore be blamed on the simplicity of the FENE-P model, based on a dumbbell, neglecting internal modes. The second observation arises from the comparison between drag reductions obtained with the minimal channel and the larger domain. For $L = 60$ and $We_\tau 0 = 84$, the difference is the largest, with the minimal channel showing 20% more reduction than the large domain. As discussed in the previous section, turbulence in the minimal channel flow under condition of drag reduction is very likely to be affected by the periodic boundary conditions. In the present case, the streamwise turbulent intensity is significantly reduced around the centerline (Fig. 2b),

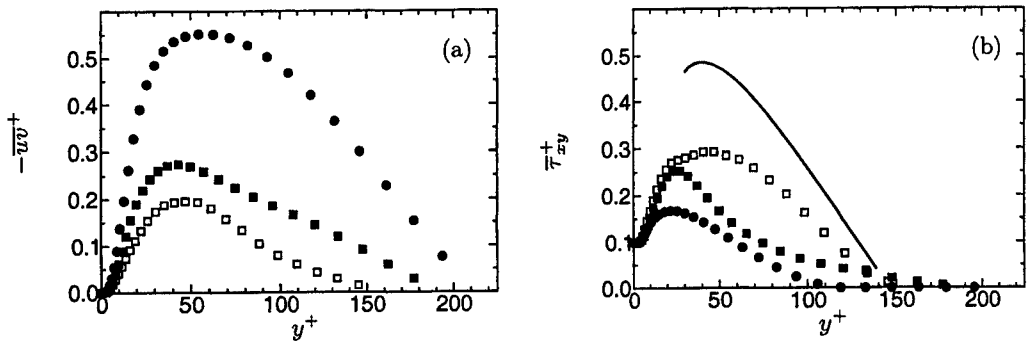


FIGURE 3. Reynolds shear stress (3a) and polymer stress (3b) normalized by u_τ and ν. Symbols are defined in Table 1. In Fig. 3b, ——— represents the contribution the polymer stress would have to Eq. (3.1) in the case of MDR defined by the velocity profile $U^+ = 11.7\ln(y^+) - 17$ and $-\overline{uv}^+ = 0$.

indicating that large scale turbulent structures which are otherwise present in the large domain cannot develop. Deprived of this energy coming from the outer region of the flow, the near-wall region produces a weaker shear.

All the mean velocity profiles domain exhibit a change of slope in the log-law region, but only the ones obtained with minimal channel flow approach Virk's asymptote, shown by a solid line in Fig. 2a. For L60W84LC ($DR = 47\%$), the slope of the log region is roughly twice that of the Newtonian, which ascertains the fact that this simulation belongs to the lower part of the HDR regime, while L100W120LC is intermediate. In the case of the minimal channel, increasing We for this simulation had no effect on the amount of drag reduction. The simulation L100W120MC seems thus representative of an asymptotic state for the constraints imposed by the boundary condition channel flow. Also plotted in Fig. 2a are some experimental data obtained at Stanford by White *et al.* (2003), showing that similar results velocity profiles can be obtained in a turbulent boundary layer with non-uniform polymer concentration.

The turbulent velocity fluctuations (Fig. 2b) behave as observed experimentally (see White *et al.* 2003). The peak of u' shifts away from the wall and its magnitude increases slowly compared to the Newtonian flow when normalized by u_τ. The wall-normal component v' follows an opposite trend; w' behaves as v' and consequently does not appear on the plot for clarity. In drag reduced flow, the maximum of u'^+ is indeed higher or comparable with the $DR = 0\%$ case, as found in experiments (Warholic *et al.* 1999; Ptasinski *et al.* 2001; White *et al.* 2003). The strong reduction of the transverse fluctuations suggests that polymers target preferentially the vortices, which have a significant contribution to the transverse velocity components.

The balance of stresses,

$$-\overline{uv}^+ - \left(1 - \frac{y^+}{h^+}\right) + \beta\frac{dU^+}{dy^+} + (1-\beta)\overline{\tau}^+_{xy} = 0\,, \tag{3.1}$$

contains significant information regarding the mechanism of polymer interaction with the mean flow. As indicated in Fig. 3a, the Reynolds shear stress reduces with increasing drag reduction. For $DR = 60\%$ (L100W120LC), $-\overline{uv}^+$ is approximately a third of its magnitude in the Newtonian case. Conversely, the polymer stress increases with increasing drag reduction (Fig. 3b). At $DR = 60\%$, its near-wall contribution to Eq. (3.1) has the same magnitude as the Reynolds shear stress. In the case of the minimal channel,

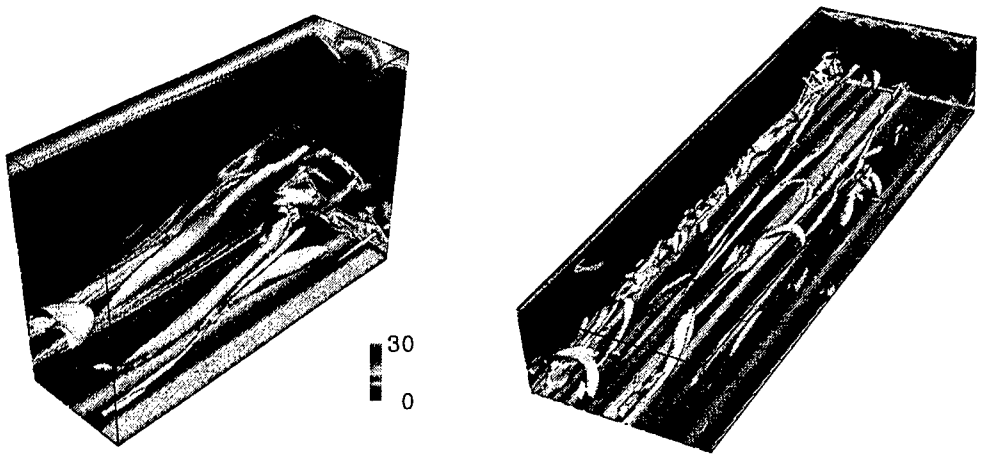


FIGURE 4. Snapshot of vortices identified by the Q-criterion (Dubief & Delcayre 2000) and the trace ($c_{kk}/L^2 \times 100$). *Left* L60W84MC; *right* L60W84LC. Vortices are only shown in the lower half of the domain.

the polymer stress is actually 1.5 higher than the Reynolds shear stress, which outlines the mechanism by which turbulence is sustained even in a minimal channel flow. The level of Reynolds shear stress and polymer stress are comparable to the ones measured by Ptasinski *et al.* (2001), even for their MDR experiment. Also plotted in Fig. 3b is the polymer stress contribution in case of zero-Reynolds shear stress as observed in the experiments of Warholic *et al.* (1999) and MDR, *i.e.* above $y^+ \sim 20$ the mean velocity profile is assumed to collapse with Virk's asymptotic profile (see Fig. 2a). In that case, the polymer stress is almost twice the one measured in the minimal channel flow for the same drag reduction. The different behavior observed in Ptasinski *et al.* (2001)'s experiment, as well as our simulation, and Warholic's demonstrates the essential role played by the polymer stress in the self-sustaining mechanism which produces the MDR turbulence.

4. Observations and perspectives on the drag reduction mechanism

The topology of the drag reduced flows is based on the same structures as Newtonian wall-turbulence: streaks and vortices. In Fig. 4, showing snapshots of L60W84MC and L60W84LC, the streaks are identified by the contours of the polymer extension c_{kk}/L^2 at the wall, where c_{kk} is the trace of c_{ij}. The regions of high and low stretch denotes high and low-speed streaks, respectively. The coherence of the streaks is rather impressive compared to Newtonian turbulence (not shown here). The streamwise persistence of the streaks has also been observed in White *et al.* (2003)'s experiments, as well as their spanwise stability. Vortices are identified using isosurfaces of the second invariant Q of the velocity gradient tensor. Positive values of $Q = \mathbf{\Omega}^2 - \mathbf{S}^2$, where $\Omega_{ij} = \partial_j u_i - \partial_i u_j$ and $S_{ij} = \partial_j u_i + \partial_i u_j$ isolate regions where the rotation rate dominates the strain rate, which provides a reliable identification method of vortices (Dubief & Delcayre 2000). The minimal channel flow contains a few, elongated vortices while the large domain has a more varied population of near-wall vortices, short and long quasi-streamwise vortices and hairpin-type vortices. These differences in the topology illustrate the different statistical behavior observed between the two simulation. On the side view, polymer extension is shown to burst away from the near-wall region intermittently in the upwash and downwash flows generated by vortices.

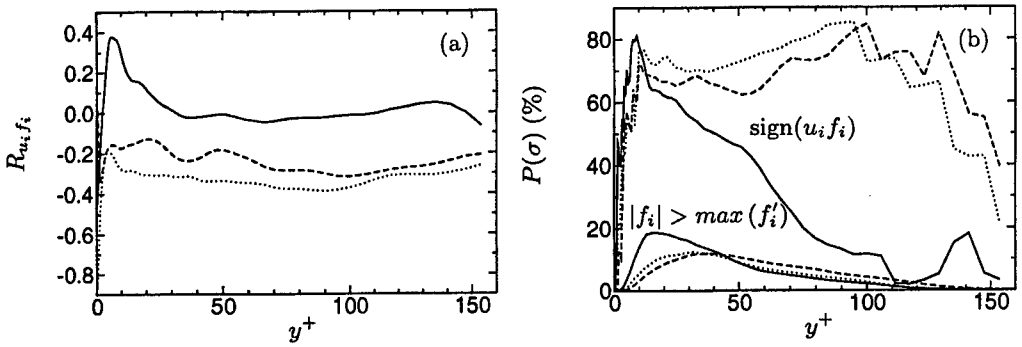


FIGURE 5. (a) Correlation velocity-viscoelastic stress in the three directions, ($R_{u_i f_i} = \overline{u_i f_i}/u_i' f_i'$, no summation on i). ——— , streamwise direction; - - - - , wall-normal; ····· , spanwise. (b) Conditional probabilities based on viscoelastic stress fluctuations satisfying $|f_i| < (\max(f_i'(y)), -h \le y \le +h)$ (the lower curves show the fraction of samples satisfying this condition). Upper curves: ——— , $P(uf_x > 0)$; - - - - , $P(vf_y < 0)$; ····· , $P(wf_z < 0)$. Data obtained from simulation L100W120MC.

The most interesting aspect of polymer drag reduction is to understand how such small concentrations of microscopic molecules can drive turbulence to states like the ones depicted in Fig. 4. One simple measure of the exchange of energy between the flow and polymers is the correlation velocity-viscoelastic stress,

$$\rho_i = \frac{\overline{u_i f_i}}{u_i' f_i'} \tag{4.1}$$

as shown in Fig. 5a (the viscoelastic stress f_i is defined in Eq. 2.1). The term $\overline{u_i f_i}$ enters the transport equation for the kinetic energy and through this term only the flow can be perturbed by polymers: when ρ_i is positive, polymers tend to enhance velocity fluctuations while $\rho_i < 0$, polymers dampen velocity fluctuations.

Only results from simulation L100W120MC are plotted since all simulations show the same trends. In the near-wall region, streamwise velocity fluctuations and viscoelastic stress fluctuations are positively correlated while, for the components normal to the mean flow, they are anti-correlated. Similar results were obtained by De Angelis *et al.* (2002) at LDR. The correlations indicates that the viscoelastic stress applies some opposition control on the transverse velocity fluctuations and plays a significant role in the increase of streamwise velocity fluctuations. Away from the viscous sublayer, the maximum correlation is about ± 0.3, ruling out the possibility that polymers enhance all streamwise velocity fluctuations nor oppose all the transverse ones.

Details of the viscoelastic stress action can only be captured by using conditional statistics. In this approach, we are interested in the large fluctuations of the viscoelastic stress, f_i since energy is exchanged between polymers and turbulence through this term. The probabilities $P((uf_x)(y) > 0, y \in [-h, +h])$, $P((vf_y) < 0, y \in [-h, +h])$ and $P((wf_z)(y) < 0, y \in [-h, +h])$ are computed over samples for which $|f_i|$ is larger than the maximum of the RMS f_i' over the entire channel. Also plotted are the fractions of samples satisfying such a condition for each component. The probability that $uf_x > 0$ peaks at 80% around $y^+ = 10$, while the probabilities that $vf_y > 0$ and $wf_z > 0$ exhibit a plateau in between 70% and 80% for $y^+ > 10$. These strong probabilities suggest that large fluctuations of viscoelastic stress are almost perfectly correlated to either turbulence enhancement for the streamwise component in the near wall region or to drag

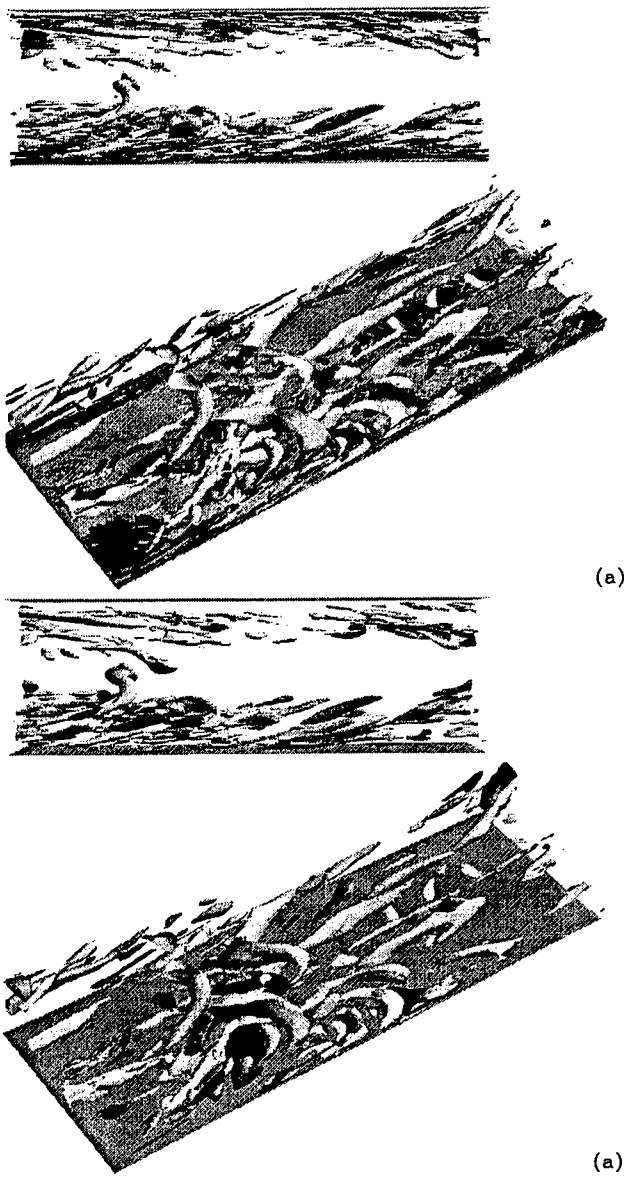


FIGURE 6. Snapshot of vortices (white isosurfaces) and isosurfaces of large viscoelastic stress fluctuations: blue, negative fluctuations; red, positive fluctuations. Fig. (a): streamwise viscoelastic stress; Fig. (b): wall-normal viscoelastic stress. The flow is from left to right, the bottom views show the lower half a portion of simulation L100W120LC, at $DR = 60\%$.

reduction for the transverse components in most of the channel. However it appears that large fluctuations of f_x away from the wall are highly anti-correlated with u fluctuations, indicating that where the mean shear is weak, f_x behaves like f_y or f_z. The separation of the drag reducing and drag enhancing activities between velocity components was also put forward by the numerical experiments (Dubief & Lele 2001) which isolated the action of polymers in the buffer region and also suggested that the drag reducing activ-

ity of the FENE-P equations comes predominantly from the wall-normal and spanwise components.

Fig. 6 illustrates the instantaneous location of large fluctuations of f_x and f_y. The view from the side gives an idea of the preferred location of these fluctuations while the view from the top indicates the relation between polymers and vortices. As observed in the correlation of u and f_x, a major portion of the large fluctuations is confined at the wall (Fig. 6a). Their occurrence is somewhat related with the presence of quasi-streamwise vortices in the buffer region and even above. The near-wall activity of the streamwise viscoelastic stress has just been shown (Fig. 5) to enhance streamwise velocity fluctuations however, away from the wall, the regions of large fluctuations are attached to the vortices in a similar way as the wall-normal viscoelastic stress (Fig. 6b). Large wall-normal viscoelastic stress appear to be produced exclusively around vortices and the same occurs for the spanwise fluctuations (not shown here). This observation holds regardless of the amount of *DR*. These visualizations show the strong correlation which exists between drag reducing polymer action and vortices.

5. Conclusion

A set of four viscoelastic simulations has been investigated, all in the high drag reduction regime, *i.e* change of slope in the log-law of the mean velocity profile and a significant decrease of Reynolds shear stress. Numerical experiment were performed in a minimal channel to show that the basic topology of drag reduced flow can be contained in a small computational domain. In its present form and for the polymer parameters under consideration, it appears that the FENE-P model does not produce enough stress to damp large scale structures in the outer region of the large domain. As drag reduction increases, the polymer stress is found to contribute as much as, and even in the minimal channel larger than, the Reynolds shear stress to the stress balance in the near-wall region. Therefore the polymer stress is essential for sustaining the weak turbulent state of MDR. The injection of energy from the polymers to the flow is confined to the very near wall region and it affects the streamwise velocity component only. Lastly, it is shown that the drag reducing activity targets exclusively the near-wall vortices, main source of turbulent friction drag (Kravchenko *et al.* 1993) and key ingredient of the autonomous regeneration cycle of near-wall turbulence (Jiménez & Pinelli 1999).

The support of DARPA and its project manager, Dr. Lisa Porter, are gratefully acknowledged. This work is sponsored by Defense Advanced Research Projects Agency, Advanced Technology Office, Friction Drag Reduction Program, DARPA order No.: K042/31, K042/13,N115/00. Issued by DARPA/CMO, Contract No.: MDA972-01-C-0041.

REFERENCES

De Angelis, E., Casciola, C. M. & Piva, R. 2002 DNS of wall turbulence: dilute polymers and self-sustaining mechanisms. *Comp. and Fluids* **31**, 495–507.

Dimitropoulos, C. D., Sureshkumar, R. & Beris, A. N. 1998 Direct numerical simulations of viscoelastic turbulent channel flow exhibiting drag reduction: Effect of variation rheological parameters. *J. Non-Newtonian Fluid Mech.* **79**, 433–468.

Dubief, Y. & Delcayre, F. 2000 On coherent-vortex identification in turbulence. *J. of Turbulence* **1** (011).

DUBIEF, Y. & LELE, S. K. 2001 Direct numerical simulation of polymer flow. In *Annual Research Briefs*, pp. 197–208. Center For Turbulence Research.

DUBIEF, Y., TERRAPON, V. E., SHAQFEH, E. S. G., LELE, S. K. & MOIN, P. 2003 The small-scale behavior of the FENE-P model in turbulent flow. *J. Comp. Phys.* To be submitted. extended version of: Dubief, Y. 2002 Direct numerical simulation of polymer flow. In *Annual Research Briefs*, pp. 197-208, Center For Turbulence Research.

JIMÉNEZ, J. & MOIN, P. 1991 The minimal flow unit in near-wall turbulence. *J. Fluid Mech.* **225**, 213–240.

JIMÉNEZ, J. & PINELLI, A. 1999 The autonomous cycle of near-wall turbulence. *J. Fluid Mech.* **389**, 335–359.

KRAVCHENKO, A. G., CHOI, H. & MOIN, P. 1993 On the relation of near-wall streamwise vortices to wall skin friction in turbulent boundary layers. *Phys. Fluids* **A 5** (12), 3307–3309.

MIN, T., YOO, J. Y. & CHOI, H. 2001 Effect of spatial discretization schemes on numerical solutions of viscoelastic fluid flows. *J. Non-Newtonian Fluid Mech.* **100**, 27–47.

PTASINSKI, P. K., NIEUWSTADT, F. T. M., VAN DEN BRULE, B. H. A. A. & HULSEN, M. A. 2001 Experiments in turbulent pipe flow with polymer additives at maximum drag reduction. *Flow, Turbulence and Combustion* **66** (2), 159–182.

SIBILLA, S. & BARON, A. 2002 Polymer stress statistics in the near-wall turbulent flow of a drag-reducing solution. *Phys. Fluids* **14** (3), 1123–1136.

SURESHKUMAR, R., BERIS, A. N. & HANDLER, R. A. 1997 Direct numerical simulations of turbulent channel flow of a polymer solution. *Phys. Fluids* **9** (3), 743–755.

TERRAPON, V. E., DUBIEF, Y., MOIN, P. & SHAQFEH, E. S. G. 2003 Brownian dynamics simulation in a turbulent channel flow. In *2003 Joint ASME/JSME Fluids Engineeing Symposium on Friction Drag Reduction*. Honolulu, Hawaii, USA.

VIRK, P. S. & MICKLEY, H. S. 1970 The ultimate asymptote and mean flow structures in Tom's phenomenon. *Trans. ASME E: J. Appl. Mech.* **37**, 488–493.

WARHOLIC, M. D., MASSAH, H. & HANRATTY, T. J. 1999 Influence of drag-reducing polymers on turbulence: effects of Reynolds number, concentration and mixing. *Exp. Fluids* **27**, 461–472.

WHITE, C. M., SOMANDEPALLI, V. S. R. & MUNGAL, M. G. 2003 The turbulence structure of drag reduced boundary layer flow. *Exp. Fluids* To be published.

MHD turbulence at moderate magnetic Reynolds number

By B. Knaepen, S. Kassinos† AND D. Carati‡

1. Introduction

1.1. *Motivation and objectives*

Magnetohydrodynamics applies to many conductive fluid and plasma flows encountered in nature and in industrial applications. In numerous circumstances, the flow is subject to a strong mean magnetic field. This happens in the earth's liquid core and is ubiquitous in solar physics for topics like sunspots, solar flares, solar corona, solar wind etc. Mean magnetic fields play an important role on even larger scales, for instance in the dynamics of the interstellar medium. Among the industrial applications involving applied external magnetic fields are drag reduction in duct flows, design of efficient coolant blankets in tokamac fusion reactors, control of turbulence of immersed jets in the steel casting process and advanced propulsion and flow control schemes for hypersonic vehicles.

Depending on the application, the magnetic Reynolds number, R_m, can vary tremendously. In astrophysical problems, R_m can be extremely high as a result of the dimensions of the objects studied. On the contrary, for most industrial flows involving liquid metal, R_m is very low, usually less than 10^{-2}. When an external magnetic field is present, it is customary at such low values of R_m to make use of the so-called quasi-static (QS) approximation. In this approximation, induced magnetic fluctuations are much smaller than the applied magnetic field and the overall magnetic effect amounts to adding in the Navier-Stokes equations an extra damping term which only affects Fourier modes having a component parallel to the magnetic field (more details below). The derivation of the QS approximation involves taking the limit of vanishing R_m and its domain of validity is thus an interesting question. Indeed certain applications, such as advanced schemes for the control of magnetogasdynamic flows around hypersonic vehicles, involve values of R_m of the order 1 to 10. It is thus valuable to possess reliable approximations in this regime that can be used in place of the full non-linear MHD.

The limit of vanishing R_m (with mean magnetic field) has been the subject of several theoretical studies in the past. In Lehnert (1955) the author concentrates on the final period of decay of a convective fluid governed by the completely linearized MHD equations ($Re \ll 1$, $R_m \ll 1$). The suppression of turbulence by a magnetic field was studied in Moffatt (1967) ($Re \gg 1$, $R_m \ll 1$) again using linearized equations. In short, both works focus on the time evolution of the energy of the Fourier modes as a function of their wave vectors. Using prescribed energy spectra, Moffatt (1967) also obtains global energy decay rates. Another theoretical investigation relevant to the present study is the work of Davidson (1995). In that article, the author derives in the quasi-static framework the conservation of momentum and angular momentum parallel to the direction of the

† Department of Mechanical and Manufacturing Engineering, University of Cyprus, 75 Kallipoleos, Nicosia 1678, Cyprus

‡ Universté Libre de Bruxelles, Statistical and Plasma Physics, CP231, Boulevard du Triomphe, Campus Plaine, 1050 Brussels, Belgium.

magnetic field (neglecting viscous dissipation). Focusing on jets and vortices, the author then describes how the flow structures need to elongate in the direction of the magnetic field in order to lower their energy loss while satisfying the above conservation laws. The elongation of structures in the direction of the magnetic field was also studied earlier in Sommeria & Moreau (1982) however in the context of linearized equations.

To our knowledge, the first numerical study of MHD turbulence in the regime $R_m \ll 1$ is due to Schumann (1976). All the simulations in that work were done using a modified 3D spectral code implementing the QS approximation. However, due to the computer resources available at that time, the resolution of the simulations was limited to 32^3. The numerical experiment of Schumann (1976) reproduces the thought experiment described in Moffatt (1967) in which an initially homogeneous isotropic flow is suddenly subjected to an applied external magnetic field. A quantitative description of the magnetic damping and building of anisotropy is presented as well as the dependence of the results on the presence or not of the non-linear term in the Navier-Stokes equation. Again considering the QS approximation, the case of forced turbulence in a 3D periodic domain has first been studied in Hossain (1991) and more recently in Zikanov & Thess (1998).

Performing FMHD simulations in the limit of low R_m is impractical. Aside from the increased complexity arising from having to carry a separate evolution equation for the magnetic field, the main problem lies in the time-scales involved in the problem. Indeed at vanishing magnetic Reynolds number, the magnetic diffusion time-scale tends to zero. The only possibility in that case is to resort to the QS approximation for which this time-scale is not explicitly relevant. Simulations of FMHD have thus been restricted so far to cases where the magnetic and kinetic time-scales are of the same order. This is the case when the magnetic Prandtl number (see below) is close to 1. Among the numerous previous numerical studies of MHD in this regime, we mention the work of Oughton *et al.* (1994) which is the most relevant to the present discussion. In that work, the authors consider the same 3D periodic geometry with an applied external magnetic field as in Schumann (1976).

In the present article we will consider the decay of MHD turbulence under the influence of a strong external magnetic field at moderate magnetic Reynolds numbers. Typical values of R_m that are considered here range from $R_m \sim 0.1$ to $R_m \sim 20$. As a comparison, the initial kinetic Reynolds number common to all our simulations is $Re_L = 199$. This means that the range of Prandtl numbers explored is 5×10^{-4} to 10^{-1}. Our motivation is mainly to exhibit how the transition from the QS approximation to FMHD occurs. At the lowest values of R_m studied here, the QS approximation is shown to model the flow faithfully. However, for the higher values of R_m considered, it is clearly inadequate but can be replaced by another approximation which will be referred to as the Quasi-Linear (QL) approximation. Another objective of the present study is to describe how variations in the magnetic Reynolds number (while maintaining all other parameters constant) affect the dynamics of the flow. This complements past studies where variations in either the strength of the external magnetic field or the kinetic Reynolds number were considered.

This article is organized as follows. In section 2 we recall the definition of the quasi-static approximation. Section 3 is devoted to the description of the numerical experiments performed using the quasi-static approximation and full MHD. In section 4 we describe the quasi-linear approximation and test it numerically against full MHD. A concluding summary is given in section 5.

2. MHD equations in the presence of a mean magnetic field

2.1. *Dimensionless parameters*

Two dimensionless parameters are usually introduced to characterize the effects of a uniform magnetic field applied to unstrained homogeneous turbulence in an electrically conductive fluid. They are the magnetic Reynolds number R_m and the interaction number N (also known as the Stuart number):

$$R_m \equiv \frac{vL}{\eta} = (\frac{L^2}{\eta})/(\frac{L}{v}), \quad N \equiv \frac{\sigma B^2 L}{\rho v} = \frac{\tau}{\tau_m}. \tag{2.1}$$

In the above expressions, $v = \sqrt{\langle u_i u_i \rangle /3}$ is the r.m.s. of the fluctuating velocity u_i; L is the integral length scale of the flow; $\eta = 1/(\sigma\mu)$ is the magnetic diffusivity where σ is the electric conductivity of the fluid, and μ is the fluid magnetic permeability; ρ is the fluid density and B is the strength of the applied external magnetic field. The magnetic Reynolds number represents the ratio of the characteristic time scale for diffusion of the magnetic field L^2/η to the time scale of the turbulence $\tau = L/v$. Related to R_m, one can also define a magnetic Prandtl number representing the ratio of R_m to the hydrodynamic Reynolds number Re_L,

$$P_m \equiv \frac{\nu}{\eta} = \frac{R_m}{Re_L}, \qquad Re_L = \frac{vL}{\nu}. \tag{2.2}$$

The interaction number N represents the ratio of the large-eddy turnover time τ to the Joule time $\tau_m = \rho/(\sigma B^2)$, i.e. the characteristic time scale for dissipation of turbulent kinetic energy by the action of the Lorentz force (Davidson 2001). N can be viewed as a measure of the ability of an imposed magnetic field to drive the turbulence to a two-dimensional three-component state. Indeed, under the continuous action of the Lorentz force, energy becomes increasingly concentrated in modes independent of the coordinate direction aligned with **B**. As a two-dimensional state is approached, Joule dissipation decreases because fewer and fewer modes with gradients in the direction of **B** are left available. In addition, the tendency towards two-dimensionality and anisotropy is continuously opposed by non-linear angular energy transfer from modes perpendicular to **B** to other modes, which tends to restore isotropy. If N is larger than some critical value N_c, the Lorentz force is able to drive the turbulence to a state of complete two-dimensionality. For smaller N, the Joule dissipation is balanced by non-linear transfer before complete two-dimensionality is reached. For very small N, the anisotropy induced by the Joule dissipation is negligible.

2.2. *The Quasi-Static approximation*

If the external magnetic field B_i^{ext} is explicitly separated from the fluctuations b_i, the MHD equations can be written as

$$\partial_t u_i = -\partial_i(p/\rho) - u_j\partial_j u_i + \frac{1}{(\mu\rho)}(B_j^{ext} + b_j)\partial_j(B_i^{ext} + b_i) + \nu\Delta u_i, \tag{2.3}$$

$$\partial_t(B_i^{ext} + b_i) = -u_j\partial_j(B_i^{ext} + b_i) + (B_j^{ext} + b_j)\partial_j u_i + \eta\Delta(B_i^{ext} + b_i), \tag{2.4}$$

where p is the sum of the kinematic and magnetic pressures and ν is the kinematic viscosity. Since we consider initially isotropic, freely decaying homogeneous turbulence there is no mean velocity field.

Also, the external magnetic field is taken to be homogeneous and stationary. Therefore,

Resolution	256^3
Box size ($l_x \times l_y \times l_z$)	$2\pi \times 2\pi \times 2\pi$
Rms velocity	1.76
Viscosity	0.006
Integral length-scale ($3\pi/4 \times (\int \kappa^{-1}E(\kappa)d\kappa / \int E(\kappa)d\kappa)$)	0.679
$Re = uL/\nu$	199
Dissipation (ϵ)	8.39
Dissipation scale ($\gamma = (\nu^3/\epsilon)^{1/4}$))	0.0127
$k_{max}\gamma$	1.62
Microscale Reynolds number ($R_\lambda = \sqrt{15/(\nu\epsilon)}u^2$)	53.5
Eddy turnover time ($\tau = (3/2)u/\epsilon$))	0.554

TABLE 1. Turbulence characteristics of the initial velocity field. All quantities are in MKS units.

(2.3) and (2.4) reduce to

$$\partial_t u_i = -\partial_i(p/\rho) - u_j\partial_j u_i + \frac{1}{(\mu\rho)}b_j\partial_j b_i + \frac{1}{(\mu\rho)}B_j^{ext}\partial_j b_i + \nu\Delta u_i, \tag{2.5}$$

$$\partial_t b_i = -u_j\partial_j b_i + b_j\partial_j u_i + B_j^{ext}\partial_j u_i + \eta\Delta b_i. \tag{2.6}$$

As pointed out in Roberts (1967), this system can be simplified considerably for flows at low magnetic Reynolds numbers. Using a Fourier representation for u_i one has in this limit,

$$\partial_t u_m(\mathbf{k},t) = -ik_m p'(\mathbf{k},t) - [u_j\partial_j u_i]_m(\mathbf{k},t) - \sigma\frac{(\mathbf{B}^{ext}\cdot\mathbf{k})^2}{\rho k^2}u_m(\mathbf{k},t) - \nu k^2 u_m(\mathbf{k},t), \tag{2.7}$$

where $p' = p/\rho$ and $u_m(\mathbf{k},t) = \sum u_m(\mathbf{x},t)e^{-i\mathbf{k}\cdot\mathbf{x}}$. Thus one can take into account the effect of the magnetic on the velocity field through a damping term and not solve explicitely the evolution equation for the magnetic fluctuations.

In the next sections, we test the QS approximation by comparing its predictions to those obtained using the full MHD equations (2.5) and (2.6).

3. Numerical Results: QS vs. FMHD

3.1. *Parameters*

To test the domain of validity of the QS approximation, we have used two different pseudo-spectral codes. The first one simulates the full MHD equations (2.5) and (2.6), while the second one simulates (2.7). All the runs presented here have a resolution of 256^3 Fourier modes in a $(2\pi)^3$ computational domain.

The initial condition for the velocity field is common to both codes. It consists of a developed turbulence field that is adequately resolved in the computational domain adopted. Some of its characteristics are listed in table 1. For the full MHD case, an initial condition for b_i has to be chosen at $t = t_0$. Here we have made the choice $b_i(t_0) = 0$. In other words, our simulations describe the response of an initially non-magnetized turbulent conductive fluid to the application of a strong magnetic field. The corresponding completely-linearized problem has been described in detail in Moffatt (1967). For the QS

#	η	B_A^{ext}	$N(t_0)$	$R_m(t_0)$
1	11.95	5.57	1	0.1
2	0.239	0.787	1	5.0
3	0.119	.557	1	10.0
4	0.0597	0.394	1	20.0
5	11.95	17.6	10	0.1
6	0.239	2.49	10	5.0
7	0.119	1.76	10	10.0
8	0.0597	1.24	10	20.0

TABLE 2. Summary of the parameters for the different runs performed

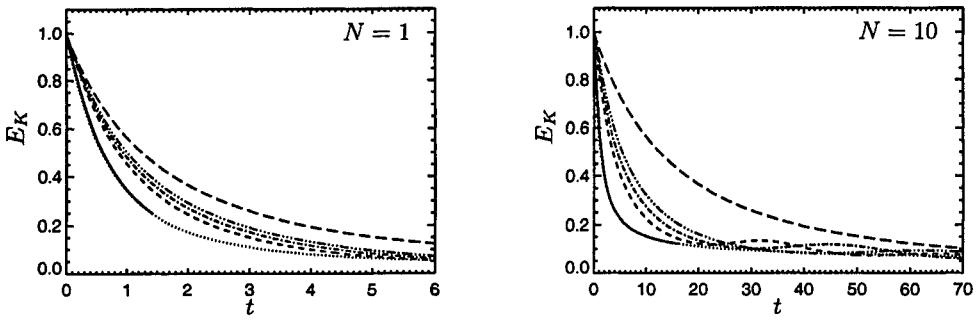


FIGURE 1. Evolution with time of the kinetic energy at different Stuart numbers and magnetic Reynolds numbers. ····· QS approximation; ——— $R_m = 0.1$; ------ $R_m = 5$; -·-· $R_m = 10$; —·—· $R_m = 20$; — — — $B^{ext} = 0$.

approximation case, an initial condition for b_i is of course not required since the equation for the velocity field is completely closed.

In order to distinguish between our numerical runs, we will vary the values of the interaction parameter and the magnetic Reynolds number (at $t = t_0$). When these two quantities are set, the only free parameters in the evolution equations (2.5), (2.6) and (2.7) are completely determined, i.e.:

$$B_A^{ext} = \frac{Nv^2}{R_m}, \quad \eta = \frac{vL}{R_m}, \tag{3.1}$$

where B_A^{ext} is the external magnetic field strength in Alfven units $B_A^{ext} = B^{ext}/\sqrt{\mu\rho}$ and the values of v and L are listed in table 1. The values of R_m and N for all our runs are listed in table 2 along with the corresponding values of η and B_A^{ext}.

3.2. *Results*

In this section we present some results obtained by performing the simulations detailed in section 3.1.

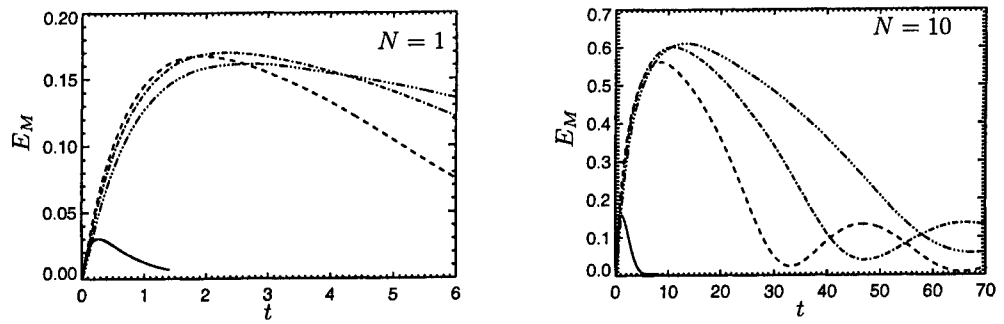


FIGURE 2. Evolution with time of the magnetic energy computed from (3.3). —— $R_m = 0.1$; ------ $R_m = 5$; -·-· $R_m = 10$; -···- $R_m = 20$

3.2.1. *Kinetic energy decay*

In fig. 1 we plot the time evolution of the normalized kinetic energy,

$$E_K = \frac{1}{E_K(0)} \int d\mathbf{x} \frac{1}{2} u_i(\mathbf{x}) u_i(\mathbf{x}). \tag{3.2}$$

In this and subsequent figures, time has been non-dimensionalized using the Joule time-scale. Keeping N constant, it is clear from the figure that as the magnetic Reynolds number is decreased, the decays converge to the quasi-static limit (dotted curve). At $R_m = 0.1$, FMHD and the QS approximation are barely distinguishable for the cases run. As expected, the discrepancy between FHMD and the QS approximation is quite severe at intermediate values of the R_m. We also note here the presence of oscillations in the kinetic energy at long times for the case $N = 10$. Their origin is well known (Lehnert 1955; Moffatt 1967) and result from the laminarization of the flow for long times. In that case the MHD equations (2.5) and (2.6) reduce to their linear versions and become (in Fourier space) a system of linear oscillators coupled through the external magnetic field. In both figures, the case $B^{ext} = 0$ has been included to emphasize the role of the magnetic field in the other runs.

3.2.2. *Magnetic energy evolution*

The next diagnostic we examine is the evolution of the energy contained in the magnetic fluctuations. This quantity is defined through,

$$E_M = \int d\mathbf{k} \frac{1}{2} |b_i(\mathbf{k}, t)|^2. \tag{3.3}$$

and its time evolution is presented in Fig. 2. After some time, the magnetic energies all reach their maximum value and then start to decrease. The rate of decay increases at lower magnetic Reynolds numbers since in the limit chosen, $\eta = vL/R_m$. Related to the oscillations in the kinetic energy we observe for $N = 10$ some oscillations in the magnetic energy at long times.

3.2.3. *Anisotropy*

A characteristic feature of MHD flows subject to a strong external magnetic field is the appearance of a strong anisotropy in the flow. In the QS approximation this is easily seen by observing that in eq. (2.7) only Fourier modes with wave vectors having a nonzero projection onto B_i^{ext} are affected by the extra Joule damping. In order to quantify the

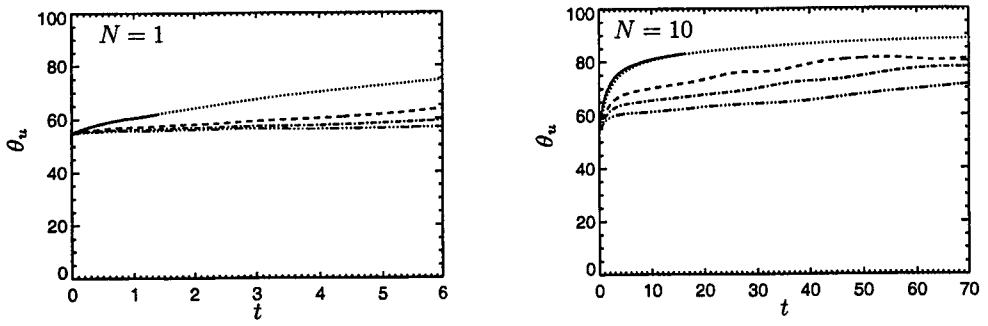


FIGURE 3. Anisotropy angle θ_u computed from (3.4). ····· QS approximation; —— $R_m = 0.1$; ------ $R_m = 5$; -·-· $R_m = 10$; -···- $R_m = 20$.

anisotropy we follow the approach of Shebalin *et al.* (1983) and Oughton *et al.* (1994) by introducing the anisotropy angles,

$$\tan^2\theta_u = \frac{\sum k_\perp^2 \|u_i(\mathbf{k})\|^2}{\sum k_z^2 \|u_i(\mathbf{k})\|^2}, \tag{3.4}$$

$$\tan^2\theta_b = \frac{\sum k_\perp^2 \|b_i(\mathbf{k})\|^2}{\sum k_z^2 \|b_i(\mathbf{k})\|^2}, \tag{3.5}$$

where $k_\perp = k_x^2 + k_y^2$ and the summations are extended to all values of $\mathbf{k}$.

When the flow is completely isotropic, one has $\tan^2\theta_u = 2$ implying $\theta_u \simeq 54.7°$. If the flow becomes independent of the z-direction then $\tan^2\theta_u \to \infty$ or equivalently $\theta_u \to 90°$. Figure 3 shows the evolution with time of θ_u for the different runs. At $N = 1$ the anisotropy is only important for the QS and $R_m = 0.1$ runs. For $N = 10$ all the runs become highly anisotropic.

The initial anisotropy in the magnetic field can also be computed exactly. At time $t_0 + \Delta t$ ($\Delta t \ll 1$), $b_i(\mathbf{k})$ is given by $b_i(\mathbf{k}, t_0 + \Delta t) = iB_z^{ext} k_z u_i(\mathbf{k}, t_0)\Delta t$. Using this form and the fact that u_i is initially homogeneous and isotropic one gets after some direct calculations,

$$\tan^2\theta_b(t_0 + \Delta t) = \frac{2}{3}, \text{ i.e., } \theta_b(t_0 + \Delta t) \simeq 39.2°. \tag{3.6}$$

Figure 4 shows the evolution with time of θ_b for the different runs. Both plots exhibit surprising behavior. In the case $N = 1$, one would expect θ_b to remain close to its initial value since the velocity field remains largely isotropic (as it is at the beginning of the simulation). Instead, θ_b evolves to a value compatible with an isotropic magnetic field. This is also the case for the runs at $N = 10$ although there the velocity field clearly evolves to an anisotropic state.

4. The Quasi-Linear approximation

4.1. *Governing equations*

The preceding section indicates that for our numerical simulations at magnetic Reynolds numbers of the order 10^{-1} the QS approximation and FMHD produce nearly identical results. For higher values of R_m the QS approximation is not valid and has to be replaced

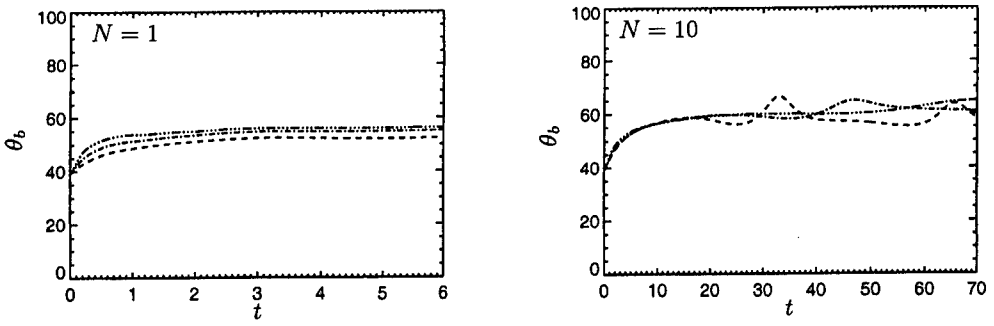


FIGURE 4. Anisotropy angle θ_b computed from (3.5). ..... QS approximation; —— $R_m = 0.1$; ------ $R_m = 5$; -·-· $R_m = 10$; —···— $R_m = 20$.

to predict the flow accurately. Since magnetic fluctuations remain small in all the runs performed, it is natural to still consider a linearized induction equation. We thus consider here an intermediate approximation which is defined by the following simplified MHD equations:

$$\partial_t u_i = -\partial_i(p/\rho) - u_j \partial_j u_i + \frac{1}{(\mu\rho)} B_j^{ext} \partial_j b_i + \nu \Delta u_i, \tag{4.1}$$

$$\partial_t b_i = B_j^{ext} \partial_j u_i + \eta \Delta b_i. \tag{4.2}$$

This approximation will be referred to as the *quasi-linear* (QL) *approximation* since only the non-linear terms involving the magnetic field are discarded whereas the non-linear convective term in the velocity equation is retained. Of course, if $\partial_t b_i$ is neglected in (4.2) one immediately recovers the quasi-static approximation.

4.2. *Results*

In order to compare the QL approximation with full MHD, we have performed the same numerical simulations as described in section 3, but this time using (4.1) and (4.2) instead of the QS approximation.

4.2.1. *Kinetic energy decay*

In fig. 5 we present the time history of the kinetic energy (as defined by (3.2)) obtained from both FMHD and the QL approximation. For reference, we have also included the predictions obtained using the QS approximation. For $N = 1$, the QL approximation and FMHD agree nearly perfectly for all values of the magnetic Reynolds number. For $N = 10$, the agreement is still very good.

4.2.2. *Magnetic energy evolution*

Figure 6 represents the time evolution of the energy of the magnetic fluctuations (defined by (3.3)) for the different runs. For $N = 1$ there is a systematic overestimate of the energy by the QL approximation which (as expected) increases with the magnetic Reynolds number. Contrary to the predictions of the kinetic energy, the performance of the QL approximation is better here when $N = 10$. Even at $R_m = 20$, the agreement between the QL approximation and FMHD is very good.

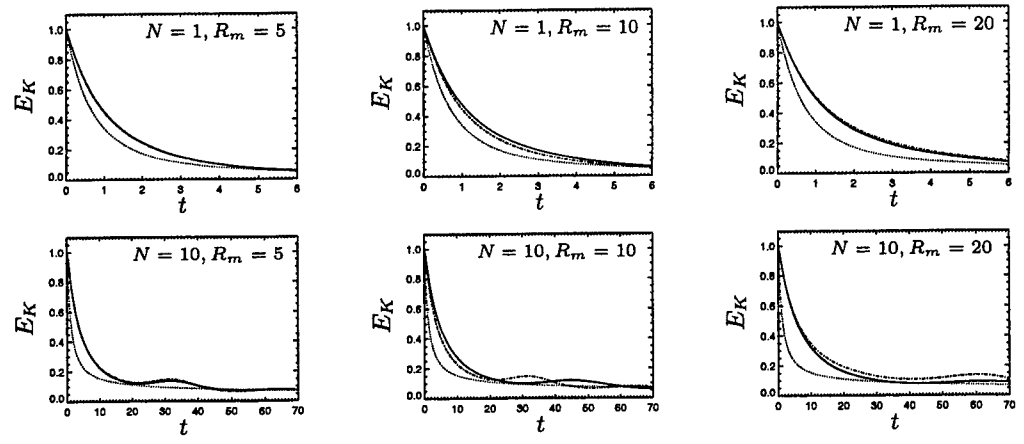


FIGURE 5. Evolution with time of the kinetic energy. —— FMHD; -·-· QL approximation; ····· QS approximation.

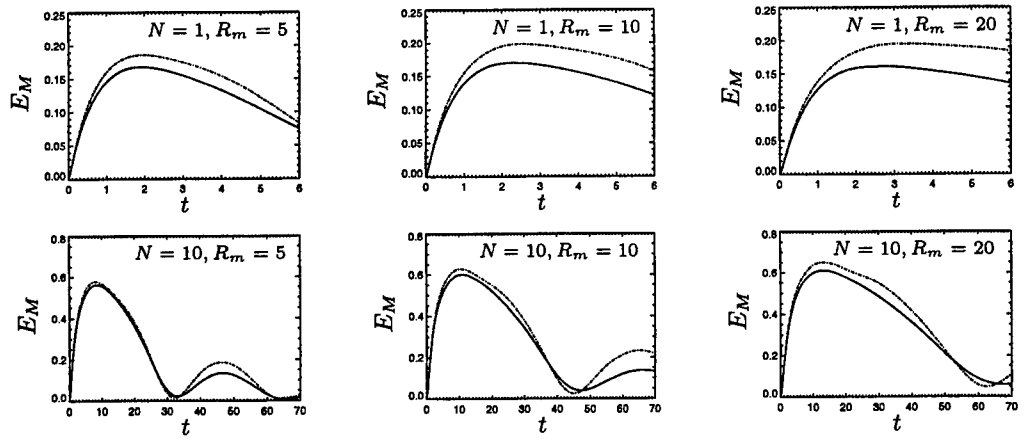


FIGURE 6. Evolution with time of the magnetic energy. —— FMHD; -·-· QL approximation.

4.2.3. *Anisotropy*

In fig. 7, the anisotropy angle θ_u computed from the QL approximation and FMHD is displayed. For reference we have also included the anisotropy evolutions predicted using the QS approximation, which as expected are inadequate especially for $R_m = 10$ and $R_m = 20$. In the runs with $N = 1$, the anisotropy predicted by the QL approximation is always more pronounced than for FMHD. For the runs at $N = 10$, the same remark holds for the beginning of the decay. After a certain amount of time, the trend inverses and the anisotropy is more pronounced in the case of FMHD. This appears to be due to a rapid saturation of anisotropy in the QL runs.

The comparison of the anisotropy angles θ_b are presented in fig. 8. Here the trend is given by an underestimate of θ_b by the QL approximation. The discrepancy is somewhat more important for the runs where $N = 1$.

The initial trends observed for both θ_u and θ_b are to be expected. Indeed, it is clear that the additional non-linear terms present in the FMHD equations tend to restore isotropy.

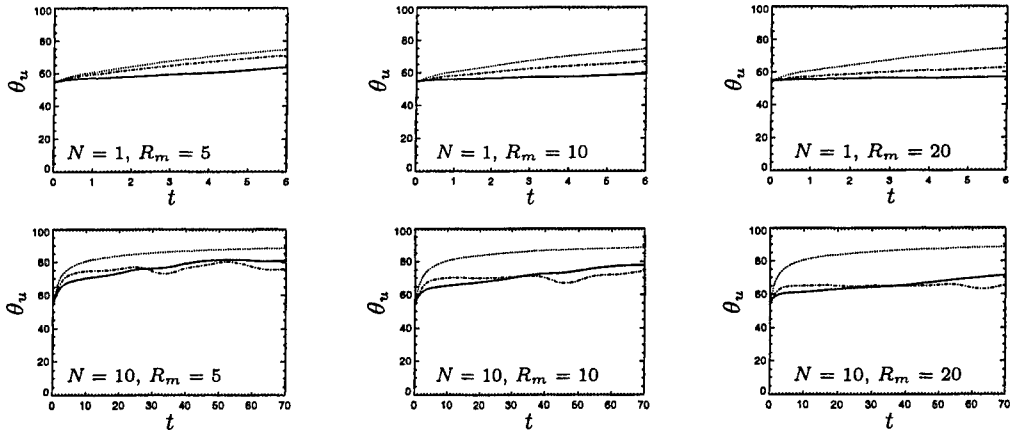


FIGURE 7. Evolution with time of the anisotropy angle θ_u. ——— FMHD; -·-·- QL approximation; ····· QS approximation.

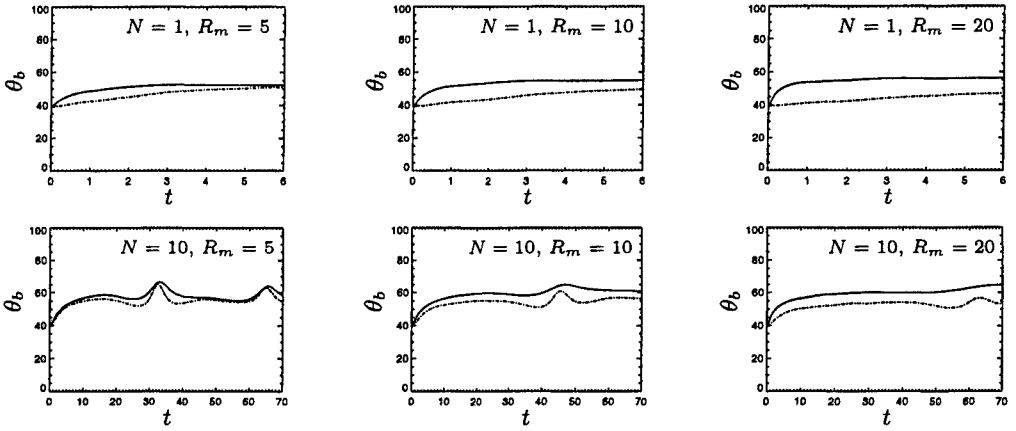


FIGURE 8. Evolution with time of the anisotropy angle θ_b. ——— FMHD; -·-·- QL approximation.

This effect will be more pronounced at the beginning of the decay when the flow is more turbulent. In the case of θ_u it is therefore natural to observe an initial overestimate of θ_u by the QL approximation. Similarly, we know from FMHD results discussed earlier that θ_b starts from an initial value of $\simeq 39.2^0$ and evolves progressively towards values close to the isotropic value of 54.7^0. This trend should be slower in the QL case because of the absence of the non-linear terms and this is exactly what is observed in fig. 8.

5. Conclusions and future plans

The Quasi-Static (QS) approximation offers a valuable engineering approximation for the prediction of MHD flows at small magnetic Reynolds numbers $R_m \ll 1$. However, important technological applications, such as advanced propulsion and flow control schemes for hypersonic vehicles, involve MHD and MGD flows at moderate magnetic Reynolds numbers $1 \lesssim R_m \lesssim 20$. In order to devise successful schemes for the prediction of these technological flows we need to understand better the intermediate regime that bridges

the domain where the QS approximation is valid and the high-R_m regime, where full nonlinear MHD (FMHD) is the only resort.

By studying the case of decaying homogeneous MHD turbulence, we have established that the Quasi-Static (QS) approximation is valid for $R_m \lesssim 1$, but progressively deteriorates as R_m is increased beyond 1. The magnetic Stuart number does not seem to have a strong effect on the accuracy of the QS approximation. That is, at a given R_m, the accuracy of the QS approximation is roughly the same for $N = 1$ as it is for $N = 10$.

We have studied another approximation, the *QL approximation*, for use at higher R_m. As with the QS approximation, this approximation assumes small magnetic fluctuations, but it resolves the time dependence of these fluctuations explicitly. The QL approximation, as we expected when we proposed it, performs like the QS approximation for $R_m \lesssim 1$, but has the advantage that it retains good agreement with FMHD for $1 \lesssim R_m \lesssim 20$. It should be noted that $R_m = 20$ is the highest value of the magnetic Reynolds number that we have tested during this effort. Therefore, our numerical simulations indicate that the QL approximation should be adopted in place of the QS approximation for flows with a moderate value of the magnetic Reynolds number ($0 \lesssim R_m \lesssim 20$).

We are currently engaged in the development of structure-based closures of the QL approximation for homogeneous turbulence in a conductive fluid subject to mean deformation and a uniform external magnetic field. This effort builds on earlier work that dealt with the modeling of decaying homogeneous MHD turbulence.

Acknowledgements

The authors are grateful G. Burton for his comments on this manuscript and to the Center for Turbulence Research for hosting and providing financial support for part of this work during the 2002 Summer Program. S.K. wishes to acknowledge partial support of this work by AFOSR. B.K. and D.C. are researchers of the Fonds National pour la Recherche Scientifique (Belgium). This work has also been supported in part by the Communauté Française de Belgique (ARC 02/07-283) and by the contract of association EURATOM - Belgian state. The content of the publication is the sole responsibility of the authors and it does not necessarily represent the views of the Commission or its services.

REFERENCES

DAVIDSON, P. 2001 *An Introduction to Magnetohydrodynamics*. Cambridge University Press.

DAVIDSON, P. A. 1995 Magnetic damping of jets and vortices. *J. Fluid Mech.* **299**, 153–186.

HOSSAIN, M. 1991 Inverse energy cascades in three dimensional turbulence. *Phys. Fluids B* **3** (3), 511–514.

KASSINOS, S. C. & REYNOLDS, W. C. 1994 A structure-based model for the rapid distortion of homogeneous turbulence. *Tech. Rep.* TF-61. Mechanical Engineering Dept.

KASSINOS, S. C. & REYNOLDS, W. C. 1999 Structure-based modeling for homogeneous MHD turbulence. In *Annual Research Briefs 1999*, pp. 301–315. Stanford University and NASA Ames Research Center: Center for Turbulence Research.

KASSINOS, S. C., REYNOLDS, W. C. & ROGERS, M. M. 2001 One-point turbulence structure tensors. *J. Fluid Mech.* **428**, 213–248.

LEHNERT, B. 1955 The decay of magneto-turbulence in the presence of a magnetic field and coriolis force. *Quart. Appl. Math.* **12** (4), 321–341.

LUMLEY, J. L. 1978 Computational modeling of turbulent flows. *Ad. Appl. Mech.* **18**, 123.

MOFFATT, H. K. 1967 On the suppression of turbulence by a uniform magnetic field. *J. Fluid Mech.* **28**, 571–592.

OUGHTON, S., PRIEST, E. & MATTHAEUS, W. 1994 The influence of a mean magnetic field on three- dimensional magnetohydrodynamic turbulence. *J. Fluid Mech.* **280**, 95.

REYNOLDS, W. C. & KASSINOS, S. C. 1995 One-point turbulence structure tensors. *Proc. Royal Society London A* **451**, 87–104.

ROBERTS, P. H. 1967 *An Introduction to Magnetohydrodynamics*. American Elsevier Publishing Company, Inc. New York.

SCHUMANN, U. 1976 Numerical simulation of the transition from three- to two-dimensional turbulence under a uniform magnetic field. *J. Fluid Mech.* **74**, 31–58.

SHEBALIN, J. V., MATTHAEUS, W. H. & MONTGOMERY, D. 1983 Anisotropy in MHD turbulence due to a mean magnetic field. *J. Plasma Phys.* **29** (3), 525–547.

SOMMERIA, J. & MOREAU, R. 1982 Why, how, and when, MHD turbulence becomes two-dimensional. *J. Fluid Mech.* **118**, 507–518.

ZIKANOV, O. & THESS, A. 1998 Direct numerical simulation of forced MHD turbulence at low magnetic Reynolds number. *J. Fluid Mech.* **358**, 299–233.

Linearly forced isotropic turbulence

By T. S. Lundgren †

Stationary isotropic turbulence is often studied numerically by adding a forcing term to the Navier-Stokes equation. This is usually done for the purpose of achieving higher Reynolds number and longer statistics than is possible for isotropic decaying turbulence. It is generally accepted that forcing the Navier-Stokes equation at low wave number does not influence the small scale statistics of the flow provided that there is wide separation between the largest and smallest scales. It will be shown, however, that the spectral width of the forcing has a noticeable effect on *inertial range* statistics. A case will be made here for using a broader form of forcing in order to compare computed isotropic stationary turbulence with (decaying) grid turbulence. It is shown that using a forcing function which is directly proportional to the velocity has physical meaning and gives results which are closer to both homogeneous and non-homogeneous turbulence.

Section 1 presents a four part series of motivations for linear forcing. Section 2 puts linear forcing to a numerical test with a pseudospectral computation.

1. Motivation for Linear Forcing

1.1. *Linearity of energy production in non-homogeneous turbulence*

In shearflow turbulence the equation for the fluctuating part of the velocity, $\mathbf{u}'$, is

$$\frac{\partial \mathbf{u}'}{\partial t} + \overline{\mathbf{u}} \cdot \nabla \mathbf{u}' + \mathbf{u}' \cdot \nabla \overline{\mathbf{u}} + \mathbf{u}' \cdot \nabla \mathbf{u}' - \nabla \cdot \overline{\mathbf{u}'\mathbf{u}'} = -\nabla p'/\rho + \nu \nabla^2 \mathbf{u}'. \tag{1}$$

The third term on the left, $\mathbf{u}' \cdot \nabla \overline{\mathbf{u}}$ appears in the turbulent energy equation as the energy production term, $< \mathbf{u}' \cdot \nabla \overline{\mathbf{u}} \cdot \mathbf{u}' >$. (Both angle brackets and overbars are used to denote averages.) In (1) it appears as a forcing term proportional to $\mathbf{u}'$. This suggests that for isotropic homogeneous turbulence it might be appropriate to force a stationary flow with a driving term proportional to the velocity. Of course, for isotropic turbulence there is no mean velocity gradient, so the only way to have the flow be isotropic and stationary is to have the forcing be isotropic. It is proposed here to use

$$\frac{\partial \mathbf{u}}{\partial t} + \mathbf{u} \cdot \nabla \mathbf{u} = -\nabla p/\rho + \nu \nabla^2 \mathbf{u} + \mathbf{f} \tag{2}$$

with the driving force

$$\mathbf{f} = Q\mathbf{u}\,, \tag{3}$$

where Q is a constant. The prime on the velocity has been omitted here and henceforth with the understanding that $< \mathbf{u} >= 0$. The turbulent energy equation is now

$$\frac{1}{2}\frac{\partial < \mathbf{u} \cdot \mathbf{u} >}{\partial t} = -\epsilon + Q < \mathbf{u} \cdot \mathbf{u} >, \tag{4}$$

where

$$\epsilon = -\nu < \mathbf{u} \cdot \nabla^2 \mathbf{u} > \tag{5}$$

† University of Minnesota

is the mean dissipation rate and the last term could be called *isotropic turbulent production.* For *stationary* turbulence therefore (setting the time derivative to zero)

$$Q = \epsilon/3U^2 \tag{6}$$

where $U^2 =< \mathbf{u} \cdot \mathbf{u} > /3$ is the mean square of one component of the velocity. The proposal is to numerically solve

$$\frac{\partial \mathbf{u}}{\partial t} + \mathbf{u} \cdot \nabla \mathbf{u} = -\nabla p/\rho + \nu \nabla^2 \mathbf{u} + (\epsilon/3U^2)\mathbf{u} \tag{7}$$

with the objective of comparing the statistics with those of grid flow turbulence. Equation (7) has the property that the rest state is unstable to long waves. Therefore solutions cannot decay to zero but must transfer energy to shorter waves in order to dissipate energy. Some reasons are given below for expecting computational results to be comparable with experiments for inertial scales of turbulence.

1.2. *Linear forcing of the Karman-Howarth equation*

A derivation of the Karman-Howarth equation, following the steps given in detail by Landau and Lifshitz (1959), but including a forcing term as in (2), gives

$$\frac{\partial U^2}{\partial t} - \frac{1}{2}\frac{\partial B_2}{\partial t} - \frac{1}{6}\frac{1}{r^4}\frac{\partial}{\partial r} r^4 B_3 =$$

$$-\nu \frac{1}{r^4}\frac{\partial}{\partial r} r^4 \frac{\partial B_2}{\partial r} + \frac{1}{r^3}\int_0^r r^2 < \mathbf{u}(\mathbf{x_2}, t) \cdot \mathbf{f}(\mathbf{x_1}, t) + \mathbf{u}(\mathbf{x_1}, t) \cdot \mathbf{f}(\mathbf{x_2}, t) > dr \tag{8}$$

where $B_2(r,t)$ and $B_3(r,t)$ are second and third order longitudinal structure functions, $\mathbf{x_2} = \mathbf{x_1} + \mathbf{r}$ and $r = |\mathbf{r}|$. With $\mathbf{f}$ given by (3), the last term can be written

$$\frac{1}{r^3}\int_0^r 2Qr^2 R_{ii}(r,t) dr \tag{9}$$

where $R_{ij}(r,t) =< u_i(\mathbf{x_1}, t) u_j(\mathbf{x_1} + \mathbf{r}, t) >$ is the velocity correlation tensor. Since the trace of the correlation tensor is related to the second order structure function by

$$R_{ii} = 3U^2 - \frac{1}{2r^2}\frac{\partial}{\partial r} r^3 B_2 \tag{10}$$

(9) can be integrated to the form

$$2QU^2 - QB_2(r,t) \ . \tag{11}$$

Using this with Q given by (6), and dropping the time derivatives for stationary turbulence, gives the result

$$-\frac{2}{3}\epsilon + \frac{\epsilon}{3U^2} B_2 = \frac{1}{6r^4}\frac{\partial}{\partial r} r^4 B_3 - \nu \frac{1}{r^4}\frac{\partial}{\partial r} r^4 \frac{\partial B_2}{\partial r} \tag{12}$$

in which ϵ is a constant given by (5). This differs from the standard decaying version of the Karman-Howarth equation which is

$$-\frac{2}{3}\epsilon - \frac{1}{2}\frac{\partial B_2}{\partial t} = \frac{1}{6}\frac{1}{r^4}\frac{\partial}{\partial r} r^4 B_3 - \nu \frac{1}{r^4}\frac{\partial}{\partial r} r^4 \frac{\partial B_2}{\partial r} \tag{13}$$

where here ϵ is a function of *time* given by

$$\epsilon(t) = -\frac{3}{2}\frac{dU^2}{dt} \equiv \frac{15\nu}{2}\frac{d^2 B_2}{dr^2}\Big|_0 \ . \tag{14}$$

The Kolmogorov $r^{2/3}$ law may be derived from (12), by the method of matched asymptotic expansions, in a manner similar to that employed by Lundgren (2002) to get that law from (13) but without the necessity of using similarity in time. The result is the same:

$$B_2 = C_2 U^2 (r/L)^{2/3} \equiv C_2 (\epsilon r)^{2/3} \tag{15}$$

where $L = U^3/\epsilon$ and ϵ and U^2 are independent of time now.

Equation(12) can be integrated to obtain B_3 in terms of B_2, as

$$B_3 = 6\nu \frac{\partial B_2}{\partial r} - \frac{4}{5}\epsilon r + \frac{2\epsilon}{U^2}\frac{1}{r^4}\int_0^r r^4 B_2 dr \ . \tag{16}$$

Using (15) for B_2 gives the simple result

$$\frac{B_3}{U^3} = \frac{4C_2}{R_L}\left(\frac{r}{L}\right)^{-1/3} - \frac{4}{5}\left(\frac{r}{L}\right) + \frac{6C_2}{17}\left(\frac{r}{L}\right)^{5/3} \ . \tag{17}$$

This may be rewritten using the Taylor microscale λ to scale r:

$$B_3 = -\frac{4}{5}\epsilon r\left(1 - R_\lambda^{-2/3}\left(2.678C_2\left(\frac{r}{\lambda}\right)^{2/3} + 2.029C_2\left(\frac{r}{\lambda}\right)^{-4/3}\right)\right) \tag{18}$$

Here $R_L = UL/\nu$; $R_L = R_\lambda^2/15$ relates R_λ and R_L and $\lambda/L = 15/R_\lambda$ relates λ and L. The corresponding result for decaying turbulence (Lundgren 2002; Lindborg 1999) is almost the same:

$$B_3 = -\frac{4}{5}\epsilon r\left(1 - R_\lambda^{-2/3}\left(2.678\left(\frac{2}{3}\,\frac{1+n}{n}\right)C_2\left(\frac{r}{\lambda}\right)^{2/3} + 2.029C_2\left(\frac{r}{\lambda}\right)^{-4/3}\right)\right) \tag{19}$$

where n is the energy decay exponent ($U^2 \propto t^{-n}$). Equations (18) and (19) would be exactly the same if $n = 2$, which is not a realistic decay exponent; $n = 1.2$ is often observed and $n = 4/3$ is the maximum value possible. These equations give a Reynolds number correction to the Kolmogorov "4/5" law showing that it is approached slowly as $R_\lambda \to \infty$. When $C_2 = 2$ and $n = 1.2$ the compensated forms have maxima at $r/\lambda = 1.23$ (for linearly forced turbulence) and $r/\lambda = 1.11$ (for decaying turbulence).

The similarity of these equations can be seen in Figure 1 where they are plotted for $R_\lambda = 350$ and compared with an experiment in a turbulent jet.

1.3. *Normalized decaying turbulence*

Consider (7) again, with and without the isotropic forcing term. In the stationary case with forcing introduce dimensionless variables

$$\mathbf{v} = \mathbf{u}/U, \quad \mathbf{x} = \mathbf{r}/L, \quad \tau = tU/L \tag{20}$$

where U and $L = U^3/\epsilon$ are constants. A simple change of variables gives

$$\frac{\partial \mathbf{v}}{\partial \tau} + \mathbf{v}\cdot\nabla\mathbf{v} = -\nabla P + R_L^{-1}\nabla^2\mathbf{u} + \frac{1}{3}\mathbf{v} \ . \tag{21}$$

Now consider the case without the forcing term, with the change of variables

$$\mathbf{v} = \mathbf{u}/U(t), \quad \mathbf{x} = \mathbf{r}/L(t), \quad \tau = \int_0^t U/L \, dt \tag{22}$$

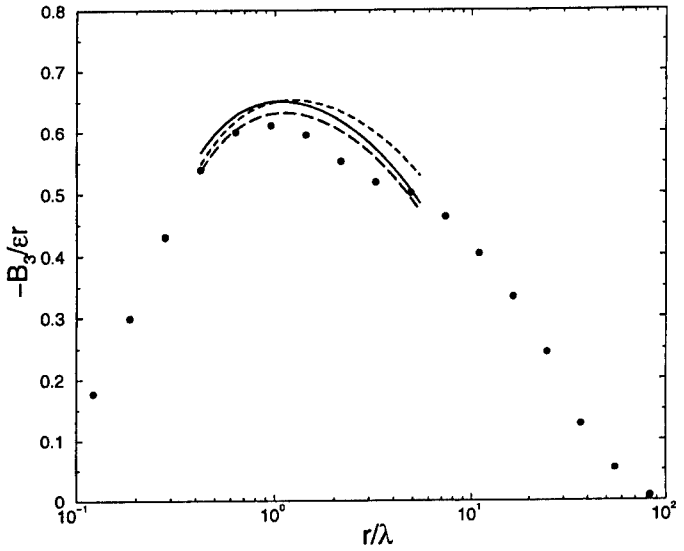


Figure 1. Compensated third order structure function vs. r/λ at $R_\lambda = 350$. The data points are from a laboratory jet (Gagne, 2002) at the same value of R_λ. The long dashed curve is from (19). The dashed curve is the linear forcing result from (18). The solid line is from the computation of section 2 using the $R_\lambda^{-2/3}$ scaling law to extrapolate from $R_\lambda = 170$ to $R_\lambda = 350$.

The equation transforms to

$$\frac{\partial \mathbf{v}}{\partial \tau} + \mathbf{v}\cdot\nabla\mathbf{v} = -\nabla P + R_L^{-1}\nabla^2\mathbf{v} - \frac{L\dot{U}}{U^2}\mathbf{v} + \frac{\dot{L}}{U}\mathbf{x}\cdot\nabla\mathbf{v}. \tag{23}$$

Using $\epsilon = -\frac{3}{2}\frac{dU^2}{dt}$ and $L = U^3/\epsilon$ the coefficient of $\mathbf{v}$ is $-\frac{1}{3}$, so

$$\frac{\partial \mathbf{v}}{\partial \tau} + \mathbf{v}\cdot\nabla\mathbf{v} = -\nabla P + R_L^{-1}\nabla^2\mathbf{v} + \frac{1}{3}\mathbf{v} \quad + \frac{\dot{L}}{U}\mathbf{x}\cdot\nabla\mathbf{v}\ . \tag{24}$$

While this is not exactly the same as (21) because of the last term, it is apparent that energy decay has the effect of an isotropic forcing term. Note also that if $U^2 \propto t^{-n}$ then $\epsilon \propto t^{-n-1}$ and $L = U^3/\epsilon \propto t^{1-n/2}$. So $\dot{L}$ would be zero if $n = 2$. In this case the equations would be the same except for the time dependence of R_L.

1.4. *Comparison with low wavenumber forcing*

In this subsection a more general forcing function is applied to the Karman-Howarth equation in order to show that the forcing range has a significant effect on the third order compensated structure function and presumably on any inertial range statistics. This analysis is carried out in detail in Appendix I and only summarized here. A Gaussian filter is applied to the velocity field, filtering out a variable part of the high wavenumber content. This filtered velocity is used as a forcing function for the Karman-Howarth equation. In one limit there is uniform linear forcing. The results of a calculation are shown in Figure 2a for different values of KL. Here K is the width of the filter; wavenumbers greater than K are filtered out. When K is small only low wavenumbers are forced, while if $K \to \infty$ forcing is uniform over all wavenumbers. The figure shows the compensated

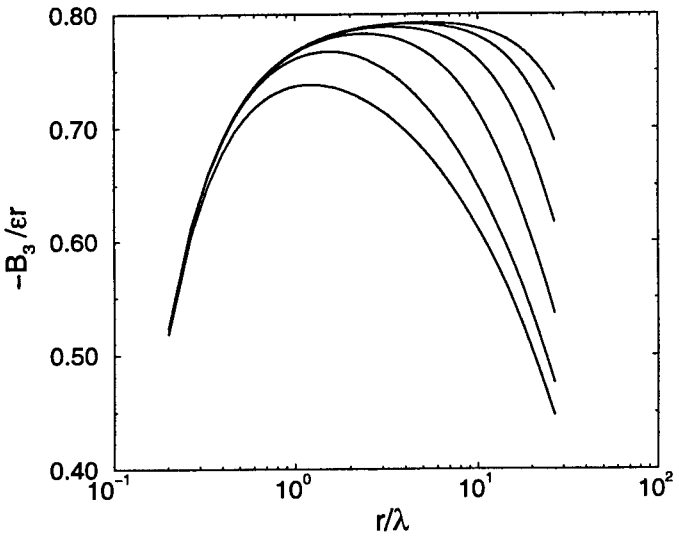


Figure 2a. Third order compensated structure functions for variations of the forcing range computed from (A17). The curves are (from the bottom) for $KL = 1000, 100, 25, 10, 5, 3$. The lowest curve ($KL = 1000$) is close to the linear forcing result from (18). All the curves are computed for $R_\lambda = 1000$.

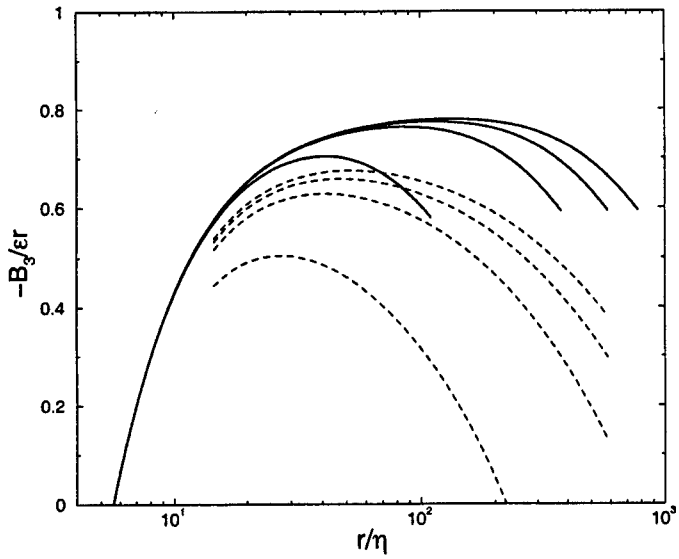


Figure 2b. Solid curves, third order compensated structure function vs. r/η for $KL = 5$ and $R_\lambda = 125, 284, 381, 460$ from the bottom up. This compares with the low wavenumber forced computation of Gotoh et. al. (2002) at the same Reynolds numbers (compare their Fig.12). The maximum values shift to the right and increase with increasing R_λ in a similar manner. The maxima are .70, .76, .77, .78 comparing with .66, .77, .78, .76 from Gotoh. The dashed curves are for linear forcing at the same values of R_λ from (18) showing the differences.

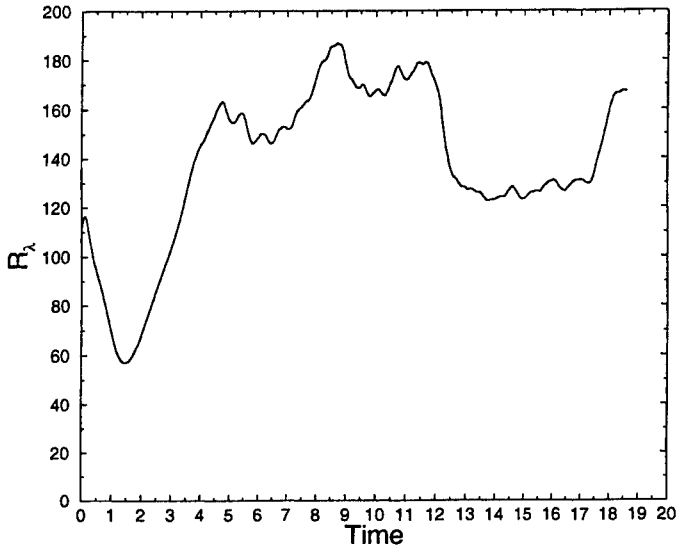


Figure 3. Time History of R_λ with linear forcing. Numerical data for the following figures was taken over a time range of about .5 near T=10, where $R_\lambda = 170$.

third order structure function for different values of KL for $R_\lambda = 1000$. When $KL = 1000$ the curve is nearly the same as computed from (18). As KL decreases the maximum value moves to the right and increases towards 4/5, greatly distorting the structure function in the inertial range.

Figure 2b shows compensated structure functions for several values of R_λ for the single value $KL = 5$. This was constructed in order to compare with the high resolution DNS of Gotoh et. al. (2002), which was driven by white noise in a low wavenumber band which corresponds roughly to a Gaussian filter with width $KL = 5$. (In their numerics at $R_\lambda = 460$ $L \sim 2.5$, making $K = 2$ which is in approximate accord with their forcing range of $1 < k < \sqrt{6}$.)

2. Pseudospectral Computation with Linear Forcing

Computations have been carried out with a Rogallo/Wray pseudospectral code, modified slightly to accomodate linear forcing. This was done with $(256)^3$ resolution with $\nu = .003$, box size 2π on a side, and time scale set by taking $Q = 1$. Figure 3 shows the time history of R_λ during a lengthy run. As can be seen the computation is not exactly stationary (but should be statistically stationary after an initial transient). The instantaneous value of $\epsilon/3U^2$ (not shown here) fluctuates about unity by about $\pm 20\%$. There are fairly stationary periods, however. Data for the following figures was taken in a relatively stationary period near $T = 10$ where $R_\lambda = 170$.

Figure 4 shows the energy spectrum versus $k\eta$. The spectrum is a little shallower than $k^{-5/3}$ (the upper straight line on the figure). Mydlarski and Warhaft (1996) indicate approximately $k^{-1.45}$ at this Reynolds number for grid flow turbulence.

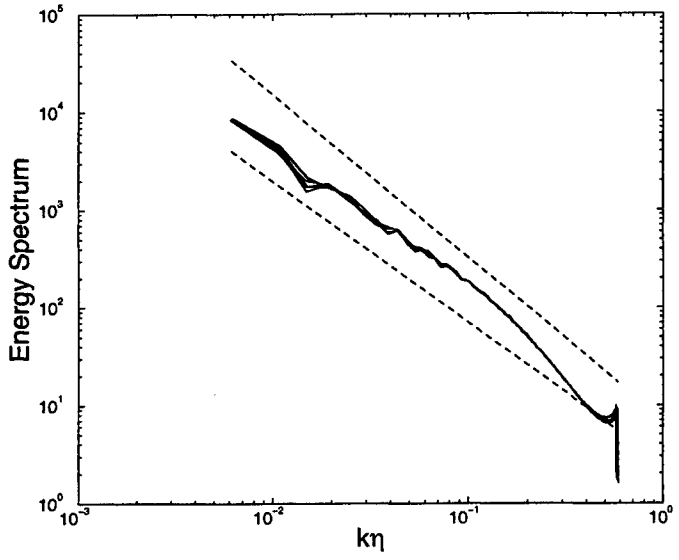


Figure 4. Energy spectrum in Kolmogorov variables for $R_\lambda = 170$. The upper straight line is $k^{-5/3}$ and the lower one is $k^{-1.45}$.

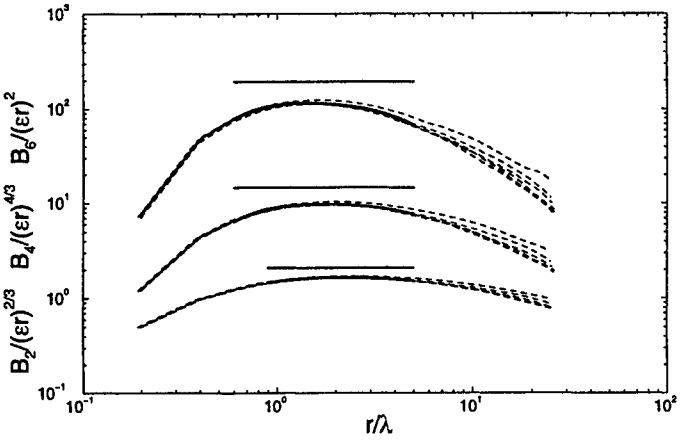


Figure 5. Compensated even order structure functions versus r/λ for $R_\lambda = 170$. Solid lines are curve fit using (25). The solid straight lines are an extrapolation to $R_\lambda = \infty$ using V_2, V_4, V_6.

In Figure 5 compensated structure functions of second, fourth, and sixth order are plotted versus r/λ. The minimum separation between two points $(2\pi/256)$ is very nearly $.2\lambda$. The output was taken by averaging over all pairs of points along the x direction with separation r (which is a multiple of $.2\lambda$). For each structure function there are six curves (the lighter long-dashed curves on the figure), one each for times separated by 1000 time steps. The total elapsed time for 5000 time steps is about .5 time units on Figure 3. The spread of these curves indicates the random nature of the output even after the spatial averaging.

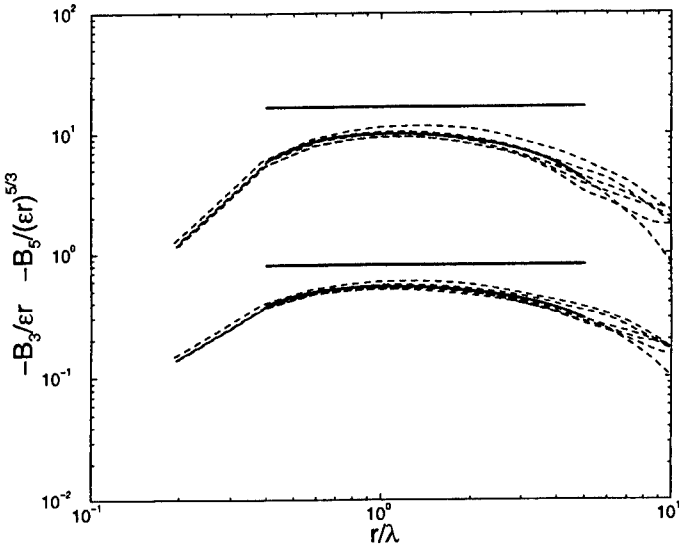


Figure 6. Odd order compensated structure functions for $R_\lambda = 170$. Curve fit same as in Figure 5.

The *pth* order compensated structure function should take the form (Lundgren 2003)

$$B_p/(\epsilon r)^{p/3} = V_p\Big(1 - R_\lambda^{-2/3}\big(A_p(r/\lambda)^{2/3} + B_p(r/\lambda)^{-4/3}\big)\Big) \quad . \tag{25}$$

This gives Reynolds number corrections to Kolmogorov (1941) theory and can be regarded as a scaling law. If the parameters V_p, A_p, B_p were determined for some Reynolds number (numerically or by experiment) one could extrapolate the data to another Reynolds number. The coefficients for $p = 2, 3, 4, 5, 6$ were determined as follows. The six time sets were truncated to about $.5 < r/\lambda < 5$ in order to get the upper parts of the sets, roughly centered about the maxima. These were accumulated into into a single set, which looks like a lot of scattered experimental points. Then using a nonlinear curve fitting algorithm (on xmgr) the coefficients V_p, A_p, B_p were determined for $R_\lambda = 170$ ($R_\lambda^{-2/3} = .033$). The values are shown in the table below.

p	V_p	A_p	B_p	$(r/\lambda)_{\max}$	$V_p/p!$
2	2.11	2.62	6.15	2.17	1.05
3	−.824	6.56	3.75	1.07	−.137
4	15.24	4.85	7.65	1.78	.635
5	−16.91	7.81	4.53	1.08	−.141
6	197.5	6.56	6.87	1.45	.274

Table 1. Coefficients for (25). Fifth column is position of maximum of $B_3/\epsilon r$. Sixth column compares V_p with $p!$.

The fit curves are shown as heavy lines which approximate the data fairly well. These should be thought of as time averages of the six curves of each set. The horizontal straight lines above each set are the curves $B_p/(\epsilon r)^{p/3} = V_p$, representing an extrapolation to

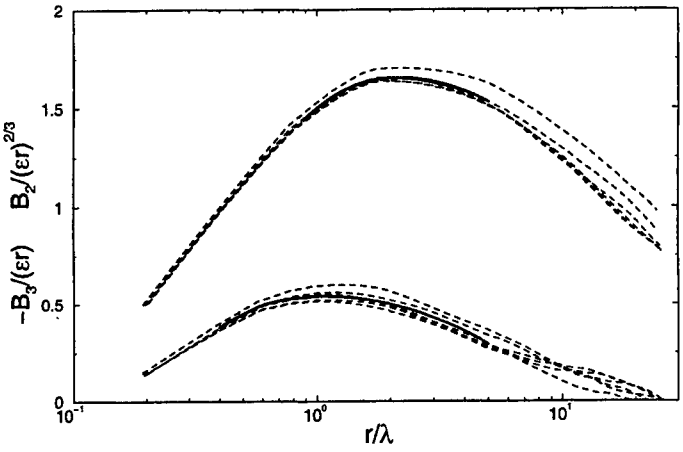


Figure 7. Second and third order structure functions repeated from figures 5 and 6 on a semilog plot in order to better show the nature of the curve fit.

$R_\lambda = \infty$. In particular note that the horizontal line above the second order stucture function, $V_2 = 2.11$, is an acceptable value for that asymptote.

The third and fifth order structure functions were treated in the same way and shown in Figure 6. The individual sets show much more scatter than the even order structure functions because of cancellation between the left and right sides of the almost symmetric pdfs. Note the value $V_3 = .824$. This should be exactly .8, the Kolmogorov "4/5" law. Figure 7 repeats the B_2 and B_3 curves from Figures 5 and 6 on a semilog plot.

The maxima of the compensated structure functions have positions which scale with λ. For even orders the positions shift towards smaller values with increasing order. For odd orders there is not much shift. The rapid increase of the magnitude of the even orders with increasing order required that they be presented on a log-log plot in order to show them on the same figure. A rapid increase of moments like $p!$, as seen in the table, is a signature for exponential tails on the pdf. This is observed approximately in Figure 8.

An example of extrapolation for the third order structure function is shown in Figure 1, where the curve fit values of V_3, A_3, B_3 are used to extrapolate to $R_\lambda = 350$ ($R_\lambda^{-2/3} = .020$).

Figure 8 is the final figure. This shows the velocity pdf versus v/σ where v is the velocity difference between two points along the x direction and σ is the standard deviation, $\sigma =< v^2 >^{1/2}$. In these variables the average and the second moment are both unity. The outermost curve is as close to the pdf of the velocity derivative as can be reached with this resolution. The fluctuations in the tails were ameliorated to some extent by accumulating the pdfs over 10 successive time steps (in addition to spatial averaging).

3. Conclusions

There were two objectives to this research. The first was to show that it is desirable and useful to compute stationary isotropic turbulence with a forcing function which is a simple linear function of velocity, which thus forces uniformly at all wavenumbers. This was done by analysis of of a forced Karman-Howarth equation, which allows calculation of third order structure functions in terms of second order structure functions. This allowed a

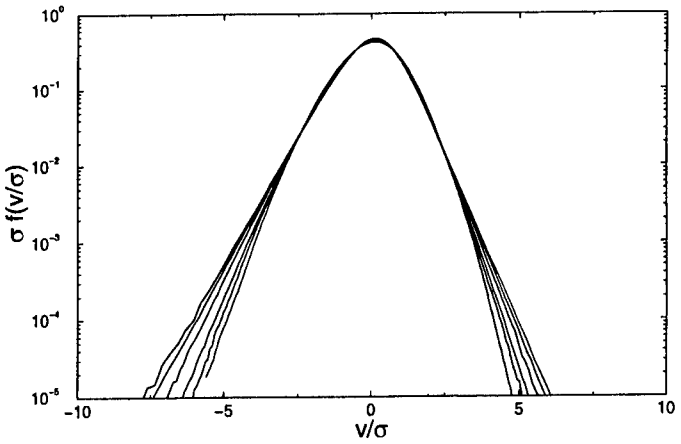


Figure 8. pdf of velocity difference vs. $v/\sigma, \sigma =< v^2 >^{1/2}$ The curves are for values of the separation. From the outside $r/\lambda = 2., .4, .6, 1.0, 1.4, 2.0, 2.4$

favorable comparison between decaying isotropic turbulence and linearly forced isotropic turbulence in subsection 1.2.

By applying filtered linear forcing to the Karman-Howarth equation it was shown that forcing at low wavenumber has a large effect on third-order structure functions, and would very likely influence all inertial range statistics, in partcular it could affect the computation of anomalous exponents. The third order structure function with low wavenumber filtered forcing was compared with high quality DNS (Gotoh et. al., 2002) and linear forcing was compared with experiments of Gagne (2002). The differences between low wave number forcing and linear forcing were considerable, as seen in Figure 2b, with low wavenumber forcing approaching the four-fifths law too rapidly with increasing Reynolds number.

The second objective was to compute a moderate resolution DNS of box turbulence with linear forcing to show the feasibility of such a computation. This was done in section 2. Compensated structure functions of second through sixth order were computed at $R_\lambda = 170$. It was shown that these could be fit with an $R_\lambda^{-2/3}$ scaling law, determining the coefficients to fit equation (25). (The analysis which produced this law (Lundgren 2003) applies equally to the forced Navier-Stokes equation.) The usefulness of the scaling law was demonstrated in Figure 1, where the third-order structure function computed at $R_\lambda = 170$ was extrapolated to $R_\lambda = 350$ (the solid curve in Figure 8 was extrapolated to the solid curve in Figure 1), where it compares with the Karman-Howarth results and with experiment.

4. ACKNOWLEDGEMENTS

The author would like to thank Bob Rogallo and Alan Wray for the use of their pseudospectral code, and Alan Wray and Nagi Mansour for help with the code and for helpful discussions during the work. Dale Pullin provided some much appreciated early encouragement.

5. Appendix I. Filtered Forcing.

With a general forcing term, the integrated Karman-Howarth equation is

$$B_3 = 6\nu\frac{dB_2}{dr} - \frac{4}{5}\epsilon r - \frac{6}{r^4}\int_0^r rdr\int_0^r < \mathbf{u}_2\cdot\mathbf{f}_1 + \mathbf{u}_1\cdot\mathbf{f}_2 > r^2dr \quad . \tag{A1}$$

It is desired to develop a general case which includes forcing at small wavenumbers and also broader forcing. A simple model takes the forcing function proportional to the velocity, but with a variable part of the high wavenumber end filtered out with a Gaussian filter. A filtered velocity in Fourier space may be written

$$\tilde{\mathbf{u}}^<(\mathbf{k}) = \tilde{g}_K(k)\tilde{\mathbf{u}}(\mathbf{k}) \tag{A2}$$

where the filter and its transform are

$$g_K(x) = \int \exp(i\mathbf{k}\cdot\mathbf{x})\tilde{g}_K(k)d\mathbf{k} \tag{A3}$$

$$\tilde{g}_K(k) = \frac{1}{(2\pi)^3}\int \exp(-i\mathbf{k}\cdot\mathbf{x})g_K(x)d\mathbf{x} \tag{A4}$$

It is assumed that $\tilde{g}_K(0) = 1$ so that

$$\int g_K(x)d\mathbf{x} = (2\pi)^3 \quad . \tag{A5}$$

For a Gaussian filter

$$\tilde{g}_K = \exp(-.5k^2/K^2) \quad . \tag{A6}$$

This filters out wavenumbers $k > K$ for $0 < K < \infty$; $K = \infty$ is the uniform forcing case. The transform of $\tilde{g}_K$ is

$$g_K(x) = (2\pi)^{3/2}K^3\exp(-K^2x^2/2) \quad . \tag{A7}$$

In general the filtered physical space velocity is given by a convolution:

$$\mathbf{u}^<(\tilde{\mathbf{x}}) = \frac{1}{(2\pi)^3}\int g_K(|\mathbf{x}-\mathbf{s}|)\mathbf{u}(\mathbf{s})d\mathbf{s} \quad . \tag{A8}$$

The forcing function will be assumed to be $\mathbf{f} = Q\tilde{\mathbf{u}}^<$, where, since $\epsilon = < \mathbf{u}\cdot\mathbf{f} >$

$$Q = \epsilon / < \mathbf{u}\cdot\tilde{\mathbf{u}}^< > \quad . \tag{A9}$$

From (A8)

$$< \mathbf{u}\cdot\mathbf{u}^< >= \frac{1}{(2\pi)^3}\int g_K(|\mathbf{x}-\mathbf{s}|) < \mathbf{u}(\mathbf{s})\cdot\mathbf{u}(\mathbf{x}) > d\mathbf{s} \tag{A10}$$

where

$$< \mathbf{u}(\mathbf{s})\cdot\mathbf{u}(\mathbf{x}) >= R_{ii}(|\mathbf{x}-\mathbf{s}|) \tag{A11}$$

is the trace of the correlation function given by (10). By using (A9) and (A10) the force correlation in (A1) may be written

$$< \mathbf{u}_2\cdot\mathbf{f}_1 + \mathbf{u}_1\cdot\mathbf{f}_2 >= 2\epsilon\frac{\int g_K(|\mathbf{x}-\mathbf{s}|)R_{ii}(s)d\mathbf{s}}{\int g_K(s)R_{ii}(s)d\mathbf{s}} \quad . \tag{A12}$$

Substituting this into (A1) gives

$$B_3 = 6\nu\frac{dB_2}{dr} -$$

$$\frac{\frac{4}{5}\epsilon r(2\pi)^3 3U^2 + \frac{12\epsilon}{r^4}\int_0^r rdr\int_0^r r^2dr\int g_K(|\mathbf{s}-\mathbf{r}|)(-\frac{1}{2}\frac{1}{s^2}\frac{d}{ds}s^3B_2(s))ds}{(2\pi)^3 3U^2 + \int g_K(s)(-\frac{1}{2}\frac{1}{s^2}\frac{d}{ds}s^3B_2(s))ds} \tag{A13}$$

where the integration over the $3U^2$ part of R_{ii} was done using (A5) and $\int_0^r rdr\int_0^r r^2dr = r^5/15$. In the upper integral do the integration over the angle variables with the Gaussian filter, obtaining

$$\int g_K(|\mathbf{s}-\mathbf{r}|)\sin(\theta)d\theta d\phi = (2\pi)^{5/2}KB(s,r) \tag{A14}$$

where

$$B(s,r) = \left(\frac{(\exp(-.5K^2(s-r)^2) - \exp(-.5K^2(s+r)^2))}{sr}\right) \tag{A15}$$

is a temporary notation. Now do the integration by parts on s, which shifts the differentiation onto $B(s,r)$. The following identity may be proved

$$\frac{\partial B(s,r)}{\partial s} = \frac{1}{K^2s^2r^2}\frac{\partial A(s,r)}{\partial r} \tag{A16}$$

where

$$A(s,r) = (1-K^2sr)\exp(-.5K^2(s-r)^2) - (1+K^2sr)\exp(-.5K^2(s+r)^2) \ .$$

Because of the $1/r^2$ factor in (A16) the inner $\int r^2dr$ may be carried out, resulting in the near-final form

$$\frac{B_3}{\epsilon r} = \frac{6L^2}{R_L}\frac{db_2}{dr} - \frac{\frac{4}{5} + (2\pi)^{-1/2}K^{-1}\frac{2}{r^5}\int_0^r rdr\int_0^\infty A(s,r)b_2(s)sds}{1-(2\pi)^{-1/2}K^5\frac{1}{3}\int_0^\infty \exp(-.5K^2s^2)b_2(s)s^4ds} \tag{A17}$$

where $b_2 = B_2/U^2$. The double integrals have to be integrated numerically with an assumed function for B_2. An appropriate form is

$$B_2 = 2U^2\tanh(.5C_2(r/L)^{2/3}) \tag{A18}$$

which gives the Kolmogorov two-thirds law for small r/L and tends to the proper limit $2U^2$ as $r/L \to \infty$.

REFERENCES

GAGNE, Y. 2002 Private communication. The data were reported in the Ph.D. Thesis of Yann Malecot (1998, U. Grenoble).

GOTOH, T., FUKAYAMA, D.& NAKANO, T. 2002 Velocity field statistics in homogeneous steady turbulence obtained using a high resolution direct numerical simulation. *Phys. Fluids* **14**, 1065–1081.

VON KARMAN, T. & HOWARTH, L. 1938 On the statistical theory of isotropic turbulence, *Proc. Roy. Soc. Lond.* A **164**, 192–215.

KOLMOGOROV, A. N. 1941 The local structure of turbulence in incompressible viscous fluid for very large Reynolds numbers, *Dokl. Akad. Nauk.*, SSSR **30**, 299-303. Reprinted in *Proc. Roy. Soc. London* A **434**, 9-13 (1991).

LANDAU, L. D. & LIFSHITZ, E. M. 1959 *Fluid Mechanics* Pergamon, London.

LINDBORG, E. 1999 Correction to the four-fifths law due to variations of the dissipation, *Phys. Fluids* **11**, 510–512.

LUNDGREN, T. S. 2002 Kolmogorov two-thirds law by matched asymptotic expansion, *Phys. Fluids*, **14**, 638-642.

LUNDGREN, T. S. 2003 Kolmogorov turbulence by matched asymptotic expansion. *Phys. Fluids*, **15**, 1074–1081.

MYDLARSKI, L. & WARHAFT, Z. 1996 On the onset of high-Reynolds-number grid-generated wind tunnel turbulence. *J. Fluid Mech.*, **320**, 331–368.

Transition in hypersonic flows including high-temperature gas effects

By Christian Stemmer †

1. Motivation and Objective

Hypersonic transition poses a special challenge for direct numerical simulations. Comparable data from Wind-tunnel tests or free-flight testing are not available or not accurate enough for comparison. The wind-tunnel testing does not allow for the exact match to the free-flight conditions at such high Mach-numbers.

Flat-plate boundary-layer transition at high Mach-numbers is investigated in this work. A simulation case was chosen where chemical non-equilibrium plays an important role but ionization can be neglected. The chosen case at an altitude of H=50Km lies close to one point on the descent path of the Space Shuttle. The failure of the Space Shuttle has shown that an improved vehicle for space transportation is imperative in the close future. Transition research for an improved space-transportation vehicle is crucial in order to estimate the heat load during re-entry.

2. Numerical Method

A sixth-order accurate numerical method (Adams & Shariff 1996; Adams 1998, 2000) is extended to incorporate chemical source terms and a conservation equation for the vibrational temperature (Stemmer & Mansour 2001). This is necessary for the simulation of chemical non-equilibrium which is present in the investigated regime.

Compact finite differences are employed and the grid is stretched in the wall-normal direction. Periodic conditions in the spanwise direction are enforced. A third-order accurate Runge-Kutta method is used for the advancement in time. Shocks can be treated separately through a hybrid ENO method, which is applied only in the areas where shocks are present.

For the presented simulation, a resolution of $1500 \times 240 \times 6$ points in x, y and z-direction was used. This yields a resolution of $\Delta x = 0.066$, $\Delta y_{min} = 7.717 \cdot 10^{-3}$ and $\Delta z = 0.146$, where the lengths are made dimensionless with the boundary-layer thickness $\delta_1 = 0.2197$m.

3. Results

A comparison for the steady base-flow results for three different cases is presented. Firstly, the **ideal-gas** case is considered. The second case considers **chemical equilibrium** and at last, the **chemical non-equilibrium** case is calculated.

The most notable difference for the three steady flows is in the temperature which is shown in the following graphs. The wall-normal profiles of the five chemical species are also shown.

† Current Address: Institut für Strömungsmechanik, Technische Universität Dresden, George-Bähr-Str. 3c, 01069 Dresden, Germany

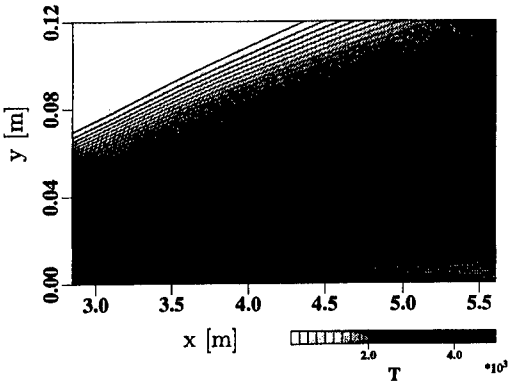


FIGURE 1. Ideal gas case; temperature in the M=20 boundary layer; contours in intervals of 200K from 200-5000K

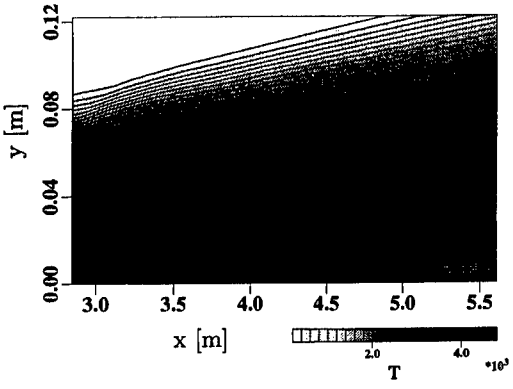


FIGURE 2. Chemical equilibrium case: temperature in the M=20 boundary layer; contours in intervals of 200K from 200-5000K

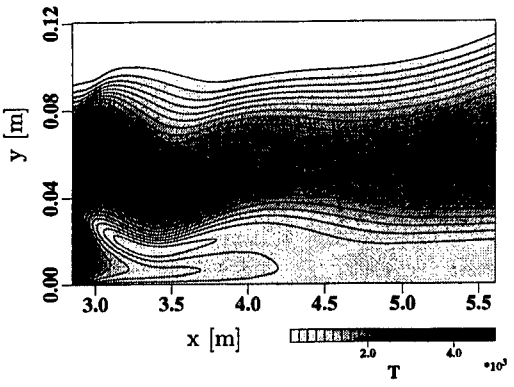


FIGURE 3. Chemical non-equilibrium case; temperature in the M=20 boundary layer; contours in intervals of 200K from 200-5000K

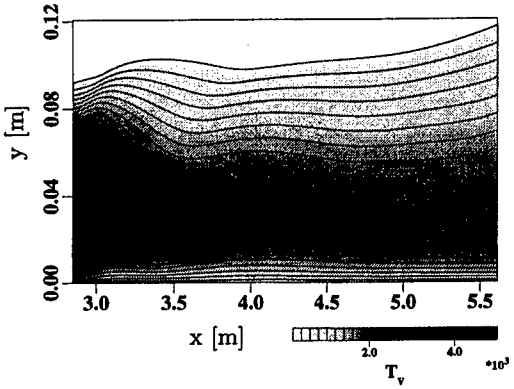


FIGURE 4. Chemical non-equilibrium case: vibrational temperature in the M=20 boundary layer; contours in intervals of 200K from 200-5000K

For the ideal-gas case (Fig.1), the similarity solution given at the inflow (Re=1.13 $\times$ 10^6) exhibits a maximum temperature of T=4773.2K at y=0.033m away from the wall. This temperature is approximately retained in the growing boundary layer.

For the chemical equilibrium case (Fig.2), after a short accommodation effect downstream of the similarity solution inflow, shows a maximum temperature of T=4478K for a given downstream location of x=5.0m at a wall-normal distance of y=0.047m. This constitutes a decrease in temperature of Δt=6.2%.

For the chemical non-equilibrium case (Fig.3), the development of the non-equilibrium conditions takes somewhat longer and the maximum temperature drops to T=2028K at y=0.066m at the same downstream location. The vibrational temperature in this case is shown in Fig.4. The vibrational temperature at T=2100K is close to the level of the translational temperature, but the maximum is observable closer to the wall at y=0.042m for the same downstream location.

The wall-normal profiles of the species concentrations for the chemical equilibrium case are shown in Fig.5 and for the non-equilibrium case in Fig.6. In both cases, the concentrations of the species N and NO are multiplied by a factor in order to make them

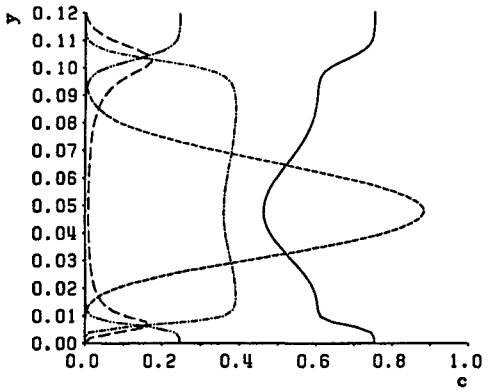


FIGURE 5. Chemical equilibrium case: concentration of chemical species ($c_N \times 5$ ---- ; c_{N2} ——— ; c_O —·— ; c_{O2} —··— ; $c_{NO} \times 10$ — — —)

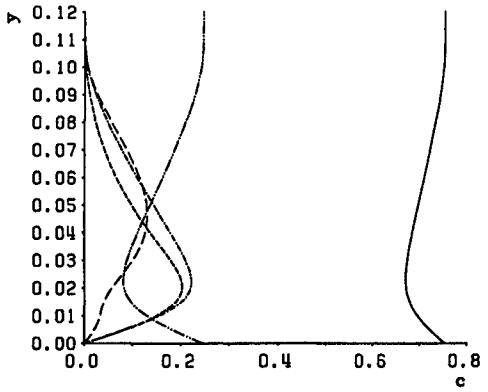


FIGURE 6. Chemical non-equilibrium case: concentration of chemical species ($c_N \times 10$ ---- ; c_{N2} ——— ; c_O —·— ; c_{O2} —··— ; $c_{NO} \times 10$ — — —)

visible in the chosen graph range. In the equilibrium case, the concentrations are a direct function of the temperature distribution as shown in Fig.2. The temperatures are high enough to almost entirely dissociate molecular oxygen inside the boundary layer. Nitrogen is dissociated to a lesser extent and the molecular level remains at almost 50% for the maximum temperature of T=4478K. For the non-equilibrium case, the deviation from the equilibrium state is most noticeable closer to the wall. The maximum dissociation levels are attained at y=0.02m and the maximum level of NO is reached a little further away from the wall at y=0.045m for the same downstream location x=5.0m.

4. Future Work

Normal and oblique mode transition studies for the described Ma=20 flow will be performed. Simulations will be undertaken to provide for chemical and thermal non-equilibrium conditions.

To mimic closer the introduction of disturbances in an experimental environment, a point source disturbance, Stemmer (2001), will be introduced. Therewith, a single frequency but all possible spanwise wave numbers can be excited simultaneously leaving it to the flow to amplify the unstable components of the disturbance.

Laminar-turbulent transition scenarios under varying disturbance conditions will be investigated to understand more about the physical behavior of chemically reacting flows in transition on a flat plate.

Qualitative comparison to the experiments by Mironov & Maslov (2000) will be conducted.

5. Acknowledgments

The author is very thankful for the support from the transition research group in Stuttgart, Germany, for advice and computing time on the NEC SX-series computers. Also, the CFD group at the AME at the University of Arizona was very helpful with numerical issues. Furthermore, the author deeply appreciates the support by Prof. N.A. Adams from the Technical University of Dresden, Germany.

REFERENCES

ADAMS, N. A. AND SHARIFF, K. 1996 A High-Resolution Hybrid Compact-ENO Scheme for Shock-Turbulence Interaction Problems. *J. of Comp. Phys.* **127**, 27-51.

ADAMS, N. A. 1998 Direct Numerical Simulation of Turbulent Compression Ramp Flow *Theor. and Comp. Fl. Dynamics.* **12**, 109-129.

ADAMS, N. A. 2000 Direct Simulation of the Turbulent Boundary Layer Along a Compression Ramp at M=3 and Re_θ=1685. *J. of Fluid. Mech.* **420**, 47-83.

ANDERSON, J. D. 1989 *Hypersonic and and High Temperature Gas Dynamics.* AIAA publication.

BLOTTNER, F. G., JOHNSON, M. & ELLIS, M. 1971 *Chemically Reacting Viscous Flow Program for Multi-Component Gas Mixtures.* SC-RR-70-754, Sandia Natl. Laboratories.

EISSLER, W. 1995 *Numerische Untersuchungen zum laminar-turbulenten Strömungsumschlag in Überschallgrenzschichten.* Dissertation, Universität Stuttgart.

GASTER, M. 1965 A Note on a Relation between Temporally Increasing and Spatially Increasing Disturbances in Hydrodynamic Stability. *J. of Fluid. Mech.* **22**, 222-224.

HIRSCHFELDER, J. O., CURTISS, C. F. & BIRD, R. A. 1964 *Molecular Theory of Gases and Liquids.* Wiley & Sons, New York.

JOHNSON, H. B., SEIPP, T. G. & CANDLER, G. V. 1998 Numerical study of hypersonic reacting boundary layer transition on cones *Physics of Fluids.* Vol. **10**(10), 2676-85.

LEES, L. & LIN, C. C. 1945 *Investigation of the stability of the laminar boundary layer in a compressible fluid.* Tech. Notes Nat. Adv. Comm. Aero. No. 1115, 85 pp.

MIRONOV, S. G. & MASLOV, A. A. 2000 Experimental study of secondary stability in a hypersonic shock layer on a flat plate. *J. of Fluid. Mech.* **412**, 259-277.

MACK, L.M. 1969 *Boundary-Layer Stability Theory.* JPL Report 900-277 Rev. A, Jet Propulsion Laboratory, Pasadena, USA.

PARK, C. 1989 A Review of Reaction Rates in High Temperature Air. *AIAA Paper 89-1740.*

SARMA, G. S. R. 2000 Physico-chemical modeling in hypersonic flow simulation. *Progress in Aerospace Science* **36**, 281-349.

SCHNEIDER, S. P. 1999 Flight data for boundary-layer transition at hypersonic and supersonic speeds. *J. of Spacecraft and Rockets* **36**, 8-20.

STEMMER, C. 2001 *Direct Numerical Simulation of Harmonic Point Source Disturbances in an Airfoil Boundary Layer with Adverse Pressure Gradient.* Dissertation, Universität Stuttgart.

STEMMER, C. & MANSOUR, N.N. 2001 DNS of transition in hypersonic boundary-layer flows including high-temperature gas effects. *Annual Research Briefs 2001* Center for Turbulence Research, Stanford University, NASA Ames, 143-150 .

STEMMER, C. 2002 Flat-Plate Boundary-Layer Hypersonic Transition. *Annual Research Briefs 2002* Center for Turbulence Research, Stanford University, NASA Ames, 389-396 .

STUCKERT, G. K. & REED, H. L. 1991 Unstable branches of a hypersonic, chemically reacting boundary layer. *Boundary Layer Transition and Control*; Proceedings of the Conference, Univ. of Cambridge, UK, Apr. 8-12, 1991, 19.1-19.13.

U.S. Standard Atmosphere, U.S. Government Printing Office, Washington, D.C., 1976.

VINCENTI, W. G. & KRUGER. C. H. 1982 *Introduction to Physical Gas Dynamics.*, Robert E. Krieger Publishing Company, Malabar, FL.

WILKE, S. P. 1950 A Viscosity Equation for Gas Mixtures. *J. of Comp. Phys.* **18**, 517-519.

APPENDIX
Roster

NAME/TERM		AREA OF RESEARCH
POSTDOCTORAL FELLOWS		
BURTON, Dr. Gregory 8/03-present	(Ph.D. Aerospace Engineering, 2003, University of Michigan)	LES based on subgrid-scale physics of turbulent flows
CROOK, Dr. Andrew 1/02-6/03	(Ph.D. Aerospace Engineering, 2001, Univ. of Manchester, UK)	Fluid mechanics of high aspect-ratio sails
DUCHAMP DE LAGENESTE, Dr. Laurent 2/00-4/03	(Ph.D. Fluid Mechanics, 1999, Ecole Centrale de Lyon, France)	LES for premixed combustion
GULLBRAND, Dr. Jessica 1/00-3/03	(Ph.D. Mechanical Engineering, 1999, Lund Institute of Technology, Sweden)	Large eddy simulation
HAM, Dr. Frank 6/02 – present	(Ph.D. Mechanical Engineering, 2001, University of Waterloo, Canada)	LES on unstructured grids & simulation of multiphase flows
HERRMANN, Dr. Marcus 3/02 – present	(Ph.D. Mechanical Engineering, 2001, University of Technology, Aachen, Germany)	Turbulent combustion
HUR, Dr. Jqseph 7/02 – present	(Ph.D. Chemical Engineering, 2001, Stanford)	Biomechanics, Bio-nano-engineering
KIRKPATRICK, Dr. Michael 4/02 – 12/03	(Ph.D. Mechanical Engineering 2001, University of Sydney, Aust.)	Turbulence modeling in LES of clouds
KNAEPEN, Dr. Bernard 7/02 –8/03	(Ph.D. Physics, 1999, University of Brussels, Belgium)	MHD turbulence
LIN, Dr. Hao 8/01-7/03	(Ph.D. Mechanical Engineering, 2001, UC Berkeley)	Protoplanetary disks
MAY, Dr. Phillipe 5/02 – 5/03	(Ph.D. Microsurgery & Biophysics, 2001, University of Paris)	Biological fluid mechanics

NAME/TERM		AREA OF RESEARCH
PAOLI, Roberto 7/03-present	(Ph.D. Aeronautical Engineering 2001, University of Rome)	Cloud physics
RAMAN, Venkatramanan 2/03-present	(Ph.D. Chemical Engineering 2003, Iowa State University)	Turbulent combustion
RIPOLL, Dr. Jean-Francois 1/ 02 – present	(Ph.D. Applied Mathematics, 2001, University of Bordeaux, France)	Radiation modeling
SENOCAK, Inanc 4/03-present	(Ph.D. Aerospace Engineering 2002, University of Florida)	LES of clouds
STEMMER, Dr. Christian 8/01-7/03	(Ph.D. Aerospace Engineering, 2001, Univ.of Stuttgart, Germany)	Hypersonic flows
TALLEY, Dr. Sharon 1/01-4/03	(Ph.D. Biology, 1999, University of Utah)	Biological fluid mechanics
USTYUGOV, Dr. Sergei 11/02-5/03	(Ph.D. Computational Physics, 1999, Keldysh Institute of Applied Math, Russia)	Solar dynamics
YOUNG, Dr. Yuan-Nan 9/02 – present	(Ph.D. Astronomy & Astrophysics, 2000, University of Chicago)	Turbulence in multi-phase flows
SR. RESEARCH ASSOC.		
WANG, Dr. Meng 9/92-present	(Ph.D. Mech. Engr., 1989, University of Colorado)	Aeroacoustics, LES
FATICA, Dr. Massimiliano 10/95-present	(Ph.D. Fluid Mechanics, 1995, Univ. of Rome, Italy)	Parallel computing
RESEARCH ASSOCIATES		
APTE, Sourabh, Dr. 9/00-present	(Ph.D. Engineering, 2000, Pennsylvania State University)	Large eddy simulation of multiphase flows
CONSTANTINESCU, Dr. George 11/99-7/03	(Ph.D. Environmental Eng. 1998 University of Iowa)	LES for complex geometries
DUBIEF, Dr. Yves 5/01-present	(Ph.D. Fluid Mechanics, 2000, Institute National Polytechnique de Grenoble, France)	Polymer drag reduction
IACCARINO, Gianluca 4/98-present	(Masters Aeronautical Engineering, 1994, University of Naples, Italy)	Turbulence modeling
KALITZIN, Dr. Georgi 1/97 – present	(Ph.D. Mechanical Engineering, 1992 University of Magdeburg, Germany)	Turbulence modeling & numerical methods
Wu, Xiaohua 7/03 – present	(Ph.D. Mechanical Engineering, 1993 Manitoba, Canada)	RANS/LES Integration

NAME/TERM		*AREA OF RESEARCH*
SCHLUTER, Dr. Jorg, 10/00-present	(Ph.D. Mechanical Engineering, 2000, CERFACS, France)	RANS/LES integration
SR. VISITING FELLOWS		
ABARZHI, Dr. Snezhana 9/02 - present	Landau Institute for Theoretical Physics, Moscow	Hydrodynamic instabilities and turbulent mixing
DIETRICH, Dr. David 2/03-3/03	Acusea Inc.	Turbulent ocean modeling
FEDOTOV, Dr. Sergei 8/03-9/03	Univ. Manchester Inst. of Science and Technology, U.K.	Turbulent combustion
HE, Dr. Guo-wei 5/1/03-10/30/03	Chinese Academy of Sciences, Institute of Mechanics, China	LES for aeroacoustics
SR. RESEARCH FELLOWS		
JIMENEZ, Prof. Javier 1987-present	University of Madrid, Spain	Wall turbulence
Lundgren, Thomas 1999-present	University of Minnesota	Turbulence & multiphase flows
NAME/TERM		**AREA OF RESEARCH**
GRADUATE STUDENTS		
BHASKARAN, Rathakrishnan 6/02 – 3/03	(Stanford University)	Plasma flow control
VENAYAGAMOORTHY, Karan 1/03-9/03	(Stanford University)	Stratified turbulence
TSENG, Yu-Heng 6/02 – 6/03	(Stanford University)	Numerical modeling of coastal ocean
KELLENERS, Philip 11/02-3/03	(University of Twente)	Multiphase flow

2003 ADVISORY COMMITTEE

Prof. Ron F. Blackwelder (Chair)
University of Southern California

Dr. Joe Adams, VP Eng. Tech.
United Technologies-Pratt & Whitney

Dr. Marvin E. Goldstein, Chief Scientist
NASA Glenn Research Center

Prof. Brian Launder
University of Manchester

Prof.. Sidney Leibovich
Cornell University

Prof. Phillip Marcus
University of California at Berkeley

Dr. Pat Purtell
Office of Naval Research

Prof. Richard A. Matzner,
Center for Relativity, U of Texas at Austin

Dr. Charles Smith
NASA Ames Research Center

Dr. Julian Tishkoff
Air Force Office of Scientific Research

Prof. Forman Williams
University of California, San Diego

Dr. Thomas Beutner (observer)
Air Force Office of Scientific Research

Dr. Julian Hunt
University College – London, England

2003 STEERING COMMITTEE

Prof. Paul A. Durbin
Mechanical Engineering, Stanford University

Prof. Sanjiva K. Lele
Mechanical Engineering Aeoronautics &
Astronautics, Stanford University

Prof. Javier Jiménez
Sr. Research Fellow, Center for Turbulence Research,
Professor, University of Madrid

Dr. Nagi N. Mansour
Deputy Director, Center for Turbulence Research
NASA Ames Research Center

Prof. Parviz Moin
Director, Center for Turbulence Research
Professor, Mechanical Engineering, Stanford.

Prof. Heinz Pitsch
Mechanical Engineering, Stanford University

Prof. William C. Reynolds
Professor, Mechanical Engineering, Stanford.

Dr. Karim Shariff
Research Scientist, NASA Ames Research Center